PHYSICS OF THE SOLID STATE VOLUME 40, NUMBER 11 NOVEMBER 1998

METALS. SUPERCONDUCTORS

Study of the critical current in YBaCuO films under reactor-neutron irradiation in the low-temperature helium circuit in the 25–300 K range

R. F. Konopleva, B. A. Borisov, I. V. Nazarkin, and V. A. Chekanov

B. P. Konstantinov Petersburg Nuclear Physics Institute, 188350 Gatchina, Leningrad Region, Russia

(Submitted April 24, 1998)
Fiz. Tverd. Tela (St. Petersburg) **40**, 1961–1967 (November 1998)

Changes in the temperature and dose dependences of I-V characteristics and of the critical current j_c of YBaCuO films on MgO and $SrTiO_3$ substrates under neutron irradiation has been studied at 25–80 K. The transport properties of YBaCuO films on MgO (M1) and $SrTiO_3$ (S1) substrates were found to behave differently. It is shown that the M1 films have granular structure, and their transport properties were considered within the concept of percolation over weak intergranular links. The S1 are single-crystal films, and their properties are analyzed within a resistive-state theory associated with thermal activation of Abrikosov vortices. It is shown that the degradation rate of the critical temperature T_c of S1 films is 3.5 times smaller than that of the M1 films. The dose dependence of j_c has an exponential character, $j_c = j_c(0)\exp(-k\Phi)$, where k is related to the number of displaced atoms per neutron and is the same for the M1 and S1 films, irrespective of the irradiation temperature. The pinning energy has been derived from the I-V characteristics and it has been found that the U/kT ratio lies within 20–25 and is independent of neutron flux. It is shown that the radiation-induced disorder changes the pinning mechanism, from pinning at the boundaries of misoriented crystals to that at spatial inhomogeneities, apparently radiation induced. © *1998 American Institute of Physics.* [S1063-7834(98)00111-7]

The current-carrying ability and magnetic properties of HTSC materials are known to be governed by interaction of magnetic flux vortices with crystal defects, acting as pinning centers. Introduction of pinning centers to increase the critical current density of HTSC materials is usually done by texturing. At the same time the desired pinning-center concentration can be reached with a high accuracy by irradiating a material with neutrons, protons, or ions. The extended pinning centers formed in this way exceed in dimensions the coherence length ξ and have therefore a strong pinning force, which is capable of affecting the critical current density j_c. The dependence on pinning centers of the current-carrying ability and magnetic properties of HTSC materials permits one to change deliberately the weak link system by irradiating the sample and, in this way, by controlling the degree of disorder in the material through introduction of defects of various types and concentrations, and to study in detail the mechanisms governing the behavior of j_c, and the nature of the high-T_c superconductivity.

The dependence of j_c on temperature and the magnitude and direction of an external magnetic field is presently analyzed by considering the superconductor as consisting of a system of grains weakly linked with one another through Josephson junctions. The onset of resistance in such a system is caused by destruction of the weak links by external magnetic field. The resistive state can form also through thermal decoupling of Abrikosov vortices from the pinning centers and their viscous flow. Therefore in order to learn the mechanisms of formation and development of the resistive state in HTSC materials and the factors responsible for the behavior and magnitude of j_c, one should carry out studies in the conditions where one of the mechanisms is dominant. Such conditions can be realized by investigating j_c and the magnetic properties under irradiation by neutrons at temperatures low enough to reduce the thermally activated processes to a minimum. We use for this purpose the low-temperature helium circuit developed and built[1,2] at the WWR-M reactor at the PNPI RAS. The helium circuit permits one to carry out experiments over a broad range of temperatures (25–300 K) and neutron fluxes (up to 10^{19} cm^{-2}).

1. EXPERIMENTAL TECHNIQUES

The studies of j_c were performed on YBaCuO films prepared by magnetron sputtering on substrates of MgO (M1) and $SrTiO_3$ (S1) with the c axis normal to the substrate.[1] The film thickness $d \sim 0.2\,\mu$m. The I-V characteristics and the temperature dependence of resistance $R(T)$ were measured by the dc four-probe technique on bridges of width $w = 100\,\mu$m and length $l = 2$ mm patterned by photolithography. The contacts were prepared by vacuum deposition of silver or gold on the M1 and S1 films, respectively. The contact resistance did not exceed 0.5 Ω. The M1 films had $T_c = 84$ K, $\Delta T_c \cong 4$ K, $j_c = 10^5$ A/cm^2, and the S1 films, $T_c \cong 91$ K, $\Delta T_c \cong 1$ K, $j_c = 5\times 10^7$ A/cm^2 at 20 K. The films

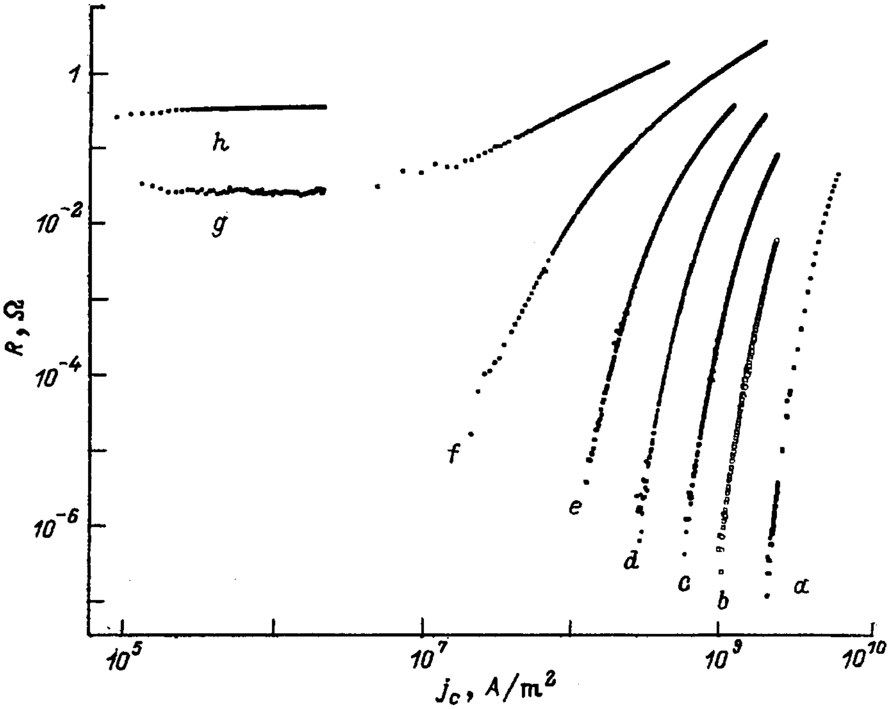

FIG. 1. *I-V* characteristic of an M1 film obtained at different temperatures T(K): *a*—77.1, *b*—77.9, *c*—78.4, *d*—78.9, *e*—79.4, *f*—79.9, *g*—80.4, *h*—80.9.

were studied in the low-temperature helium circuit of the WWR-M reactor of PNPI (Ref. 1) in a fast neutron flux ($E > 0.1$ MeV) $\sim 1\times 10^{13}$ cm^{-2} s^{-1} up to fluxes $\Phi \sim 5\times 10^{18}$ cm^{-2} at temperatures of 25–300 K. The *I-V* characteristics were measured at a temperature maintained to within ±0.1 K. The magnetic field was normal to the film plane (along the *c* axis).

2. EXPERIMENTAL RESULTS AND DISCUSSION

A. Transport properties of irradiated YBaCuO films

1) Films on MgO substrates.

Figure 1 presents $R(j_c)$ plots obtained on unirradiated M1 films at different temperatures. The pattern of the $R(j_c)$ relation suggests that the M1 films are granular, and that their transport properties are governed by weak intergranular links making up a Josephson-junction array. Energy dissipation (and, hence, active resistance) in such a Josephson medium sets in when the currents through the intergranular links exceed their critical values, with the grains themselves remaining superconducting. An analysis of the percolative path through a disordered three-dimensional array of superconductors with different local critical currents characterizing the intergranular weak links (made under the assumption of their uniform distribution) yielded the following expression for the *I-V* characteristic in the case of low voltages^{3,4}

$$V \cong (j - j_c)^n, \qquad (1)$$

where j is the current density, and exponent $n > 1$ depends on the dimension of the system and the type of the weak links, as well as on the temperature and external magnetic field. As the temperature and magnetic field increase, parameter n decreases and approaches the Ohmic value $n \cong 1$. A similar expression for the *I-V* characteristic in the vicinity of j_c was obtained also by computer simulation.^{5} *I-V* characteristics described by Eq. (1) were observed experimentally in both ceramic HTSC samples^6 and in granular films,^{7} with parameter n varying within a broad range $1 < n < 4$. Fitting Eq. (1) to the *I-V* characteristic of an unirradiated M1 film showed that this relation approximates the initial portions of the characteristic fairly well. The temperature dependences of j_c and of parameter n obtained from a fit of Eq. (1) are shown in Fig. 2. Exponent n, which was found to be somewhat larger (~ 7) than those quoted in other papers,^{6,7} decreases as one approaches T_c.

It is known that the temperature dependence of the criti-

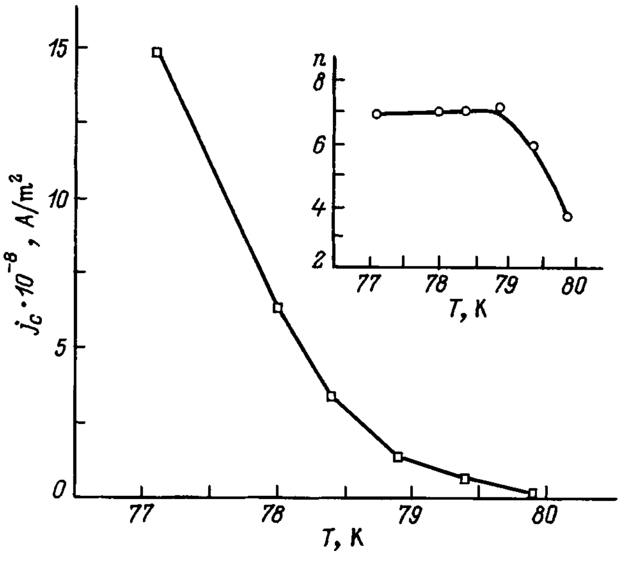

FIG. 2. Temperature dependence of critical-current density and exponent n (in the inset) in Eq. (1) for an M1 film. j_c was derived from a fit of the $I-V$ curve to Eq. (1).

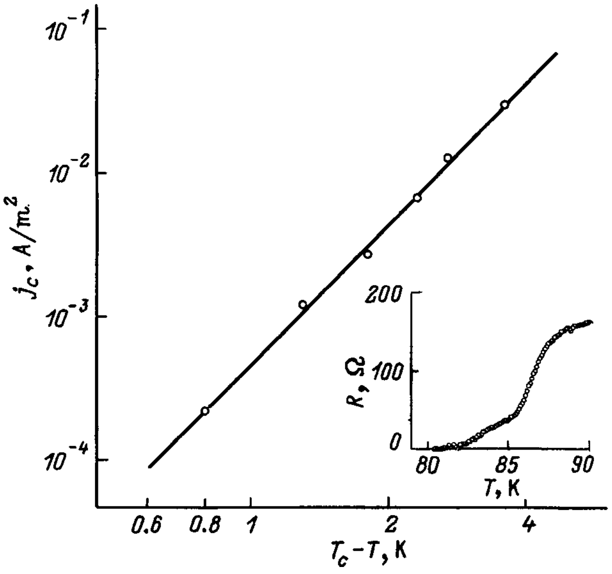

FIG. 3. Temperature dependence of critical-current density of an unirradiated M1 film (plotted to test Eq. (2)); $x=3.3, T_c=80.7$ K. Inset: $R\,(T)$ relation in the region of the transition.

cal current in a Josephson-junction system can be described by a relation of the type

$$j_c \cong (T_c - T)^x . \tag{2}$$

Parameter x is governed by the actual weak-link type (S–I–S, S–N–S, S–N–I–N–S). For instance, Ambegaokar-Baratoff theory[8] yields $x=1$ for a S–I–S contact system. For an S–N–S–type system a relation similar to (2) with $x=2$ was obtained.[9] In most experiments, relation (2) is found to describe appropriately the temperature dependence of the critical current in YBaCuO systems. At the same time some of the quoted figures for x, e.g. $x \cong 3.5$ (Ref. 10), are in excess of the values predicted by theory for S–I–S, S–N–S, S–N–I–N–S–type contacts, which may be due to a more complex structure of the intergranular links not included in theoretical models (for example, an asymmetry between N–I–N layers). In our case the temperature dependence of the critical current for the M1 film (Fig. 3) is likewise fitted well by relation (2), but at the same time the value $x=3.3$ exceeds those predicted by the above models. The critical temperature T_c calculated from Eq. (2) agrees well with the zero-resistance temperature in the $R\,(T)$ relation (see inset to Fig. 3).

2) Films on $SrTiO_3$ *substrates.*

In contrast to M1 films, the I-V curves of unirradiated S1 films exhibit for $I > 0.5$ A a switching effect within a broad temperature interval, which suggests that these films are single crystal. The mechanism of destruction of superconductivity in such single-crystal systems by current is related to the onset of kinetic depairing at film edges,[11] and the critical current itself, to the beginning of vortex flow. Estimation of the physical limit for j_c determined by the condition of the depairing current density at the film edge reaching the level $J\,(w/2) = \Phi_0\,(3\sqrt{3}\,\pi\mu_0\lambda^2\xi)$, taking into account the relation[12] $J\,(w/2) = I\,(2\pi\lambda^2 wd)$ (where Φ_0 is the magnetic flux quantum, λ is the field penetration depth, and ξ is the coherence length), yields $j_c \approx 3\times10^7$ A/cm^2 for $w=100\,\mu$m, $d=0.2\,\mu$m, $\lambda=10^3$ Å, and $\xi=20$ Å, which agrees in order of magnitude with experimental data. The values of j_c and $J\,(w/2)$ thus obtained permit one actually to relate the mechanism of destruction by a superconductivity current in grains to the onset of kinetic depairing at the film edge.[11] All this made possible application to the analysis of I-V characteristics of single-crystal films S1 the continuous-medium model,[13] which attributes the resistive state to thermal decoupling of Abrikosov vortices. Within this model, the field induced by a vortex pinned at a center is written

$$E \sim \tau^{-1} = \omega_0 \exp[-(U - \alpha j)/kT] , \tag{3}$$

where τ^{-1} is the time a vortex remains pinned at the center, ω_0 is the characteristic vibrational frequency of flux lines, U is the pinning activation energy, and αj is the work done by the vortex acted upon by the Lorentz force at a current density j. In a general case, one has to consider a more detailed I-V model including a crossover from occasional depinnings of the vortex to its practically free flow under the action of the Lorentz force. Taking into account the possibility of vortex repinning by the center, we obtain for the I-V characteristic[14]

$$E = B\nu \left[1 + \left(\frac{\nu}{\omega_0 \lambda} \right) \frac{\exp(U/kT)}{\exp(\alpha j/kT)} - \exp(-\alpha j/kT) \right]^{-1} , \tag{4}$$

where ν is the vortex velocity, and $B = \mu_0 H$ is the external magnetic field, which is assumed to penetrate throughout the film. In the limit where the vortex pinning time τ exceeds the drift time τ_a ($\tau_a \ll \tau$), and for not too weak currents ($j \gg kT/\alpha$), the I-V characteristics follow an exponential behavior[12]

$$E = B\omega_0 \lambda \exp[-(U - \alpha j)/kT] = B\nu_c , \tag{5}$$

where ν_c is the flux creep velocity. The quantities U and α in Eq. (5) do not depend on B. In applying Eq. (5) to description of the I-V characteristic we assume the existence of magnetic fields weak enough to justify neglect of cooperative effects and consideration of a single vortex. This implies that the critical current practically does not vary with the field, and argues for the validity of the independent-vortex approximation. In this region of magnetic fields, the I-V curves are described by an exponential relation of the type $V \propto \exp(j_c/j_1)$, where parameter j_1 is field independent. For fields $B > 80$ mT, the I-V characteristics are no longer exponential.

In our experiment, the $j_c\,(B)$ relations were found to be well approximated by the classical relation

$$j_c(B) = j_c(0)(1 + B/B_0)^{-1} . \tag{6}$$

The inset to Fig. 4 plots the temperature dependence of U/kT derived from a fit of Eq. (5) to the I-V characteristic (for $U/kT \gg 1$). The value $U/kT \approx 25$ thus found is in agreement with the estimate $15 < U/kT < 50$ quoted in Ref. 14. The temperature behavior of j_c (determined by a 1 μV/mm criterion) and $j_1 = kT/\alpha$ (Fig. 4) are in accord with Eq. (2). A relation of type (2) can fit a variety of pinning mechanisms.

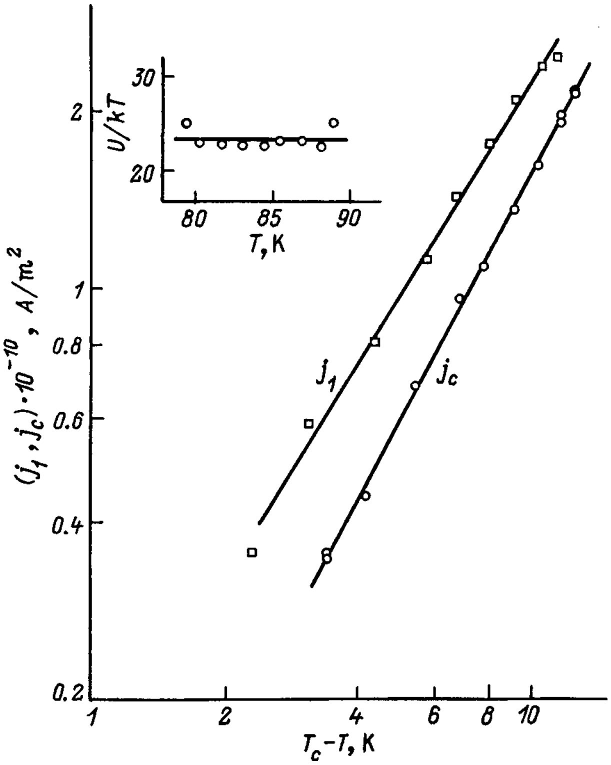

FIG. 4. Temperature dependence of j_c and j_1 for an unirradiated S1 film. Inset: temperature dependence of U/kT. $B=50$ mT.

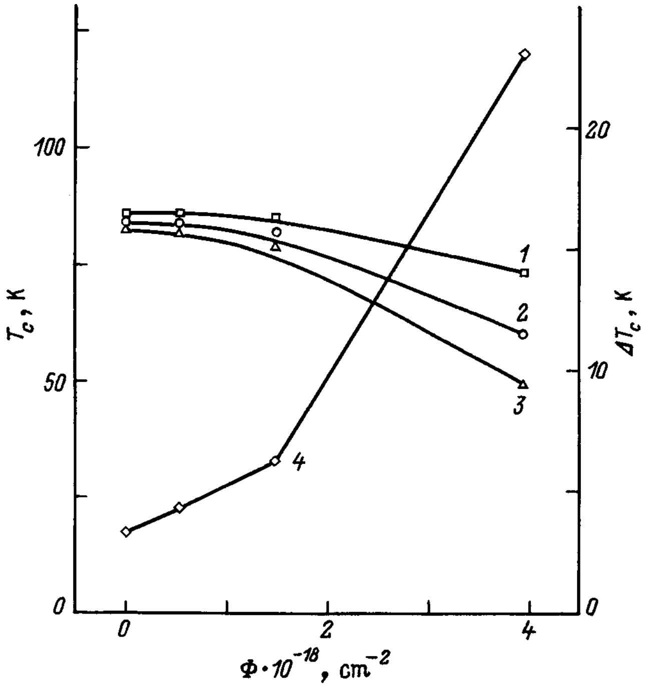

FIG. 5. Temperature of (1) the onset, $T_c^{0.9}$, (2) midpoint, $T_c^{0.5}$, (3) end, $T_c^{0.1}$, and (4) width, ΔT_c, of the superconducting transition in an M1 film as a function of fast-neutron flux.

For instance, for pinning at normal inclusions and spatial inhomogeneities with dimensions of the order of the mean-free path $x=2$,[12] for pinning at boundaries of misoriented crystallites $x=1.5$ (Ref. 15). In our case, the temperature dependences of j_c and j_1 before irradiation are well approximated by Eq. (2) with $x=1.5$ and 1.2, respectively. Our experimental relations $j_c(T)$ and the value $x=1.5$ are apparently appropriate for vortex pinning at plain grain boundaries, and the weak temperature dependence of the pinning activation energy U/kT indicates three-dimensional character of the pinning potential.[14]

B. Effect of irradiation on the transport properties of YBaCuO films

1) Films on MgO substrates.

Figures 5 and 6 display $T_c(\Phi)$ and $j_c(\Phi)$ relations obtained on the M1 film under irradiation at $T=25$ K by various neutron fluxes. The superconducting properties are seen to degrade monotonically (T_c and j_c decrease) with increasing neutron flux. At a flux of 4.5×10^{18} cm^{-2}, an Ohmic region is seen to appear in the I-V characteristic in the low-current domain, but the nonlinearity typical of the superconducting state sets in again as the current increases. The critical current degradation in this flux region can be associated not only with a change in the properties of superconducting grains and of the weak Josephson junctions coupling them but also with decreasing effective cross section of the superconducting path for the transport current, whereas degradation of T_c and the change in shape of the resistive transition depend on the change in the characteristics of the grains and of intergranular links. Figure 5 presents dose dependences of $T_c^{0.9}$, $T_c^{0.1}$, and $T_c^{0.5}$ (the transition onset, end, and midpoint temperatures, respectively) and of the width ΔT_c of the superconducting resistive transition. The average degradation rate of the critical temperature $T_c^{0.5}$ for the M1 film, $\Delta T/\Delta\Phi$, was found to be 9.2×10^{-18} K$\cdot$cm^2. It is known that the onset of the resistive superconducting transition is identified by the onset of superconductivity in the bulk of the grains,

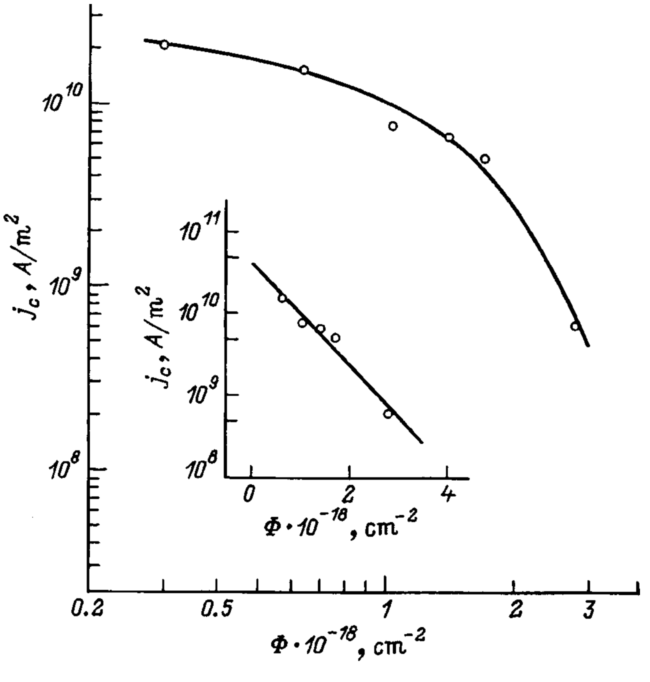

FIG. 6. Dose dependence of the critical-current density of an M1 film. Inset: a fit of Eq. (6) to the dose dependences.

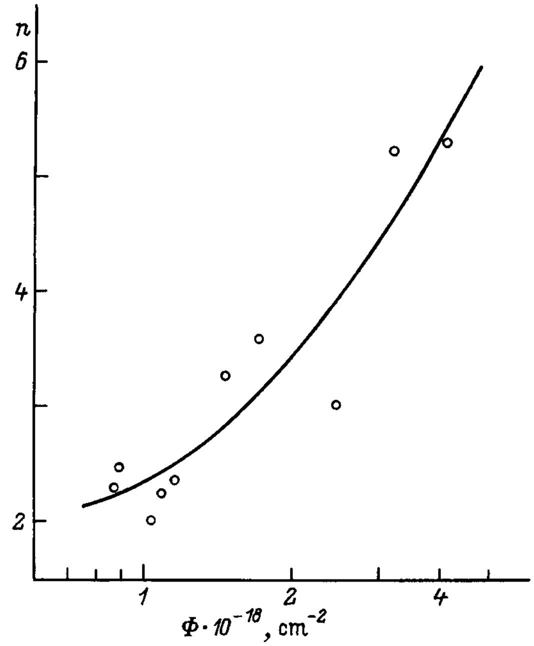

FIG. 7. Dose dependence of exponent n with I-V characteristics of an M1 film approximated by Eq. (1).

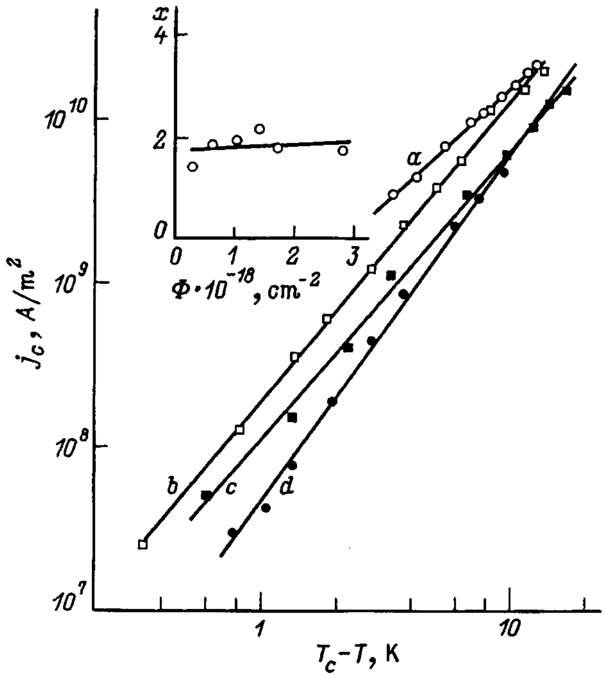

FIG. 8. Approximation of the $j_c(T)$ relations of an S1 film with Eq. (2) for different neutron fluxes ($\Phi\times10^{-18}$ cm^{-2}): *a*—0.3, *b*—0.64, *c*—1.4, *d*— 1.7. Inset shows the dose dependence of exponent x.

and its end, by that over the weak intergranular links. Hence neutron irradiation affects intergranular links to a larger extent than the grain bulk.

I-V curves of the M1 film obtained at different neutron fluxes were treated by percolation theory using Eq. (1). Figures 6 and 7 present dose dependences of the critical current density j_c and of exponent n. One clearly sees exponent n to grow rapidly with neutron flux, which indicates a considerable modification of the properties of weak intergranular links by irradiation.

The $j_c(\Phi)$ relation follows exponential behavior

$$j_c(\Phi)=j_c(0)\exp(-k\Phi), \tag{7}$$

where $j_c(0)$ is the critical current density before irradiation, and coefficient $k=7\times10^{-19}$ cm^2. Critical current should vary with dose in this way if the current-carrying ability of a material is dominated by the fraction of the superconducting phase. Assuming that the critical current density in the superconducting region does not depend on irradiation $[j_c^s(\Phi)=j_c^s(0)=\text{const}]$, one readily obtains for $j_c(\Phi)$ relation (6).[16] In this case, coefficient k is related to the number of displaced atoms per neutron.

2) Films on SrTiO$_3$ *substrates.*

The $T_c(\Phi)$ and $j_c(\Phi)$ relations obtained for S1 films under irradiation at 25 K exhibited the same pattern as those for the M1 film. Note that the increase in transition width ΔT_c with neutron flux in *S*-type films is three times smaller than that in M films. The average degradation rate of the critical temperature $T_c^{0.5}$ for the S1 film was found to be 2.5×10^{-18} K·cm^2, i.e., a factor 3.5 smaller than that for the M1 films. Figure 8 shows the fits of the temperature dependences of the critical current density obtained for an S1 film at different fast-neutron fluxes against Eq. (2). The critical-current density was found from I-V curves based on a threshold criterion of 1 μV. The $j_c(T)$ relation is seen to be fairly well approximated with a power law, with the exponent $x\cong2$ being independent of neutron flux (see inset in Fig. 8). The $j_c(\Phi)$ relation measured on an S1 film at 80 K is displayed in Fig. 9. The critical current decreases exponentially, (7), with increasing flux (see inset to Fig. 9). The parameter $k=1\times10^{-18}$ cm^2 is slightly in excess of the values obtained for the M1 films.

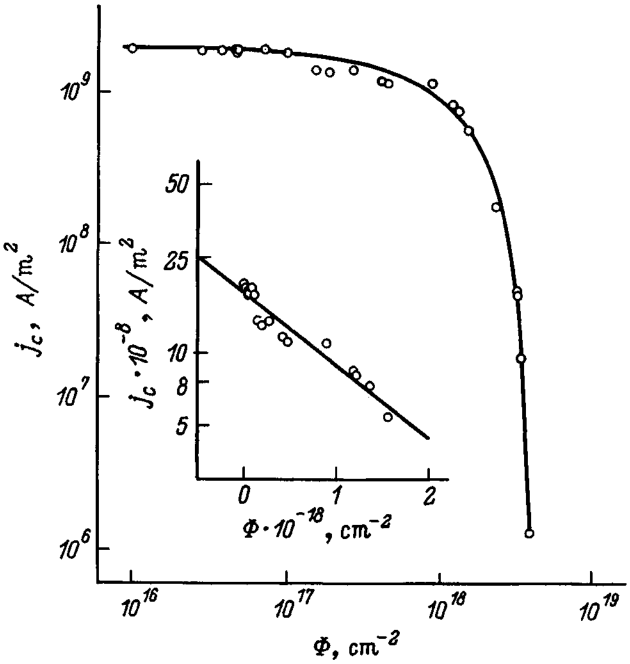

FIG. 9. Dose dependence of the critical-current density of an S1 film obtained at $T=80$ K. Inset shows a fit of the dose dependence to Eq. (6).

The I-V characteristics of S1 films obtained at various neutron fluxes were treated within the model of resistive state based on thermal activation of Abrikosov vortices.[13] Calculations made using Eq. (5) showed the pinning activation energy U to be independent of flux, and the U/kT ratio to lie within the 20–25 interval, as is the case with the M1 films. A similar result was obtained when YBaCuO single crystals were irradiated by 3-MeV protons.[17] One could expect the collective-pinning theory,[18] by which the dose dependence of the pinning activation energy should behave as $U \propto 1/\Phi$, to become valid for high pinning-center densities; this prediction does not agree, however, with the independence of the pinning activation energy from flux obtained in this experiment, which argues against the model of three-dimensional collective pinning.

Thus the observed difference in behavior between the transport properties of YBaCuO films grown on MgO (M1) and $SrTiO_3$ (S1) films is determined primarily by their crystal structure which, in turn, depends on substrate structure and the preparation technology employed. It has been shown that M1 films are granular systems, and that their transport properties are dominated by weak intergranular links, which represent an array of Josephson junctions described adequately by percolation theory.[3,4] S1 films have a single-crystal structure, and the continuous-medium model,[13] according to which the resistive state is due to thermal decoupling of Abrikosov vortices, offers a good approximation to their transport characteristics. The differences in the crystal structure between M1 and S1 films accounts also for the different degree of their degradation under low-temperature neutron irradiation. It has been shown that disorder in S1 films changes the mechanism of pinning, from that at the boundaries of disordered crystallites in unirradiated films to pinning at spatial inhomogeneities on the scale of the mean-free path produced by neutron irradiation. This change in the pinning mechanism in single-crystal YBaCuO films resulted not in the expected growth of j_c with increasing neutron flux but only in a degradation of j_c throughout the flux variation range studied (from 3×10^{17} to 3×10^{18} cm^{-2}). The absence of a maximum in the $j_c(\Phi)$ relation may apparently be due to the high structural perfection of the films under study.

A nonmonotonic $j_c(\Phi)$ relation with a maximum at a neutron flux $\Phi \sim 2\times10^{17}$ cm^{-2} was shown[19] to be observed only in strongly granulated materials, a class into which one can place ceramic systems, as well as imperfect films and single crystals.

Thus, in order to increase the critical current in HTSC materials through disorder produced by reactor-neutron irradiation, one should use granular materials with grain size above 8–10 μm.

Support of the Interdepartmental R&D Program "Neutron Studies of Matter" is gratefully acknowledged.

[1)] The authors are grateful to F. F. Karmonenko (St. Petersburg SEU) and S. Yu. Klimov (IFM, N. Novgorod) for providing M1 and S1 films, respectively.

[1] A. K. Pustovoĭt, B. A. Borisov, R. F. Konopleva, G. D. Porsev, V. A. Chekanov, S. O. Bokhanov, and M. V. Chudakov, LNPI Preprint No. 1749 (1991).

[2] R. F. Konopleva, B. L. Oksengendler, A. K. Pustovoĭt, B. A. Borisov, V. A. Chekanov, and M. V. Chudakov, Sverkhprovodimost': (KIAE) **6**, 568 (1993).

[3] E. Guyon, S. Roux, A. Hansen, D. Bideau, J.-P. Troadec, and H. Crapo, Rep. Prog. Phys. **53**, 373 (1990).

[4] A. D. Caplin, S. S. Bungre, S. M. Cassidy, J. R. Laverty, and Z. X. Shen, Physica A **168**, 268 (1990).

[5] M. I. Gurevich, E. Z. Meĭlikhov, O. V. Tel'kovskaya, and V. V. Yan'kov, Sverkhprovodimost': (KIAE) **1**, 80 (1988).

[6] E. Babič, M. Prester, and N. Biškup, Solid State Commun. **77**, 849 (1991).

[7] P. England, T. Venkatesan, X. D. Wu, and A. Inam, Phys. Rev. B **38**, 7125 (1988).

[8] V. Ambegaokar and A. Baratoff, Phys. Rev. Lett. **10**, 486 (1963).

[9] S. Greenspoon and J. T. Smith, Can. J. Phys. **49**, 1350 (1971).

[10] L. H. Allen, P. R. Broussard, J. H. Claassen, and S. A. Wolf, Appl. Phys. Lett. **53**, 1338 (1988).

[11] M. M. Gaĭdukov, E. F. Gatsura, E. K. Gol'dman, L. Kovalevich, A. B. Kozyrev, A. Yu. Popov, and T. B. Samoĭlova, Sverkhprovodimost': (KIAE) **3**, 2191 (1990).

[12] A. I. Larkin and Yu. N. Ovchinnikov, Zh. Éksp. Teor. Fiz. **61**, 1221 (1971) [Sov. Phys. JETP **34**, 651 (1971)].

[13] P. W. Anderson and Y. W. Kim, Rev. Mod. Phys. **36**, 39 (1964).

[14] A. V. Bezvinner, S. V. Gaponov, M. A. Kalyagin, V. Ya. Kosyev, L. A. Mazo, and M. D. Strikovskiĭ, Sverkhprovodimost': (KIAE) **3**, 2332 (1990).

[15] S. V. Gaponov, G. G. Kaminskiĭ, E. B. Klyuenkov, D. V. Kuzin, V. I. Matsuĭ, V. M. Pan, V. G. Prokhorov, and M. D. Strikovskiĭ, Zh. Éksp. Teor. Fiz. **95**, 2191 (1989) [Sov. Phys. JETP **68**, 1266 (1989)].

[16] B. D. Weaver, M. E. Reeves, D. B. Chrisey, G. P. Summers, W. L. Olson, M. M. Eddy, T. W. James, and E. J. Smith, J. Appl. Phys. **69**, 1119 (1991).

[17] L. Civale, A. D. Marwick, M. W. McElfresh, T. K. Worthington, A. P. Malozemoff, F. H. Holtzberg, J. R. Thompson, and M. A. Kink, Phys. Rev. Lett. **65**, 1164 (1990).

[18] M. V. Feigelman and V. M. Vinokur, Phys. Rev. B **41**, 8986 (1990).

[19] R. F. Konopleva, I. V. Nazarkin, and V. A. Chekanov, Perspekt. Mater. No. 6, 34 (1997).

Translated by G. Skrebtsov

PHYSICS OF THE SOLID STATE VOLUME 40, NUMBER 11 NOVEMBER 1998

Different path of pressure-induced oxygen ordering and disordering processes in $YBa_2Cu_3O_{6+x}$ near a metal–insulator transition

I. M. Fita*) and V. P. D'yakonov

Donetsk Physicotechnical Institute, Ukrainian Academy of Sciences, 340114 Donetsk, Ukraine

R. Puznyak and G. Szymczak

Institute of Physics, Polish Academy of Sciences, 02-668 Warsaw, Poland

(Submitted April 29, 1998)
Fiz. Tverd. Tela (St. Petersburg) **40**, 1968–1973 (November 1998)

The relaxation of the superconducting transition temperature T_c in $YBa_2Cu_3O_{6.38}$ is investigated with increasing oxygen order in the CuO_x plane under 1 GPa pressure and with decreasing oxygen order after the pressure is relieved. It is established that the oxygen disordering process is more rapid than the pressure-induced ordering process: The ratio of the relaxation times of T_c in these processes $\tau_{ord}/\tau_{disord} \approx 5$. This behavior could be caused by different mechanisms of the pressure-induced increase in the Cu–O chain length and decrease of this length after pressure relief. © *1998 American Institute of Physics.* [S1063-7834(98)00211-1]

After the experiment of Ref. 1, which showed a direct connection between superconducting order and local oxygen order in the oxygen-deficient compound $YBa_2Cu_3O_{6+x}$, a large number of works were performed on the problem of oxygen ordering in Y123. These were primarily experiments on aging of samples in which the relaxation of superconducting structural, electronic, and other physical properties was observed at room temperature T_{RT} over several days[2–8] in nonequilibrium quenched disordered $YBa_2Cu_3O_{6+x}$ samples as the equilibrium state was approached by increasing the oxygen order (Cu–O chain length) in CuO_x planes. These time-dependent phenomena are ordinarily interpreted in a charge-transfer model according to which the system Y123 is represented by conducting CuO_2 layers and insulting CuO_x layers, which are a reservoir for holes. Oxygen ordering, corresponding to an increase in the lengths of Cu–O chain fragments at the first stage followed by the formation of a two-dimensional superstructure, materializes by diffusion hops of oxygen atoms from O(5) into O(1) positions, as a result of which some triply oxygen-coordinated Cu(1) atoms transform into doubly coordinated atoms with their valence changing from +2 to +1. This requires transfer of electronic charge from the CuO_2 plane to the CuO_x plane. Thus, during aging, as the system relaxes into the equilibrium state, the CuO_2 planes are continuously doped with holes.

A similar charge transfer mechanism is also proposed to explain the experiments on photoinduced superconductivity[9] and the effect of an electric field on the properties of superconducting films.[10]

Ordering of Cu–O chains in the system Y123 can also be induced by external pressure, causing nonequilibrium by decreasing the unit-cell volume.[11,12] The degree of order of the mobile oxygen system in a sample subjected to compression will increase, approaching an equilibrium value corresponding to the new volume. This occurs because the unit cell volume decreases upon the transformation $Cu^{2+} \rightarrow Cu^{1+}$ in the CuO_x plane. The effect of oxygen ordering in T_c is greatest near the metal–insulator transition, where the state of the system depends most sharply on the current-carrier density. The highest values $dT_c/dP \approx 30$ K/GPa were observed in single-crystal $YBa_2Cu_3O_{6.4}$[13] and in $NdBa_2Cu_3O_{6.67}$.[14]

In experiments studying the aging of quenched samples, only the direct process leading to an increase in oxygen order can be observed, whereas the pressure method makes it possible to follow also the reverse process leading to disordering of oxygen chains after relief (or lowering) of the pressure, and it also makes it possible to regulate the change in the oxygen order by varying the magnitude of the applied pressure for a fixed oxygen content in the sample. In this way, the pressure method is promising for studying oxygen ordering processes in Y123.

In a previous work[14] we realized a transition into the superconducting state in an initially nonsuperconducting $NdBa_2Cu_3O_{6.67}$ sample exclusively by pressure-induced oxygen ordering. The transition between the superconducting and nonsuperconducting phases was completely reversible with respect to pressure and showed good reproducibility. After pressure relief, T_c relaxed to zero, but more rapidly than it increased under pressure. This asymmetry of the time dependence of $T_c(T)$ under pressure and after pressure relief shows that the oxygen ordering and disordering processes follow different paths. It is known that a O-II superstructure does not materialize in Nd123,[15] since the Nd ion, which has a large radius, actively influences the oxygen order, changing the interaction between neighboring O(1) in the CuO_x plane. In the present work we checked the manner in which the ordering and disordering of oxygen occur in the O-II structure in Y123. The measurements of the time dependence $T_c(t)$ were performed under pressure $P=1$ GPa and after pressure relief (at $P=0$) on a $YBa_2Cu_3O_{6.38}$ sample with $T_c \approx 8$ K in the equilibrium state at atmospheric pressure.

1. EXPERIMENTAL PROCEDURE

The ceramic $YBa_2Cu_3O_{6+x}$ was prepared by the standard method. A sample with oxygen index $x=0.38$ was chosen for the investigations. The sample was obtained by rapid quenching in liquid nitrogen after appropriate heat treatment of an optimally doped sample with index $x=0.95$, determined by iodometric titration. After prolonged holding (several weeks) at room temperature, $T_c \approx 8$ K in the equilibrium sample, which agrees well with the data of Ref. 2, indicating the appearance of superconductivity in Y123 for $x \geqslant 0.35$.

Magnetic measurements under pressure were performed at the Institute of Physics of the Polish Academy of Sciences on a PAR model 450 vibrating-reed magnetometer in the temperature range 4.2–100 K. The method used a miniature piston–cylinder container made of a negative beryllium bronze, in which a hydrostatic pressure up to 1 GPa was produced at room temperature. A 1:1 mixture of transformer oil and kerosene was used as the pressure-transmitting medium. The experimental sample ($m=0.029$ g) had a cylindrical shape with diameter $d=1.1$ mm and length $l=5$ mm. The pressure was determined at low temperatures according to the known pressure dependence $T_c(P)$ of pure tin, a sample of which ($m \approx 0.01$ g) was placed next to the experimental sample of Y123.

In the experiment, the temperature dependences of the magnetization $M(T)$ of the sample in a 10 Oe field at fixed pressure 1 GPa were measured. Prior to each measurement the container with the sample was cooled to 4.2 K in zero magnetic field (ZFC). The time interval during which the sample was at room temperature $T_{RT}=295$ K was measured between changes of $M(T)$, whereas the time the sample was in the cryostat was neglected, since virtually no oxygen diffusion is observed at $T<240$ K.[2] The total duration of the experiment under pressure was about 5 days. The transition temperature T_c with different residence time t under 1 GPa pressure at T_{RT} and the time dependence of T_c, reflecting the character of the variation of oxygen order at 1 GPa pressure, were determined from the $M(T,t)$ data. A similar sequence of measurements was performed immediately after pressure relief to zero in order to determine the reverse relaxation of T_c to its equilibrium value at $P=0$.

2. RESULTS AND DISCUSSION

Figure 1a displays the temperature dependences of the ZFC magnetization $M(T)$ of a $YBa_2Cu_3O_{6.38}$ sample which were measured in a 1 mT field at atmospheric pressure in the equilibrium state (curve *0*) and under 1 GPa pressure after definite holding periods at T_{RT} in a period ~ 5 days (curves *1–4*). One can see that the superconducting transition is strongly broadened. This is generally characteristic of ceramic samples because of stresses existing at grain boundaries, which lead to oxygen-order gradients,[2] as well as because of the high measuring field 1 mT required to maintain adequate sensitivity.

The temperature T_c was determined by extrapolating the line of maximum slope on the $M(H)$ curve to zero magnetization. During the experiment T_c asymptotically approached its equilibrium value ≈ 21 K at 1 GPa. In the process, the superconducting transition narrowed. The first critical field H_{c1}, roughly estimated from the deviation of $M(H)$ from linearity at 4.2 K and normalized to the value at $T=0$ according to $H_{c1}(T)=H_{c1}(0)[1-(T/T_c)^2]$ varied from ≈ 4 Oe ($T_c \approx 8$ K) at $P=0$ to ≈ 18 Oe ($T_c \approx 21$ K) at $P=1$ GPa . The change in T_c and H_{c1} was no longer distinguishable, within the limits of experimental error, after holding at 1 GPa for longer than 100 h. At $t=118$ h the pressure on the sample was relieved, after which the system relaxed at $P=0$ to the equilibrium state. Figure 1b shows how the temperature dependence of the magnetization changes in time after pressure relief (curves *5–7*) relative to the state at $P=1$ GPa with the maximum holding time in the experiment (curve *4*).

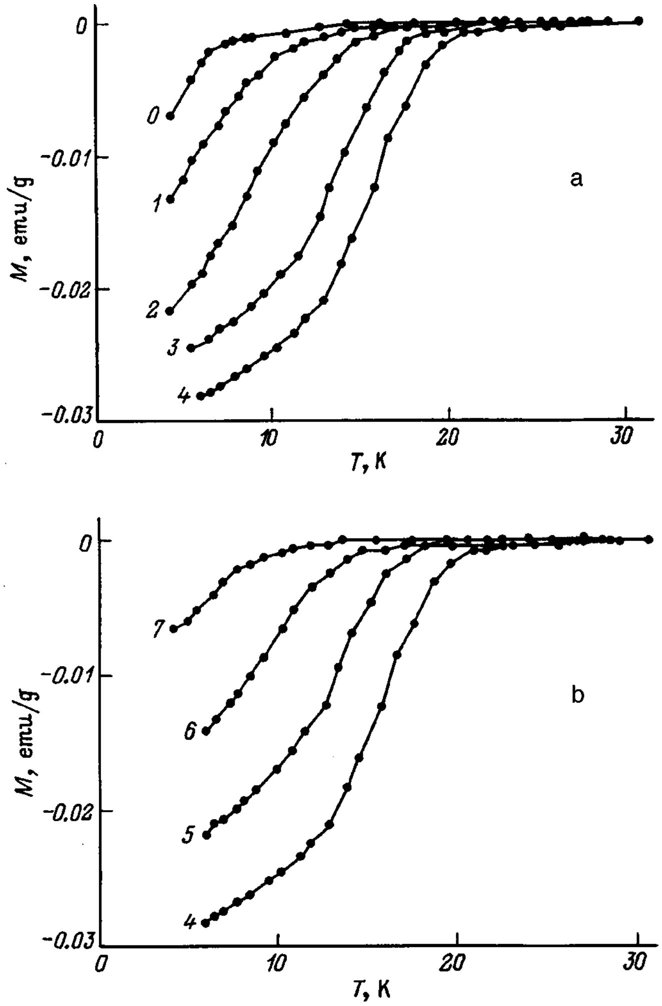

FIG. 1. Temperature dependence of the magnetization of a $YBa_2Cu_3O_{6.38}$ sample measured at 1 mT (ZFC). a) At $P=0$ in the equilibrium state (curve *0*); under pressure $P=1$ GPa with different holding times t at T_{RT}. t (h): *1* — 0.25, *2* — 7.7, *3* — 39, *4* — 81. b) After pressure relief with holding times at T_{RT}. t (h): *5* — 0.15, *6* — 21, *7* — 52.8, curve *4* — same as curve *4* in Fig. 1a.

The results of the T_c measurements in the pressure change cycle described $0 \rightarrow 1$ GPa$\rightarrow 0$ are displayed in Fig. 2. The relaxational character of the change in T_c under pressure and after pressure relief is described well by a simple exponential function, which was checked quite reliably on the relaxation of T_c, the structural properties, and conduc-

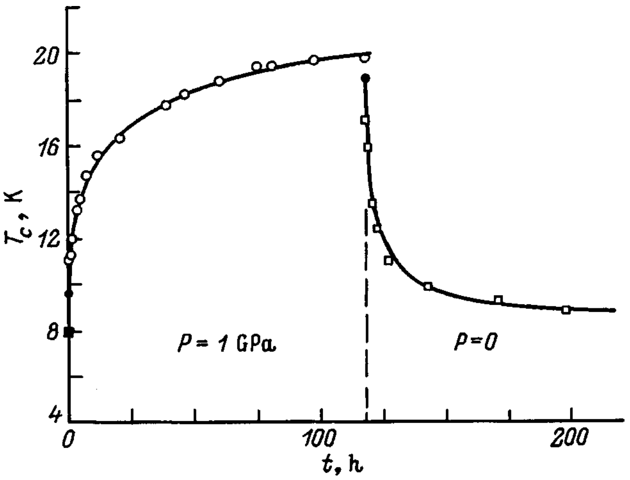

FIG. 2. Time dependence of T_c during restructuring of the oxygen subsystem CuO_x in $YBa_2Cu_3O_{6.38}$. Open circles — under 1 GPa pressure, open squares — after pressure relief ($P=0$), filled square — equilibrium value of T_c at $P=0$. The solid lines were calculated using Eq. (1) with the parameters presented in Table I; the filled circles show the computed values of T_c at $t=0$ (at the start of the oxygen ordering process at 1 GPa) and at $t=118$ h (at the start of oxygen disordering after pressure relief).

tivity in experiments on aging of Y123 samples[1–5,8] and under pressure,[11–14]

$$T_c(t)=T_c(\infty)-[T_c(\infty)-T_c(0)]\exp[-(t/\tau)^{0.5}], \tag{1}$$

where t is the holding time at T_{RT}, $T_c(0)$ is the value of T_c at the start of the nonequilibrium oxygen ordering (or disordering) process, $T_c(\infty)$ is the equilibrium value of T_c, and τ is the relaxation time. The parameters $T_c(0)$, $T_c(\infty)$, and τ that best describe the behavior of T_c at 1 GPa and after pressure relief (solid lines in Fig. 2) are presented in Table I. We note that $T_c(0)$ is an adjustable parameter, since in our procedure we could not determine T_c immediately after applying (or relieving) the pressure. Ordinarily, before cooling the sample was at temperature T_{RT} for about 0.2 h. Figure 2 shows (filled circles) the computed values of $T_c(0)$. The equilibrium values of $T_c(\infty)$ were also calculated, since the duration of the experiment was limited.

The change in T_c, which is reversible with respect to pressure within the limits of error in determining T_c, occurs mainly as a result of a change in the oxygen order. As first shown by Metzger et al.,[11] the complicated effect of pressure on T_c in oxygen-deficient Y123 can be represented by a sum of two contributions that are of different nature: one due to pressure-induced oxygen ordering $(dT_c/dP)_0$ and the other due to the intrinsic pressure $(dT_c/dP)_i$. The second term, $(dT_c/dP)_i$, is due to changes in the interactions (between CuO_2 planes, electron-phonon interaction, and others), which are directly responsible for superconductivity, as well as to charge redistribution as a result of a pressure-induced decrease of the lattice parameters. We note that these contributions are not completely independent, if the structural relaxation accompanying oxygen ordering is taken into account. The quantity $(dT_c/dP)_i$, which we estimated with increasing and decreasing pressure, is 1.7 and 1.2 K/GPa, respectively. The values obtained are close to $(dT_c/dP)_i=1.8$ K /GPa, measured on a $YBa_2Cu_3O_{6.4}$ single crystal.[13]

TABLE I. The parameters $T_c(0)$, $T_c(\infty)$, and τ for which Eq. (1) best describes the relaxation of $T_c(t)$ under 1 GPa pressure and after pressure relief (see curve in Fig. 2).

P, GPa	$T_c(0)$, K	$T_c(\infty)$, K	τ, h
1	9.56	21.5	27.7
0	18.8	8.55	5.4

Conversely, the effect of oxygen ordering at 1 GPa, $(dT_c/dP)_0$, is ≈ 12 K/GPa, which is two times lower than the value obtained in Ref. 13 at $P=0.43$ GPa. The difference can be due to the influence of grain boundaries and other microstructural defects in ceramic on the pressure-induced change of oxygen order. Another reason for the observed difference could be that dT_c/dP is not constant but rather always decreases with pressure and is maximum in the limit $P\rightarrow 0$. This was recently well substantiated by Gupta et al.,[16] who took into consideration the parabolic dependence $T_c \sim (n_{\mathrm{opt}-n})^2$ characteristic for high-T_c superconductors (where n is the hole density in the CuO_2 plane, $n_{\mathrm{opt}}=0.25$ holes/CuO_2 is the optimal density at $T_c=T_{c,\max}$).[17,18] Indeed, $dT_c/dP=(dT_c/dn)(dn/dP)\sim(n_{\mathrm{opt}}-n)$, since $dn/dP\approx$ const (which is valid for not very high values of P), and therefore dT_c/dP decreases under pressure all the more rapidly, the greater the pressure-induced charge redistribution dn/dP. This effect, i.e. essentially the nonlinearity of $T_c(P)$, should be easily noticeable near the metal–insulator transition, where dn/dP due to oxygen ordering is maximum, and the compressibility is also maximum (for $x\sim 0.3$ Y123 is the ''softest'' material).[19] Thus, we observed in $NdBa_2Cu_3O_{6.67}$ at a pressure-induced metal-insulator transition that values of $(dT_c/dP)_0$ at 1 GPa (≈ 30 K/GPa) and 0.55 GPa (≈ 43 K/GPa) differ by approximately a factor of 1.5.[20] In reality, this difference is even larger, since the quantities $(dT_c/dP)_0$ were determined by averaging over the indicated pressure intervals, i.e. as $\Delta T_c/\Delta P$. On the basis of these considerations and the experimental results of Ref. 20, we infer a nonlinear pressure dependence $T_c(P)$ in $YBa_2Cu_3O_{6.4}$ and the difference, originating therefrom, between the effect of dT_c/dP that we observed at 1 GPa and the value measured at 0.43 GPa in Ref. 13.

The relaxation time τ in the oxygen ordering process is, to a first approximation, often associated to the activation energy of the O(5)→O(1) transition, $E\approx 1$ eV, according to the Arrhenius law $\tau=\tau_0\exp(E/kT)$, where $\tau_0\approx 1.4\times 10^{12}$ s.[2] However, Monte Carlo simulation of oxygen ordering in aging experiments[21] predicts a more complicated process occuring in two stages: a relatively fast process leading to ordering of the O(1)/O(5) sublattice, where only transitions between neighboring O(1) and O(5) positions occur, and a slower process leading to the formation of an O-II superstructure in which the Cu–O chains elongate so as to minimize the number of energetically unfavorable chain ends. The large variance in the observed values of τ in different experiments on Y123 does not make it possible to determine accurately which process is observed in reality. Monte Carlo estimates[21] show that τ corresponds in aging experiments to the process leading to the formation of an O–II superstruc-

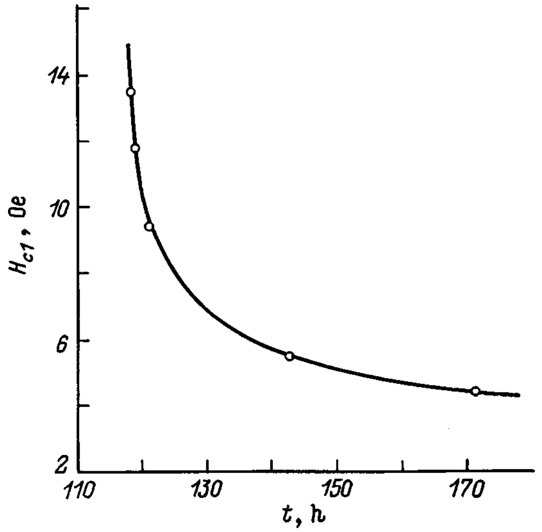

FIG. 3. Relaxation of the first critical field H_{c1} during oxygen disordering after relief of 1 GPa pressure to zero. Circles — experimental values of H_{c1}, normalized to the values at $T=0$; the solid line was computed using Eq. (1) with the parameters $H_{c1}(t=0)=15$ Oe, $H_{c1}(\infty)=3.55$ Oe, $\tau=7.8$ h.

ture with a long relaxation time, but it follows from the experiment of Ref. 4 that such a process at T_{RT} occurs much too slowly (several weeks). The variance of the experimental values of τ is associated with the influence of microstructural defects, Al and Au impurity atoms in the experimental samples, on oxygen diffusion as well as with the different oxygen deficits. Recently,[13] a strong dependence $\tau(x)$ was observed in a $YBa_2Cu_3O_{6+x}$ single crystal: As the oxygen content increased, τ rapidly decreased from $\tau\approx10$ h at $x=0.4$ to $\tau\approx0.5$ h at $x=0.7$. Monte Carlo calculations also predict a maximum of τ due to large fluctuations near a $T-O$ transition (between the tetra- and orthophases at $x\sim0.35$).[22]

We determined the relaxation time in the process of oxygen ordering at $P=1$ GPa by analyzing the time dependence $T_c(t)$ in Fig. 2: $\tau_{\mathrm{ord}}=27.7$ h (see Table I). This value of τ is higher than in a $YBa_2Cu_3O_{6.4}$ single crystal,[13] probably for the reasons discussed above (due to the influence of defects: boundaries, impurities, and so on in the ceramic) as well as because in our experiment the pressure was more than two times higher than in Ref. 13. The latter supposition agrees with the Monte Carlo calculations,[22] showing that near a $T-O$ transition τ increases strongly with increasing annealing temperature T_a, which fixes the degree of oxygen disorder at the start of the aging process. In our case the degree of disorder is fixed by the pressure P.

In the reverse process leading to disordering of the oxygen subsystem after pressure relief to zero, we calculated $\tau_{\mathrm{disord}}=5.4$ h, i.e., the disordering process is much more rapid, $\tau_{\mathrm{ord}}/\tau_{\mathrm{disord}}\approx5$. The discrepancy with respect to the time dependence $T_c(t)$ at $P=1$ GPa and $P=0$ is even noticeable visually (Fig. 2). We also check the rate of the reverse process according to the relaxation of the first critical field H_{c1}, determined from the dependence $M(H)$ at 4.2 K in different nonequilibrium states. Figure 3 shows the variation of the parameter H_{c1} accompanying oxygen disordering after relief of 1 GPa pressure, starting at time $t=118$ h (the values of H_{c1} are normalized to $T=0$ according to the relation $H_{c1}(T)=H_{c1}(0)[1-(T/T_c)^2]$). The solid line in Fig. 3 was calculated according to Eq. (1) with the substitutions $H_{c1}\rightarrow T_c$ and $t\rightarrow t-118$ h and the parameters $H_{c1}(t=0)=15$ Oe, $H_{c1}(\infty)=3.55$ Oe, $\tau=7.8$ h, i.e., we obtained that in the reverse process the parameters T_c and H_{c1} relax to equilibrium values at close rates.

In summary, the pressure-induced oxygen ordering relaxation process and the reverse disordering relaxation process after pressure relief occur differently. This follows from the large difference between the relaxation times T_c in the direct and reverse processes. A similar behavior under pressure (i.e. more rapid drop of T_c after pressure relief) was observed at a metal–insulator transition in $NdBa_2Cu_3O_{6.67}$,[14] which has a different type of oxygen order, different from the superstructure O-I, as a result of the strong influence of the large-radius Nd ion.[15] We add that in a $YBa_2Cu_3O_{6.5}$ film the disordering of Cu–O chains after removal of photoirradiation likewise is more rapid than irradiation-induced oxygen ordering,[9] i.e. there is an analogy with the pressure-induced behavior. Asymmetry of the electric-field-induced oxygen ordering and disordering in Y123 has also been observed.[10]

From the oxygen-ordering picture presented in Ref. 21, a simple inference can be drawn about the nature of the asymmetric dependence $T_c(t)$ in the direct and reverse oxygen-ordering processes. As the Cu–O chain fragments increase in length by an oxygen atom attaching to the end of a chain, the average diffusion length of the transition O(5)→O(1) should be longer than in the case of shortening of Cu–O chains, since in the former case an oxygen atom must traverse a longer distance in order to find a vacant location in O(1) positions. In the reverse chain-shortening process, however, O(1)→O(5) transitions can be easily accomplished between neighboring oxygen atoms, so that the charge redistribution process between CuO_2 and CuO_x planes will be more rapid. The relaxation will also speed up if the possibility of destruction of a Cu–O chain by rupture is taken into account. In this case the chain lengths and correspondingly the hole density in the CuO_2 plane effectively decrease. This simple scheme, however, requires a detailed examination.

In conclusion, we shall note the characteristic features, investigated here, of the pressure-induced restructuring of the oxygen sublattice in $YBa_2Cu_3O_{6+x}$ near the metal–insulator transition. The change in T_c due to the change in the degree of oxygen order in the CuO_x plane is completely reversible with respect to pressure, showing that the displacement of electronic charge between CuO_2 and CuO_x planes is reversible. However, the process leading to disordering of the oxygen subsystem occurs much more rapidly than the direct process leading to ordering, the ratio of the relaxation times in these processes being $\tau_{\mathrm{ord}}/\tau_{\mathrm{disord}}\approx5$. The asymmetry of the temporal variation of the pressure-induced oxygen ordering and disordering processes could be due to the fact that the mechanism leading to an increase of the Cu–O chain length (by oxygen atom attachments to chain ends) is different from the mechanism leading to more rapid shortening of the chain (by removal of oxygen from a chain end to a neighboring

O(5) position or rupture of a long C–O fragment).

This kind of behavior is evidently characteristic for the 1–2–3 system, since a difference between the rates of the direct and reverse oxygen-ordering processes was observed earlier in the case of the effect of photoirradiation in $YBa_2Cu_3O_{6+x}$ films[9] and in the appearance of pressure-induced superconductivity in $NdBa_2Cu_3O_{6.67}$[14] with O-I structure.

We also note that the present discussion of the results is based on the model of charge transfer between conducting CuO_2 and insulating CuO_x planes, though recently it has been asserted that Cu–O chains have conductivity and a superconducting density exists in CuO_x layers.[23,24] In any case, it is urgent to study the character of oxygen ordering in a system Y123.

We are grateful to N. A. Doroshenko for preparing the samples.

This work was supported in part by the Polish State Committee on Science (KBN) under grant N 2 P 03 B 09514.

*⁾E-Mail: fita@host.dipt.donetsk.ua

---

[1] J. D. Jorgensen, S. Pei, P. Lightfoot, Hao Shi, A. P. Paulikas, and B. W. Veal, Physica C **167**, 571 (1990).

[2] B. W. Veal, A. P. Paulikas, Hoydoo You, Hao Shi, Y. Fang, and J. W. Downey, Phys. Rev. B **42**, 6305 (1990).

[3] H. Claus, S. Yang, A. P. Paulicas, J. W. Downey, and B. M. Veal, Physica C **171**, 205 (1990).

[4] S. Yang, H. Claus, B. W. Veal, R. Wheeler, A. P. Paulikas, and J. W. Downey, Physica C **193**, 243 (1992).

[5] H. Shaked, J. D. Jorgensen, B. A. Hunter, R. L. Hitterman, A. P. Paulicas, and B. W. Veal, Phys. Rev. B **51**, 547 (1995).

[6] A. N. Lavrov and L. P. Kozeeva, Physica C **253**, 313 (1995).

[7] J. Kircher, M. Cardona, A. Zibold, K. Widder, and H. P. Geserich, Phys. Rev. B **48**, 9684 (1993).

[8] S. Libbrecht, E. Osquiguil, B. Wuyts, M. Maenhoudt, Z. X. Gao, and V. Bruynseraede, Physica C **206**, 51 (1993).

[9] V. V. Eremenko, E. S. Kachur, V. G. Piryatinskaya, A. M. Ratner, and V. V. Shapiro, Physica C **262**, 54 (1996).

[10] N. Chandrasekhar, Oriol T. Walls, and A. M. Goldman, Phys. Rev. Lett. **71**, 1079 (1993).

[11] J. Metzger, T. Weber, W. H. Fietz, K. Grube, H. A. Ludwig, T. Wolf, and H. Wühl, Physica C **214**, 371 (1993).

[12] W. H. Fietz, R. Quenzel, K. Grube, J. Metzger, T. Weber, and H. A. Ludwig, Physica C **235–240**, 1785 (1994).

[13] W. H. Fietz, R. Quenzel, H. A. Ludwig, K. Grube, S. I. Schlachter, F. W. Hornung, T. Wolf, A. Erb, M. Kläser, and G. Müller-Vogt, Physica C **270**, 258 (1996).

[14] V. P. D'yakonov, I. M. Fita, N. A. Doroshenko, M. Baran, and G. Shimchak, JETP Lett. **63**, 784 (1996); Physica C **270**, 285 (1997).

[15] H. Lütgemeier, S. Schmenn, P. Meuffels, O. Storz, R. Schölhorn, Ch. Niedermayer, I. Heinmaa, and Yu. Baikov, Physica C **267**, 191 (1996).

[16] R. P. Gupta and M. Gupta, Phys. Rev. B **51**, 11 760 (1995).

[17] J. L. Tallon, C. Berbhard, H. Shaked, R. L. Hitterman, and J. D. Jorgensen, Phys. Rev. B **51**, 12 911 (1995); M. R. Presland, J. L. Tallon, R. G. Buckley, R. S. Liu, and N. D. Frower, Physica C **176**, 95 (1991).

[18] B. W. Veal and A. P. Paulikas, Physica C **184**, 321 (1991).

[19] K. Suenaga and G. Oomi, J. Phys. Soc. Jpn. **60**, 1189 (1991).

[20] I. M. Fita, V. P. D'yakonov, M. Baran, and G. Szymczak, Fiz. Tverd. Tela (St. Petersburg) **39**, 1328 (1997) [Phys. Solid State **39**, 1178 (1997)].

[21] C. Ceder, R. McCormack, and D. de Fontaine, Phys. Rev. B **44**, 2377 (1991).

[22] E. E. Tornau, P. J. Kundrotas, and A. Rosengren, Physica C **269**, 198 (1996).

[23] D. N. Basov, R. Liang, D. A. Bonn, W. N. Hardy, B. Dabrowski, M. Quijada, D. B. Tanner, J. P. Rice, D. M. Ginsberg, and T. Timusk, Phys. Rev. Lett. **74**, 598 (1995).

[24] G. V. M. Williams and J. L. Tallon, Physica C **258**, 41 (1996).

Translated by M. E. Alferieff

PHYSICS OF THE SOLID STATE VOLUME 40, NUMBER 11 NOVEMBER 1998

Study of the photovoltaic frequency-response function in thin YBCO films

A. I. Grachev, P. M. Karavaev, and S. G. Shul'man

A. F. Ioffe Physicotechnical Institute, Russian Academy of Sciences, 194021 St. Petersburg, Russia

(Submitted February 25, 1998; resubmitted May 12, 1998)
Fiz. Tverd. Tela (St. Petersburg) **40**, 1974–1979 (November 1998)

The frequency response of the photovoltaic component of light-induced voltages in superconducting YBCO films having different morphologies has been measured for the first time over a broad range of 1.5 Hz to 150 kHz. It is shown that the deviation of the high-frequency response from the conventional relaxation dependence observed in one of the samples can be due to a spread in parameters of the elementary photoemfs generated in different regions of the film. The data obtained permitted estimation of a number of quantities characterizing the photoconducting properties of the nonmetallic regions with extended inhomogeneities which are responsible for the onset of the photovoltaic signal. © *1998 American Institute of Physics.* [S1063-7834(98)00311-6]

As shown by our earlier studies[1–3] of light-induced in-plane voltages generated in superconducting YBCO films, the observed signals are associated with at least three mechanisms, one of which is the photovoltaic effect. The photovoltaic effect is assumed to be due to the existence of internal interfaces (of the type metal–semiconductor–metal) in the bulk of the superconducting phase, which form at extended (planar) defects or inhomogeneities (we shall refer to these regions in what follows as ″inhomogeneities″, and understand by the ″properties of inhomogeneities″ the corresponding properties of the semiconducting layers).[3] An analysis of some inhomogeneities of this kind known to exist in YBCO films, made from the standpoint of their possible contribution to the photovoltaic effect, was reported in Ref. 3.

The main experimental tool capable of separating the various mechanisms for generation of light-induced voltages in YBCO is based presently on measuring the frequency response of the variable signals generated in a film illuminated by an intensity-modulated light beam.[1] Because the light source used in these experiments was a standard halogen lamp, the intensity was modulated by a mechanical chopper, which did not permit one to reach beyond $f\sim 1$ kHz. With such a limitation of the frequency range, no full pattern of the behavior of the photovoltaic component which would include the frequency-response roll-off region could be obtained. At the same time the significance of such information to unraveling the nature of the photovoltaic effect in YBCO films is obvious, particularly if one takes into account the difficulties involved in spectral measurements of low induced voltages. Therefore the main object of this work was to study the frequency response of light-induced voltages in YBCO films over a considerably broader frequency range, from 1.5 Hz to 150 kHz.

The measurements were performed on three YBCO films with different morphology. The response functions obtained reveal both some common features and certain differences, the most essential of them concerning the high-frequency roll-off of the response. For instance, one of the samples, measured in the conditions where the signals varied linearly with illumination intensity, exhibited, in place of the expected frequency relation of the type $(1+\omega^2\tau^2)^{-1/2}$ ($\omega=2\pi f$, and τ is the relaxation time), a steeper decay of the signal close to ω^{-2}. It was shown that this feature of the response function may be due to the statistical nature of detected signals, which are actually the results of summation of elementary photoemfs generated by individual inhomogeneities. For this interpretation to be valid, these photoemfs must differ not only in relaxation times but in the sign as well. Subsequent treatment of the response function and of other experimental data pertaining to the photoconducting properties of the samples permitted estimation of a number of parameters (e.g. the lifetime of minority carriers), which characterize the semiconducting properties of the inhomogeneities under study.

1. SAMPLES AND EXPERIMENTAL TECHNIQUES

Light-induced voltages were measured on three YBCO films, two of which were studied earlier[1–3] (the films on MgO and $LaAlO_3$ substrates were denoted in Refs. 1–3 by $S2$ and $S3$, respectively) and, therefore, their structural, geometric, and physical characteristics were already presented. The third sample, although used for the first time, was one of the lot investigated previously and prepared by laser ablation on $NdGaO_3$ substrates. Considered from the standpoint of morphology, the latter sample, denoted subsequently by $S4$ (for the other samples the old notation has been retained), had the weakest-pronounced texture, but, in contrast to $S2$ and $S3$, did not exhibit residual resistivity below the superconducting transition point ($T_c\sim 90$ K).

The geometry of the experiment and the general scheme for measurement of light-induced voltages were described elsewhere.[1–3] All measurements were carried out at room temperature. A new aspect of the experimental technique was the use of a He-Ne laser ($\sim 10^{-2}$ W) for sample illumination, with an electro-optical modulator serving for intensity modulation. This permitted broadening substantially the measurement range (from 1.5 Hz to 150 kHz), as well as

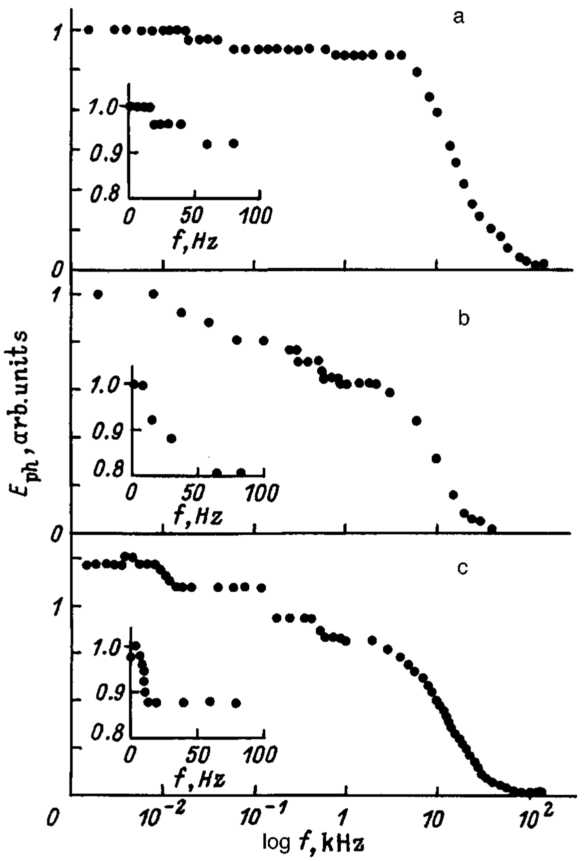

FIG. 1. Frequency response of light-induced voltages ($T = 300$ K) in samples $S2$ (a), $S3$ (b), and $S4$ (c). The insets display on standard scale the response in the low-frequency range.

to improve the reliability. Besides, by focusing the laser beam properly, one could investigate the spatial distribution of the photovoltaic effect over the film surface.

2. RESULTS AND DISCUSSION

Figure 1 displays frequency response measurements made on the samples under study. (Note that the signal in $S2$ and $S3$ was measured between the contacts on which the light-induced voltages are the largest.[3]) The responses of all the samples are seen to follow the same pattern. Within the initial region ($1.5 \leqslant f \leqslant 100$ Hz), the signal falls off to reach a relatively smooth plateau exhibiting one or several steps, depending on the sample, after which (for $f \geqslant 10^4$ Hz) the induced voltages decay to zero.

The low-frequency roll-off of the frequency response was observed earlier[1] and was attributed to the signal of steady-state thermopower superimposing on the photovoltaic component of the light-induced voltage. This explanation was supported by measurements of the frequency dependence of the bolometric response V_b (i.e. the signal which is generated by thermal modulation of the resistance of an illuminated sample connected to an external current source), which were performed in the same conditions as the study[1] of the light-induced voltages. Similar experiments were carried out in this work as well, and their results for one of the samples ($S3$) are displayed in Fig. 2. Also shown is the low-frequency part of the response of the light-induced component, where the reckoning is done from the plateau level. As follows from a comparison of these relations, the characteristic frequency of the cut-off, which is determined by the thermal time constant τ_{th} of the sample, is practically the same for both signals.

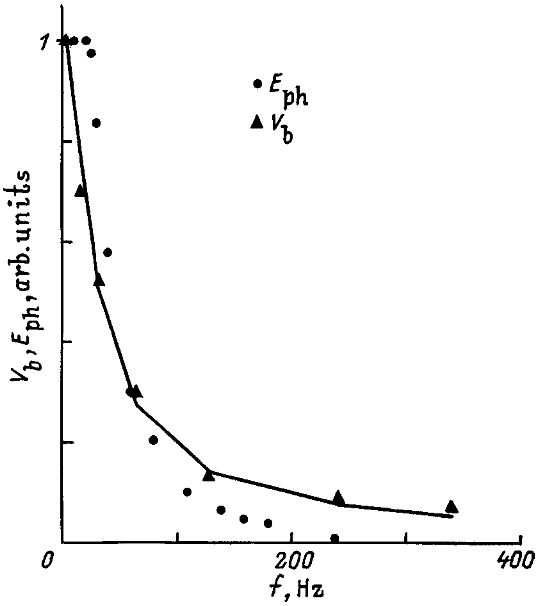

FIG. 2. Frequency dependence of the bolometric component V_b and of the low-frequency component of light-induced voltages (E_{ph}) in $S3$. The solid line is a fit of relation (1) to the bolometric response with a fitting parameter $\tau_{\mathrm{th}} = 8.8 \times 10^{-3}$ s.

A comprehensive study of the origin of the steady-state thermoelectric component of light-induced voltages is beyond the scope of this work. Therefore we shall limit ourselves to repeating the conjecture put forward in Ref. 1 that since the thermopower signal is seen also with the light spot focused symmetrically between the measuring contacts, it most probably is due to the presence of spatial inhomogeneities in the samples.

Turning now to a discussion of the photovoltaic response of the light-induced voltage (E_{ph}), one should stress the practically linear dependence of E_{ph} on the incident light intensity I ($I_{\max} \sim 10$ W$\cdot$cm^{-2}). Therefore we could expect the frequency dependence of E_{ph} to follow the standard relaxation relation

$$E_{\mathrm{ph}}(\omega) = E_{\mathrm{ph}}(0)(1 + \omega^2 \tau^2)^{-1/2}, \qquad (1)$$

where τ is a certain characteristic relaxation time. An attempt at fitting this relation to the experimental frequency responses (after subtraction from them of the thermoelectric component) met with success, however, only for $S2$ and $S4$ (Fig. 3). The steeper roll-off of the response of sample $S3$ did not permit a satisfactory fit (Fig. 4).

We believe the reason for such an unconventional behavior of the photovoltaic response in $S3$ to originate from an integrated character of the E_{ph} component, which represents actually the result of averaging of the contributions from elementary photoemf's (e_i) generated by individual inhomogeneities. Obviously enough, parameters e_i may exhibit a certain spread over a sample, both in their sign and

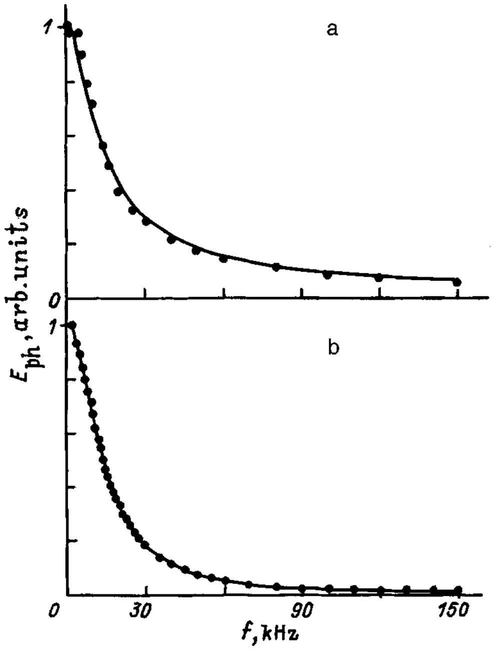

FIG. 3. Frequency response of the photovoltaic component in samples (a) $S2$ and (b) $S4$ fitted by relation (1) with the fitting parameter τ of 1.7 $\times 10^{-5}$ and 1.45×10^{-5} s for $S2$ and $S4$, respectively.

the magnitude of τ. To see how this may affect the frequency dependence of the resultant signal, consider a few simple examples.

We start with the case of two photoemfs (e_1 and e_2) of the same sign but differing in the relaxation times, τ_1 and τ_2. The frequency dependence of the resultant photoemf e_Σ can be derived by Fourier transforming the response of our system $[u(t)]$ to a single pulse

$$u(t)=u_1(t)+u_2(t)=\exp(-t/\tau_1)s(t)+\exp(-t/\tau_2)s(t),$$

or

$$U(\omega)=U_1(\omega)+U_2(\omega)=\tau_1/(1+i\omega\tau_1)+\tau_2/(1+i\omega\tau_2)$$
$$=[(\tau_1+\tau_2)+i2\omega\tau_1\tau_2]/(1+i\omega\tau_1)(1+i\omega\tau_2), \quad (2)$$

where $s(t)$ is the Heaviside function.

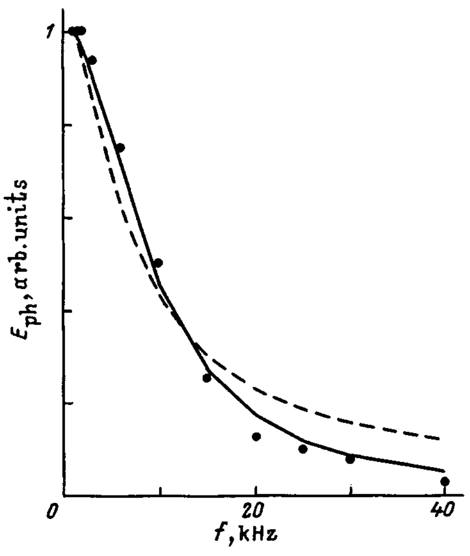

FIG. 4. Frequency response of the photovoltaic component in sample $S3$ fitted by relation (1) (dashed line) and (7) (solid line). In the latter case the curve was obtained with the following fitting parameters: $\tau_1=1.65\times 10^{-5}$ s, $\tau_2=1.8\times 10^{-5}$ s, $g_1=g_2$.

The $e_\Sigma(\omega)$ relation is determined by the modulus $|U(\omega)|$:

$$e_\Sigma(\omega)\sim|U(\omega)|\sim[1+\omega^2\tau^{*2}]^{1/2}/(1+\omega^2\tau_1^2)^{-1/2}$$
$$\times(1+\omega^2\tau_2^2)^{-1/2}, \quad (3)$$

where $\tau^*=2\tau_1\tau_2/(\tau_1+\tau_2)$.

For $\delta\tau=|\tau_1-\tau_2|\ll\tau_{1,2}$, Eq. (3) can be recast, to second-order terms, to an expression of the type (1):

$$e_\Sigma(\omega)\sim(1+\omega^2\tau_{av}^2)^{-1/2}, \quad (4)$$

where $\tau_{\mathrm{av}}=(\tau_1+\tau_2)/2$.

If, however, $\delta\tau\sim\tau_{1,2}$, the $e_\Sigma(\omega)$ relation may take on a two- (in a general case, a many-) step shape. In our opinion, it is this factor, i.e. the presence in a sample of several (at least two) types of elementary photoemf's with essentially different relaxation times that can account for the steps in the frequency response function in the plateau region (Fig. 1).

Consider now what will happen if e_1 and e_2 have opposite signs, all the other conditions remaining unchanged. For $U(\omega)$ we now obtain

$$U(\omega)=(\tau_1-\tau_2)/(1+i\omega\tau_1)(1+i\omega\tau_2), \quad (5)$$

whence it follows that

$$e_\Sigma(\omega)\sim|U(\omega)|\sim[1+\omega^2(\tau_1^2+\tau_2^2)+\omega^4\tau_1^2\tau_2^2]^{-1/2}. \quad (6)$$

We readily see that for frequencies $\omega\gg(\tau_1^{-2}+\tau_2^{-2})^{1/2}$ the resultant photoemf should exhibit a steeper decay, $\sim\omega^{-2}$.

Obviously enough, this consideration can be extended to any number of e_i. To do this, one will have to sum consecutively the complex amplitudes for e_i of either sign (after arranging them in groups close in magnitude of e_i and of τ_i) and introduce the properly averaged times τ_{av}, thus reducing the problem to the case of two (or several) photoemfs. The results thus obtained will naturally remain valid, at least from the qualitative standpoint. Thus the unusual high-frequency behavior of the photovoltaic effect in sample $S3$ can be accounted for by generation of elementary photoemfs of opposite signs, which produce at least two sum signals, e_Σ^+ and e_Σ^-, which are close in absolute magnitude and differ in statistically averaged relaxation times.

The existence of elementary photoemfs with opposite signs follows from the model[3] of the photovoltaic effect in YBCO films, which assumes generation at opposite interfaces of an inhomogeneity of counter-streaming photocurrents. The scatter in τ likewise does not come as a surprise, particularly since any degree of scatter will, in principle, be sufficient. The need of taking into account experimentally the statistic nature of photovoltaic signals in our samples is buttressed convincingly by the results of scanning the film surface with a focused laser beam (with the spot area $\sim$100 $\times$100 μm). All samples exhibited a noticeable variation of E_{ph} in magnitude, with even a sign reversal observed in sample $S4$ (a similar result was obtained also in Ref. 4), which correlates with the weaker-pronounced texture of this sample.

Thus application of the above results obtained on our samples, in particular, of Eq. (6), to approximating the frequency response in $S3$ appears well substantiated. In actual fact one used in place of Eq. (6) a more general expression, which included weighing coefficients g_1 and g_2 to take into account the spread in other (besides τ_{av}) parameters determining e_{Σ}^{+} and e_{Σ}^{-} (for instance, the number of the elementary component photoemfs):

$$E_{\mathrm{ph}}(\omega)=[(g_1\tau_1-g_2\tau_2)^2+\omega^2\tau_1^2\tau_2^2(g_1-g_2)^2]^{1/2} \times(1+\omega^2\tau_1^2)^{-1/2}(1+\omega^2\tau_2^2)^{-1/2}. \quad (7)$$

The fitting parameters $g_{1,2}$ and $\tau_{1,2}$ are connected through an obvious relation $E_{\mathrm{ph}}(0)=g_1\tau_1-g_2\tau_2$. The solid line in Fig. 4 is a fit by Eq. (7) to the frequency response of $S3$; also presented are the fitting parameters used.

An analysis of the frequency-response fitting for the samples under study shows that despite the considerable differences in their morphology, the values of τ obtained are fairly close. Taking into account the differences between the inhomogeneities (at least in $S2$ and $S3$, Ref. 3) contributing to the photovoltaic effect, this result, like the nature of τ itself, requires interpretation. One would need for this, however, information on the electronic properties of the inhomogeneities under study, which are practically lacking at present. Therefore the above results can be analyzed only within the general concepts of the photovoltaic response.

It is known[5] that the relaxation mechanism of the photovoltaic effect (forming in the region of the *p-n* junction, or of the metal-semiconductor contact, as is assumed in our case) depends in a general case on the relation between the width of the space-charge region (SCR) of the rectifying barrier, w, and the diffusion length of minority carriers, l (which in our case are generated in the semiconducting layer). For $w \gg l$, τ is determined by the transit time t_d through the SCR for the slowest carriers. In the opposite case ($w \ll l$), the photovoltaic effect is dominated by diffusion to the SCR of light-generated minority carriers, and it is their lifetime that determines τ.

As follows from the model of the photovoltaic effect in YBCO,[3] generation of the experimentally observed voltages requires that the effective inhomogeneity width d exceed 10^{-5} cm. Application of this criterion to data on the morphology of samples $S2$ and $S3$ permitted identifying the types of the inhomogeneities most likely to contribute to the photovoltaic effect. Their thickness (which does not exceed a few microns) determines the maximum value of w, which can then be used to estimate the carrier mobility μ satisfying the relation $t_d \sim w^2/\mu\varphi \sim \tau$ (here φ is the height of the barrier bounding the inhomogeneity). For $w \sim d \sim 10^{-4}$ cm, $\tau \sim 10^{-5}$ s, and $\varphi \sim 10^{-1}$ V, we obtain $\mu \sim 10^{-2}$ cm^2 $\cdot$V^{-1}s^{-1}. Although such a small value of μ is, in principle, reconcilable with carrier mobility in disordered media, it was obtained for a clearly overestimated w. Indeed, a priori one should expect values $w \sim 10^{-6}$ cm. In this case the corresponding estimate of μ becomes physically unacceptable, which should be considered as an argument for the validity of the second mechanism of the photovoltaic effect in our films.

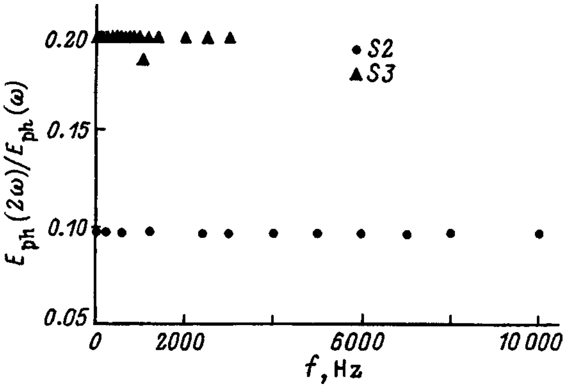

FIG. 5. Ratio of the light-induced signal measured at double modulation frequency to that at the fundamental-frequency plotted vs frequency for samples $S2$ and $S3$.

The above estimate of w follows from the expected high concentration of free (n) and/or localized (n_{loc}) carriers making up the SCR. Indeed, using for w the well-known expression[6] for the width of the Schottky-barrier SCR, the above value of w is obtained with n (n_{loc})$\sim 10^{19}$ cm^{-3} (for reasonable estimates of the dielectric permittivity). The existence of such free-carrier concentrations in these regions has been confirmed to a certain extent by the discovery in our samples of a photovoltaic signal at the double modulation frequency.

In principle, the presence of higher harmonics in the photovoltaic signal does not come as a surprise, if one takes into account the nonlinear dependence of photodiode current density on voltage V_0 across it.[5] The amplitude ratio of the fundamental to second harmonic, $E_{\mathrm{ph}}(2\omega)$, is determined by a parameter eV_0/kT (here e is the electronic charge, k is the Boltzmann constant, and T is temperature), which in our case ($V_0 \sim E_{\mathrm{ph}} \sim 3\times10^{-7}$ V and $T=300$ K) is, in order of magnitude, 10^{-5}. At the same time the experimental values of $E_{\mathrm{ph}}(2\omega)/E_{\mathrm{ph}}(\omega)$ were found to be about four orders of magnitude larger (Fig. 5). In the conditions where $E_{\mathrm{ph}}(I)$ is a linear relation, the only reason for such large $E_{\mathrm{ph}}(2\omega)$ signals can lie in sample resistance modulation. Note also that, while for $f<100$ Hz the change in the resistance could be assigned to heating of the films, at higher frequencies it could be associated only with photoconductivity of the nonmetallic regions in the samples. This posturate was supported by measurements of V_b in $S2$ and $S3$ carried out over a broader frequency range (Fig. 6). As seen from the figure, at $f \sim 100-300$ Hz the signal reaches a plateau, and only after this it decays for $f>0.5-1$ kHz. Fitting the points in Fig. 6 with a relation of the type (1) permitted estimation of the time τ_{ph} associated with relaxation of photoexcited carriers (n_{ph}). Their concentration can be estimated from the expression $n_{ph}=\beta\alpha I\tau_{\mathrm{ph}}$ by substituting into it the absorption coefficient $\alpha \sim 10^5$ cm^{-1} (which, in order of magnitude, is equal to the value of α for bulk YBCO) and incident intensity I ~ 3 W$\cdot$cm$^{-2} \sim 3\times10^{19}$ photons/(cm^{2}s) (the quantum yield β is assumed to be one), which yields

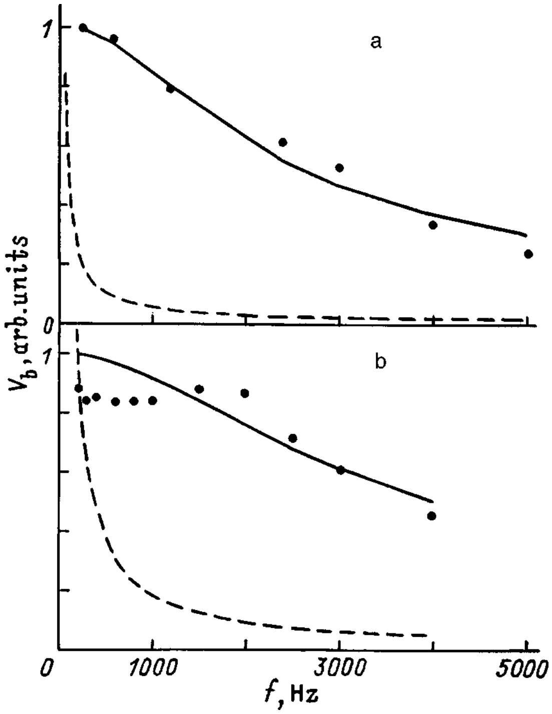

FIG. 6. High-frequency behavior of the signal corresponding to the bolometric component in sample $S2$ (a) and $S3$ (b). The solid line displays the fit using relation of the type (1) obtained with the fitting parameters $\tau_{\mathrm{ph}}=1.0\times10^{-4}$ s and $\tau_{\mathrm{ph}}=7\times10^{-5}$ s for $S2$ and $S3$, respectively. The dashed lines correspond to the frequency dependence of the thermal V_b component obtained by extrapolating low-frequency data (obtained with $\tau_{\mathrm{th}}=8.8\times10^{-3}$ s and $\tau_{\mathrm{th}}=1.25\times10^{-2}$ s for $S2$ and $S3$, respectively).

$n_{\mathrm{ph}}\sim10^{20}$ cm^{-3}. Considering that the $E_{\mathrm{ph}}(2\omega)$ signal observed in these conditions corresponds to a change in sample resistance by about 5–10%, the equilibrium carrier concentration in the nonmetallic (photoconducting) regions corresponds to $n\sim10^{21}$ cm^{-3}.

We are naturally interested in the extent to which the inhomogeneities under study here contribute to total resistance [which manifests itself, for instance, in the existence of residual resistance in samples $S2$ and $S3$ below T_c (Figs. 1 and 2 in Ref. 3) and of photoconductivity in the nonmetallic volume of the films. In this sense the situation with $S2$ appears easier to understand. A comparison of Raman spectra [which show a superconducting phase to be dominant (see Fig. 5 in Ref. 3)] with electron microscope images of $S2$ (Fig. 3 in Ref. 3) suggests that the bulk of the sample is mostly occupied by superconducting microcrystals, which are surrounded by nonmetallic layers suppressing superconducting current through the film. Obviously enough, it is with these layers that one should associate the sample photoconductivity as well. On the other hand, these inhomogeneities were considered[3] as the most likely sources of the photovoltaic effect in $S2$. In this case one could apply to them, with good reason, the above estimate of n arguing for the validity of $w\lesssim10^{-6}$ cm which, as already pointed out, excludes any connection of the photovoltaic effect in $S2$ with carrier generation in the SCR and permits identification of τ with the lifetime of minority carriers. It is unlikely that the situation with $S3$ and $S4$ is different, and this is suggested, in particular, by the above-mentioned closeness of the values of τ in all the samples studied. It thus appears that the mechanism of the photovoltaic effect in the YBCO films under study involves diffusion of minority carriers generated by light in the nonmetallic regions of the internal interfaces, which exist in the bulk of the superconducting phase in YBCO.

In conclusion, it appears useful to compare our values of τ_{ph} with photoconductivity relaxation studies performed on samples of the tetragonal, partially oxidized, YBCO phase. (It should be pointed out that the true lifetimes dominated by the recombination time may differ from the ones obtained here because of the multiple release and recapture of carriers by shallow levels.) For instance, Ref. 7 quotes $\tau_{ph}\sim2\times10^{-4}$ s for $\mathrm{YBa_2Cu_3\ O_x}$ films ($x<6.4$). At the same time, as follows from data[8] obtained for $\mathrm{YBa_2Cu_3O_{6.3}}$ crystals, τ_{ph} is of the order of a few microseconds at $T=300$ K. The values of τ_{ph} obtained by us lie in between, which, in principle, does not exclude the nonmetallic regions in the samples (including the inhomogeneities under study) to be close in properties to the insulating phase of YBCO.

Thus our study of the response of light-induced voltages in superconducting YBCO films performed at frequencies from 1.5 Hz to 150 kHz has confirmed the existence in them of photovoltaic voltages assumed[3] to be due to the rectifying barriers at internal interfaces in the bulk of the superconducting YBCO phase, which exist at extended inhomogeneities. The observed deviation of the frequency response curves from the conventional relaxation behavior is a consequence of the statistical nature of the signals, which represent actually the sum of elementary photoemfs generated by individual inhomogeneities differing both in the sign and magnitude of the relaxation times. Measurements of photoemfs generated at the double modulation frequency, as well as of the photoresponse of samples connected to an external current source, have yielded additional information on the photoconducting properties of the samples. An analysis of the totality of the experimental data obtained permitted relating the mechanism of the photovoltaic effect to the diffusion of minority carriers created at the inhomogeneities under study, and estimation of their lifetime.

[1] A. I. Grachev, I. V. Pleshakov, A. P. Paugurt, and S. G. Shul'man, Fiz. Tverd. Tela (St. Petersburg) **38**, 2922 (1996) [Phys. Solid State **38**, 1598 (1996)].
[2] A. I. Grachev and I. V. Pleshakov, Solid State Commun. **101**, 507 (1996).
[3] A. I. Grachev, V. Yu. Davydov, P. M. Karataev, S. F. Karmanenko, A. P. Paugurt, and I. V. Pleshakov, Physica C **288**, 268 (1997).
[4] H. S. Kwok, J. P. Cheng, and S. Y. Dong, Phys. Rev. B **43**, 6270 (1991).
[5] T. S. Moss, G. J. Burrell, and B. Ellis, *Semiconductor Opto-Electronics* (Butterworths, London, 1973).
[6] E. H. Roderick, *Metal-Semiconductor Contacts* (Clarendon Press, Oxford, 1978; Radio i Svyaz', Moscow, 1982).
[7] R. Boyn, K. Löbe, H.-U. Habermeier, and N. Pruß, Physica C **181**, 75 (1991).
[8] G. Yu, A. J. Heeger, G. Stucky, N. Herron, and E. M. McCarron, Solid State Commun. **72**, 345 (1989).

Translated by G. Skrebtsov

PHYSICS OF THE SOLID STATE VOLUME 40, NUMBER 11 NOVEMBER 1998

Pressure- and doping-induced interlayer charge transfer in mercury cuprates

S. Sh. Shil'shteĭn

Russian Scientific Center ''Kurchatov Institute'', 123182 Moscow, Russia

(Submitted February 10, 1998; resubmitted May 14, 1998)
Fiz. Tverd. Tela (St. Petersburg) **40**, 1980–1983 (November 1998)

An analysis of the variation of site parameters has permitted determination of the interlayer charge transfer in mercury cuprates induced by pressure and incorporation of superstoichiometric oxygen and fluorine anions into $HgBa_2CuO_4$. It is shown that the charge transfer is governed by charge balance between the mixed-valence cations, namely, the mercury in the charge reservoir and the copper in the conducting layers. © *1998 American Institute of Physics.* [S1063-7834(98)00411-0]

The crystal structure of mercury cuprates, which have the highest superconducting transition temperatures to date, has been studied intensively in recent years, primarily in the simplest compound $HgBa_2CuO_{4+\delta}$. Neutron diffraction measurements yielded detailed information on the site parameters of all atoms and on their dependence on stoichiometry and external pressure, as well as on the position of superstoichiometric oxygen.[1–6] The correlations between the amount of this oxygen and the critical transition temperature were established, but, in contrast to yttrium-barium cuprates, structural data did not provide an unambiguous answer for how this interlayer charge transfer takes place. The objective of the present work was to determine from high-precision neutron-diffraction data the in-plane and ionic charge in the mercury cuprates and the amount of interlayer charge transfer induced by pressure and incorporation of superstoichiometric anions,[2,5–7] using the model[8] of Coulomb-induced layer splitting.

The (HgO_δ) and (CuO_2) layers in the mercury cuprates $HgBa_2Ca_{n-1}Cu_nO_{2n+2+\delta}$ sandwich a (BaO) layer split into separate Ba^{+2} and O^{-2} sheets (Fig. 1) by Coulomb interaction between the positively charged (HgO_δ) and negatively charged (CuO_2) layers.

The splitting of the (BaO) layer is connected with the charge difference between the adjacent layers, $Q = Q_m - Q_c$, through an empirical relation[9]

$$\Delta = -0.045 + 0.2475\,Q, \qquad (1)$$

where the splitting Δ is in Å, and the charge is expressed in units of electronic charge. In accordance with Eq. (1), a change in the (BaO) layer splitting implies a change in the charge on the adjacent layers. Thus one can, based on the site parameters determined from diffraction measurements, derive direct information on charge transfer from the (HgO_δ) reservoir to the (CuO_2) conducting layers. This provides a possibility of following the variation of the charge on the layers and on individual ions, as this was done[9] for $YBa_2Cu_3O_{7-y}$ by changes in the oxygen stoichiometry $(0<y<1)$.

Diffraction data on the site parameters in various mercury cuprates obtained at high pressures indicate that the (BaO) splitting in all these compounds varies similarly with pressure (Fig. 2).[6] The splitting at $P=5$ GPa decreases by more than 10%, whereas the cell dimensions decrease only by 1–1.5%.

This implies nonuniform deformation of the crystal, and the presence of a ''weak'' element, which is the spacing between the Ba^{2+} and O^{-2} layers, is due to a change of some interactions in the crystal rather than simply to a decrease in volume. The Coulomb model assigns this to a weakening of the coupling between adjacent layers, which is caused, in its turn, by the reduced difference between the charges of the mercury and copper layers. Because the mercury layer is charged positively, and the copper one, negatively, the decrease of Q may be considered as an unambiguous indication that application of a high pressure or a reduction of the volume initiates transfer of a positive charge from the reservoir (the mercury layer) to the conducting copper layers.

The change in the (BaO) layer splitting in mercury cuprates is $d\Delta/dP \cong -0.02$ Å/GPa. According to Eq. (1), the pressure-induced interlayer charge transfer in all cuprates is $-dQ/dP \cong 0.08$/GPa. At $P=10$ GPa, the charge transferred from the mercury to the copper layers is 0.8. This means that the ionic charge of mercury changes from close to $+2$ at

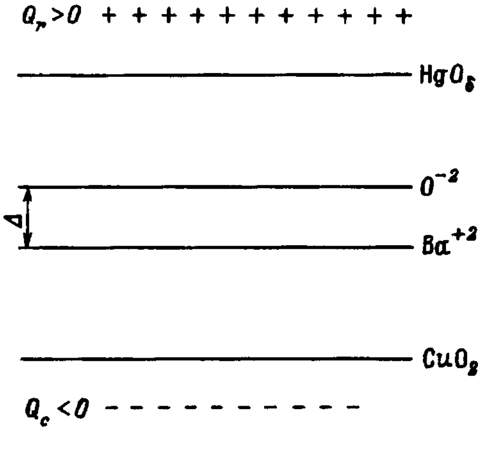

FIG. 1. Layer arrangement in mercury cuprate lattice (fragment of the structure). Q_m — mercury-layer charge, Q_c — copper-layer charge (both are reduced to the area of the unit-cell basal plane).

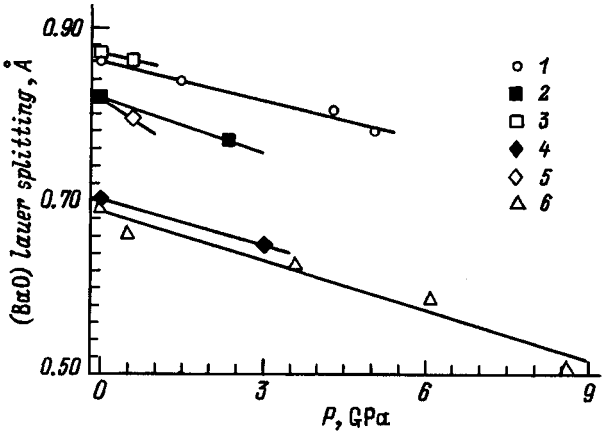

FIG. 2. (BaO) layer splitting in (*1–3*) $HgBa_2CuO_{4+\delta}$, (*4,5*) $HgBa_2CaCu_2O_{6+\delta}$, and (*6*) $HgBa_2Ca_2Cu_3O_{8+\delta}$ vs pressure.[6]

zero pressure to a value close to $+1.2$. Thus most of the mercury ions in the reservoir layer are transferred by this pressure from the $+2$ to $+1$ state. A similar transfer of positive charge from the (CuO_y) reservoir layers to the conducting (CuO_2) layers induced by an external pressure occurs also in the yttrium-barium cuprates,[10] although the transferred charge and the variation of the ionic charges in the latter are smaller. The qualitative changes, however, are the same, namely, in the mercury cuprates a decrease of the mercury ion charge brings about an increase of the ionic charge on copper, whereas in the yttrium-barium cuprates a decrease of the chain-copper ion charge results in an increase of the plane-copper charge.

Neutron diffraction studies of $HgBa_2CuO_{4+\delta}$, the simplest representative of the mercury cuprate family, yielded the site parameters of all atoms for the compositions $0.06 < \delta < 0.19$.[2] They were used to construct the dependence of the (BaO) layer splitting on composition displayed in Fig. 3a. One readily sees a decrease of the splitting with increasing amount of oxygen doped into the mercury layer. This indicates a transfer of positive charge to the copper layers from the mercury reservoir when superstoichiometric oxygen is incorporated into it. In accordance with the universally accepted concepts, transfer of a positive charge results in an increase in hole concentration in the conducting layer, and this can be responsible for the change of the superconducting transition temperature in superstoichiometric mercury cuprates.

Incorporation of superstoichiometric oxygen reduces the lattice periods, i.e. reduces the volume. The linear compression induced by oxygen doping is, however, 0.1–0.2%, i.e. it is still smaller than that produced by application of pressure, while the (BaO) layer splitting decreases by more than 10%. Hence the effect of doping cannot be reduced to a change in volume only, and instead is due to a change in the ionic charges.

To approach quantitative determination of the layer charges Q_m and Q_c, one has to take into account, besides condition (1), the charge neutrality condition as well. Assuming the barium ionic charge to be $+2$, and the charge on the oxygen ions, -2, we obtain for the charge neutrality condition

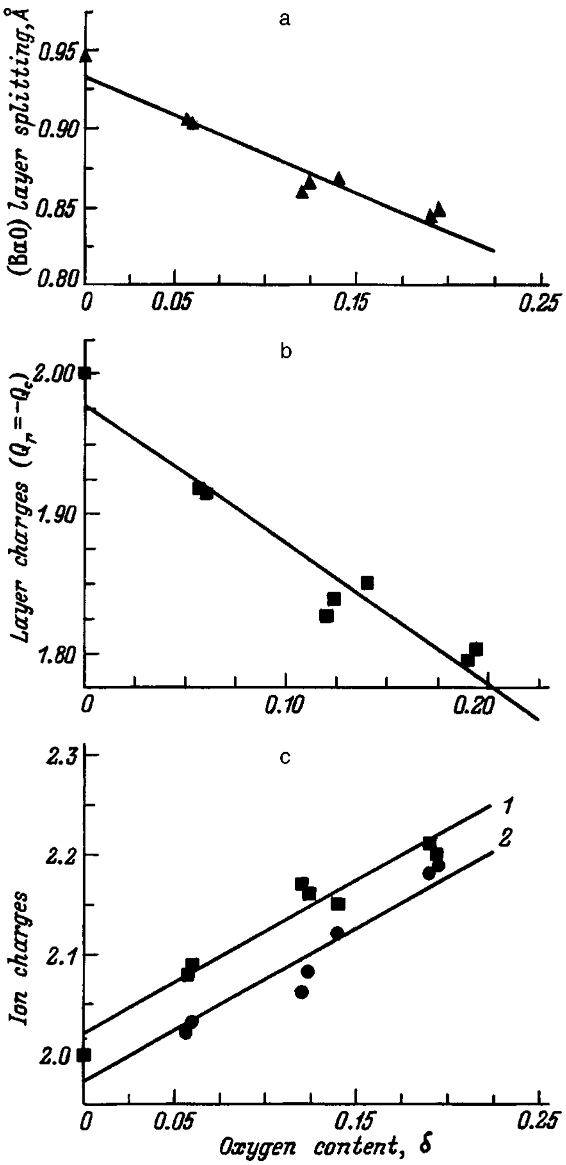

FIG. 3. (a) (BaO) layer splitting, (b) mercury, Q_m, and copper, Q_c, layer charge, and (c) charge on (*1*) copper and (*2*) mercury ions in $HgBa_2CuO_{4+\delta}$ vs the content of superstoichiometric oxygen.

$$Q_m + Q_c = 0\,. \tag{2}$$

Solving Eqs. (1) and (2) yields the layer charge distribution as a function of composition (Fig. 3b). For $\delta = 0.2$, the charge transfer is 0.2 per (CuO_2) layer. Hence it is close to that occurring under a pressure of a few GPa, and this correlates with the observation that application of this pressure and incorporation of excess oxygen result in an increase of the critical temperature in $HgBa_2CuO_{4+\delta}$.

Knowing the layer charge [and assuming that $q(O) = -2$], one can readily find the copper and mercury ionic charges in $HgBa_2CuO_{4+\delta}$. It turns out that the charges of both ions are slightly larger than $+2$ (Fig. 3c) and do not differ much from one another. Thus when excess oxygen ions are doped into the mercury cuprate, their negative charge is compensated approximately equally by an increase

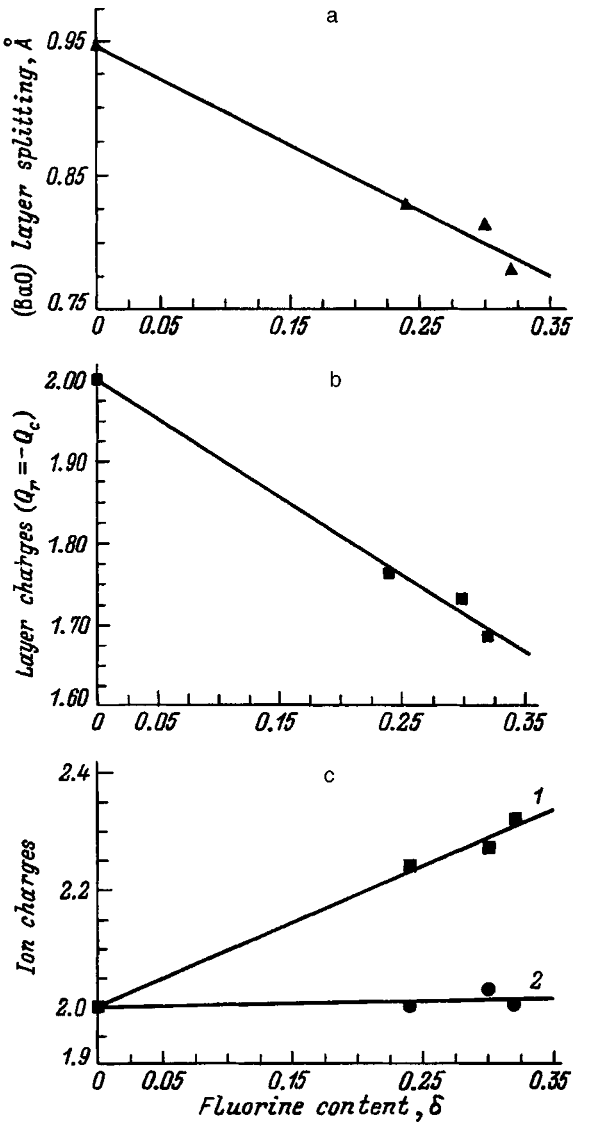

FIG. 4. (a) (BaO) layer splitting, (b) mercury, Q_m, and copper, Q_c, layer charge, and (c) charge on (*1*) copper and (*2*) mercury ions in $HgBa_2CuO_4F_\delta$ vs the content of superstoichiometric fluorine.

of the charge on the mercury and copper ions. In other words, only half of the positive charge produced in ionization of the superstoichiometric oxygen transfers to the (CuO_2) conducting layer, with the other part remaining in the charge reservoir layer. As a result, only a small fraction (about 10%) of ions of both species, copper in the conducting layer and mercury in the reservoir, reside in the $+3$ state, while the state of the others is $+2$. It is universally believed that copper ions with a charge of $+3$ are present in high-T_c superconductors. For mercury ions this charge is apparently less typical, but one obtained direct evidence[11] for their existence in $HgBa_2CuO_{4+\delta}$ from XPS spectra of this compound.

A neutron diffraction study of $HgBa_2CuO_4F_\delta$ yielded its site parameters for compositions $0.24<\delta<0.32$.[7] These data were combined with the results of Ref. 2 to construct the dependence of (BaO) splitting on the amount of fluorine in the mercury layer (Fig. 4a). Fluorine incorporation affects the splitting too, and its decrease reaches the same value (about 10%) for the excess anion concentration of 0.2 per formula unit for both fluorine and oxygen. Hence in both cases incorporation of superstoichiometric anions results in a transfer of positive charge to the copper layers. We used the procedure described above to construct the dependences of the charge in the layers and on cations of both species on composition (Fig. 4b and 4c). It was found that the ionic charge of mercury in the cuprate with excess fluorine remains $+2$, whereas the charge on copper ions increases with the amount of fluorine. This means that the negative charge of the fluorine ions is compensated in this case only by an increase of the copper charge.

The above results permit one to describe the ionic charge balance in mercury cuprates setting in under changes in pressure and composition in the following way. Application of an external pressure transfers positive charge from the mercury layers, which act as charge reservoirs, to the conducting copper layers. This transfer is realized only through charge exchange between the mercury and copper ions, in which the charge on the copper ions increases, and that on the mercury ions, decreases. The positive charge created in the ionization of oxygen or fluorine atoms when superstoichiometric anions are incorporated into $HgBa_2CuO_4$ becomes redistributed differently between the mercury and copper layers. While in the case of fluorine all of the charge transfers to the copper layers, incorporation of oxygen leaves about half of the charge on mercury ions in the mercury layers. This difference accounts for the independence of the hole concentration in copper layers on the charge of superstoichiometric ions pointed out in Ref. 7. Another difference between the cuprates with excess oxygen and fluorine consists in that incorporation of oxygen into mercury layers, in contrast to fluorine, results in the formation in them of Hg^{+3} ions. It may be conjectured that the presence of negative ions with a higher charge in the nearest environment favors the $Hg^{+2}\rightarrow Hg^{+3}$ transition.

Interlayer charge transfer induced by doping or a decrease in volume is made possible by the presence of mixed-valence atoms both in the reservoir and in the conducting layers. While the mixed valence of copper and the part played by it in carrier generation in (CuO_2) layers is being discussed by most authors, the significance of the mixed valence of the cation reservoir is recognized to a lesser degree. For instance, the difficulties met in the attempt to explain the structural transformations induced by doping of copper cuprates stem from the a priori rejection of the possibility that the charge on the mercury ions can change.

It appears of interest to compare interlayer charge transfer initiated by a change in the anion stoichiometry in mercury cuprates and in the most intensively studied cuprate $YBa_2Cu_3O_{7-y}$. In both cases, the interlayer transfer is driven by balance in the cation charge. The positive charge of $+2$ released when an additional oxygen ion is doped into $YBa_2Cu_3O_6$ is distributed in such a way that two (CuO_2) layers gain a net charge of $+0.5$, and the remainder is expended in increasing the ionic charge of the chain copper.[9] In other words, about a fourth of the charge coming from the excess anions transfers to the conducting layers. When excess oxygen is doped into $HgBa_2CuO_4$, the charge, which is $+0.4$ for $\delta=0.2$, divides into two approximately equal parts, with one of them increasing the copper ionic charge in the (CuO_2) layers, and the other, increasing the charge on mercury ions in the layers receiving the excess oxygen. The charge produced in incorporation of excess fluorine into $HgBa_2CuO_4$ ($+0.3$ for $\delta=0.3$) increases the charge on the copper ions, while the charge of the mercury ions in fluorine-doped layers remains unchanged.

The above data on interlayer charge transfer have been obtained from an analysis of bond lengths and ion layer splitting. They stress the need of high-precision determination of structural parameters.

Coexistence in superstoichiometric mercury cuprates of copper and mercury ions with different charges may give rise to a variety of effects, such as crystal-field rearrangement, features in the Debye–Waller factor, a change in heat capacity, optical, and other physical properties, as this occurs in ionic crystals with charged defects.

Thus interlayer charge transfer in high-T_c superconductors is dominated by the charge balance between mixed-valence cations. Application of a high pressure transfers positive charge from the cations in the reservoir to those in the conducting layers. The actual results of incorporating extra dopant anions into the reservoir depend on what fraction of the excess positive charge is transferred from the reservoir to the conducting layers. In the yttrium-barium cuprates this fraction does not exceed one fourth, whereas in the mercury cuprates it may be as high as one half to one, depending on the excess anion species.

The author is grateful to A. M. Balagurov and V. A. Somenkov for fruitful discussions.

Support of the Russian Fund for Fundamental Research (Grants 96038 and 96-15-96473) is gratefully acknowledged.

[1] Q. Huang, J. W. Lynn, Q. Xiong, and C. W. Chu, Phys. Rev. B **52**, 462 (1995).

[2] A. M. Balagurov, V. V. Sikolenko, V. G. Simkin, V. V. Alyoshin, E. V. Antipov, A. A. Gippius, D. A. Mikhaĭlova, S. N. Putilin, and F. Boure, Physica C (in press).

[3] J. L. Wagner, P. G. Radaelli, D. G. Hinks, J. D. Jorgensen, J. F. Mitchell, B. Dabrowski, G. S. Knapp, and M. A. Beno, Physica C **210**, 447 (1993).

[4] V. L. Aksenov, A. M. Balagurov, B. N. Savenko, V. P. Glazkov, I. N. Goncharenko, V. A. Somenkov, E. A. Antipov, S. N. Putilin, and J. J. Capponi, High Press. Res. **14**, 127 (1995).

[5] A. R. Armstrong, W. I. F. David, I. Gameson, P. P. Edwards, J. J. Capponi, P. Bordet, and M. Marezio, Phys. Rev. B **52**, 15551 (1995).

[6] V. L. Aksenov, A. M. Balagurov, B. N. Savenko, D. V. Sheptyakov, V. P. Glazkov, V. A. Somenkov, S. Sh. Shilstein, E. V. Antipov, and S. N. Putilin, Physica C **275**, 87 (1997).

[7] A. M. Abakumov, V. L. Aksenov, V. A. Alyoshin, E. V. Antipov, A. M. Balagurov, D. A. Mikhaĭlova, S. N. Putilin, and M. G. Rozova, Preprint JINR, E14-97-234, Dubna (1997), 13 pp.

[8] S. Sh. Shil'shtein, A. S. Ivanov, and V. F. Somenkov, Sverkhprovodimost' (KIAE) **7**, 903 (1994); Physica C **245**, 181 (1995).

[9] S. Sh. Shil'shtein and A. S. Ivanov, Fiz. Tverd. Tela (St. Petersburg) **37**, 3268 (1995) [Phys. Solid State **37**, 1796 (1995)].

[10] S. Sh. Shil'shtein, Fiz. Tverd. Tela (St. Petersburg) **38**, 1724 (1996) [Phys. Solid State **38**, 951 (1996)].

[11] C. S. Gopinath and S. Subramanian, Physica C **232**, 222 (1994).

Translated by G. Skrebtsov

PHYSICS OF THE SOLID STATE VOLUME 40, NUMBER 11 NOVEMBER 1998

SEMICONDUCTORS AND INSULATORS

Structural study of thermal-oxide films on silicon by cathodoluminescence

M. V. Zamoryanskaya and V. I. Sokolov

A. F. Ioffe Physicotechnical Institute, Russian Academy of Sciences, 194021 St. Petersburg, Russia

(Submitted April 3, 1998)
Fiz. Tverd. Tela (St. Petersburg) **40**, 1984–1989 (November 1998)

A study of cathodoluminescence spectra of silicon oxide films grown thermally on silicon is reported. It has been established that the cathodoluminescence properties of thermal films are nonuniform in depth and depend on the growth conditions and characteristics of the silicon substrate. © *1998 American Institute of Physics.* [S1063-7834(98)00511-5]

Growth of thermal oxide on silicon involves a variety of physicochemical processes, whose nature largely remains unclear. The electrophysical characteristics of the interface, which determine the parameters of planar devices, however, reflect the structure of the oxide film.[1]

Luminescence is one of the most informative tools for probing defects in the structure and composition. Using a focused, high-energy electron beam for luminescence excitation offers a number of advantages over photoluminescence. First, the high-energy of electrons (from 1 keV up) permits one to excite all luminescence centers existing in the oxide, including those excited in the intrinsic-absorption band (6–8 eV). Second, one can obtain emission spectra from various depths in the film, because electrons penetrate into the sample to distances depending on electron energy.[2] Electrons of 1-keV energy penetrate into SiO_2 to a depth of about 200 Å.

The main objective of this work was to probe by cathodoluminescence the structure of thermally generated SiO_2 films (defect distribution throughout the film thickness).

1. EXPERIMENTAL TECHNIQUES

The experimental samples were films of thermally produced silicon oxide 0.15–0.4 μm thick, which were grown by oxidation in dry and humid oxygen at 1050 °C. As substrates served plates of *n* silicon (BKEF-0.01 and KÉ-100) and *p* silicon (KDB-1 and KDV-0.1) with (111) orientation of the operating surface.

The cathodoluminescence studies were carried out on a CAMEBAX electron probe microanalyzer provided with a built-in optical microscope and a cathodoluminescence spectrometer which permits measurements within the 270–800-nm range.[3] To study the variation of cathodoluminescence spectra with depth, the sample was made wedge-shaped with a small angle by chemical etching. The spectra were taken at an electron energy of 1 keV. The electron beam scanned the wedge in steps of a few microns. This provided a resolution in depth of 40–100 Å, depending on the wedge angle.

2. MAIN RESULTS AND DISCUSSION

Two emission bands associated with intrinsic structural defects, at 450 nm (2.65 eV) and 640 nm (1.9 eV), were reliably identified in the luminescence spectra of amorphous SiO_2 films, glass, and quartz. The blue band (2.65 eV) originates from the forbidden singlet-triplet transition in the doubly-coordinated silicon molecular complex, and the red band (1.9 eV) is due to the presence of nonbridging oxygen.[4] High-energy excitation gives rise to the appearance of self-trapped exciton emission in the 2.2–2.6-eV region, namely, at 2.6 eV for quartz, at 2.3 eV for amorphous SiO_2, and at 2.2 eV for crystobalite.[5]

The spectra obtained by us exhibit both bands associated with intrinsic film defects, at 1.9 and 2.65 eV. The latter band is the strongest in thermal films. In many spectra it shows an asymmetry on the side of lower energies, which could be attributed to exciton emission in the 2.6–2.1-eV interval.

A. Cathodoluminescence of films grown in dry and humid oxygen

Figures 1 and 2 display cathodoluminescence spectra obtained from different depths of films grown in humid (Fig. 1) and dry (Fig. 2) oxygen on *p* silicon (type KDB-0.1).

The spectra of humid-grown films obtained from the region close to the interface are dominated by a band peaking at 2.2–2.3 eV (spectra *1* and *2*). The spectra obtained from central regions of the film no longer contain this band. In spectra *3* and *4*, a band peaking at 1.9 eV becomes prominent, and spectrum 5 exhibits one symmetrical band at 2.65 eV. On the surface (spectrum *6*), a new band at 3 eV appears, which is possibly due to a boron impurity.

The films grown in dry oxygen have a five times higher intensity. The spectrum is dominated by a band peaking at 2.65 eV. The emission of the nonbridging oxygen is very weak.

The maximum of the ''exciton'' luminescence shifts from 2.14 eV at the interface to 2.45 eV on the surface.

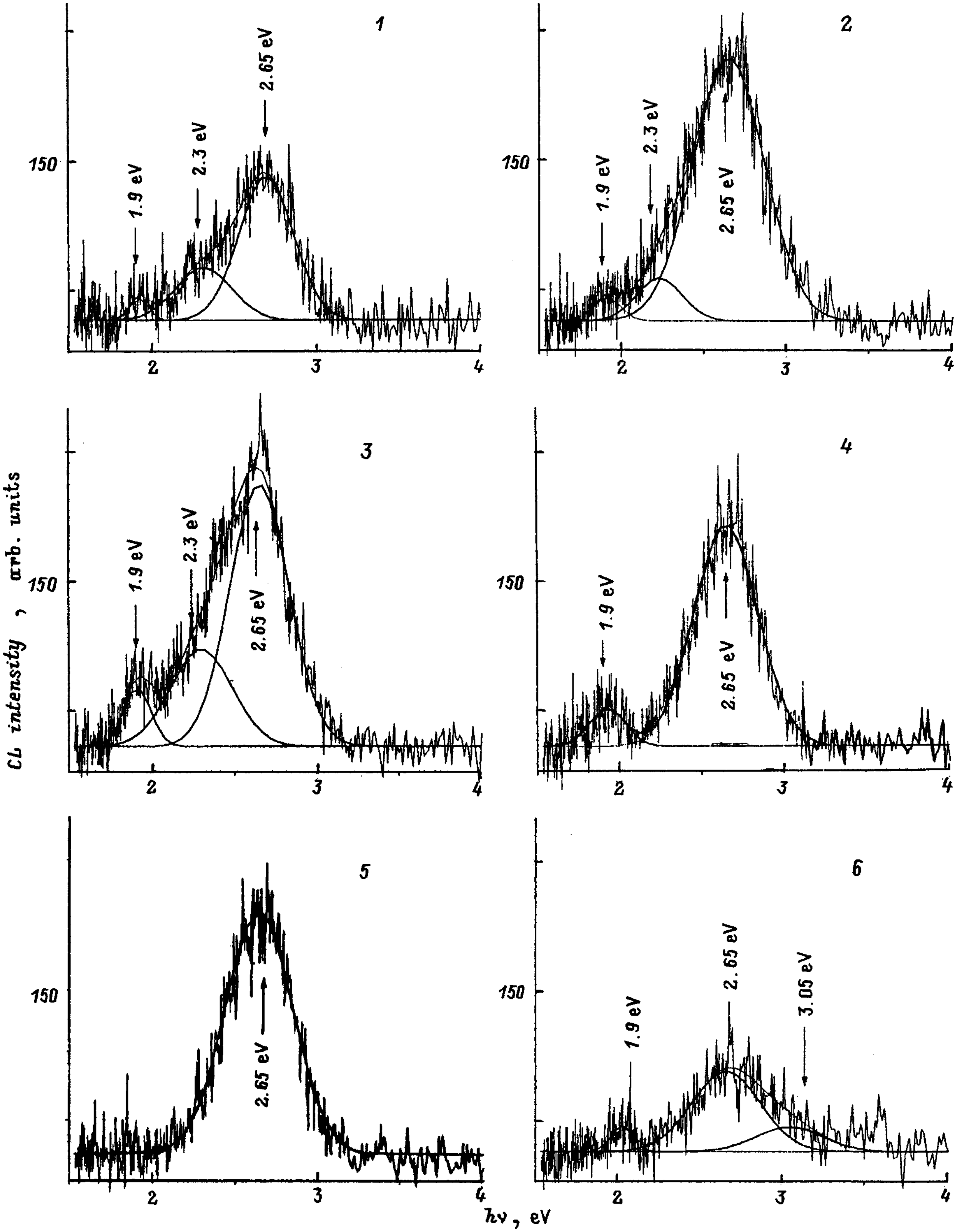

FIG. 1. Cathodoluminescence spectra of a thermally oxidized film grown on *p* silicon (KDV-0.1) in humid oxygen. *1* — spectrum obtained near the interface, *2,3,4,5* — spectra measured from different depths of the film progressively farther away from the interface, *6* — near-surface spectrum.

B. Dependence of film cathodoluminescence spectra on the silicon type

Figure 3 displays cathodoluminescence spectra obtained near the interface from films grown on different types of silicon: *1* — KDV-0.1, *2* — BKEF-0.01, and *3* — KE-100 in dry oxygen. The spectra differ primarily in the change of the 2.2–2.4-eV band in position and relative intensity. Films prepared of *n* silicon exhibit this band at 2.2 eV, and the higher is its relative intensity, the lower is the free-carrier concentration in the substrate.

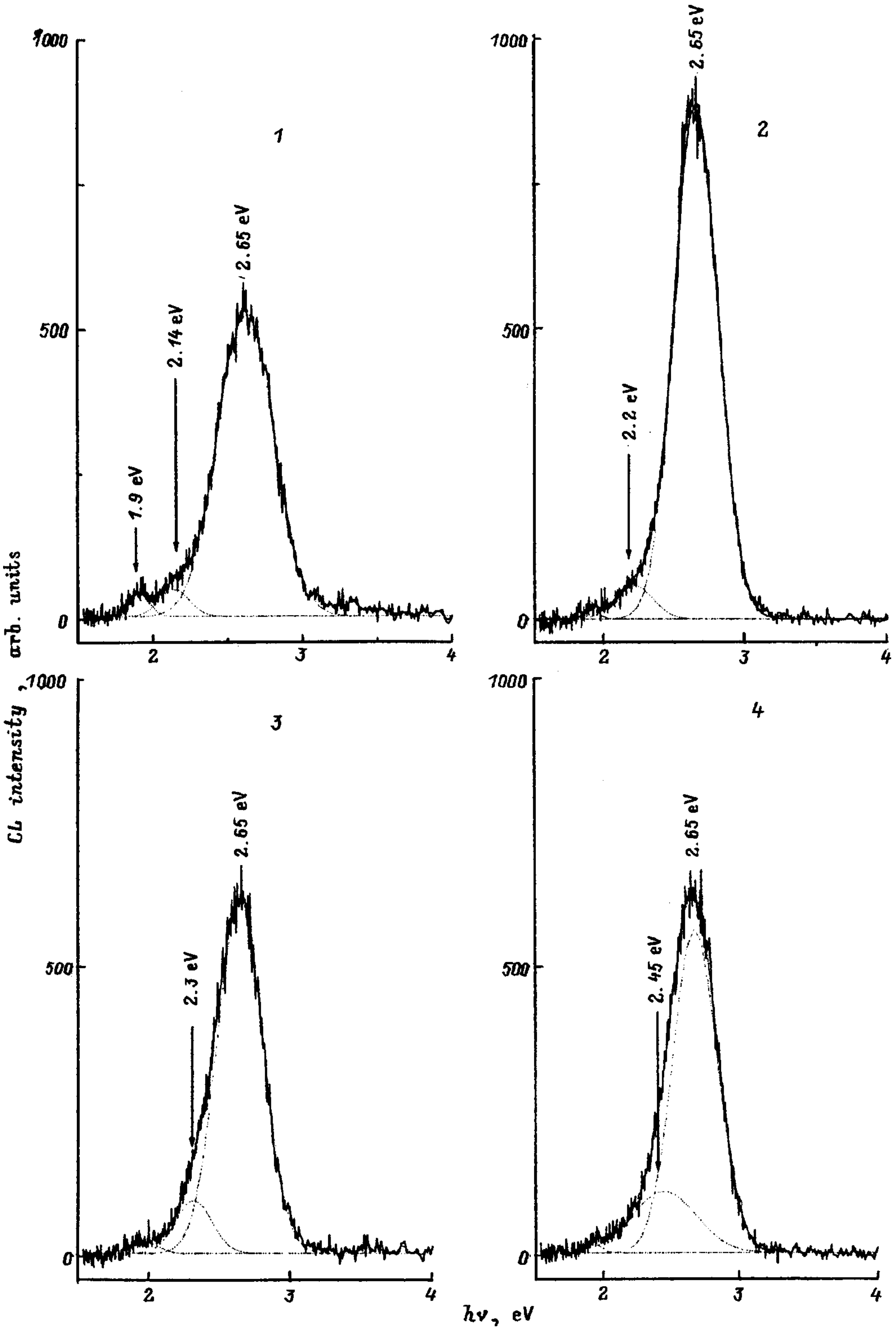

FIG. 2. Cathodoluminescence spectra of a thermally oxidized film grown on *p* silicon (KDV-0.1) in dry oxygen. *1* — spectrum obtained in the vicinity of the interface, *2,3* — spectra measured from different depths of the film progressively farther away from the interface, *4* — near-surface spectrum.

In the film grown on *p* silicon, this band is shifted up to 2.4 eV and has a comparatively lower intensity. If it originates from the self-trapped exciton emission, then the enhancement of its intensity in a film with a lower impurity concentration is only natural. Note that oxidation performed under our conditions produces on the interface a thin low-defect SiO_2 layer. It is likely that this layer is made up of fine crystallites.[5] The shift and change in intensity of the exciton band may be associated with a change in the layer thickness and the size of these crystallites.

C. Effect of boron impurity on cathodoluminescence spectra

Figure 4 presents a cathodoluminescence spectrum of an oxide film containing borosilicate glass. To study the effect

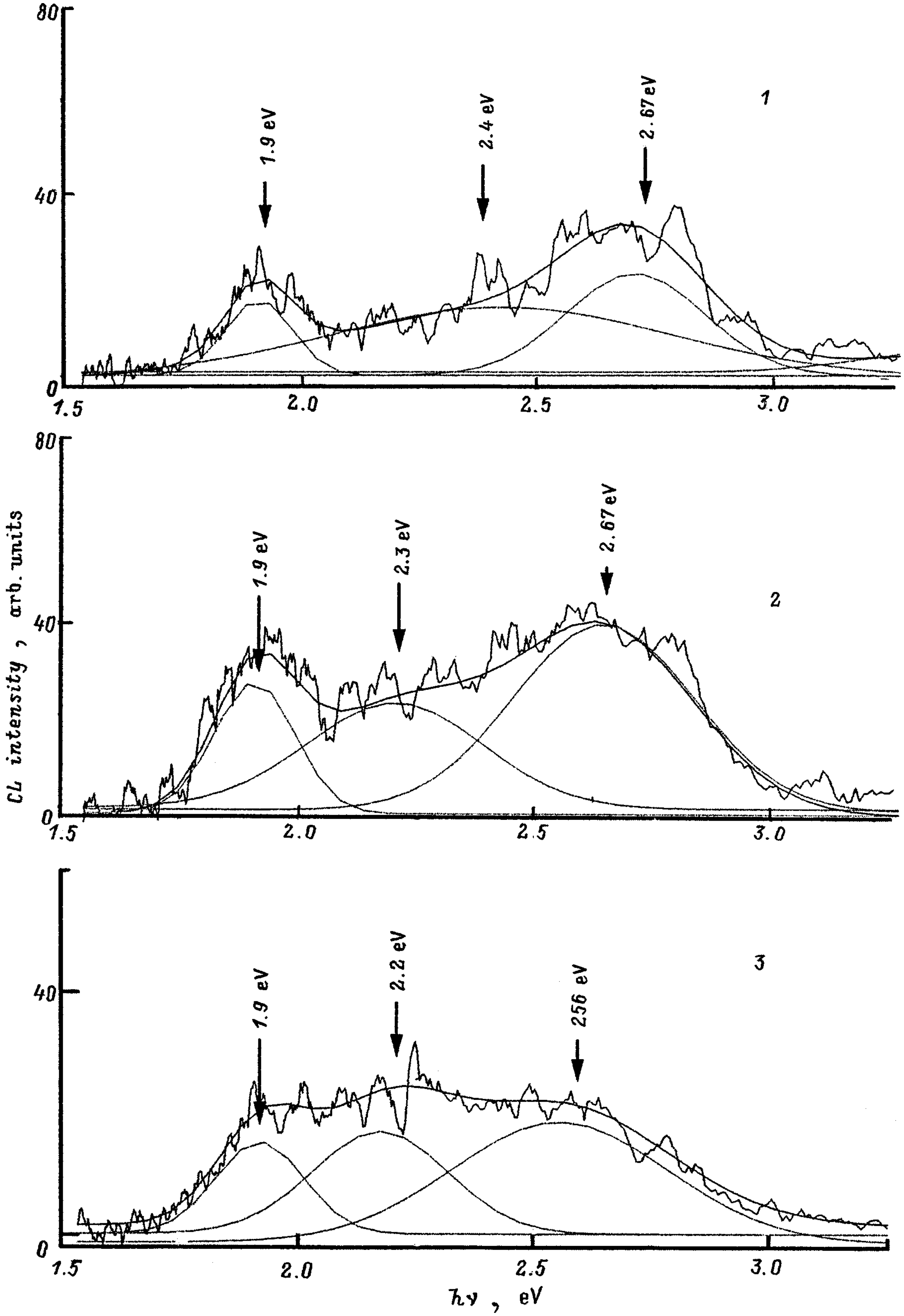

FIG. 3. Cathodoluminescence spectra obtained near the interface on films grown in dry oxygen on different types of silicon: *1* — KDV-0.1, *2* — BKEF-0.01, and *3* — KE-100.

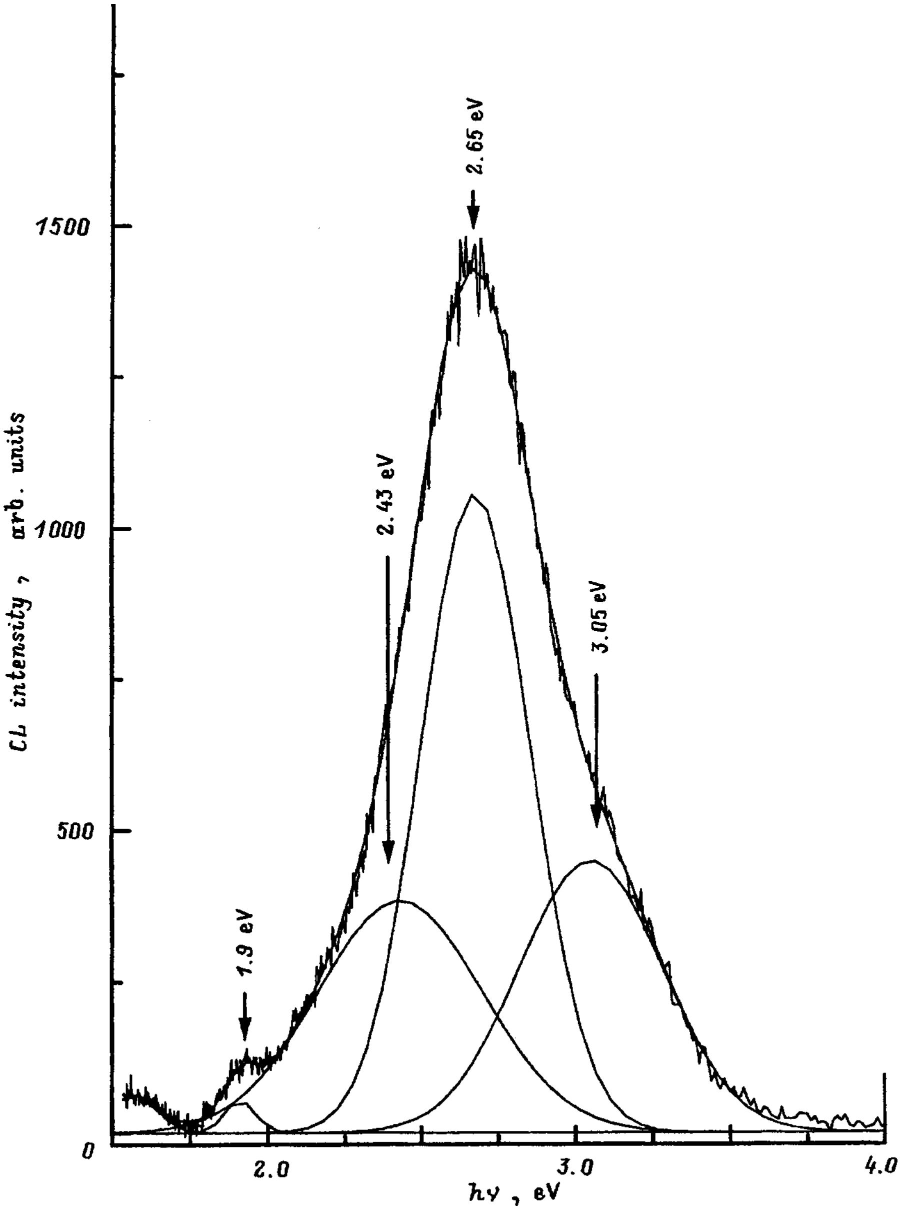

FIG. 4. Cathodoluminescence spectra of a thermally oxidized film containing borosilicate glass.

of boron impurity on cathodoluminescence spectra, boron was diffused into the oxide film. We readily see that the presence of boron in the film gives rise to an enhancement of total spectral intensity and appearance of a shoulder on the short-wavelength side of the 2.65-eV band. This can be regarded as the formation of a new band at 3.05 eV. A similar spectrum was obtained for a film grown on KDB-type silicon (Fig. 2). This means that the impurities contained in the substrate enter the growing oxide film under thermal oxidation, and modify its structure bringing about an intensity increase of the band peaking at 2.65 eV and appearance of a new band at 3.05 eV.

To sum up, (1) films grown on silicon by thermal oxidation differ in cathodoluminescence properties throughout their thickness, and (2) oxides grown on different substrates exhibit different cathodoluminescence spectra for all excitation conditions used by us.

[1] V. I. Sokolov and N. A. Fedorovich, Phys. Status Solidi A **99**, 151 (1987).
[2] F. Maurice, L. Mény, and R. Tixier, *Microanalysis and Scanning Electron Microscopy* (Les Éditions de Physique, 1978), p. 527.
[3] M. V. Zamoryanskaya, A. N. Zamoryanskiĭ, and I. A. Vaĭnshenker, Prib. Tekh. Éksp. No. 4, 161 (1987).
[4] A. R. Silin' and A. N. Trukhin, *Point Defects and Elementary Excitations in Crystalline and Glassy* SiO_2 [in Russian] (Riga, Zinatne, 1985), 243 pp.
[5] A. N. Trukhin and A. É. Plaudis, Fiz. Tverd. Tela (Leningrad) **21**, 1109 (1979) [Sov. Phys. Solid State **21**, 644 (1979)].

Translated by G. Skrebtsov

PHYSICS OF THE SOLID STATE VOLUME 40, NUMBER 11 NOVEMBER 1998

Exchange and correlation interactions and band structure of non-close-packed solids

G. V. Grushevskaya*) and L. I. Komarov

Belorussian State University, 220050 Minsk, Belorus

L. I. Gurskiĭ

Physicotechnical Institute, Belorussian Academy of Sciences, Minsk, Belorus

(Submitted November 19, 1997; resubmitted April 7, 1998)
Fiz. Tverd. Tela (St. Petersburg) **40**, 1990–1994 (November 1998)

The electronic properties of solids are calculated by the Green's function method taking account of the deformation of the atomic spheres to atomic ellipsoids by the crystal field. It is shown that the ratio of the correlation and exchange interactions in the crystal influences the nature of the band structure in non-close-packed solids. [S1063-7834(98)00611-X]

Modeling of the electrophysical properties of solids is topical in connection with the appearance and use of new materials with high structural anisotropy (for example, graphite composites[1]). However, a correct description of the crystal-field-induced correlations, which lower the spherical symmetry of the atomic potential, is absent. At the same time, exchange in such materials likewise is highly anisotropic.

In the Hartree–Fock approximation the exchange potential can be interpreted as the appearance of a ''hole'' in the halo of positive charge of an electron interacting with an electron whose spin is parallel to that of the first electron. The correlation potential, which is neglected in the Hartree–Fock approximation, can be interpreted as the appearance of a ''hole'' in the halo of positive charge of an electron interacting with an electron possessing antiparallel spin.[2]

An analysis employing a Heisenberg Hamiltonian is used for the total exchange energy. It is known that the competition between exchange and correlations plays a large role in the theory of the magnetic properties of materials.[2] On the other hand, polarization effects due to correlations between electrons determine the dielectric properties and the conditions of absorption of electromagnetic radiation in a solid. The complex permittivity ε can be written in the form

$$\varepsilon(p,z)=1-V(p)\Pi(p,z),$$

where V is the Fourier transform of the Coulomb potential, Π is the polarization operator, p is the momentum, and z is the complex frequency. This suggests that the electrophysical properties should also depend substantially on the competition between exchange and correlations.

Thus the nature of the band structure depends on the characteristic features of the correlation potential. However, it is not enough to know the correlation potential to describe the electrophysical properties of a solid as a whole. The objective of the present work is to show how the exchange and correlation interactions influence the characteristics of the band structure.

1. GREEN'S FUNCTIONS METHOD

We employed the method of Green's functions to reach our stated goal.[3] The electronic properties of solids are calculated taking into account the nonspherical nature of the distribution of the electron density in an atom. The nonsphericity of the electron density distribution in a solid is due to the crystal field, which deforms atomic spheres to atomic ellipsoids.

The characteristic features of electron scattering were studied taking into account the nonsphericity of the electron density distribution in the crystal. The self-consistent correlation potential is determined by the value of the characteristic correlation energy due to polarization effects, including taking account of the ellipsoidal shape of the atoms, and is found by the method of Green's functions.[3] The peturbed Green's function $G_1(1,2)$ was found from Dyson's equation

$$G_1(1,2)=G_1^0(1,2)+\int d\bar{1}d\bar{2}G_1^0(1,\bar{1})\Sigma(\bar{1},\bar{2})G_1(\bar{2},2),$$

where $G_1^0(1,2)$ is the free (unperturbed) Green's function and $\Sigma(\bar{1},\bar{2})$ is the self-energy operator.

The Fourier–Laplace transform of the electron self-energy Σ^{HFSP}, which is the correlation part of the Hamiltonian in the self-consistent Hartree-Fock approximation, is

$$\Sigma^{\mathrm{HFSP}}(p,z)=\int\int\frac{V(p-k)G_1(z-\omega)dkd\omega}{1-V(p-k)\Pi(p-k,\omega)}.$$

Here V is the Fourier transform of the Coulomb potential, Π is the polarization operator, k and p are momenta, and z and ω are complex frequencies.

The polarization operator describes the contribution of polarization effects calculated taking account of the nonsphericity of the potential and the electron density of the atomic shells in a crystal which are deformed by the crystal field. In the random-phase approximation it has the form[4]

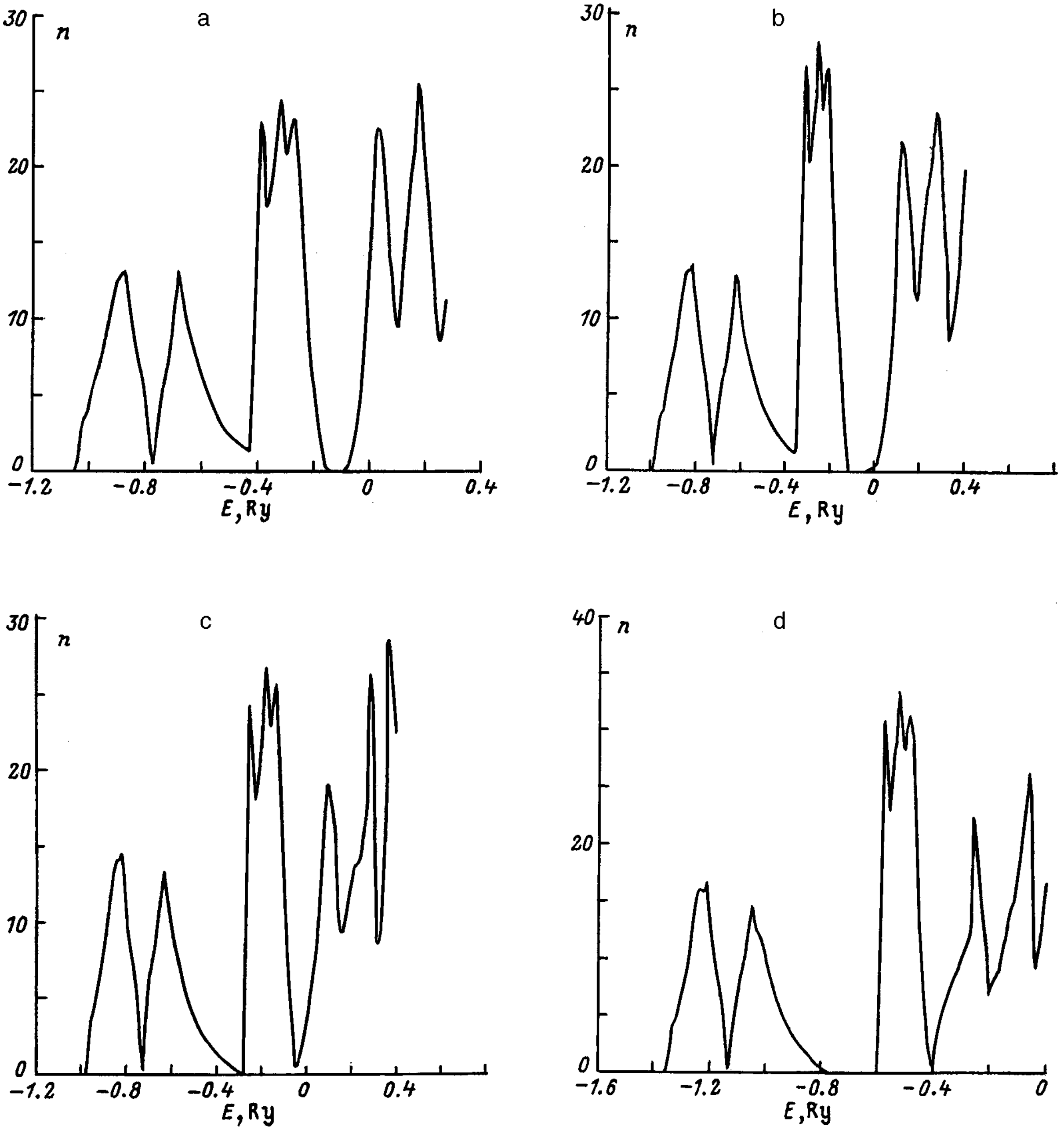

FIG. 1. One-electron density of states *n* in a unit cell of germanium. a — Self-consistent correlation potential: $\alpha_X=2/3$, $\alpha_c=1$; b–d — non-self-consistent correlation potential: b — $\alpha_X=2/3$, $\alpha_c=1(1600\pi)$; c — $\alpha_X=2/3$, $\alpha_c=1/16\pi$; d — $\alpha_X=1$, $\alpha_c=1/16\pi$.

$$\Pi^{\mathrm{ARPH}}(q,z)=\int dp\,\frac{f(E_n,p)-f(E_n,p+q)}{-\hbar z+E_n(p)-E_n(p+q)}$$
$$-(C^{20}_{20,20})^2\sum_{n''}\frac{4b_0}{3e^2\varepsilon_0}e_c|d_{n'',n}|^2\cos^2(\Theta_{qr})$$
$$\times\int dp_1\,\frac{f(E_n,p)-f(E_{n''},p_1+q)}{-\hbar z+E_n(p)-E_{n''}(p_1+q)}. \qquad (1)$$

Here $E_n(E_{n''})$ are the eigenvalues of the Hamiltonian of the problem, *n* is the band index, $f(E_n,p)$ is the Fermi distribution of the electron energies and momenta, *e* is the electron charge, ε_0 is the permittivity, b_0 is the semiaxis of the ellipsoid used to model the atoms of clusters of a solid in first-principles calculations, e_c is the eccentricity of the ellipsoid, $C^{20}_{20,20}$ is a Clebsch–Gordan coefficient, $\mathbf{d}_{n',n}$ is the dipole moment, and Θ_{qr} is the angle between the dipole moment $\mathbf{d}_{n'',n}$ and the wave vector $\mathbf{q}$. The first term in Eq. (1) describes the local polarization contribution of Bloch electrons. The second term in Eq. (1) describes polarization effects which appear as a result of the nonsphericity of the interatomic potential and are due to the dipole moments of the electric charges.

The self-energy is the Fourier transform of the correlation potential of the interatomic interaction obtained from a series expansion in terms of the periodic Bloch functions $u_n(q)$. For this reason, the correlation potential of the interatomic interaction is found from the equation

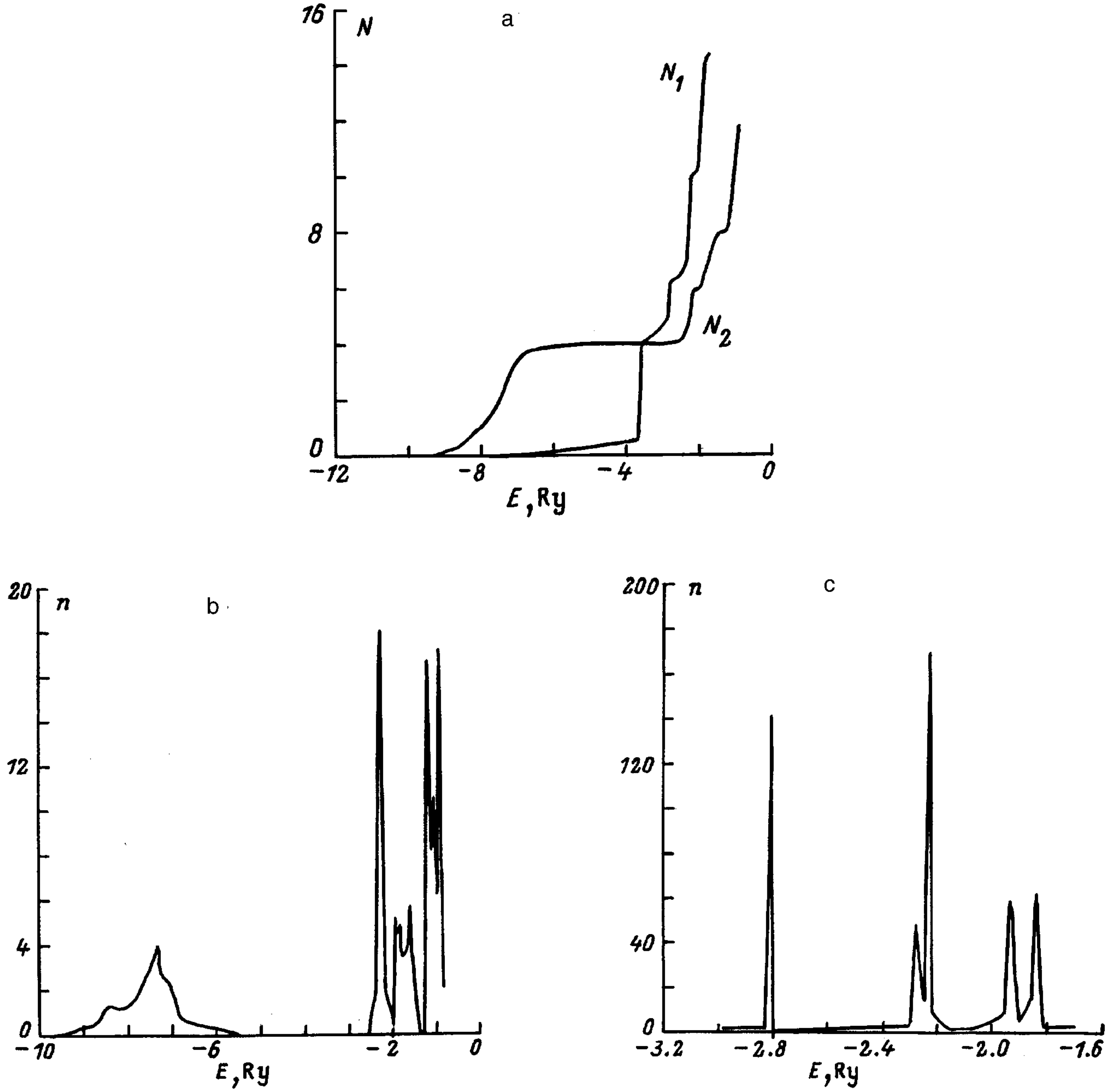

FIG. 2. N_1, N_2, and the one-electron density of states n of graphite versus energy E taking account of the correlation interactions of rotated and nonrotated layers. a) N_1 — for graphite taking account of correlations determined by the rotated layers, N_2 — energy dependence of the number of one-electron states for two-dimensional graphite; b) one-electron density of states n for graphite neglecting correlations; c) one-electron density of states n for graphite taking account of correlations determined by the rotated layers.

$$V_c(r)=\frac{1}{V_{\mathrm{BZ}}(2\pi)^3}\sum_n \int |u_n(q)|^2\Sigma_n^{\mathrm{HFSP}}(q,z)e^{i\mathbf{q}\cdot\mathbf{r}}d\mathbf{q}. \tag{2}$$

The plasmon frequencies, at which resonance occurs, make the main contribution to the integral. The plasmon frequencies were found numerically from the expression

$$1-(2s+1)V(q)\Pi_n^{\mathrm{ARPH}}(q,z)=0,$$

where s is the electron spin. In what follows, the dependence of the plasmon frequency on the wave number q, $z=z(q)$, is used as the dispersion relation.

In summary, in the random-phase approximation, the correction for the nonsphericity of the interatomic interaction potential changes the self-consistent potential of the electrons in a Wigner–Seitz cell. The change in the potential of electrons in the Wigner–Seitz cell is directly related to the phenomena giving rise to a change in the band width and the appearance of a band gap.

2. NUMERICAL MODELING

At the present time, the Kohn–Sham density functional theory is the most widely used theory for performing self-consistent calculations of the band structure of a solid (see, for example, Refs. 5–7). In principle, an exact theory requires approximations of the exchange-correlation energy. However, the existing approximations, such as the local spin density and gradient approximations,[8] neglect the deviations from sphericity of the electronic density of an atom deformed by the crystal field. Taking account of the electronic correlations (2) of the electrons in the atoms of a crystal, which are modeled by atomic ellipsoids, we found the eigenfunctions of the Kohn–Sham equations for a density functional in the form of an expansion in linear muffin-tin orbitals. The Hamiltonian H of the system was represented in the form

$$H=H_0+\varphi_{\mathrm{sc}}+V_x+V_c, \tag{3}$$

where H_0 is the Hamiltonian of the free valence electrons and atomic cores, φ_{sc} is the self-consistent potential calculated using the Poisson equation, V_x is the exchange potential, and V_c is the correlation energy (2). The calculations were performed using the Slater $X\alpha$-exchange potential for spin-unpolarized single-electron states. The following results were obtained.

The energy distribution function n of one-electron states in a unit cell of germanium has an energy gap 0.0536 Ry (0.73 eV), which is in good agreement with the experimental data (Fig. 1a). The gap localizes a system of eight electrons. Subsequently, to investigate separately the contributions of exchange and correlations to the behavior of the electronic subsystem for germanium, the correlation potential was chosen to be non-self-consistent but with a correction factor α_c. For $\alpha_c=1/(1600\pi)$ the distribution function n of single-electron states is shown in Fig. 1b. An energy gap of 0.065 Ry is present, and the charge density remains qualitatively the same as before. The exchange constant α_X in the Slater potential equals 2/3. Figure 1c shows the result of increasing the correlation energy by a factor of 100. One can see that the gap closes. Increasing exchange to 1 results in the appearance of a gap which separates a subsystem of four electrons (Fig. 1d). Therefore increasing the exchange energy leads to the appearance of a gap in the band structure, and the location of this gap is determined by the magnitude of the correlation energy. The effective exchange is underestimated by the amount of the correlation energy, which the initial exchange increases by localization. It can be concluded that the electrophysical properties of solids are determined by the ratio of the correlation interaction of antiparallel spins and the exchange interaction of uncompensated spin magnetic moments of the atomic electrons in the crystal. In addition, weak exchange strives to localize a subsystem of atomic electrons.

We shall study graphite as a real non-close-packed structure where it is important to take account of the nonspherical distribution of the electron density in atoms. Since graphite has a layered structure, the exchange interaction between layers is weak. Neglecting the correlation interaction between layers, graphite can be treated in a two-dimensional approximation. This was implemented numerically by calculating the structure of graphite with nonrotated layers. For three-dimensional graphite it is then necessary to solve the two-dimensional Dyson equation for the Green's functions of an electron in graphite with layers rotated by ±60° with respect to one another, treating the correlation potential as an external potential. The calculation was performed for s and p electrons. The computational results show that two-dimensional graphite is an insulator (Fig. 2). The highest valence band is separated from the lowest conduction band by an energy gap of 0.063 Ry (0.85 eV). It is interesting that the exchange is so strong that besides localization of the entire electronic system of eight electrons of a crystal cell of graphite, localization of an electronic subsystem of four electrons also occurs. For three-dimensional graphite, layers with the same orientation are separated by layers rotated by 60°. Calculation of the number N of one-electron states (Fig. 2a) shows that correlations, as a counterbalance to the exchange interactions, decrease the gap in the band structure and lead to overlapping of the energy bands. For two-dimensional graphite the peaks in the single-electron density of states n form two groups (Fig. 2b), and taking account of the interaction with rotated layers leads to the formation of three groups of peaks (Fig. 2c).

Thus the lifting of degeneracy for $p_{x,y}$ electrons, which results in doubling of the corresponding peak in the electron density of states, is due to narrowing, right up to complete vanishing, of the exchange energy gap as a result of the correlation interaction of atomic electrons belonging to different layers of the crystal structure of graphite. The latter forms the semimetallic properties of graphite.

So, the proposed method of numerical modeling of the electrophysical properties of non-close-packed systems can be used to investigate the ratio of the correlation interaction for antiparallel spins and the exchange interaction of uncompensated spin moments of electrons and their influence on the nature of the band structure.

This work was supported by the Belorussian Fund for Fundamental Research (Project No. F94-096).

*⁾E-Mail: Grushevskaja@phys.bsu.unibel.by

---

[1] D. Fristot, A. Charlier, M. F. Charlier, L. Lang, and S. Doyen-Lang, J. Phys.: Condens. Matter **3**, 5323 (1991).

[2] A. O. Animalu, *Intermediate Quantum Theory of Crystalline Solids* (TechBooks, 1977; Mir, Moscow, 1981, 574 pp.).

[3] G. V. Grushevskaya, L. I. Gurskiĭ, L. I. Komarov, and G. G. Krylov, Dokl. Akad. Nauk Belarusi **40**(5), 58 (1996).

[4] G. V. Grushevskaya, L. I. Gurskiĭ, L. I. Komarov, and G. G. Krylov, Dokl. Akad. Nauk Belarusi **40**(6), 49 (1996).

[5] H. L. Skriver, *The LMTO Method: Muffin-Tin Orbitals and Electronic Structure* (Springer-Verlag, Berlin, 1984), 279 pp.

[6] M. Sprinborg, Physica B **172**, 225 (1991).

[7] B. V. Novysh, N. N. Dorozhkin, E. M. Gololobov, and V. M. Anishchik, Physica B **195**, 209 (1996).

[8] J. P. Perdew, J. A. Chavary, S. H. Vosko, K. A. Jackson, M. R. Rederson, and D. J. Singh, Phys. Rev. B **46**, 6671 (1992).

Translated by M. E. Alferieff

Model of the pair phosphorus atom–interstitial silicon atom

A. R. Chelyadinskiĭ and V. A. Burenkov

Belorussian State University, 220050 Minsk, Belorus

(Submitted April 7, 1998)
Fiz. Tverd. Tela (St. Petersburg) **40**, 1995–1998 (November 1998)

Interstitial defects in silicon implanted with P and Si ions are investigated by x-ray diffraction. It is established that the interstitial complexes formed by implantation and in subsequent heat treatment do not contain a P atom. A model is proposed for the pair PI: P atom–institial Si atom. The pair PI consists of P and Si atoms at the same interstice which are not bound to one another by a covalent bond. The pair model accounts for the characteristic features of the diffusion of implanted phosphorus in silicon. © *1998 American Institute of Physics.* [S1063-7834(98)00711-4]

It is now thought that the anomalous diffusion of phosphorus implanted in silicon occurs via the pair P atom–interstitial Si atom.[1–3] However, in the literature there is still no information about the structure of this pair.

The following features are observed in the diffusion of implanted phosphorus: 1) anomalously high values of the effective diffusion coefficient: with rapid thermal annealing (RTA) with a duration of the order of 10 s at 900 °C it is 1000 times larger than the intrinsic value (i.e., the value for ordinary thermal diffusion from an external source); 2) as the annealing time increases, the diffusion coefficient approaches the intrinsic value; 3) for RTA the effective phosphorus diffusion coefficient is temperature independent in the range 800–1050 °C; and, 4) as a result of annealing, the maximum of the phosphorus distribution shifts toward the surface.

The experimentally established temperature independence of the effective diffusion coefficient indicates that diffusion occurs by means of a complex. As temperature increases, the exponential growth in the migration rate of the complex is compensated by a similar decrease in the lifetime of the complex. At the same time, the diffusion activation energy of the complex must equal the annealing activation energy of the complex.[3]

As assumed earlier,[4–6] the following data attest to the fact that this complex must be interstitial and not an *E* center (a complex consisting of a P atom and a vacancy). The phosphorus diffusion coefficient increases if the silicon surface oxidizes in the process of diffusion.[7] It is known that in silicon excess interstitial atoms are generated in the process of oxidation. Conversely, the implanted-phosphorus diffusion coefficient can be considerably decreased (by a factor of 100[3,8]) by predoping the layer with group-IV elements (Ge, C). According to the data of Refs. 9 and 10 , these impurities are traps of interstitial Si atoms operating by the Watkins substitution mechanism.

The structure of a number of interstitial complexes has been established by electron spin resonance (ESR) in irradiated silicon. However, the literature contains no data on an interstitial complex containing a P atom.

In Refs. 1 and 12 it was shown that interstitial complexes can be investigated by studying the Watkins effect — displacement of group-III elements out of the lattice sites by interstitial Si atoms. Interstitial Si atoms arise as a result of the decomposition of complexes during heat treatment of irradiated samples. The process of displacing group-III elements was monitored by observing the change in the lattice period of the crystal. In the present work we used this method to investigate interstitial defects in silicon irradiated with Si^+ and P^+ ions.

1. EXPERIMENTAL PROCEDURE

The x-ray diffraction investigations were performed with a two-crystal spectrometer with parallel arrangement of crystals, using Cu $K\alpha_1$ radiation, in fourth-order reflection from (111) planes. The lattice period was determined from the angular distance between the reflection maxima from the implanted layer and substrate to within $\pm 1\times 10^{-6}$ nm.

Samples of *p*-type silicon lightly doped ($\rho_0=10$ Ω-cm) and strongly doped ($\rho_0=0.005$ Ω-cm) with boron and irradiated with different ions were investigated. The energy of the P^+ and Si^+ ions was 200 keV and the energy of the B^+ ions was 100 keV. The effective density of the scanning ion beam was 0.2 $\mu A\cdot cm^{-2}$.

Isochronous annealing for 15 min was performed in evacuated quartz ampuls. The temperature was maintained to within ±2 °C.

2. RESULTS AND DISCUSSION

Ion implantation increases the lattice period (LP) of silicon. The restoration of the LP in lightly doped silicon ($\rho_0=10$ Ω-cm), irradiated with Si^+, P^+, and B^+ ions, during isochronous annealing is presented in Fig. 1. Similar curves for silicon lightly doped with boron (Si:B) are shown in Fig. 2. Curve *3* in Fig. 2 shows the restoration of the LP in Si:B, irradiated with Si^+ ions, in the process of isochronous annealing with simultaneous irradiation with 10 keV electrons with current density 2 $\mu A\cdot cm^{-2}$.

In the silicon layers irradiated with Si^+ ions (curve *1* in Fig. 1), the first stage (100–280 °C) is due to annealing of predominantly divacancies.[11] At the second stage (380–600

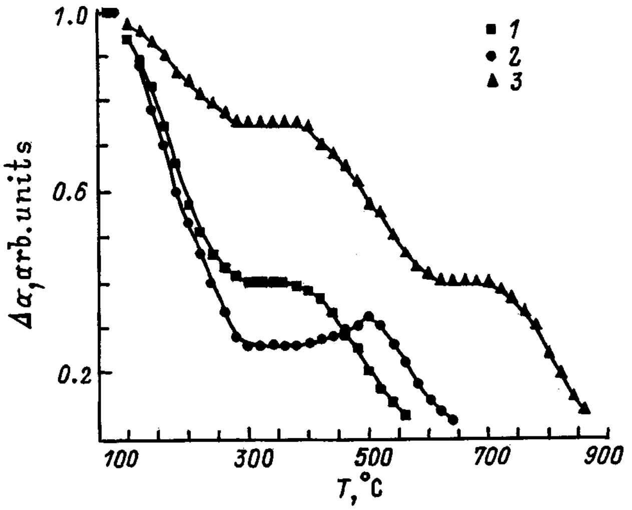

FIG. 1. Restoration Δa of the lattice period during isochronous annealing in silicon irradiated with ions. *1* — Si$^+$ (1×10^{14} cm^{-2}), *2* — P$^+$ (1×10^{14} cm^{-2}), *3* — B$^+$ (1×10^{15} cm^{-2}).

°C) multiple-vacancy complexes are annealed, for example, five-vacancy (Si–*P*1 centers) and others still unidentified.[13] In silicon irradiated with P$^+$ ions (curve *2* in Fig. 1), besides divacancies, *E* centers are also annealed at the first stage; phosphorus is present in the multiple-vacancy complexes, increasing their annealing temperature by 100 °C. An annealing stage with 700–900 °C (curve *3* in Fig. 1) is characteristic for silicon crystals irradiated with B$^+$ ions.

In silicon heavily doped with boron, ''reverse'' annealing stages are superposed on the LP restoration curves. These stages are due to the displacement of boron atoms from lattice sites in silicon by interstitial Si atoms freed as a result of the decomposition of interstitial complexes. The boron atoms located in sites compress the silicon lattice. The tetrahedral covalent radius of boron (0.08 nm) is shorter than that of the Si atom (0.1175 nm). When boron atoms leave the sites, the LP of silicon increases. The two stages of ''reverse'' annealing with 120 and 480 °C centers are the same as the annealing temperatures of the paramagnetic centers Si–*P*6[14] and Si–*B*3,[15] respectively. The Si–*P*6 and Si–*B*3 centers are split di-interstitial complexes. The complex Si–*B*3 is more symmetric and stable, and according to ESR data[15] it forms during heat treatment as a result of restructuring of Si–*P*6 defects. These centers are both observed in a positively charged state.

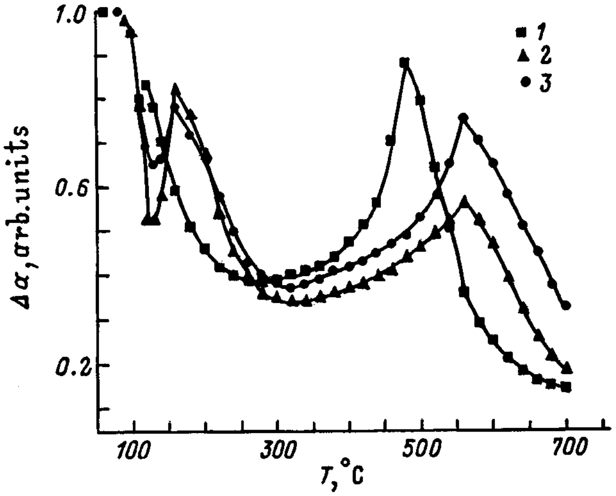

FIG. 2. Restoration Δa of the lattice period during isochronous annealing in silicon heavily doped with boron and irradiated with ions. *1* — Si$^+$ (1×10^{14} cm^{-2}), *2* — P$^+$ (1×10^{14} cm^{-2}), *3* — Si$^+$ (1×10^{14} cm^{-2}, annealing with simultaneous electron irradiation).

In P$^+$ irradiated Si:B crystals, the boron displacement stages lie at higher temperatures: 160 and 560 °C (curve *2* in Fig. 2). These stages coincide with the annealing temperatures of Si–*A*5[16] and Si–*O*2[17] paramagnetic centers, respectively, observed in a neutral charge state. The authors of Ref. 16 assumed that the Si–*A*5 defect consists of two interacting, split di-interstitial complexes separated by 0.9 nm. The paramagnetic center Si–*O*2 is, according to ESR data, an interstitial complex but its structure has still not been determined. The concentrations of all interstitial centers identified by ESR are two to three orders of magnitude lower than the concentrations of divacancies. However, estimates obtained from data on the displacement of boron from lattice sites show that the concentrations of interstitial complexes are comparable to the divacancy concentrations.[11] The disparity is evidently due to the fact that interstitial complexes are concentrated predominantly in regions of defect accumulations and, because of high local concentrations, the complexes interact with one another and their individual properties are not manifested in the ESR spectra.

The differences in the annealing temperatures of interstitial complexes in silicon irradiated with Si$^+$ and P$^+$ ions (curves *1* and *2* in Fig. 2), at first glance, admit the idea that P atoms are constituents of Si–*A*5 and Si–*O*2 complexes, especially since according to ESR data these centers were observed in phosphorus-doped silicon.[16,17] However, these differences in the annealing temperatures could be due to the charge states of the defects. In silicon heavily doped with boron and irradiated with Si$^+$ ions, the interstitial defects are in a positively charged state. The densities of radiation defects estimated from the magnitude of the change in the LP and the displacements of atoms near the predominant defects [0.02 nm (Ref. 18)] are of the same order of magnitude as the initial charge carrier density (4×10^{19} cm^{-3}) in Si:B crystals. Correspondingly, the annealing temperatures of the interstitial defects are identical to the annealing temperatures of the paramagnetic centers Si–*P*6 and Si–*B*3. In Si:B crystals irradiated with P$^+$ ions, the defects are in a neutral charge state. It is known that even during implantation a substantial fraction of the phosphorus (up to 70%[19]) occupies lattice sites, and as a result charge compensation occurs. This assumption is confirmed by experiments on annealing of defects with simultaneous irradiation by low-energy electrons in Si:B crystals irradiated by Si$^+$ ions (curve *3* in Fig. 2). In this case the annealing temperatures of the defects are the same as in silicon irradiated by P$^+$ ions. This is explained by the fact that the interstitial defects Si–*P*6 and Si–*B*3 trap nonequilibrium electrons and are transferred into neutral charge states Si–*A*5 and Si–*O*2 with their characteristic annealing temperatures. It is interesting that the low-temperature (120 °C) ''reverse'' annealing stage (curve *1* in

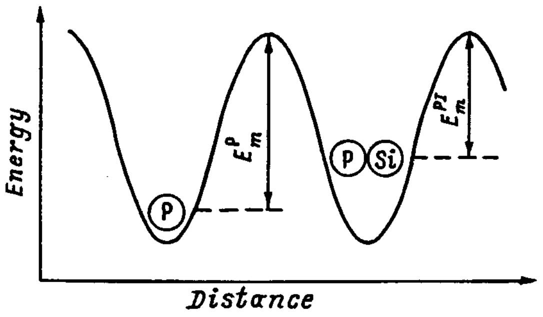

FIG. 3. Energy barrier for migration of a phosphorus atom and a pair, E_m^{P} and E_m^{PI}, respectively, in a silicon lattice.

Fig. 2) is weak. When defects are transferred into a neutral charge state, however, the boron displacement stage (160 °C) is much more intense (curve *3*). The small amplitude of the ''reverse'' annealing at 120 °C can be explained by the fact that during heat treatment the Si–*P*6 defects are rearranged predominantly into Si–*B*3 complexes. This agrees with the ESR data.[15] As follows from our data, in the case of the neutral state Si–*A*5 these defects decompose during heat treatment and mobile Si atoms are freed and participate in the substitution process.

It follows from our experiments that the pairs Si–*P*6 and Si–*A*5 as well as Si–*B*3 and Si–*O*2 are one and the same defects but in different charge states. It also follows from these experiments that the interstitial complexes do not contain a P atom. If stable interstitial complexes with a P atom are not formed, then what is the pair *PI* which gives rise to the anomalous diffusion of phosphorus? We think that the pair arises when P and Si atoms occupy the same interstice. The P and Si atoms are not bound to one another by a covalent bond. The bond is determined by the potential relief of the crystal (Fig. 3). In this scheme, the barrier for migration of an individual phosphorus atom is E_m^{P}. For the pair *PI* this barrier E_m^{PI} is, evidently, lower. This determines the higher mobility of a *PI* pair compared with an isolated P atom. For this pair, as follows from experiment, the annealing activation energy of the complex equals its diffusion activation energy. When the pair *PI* acquires energy above the barrier E_m^{PI}, it can hop into a neighboring interstice as a whole or the atoms P and Si can hop into different interstices (decomposition of a pair). The probabilities of these processes do not depend on temperature.

The pairs *PI* can form not only as a result of two atoms randomly occupying the same interstice. This process can and must occur if P atoms are present in lattice sites in the crystal and excess interstitial Si atoms arise. A P atom at a lattice site in silicon, just as any other substitution atom with a covalent radius different from that of the matrix, creates an elastically deformed region around itself. According to the ideas developed in Ref. 10, an interstitial Si atom which enters a distorted sphere of radius *R* moves in a directed manner in the field of the elastic deformations toward their source. For a P atom in silicon the radius *R* is 4 nm. If two Si atoms enter this sphere, both atoms move toward the P atom. One of them displaces the P atom into an interstice, and the other Si atom is found in the same interstice. A *PI* pair arises as a result. The concentrations of defects in the implanted layer are sufficiently high for this mechanism to materialize. For a P^+ dose of $1 \times 10^{14}\ \mathrm{cm}^{-2}$ and an energy of the order of 100 keV, the volume density of phosphorus atoms in the layer is about $10^{19}\ \mathrm{cm}^{-3}$ and the defect density is of the order of $10^{20}\ \mathrm{cm}^{-3}$.[3] The *PI* pairs are formed in appreciable concentrations as long as an excess concentration of interstitial Si atoms exists. As the pairs are annealed, their concentration decreases and the effective diffusion coefficient approaches the intrinsic value.

In summary, the experimental results obtained and their comparison with published ESR data allow us to conclude that as a result of implantation and subsequent heat treatment stable interstitial complexes containing a phosphorus atom do not form in silicon. The pair P atom–interstitial Si atom forms when P and Si atoms appear at the same interstice. The P and Si atoms are not bound to each other by a covalent bond. The bond is determined only by the potential relief of the crystal. The proposed model of the pair corresponds to all characteristic features of the diffusion of implanted phosphorus in silicon.

[1] F. F. Morehead and R. F. Lever, Appl. Phys. Lett. **48**, 151 (1986).
[2] H. U. Jager, T. Fendel, and S. Ulbricht, Phys. Status Solidi A **116**, 571 (1989).
[3] A. R. Chelyadinskii and H. I. Haki Taher, Phys. Status Solidi A **142**, 331 (1994).
[4] F. N. Schwettmann and D. L. Kendall, Appl. Phys. Lett. **19**, 218 (1971).
[5] M. Yoshida, J. Appl. Phys. **48**, 2169 (1977).
[6] R. B. Fair and C. C. Tsai, J. Electrochem. Soc. **124**, 1107 (1977).
[7] D. A. Antoniadis and Moskowitz, J. Appl. Phys. **53**, 6788 (1982).
[8] V. A. Burenkov, M. Jadan, and A. R. Chelyadinskii, in *Proceedings of the Conference on Ion Implantation of Science and Technology*, Naleczow, Polska, 1997, p. 108.
[9] G. D. Watkins and K. L. Brower, Phys. Rev. Lett. **36**, 1329 (1976).
[10] N. I. Berezhnov, A. R. Chelyadinskii, M. Jadan, and Yu. R. Suprun-Belevich, Nucl. Instrum. Methods Phys. Res. B **73**, 357 (1993).
[11] N. I. Berezhnov, V. F. Stelmakh, and A. R. Chelyadinskii, Phys. Status Solidi A **78**, K121 (1983).
[12] N. I. Berezhnov, Yu. R. Suprun-Belevich, A. R. Chelyadinskiĭ, and Kh. I. Khaki Takher, Izv. Vyssh. Uchebn. Zaved. Fiz. **4**, 55 (1991).
[13] V. A. Botvin, Yu. V. Gorelkinskiĭ, V. O. Sigle, and M. A. Chubisov, Fiz. Tekh. Poluprovodn. **6**, 1683 (1972) [Sov. Phys. Semicond. **6**, 1453 (1972)].
[14] Y. H. Lee, N. N. Gerasimenko, and J. W. Corbett, Phys. Rev. B **14**, 4506 (1976).
[15] K. L. Brower, Phys. Rev. B **14**, 872 (1976).
[16] Y. H. Lee, Y. M. Kim, and J. W. Corbett, Radiat. Eff. **15**, 77 (1972).
[17] J. W. Corbett and J. P. Karins, Nucl. Instrum. Methods Phys. Res. **182-183**, 457 (1981).
[18] A. N. Zhevno, V. V. Sidorik, and V. D. Tkachev, Dokl. BSSR **20**, 409 (1976).
[19] J. C. North and W. M. Gibson, Appl. Phys. Lett. **16**, 126 (1970).

Translated by M. E. Alferieff

PHYSICS OF THE SOLID STATE VOLUME 40, NUMBER 11 NOVEMBER 1998

Nonlinear propagation of light in semiconductors in the presence of two-photon excitation of biexcitons

A. Kh. Rotaru

Moldavian State University, Kishinev, Moldavia

V. Z. Tronchu

Institute of Applied Physics, Moldavian Academy of Sciences, 277028 Kishinev, Moldavia

(Submitted April 7, 1998)
Fiz. Tverd. Tela (St. Petersburg) **40**, 1999–2002 (November 1998)

The steady- and nonsteady-state passage of light through a ring resonator in the presence of two-photon excitation of biexcitons from the ground state of the crystal is studied. The values of the parameters for which complicated nonlinear temporal formations are possible in the system are found. The possibility of observing the predicted effects experimentally is discussed.

In the last few years a great deal of attention has been devoted to cooperative processes in the excitonic region of the spectrum. In Refs. 1 and 2, a theory of optical bistability and dynamic chaos in the excitonic region of the spectrum is constructed in the ring-resonator geometry on the basis of the Keldysh equations. In Ref. 3 it is predicted that the observation and breakdown of dynamic optical chaos are possible in a system of coherent excitons and photons exposed to an external periodic force. Reference 4 is devoted to the study of steady- and nonsteady-state optical bistability (OB), multistability, optical switchings, and self-pulsations in a system of coherent excitons and biexcitons in semiconductors, taking account of the exciton-photon interaction and optical conversion of excitons into biexcitons. In Ref. 5 a theory of OB and autooscillations in condensed media with the participation of excitons and biexcitons is constructed. A CuCl crystal, for which convincing experimental proofs of the existence of a biexciton are available, is chosen as the model. It is shown that both regular and stochastic self-pulsations with formation of complicated limit cycles and strange attractors in phase space are possible depending on the parameters of the system.

Biexcitons, predicted by Moskalenko[6] and Lampert,[7] are widely used to interpret new absorption and luminescence bands in semiconductors. Biexcitonics has essentially become an independent field of condensed-state physics. The most convincing experimental proofs of the existence of biexcitons are based on observations of two-phonon excitation of biexcitons from the ground state of the crystal (CuCl, CuBr, and others).[8–11] Moreover, Hanamura[12] was the first to show that the process of two-photon excitation of biexcitons from the ground state of the crystal is characterized by a gigantic oscillator strength. As a result, the method of two-photon excitation of biexcitons is now widely used for the experimental investigation of biexciton states. Here the absorption band has a narrow δ-function-like shape. The direct creation of biexcitons on account of the giant two-photon absorption of light in CuCl crystal was first observed by Gale and Mysyrowicz.[13–15]

The present work is devoted to the study of the steady- and nonsteady-state passage of light through a ring resonator in the presence of two-photon excitation of biexcitons from the ground state of the crystal. The values found for the parameters for which complex nonlinear temporal formations are possible in the system are found. The possibility of observing the predicted effects experimentally is discussed.

Let us consider the phenomenon of optical self-organization in the simplest model of a ring resonator. The photons of the propagating pulse excite biexcitons from the ground state of the crystal as a result of the two-photon absorption process.

The Hamiltonian of the problem consists of a sum of Hamiltonians of free biexcitons and the field and the Hamiltonian describing the interaction of the field with a system of coherent biexcitons. In the model adopted the interaction Hamiltonian has the form

$$H_{\text{int}} = -\hbar\mu(E^- E^- b + b^+ E^+ E^+), \tag{1}$$

where b^+ is the biexciton creation operatore and μ is a constant characterizing two-photon excitation of biexcitons from the ground state of the crystal,[12] and $E^+(E^-)$ are the positive (negative)-frequency component of the electric field of the electromagnetic wave.

The equation of motion for the amplitude of the biexciton wave b has the form

$$i\frac{\partial b}{\partial t} = \omega_{\text{biex}} b - i\gamma_m b - \mu E^+ E^+, \tag{2}$$

where $\hbar\omega_{\text{biex}}$ is the biexciton formation energy and γ_m is the biexciton decay constant, which determines the rate at which quasiparticles leave the coherent mode into incoherent modes and was introduced into the equation of motion phenomenologically.

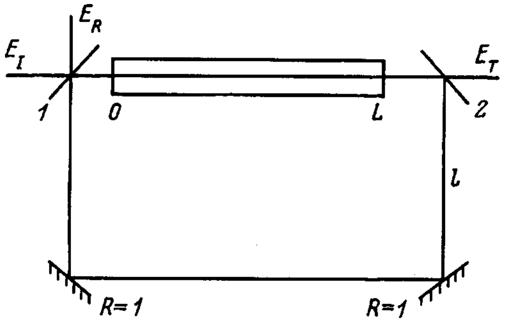

FIG. 1. Diagram of the ring resonator. E_1, E_R, and E_T — amplitudes of the incident, reflected, and transmitted fields, respectively.

Since the photon mode is coherent and its amplitude is macroscopically large, the problem can be solved semiclassically using the wave equation

$$c^2\frac{\partial^2 E^+}{\partial z^2}-\frac{\partial^2 E^+}{\partial t^2}=8\pi\bar{h}\mu\frac{\partial^2 E^- b}{\partial t^2}. \qquad (3)$$

We shall represent the solutions of Eqs. (2) and (3) in the form of a product of slowly varying envelopes and rapidly oscillating components

$$E^+=e^+\exp(ikz-i\omega t),\quad b=\tilde{B}\exp(2ikz-2i\omega t), \qquad (4)$$

where ω is the frequency of the electromagnetic wave.

For the subsequent analysis we shall use the approximation of slowly varying envelopes, which is valid if

$$\left|\frac{\partial e^+}{\partial t}\right|\ll\omega|e^+|,\quad \left|\frac{\partial e^+}{\partial z}\right|\ll k|e^+|\ \ldots\ .$$

This means that the envelopes are quite smooth functions compared with the rapidly oscillating part.

Since the study of OBs, optical switchings, and self-pulsations presently is characterized by the fact that these phenomena are studied for specific optical devices with the appropriate experimental geometry, we shall study biexcitons in the ring-resonator geometry. Let a sample of length L be positioned between the entrance and exit mirrors of the resonator, which are characterized by a transmission coefficient T. The two other mirrors are assumed to be ideally reflecting (Fig. 1). The boundary conditions for the ring resonator have the form

$$E(0,t)=\sqrt{T}E_I+RE(L,t-\Delta t)e^{iF},\quad E_T=\sqrt{T}E(L,t),$$

where E_I is the field amplitude at the resonator entrance (pump), E_T is the field amplitude at the resonator exit, $R=1-T$ is the reflection coefficient of the mirrors *1* and *2* of the resonator, Δt is the delay time due to feedback, $\Delta t=(L+2l)/c_0$, c_0 is the speed of light in vacuum, $F=kL+k_0(2l+L)$ is the phase shift of the field in the resonator, and k_0 is the wave vector of the field in vacuum.

Substituting the expressions (4) into Eqs. (2) and (3) in the slowly-varying-amplitudes approximation, neglecting effects due to spatial dispersion of the biexcitons, which in the essential region of the spectrum are of no consequence, and switching to the dimensionless quantities

$$\delta=\frac{2\omega-\omega_{\text{biex}}}{\gamma_m},\quad C=\frac{\alpha L}{T},\quad \alpha=\frac{4\pi\bar{h}\omega\gamma_m}{kc^2\mu},$$

$$\tau=t\gamma_m,$$

$$\sigma=\frac{c^2kT}{L\gamma_m},\quad \Delta=\frac{\omega^2-c^2k^2}{2\omega\gamma_m},\quad B=\frac{\tilde{B}}{B_s},\quad B_s=\sqrt{\frac{\gamma_m}{\mu}},$$

we obtain the following shortened equations:

$$\frac{\partial X_1}{\partial\tau}=\sigma C(X_2B_1-X_1B_2)-\frac{\sigma}{T}\frac{\partial X_1}{\partial Z}-\Delta X_2, \qquad (5)$$

$$\frac{\partial X_2}{\partial\tau}=\sigma C(X_1B_1-X_2B_2)-\frac{\sigma}{T}\frac{\partial X_2}{\partial Z}+\Delta X_1, \qquad (6)$$

$$\frac{\partial B_1}{\partial\tau}=-\delta B_2-B_1-2X_1X_2, \qquad (7)$$

$$\frac{\partial B_2}{\partial\tau}=\delta B_1-B_2-X_2^2+X_1^2, \qquad (8)$$

where $X_1=\mathrm{Re}e^+$, $X_2=\mathrm{Im}e^+$, $B_1=\mathrm{Re}\tilde{B}$, and $B_2=\mathrm{Im}\tilde{B}$.

The system of nonlinear differential equations (5)–(8) describes the spatiotemporal evolution of coherent biexcitons and photons in condensed media in the approximation of smooth envelopes and is the basis for the subsequent analysis. Finding the exact analytical solutions of a system of nonlinear partial differential equations is a very difficult problem. However, the main features of the nonlinear passage of light can be found in the mean-field model, widely employed in the theory of optical bistability. Mathematically, it corresponds to replacing $\int_0^L E(X)dX$ by $E(L)L$.

In this approximation, Eqs. (5) and (6) can be integrated over the coordinate

$$\frac{dX_1}{d\tau}=\sigma\Bigg(C(X_2B_1-X_1B_2)-\frac{X_1}{T}+\frac{R}{T}(X_1\cos F-X_2\sin F)-\Delta X_1-Y\Bigg), \qquad (9)$$

$$\frac{dX_2}{d\tau}=\sigma\Bigg(C(X_1B_1+X_2B_2)-\frac{X_2}{T}+\frac{R}{T}(X_2\cos F+X_1\sin F)+\Delta X_1\Bigg), \qquad (10)$$

where boundary conditions were used for the normalized amplitudes

$$TY+R[X_1(L,t-\Delta t)\cos F-X_2(L,t-\Delta t)\sin F]=X_1(0,t),$$

$$R[X_2(L,t-\Delta t)\cos F+X_1(L,t-\Delta t)\sin F]=X_2(o,t),$$

$$E_1=Y\left(\frac{\gamma_m}{\mu}\right)^{\frac{1}{4}},\quad E_T=X\left(\frac{\gamma_m}{\mu}\right)^{\frac{1}{4}}.$$

The equations (7)–(10) describe the dynamical evolution of coherent photons and biexcitons in the mean-field approximation. In the stationary case $(dX_1/d\tau=dX_2/d\tau=dB_1/d\tau=dB_2/d\tau=0)$ we obtain an equation of state that

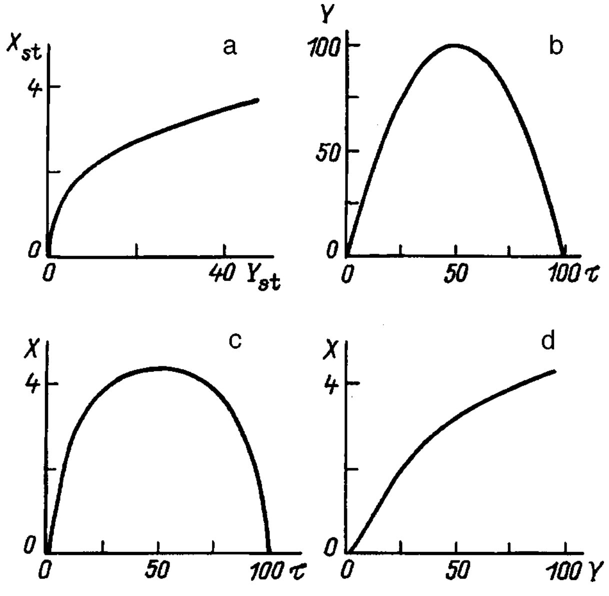

FIG. 2. Steady-state dependence of the amplitude X_{st} of the radiation exiting from the resonator on the amplitude Y_{st} of the incident radiation for the parameters $C=2$, $F=\pi/2+2\pi n$, $\delta=2$, $\sigma=0.1$, $T=0.1$ (a), parabolic shape of the external pulse Y (b), shape X of the pulse at the resonator exit (c), and the dynamical dependence $X(Y)$ (d).

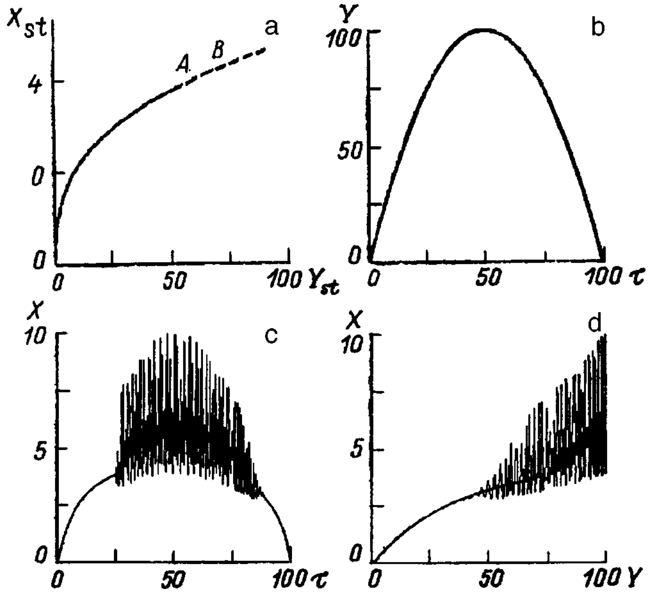

FIG. 3. Steady-state dependence $X_{st}(Y_{st})$ with parameters $F=2\pi n$, $c=2$, $\delta=2$, $\sigma=1$, $T=0.1$ (a), parabolic shape of the external pulse Y (b), pulse shape X at the resonator exit (c), and dynamical dependence $X(Y)$ (d).

determines in the mean-field approximation the amplitude X_{st} of the output radiation as a function of the amplitude Y_{st} of the incident radiation:

$$Y_{st}^2=X_{st}^2\left(\frac{1-R\cos F}{T}+C\frac{X_{st}^2}{1+\delta^2}\right)^2+\left(\frac{R\sin F}{T}+\frac{\Delta}{\sigma}-C\frac{X_{st}^2\delta}{1+\delta^2}\right). \qquad (11)$$

Figure 2a displays the steady-state dependence of the amplitude X_{st} on the amplitude Y_{st} for low intensities of the incident signal. As one can see from the plot, this dependence is single-valued.

An important and fundamental question is to investigate the stability of stationary states. The investigation of the stability of stationary states with respect to small perturbations is determined by the characteristic equation for the Jacobian of the system (7)–(10). If all roots of the characteristic equation have a negative real part, then the corresponding stationary solutions are stable with respect to small disturbances. The stability of the stationary state for different values of the parameters and with different intensities of the incident radiation was investigated using the Routh–Hurwitz criterion. As one can see from Fig. 2a, all stationary points are stable for low incident-radiation intensities.

As a rule, in an experiment, pulses having different shapes are fed into the resonator and their deformation at the exit is analyzed. Such an experiment was first performed by Bischofberger and Shen.[16] The behavior of a nonlinear Fabry–Perot interferometer, filled with a Kerr medium, under the action of pulses of different shape was studied theoretically and experimentally. The authors obtained excellent agreement between theory and experiment. We performed a computer experiment in which the system of nonlinear differential equations (7)–(10), which describes the dynamics of coherent photons and biexcitons, taking acount of the boundary conditions for a ring resonator is solved numerically with the external pump $Y(\tau)$ being a parabolic function of time (Fig. 2b). The result of the experiment is presented in Figs. 2b–d. A deformation of the initial pulse is observed (Fig. 2c), and the system tends toward stationary behavior (Fig. 2d). The result of the computer experiment can be compared with the experimental results of Refs. 17–19.

For high incident-radiation intensities there appears a section where the stationary states are unstable (Fig. 3a). The

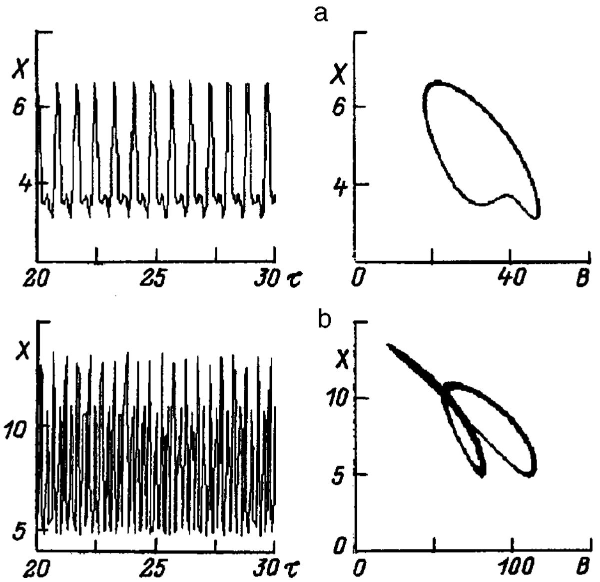

FIG. 4. Temporal evolution of the system with a constant pump and parameters $F=2\pi n$, $C=2$, $\delta=2$, $\sigma=1$, $T=0.1$. a—$Y=60$, evolution of the point A (Fig. 3a), b—$Y=65$, evolution of the point B (Fig. 3a).

dynamics of the process, where an unstable section is present in the system, is displayed in Fig. 3b–d. Nonlinear self-pulsations arise on the unstable section in the presence of a constant pump, and intime the phase trajectory reaches a stable limit cycle (Fig. 4a) (evolution of the point A, shown in Fig. 3a). As the image point moves toward the right, the oscillations become more complicated, newer and newer harmonics appear in the spectrum (Fig. 4b). A period doubling bifurcation occurs and a chaotic regime appears. At the same time, it is necessary to increase the intensity of the incident radiation, which results in a rapid increase in the density of quasiparticles.

In conclusion, we shall discuss the possibility of observing self-pulsations of biexcitons experimentally. Our model is best suited to CuCl-type crystals, where the biexciton binding energy is of the order of 40 MeV, the sample length $L=900$ Å, $\gamma_m=10^{12}\ \mathrm{s}^{-1}$, and $T=0.1$. Then, we obtain that the critical power at which the nonlinear phenomena under study can be observed is of the order of 7 mW/cm^2, while the biexciton density is of the order of $10^{15}\ \mathrm{cm}^{-3}$, which corresponds to the values of our parameters: $F=2\pi n$, $C=2$, $\delta=2$, $\sigma=1$, and $T=0.1$.

In summary, our numerical estimates allow us to conclude that it is actually possible to observe self-pulsations in a system of coherent biexcitons in condensed media.

[1] B. Sh. Parkanskiĭ and A. Kh. Rotaru, Zh. Éksp. Teor. Fiz. **99**, 899 (1991) [Sov. Phys. JETP **72**, 499 (1991)].

[2] S. A. Moskalenko, A. Kh. Rotaru, and V. A. Zalozh, Fiz. Tverd. Tela (Leningrad) **31**, 265 (1989) [Sov. Phys. Solid State **31**, 500 (1989)].

[3] A. Kh. Rotaru and V. Z. Tronchu, Fiz. Tverd. Tela (St. Petersburg) **36**, 90 (1994) [Phys. Solid State **20**, 10 (1994)].

[4] V. A. Zalozh, A. Kh. Rotaru, and V. Z. Tronchu, Zh. Éksp. Teor. Fiz. **103**, 994 (1993) [JETP **76**, 487 (1993)].

[5] V. A. Zalozh, A. Kh. Rotaru, and V. Z. Tronchu, Zh. Éksp. Teor. Fiz. **105**, 260 (1994) [JETP **78**, 138 (1994)].

[6] S. A. Moskalenko, Opt. Spektrosk. **5**, 147 (1958).

[7] M. Lampert, Phys. Rev. Lett. **1**, 450 (1958).

[8] S. Nikitine, A. Mysyrowicz, and J. Grun Helvetica, Phys. Acta. **41**, 1058 (1968).

[9] R. Knox, S. Nikitine, and A. Mysyrowicz, Opt. Commun. **1**, 19 (1969).

[10] H. Souma, J. Phys. Soc. Jpn. **29**, 697 (1970).

[11] N. Nagasawa, J. Lumin. **12/13**, 587 (1976).

[12] E. Hanamura, Solid State Commun. **12**, 951 (1973).

[13] G. Gale and A. Mysyrowicz, J. Phys. **35**, *4 Suppl.*, 43 (1974).

[14] G. Gale and A. Mysyrowicz, Phys. Rev. Lett. **32**, 724 (1974).

[15] G. Gale and A. Mysyrowicz, Phys. Lett. A **54**, 321 (1975).

[16] T. Bischofberger and Y. Shen, Phys. Rev. A **19**, 1169 (1979).

[17] B. Levy, J. Bigot, and B. Henerłag, Solid State Commun. **48**, 705 (1983).

[18] N. Peyghambarian and H. Gibbs, Phys. Rev. Lett. **51**, 1692 (1983).

[19] H. M. Gibbs, G. Khitrova, and N. Peghambarian, *Nonlinear Photonics*, Springer Series in *Electronics and Photonics*, Vol. 30, Springer-Verlag, Berlin, 1990, 210 pp.

Translated by M. E. Alferieff

Resonance states of the continuous spectrum of a bounded crystal near the critical points of volume bands

G. V. Vol'f and Yu. P. Chuburin

Physicotechnical Institute, Ural Branch of the Russian Academy of Sciences, 426001 Izhevsk, Russia

(Submitted February 2, 1998; resubmitted May 14, 1998)
Fiz. Tverd. Tela (St. Petersburg) **40**, 2003–2007 (November 1998)

The conditions for the existence of resonance electronic states near the critical points of volume bands are obtained. It is shown that resonances of this type are qualitatively different from surface resonances associated with states induced by an image potential. The manifestation of such ''volume'' resonances in the scattering of very slow electrons by a TiS_2 surface is studied.

It is important to study the manifestations of the electronic energy bands of an unbounded crystal in the continuous spectrum of a semiinfinite crystal, in the first place, from the stand point of general theory in order to clarify the ''arrangement'' of the states of the continuous spectrum of a bounded crystal, this ''arrangement'' being in may respects very different from that obtained in the often employed free-electron model.[1–4] In the second place, this information is necessary in order to interpret the experimental data correctly because states of this type are directly involved in electronic scattering processes (low-energy electron diffraction (LEED)) or photoelectronic emission. Specifically, the extrema of volume bands that fall within the energy range of the continuous spectrum are responsible for the peaks of the effective cross section of phototransitions from surface states.[5] The position of the critical points of the volume dispersion law of electrons is clearly correlated with the fine structure of the energy dependence of the very-low-energy electron-reflection coefficient of a crystal surface.[1,6] This circumstance is now used successfully to determine experimentally the final states of the photoemission process. In combination with photoelectron spectroscopy this opens up the possibility of reliable experimental reconstruction of the energy bands in the near-Fermi region.[7]

The source of the connection between the states in the continuous spectrum of a bounded crystal and the states of an infinite crystal is the asymptotic behavior of the wave function of the scattering electron in the interior of the crystal, or in the language of the dynamical theory of diffraction, the relation between the transfer matrix and the ''matching'' matrix.[8] It is known that, in principle, the quasistationary (resonant) states can strongly influence the scattering amplitude and the wave functions of the continuous spectrum.[3,9] However, their manifestation in a concrete physical situation is by no means always clear. An example is the discussion that took place at the beginning of the 1980s of the role of surface resonances in the formation of the LEED fine structure near diffraction thresholds.[10–12] As a result, the point of view developed that interference processes play the leading role and the contribution of surface resonances to the ''threshold'' effect is negligibly small.

The extension of this view to all situations of electronic scattering by the surface of a crystal is not justified, either theoretically[2–4,10] or experimentally. The latter is demonstrated by recent investigations of surface states by polarized-electron spectroscopy[13] or by the method of Ref. 14, where selective adsorption and desorption of low-energy electrons in the scattering by the surface of a crystal were first observed and it was shown clearly that capture of electrons into quasistationary Rydberg-type states does indeed take place and is responsible for the observed effect.

In the present work the conditions for the appearance and the character of long-lived resonances near the critical points of volume bands are investigated.

1. MODEL

For mathematical convenience we shall consider two semiinfinite crystals (SICs), occupying the spaces $z \leqslant -L/2$ and $z \geqslant L/2$. The width L of the vacuum gap is assumed to macroscopically large, so that the crystals do not interact with one another. If the source of electrons lies near the right-hand SIC ($z \geqslant L/2$), then the observation time $t < 2L/|V_z|$, where V_z is the velocity component of the reflected electrons that is perpendicular to the surface, the left-hand crystal does not contribute to the measurement results and the wave packet of the scattered electron in this system is the same as the wave packet corresponding to only the SIC occupying the half-space $z \geqslant L/2$.

The quasistationary states satisfy the Lippman–Schwinger equation, not containing the incident wave, with complex energy E.[9] In the unit cell Ω of the SIC we have

$$\Psi(\mathbf{r};\mathbf{k},E) = -\int_\Omega G_{\mathbf{k}}(\mathbf{r},\mathbf{r}';E)[V_+(\mathbf{r}') + V_-(\mathbf{r}')]\Psi(\mathbf{r}';\mathbf{k},E)\,d\mathbf{r}',$$

$$\Psi(\mathbf{r}+\mathbf{R}_n;\mathbf{k},E) = \exp(i\mathbf{k}\cdot\mathbf{R}_n)\Psi(\mathbf{r};\mathbf{k},E), \qquad (1)$$

where $\mathbf{k}$ is a two-dimensional reduced quasimomentum, $\mathbf{R}_n$ is the translation vector of the Bravais lattice of the SIC, $G_{\mathbf{k}}(\mathbf{r},\mathbf{r}';E)$ is a Bloch Green's function in the variable $\mathbf{u} = (x,y)$ for free electrons

$$G_{\mathbf{k}}(\mathbf{r},\mathbf{r}';E)=\frac{i}{2S}\sum_{\mathbf{g}_\mu} e^{i(\mathbf{k}+\mathbf{g}_\mu)\cdot(\mathbf{u}-\mathbf{u}')}\frac{e^{i\sqrt{E-(\mathbf{k}-\mathbf{g}_\mu)^2}|z-z'|}}{\sqrt{E-(\mathbf{k}-\mathbf{g}_\mu)^2}}, \tag{2}$$

S is the area of a section of the cell Ω by the surface plane of the crystal, $\mathbf{g}_\mu$ is a two-dimensional reciprocal-lattice vector of the SIC, and $V_{+(-)}(\mathbf{r})$ is the potential of the right- (left) hand SIC.

Of course, the solutions of Eq. (1) with zero and nonzero V_- are not the same. The wave packets of the scattered states corresponding to the two formulations of the problems are equivalent only in the sense indicated above. When vacuum absorption, which is always present in real experiments and is taken into account below by introducing the appropriate optical potential, is taken into account, there is actually no limit on the measurement time for macroscopically large L.

We represent the potential of the SIC in the form

$$V_\pm(\mathbf{r})=[V^{(\infty)}(\mathbf{r})+i\sigma_B]\Theta(\pm z-L/2) + i\sigma_\nu\Theta(\mp z+L/2)+U_\pm(\mathbf{u},L/2\pm z), \tag{3}$$

where $\Theta(x)$ is the Heaviside function, $V^{(\infty)}(\mathbf{r})$ is the potential of an unbounded crystal, $\sigma_{B,(\nu)}>0$ is the imaginary part of the optical potential[15] that describes absorption in the three-dimensional (vacuum) region, $\sigma_\nu\ll\sigma_B$; $U_\pm(\mathbf{u},L/2\pm z)$ is the surface-screening function, which is zero sufficiently far from the crystal surface. We assume that the real part of the optical potential is included in $V^{(\infty)}$ and $U_\pm$.

2. CONDITION FOR THE EXISTENCE OF RESONANCES NEAR THE CRITICAL POINTS OF VOLUME BANDS

It follows from Eq. (1) that

$$[1+\hat{G}_{\mathbf{k}}(E)(V_+ + V_-)]\Psi \equiv \hat{G}_{\mathbf{k}}(E)\hat{G}_{\mathbf{k}}^{(\infty)^{-1}}(E-i\delta)[1+\hat{G}_{\mathbf{k}}^{(\infty)}(E-i\delta)W]\Psi, \tag{4}$$

where $\hat{G}_{\mathbf{k}}$ and $\hat{G}_{\mathbf{k}}^{(\infty)}$ are the Green’s operators of a free electron and an electron in an infinite crystal with the Hamiltonian

$$\hat{H}^{(\infty)}=-\Delta+V^{(\infty)}(\mathbf{r}),$$

and $\delta=\sigma_B-\sigma_\nu>0$. The function

$$W(\mathbf{r};\sigma_B,\sigma_\nu)=[V^{(\infty)}(\mathbf{r})+i(\sigma_B-\sigma_\nu)][\Theta(z-L/2) -\Theta(z+L/2)]+U_+(\mathbf{u},z)+U_-(\mathbf{u},z) \tag{5}$$

vanishes for sufficiently large $|z|$.

Therefore if a solution of the equation

$$[1+\hat{G}_{\mathbf{k}}^{(\infty)}(E-i\delta)W(\mathbf{r})]\Psi_{\mathbf{k}}(\mathbf{r},E)=0, \tag{6}$$

exists, then a solution of Eq. (1) also exists.

Let us consider the conditions under which a nontrivial solution of Eq. (6) exists. At the critical point of the n-th band of an unbounded crystal $\partial\mathcal{E}(\mathbf{K}_c)/\partial k_z=0$, where $\mathbf{K}_c=(\mathbf{k},k_z^{(c)})$, while $\mathcal{E}_n(\mathbf{k},k_z)$ is the volume dispersion law for electrons. Then, near $\mathbf{K}_c$ the Green’s function of an infinite crystal can be represented as[16]

$$G^{(\infty)}(\mathbf{r},\mathbf{r}';\mathbf{k},k_z^{(1)},E-i\delta)=\frac{id\phi_n(\mathbf{K}_c,\mathbf{r})\phi_n(\mathbf{K}_c,\mathbf{r}')}{(k_z^{(1)}-k_z^{(c)})\partial^2\mathcal{E}_n(\mathbf{K}_c)/\partial k_z^2} +\tilde{G}(\mathbf{r},\mathbf{r}';\mathbf{k},k_z^{(1)},\ E-i\delta), \tag{7}$$

where d is the interplanar spacing in the SIC, ϕ_n are the wave functions of an infinite crystal, and $k_z^{(1)}$ is a solution of the equation

$$\mathcal{E}_n(\mathbf{k},k_z)=E-i\delta, \tag{8}$$

such that $\mathrm{Im}(\partial\mathcal{E}_n(\mathbf{k},k_z^{(1)}(E,\delta))/\partial k_z)<0$, which gives the ‘‘correct’’ (increasing)[9,16,17] asymptotic behavior of the quasistationary states in the limit $|z|\to\infty$; $\tilde{G}(\mathbf{r},\mathbf{r}';\mathbf{k},k_z^{(1)},E-i\delta)$ is an analytic function of $k_z^{(1)}$.

Using Eq. (7), we write Eq. (6) for the function $F(\mathbf{r};\mathbf{k},E)\equiv\sqrt{|W(\mathbf{r})|}\Psi_{\mathbf{k}}(\mathbf{r},E)$ as

$$F(\mathbf{r};\mathbf{k},E)=\hat{K}(\mathbf{k},k_z^{(1)}(E,\delta)F(\mathbf{r};\mathbf{k},E)) +\frac{id\phi_n(\mathbf{r},\mathbf{K}_c)\sqrt{|W(\mathbf{r})|}}{(k_z^{(1)}(E,\delta)-k_z^{(c)})\partial^2\mathcal{E}_n(\mathbf{K}_c)/\partial k_z^2} \times\int_\Omega\phi_n^*(\mathbf{r}',\mathbf{K}_c)\sqrt{W(\mathbf{r}')}F(\mathbf{r}';\mathbf{k},E)d\mathbf{r}', \tag{9}$$

where $\hat{K}$ is an integral operator with the kernel $\sqrt{|W(\mathbf{r})|}\tilde{G}(\mathbf{r},\mathbf{r}';\mathbf{k},k_z^{(1)},(E-i\delta))\sqrt{W(\mathbf{r}')}$ which is analytic as a function of $k_z^{(1)}$ and, by virtue of Eq. (5), vanishes for sufficiently large $|z|$ and $|z'|$. Under these conditions the bounded inverse operator $(1-\hat{K})^{-1}$ exists,[18] and Eq. (9) becomes

$$k_z^{(1)}(E,\delta)-k_z^{(c)}=\frac{\beta_n(\mathbf{k},k_z^{(1)}(E,\delta))}{1/2\partial^2\mathcal{E}(\mathbf{K}_c)/\partial k_z^2}, \tag{10}$$

where

$$\beta_n(\mathbf{k},k_z^{(1)})=\frac{id}{2}\int_\Omega\sqrt{W(\mathbf{r})}\phi_n^*(\mathbf{r},\mathbf{K}_c)(1-\hat{K})^{-1} \times\sqrt{|W(\mathbf{r})|}\phi_n(\mathbf{r},\mathbf{K}_c)d\mathbf{r}.$$

The condition for Eq. (10) to be solvable is the condition for the existence of a resonance.

If the z component of the reciprocal effective mass tensor is large at the critical point, more precisely, if

$$\left(\frac{m_0}{m^*}\right)_z=\frac{1}{2}\frac{\partial^2\mathcal{E}_n(\mathbf{K}_c)}{\partial k_z^2}\gg\beta_n(\mathbf{k},k_z^{(1)}), \tag{11}$$

then, as follows from a theorem due to Rouché,[19] Eq. (10) has as many zeros as the function $k_z^{(1)}(E,\delta)-k_z^{(c)}$, i.e. one. Hence, for fixed $\mathbf{k}$ and E there is precisely one quasistationary solution.

In the opposite case of large effective masses, small changes in $W(\mathbf{r})$ will take the root of Eq. (10) out of the vicinity of the critical point. This indicates that the probability for resonance features to appear in the scattering of an

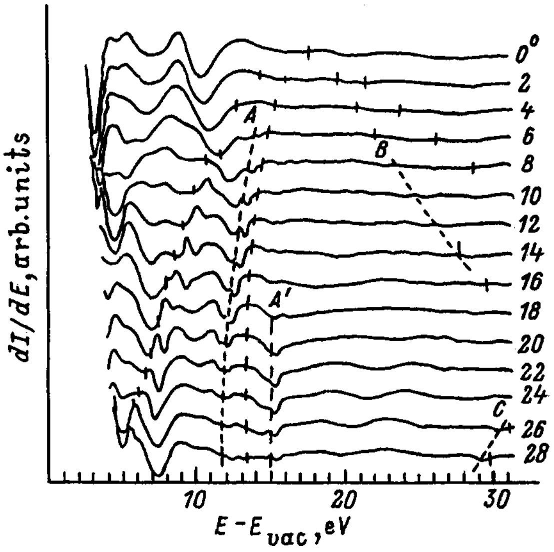

FIG. 1. $\partial I/\partial E$ spectrum of $1T$-TiS_2. The polar angles of incidence of the primary beam are indicated near the curves. The bars mark the diffraction thresholds corresponding to the vectors $\mathbf{g}_1$, $\mathbf{g}_2(\mathbf{g}_2')$, $\mathbf{g}_3(\mathbf{g}_3')$, $\mathbf{g}_4$, and $2\mathbf{g}_1$ in Fig. 2.

electron beam with momentum $\mathbf{p}\approx(\mathbf{k},\sqrt{E_c-\mathbf{k}^2})$ is low on account of the short lifetime of the quasistationary state in this case.

We note that because the solution of Eq. (10) is a continuous function of $\mathbf{k}$ the resonance states (in any case locally) form a band $E_R=E_R(\mathbf{k},\delta)$ which is imbedded in the continuum of the states of the continuous spectrum of the SIC.

3. COMPARISON WITH EXPERIMENT

In the context of the present work, we shall examine experiments on the diffraction of very-low-energy electrons ($E\leqslant 10-15$ eV), where the critical points of volume bands appear explicitly[1] and therefore resonances associated with them can also appear.

Figure 1, which is taken from Ref. 20, displays the energy dependence of the absorbed current $I(E)$ in the $1T$ phase of TiS_2 for different polar angles of incidence of the initial beam, propagating in the direction $\overline{\Gamma}-\overline{M}$ of the two-dimensional Brillouin zone (Fig. 2).

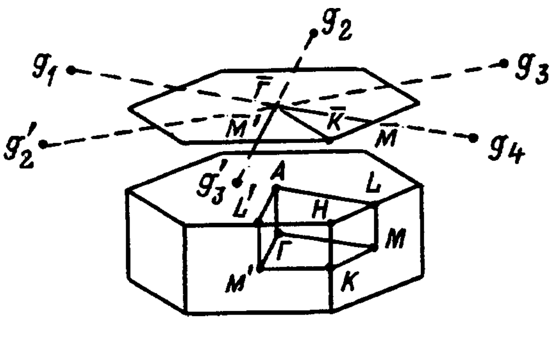

FIG. 2. Surface and volume Brillouin bands of the compound $1T$-TiS_2. $\mathbf{g}_i$ — two-dimensional vectors in the reciprocal lattice of a semiinfinite crystal.

Three types of peaks can be clearly seen in the structure of $\partial I/\partial E$: 1) a dominating structure, corresponding to peaks in $I(E)$ with half-width greater than 1 eV (the distance between the nearest extrema in the curve $\partial I/\partial E$); such a width of the peaks shows that the electrons penetrate quite deeply into the crystal and this, together with the elastic character of the interaction, manifested in the clearly expressed dependence on $\mathbf{k}$, indicate that the peaks are associated with the volume band structure;[20] 2) narrow peaks, which are very sensitive to the surface state, near the diffraction thresholds (A, A', B, and C in Fig. 1); these peaks are entirely justifiably attributed in Ref. 20 to the threshold defect,[10–12] which the authors, following convention, sometimes term a surface resonance; and, 3) the third type of structure, lying in Fig. 1 to the left of the lower diffraction threshold, corresponds to peaks in $I(E)$ with width less than that of the type-I peaks but much greater than that of the type-II peaks. In Ref. 20 this structure is hypothetically interpreted as a surface resonance with large electron penetration into the interior of the crystal.

It is evident from Fig. 1 that the type-III peaks lie next to the maxima or minima of the type-I structure of $\partial I/\partial E$, i.e. they are located near the critical points of volume bands. According to Eq. (10), for a definite character of the volume bands ($m^*\beta\ll 1$), a quasistationary state with a comparatively long lifetime τ exists in a small neighborhood of the real energy $E_c=\mathcal{E}_n(\mathbf{K}_c)$ (the energy of the resonance E_R is close to E_c and therefore $\mathrm{Im}(E_R)\sim 1/\tau$ is small). This situation is probably develops in the experiment under study.

It is important to note that according to Eq. (10) the energy ($\mathrm{Re}[E(\mathbf{k},k_z^{(c)};\delta)]$) and width ($\mathrm{Im}[E(\mathbf{k},\mathbf{k}_z^{(c)};\delta)]$) of the resonance peak are determined by the quantities that characterize the volume band structure, though, of course, according to the derivation of Eq. (10), the presence of the crystal surface is necessary. This qualitatively distinguishes resonances of this type from surface resonances, which depend strongly on the form of the potential barrier. Following Ref. 21, it should be called a "volume resonance." The hypothesis that such resonances could exist was advanced in Ref. 22 on the basis of an analogy with single-center scattering under the condition that the resonance falls within a neighborhood of the branch point of the scattering amplitude of a SIC, which the critical point of the volume bands is.[16]

If the splitting between E_R and E_c is not too small, then the intensity of the resonance peak has the Breit–Wigner form[3]

$$I_R(E)=\frac{b(E,\delta)}{(E-\mathcal{E}_R(\mathbf{k}))^2+\Gamma^2}, \tag{12}$$

where $b(E,\delta)$ depends weakly on the energy, $\mathcal{E}_R(\mathbf{k})=\mathrm{Re}[E_R(\mathbf{k},\delta)]$ is the real projection of the dispersion law of quasistationary states,[3] and $\Gamma=\mathrm{Im}[E_R(\mathbf{k},\delta)]$ is small. This situation is closest to the case of normal incidence of electrons on the TiS_2 surface (Fig. 1). In Fig. 3, the contribution extracted from the experimental curve to the structure of $\partial I/\partial E$ at $E\approx 4$ eV is compared with the energy derivative of

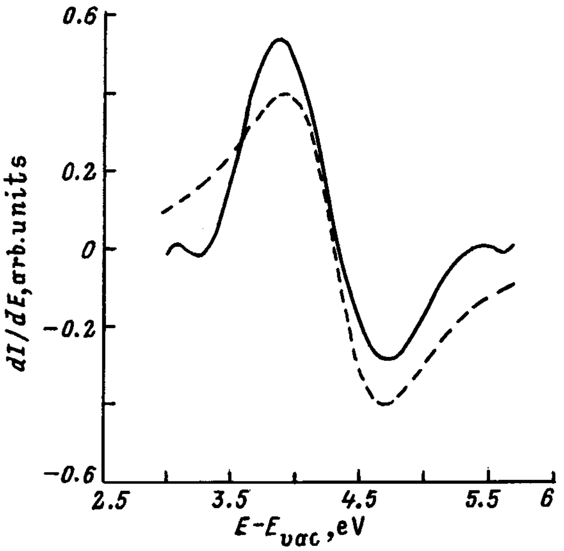

FIG. 3. Contribution of a low-energy resonance to $\partial I/\partial E$ for normal incidence of the primary beam. Solid line — experiment, dashed line — theory.

the intensity calculated from Eq. (12) in the approximation that $b(E,\delta)$ is constant. The theoretical curve corresponds to $b=0.37$, $\delta=0.67$ eV, and $\mathcal{E}_R(0)=4.3$ eV.

The qualitative agreement of the results is obvious. The quantitative differences between the computed and experimental curves are due both to the error in extracting the resonance contribution from the experimental data and to the facts that the energy dependence of $b(E,\delta)$ was neglected and the isolated-resonance approximation was used.

In summary, the following results were obtained: 1) For a definite character of the dispersion law $(m^*\beta\ll 1)$ of the excited bands of an unbounded crystal, comparatively long-lived resonances arise near the critical points; 2) the energy and lifetime of such resonances are determined by the electronic states in the volume of the crystal; 3) these ‘‘volume resonances’’ are manifested in very-low-energy electron diffraction as a fine structure of intermediate width compared with the surface resonances and peaks associated with the critical points of volume bands; 4) sufficiently far from a critical point, the resonance contribution to the scattering intensity is escribed by the crystal analog of the Breit–Wigner formula; and, 5) it follows on this basis that resonances of the indicated type must be taken into account in order to extract the structure of $\partial I/\partial E$ that is associated with the critical points of volume bands in the experimental determination of the dispersion of the final states of the photoelectron emission process[1] and reconstruction of the occupied bands.

E-mail: tv@otf.fti.udmurtia.su

---

[1] V. N. Strocov, Int. J. Mod. Phys. B **9**, 1755 (1995).
[2] G. V. Vol'f, Yu. P. Chuburin, and L. A. Rubtsov, Poverkhnost', No. 10, 81 (1991).
[3] G. V. Vol'f, Yu. P. Chuburin, A. E. Pablov, and L. A. Rubtsova, Poverkhnost', No. 12, 24 (1992).
[4] Yu. P. Chuburin and G. V. Wolf, J. Phys.: Condens. Matter **8**, 631 (1996).
[5] S. G. Louie, T. Thiry, R. Pinchaux, Y. Petroff, D. Chandesris, and J. Lecante, Phys. Rev. Lett. **44**, 549 (1980).
[6] V. N. Strocov and H. I. Starnberg, Phys. Rev. B **52**, 8759 (1995).
[7] V. N. Strocov, H. I. Starnberg, P. O. Nilsson, H. E. Brauer, and L. J. Hollebom, Phys. Rev. Lett. **79**, 467 (1997).
[8] E. G. McRae, Surf. Sci. **11**, 479 (1968).
[9] J. R. Taylor, *Scattering Theory: The Quantum Theory of Nonrelativistic Collisions* (Wiley, N.Y., 1972; Mir, Moscow, 1975, 566 pp.).
[10] E. G. McRae, Rev. Mod. Phys. **51**, 541 (1979).
[11] J. C. Le Bosse, J. Lopez, C. Gaubert, Y. Gauthier, and R. J. Baudoing, J. Phys. C.: Sol. Stat. Phys. **15**, 3425 (1982).
[12] J. C. Le Bosse, J. Lopez, C. Gaubert, Y. Gauthier, and R. J. Baudoing, J. Phys. C.: Sol. Stat. Phys. **15**, 6087 (1982).
[13] V. N. Petrov, S. A. Starovoĭtov, M. S. Galaktionov, B. V. Yushenkov, and Yu. A. Mamaev, Fiz. Tverd. Tela (St. Petersburg) **38**, 1423 (1996) [Phys. Solid State **38**, 787 (1996)].
[14] M. Rossa and F. Moresco, Phys. Rev. Lett. **73**, 822 (1994).
[15] J. B. Pendry, *Low Energy Electron Diffraction,* Academic Press, N.Y., 1974, 406 pp.
[16] Yu. P. Chuburin, Teor. Mat. Fiz. **110**, 443 (1997).
[17] A. I. Baz', Ya. B. Zel'dovich, and A. M. Perelomov, *Scattering, Reactions, and Decays in Nonrelativistic Quantum Mechanics* [in Russian], Nauka, Moscow, 1966, 339 pp.
[18] M. Reed and B. Simon, *Methods of Modern Mathematical Physics* (Academic Press, N.Y., 1972; Moscow, 1977, Vol. 1, 360 pp.).
[19] M. A. Lavrent'ev and B. V. Shabat, *Methods of the Theory of Functions of a Complex Variable* [in Russian], Moscow, 1973, 736 pp.
[20] V. N. Strocov, H. I. Starnberg, and A. R. H. F. Ettema, Solid State Commun. **96**(9), 659 (1995).
[21] G. Capart, Surf. Sci. **13**, 361 (1969).
[22] J. I. Gersten and E. G. McRae, Surf. Sci. **29**, 483 (1972).

Translated by M. E. Alferieff

Recombination kinetics in nonlinear defective LiB_3O_5 crystals

I. N. Ogorodnikov,*) A. V. Porotnikov, and A. V. Kruzhalov

Ural State Technical University, 620002 Ekaterinburg, Russia

V. Yu. Yakovlev

Tomsk Polytechnical University, 634021 Tomsk, Russia

(Submitted January 23, 1998)
Fiz. Tverd. Tela (St. Petersburg) **40**, 2008–2014 (November 1998)

A study of recombination kinetics in LiB_3O_5 (LBO) crystals by time-resolved luminescence and absorption spectroscopy is reported. An investigation of the kinetics of transient optical absorption (TOA) and luminescence under ns-scale electron-beam excitation performed within a broad temperature range of 77–500 K and a 1.2–5-eV spectral interval has established that the specific features in the recombination kinetics observed in LBO involve electronic, B^{2+}, and hole, O^-, trapping centers. The TOA and luminescence kinetics, as well as their temperature dependence, are interpreted by a model of competing hole centers. Relations connecting the kinetics parameters and the temperature dependence to the parameters of the main LBO point defects are presented. © *1998 American Institute of Physics.* [S1063-7834(98)01011-9]

The very first publications reporting development of a technology for growing massive lithium triborate LiB_3O_5 (LBO) crystals of optical quality, and investigation of the main physical properties of this compound, have established LBO as one of the most promising optical materials for use in present-day nonlinear and integrated optics.[1] Indeed, this crystal combines unique characteristics, such as comparatively high nonlinear coefficients, a broad optical transmission band (159–3500 nm), a high surface-destruction threshold (24.6 $J\cdot cm^2$ for a laser pulse duration $\tau_{ex}=1.3$ ns and 25 $GW\cdot cm^2$ for $\tau_{ex}=0.1$ ns), chemical and mechanical stability and moisture resistance.[2,3] Not the least in this list is the large width of the angular and temperature phase-synchronism ranges; for example, the conditions for noncritical phase synchronism for wavelengths from 1025 to 1340 nm are reached within a temperature region from -50 to 180 °C.[4] At the same time our knowledge of the nature of the radiation hardness and optical stability of LBO, electronic-excitation dynamics, electronic structure, point defects, and recombination processes is still inadequate. For instance, Ref. 5 reports a preliminary investigation of point defects, broad-band UV luminescence was revealed and its main properties studied,[6–8] and the electronic structure of perfect and defective LBO crystals were examined experimentally and theoretically.[9–12] Transient optical absorption of LBO was detected, and its study begun.[13]

The objective of this work was to study the kinetics of recombination processes in LiB_3O_5 crystals by time-resolved luminescence and absorption spectroscopy.

1. EXPERIMENTAL DETAILS

The study made use primarily of luminescence and absorption spectroscopy with nanosecond-scale resolution. The excitation was provided by an accelerated ns-scale electron beam with $E_{ex}=0.25$ MeV, $t_{1/2}=3-130$ ns, and $j_{max}=2\times10^3$ $A\cdot cm^{-2}$. The shortest time resolution in these conditions was 4 ns. The measurements were carried out in vacuum within the 1.2–5.0-eV spectral interval at temperatures from 77 to 500 K. A detailed description of the experimental set-up is presented elsewhere.[14]

LiB_3O_5 crystals of high optical quality were grown by Ol'khovaya and Maslov by a modified melt-solution method.[15] The main crystallographic parameters of the LBO crystals produced were in close agreement with those in Ref. 16.

2. EXPERIMENTAL RESULTS

Irradiation of LBO crystals with an electron beam at 77 K results in a build-up of induced optical density with increasing number of excitation pulses (Fig. 1). No decay of the optical density at 77 K on the time scale studied has been found. At the same time the induced optical density saturates with electron flux increasing by less than an order of magnitude (Fig. 1). Above the temperature interval within which carriers are released from the main trapping centers (130–240 K, Ref. 17), one observes transient optical absorption (TOA) assigned[13] to electronic transitions from LBO valence-band states to a local level of the hole O^- center. It was proposed[13] to approximate the TOA decay of LBO at 298 K within the 0.1 μs–10-ms range with a sum of two exponentials in the μs range and one exponential in the ms range. To test the validity of this approach, we have estimated the effect of excitation density and temperature on the TOA kinetics. Indeed, variation of the electron beam current (excitation density) from 12.5 to 23% of the maximum level changes not only the magnitude of the induced optical density but, to a certain extent, the parameters of the decay kinetics (Table I). The best fit to the TOA decay curve in the μs range is obtained by using a sum of two exponentials whose time constants are comparable in order of magnitude

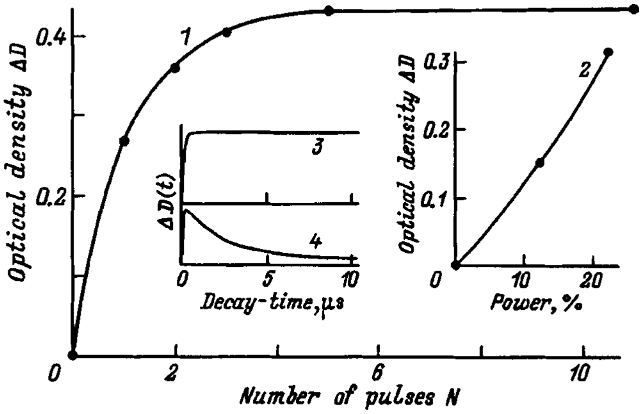

FIG. 1. (*1*) Build-up of induced optical density in LBO in the 3.8-eV region measured at 77 K vs excitation pulse number N at 23% beam power, (*2*) variation of initial TOA intensity ΔD with beam power at 298 K, and characteristic TOA decay kinetics pattern obtained in the 3.8-eV band at (*3*) 77 K and (*4*) 298 K.

to the carrier lifetimes for the trapping centers involved. Besides, while the parameters of the exponentials in the μs range depend to some extent on excitation density (see Table I), they exhibit noticeable stability. Therefore in the study of the temperature dependence of LBO TOA decay in the μs range we used an approximation of the form

$$D(t)=D_{10}\exp(-t/\tau_{a1})+D_{20}\exp(-t/\tau_{a2})+D_3, \quad (1)$$

where D_{10} and D_{20} are the initial values and τ_{a1}, τ_{a2} are the time constants of the LBO TOA decay components, and D_3 is the constant component (of the ms-range exponentials which do not decay significantly on the time scale under study). Table I presents these values for room temperature. The initial TOA level, $D_0=D(t=0)$, decreases with increasing temperature in the 298–500 K range. One can separate three characteristic portions in the $D_0(T)$ curve: 298–370 K, 370–440 K, and above 440 K. The first of them exhibits insignificant change in $D_0(T)$. Within the second and third portions, $D_0(T)$ decreases by a few times, with the rate of this decrease increasing considerably for $T>440$ K. The corresponding activation energies for these portions are estimated as 60 and approximately 400 meV, respectively (Fig. 2). The fitting parameters likewise exhibit a dependence on temperature. For instance, the initial intensities of the D_{20} and D_3 components decrease with increasing temperature, with an activation energy of about 60 meV. The intensity of the fast component $D_{10}(T)$ varies within the 280–370 K interval in opposite relation with $D_{20}(T)$. As the temperature is increased still more, $D_{10}(T)$ and $D_{20}(T)$ begin to vary in a similar way (Fig. 2). The characteristic temperature intervals near 440 and 500 K are not accidental. Indeed, trapping centers with delocalization temperatures of 450 and 510 K were found to exist.[18] The time constants of both TOA decay components decrease monotonically with increasing temperature with close activation energies of about 200 meV (Fig. 2). At the same time the prefactors for the fast and slow components are different, 1.0 and 0.05 GHz, respectively. This indicates a complex decay pattern for TOA centers, with more than one type of defects involved in recombination.

TABLE I. Effect of excitation power on LBO TOA decay kinetics at 298 K.

P_{ex},%	D_1	D_2	D_3	τ_{a1}, μs	τ_{a2}, μs
12.5	0.03	0.06	0.06	1.2	10
23.0	0.11	0.11	0.12	1.5	15

Note: P_{ex} — excitation power; D_1, D_2 — initial values, and τ_{a1}, τ_{a2} — time constants of the exponential TOA decay components; D_3 — constant component of the ms-range exponentials.

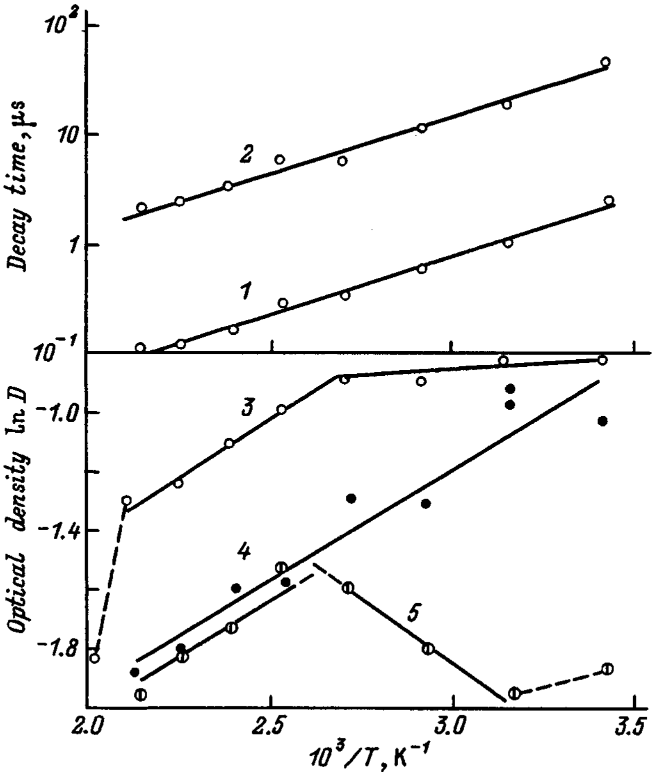

FIG. 2. Temperature behavior of (*1,2*) time constants and (*3–5*) initial intensities for (*1,5*) the first, (*2,4*) the second components, and (*3*) experimental TOA decay kinetics $D(t)$. Symbols — experimental data, solid line — assumed relation.

Excitation of the LBO crystal within the 77–350 K interval was shown[19] to produce a fairly strong pulsed cathodoluminescence. One could expect that its manifestation in this experiment, with the sample excited by a heavy-current electron beam, would be still stronger. An additional contribution to the detected light signal due to pulsed cathodoluminescence could affect considerably the TOA kinetics. An estimation of this contribution showed, however, that even in the short-wavelength region of the spectrum it does not exceed a few percent of the probing light beam and, therefore, cannot affect noticeably the observed TOA kinetics. Figure 3 presents pulsed-cathodoluminescence spectra measured directly after the end of the excitation pulse and 1 μs later. One observes a certain broadening of the spectrum of the fast component compared to that of the slow one. At the same time their spectral profiles are basically similar and consist of the same main elementary bands of Gaussian shape, G_1 and G_2, with maxima at 3.5 and 4.2 eV. Their amplitude ratio $I_m(G_1)/I_m(G_1)=0.23$, and the degree of polarization at 3.8

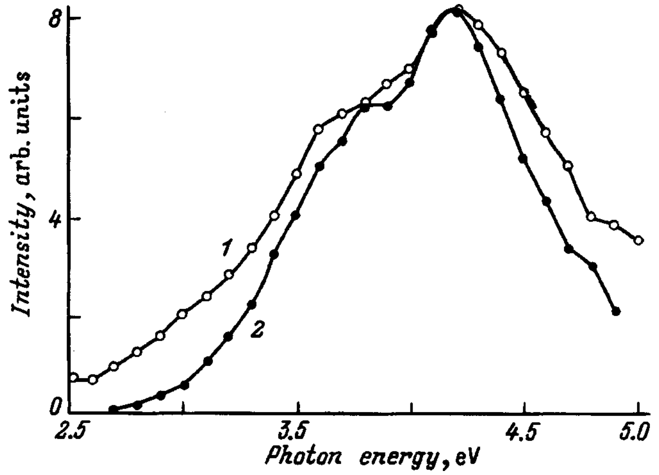

FIG. 3. Normalized LBO pulsed-cathodoluminescence spectra measured at 298 K (*1*) immediately after the excitation pulse and (*2*) 1 μs later.

eV is 60%. The observed luminescence is close in its spectral characteristics to that obtained[20] under synchrotron excitation of LBO. At the same time an analysis of the pulsed-cathodoluminescence kinetics under heavy-current excitation revealed additional details, which are essential for understanding the recombination decay in LBO. For instance, besides the fast exponential with a characteristic decay time shorter than the excitation pulse ($t_{1/2}=7$ ns) one observed μs-range components. Figure 4 shows graphically the kinetics of pulsed-cathodoluminescence decay at 3.8 eV measured at different temperatures in the above time range. These kinetics are characterized by a region of a particularly fast rise, whose parameters depend on temperature. A formal analysis of these kinetics fitted them to a relation

$$I(t)=I_0[1-I_1\exp(-t/\tau_1)]\exp(-t/\tau_2), \qquad (2)$$

where τ_1 and τ_2 are the cathodoluminescence rise and decay time constants, which at 298 K are 1.5 and 25 μs, respectively, and I_0 and I_1 are parameters characterizing the initial pulsed-cathodoluminescence intensity and the relative amplitude of the rise in absorption. The temperature dependences of the experimental $[I(0)=I(t=0)]$ and calculated parameters (τ_1, τ_2, I_0) plotted in Arrhenius coordinates are straight lines (Fig. 4) with activation energies of 130 meV $[I(0)]$, 310 meV (τ_1), 400 meV (τ_2), and 90 meV (I_0). Parameter I_1 does not exhibit any particularly pronounced temperature dependence, namely, it increases from 0.46 at room temperature to 0.60 at 400 K, to decline thereafter to 0.50 at 490 K. The prefactors for τ_1 and τ_2 were found to be 34 and 140 GHz. Close to 440 K the pulsed-cathodoluminescence intensity reaches a maximum, and a further increase of temperature brings about its falloff. It should be pointed out that the position of the luminescence maximum has a tendency to decrease with decreasing excitation power; indeed, it is 440 K in this work, 330 K when excited with a low-current electron beam,[19] and 240 K under x-ray excitation.[6] This may indicate the existence of an external mechanism of thermal luminescence quenching.

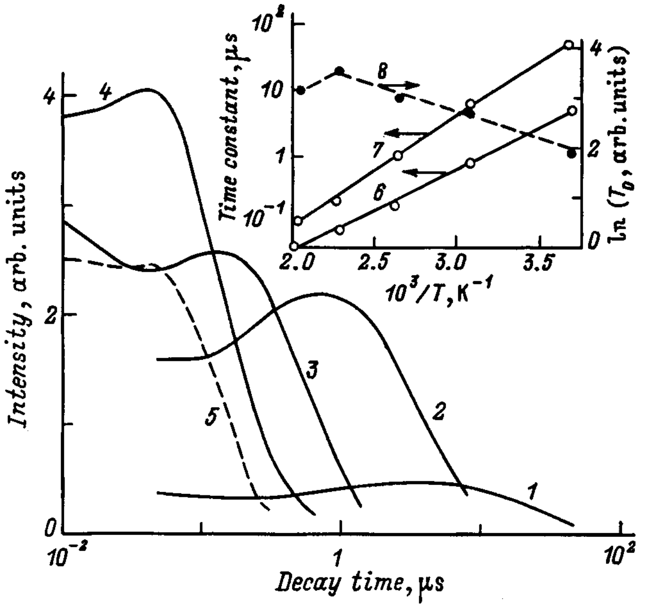

FIG. 4. Pulsed-cathodoluminescence decay in the 3.8-eV band at (*1*) 298 K, (*2*) 348 K, (*3*) 398 K, (*4*) 448 K, and (*5*) 493 K. Inset shows the temperature behavior of the fitting parameters (*6*) τ_1, (*7*) τ_2, and (*8*) I_0.

3. DISCUSSION OF RESULTS

An analysis of available experimental results on the dynamics of electronic excitations and defects in LBO, both published earlier (see, e.g., Refs. 13 and 17–21) and presented here, indicates participation of the main intrinsic lattice defects, B^{2+} and O^-, in energy transport to luminescence centers and a possible involvement of the radiative annihilation of defect-bound excitons in the luminescence. This accounts for the pronounced effect of localized states on the luminescence kinetics. A similar pattern of luminescence processes has recently been established for some other nonlinear crystals (for example, for $\beta=BaB_2O_4$, Ref. 22). Recalling the experimentally observed correlations between the main kinetics parameters of the luminescence and TOA in LBO, it appears reasonable to conjecture that both phenomena originate from the same recombination processes involving the main point defects in LBO, namely, the B^{2+} and O^- centers and, probably, trapping centers annealing at 440 and 510 K. One of the most noticeable features in the kinetics of recombination in LBO observed in this work is the existence of a rising portion in the pulsed-cathodoluminescence decay. Basically, one could propose a number of different explanations for this process (see, e.g., Refs. 23 and 24). At the same time the absence of such a rising portion in the TOA decay, as well as the available additional experimental material,[13,17–21] narrows substantially the range of acceptable hypotheses. We note also that the luminescence and TOA decay time constants are comparable, and that the pulsed-cathodoluminescence rising component is comparable to the first component of TOA decay. At the same time the activation energies derived from the temperature dependence of the luminescence and TOA do not coincide in most cases with those obtained for the main LBO defects and take on some intermediate values. This suggests that the luminescence and TOA decay kinetics cannot be adequately described within

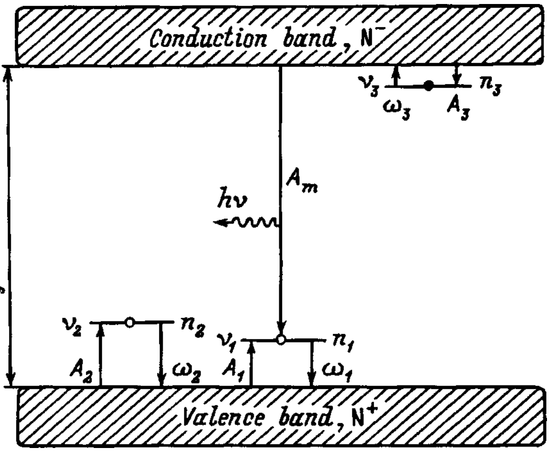

FIG. 5. Energy level diagram for the recombination processes in LBO (see text).

simple model concepts based on independent elementary relaxation processes and isolated trapping centers. One should consider instead a system of balance equations for the case of several local levels.

Figure 5 presents a qualitative energy-level diagram for the assumed recombination processes in LBO. The balance equations describing this system were augmented by a charge neutrality condition to give

$$\begin{cases} \dfrac{dn_1}{dt} = -\omega_1 n_1 + A_1(\nu_1 - n_1)N^+ - A_m n_1 N^-, \\ \dfrac{dn_2}{dt} = -\omega_2 n_2 + A_2(\nu_2 - n_2)N^+, \\ \dfrac{dn_3}{dt} = -\omega_3 n_3 + A_3(\nu_3 - n_3)N^-, \\ \dfrac{dN^-}{dt} = \omega_3 n_3 - A_3(\nu_3 - n_3)N^- - A_m n_1 N^-, \\ \dfrac{dN^+}{dt} = \sum_{i=1}^{2} [\omega_i n_i - A_i(\nu_i - n_i)N^+], \\ n_1 + n_2 + N^+ = n_3 + N^-, \end{cases} \tag{3}$$

where ν_i and n_i are the concentrations of defects and carriers trapped by them (in cm^{-3}), with $n_i(t=0) = n_{i0}$ being the initial carrier concentration, A_i are electron and hole trapping coefficients for the ith level ($\text{cm}^{-3}\cdot\text{s}^{-1}$), A_m is the recombination coefficient, $\omega_i = \omega_{i0}\exp(-E_i/k_B T)$, ω_{i0} and E_i are the frequency factor and activation energy, k_B is the Boltzmann constant, N^- and N^+ are the carrier concentrations in the conduction and valence bands, respectively, and i labels the trapping center (Fig. 5).

According to this level diagram, local centers of three types can be operative here: a shallow electronic trapping center B^{2+} and two moderately deep hole centers. One of the latter, the paramagnetic O^- center, was studied earlier by EPR.[21] As follows from Ref. 13, the observed optical absorption in LBO in the transmission band is due to electronic optical transitions from valence-band states to a local level of the hole O^- center. Therefore, the TOA kinetics were identified with the $n_2(t)$ relation. Within the concept being developed here, the pulsed-cathodoluminescence decay is due primarily to electronic recombination at the hole centers, n_1. It is known that competition between the main, n_2, and additional, n_1, trapping levels may in certain conditions initiate a rise in the luminescence kinetics.[23,24] Consider this point in more detail.

Assuming $A_m n_1 N^- \ll |\omega_1 n_1 - A_1 \nu_1 N^+|$, we use the solution[24] of the problem of two competing trapping centers, which in the notation of Fig. 5 can be written

$$n_1(t) = (n_{10} - A)\exp(-\lambda_1 t) + A\exp(-\lambda_2 t), \tag{4}$$

$$n_2(t) = (n_{20} - B)\exp(-\lambda_1 t) + B\exp(-\lambda_2 t), \tag{5}$$

where λ_1, λ_2 are constants determined from the relations[24]

$$\lambda_1 = a_1 + a_2, \quad \lambda_2 = a_1 - a_2, \tag{6}$$

$$a_1 = \frac{1}{2}[\omega_1(1-\delta_1) + \omega_2(1-\delta_2)], \tag{7}$$

$$a_2 = \left[\frac{1}{4}[\omega_1(1-\delta_1) - \omega_2(1-\delta_2)]^2 + \omega_1\omega_2\delta_1\delta_2\right]^{1/2}, \tag{8}$$

$$\delta_k = A_k\nu_k \Big/ \sum_{i=1}^{2} A_i\nu_i. \tag{9}$$

The coefficients A and B are functions of the trapping-center parameters

$$A = [\omega_2\delta_1 n_{20} - (\omega_1(1-\delta_1) - \lambda_1)n_{10}]/(\lambda_1 - \lambda_2), \tag{10}$$

$$B = [\omega_1\delta_2 n_{10} - (\omega_2(1-\delta_2) - \lambda_1)n_{20}]/(\lambda_1 - \lambda_2). \tag{11}$$

Recalling that TOA is proportional to the trapping-center concentration, $n_2(t)$, we obtain

$$D(t) = \gamma_a[(n_{20} - B)\exp(-\lambda_1 t) + B\exp(-\lambda_2 t)], \tag{12}$$

where γ_a is a coefficient of proportionality. As evident from Eq. (12), the TOA decay kinetics contain two exponential components with time constants

$$\tau_{a1} = \lambda_1^{-1}, \quad \tau_{a2} = \lambda_2^{-1}. \tag{13}$$

The initial TOA intensities are found from Eq. (12) for $t \to 0$

$$D_0 = \gamma_a n_{20}, \quad D_{10} = \gamma_a(n_{20} - B), \quad D_{20} = \gamma_a B. \tag{14}$$

The pulsed-cathodoluminescence kinetics are governed within this model by the relation

$$I(t) = \gamma A_m n_1 N^-, \tag{15}$$

where γ has the meaning of the quantum yield of recombination luminescence. To find $N^-(t)$, we use the third and fourth equations of (3) under the assumption that $\nu_i \gg n_i$, and $dN^-/dt \to 0$. One readily sees that

$$\frac{dn_3}{dt} = -\lambda_3 n_3, \quad \text{where } \lambda_3 = (1-\delta_3)\omega_3. \tag{16}$$

The relative trapping coefficient δ_3 is defined similar to (9). Integrating (16) from $t=0$ to t and substituting the result into the fourth equation of (3) yield

$$N^- = C\exp(-\lambda_3 t), \quad \text{where } C = n_{30}\omega_3/(A_3 n_3). \tag{17}$$

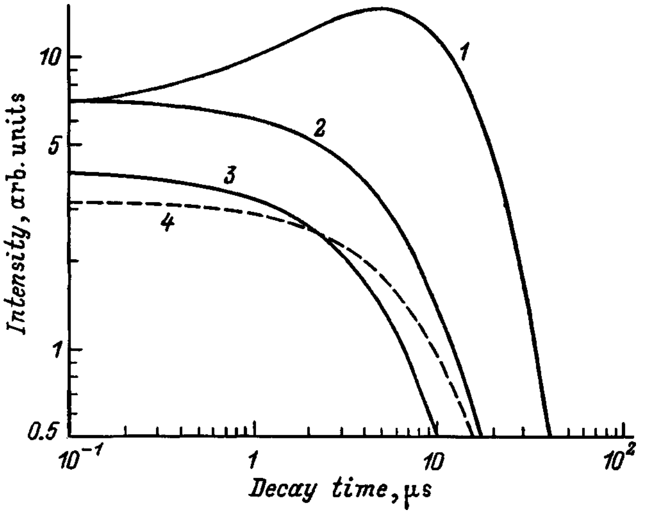

FIG. 6. Model decay kinetics for pulsed cathodoluminescence and TOA obtained for $E_1=300$ meV, $E_2=400$ meV, $E_3=130$ meV, $\omega_1=28.5$ GHz, $\omega_2=1000$ GHz, $\omega_3=0.005$ GHz, $\delta_1=0.4$, $\delta_2=0.1$, $\delta_3=0.5$, $A_m=5\times10^{-7}$ $\mathrm{cm^3\cdot s^{-1}}$, $\nu_1=\nu_2=\nu_3=5\times10^{14}$ $\mathrm{cm^{-3}}$, $n_1=n_3=10^9$ $\mathrm{cm^{-3}}$, $n_2=10^{10}$ $\mathrm{cm^{-3}}$.

Substituting n_1 and N^- in their explicit forms from Eqs. (4) and (17), respectively, into Eq. (15), we obtain a relation for the pulsed-cathodoluminescence kinetics as a sum of two exponentials

$$I(t)=\gamma C[(n_{10}-A)\exp(-\lambda_1^*t)+A\exp(-\lambda_2^*t)]; \quad (18)$$

$$\lambda_1^*=\lambda_1+\lambda_3, \quad \lambda_2^*=\lambda_2+\lambda_3. \quad (19)$$

The condition for the observed rise to occur is $A>n_{10}$. By comparing Eq. (18) with experimental curve (2) one can obtain expressions relating the corresponding coefficients:

$$I(0)=\gamma n_{10}C, \quad I_0=\gamma CA, \quad I_1=1-n_{10}/A; \quad (20)$$

$$\tau_1=(\lambda_1-\lambda_2)^{-1}, \quad \tau_2=(\lambda_2+\lambda_3)^{-1}. \quad (21)$$

The position of the maximum of the rising portion in the pulsed-cathodoluminescence kinetics is determined from the condition of the extremum of function (18)

$$t_m=(\lambda_1-\lambda_2)^{-1}\ln\left(I_1\frac{\lambda_1+\lambda_3}{\lambda_2+\lambda_3}\right). \quad (22)$$

Summing up, we can conclude that the theoretical relations (12) and (18) provide an adequate interpretation for the appearance of two exponentials in the TOA decay and the rise in pulsed cathodoluminescence within the time range under study (Fig. 6), as well as establish dependence of the kinetics parameters on point defect characteristics and experimental conditions. In particular, a comparison of Eqs. (13) and (20) suggests that the theoretical time constants of TOA and pulsed cathodoluminescence should differ somewhat, $\tau_1>\tau_{a1}$ and $\tau_2<\tau_{a2}$. It is this relation that is observed in experiment.

Having established an approximate analytic form for the TOA and pulsed-cathodoluminescence decay, one can now discuss their temperature dependence. For constant γ_a and n_{20}, the initial TOA intensity D_0 should not depend on temperature, whereas the D_{10} and D_{20} components should vary in opposite relation with increasing temperature as $B=B(T)$. Below 400 K, this prediction is seen to agree with experiment (Fig. 2). As the temperature is raised still more, however, D_0 and D_{10} decrease following the same course as the D_{20} component. Thus the kinetics at 400 K are clearly seen to be dominated by some thermal fluctuation process with an activation energy of about 60 meV, which accounts for the decrease of induced optical density with increasing temperature.

A more satisfactory agreement with experiment is obtained by simulating the temperature dependence of the pulsed- cathodoluminescence decay. Indeed, assuming the quantum yield of recombination luminescence γ and the initial concentrations n_{10} and n_{30} to be temperature independent, the factor $C=C(T)$ will dominate the temperature dependence of the initial pulsed-cathodoluminescence intensity $I(0)$. As follows from Eq. (17), an Arrhenius plot of C is a straight line with a slope $-E_3/k_B$. The experimental value of the activation energy of the process (130 meV) agrees well with that of the electronic trapping center B^{2+} in LBO, which is identified in our model with n_3. At the same time the deviation from a straight-line relation at temperatures above 440 K (Fig. 4) suggests that at these temperatures either γ, or n_{10}, or n_{30} are no longer constant. This may be due both to thermal quenching of the luminescence and to some deeper trapping centers becoming active. As follows from Eq. (20), the temperature dependence of the pulsed-cathodoluminescence parameter I_0 is close to that of the initial intensity $I(0)$, but $I_0(T)$ should have a somewhat lower activation energy, exactly what is observed in the experiment. An analysis of the temperature dependence of parameter $I_1(T)$ [Eq. (20)] shows that, for constant n_{10}, $I_1(T)$ should vary in opposite relation to $I_0(T)$. At the same time one cannot expect a noticeable change in I_1, because $A\gg n_{10}$. For temperatures below 400 K, this is in good agreement with experiment. The temperature dependences of the time constants τ_1 and τ_2 estimated from (21) have thermal activation energies $E_1=300$ meV and $E_2=400$ meV and fit well to the experimental relations (Fig. 4).

Thus a combined study of the kinetics of transient absorption and luminescence of LBO crystals excited by an electron beam suggest that the TOA and luminescence of LBO are produced in the same recombination processes involving the main point defects, namely, the electronic B^{2+} and hole O^- centers. The specific features in the TOA and luminescence kinetics, their interrelation and dependence on the point-defect parameters, temperature, and excitation conditions can be described within the model of competing hole centers. The most satisfactory numerical agreement with experiment has been reached in simulation of the luminescence kinetics and of its temperature dependence. At the same time, some of the features observed in the temperature dependence of the TOA decay kinetics cannot be accounted for by this model and require further investigation of the optical and luminescence transitions in TOA centers and of the luminescence of lithium triborate.

The authors express gratitude to V. A. Maslov for providing LBO crystals for the present study.

Support of the INCO-COPERNICUS program (Grant IC15CT960721) is gratefully acknowledged.

*⁾E-mail: ogo@dpt.ustu.ru

---

[1] C. Chen, Y. Wu, A. Jiang, B. Wu, G. You, R. Li, and S. Lin, J. Opt. Soc. Am. B **6**, 616 (1989).

[2] L. Wei, D. Guiqing, H. Qingzhen, Z. An, and L. Jingkui, J. Phys. D **23**, 1073 (1990).

[3] Z. Shuqing, H. Chaoen, and Z. Hongwu, J. Cryst. Growth **99**, 805 (1990).

[4] T. N. Khartsieva, Laz. Tekhn. Optoél. No. 1/2, 76 (1992).

[5] M. P. Scripsick, X. H. Fang, G. J. Edwards, L. E. Halliburton, and J. K. Tyminsky, J. Appl. Phys. **73**, 1114 (1993).

[6] I. N. Ogorodnikov, V. Yu. Ivanov, A. Yu. Kuznetsov, A. V. Kruzhalov, V. A. Maslov, and L. A. Ol'khovaya, Pis'ma Zh. Tekh. Fiz. **19**, No. 2, 14 (1993) [Tech. Phys. Lett. **19**, 77 (1993)].

[7] I. N. Ogorodnikov, A. Yu. Kuznetsov, A. V. Kruzhalov, and V. A. Maslov, Radiat. Meas. **24**, 423 (1995).

[8] V. Yu. Ivanov, I. N. Ogorodnikov, V. A. Pustovarov, and A. V. Kruzhalov, Nucl. Instrum. Methods Phys. Res. A **359**, 339 (1995).

[9] A. Yu. Kuznetsov, M. V. Kuznetsov, I. N. Ogorodnikov, A. V. Kruzhalov, and V. A. Maslov, Fiz. Tverd. Tela (St. Petersburg) **36**, 845 (1994) [Phys. Solid State **36**, 465 (1994)].

[10] A. B. Sobolev, A. Yu. Kuznetsov, I. N. Ogorodnikov, and A. V. Kruzhalov, Fiz. Tverd. Tela (St. Petersburg) **36**, 1517 (1994) [Phys. Solid State **36**, 829 (1994)].

[11] A. Yu. Kuznetsov, A. B. Sobolev, I. N. Ogorodnikov, and A. V. Kruzhalov, Fiz. Tverd. Tela (St. Petersburg) **36**, 3530 (1994) [Phys. Solid State **36**, 1876 (1994)].

[12] A. Yu. Kuznetsov, A. B. Sobolev, I. N. Ogorodnikov, and A. V. Kruzhalov, Radiat. Eff. Defects Solids **134**, 69 (1995).

[13] I. N. Ogorodnikov, A. V. Porotnikov, S. V. Kudyakov, A. V. Kruzhalov, and V. Yu. Yakovlev, Fiz. Tverd. Tela (St. Petersburg) **39**, 1535 (1997) [Phys. Solid State **39**, 1366 (1997)].

[14] V. Yu. Yakovlev, Fiz. Tverd. Tela (Leningrad) **26**, 3334 (1984) [Sov. Phys. Semicond. **26**, 2003 (1984)].

[15] V. A. Maslov, L. A. Olkhovaya, V. V. Osiko, and E. A. Shcherbakov, in *Abstracts of the 10th International Conference on Crystal Growth* (San Diego, 1992), p. 11.

[16] S. F. Radaev, N. I. Sorokin, and V. I. Simonov, Fiz. Tverd. Tela (Leningrad) **33**, 3597 (1991) [Sov. Phys. Solid State **33**, 2024 (1991)].

[17] I. N. Ogorodnikov, A. Yu. Kuznetsov, A. V. Kruzhalov, and V. A. Maslov, Radiat. Eff. Defects Solids **136**, 233 (1995).

[18] I. N. Ogorodnikov, V. I. Kirpa, A. V. Kruzhalov, and A. V. Porotnikov, Zh. Tekh. Fiz. **67**, No. 7, 121 (1997) [Tech. Phys. **42**, 832 (1997)].

[19] I. N. Ogorodnikov, A. Yu. Kuznetsov, A. V. Kruzhalov, and V. A. Maslov, Pis'ma Zh. Tekh. Fiz. **20**, No. 5, 62 (1994) [Tech. Phys. Lett. **20**, 368 (1994)].

[20] I. N. Ogorodnikov, A. V. Porotnikov, V. A. Pustovarov, and A. V. Kruzhalov, J. Lumin. **72-74**, 703 (1997).

[21] A. V. Porotnikov, I. N. Ogorodnikov, S. V. Kudyakov, A. V. Kruzhalov, and S. L. Votyakov, Fiz. Tverd. Tela (St. Petersburg) **39**, 1380 (1997) [Phys. Solid State **39**, 1224 (1997)].

[22] V. Kisand, R. Kink, M. Kink, J. Maksimov, M. Kirm, and I. Martinson, Physica Scripta **54**, 542 (1996).

[23] M. V. Fock, *Introduction to the Luminescence Kinetics of Crystalline Phosphors* [in Russian] (Nauka, Moscow, 1964), 283 pp.

[24] V. V. Antonov-Romanovskiĭ, *Photoluminescence Kinetics of Crystalline Phosphors* [in Russian] (Nauka, Moscow, 1966), 324 pp.

Translated by G. Skrebtsov

Build-up of *F* and *M* color centers in KCl single crystals under combined electron and proton irradiation

M. M. Mikhaĭlov and V. M. Ardyshev

Tomsk Polytechnical University, 634004 Tomsk, Russia

(Submitted January 8, 1998; resubmitted March 17, 1998)
Fiz. Tverd. Tela (St. Petersburg) **40**, 2015–2018 (November 1998)

The *F* and *M* color-center build-up kinetics in KCl crystals under combined irradiation with electrons of energy 15 and 100 keV and 100-keV protons have been studied in the flux range of $10^{13}-10^{15}\,\mathrm{cm}^{-2}$ and at a flux density of $3\times10^{11}\,\mathrm{cm}^{-2}\,\mathrm{s}^{-1}$. It is shown that consecutive irradiation with electrons and protons produces results not obtainable under electron or proton irradiation alone. [S1063-7834(98)01111-3]

Studies of the degradation of optical properties of solids under combined irradiation by low- and medium-energy electrons and protons, which are the major components of cosmic rays in the Earth's radiation belts and other regions of space, are of interest for both basic and applied research. Because of the very complex composition of the materials used in space technology, investigation of the effect of combined action of various radiations should preferably be done on model objects such as alkali halide crystals.

It is known that proton irradiation of alkali halide crystals produces defects both by ionization by a below-threshold mechanism (similar to irradiation by electrons) and through elastic displacement of atoms from their lattice positions.[1,2] Therefore, for comparable energies released in irradiation, protons can be expected to create higher absorption-center concentrations in alkali halides than electrons.

The objective of this work was to study the build-up kinetics of simple (*F*) and complex (*M*) color centers in KCl single crystals under irradiation only by electrons and only by protons, as well as consecutively, by 15- and 100-keV electrons and 100-keV protons.

1. EXPERIMENTAL TECHNIQUES

The study was carried out on a SPEKTR set-up (Ref. 3) provided by an additional source of protons with energy of up to 140 keV. The crystals were 15-mm dia. discs with thickness of 1.0 to 2.5 mm, with an aluminum layer opaque to light deposited on one of the sides in vacuum. Up to 20 samples could be fixed on the stage at one time, and they were irradiated by 15- and 100-keV electrons, 100-keV protons, or consecutively first by electrons, and then by protons of the same particle energies. The incident particle fluxes was $10^{13}-10^{15}$ cm^{-2}, and the flux density, 3×10^{11} $\mathrm{cm}^{-2}\,\mathrm{s}^{-1}$. Irradiation was carried out in vacuum better than 10^{-5} Pa at room temperature. The hemispherical reflectivity (ρ_λ) of samples in the 300–900-nm range was measured directly in vacuum both before and after the irradiation. The values of ρ_λ were converted to the transmissivities τ_λ. Then difference spectra of diffuse reflectivity ($\Delta\rho_\lambda$) or transmissivity ($\Delta\tau_\lambda$) were obtained by subtraction of the corresponding spectra taken before and after irradiation, and they were compared with the induced absorption spectra. The spectra thus obtained were subsequently treated by the ORANG program which included the parameters of all known elementary bands to deconvolute the *F* and *M* absorption features.

The halfwidth and positions of the maxima of the bands were taken equal to 0.35 and 2.23 eV (*F* band) and 0.12 and 1.49 eV (*M*).[4]

2. EXPERIMENTAL RESULTS AND THEIR DISCUSSION

Figure 1a,b presents the build-up kinetics of *F* and *M* centers in samples irradiated only by electrons of energy 15 and 100 keV, only by protons of energy 100 keV, and consecutively first by electrons, and after that by protons of the same energies. Figure 2a,b compares the sum of concentrations of these centers produced by irradiation only with electrons and only with protons with the results of consecutive irradiation first by electrons, and then by protons. The oscillator force *f* was accepted equal to 0.8 for the *F* centers,[4] and to 2/3 of *f* for the *M* centers (Ref. 5). Table I lists the values of the additivity coefficient *A* calculated from the expression

$$A=n_{F,M}^{e\to p}/(n_{F,M}^{e}+n_{F,M}^{p})\,, \tag{1}$$

where $n_{F,M}^{e\to p}$ is the concentration of the *F* and *M* centers created in consecutive irradiation by electrons and protons, and $n_{F,M}^{e}$ and $n_{F,M}^{p}$ are the *F* and *M* center concentrations produced in irradiation by electrons or protons only, respectively.

These data lead to the following conclusions:

1) For fluxes $\Phi\leqslant10^{14}$ cm^{-2} ($t\leqslant330$ s), the concentration of *F* and *M* centers produced by protons is higher than that created under electron irradiation. For larger Φ, the quasi-stationary concentrations n_F and n_M of these centers are higher than those generated by 15-keV electrons but lower than those due to 100-keV electrons (curves *1–3* in Fig. 1a,b);

2) The concentrations of *F* and *M* centers produced in consecutive irradiation with 15-keV electrons and protons within the flux range studied are higher than those due to electrons or protons only (curves *1,3,4* in Fig. 1a and 1b);

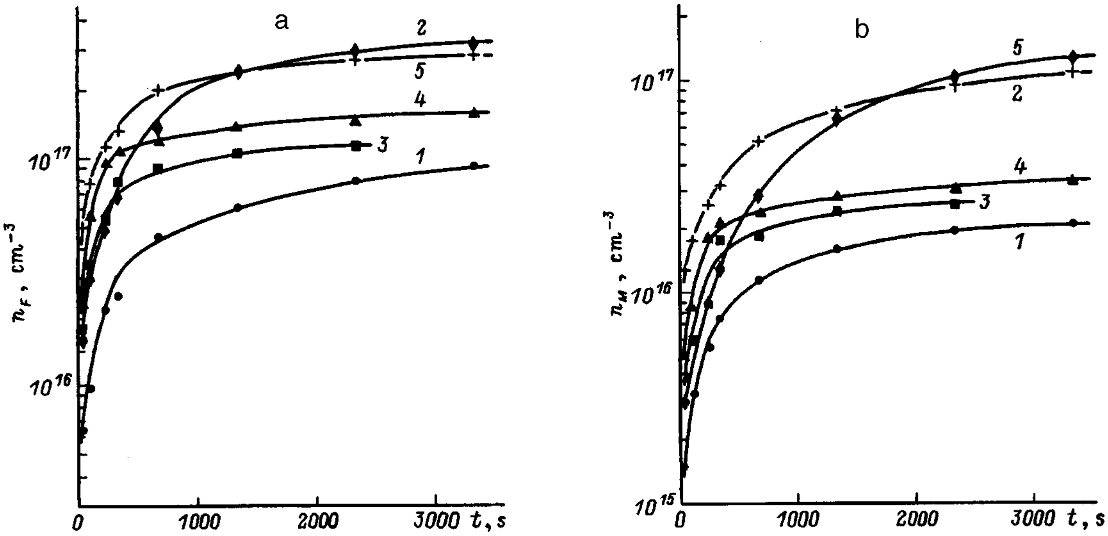

FIG. 1. Dependence of the concentration of (a) *F* centers and (b) *M* centers in KCl on irradiation time (flux) by (*1*) 15-keV electrons, (*2*) 100-keV electrons, (*3*) 100-keV protons, (*4*) consecutively by 15-keV electrons and 100-keV protons, and (*5*) consecutively by 100-keV electrons and 100-keV protons.

(3) For fluxes $\Phi \leqslant 10^{14}$ cm^{-2}, the sum of the *F* center concentrations (Σn_F) produced separately by electrons (15 keV) and by protons is less than the n_F observed under consecutive irradiation first by electrons, and thereafter by protons of the same energy. As the flux increases, Σn_F becomes larger than n_F generated under consecutive irradiation (curves *1* and *2* in Fig. 2a);

(4) The sum of the *M* center concentrations (Σn_M) created under separate irradiation by electrons and protons (15 keV) within the Φ range studied is larger than that produced under consecutive irradiation (curves *3* and *4* in Fig. 2b);

(5) The additivity coefficient *A* for *F* centers decreases from 1.2 to 0.7 with the flux increasing from 10^{13} to 10^{15} cm^{-2}. For *M* centers, $A < 1$ (Table I);

(6) In the case of consecutive irradiation by 100-keV electrons and, after that, by protons the concentration of *F* centers produced for $\Phi \leqslant 10^{14}$ cm^{-2} and that of *M* centers created for $\Phi < 5 \times 10^{14}$ cm^{-2} are larger than those produced only by electrons and only by protons (curves *2,3,5* in Fig. 1a,b). At the same time for $\Phi > 5 \times 10^{14}$ cm^{-2} the values of n_F and n_M practically coincide with those obtained under irradiation with 100-keV electrons (curves *2* and *5* in Fig. 1a,b);

(7) The sums of the concentrations Σn_F and Σn_M created only by electrons (100 keV) and only by protons are initially, for $\Phi < (1-2) \times 10^{14}$ cm^{-2}, smaller than the *F* and *M* center concentrations produced under consecutive irradiation by electrons and protons of the same energies, but be-

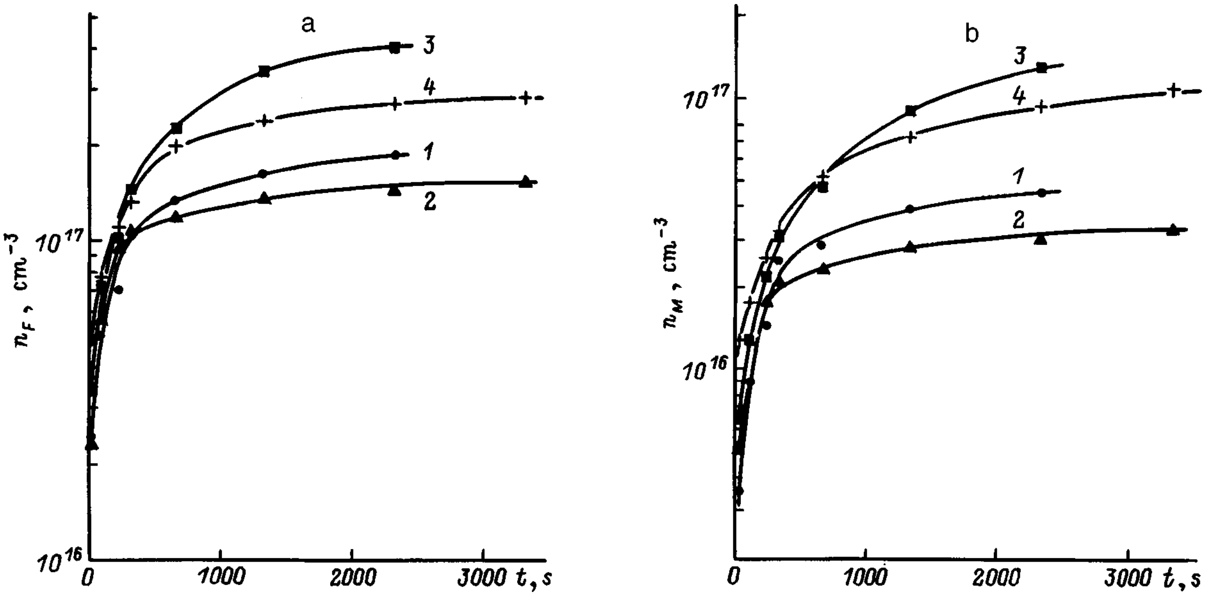

FIG. 2. Dependence of (a) the sum of *F* center concentrations and (b) the sum of *M* center concentrations in KCl on irradiation time (flux) by (*1*) 15-keV electrons and 100-keV protons, (*3*) 100-keV electrons and 100-keV protons, and of *F* and *M* center concentrations under consecutive irradiation (*2*) by 15-keV electrons and 100-keV protons and (*4*) by 100-keV electrons and 100-keV protons.

TABLE I. Additivity coefficient A for combined irradiation of KCl crystals by electrons and protons.

Irradiation regime	Centers	Φ, cm^{-2}							
		1×10^{13}	3×10^{13}	7×10^{13}	1×10^{14}	2×10^{14}	4×10^{14}	7×10^{14}	1×10^{15}
Electrons 15 keV	F Centers	1.20	1.06	1.02	1.00	0.88	0.83	0.76	0.7
Protons 100 keV	M Centers	0.70	0.80	0.84	0.82	0.79	0.70	0.67	⋯
Electrons 100 keV	F Centers	⋯	1.34	1.12	0.98	.084	0.69	0.66	⋯
Protons 100 keV	M Centers	⋯	1.60	1.25	1.12	1.10	0.80	0.72	⋯

come larger with increasing Φ (curves *3* and *4* in Fig. 2a,b);

(8) The additivity coefficient for the F and M centers decreases with increasing flux and approaches one for $\Phi=(1-2)\times10^{14}$ cm^{-2} (Table I);

(9) M centers start to form already at low fluences ($\sim10^{13}$ cm^{-2}), both under separate and consecutive irradiation by electrons and protons.

The above features in defect formation observed under irradiation of KCl crystals both separately by electrons and protons and consecutively, first by electrons, and thereafter by protons, are apparently due to differences in the slowing-down parameters of these particles in solids. Table II presents the first two moments of the distributions of specific energy losses, R_p and ΔR_p, integrated energy losses for ionization, $(dE/dx)_i$, and KCl atom displacement, $(dE/dx)_d$, integrated cross sections for ionization, σ_i, and displacement, σ_d, as well as integrated concentrations of ionized, N_i, and elastically displaced, N_d, atoms calculated taking into account the average number of displacements per atom ν.

σ_i was calculated from the expression

$$\sigma_i=(N_0ZI)^{-1}(dE/dx)_i, \tag{2}$$

where N_0 is the atomic concentration (3.2×10^{22} cm^{-3}), Z is the effective atomic charge (18), and I is the hydrogen ionization potential.

As seen from Table II, the layer thickness a ($a=R_p+\Delta R_p$) in the case of irradiation by 100-keV protons practically coincides with that for 15-keV electrons, while being considerably less than that for 100-keV electrons. The values of σ_i and N_i calculated in different approximations for the case of proton irradiation differ from one another by not more than a factor three. These values exceed, however, by two to three orders of magnitude the ones obtained for irradiation by 15- and 100-keV electrons.

The values of σ_d and N_d for protons differ from one another by about an order of magnitude and are less than the corresponding values for ionization by two to three orders of magnitude. It thus follows that the integrated energy losses of 100-keV protons in KCl are due primarily to ionization.

Based on the data of Table II, our experimental results can be explained by assuming the existence of additional recombination channels associated with surface local levels, as well as with defects which form in elastic displacement of atoms under proton irradiation. Surface recombination is most effective in the case of irradiation by 15-keV electrons and 100-keV protons, because the electronic excitations and the associated defects lie close to the surface. For this reason the F and M center concentrations observed in these conditions are lower than those produced by 100-keV electrons.

For low proton fluxes, the defect concentration is comparatively small, thus making surface recombination dominant. The concentration of electronic excitations in this case is higher than that obtained under 15-keV electron irradiation, and this favors production of F and M centers in higher concentrations. The recombination rate via defects increases

TABLE II. Slowing-down parameters for KCl irradiation by electrons and protons.

Parameter	Electrons		Protons	Method of calculation
	15 keV	100 keV	100 keV	
R_p, cm	2.8×10^{-5}	1×10^{-3}	1.4×10^{-4}	Refs. 6 and 7
ΔR_p, cm	9.4×10^{-5}	3×10^{-3}	1.9×10^{-5}	Refs. 6 and 7
$(dE/dx)i$,eV/cm	2.1×10^{7}	4.6×10^{6}	1.8×10^{9}	Ref. 8
$(dE/dx)_d$, eV/cm	⋯	⋯	2.4×10^{6}	Refs. 6 and 7
σ_i, cm^2	2.7×10^{-18}	5.9×10^{-19}	2.3×10^{-16}	Ref. 8
			5.8×10^{-16}	By Lindhard[1,2]
			2.1×10^{-16}	By Firsov[1,2]
σ_d, cm^2	⋯	⋯	5.6×10^{-19}	By Rutherford[1,2]
			7.6×10^{-18}	Refs. 6 and 7
N_i, cm^{-3}	$8.8\times10^{4}\Phi$	$1.9\times10^{4}\Phi$	$6.7\times10^{6}\Phi$	By Firsov[1,2]
			$1.9\times10^{7}\Phi$	By Lindhard[1,2]
			$7.4\times10^{6}\Phi$	Ref. 8
N_d, cm^{-3}	⋯	⋯	$6.2\times10^{4}\Phi$	By Rutherford[1,2]
			$8.4\times10^{5}\Phi$	Refs. 6 and 7
ν			3.46	Ref. 9

with increasing proton flux. However, if the electronic excitation level is high, the *F* and *M* center concentration will remain higher than that produced by 15-keV electrons.

The decrease of the additivity coefficient *A* with increasing flux can be assigned to recombination-stimulated destruction of defects. In the case of nonradiative recombination at defects, the released energy directly transforms into lattice vibrations. Localized initially near the recombination center, this vibrational energy dissipates in the form of phonons. An increase in vibrational energy can result in destruction of the complex *M* centers, as well as in annihilation of vacancies and interstitials (destruction of *F* centers).

This mechanism should be more efficient for comparable thicknesses of the defected layers produced by 15-keV electrons and 100-keV protons, and this is confirmed by the experiment.

The above results can be summed up as follows.

1) The concentration of *F* and *M* centers produced under consecutive irradiation of KCl crystals by electrons and protons is not equal to the sum of the concentrations of these centers when using electrons or protons only;

2) For $\Phi = 1 \times 10^{13} - (1-2) \times 10^{14}$ cm^{-2}, the additivity coefficient *A* for *F* and *M* centers (15- and 100-keV electrons and 100-keV protons), as well as for *M* centers (electrons and protons of 100 keV), exceeds one, while for $\Phi = (1-2) \times 10^{14} - 10^{15}$ cm^{-2} it is less than one. For *M* centers (15-keV electrons and 100-keV protons), $A < 1$ within the flux range studied.

The authors express their gratitude to M. I. Dvoretskiĭ and E. V. Komarov for assistance in measurements, and to M. V. Belyakov for calculation of the absorption spectra.

[1] I. A. Abroyan, A. N. Andronov, and A. I. Titov, *Physical Foundations of Electronic and Ionic Technology* [in Russian] (Vysshaya Shkola, Moscow, 1984), 319 pp.

[2] V. L. Vinetskiĭ and G. A. Kholodar', *Radiation Physics of Semiconductors* [in Russian] (Naukova Dumka, Kiev, 1979), 332 pp.

[3] L. G. Kositsyn, M. M. Mikhaĭlov, N. Ya. Kuznetsov, and M. I. Dvoretskiĭ, Prib. Tekh. Ėksp. No. 4, 176 (1985).

[4] A. A. Vorob'ev, *Color Centers in Alkali Halide Crystals* [in Russian] (TGU, Tomsk, 1968), 387 pp.

[5] C. Z. van Doorn, Phys. Rev. Lett. **4**, 236 (1960).

[6] V. V. Yudin, in *Physical Foundations of Ion-Beam Doping* [in Russian] (Gor'kiĭ, 1972), p. 10.

[7] V. V. Yudin, Ėlektronn. Tekhn., Ser. 2 (No. 2, 3, 1974).

[8] V. V. Yudin, Ėlektronn. Tekhn., Ser. 2 (No. 4, 15 198‘5).

[9] J. F. Gibbons, IEEE **60**, No. 9, 53 (1972).

Translated by G. Skrebtsov

PHYSICS OF THE SOLID STATE VOLUME 40, NUMBER 11 NOVEMBER 1998

First-principles calculations of the electronic structure of fluorite-type crystals (CaF_2, BaF_2, SrF_2, and PbF_2) containing Frenkel defects. Analysis of optical and transport properties

V. P. Zhukov and V. M. Zaĭnullina

Institute of Solid-State Chemistry, Ural Branch of the Russian Academy of Sciences, 620219 Ekaterinburg, Russia

(Submitted November 3, 1997; resubmitted March 23, 1998)
Fiz. Tverd. Tela (St. Petersburg) **40**, 2019–2025 (November 1998)

The electronic structure of the alkali-earth fluorides CaF_2, BaF_2, SrF_2, and PbF_2 with Frenkel defects is investigated in the tight-binding approximation by the LMTO method. The defect formation and migration energies are calculated. The electronic structure and optical excitations of a *H* center in a defective fluorite structure are examined. It is shown on the basis of calculations of the binding energies that CaF_2, BaF_2, and SrF_2 are ionic compounds, while the chemical bond in PbF_2 is partially covalent. Possible methods of displacement of interstitial fluorine atoms that lead to the observed optical spectra of an *H* center are investigated. © *1998 American Institute of Physics.* [S1063-7834(98)01211-8]

The fluorides of alkali-earth (AE) elements possess anomalously high ionic conductivity[1,2] and are promising optical materials for the vacuum ultraviolet range.

Anionic Frenkel defects (anti-Frenkel defects—AFDs) —interstitial ions F^- and vacancies bound with them—play the dominant role in the formation of ionic transport in AE fluorides.[3] It has also been established experimentally that *F*, V_{k^-}, and *H* centers are present in the fluorides CaF_2, BaF_2, and SrF_2 which have undergone special treatment.[4–6] In investigations of ionic conductivity, the *H* center, whose structure is close to that of the AFD structure, is of most interest. According to ESR and optical spectroscopy data,[7] the *H* center is a molecular ion F_2^- oriented along the [111] direction.

A series of investigations of ionic transport has been conducted by classical molecular dynamics (MDs).[8,9] Spatiotemporal modeling of ionic conductivity by MD was performed in Ref. 10 for CaF_2, in Ref. 11 for BaF_2, in Ref. 12 for SrF_2, and in Ref. 13 for PbF_2. The classical MD method permits calculating a variety of thermodynamic characteristics of crystals. However, the applicability of the MD method is considerably limited by the need to fit empirical pair potentials for the interionic interaction, which presents substantial diffculties for compounds where the chemical bond has partial covalent character.

In Refs. 14 and 15 the semiempirical methods of quantum chemistry were used to study the electronic structure of defects in alkali-metal and AE fluorides. These methods have a number of well-known drawbacks which limit their accuracy and sphere of application.

Systematic calculations of the electronic structure of AE fluorides by nonempirical computational methods were initiated in the 1970s,[16–19] but there are no earlier attempts to calculate the electronic structure of defects in AE fluorides or the characteristics of ionic transport by nonempirical methods. An exception is Ref. 19, where calculations of the formation energy of defects in MgO were performed by a nonempirical Hartree–Fock method using the cluster approximation. We have made the first ab initio investigation of the band structure of defective fluorides CaF_2, BaF_2, SrF_2, and PbF_2 by the linear muffin-tin orbitals method (LMTO). In the present paper it is shown that this method permits calculating in reasonable agreement with experiment the energy of formation and migration of Frenkel defects, to determine the reason for the different stability of cationic and anionic sublattices, and to determine the possible atomic displacments that occur in an anti-Frenkel defect.

1. CRYSTAL STRUCTURE

The structure of fluorite consists of a superposition of two cubic sublattices formed by cations and anions (Fig. 1). Anions form a primitive cubic sublattice, while cations occupy positions at the centers of cubes formed by eight anions (i.e. they occupy locations only in half of all anionic cubes), forming a face-centered cubic sublattice. The fluorite unit cell consists of four formula units MF_2, where M is a cation. A face-centered cubic sublattice formed by empty positions (interstices) can also be distinguished in the fluorite lattice. In our calculations, a so-called extrasphere—a pseudoatom with zero nuclear charge and a basis of self-consistent atomic orbitals—is placed in each interstice. This quite ''loose'' structure makes possible ionic transport in fluorite crystals. The lattice periods for CaF_2, BaF_2, SrF_2, and PbF_2 crystals are, respectively, 5.45, 5.78, 6.18, and 5.93 Å.[20]

As a result of thermal excitations, some interstices are occupied in a disordered manner by cations (Frenkel defects — FDs) or anions (anti-Frenkel defects). At low temperatures the concentration of Frenkel defects is low, but there are experimental and theoretical indications that in the superionic phase the degree of occupation of interstices can reach 0.3.[3]

At present there are no accurate nonempirical methods for calculating the total electronic-nuclear energy of disor-

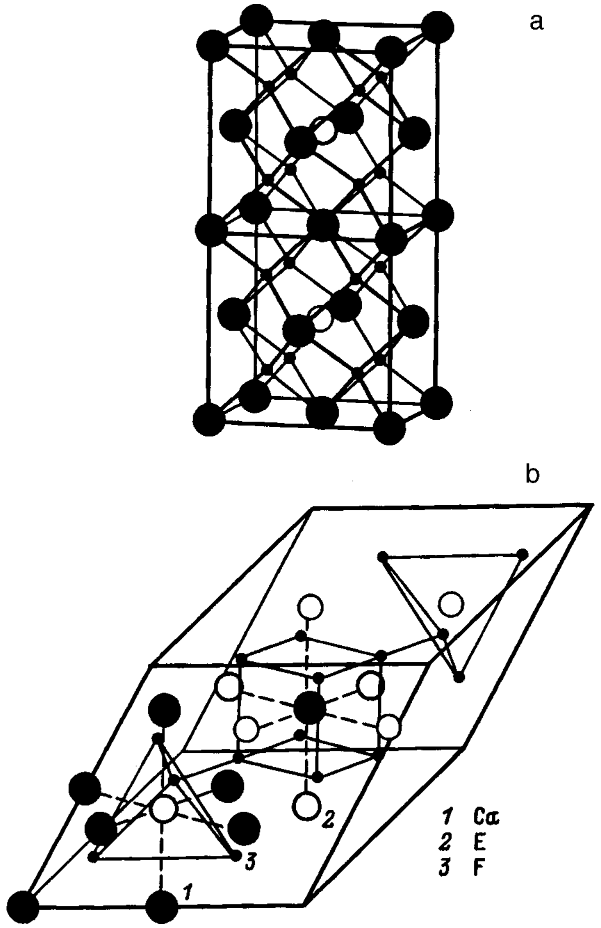

FIG. 1. Fragment of the crystal structure of fluorite (a) and a 2×2×2 supercell used in the LMTO calculations (b).

dered solids. To be able to use the band methods developed for periodic crystals to calculate the electronic structure, we employed the supercell method. The 2×2×2 rhombohedral supercell (Fig. 1) which we employed is obtained by double translation along primitive vectors. Thus, the atomic bases in the present calculations have the form $M_8F_{16}E_8$, where M = Ca, Sr, Ba, and Pb, while E is an extrasphere. An AFD in such a cell is obtained by transferring a fluorine ion into a neighboring interstice; in so doing, a vacancy is formed in the anionic sublattice. The dimensions of the supercell make it possible to place an interstitial fluorine ion in the first or second coordination sphere relative to the lattice vacancy.

In our calculations the Frenkel defects are separated by a distance of at least two primitive-translation vectors. We shall present below data showing that the interaction between defects at such distances can be taken as negligibly small, at least for the structure of single-electron states, i.e. the defects can be assumed to be isolated from one another.

2. COMPUTATIONAL METHOD

The calculations of the electronic band structure of CaF_2, BaF_2, SrF_2, and PbF_2 were performed by the linear muffin-tin orbitals method in the tight-binding approximation (LMTO–TB), the mathematical principles of which are expounded in Ref. 21. The computational method as a whole corresponds to that described in Ref. 22, so that we shall only describe the computational details that permit choices.

The set of atomic orbitals (AOs) which are employed for constructing the Bloch functions of the crystal included the valence *ns*-AOs of the Ca, Sr, and Ba atoms, $n=4, 5, 6$; the *np* and $(n-1)d$ AOs of Ca, Sr, and Ba were not included in the basis of Bloch functions and were included in the construction of the Hamiltonian matrices by down-folding,[23] based on the Löwdin perturbation theory.[24] The *s* states of the extra spheres were also included in the atomic basis, while the *p* and *d* states of the extraspheres were taken into account only as part of the down-folding procedure. The $6s$ $6p$, and $5d$ AOs of the lead atoms were included in the atomic basis. The $2p$ AOs from the fluorine atoms were included in the basis, while the $2s$ and $3d$ orbitals of fluorine were taken into account of the basis of the down-folding model.

The calculations were performed for 64 *k* vectors per Brillouin zone (eight *k* vectors for its irreducible part). The radii of the atomic spheres were determined by an automatic procedure described in Ref. 22, from the condition that these spheres fill the volume of a defect-free crystal. The values obtained by this procedure for the radii of AE atoms and extra spheres differ by 5–15%, while the radii of the extra spheres and fluorine atoms differ by 37–41%. The correct choice of the radii of the extraspheres and the real atoms, which change places, forming an AFD, plays an important role in obtaining results of adequate accuracy for the defect formation energy. We assumed that a real atom occupying the position of an extra sphere acquires its radius and, conversely, the radii of the atoms and the extra spheres that do not participate in defect formation remain unchanged. It is known that in the LMTO method the errors due to overlapping of atomic spheres grow as the cube of the overlapping.[25] Since in our work the differences of the total energy of an ideal crystal and a crystal with a defect are analyzed, the indicated scheme for calculating the atomic radii makes it possible to reduce the error to a minimum. Other methods of determining the atomic radii for crystals with defects give defect formation energies which are two to three times higher than the values presented below.

3. ELECTRONIC BAND STRUCTURE OF IDEAL AE FLUORIDES AND CRYSTALS WITH DEFECTS. STRUCTURE OF *H* CENTERS IN AE FLUORIDES AND THEIR OPTICAL SPECTRA

Calculations of the band structure of ideal CaF_2, SrF_2, and BaF_2 crystals show that the $2p$ states of fluorine form the valence band and the *s* states of the cation form the conduction band. In the case of a PbF_2 crystal the valence-band bottom consists of the $2p$ orbitals of fluorine, while the $6p$ AOs of lead correspond to the conduction band. The typical total density of states for CaF_2 for the present calculations is displayed in Fig. 2. The total densities of states for the other fluorides differ mainly by the band gap (E_g), which is compared in Table I with the experimental data of Refs. 26–28. One can see that the calculations to decrease the band gap from CaF_2 to SrF_2 and then increase to BaF_2. A PbF_2 crystal is characterized by a small band gap. The computed

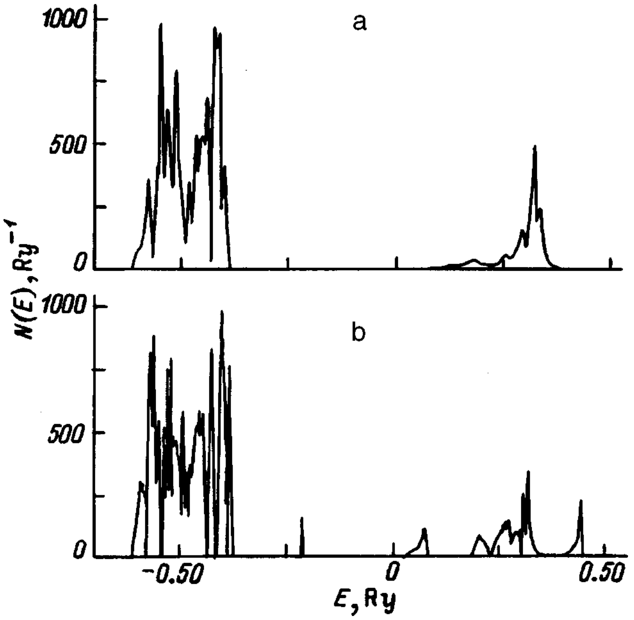

FIG. 2. Total density of states for an ideal CaF_2 crystal (a) and a crystal with an anti-Frenkel defect (b).

values of the band gap are lower than the experimental data. This is a systematic error of electron-density-functional methods.

When FDs and AFDs appear, the calculations show an appreciable narrowing of the band gap. On this basis it can be expected that as temperature increases, especially with a sharp increase in defect density near the superionic transition temperature, the energy of the fundamental absorption edge should decrease. However, an intense excitonic absorption peak is superposed on the fundamental absorption edge in fluorides.[28] Moreover, the AFD density in AE fluorides is low, which makes it difficult to check this result experimentally.

One can see from Fig. 2 that the appearance of AFDs in an AE fluoride crystal also results in the appearance of a peak (to which an interstitial fluorine ion makes the main contribution) in the density of states in the band gap. Interestingly, the width of this peak is very small and does not exceed the step size, 0.005 Ry = 0.068 eV, used in our calculations to construct the histogram of the density of states. The very weak dispersion with respect to the k vector of the states of this peak shows that the interaction between anti-Frenkel defects in amounts of one per 32-atom cell (the degree of filling of interstices by defects is 0.125) leads to very small errors in analyzing the electronic excitations.

TABLE I. Band gap E_g in CaF_2, SrF_2, BaF_2, and PbF_2 crystals.

Crystal	E_g, eV	
	Exp.	Theory
CaF_2	12.10	6.11
SrF_2	11.25	6.02
BaF_2	10.57	6.37
PbF_2	3.00	3.64

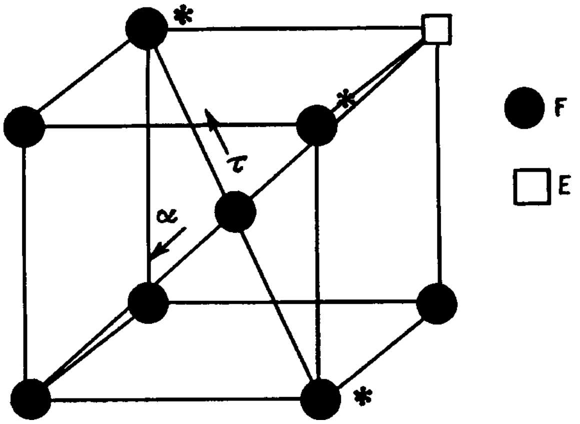

FIG. 3. Possible displacements of an interstitial fluorine atom which lead to the formation of a molecular ion F_2^- : α — axial, τ — tangential.

Although the AFDs are high-temperature formations, numerous investigations have shown that stabilization of AFD-like defects is possible. Thus, in Ref. 29 impurity centers were stabilized by doping rare-earth elements with trivalent ions, followed by x-ray irradiation. It was shown that impurity centers have ESR spectra and quasimolecular optical spectra. These spectra were interpreted by comparing with the results of Hartree–Fock calculations of the F_2^- ion. However, this approach, which neglects the interaction of the ion with its surroundings, is limited. Specifically, the fine structure of optical spectra is ignored; it is impossible to determine the type of atoms (site or interstitial) on which the unpaired electron is localized; and, the orientation of the interstitial ion relative to the vacancy bound to it in the fluorine sublattice cannot be determined.

It follows from the fact that only one ''impurity'' level is observed when an interstitial fluorine ion is localized precisely at the center of the cube of the nearest-neighbor lattice fluorine ions that displacements of interstitial ions play an important role in the formation of the quasimolecular spectra of a H center. One can see from Fig. 3 that if an axis is drawn from the center of the above-mentioned cube in the direction of the interstitial vacancy, then it can be assumed a priori that a molecular ion F_2^- can form by a displacement of an interstitial fluorine ion both along the axis (axial displacement α) and perpendicular to the axis (tangential displacement τ). Calculations performed for a set of such displacements in CaF_2 show that the impurity level splits into several quasimolecular levels even for small displacements of both types. The optimal (for agreement with optical experimental data) values of the electron transition energies between quasimolecular levels are obtained with a tangential displacement $\tau = 0.1$ from the F–F axis in an ideal cube. Neutron diffraction investigations of powder fluoride samples confirm the displacement of an interstitial fluorine atom by $0.07a$ (a — lattice period) from the position at the center of the cube.[3] The position of the computed quasimolecular levels with such a displacement is shown in Fig. 4. The types of symmetry of the levels here were obtained by constructing charts of the spatial distribution of the wave functions for the center of the Brillouin zone. One can see that the order of the

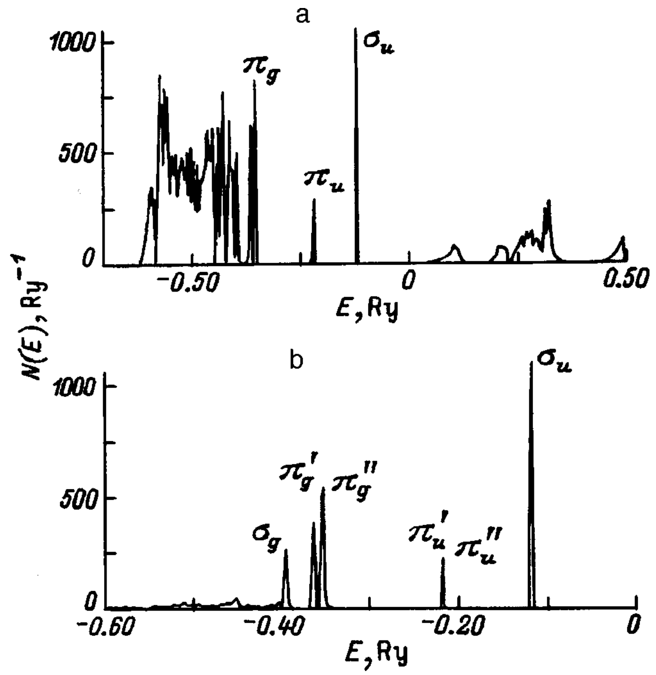

FIG. 4. Total density of states for a CaF_2 crystal with AFDs with displacement of an interstitial fluorine atom by $\tau = 0.1$ (a) and the sum of the densities of states for the fluorine atoms in a F_2^- molecule (b).

levels with increasing energy corresponds to that obtained for the F_2^- ion without exact calculations and taking account of only the spatial orientation of the lobes of the $2p$ valence orbitals of the fluorine atoms (Fig. 5).

The construction of the total density of states for a pair of fluorine atoms, forming an *H* center, in the low-energy range shows (Fig. 4b) that an interaction of a F_2^- ion with the crystal environment results in splitting of the π_g level into two levels π_g' and π_g'', symmetric and antisymmetric with respect to a plane passing through the axially-displaced fluorine ion and the nearest site atoms, marked by asterisks in Fig. 3. At the same time the splitting of the high-energy level π_u is very small.

The computed excitation energies are presented in Table II together with the types of transitions that follow from our calculations and from the experimental work in Ref. 29. Comparing them shows that the identification of the low-energy excitation 1.65 eV, made in Ref. 29 on the basis of the molecular Hartree–Fock calculations, is wrong. The work in Ref. 9 also has the drawback that the splitting of the π_g level is ignored, which results in a not entirely correct interpretation of the high-energy excitation at 3.87 eV. At the same time, the optical spectra presented in Ref. 29 clearly show the complicated character of the high-energy excitation.

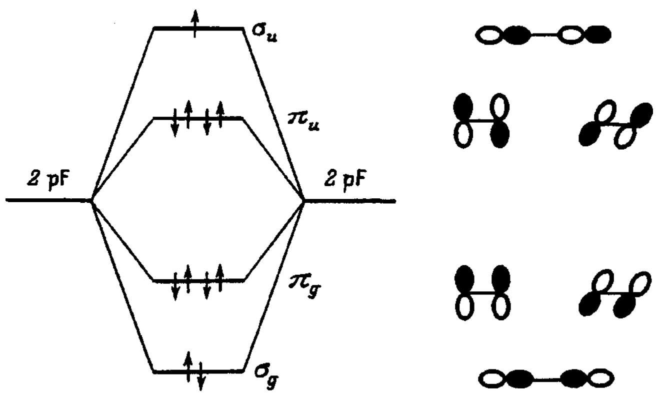

FIG. 5. Qualitative scheme leading to the formation of the energy levels of a F_2^- molecule.

TABLE II. Optical excitation energies for an *H* center in CaF_2 according to LMTO calculations.

Computed excitation energy, eV	Type of transition	Experimental excitation energy,[29] eV	Identification of excitation according to Ref. 29
1.77	$\pi_u \rightarrow \sigma_u$	1.65	$\pi_g \rightarrow \sigma_u$
3.34, 3.20	$\pi_g \rightarrow \sigma_u$	3.87	$\sigma_g \rightarrow \sigma_u$
3.78	$\pi_g \rightarrow \sigma_u$		

Comparing with the experimental data the energies of the optical excitations with a variable axial displacement of the interstitial atoms also makes it possible to estimate the probability of the presence of such displacements. Specifically, as the axial displacement α increases from 0 to 0.2, the energy of the low-energy excitation remains too low, equal to 1.36 eV at $\alpha = 0.2$. However, at $\alpha = 0.2$ the computed energy of the next excitation (4.15 eV) is now higher than the experimental values. Therefore the good agreement with experiment that obtains for tangential displacement cannot be obtained by varying the axial displacement. An additional argument in favor of tangential displacement is that for all values of the axial displacements the total energy of a supercell is appreciably higher than in the case of tangential displacements (for $\alpha = 0.2$ by 2.08 eV).

According to the experimental data and their interpretation of the basis of Hartree–Fock calculations, the intermolecular level σ_u, to which electrons are transferred in optical excitations, is occupied in the normal state by an unpaired electron, which gives rise to an ESR spectrum (the second electron is captured by the rare-earth dopant atom). According to the data of Ref. 7, the unpaired electron is delocalized between a pair of fluorine atoms, forming a *H* center, in the ratio 6:4. Our calculations show that the contributions of interstitial and site fluorine ions to the maximum of the electronic density of states in the range of the peak σ_u are 698 and 407 Ry^{-1}, respectively, i.e. the calculations show delocalization of the unpaired electron between the atoms of a *H* center in a ratio close to 6:4 in favor of the interstitial fluorine ion.

4. CHEMICAL BOND AND CHARACTERISTICS OF THE IONIC CONDUCTIVITY IN AE FLUORIDES

One of the predominant views concerning the mechanism of ionic conduction in AE fluorides is that cationic sublattice is more stable than the anionic sublattice, which ‘‘melts’’ at high temperatures, giving rise to ionic conduction. Simulation of ionic conduction by classical molecular dynamics completely confirms this view.[8–13] However, the reason why the cationic sublattice is more stable remains

TABLE III. Formation and migration energies of defects in CaF_2, SrF_2, BaF_2, and PbF_2 crystals.

		CaF_2	SrF_2	BaF_2	PbF_2
AFD energy,	Theory	4.37	3.57	2.55	2.58
eV	Exp.	2.2−3.1	1.7−2.3	1.6−1.9	1.1
FD energy,	Theory	9.47	8.56	4.40	9.79
eV	Exp.	6.0	⋯	⋯	⋯
Migration	Theory	0.84	0.66	0.45	0.37
energy, eV	Exp.	0.52	0.47	0.58	0.23−0.33

unclear. Specifically, their arises the question of whether or not there exists a chemical bond inside the cationic sublattice.

We checked the validity of such assumptions by estimating the strength of the chemical bond. More accurately, we estimated its covalent component in the binding energy, which is determined for a pair of atoms R and R' as

$$U_{RR'}=\int^{E_F} d\varepsilon \sum_{lm\in R} \sum_{l'm'\in R'} H_{Rlm,R'l'm'} D_{Rlm,R'l'm'}(\varepsilon).$$

Here $H_{Rlm,R'l'm'}$ are the matrix elements of the Hamiltonian, and $D_{Rlm,R'l'm'}$ are the density matrix elements. Orbitals with quantum numbers l and m belong to atom R, while orbitals with quantum numbers $l'm'$ belong to the atom R'. The integration extends over the entire energy range of the valence states, up to the Fermi level. Previously, similar calculations were used to investigate the chemical bond in refractory transition-metal compounds.[30]

As an example, we shall present typical results for SrF_2. Here the energy of the chemical bond for the Sr–Sr pair of atoms is -0.037 eV, while the energy of Sr–F is -0.028 eV. The very low values of these energies ascompared with their coupling energy or thermal atomization energy show that the chemical bond Sr–F is almost purely ionic, while the Sr–Sr bond is essentially absent. PbF_2 is an exception. While the Pb–Pb bond is negligible, the covalent component of the Pb–F bond is -0.58 eV.

Thus, the calculations show that the higher stability of the cationic sublattice in AE fluorides cannot be explained by the presence of any chemical bond in this sublattice, i.e. the stability of the crystals as a whole is determined by the electrostatic interaction between the sublattices. Nonetheless, the calculations show that the sublattices differ greatly with respect to the formation of Frenkel defects with their participation.

In Table III we compare with experimental data our computed values of the FD energy (transfer of a cation into an interstice) and the AFD energy (transfer of an anion). There is a large variance in the experimental values of the AFD formation energies. The computed values are systematically higher than the experimental values by a factor of 1.5–2, but they correctly reproduce the fact that the AFD formation energy decreases from Ca to Ba. The FD formation energies are approximately two times higher than the AFD formation energies. The experimental value, available only for CaF_2 (6.0 eV[31]), also confirms that the probability of FD formation is low compared with that of AFD formation.

The somewhat large size of the supercell employed in the calculations also makes it possible to estimate the potential barriers for migration of anions in AE fluorides. The lattice vacancy formed with the transition of a fluorine ion to an interstitial position could be located in the first or second coordination sphere with respect to an interstitial atom at distances of 2.72 and 4.72 Å, respectively, for the case of CaF_2. According to calculations, for all crystals studied, the total crystal energy with the vacancy in the second coordination sphere is higher than the energy with the vacancy in the first coordination sphere.

Since the transfer of a vacancy from the first to the second coordination sphere is equivalent to the opposite motion of fluorine ions, the potential barriers at the first step of migration of fluorine ions can be estimated as the difference of the total energies for the two indicated variants of the relative arrangement of an interstitial ion and the corresponding vacancy. The potential barriers estimated in this manner are presented in Table III. The experimental values of the migration energy are most often obtained from measurements of the ionic conductivity.[31] In so doing, two possible ion-conduction mechanisms are distinguished: motion of vacancies formed with the appearance of AFD and motion of interstitial ions. The results of both analysis of the experimental data and molecular-dynamic simulation[32,33] show that the first ion-conduction mechanism, characterized by lower migration energies, dominates. The experimental values of the vacancy migration energy[33] are also presented in Table III. Just as our calculations, experiments show that the migration energy decreases from CaF_2 to SrF_2 and PbF_2. A discrepancy exists only for BaF_2: The experimental value of the migration energy is too high.

We note that the discrepancy between our computational characteristics and their experimental analogs is on the whole systematic: The formation energies of defects and the migration energies are typically too high by a factor of 1.3–1.6. This casts doubt on the reliability of the experimental value of the migration energy in BaF_2.

The data obtained correspond to ionic conductivity increasing from CaF_2 to SrF_2 and BaF_2 in a wide temperature interval.[31] The lowest computed value of the migration energy corresponds to the highest ionic conductivity, observed for PbF_2.[33]

In summary, the following results have been obtained in this work: 1) The electronic structure of CaF_2, SrF_2, BaF_2, and PbF_2 crystals with Frenkel defects was calculated for the first time by a nonempirical method; 2) it was shown that the chemical bond in the compounds CaF_2, SrF_2, and BaF_2 is ionic, covalence effects are important only for PbF_2, and there are no bonds between the AE atoms; 3) the formation and migration energies of defects have been calculated for the first time by a nonempirical method, and AFD formation occurs preferentially in the series of compounds investigated; 4) the preferred direction of displacement of an interstitial fluorine ion accompanying the formation of H centers was determined and it was found that localization of an unpaired electron on an interstitial fluorine ion in an H center predominates; and, 5) the errors made in identifying bands in the optical spectra of *H* centers on the basis of molecular Hartree–Fock calculations were exposed.

The results obtained indicate that investigations of the properties of defects in ionic crystals and characteristics of ionic conduction by electronic density functional methods in combination with the supercell method hold promise. One reason that the values of the AFD formation energies are too high is that in our work the interaction between AFDs was neglected. It is assumed that this interaction, which likewise can be analyzed on the basis of our approach, at high temperatures lowers the AFD formation energy, which ultimately results in a transition to the superionic state. It is known, for example, that lead fluoride undergoes a transition to a superionic state starting at 500 K, while the phase transition temperature of other fluorides is about 1200 K. For this reason, a higher concentration of anti-Frenkel defects can be expected for PbF_2 at the temperatures at which the conductivity is estimated, and for this reason the formation energy of defects should be larger because of the interaction between defects. This can explain why our computed value of the FD formation energy is too high. It is also necessary to take account of the fact that the interstitial ions can occupy not only interstices with octahedral symmetry but also positions in directions with three- and two-fold symmetry.[7] On the other hand, the too high values of the computed defect formation energies and migration energies can be explained in part by the fact that the nonspherical components of the potential inside the atomic spheres and the relaxations of ions in the first coordination sphere of an interstitial atom were neglected. This is impossible in the LMTO method in the tight-binding basis, which is not intended for calculating interatomic forces. But it is entirely possible to take account of these effects in more laborious methods, for example, in the total-potential LMTO[34] or LAPW methods.[35] The main advantage of nonempirical approaches over molecular statics or dynamics methods[36] is that there is no need to fit empirical parameters, which makes it much more difficult to use semiempirical methods for systems with a partially covalent or metallic chemical bond.

This work was supported by a Russian Fund for Fundamental Research, Grant No. 98-03-33188a.

*) E-Mail: ntst@ihim.ural.ru

---

[1] A. V. Chadwick, Solid State Ionics **8**, *3*, 209 (1983).

[2] W. Hayes, *Crystals with the Fluorite Structure*. Clarendon, Oxford (1974).

[3] M. B. Salamon [Ed.], *Physics of Superionic Conductors* [in Russian], Znanie, Riga, 1982, 315 pp.

[4] W. Hayes and F. R. Lambourn, Solid State Phys. **6**, 11 (1973).

[5] N. Iton and K. Tanimura, J. Phys. Chem. Solids **51**, 717 (1990).

[6] A. C. Lewandowski and T. M. Wilson, Phys. Rev. B **52**, 100 (1995).

[7] A. M. Stoneham, *Theory of Defects in Solids: The Electronic Structure of Defects in Insulators and Semiconductors* (Clarendon Press, Oxford, 1975; Mir, Moscow, 1978, Vol. 2).

[8] R. E. Boyett, M. G. Ford, and P. A. Cox, Solid State Ionics **81**, 61 (1995).

[9] C. A. J. Fesher, M. S. Islam, and R. J. Brook, J. Solid State Chem. **128**, 137 (1997).

[10] Y. Kaneco and A. Ueda, J. Phys. Soc. Jpn. **57**, 3064 (1988).

[11] S. Ch. Aĭt'yan and A. K. Ivanov-Shits, Fiz. Tverd. Tela (Leningrad) **32**, 1360 (1990) [Sov. Phys. Solid State **32**, 795 (1990)].

[12] D. Bingham, A. N. Cormack, and C. R. A. Catlow, J. Phys.: Condens. Matter **1**, 1213 (1989).

[13] A. B. Walker, M. Dixon, and M. J. Gillan, J. Phys. C **15**, 4061 (1982).

[14] J. L. Gavartin, E. K. Shidlovskaya, A. L. Shluger, and A. N. Varaksin, J. Phys.: Condens. Matter **3**, 2237 (1991).

[15] E. A. Kotomin, A. Stashans, L. N. Kantorovich, A. I. Lifshitz, A. I. Popov, and I. A. Tele, Phys. Rev. B **51**, 8770 (1995).

[16] V. V. Nemoshkalenko, V. G. Aleshin, and M. T. Panchenko, Dokl. Akad. Nauk SSSR **231**(3), 585 (1976) [Sov. Phys. Dokl. **21**, 660 (1976)].

[17] N. V. Starostin and M. P. Shepilov, Fiz. Tverd. Tela (Leningrad) **17**, 822 (1975) [Sov. Phys. Solid State **17**, 523 (1975)].

[18] J. Kudrnovsky, N. E. Christensen, and J. Masek, Phys. Rev. B **43**, 12 597 (1991).

[19] R. W. Grimes, C. R. A. Catlow, and A. M. Stoneham, J. Phys.: Condens. Matter **1**, 7367 (1989).

[20] G. B. Bokiĭ, *Introduction to Crystal Chemistry* [in Russian], Moscow State University, Moscow, 1954, 367 pp.

[21] O.-K. Andersen, Z. Pawlowska, and O. Jepsen, Phys. Rev. B **34**, 5253 (1986); O.-K. Andersen, O. Jepsen, and M. Sob, in *Electronic Band Structure and Its Applications,* edited by M. Yussouf, Springer, Berlin, 1987; O.-K. Andersen, in *The Electronic Structure of Complex Systems,* edited by P. Phariseau and W. M. Temmerman (Plenum Press, N.Y., 1984).

[22] V. P. Zhukov, Fiz. Tverd. Tela (St. Petersburg) **38**, 166 (1996) [Phys. Solid State **38**, 90 (1996)].

[23] W. R. L. Lambrecht and O.-K. Andersen, Phys. Rev. B **34**, 2439 (1986).

[24] P.-O. Löwdin, J. Chem. Phys. **19**, 1396 (1951).

[25] O.-K. Andersen, A. V. Postnikov, and S. Yu. Savrasov, Mater. Res. Soc. Symp. Proc. **253**, 37 (1992).

[26] R. T. Pool, J. Szajman, R. C. G. Leckey, J. G. Jenkin, and J. Liesgang, Phys. Rev. B **12**, 5872 (1975).

[27] M. Scrocco, Phys. Rev. B **26**, 1535 (1982).

[28] G. W. Rubloff, Phys. Rev. B **5**, 663 (1972).

[29] J. H. Beaumont, W. Hayes, D. L. Kirk, and G. P. Summers, Proc. R. Soc. London, Ser. A **315**, 69 (1970).

[30] R. F. Sabiryanov, O. N. Mryasov, A. L. Ivanovskiĭ, and G. P. Shveĭkin, Metallofiz. **13**, 77 (1991); R. F. Sabiryanov and A. L. Ivanovskiĭ, Metallofiz. **14**, 7 (1991).

[31] V. N. Chebotin and M. V. Perfil'ev, *Electrochemistry of Solid Electrolytes* [in Russian], Khimiya, Moscow, 1978.

[32] M. J. Gillan, Solid State Ionics **9/10**, 755 (1983).

[33] P. Hagenmuller, *Inorganic Solid Fluorides. Chemistry and Physics* (Academic Press, N.Y., 1985, p. 260).

[34] M. Methfessel, Phys. Rev. B **38**, 1537 (1988).

[35] H. Krakauer, M. Posternak, and A. J. Freeman, Phys. Rev. B **19**, 1706 (1979); M. Weinert, J. Math. Phys. **22**, 2433 (1981).

[36] A. N. Varaksin, *Interaction and Migration of Point and Structural Defects in Insulators Based on Alkali-Halide Crystals: Computer Modeling* [in Russian], Ekaterinburg, 1977.

Translated by M. E. Alferieff

PHYSICS OF THE SOLID STATE VOLUME 40, NUMBER 11 NOVEMBER 1998

Effect of Mo^{3+} ions on Nd^{3+} spin-lattice relaxation in $Y_3Al_5O_{12}$

L. K. Aminov, I. N. Kurkin, S. P. Kurzin, and D. A. Lukoyanov

Kazan State University, 420008 Kazan, Russia

(Submitted March 27, 1998)
Fiz. Tverd. Tela (St. Petersburg) **40**, 2026–2028 (November 1998)

The content of Mo^{3+} ions in YAG:Nd garnet samples prepared by different technologies has been studied, and the spin-lattice relaxation rate of these ions at temperatures of 4–5 K measured. It is concluded is drawn that Mo^{3+} ions can play the part of rapidly relaxing centers mediating the Nd^{3+} spin-lattice relaxation at liquid-helium temperatures. This may account for a number of features in the spin-lattice relaxation of rare-earth ions in garnets, observed earlier at low temperatures. © *1998 American Institute of Physics.* [S1063-7834(98)01311-2]

Nd^{3+}-doped YAG ($Y_3Al_5O_{12}$) crystals find broad application in quantum electronics.[1] These crystals were studied in considerable detail by various techniques, including EPR and electron spin-lattice relaxation (SLR).[2–5]

Relaxation occurring at liquid-helium temperatures was found to exhibit a number of features. The relaxation rate was reported to depend nonlinearly on temperature, and nonmonotonically on Nd^{3+} concentration.[3] The relaxation rates measured in samples grown in different ways were observed to differ noticeably even at nominally equal Nd^{3+} concentrations.[4,5] This permits a conclusion that the ″anomalous″ behavior of relaxation at low temperatures is due to crystal defects which may not be directly associated with the Nd^{3+} impurity ions themselves. Such active defects may be localized vibrations, two-level systems, and foreign ions present in the crystal.

In some technologies, crystals are grown in molybdenum crucibles,[3] which enables incorporation of molybdenum ions into the crystal matrix. A comprehensive study of the EPR spectrum of Mo^{3+} ions in YAG revealed that molybdenum substitutes for aluminum in the octahedral position, and that the lowest levels of Mo^{3+} are two doublets with an initial splitting of $8-10\,\mathrm{cm}^{-1}$.[6] It thus appears reasonable to assume that at least some of the features in the SLR of Nd^{3+} ions in garnets are being affected by Mo^{3+} ions. The present work was aimed at testing this hypothesis. With this purpose in mind, we studied the Mo^{3+} content in various YAG:Nd samples, as well as measured the SLR time of these ions at helium temperatures and made simple theoretical estimates.

1. EXPERIMENTAL RESULTS

We continued our investigation of YAG:Nd^{3+} crystals grown by different methods, namely, A and A' were YAG:1 at.%Nd^{3+} samples grown by horizontal directed crystallization (HDC), and the B sample (YAG:1 at.%Nd^{3+}) was pulled by the Czochralski method. Besides the above samples (used in our earlier spin-lattice relaxation time measurements[4,5]), we studied also HDC-grown A'' samples (YAG:0.1 at.%Nd^{3+}). EPR and spin-lattice relaxation measurements were performed on an IRÉS-1003 spectrometer-relaxometer at a frequency ~9.25 GHz. The temperature was varied within the 4–50 K interval. We also present the results of our measurements on sample A carried out within the 1.5–10 K interval on a custom-built relaxometer, which likewise operated at ~9.25 GHz.

The actual Nd^{3+} concentration in sample A'' was found to be substantially lower than 0.1 at.%. The Nd^{3+} EPR intensity of this sample was low enough to permit observation of the EPR spectrum of foreign impurities. The characteristics of this spectrum (the g factors, the number of magnetically inequivalent centers, hyperfine structure) argued unambiguously for the presence in crystal A'' of a Mo^{3+} impurity. The effective g factors of the lowest Mo^{3+} doublet are $g_{\|}=1.967$, $g_{\perp}=3.91$.[6] The principal value of $g_{\|}$ corresponds to the C_3 axis of the nearest neighbors. We may recall that the Nd^{3+} SLR measurements reported in Refs. 4,5 were made in the H$\|$[100] orientation. The resonant magnetic fields for the Nd^{3+} ion measured at 9.25 GHz in this orientation are $H=1685$ Oe (twofold-degenerate line) and $H=4480$ Oe (fourfold-degenerate line). The Mo^{3+} EPR spectrum taken in this orientation consists of one fourfold-degenerate line in a magnetic field $H=1950$ Oe.

The Mo^{3+} concentration in sample A'' was found to be $1.2\times10^{17}\,\mathrm{cm}^{-3}$, or ~0.0013% of octahedral Al^{3+} ions. The concentrations were obtained by comparing the intensity of the Mo^{3+} EPR spectrum with that of a reference sample with a known paramagnetic-center concentration.

We needed data on foreign impurities in samples A, A', and B containing 1 at.% Nd^{3+}, whose EPR spectrum is so strong as to mask the presence of small amounts of other impurities. Therefore the search for foreign impurity centers in these samples was done at $T\sim40-50$ K, where the EPR spectrum of Nd^{3+} is not observed because of the fast SLR of these ions. The results obtained are as follows. In samples A and A', the Mo^{3+} EPR spectrum is observed. The Mo^{3+} concentration in sample A is $\sim2.2\times10^{17}\,\mathrm{cm}^{-3}$, or ~0.002% of the Al^{3+} ions. In sample A', the Mo^{3+} concentration is somewhat higher than that in A. No Mo^{3+} ions (or other impurities) were found in sample B.

It is in the Mo^{3+}-containing samples A and A' that one

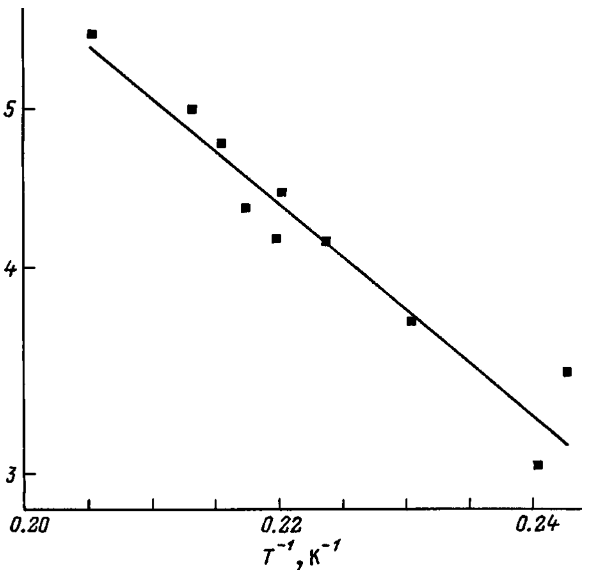

FIG. 1. Spin-lattice relaxation of Mo^{3+} ions in $Y_3Al_5O_{12}$ single crystals. The straight line is a plot of Eq. (1).

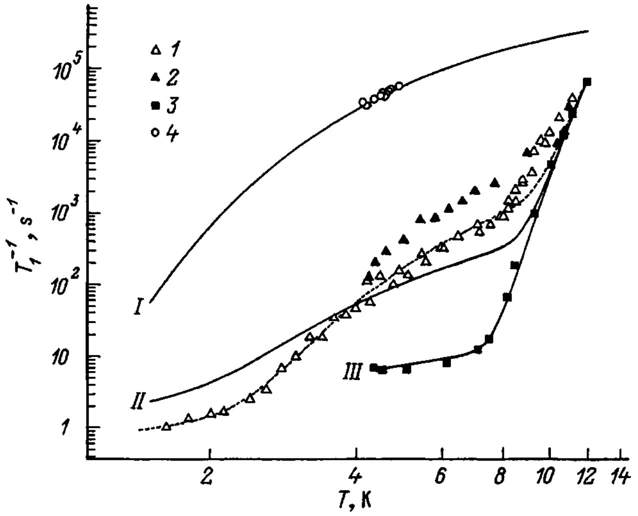

FIG. 2. Spin-lattice relaxation of Nd^{3+} and Mo^{3+} ions in $Y_3Al_5O_{12}$ single crystals. *1* — Nd^{3+}, sample *A*; *2* — Nd^{3+}, sample *A′*; *3* — Nd^{3+}, sample *B*; *4* — Mo^{3+}, sample *A″*. Solid lines I–III are plots of Eqs. (1), (6), and (4), respectively. Dashed line is a plot of Eq. (7).

observes a faster spin-lattice relaxation of Nd^{3+} ions which depends anomalously on temperature, while sample *B* did not exhibit any anomalies. It appears natural to assume that the anomalies are caused by cross relaxation via the Mo^{3+} ions. For this to occur, the SLR rate of Mo^{3+} ions should be high enough. Because information on the SLR of Mo^{3+} ions in YAG is lacking, we made an attempt at performing such measurements. The time T_1 was measured by the pulsed saturation technique. We took for this purpose sample *A″*, which did not contain Nd^{3+} ions. Because the Mo^{3+} concentration was low, the YAG crystal chosen had a large enough volume (~ 100 mm^3). The resonator design permitted EPR (and relaxation) measurements of such a large sample only for one fixed orientation of the external magnetic field in the horizontal plane.

The times T_1 of Mo^{3+} ions turned out to be very short ($T_1 \sim 30\times 10^{-6}$ s at $T\sim 4.2$ K). The measurements, which are presented in Fig. 1, were carried out within a narrow temperature interval of 4–5 K, because the IRES-1003 set-up does not permit studies for $T<4$ K, while for $T>5$ K the Mo^{3+} times T_1 turned out to be shorter than 10^{-5} s and also could not be measured. In the presence of an excited doublet with energy ~ 10 cm^{-1}, relaxation of the Mo^{3+} ion in this temperature interval should occur in a process of the type of resonant fluorescence. It appears reasonable, therefore, to describe the temperature behavior of the relaxation rate by an exponential. The experimental data presented in Fig. 1 are fitted well by the relation

$$T_1^{-1} = 1.1\times 10^6 \exp(-10\times 1.44/T)\,. \tag{1}$$

2. DISCUSSION OF RESULTS

The effect of cross relaxation on SLR was considered in detail, for example, in Refs. 3,7–9. As follows from these studies, the recovery of *a* spin magnetization to the equilibrium level via cross relaxation through the *b* spins is described by a sum of two exponentials with two time parameters. Assuming the *b* spin concentration to be small ($N_a \gg N_b$), these parameters are

$$\lambda_- \cong T_{1a}^{-1} + \frac{T_{12}^{-1}(T_{1b}^{-1}-T_{1a}^{-1})}{T_{12}^{-1}+T_{1b}^{-1}-T_{1a}^{-1}}\,\frac{N_b}{N_a}, \tag{2}$$

$$\lambda_+ \cong T_{1b}^{-1} + T_{12}^{-1}\,. \tag{3}$$

Here T_{1a}^{-1} is the relaxation rate of the *a* spins under study, T_{1b}^{-1} is that of *b* spins, and T_{12}^{-1} is the cross-relaxation rate.

In experiments one measures, as a rule, the ″long″ relaxation time corresponding to the rate λ_-.

We used Eq. (2) to calculate the temperature dependence of the Nd^{3+} relaxation rate in the YAG sample *A*, for which the measurements of T_1 were made within a broader temperature range, and where the relaxation follows an anomalous pattern. We identified the ″true″ relaxation rate T_{1a}^{-1} of Nd^{3+} ions in YAG with the relaxation in sample *B* (where no Mo^{3+} impurity was detected), which can be described by the relation [see Eq. (6) in Ref. 4]

$$T_{1a}^{-1} = 1.5\,T + 3.1\times 10^{11}\exp(-128\times 1.44/T)\,. \tag{4}$$

The relaxation rate of rapidly relaxing centers, T_{1b}^{-1}, is determined by that of the Mo^{3+} ions and given by Eq. (1).

The cross-relaxation rate T_{12}^{-1} is estimated as the width of the resonant line of *a* spins multiplied by the overlap function $f(\omega_a-\omega_b)$.[7] Assuming f to be a Lorentzian (cf. Ref. 9) for a Nd^{3+} concentration of 1 at.%, we obtain $T_{12}^{-1} \sim 10^5$ s^{-1} for the largest possible separation between the Mo^{3+} and Nd^{3+} resonant lines (the Nd^{3+} fourfold-degenerate line for $H\|C_4$). Thus at low temperatures one can use the approximation $T_{12}^{-1} \gg T_{1b}^{-1} \gg T_{1a}^{-1}$, with

$$\lambda_- \cong T_{1a}^{-1} + T_{1b}^{-1}\frac{N_b}{N_a}\,. \tag{5}$$

The Nd^{3+} ion concentration N_a was taken equal to $1.4\times10^{20}\ \mathrm{cm}^{-3}$, which is 1 at.% of Y^{3+} ions in the crystal. $N_b\sim2.2\times10^{17}\ \mathrm{cm}^{-3}$ is the Mo^{3+} concentration in sample A. This yields the following expression for the "anomalous" spin-lattice relaxation of Nd^{3+} ions in sample A occurring by way of cross-relaxation via Mo^{3+} ions:

$$T_1^{-1}=1.5\,T+3.1\times10^{11}\exp(-128\times1.44/T)+1.73\times10^{3}\exp(-10\times1.44/T)\,. \tag{6}$$

Figure 2 shows experimental data on the SLR of Nd^{3+} ions (for the fourfold-degenerate line) in YAG samples B, A, and A', and of Mo^{3+} ions in YAG sample A'', as well as their fitting with Eqs. (4), (6), and (1).

We readily see that Eq. (6) describes fairly well the SLR of Nd^{3+} ions in samples A, which argues for the anomaly being due to cross-relaxation via the rapidly relaxing Mo^{3+} centers. One can achieve a practically perfect fit to the experimental data by taking the quantities T_{12}^{-1}, the Mo^{3+} excited-doublet energy Δ, and the relative ion concentration N_b/N_a as fitting parameters. The dashed line in Fig. 2 is a plot of the fitting relation

$$T_1^{-1}=0.64\,T+3.1\times10^{11}\exp(-128\times1.44/T)+1.7\times10^{4}\exp(-16\times1.44/T)\,. \tag{7}$$

The authors express their gratitude to G. A. Ermakov, E. V. Antonov, and G. A. Denisenko for providing the single crystals, and to R. Yu. Abdulsabirov and M. R. Gafurov for assistance in measurements.

[1] A. A. Kaminskiĭ, *Laser Crystals* [in Russian] (Nauka, Moscow, 1975).
[2] C. Y. Huang, Phys. Rev. A **139**, A241 (1965).
[3] Kh. S. Bagdasarov, D. M. Daraseliya, and A. A. Manenkov, JETP Lett. **8**, 323 (1968).
[4] L. K. Aminov, I. N. Kurkin, S. P. Kurzin, D. A. Lukoyanov, I. Kh. Salikhov, and R. M. Rakhmatullin, Zh. Éksp. Teor. Fiz. **111**, 332 (1997) [JETP **84**, 183 (1997)].
[5] L. K. Aminov, I. N. Kurkin, and D. A. Lukoyanov, Appl. Magn. Res., 1998 (in press).
[6] Kh. S. Bagdasarov, Yu. N. Dubrov, I. N. Marov, V. O. Martirosyan, and M. L. Meilman, Phys. Status Solidi B **56**, K65 (1973).
[7] G. H. Larson and C. D. Jeffries, Phys. Rev. **145**, 311 (1966).
[8] M. B. Schulz and C. D. Jeffries, Phys. Rev. **149**, 270 (1966).
[9] A. A. Antipin and V. A. Skrebnev, Fiz. Tverd. Tela (Leningrad) **12**, 2166 (1970) [Sov. Phys. Solid State **12**, 1728 (1970)].

Translated by G. Skrebtsov

Optical spectra of octahedral cubic and trigonal Yb^{3+} impurity centers in $KMgF_3$ and $KZnF_3$ crystals

B. N. Kazakov, A. M. Leushin, G. M. Safiullin, and V. F. Bespalov

Kazan State University, 420008 Kazan, Russia

(Submitted April 7, 1998)
Fiz. Tverd. Tela (St. Petersburg) **40**, 2029–2034 (November 1998)

Groups of lines corresponding to octahedral cubic and trigonal impurity centers have been isolated in complex many-center luminescence and excitation spectra of Yb^{3+}-doped $KMgF_3$ and $KZnF_3$ crystals. The crystal-field potentials derived from the spectra are in good agreement with those of similar centers in $CsCaF_3$:Yb^{3+} crystal studied earlier. © *1998 American Institute of Physics.* [S1063-7834(98)01411-7]

1. Luminescence spectra of the impurity centers of cubic and trigonal symmetry produced by incorporating Yb^{3+} ions in the octahedral positions of the doubly charged cations in $KMgF_3$ and $KZnF_3$ were first studied in Ref. 1. The crystal-field parameters were derived in Ref. 1 from the experimental $^2F_{5/2}$, $^2F_{7/2}$ Stark multiplets and g factors of the lowest Yb^{3+} Kramers doublets. Our EPR and optical-spectroscopy studies[2] of similar impurity centers in the somewhat looser but cubic crystal $CsCaF_3$, combined with their interpretation within crystal-field theory,[3] revealed that the crystal-field potential of this compound differs substantially from those reported in Ref. 1. Some of the crystal-field parameters coincide neither in sign nor in magnitude, and these differences cannot be assigned to the lattice constant changes involved in the transition from the $KMgF_3$ and $KZnF_3$ matrices to $CsCaF_3$.

We also noticed that the experimental energy-level schemes presented in Ref. 1 are not complete, indeed, they do not contain the upper Stark levels of the excited-state $^2F_{5/2}$ multiplets of Yb^{3+} ions. Besides, the assignment of the cubic impurity-center lines is wrong. In particular, one of the lines observed at liquid-nitrogen temperature was assigned to a transition from an excited level of the $^2F_{5/2}$ multiplet (which is distant from the lowest level of this multiplet by approximately 1000 cm^{-1}) to a level of the $^2F_{7/2}$ ground-state multiplet. Obviously enough, such a transition is hardly likely to occur at nitrogen temperature.

This stimulated us to carry out a more comprehensive study of the luminescence and excitation spectra of octahedral cubic and trigonal Yb^{3+} impurity centers in $KMgF_3$ and $KZnF_3$ crystals using modern experimental and theoretical methods of analysis of many-center spectra. This study has produced a more complete experimental information compared to Ref. 1, and it was subsequently employed to determine for both impurity centers their crystal-field parameters, which agree with those of similar centers in the $CsCaF_3$ crystal.

2. Optical spectra were measured with a spectrometer described elsewhere.[2,4] Because Yb^{3+} ions allow only resonant excitation, the luminescence and excitation spectra were obtained by the gating technique. The separation of spectral lines according to the types of impurity centers was achieved by the phase modulation method.[4]

Figures 1a and 2a display, respectively, the complex luminescence spectra observed in $KMgF_3$ and $KZnF_3$ crystals in the near IR region at liquid-nitrogen and helium temperatures. These spectra are similar to the luminescence spectra of cubic (aI type) and trigonal (aII type) impurity centers in the isostructural matrix $CsCaF_3$.[2] The phase modulation technique made possible separation of the spectral lines relating to cubic (Figs. 1d and 2d) and trigonal (Figs. 1c and 2c) impurity centers. This permitted us to construct empirical schemes of the Stark ground-state multiplet $^2F_{7/2}$ of the impurity centers under study, and to assign the observed spectral lines to transitions from the lowest state of the excited-state $^2F_{5/2}$ multiplet to the corresponding levels of the $^2F_{7/2}$ multiplet (see insets to Fig. 1c,d). As seen from this assignment, the lowering of the point-group symmetry to C_{3v} involved in going from a cubic to a trigonal impurity center brings about an insignificant line splitting for the cubic impurity center. For instance, line *1* splits into lines *6* and *10*, line *2* into lines *7*, *8*, *11*, *12*, and line *3* into lines *9* and *13* (Figs. 1 and 2). This experimental observation allows the following conclusions. First, the trigonal distortion of the cubic crystal-field potential involved in going from an aI to aII impurity center is insignificant. This conclusion is supported also by the weak anisotropy of the g factors.[1,5] Second, the luminescing level and the first excited Stark level of the ground-state multiplet $^2F_{7/2}$ of Yb^{3+} cubic-impurity centers are quartets.

The luminescence spectra (Figs. 1 and 2) have permitted construction of the complete energy-level scheme only for the ground-state multiplets of the impurity centers under study. Determination of the structure of the excited-state multiplets of these centers would require the knowledge of the absorption spectra of these crystals. We did not, however, succeed in measuring the corresponding absorption spectra because of the low concentration of the Yb^{3+} impurity ions. We used, therefore, the excitation spectra of the crystals in which, in contrast to the absorption spectra, it

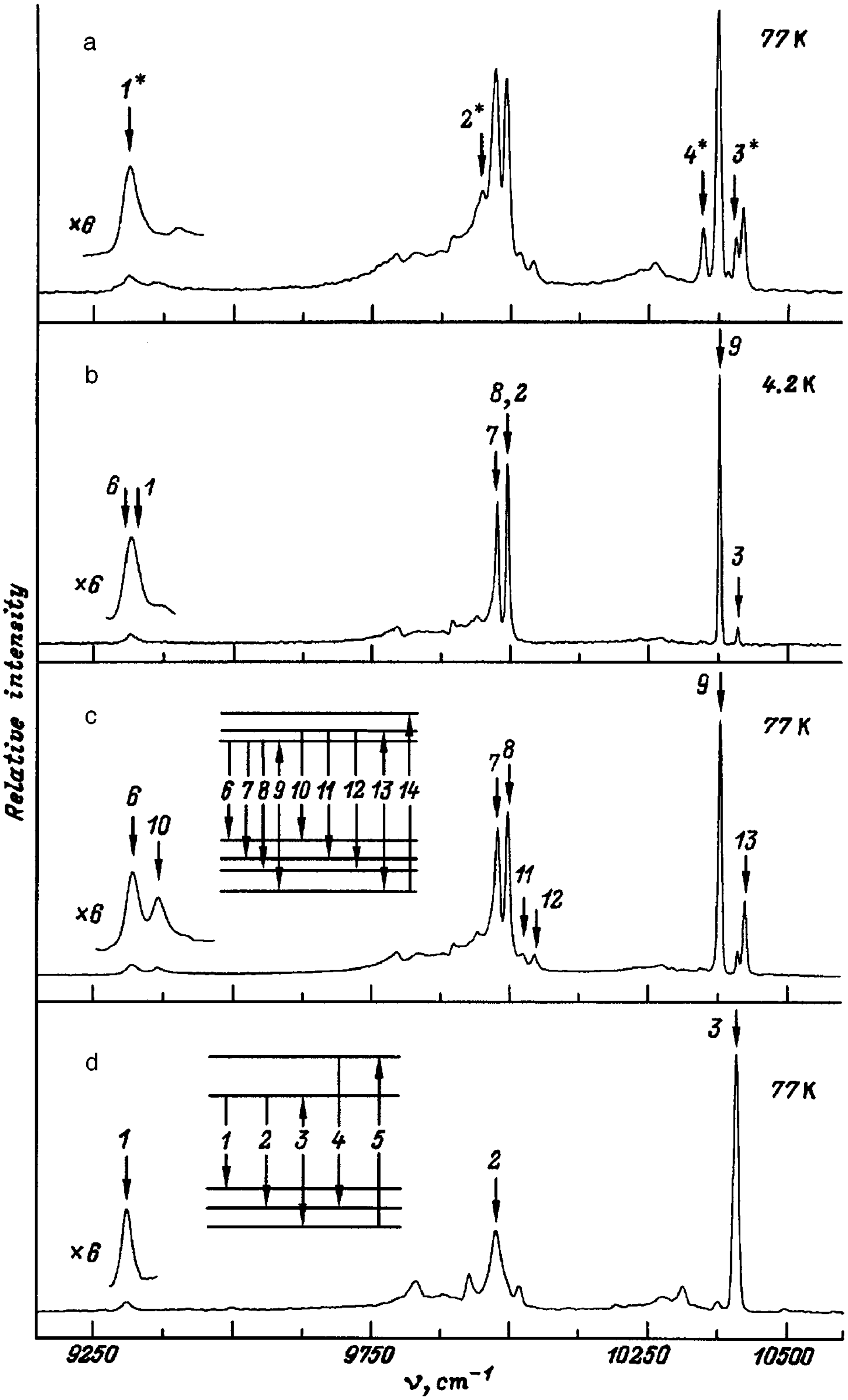

FIG. 1. (a, b) Luminescence spectra of $KMgF_3$:Yb^{3+}; (c, d) spectral lines of predominantly octahedral trigonal and cubic Yb^{3+} impurity centers, respectively, isolated by phase modulation. Here and subsequently, the line number refers to the number of the transition between the energy levels to which they were assigned. Asterisk identifies the lines interpreted in Ref. 1 as belonging to the octahedral cubic impurity center.

was found possible to isolate by the phase modulation technique the spectral lines belonging to the octahedral cubic and trigonal Yb^{3+} impurity centers (Figs. 3 and 4).

We were able to determine the absorption and emission transitions connecting the same energy levels of the impurity centers from a comparison of the luminescence spectra (Figs. 1 and 2) with excitation spectra (Figs. 3 and 4). For the cubic center, these are lines *3*, and for the trigonal one, lines *9* and *13* (Figs. 1–4). Spectral line *5* (Figs. 3a and 4a) is radiated in the transition from the ground state of the excited-state mul-

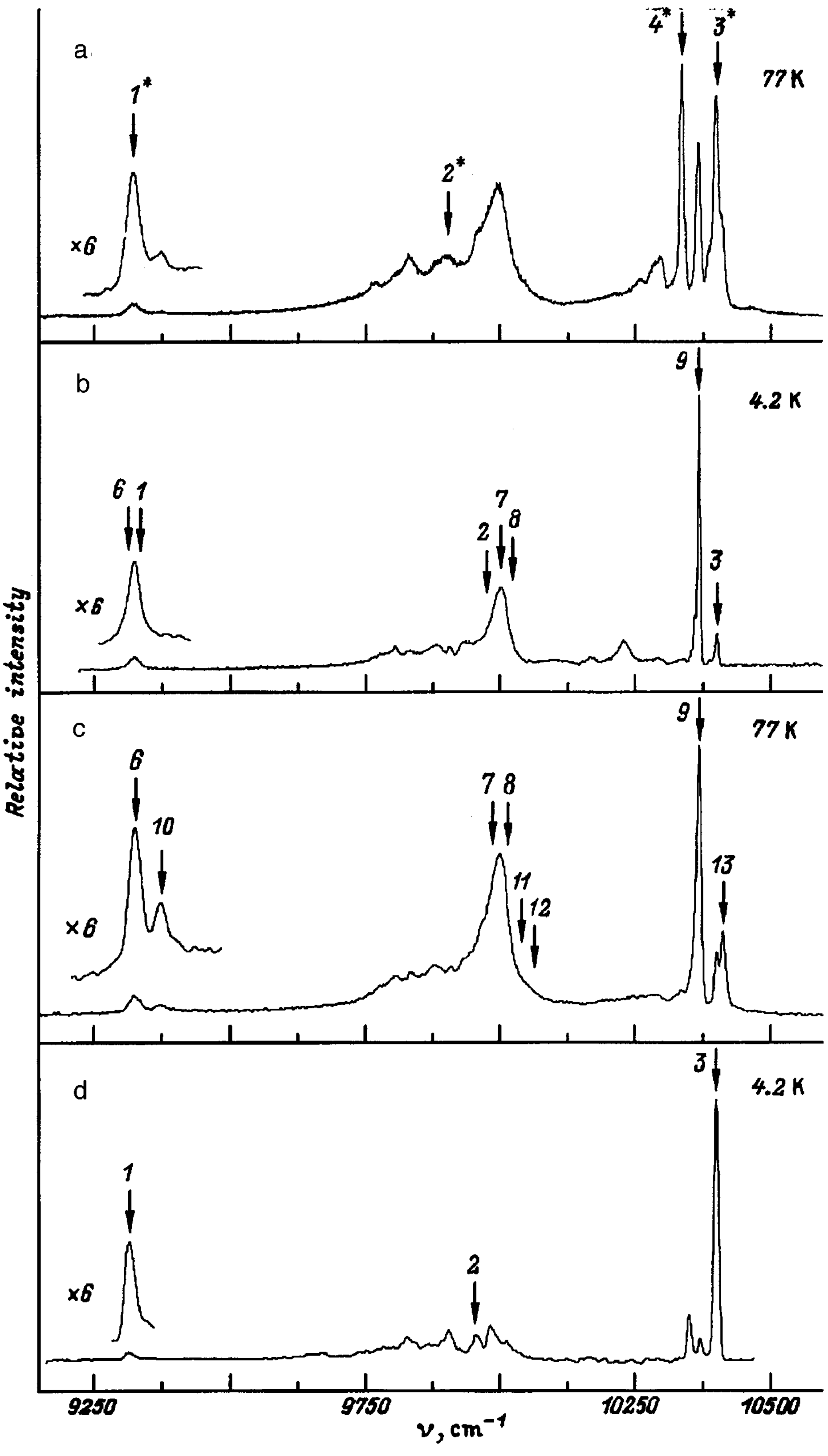

FIG. 2. (a, b) Luminescence spectra of $KZnF_3$:Yb^{3+}; (c, d) spectral lines of predominantly octahedral trigonal and cubic Yb^{3+} impurity centers, respectively, isolated by phase modulation.

tiplet $^2F_{5/2}$ of the cubic Yb^{3+} impurity center, and line *14*, in that of the trigonal center (Figs. 3b and 4b).

The experimental level energies and the g factors measured in Refs. 1 and 5 are listed in Table I.

3. To assign the experimental optical and EPR spectra produced by transitions between the states of the ^2F term of $4f^{13}$ configuration, an energy matrix including spin-orbit coupling of the Yb^{3+} ion and its interaction with the crystal and external magnetic fields was constructed. The crystal-field potentials were constructed in the standard way through V_k^q harmonic polynomials.[6] The Cartesian coordinates of the $4f$ hole in cubic impurity centers were reckoned from the

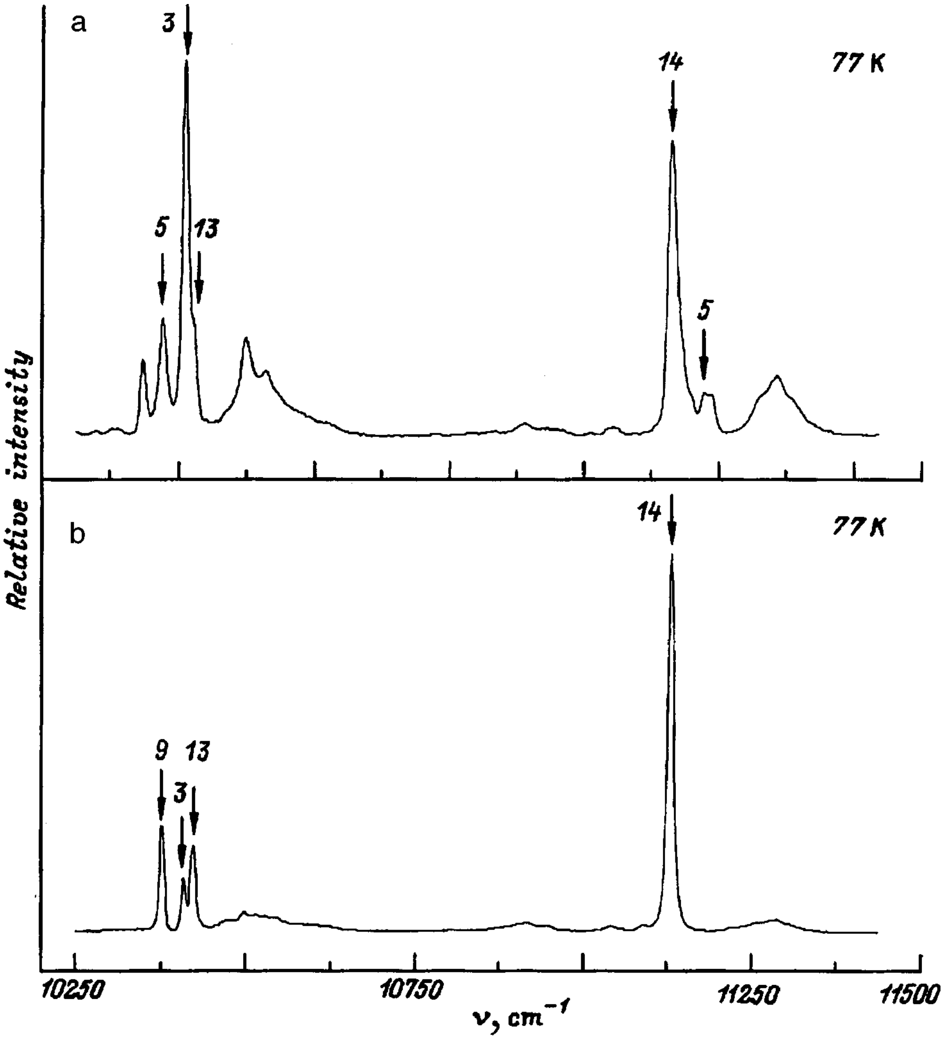

FIG. 3. (a) Excitation spectra of $KMgF_3$: Yb^{3+}; (b) spectral lines of predominantly octahedral trigonal Yb^{3+} impurity centers isolated by phase modulation.

cubic axes of the crystal. For trigonal centers, the z axis of the frame was aligned with the symmetry axis of the impurity center, and the other two were oriented so that one of the ligands in the nearest-neighbor octahedral environment lies within the $-xz$ quadrant in the zx plane.

The parameters of the crystal-field potential and spin-orbit interaction ξ were obtained from the best fit to the experimental energy-level diagrams and g factors by the procedure described in Ref. 3. Table I presents the calculated level energies and g factors together with the wave-function symmetry characteristics. The quality of fit to the experimental Stark energy-level schemes is seen from the fact that the rms deviation σ did not exceed 3 cm^{-1} for all four types of impurity centers. The calculated crystal-field and spin-orbit coupling parameters are listed in Table II. Also presented are the crystal-field parameters for the $KMgF_3$ and $KZnF_3$ crystals obtained in Ref. 1 and for the $CsCaF_3$ matrix, which is isomorphic with the matrices under study here.

Our crystal-field potentials (see Table II) for the Yb^{3+} impurity centers in all three matrices agree well with one another and follow the general trend to decrease with increasing lattice constant. The slight deviations from this trend observed for the B_2^0, B_6^0, and B_6^3 parameters increase somewhat in absolute magnitude in going from the $KMgF_3$ to $KZnF_3$ matrix.

As seen from Table II, our crystal-field potentials differ noticeably from those quoted in Ref. 1, particularly the B_6^0 and B_6^6 parameters. The signs of the parameters obtained in the two works coincide, with the exception of that of B_2^0. The negative sign of B_2^0 was, however, confirmed by microscopic calculations.[7] The crystal-field characteristics obtained in Ref. 7 agree satisfactorily with our empirical parameters. The only exception is the B_2^0 parameter, which is smaller than the value obtained by us.

Note also that our theoretical values of the g factors for the type aII trigonal impurity centers agree considerably better with experiment than the ones obtained in Ref. 1. For example, the deviation of the experimental g factors from the calculated values is 0.031 in our case (see Table II), whereas in Ref. 1 it is 0.15.

Thus we have obtained reliable crystal-field parameters for octahedral cubic and trigonal Yb^{3+} impurity centers for a number of perovskite-type cubic crystals. These parameters can be used in spectral assignments for similar impurity cen-

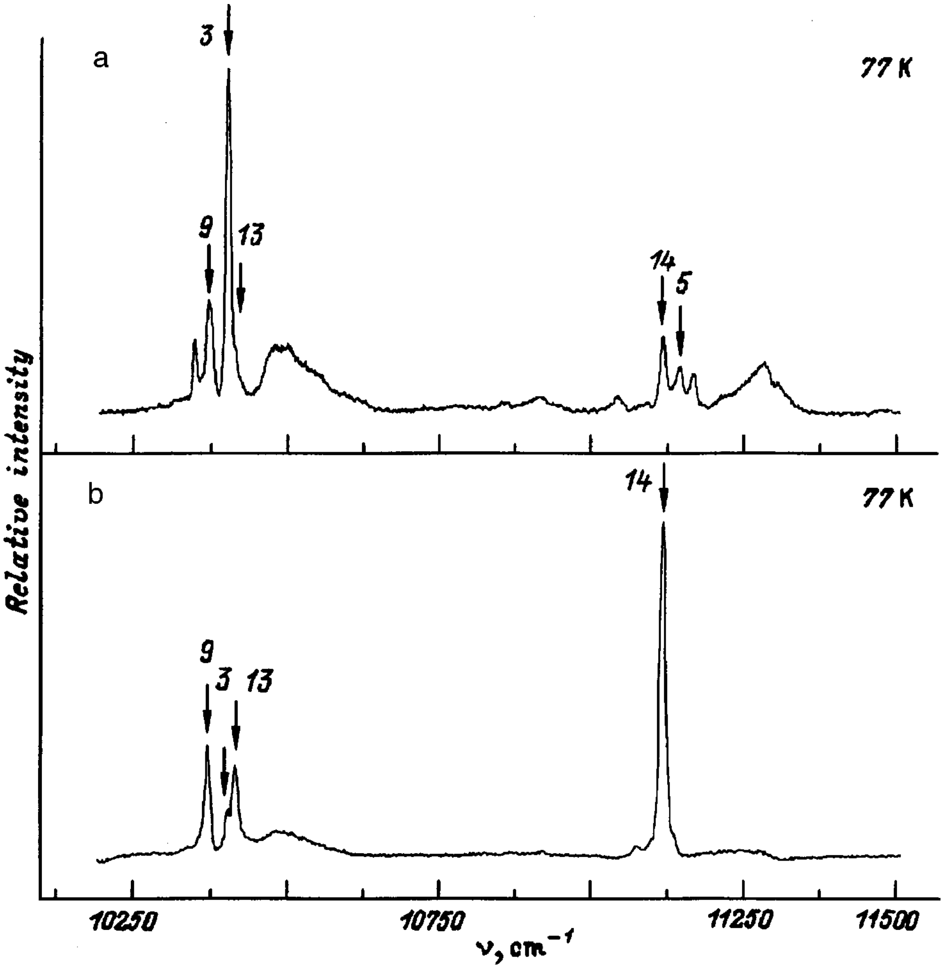

FIG. 4. (a) Excitation spectra of $KZnF_3$:Yb^{3+}; (b) spectral lines of predominantly octahedral trigonal Yb^{3+} impurity centers isolated by phase modulation.

TABLE I. Energy levels (in cm^{-1}) and g factors of Yb^{3+} impurity centers in $KMgF_3$ and $KZnF_3$ crystals.

		$KMgF_3$		$KZnF_3$	
J	Symmetry characteristics	Experiment	Theory	Experiment	Theory
1	2	3	4	5	6
Type *a*I cubic impurity center					
5/2	$^2\Gamma_7^-$	11179	11176	11145	11145
	$^2\Gamma_8^-$	10409	10409	10403	10401
7/2	$^1\Gamma_7^-$	1100	1103	1084	1082
	$^1\Gamma_8^-$	433	433	443	442
	Γ_6^-	0	0	0	0
	$^g\Gamma_6^-$	−2.584 (Ref. 5)	−2.667	−2.582 (Ref. 1)	−2.667
Type *a*II trigonal impurity center					
5/2	$^5\Gamma_4$	11131	11133	11118	11119
	$^2\Gamma_{56}$	10421	10418	10412	10412
	$^4\Gamma_4$	10376	10374	10368	10366
7/2	$^3\Gamma_4$	1062	1058	1044	1041
	$^1\Gamma_{56}$	402	401	374	373
	$^2\Gamma_4$	383	383	366	366
	$^1\Gamma_4$	0	0	0	0
	$^{g\|1}\Gamma_4$	−1.844 (Ref. 5)	−1.844	−1.82 (Ref. 1)	−1.824
	$^{g|1}\Gamma_4$	−2.896 (Ref. 5)	−2.928	−2.90 (Ref. 1)	−2.931

TABLE II. Crystal-field and spin-orbit interaction parameters (in cm^{-1}) of Yb^{3+} octahedral impurity centers in $KMgF_3$, $KZnF_3$, and $CsCaF_3$ crystals.

	Type *a*I cubic impurity center			Type *a*II trigonal impurity center.						
Matrix	ξ	B_4	B_6	ξ	B_2^0	B_4^0	B_4^3	B_6^0	B_6^3	B_6^6
$KMgF_3$ (Ref. 1)		311	9		40	−185	−6050	−10	−90	30
$KZnF_3$ (Ref. 1)		318	8		35	−188	−6200	−9	−70	20
$KMgF_3$ (Ref. 7)					−63	−176	−5568	42	−246	389
$KMgF_3$	2900	334	4	2903	−278	−221	−5450	−42	−220	490
$KZnF_3$	2897	325	7	2905	−282	−218	−5351	−50	−246	454
$CsCaF_3$	2905	293	−2	2906	−232	−203	−5004	−34	−112	352

Note: 1. The signs of parameters B_4^3 and B_6^3 calculated[7] with inclusion of lattice strain were reversed in accordance with our choice of the axes of the type *a*II impurity center. 2. The difference of the crystal-field parameters for $CsCaF_3$ from the corresponding figures quoted in Ref. 3 is due to the fact that we reached a better fit to experimental values owing to a better convergence of the variational procedure.

ters with other rare-earth ions injected into fluoride matrices of perovskite structure.

[1] A. A. Antipin, A. V. Vinokurov, M. P. Davydova, S. L. Korableva, A. L. Stolov, and A. A. Fedii, Phys. Status Solidi B **81**, 287 (1977).

[2] V. F. Bespalov, M. L. Falin, B. N. Kazakov, A. M. Leushin, I. R. Ibragimov, and G. M. Safiullin, Appl. Magn. Reson. **11**, 125 (1996).

[3] V. F. Bespalov, B. N. Kazakov, A. M. Leushin, and G. M. Safiullin, Fiz. Tverd. Tela (St. Petersburg) **39**, 1030 (1997) [Phys. Solid State **39**, 925 (1997)].

[4] B. N. Kazakov, A. V. Mikheev, G. M. Safiullin, and N. K. Solovarov, Opt. Spektrosk. **79**, 426 (1995) [Opt. Spectrosc. **79**, 392 (1995)].

[5] M. M. Abraham, C. B. Finch, J. L. Kolopus, and J. T. Lewis, Phys. Rev. B **3**, 2855 (1971).

[6] S. A. Al'tshuler and B. M. Kozyrev, *Electronic Paramagnetic Resonance* [in Russian] (Nauka, Moscow, 1972), 672 pp.

[7] M. L. Falin, M. V. Eremin, M. M. Zaripov, I. R. Ibragimov, and M. P. Rodionova, J. Phys.: Condens. Matter **2**, 4613 (1990).

Translated by G. Skrebtsov

PHYSICS OF THE SOLID STATE VOLUME 40, NUMBER 11 NOVEMBER 1998

Anisotropy of the Faraday effect in crystalline quartz

M. A. Novikov and A. A. Khyshov

Institute of Microstructure Physics, Russian Academy of Sciences, 603600 Nizhniĭ Novgorod, Russia

(Submitted April 10, 1998)
Fiz. Tverd. Tela (St. Petersburg) **40**, 2035–2036 (November 1998)

The anisotropy of the Faraday effect in crystalline quartz was measured for the first time. The optical-wedge method was used to investigate the Faraday effect under conditions of strong linear birefringence and optical activity. © *1998 American Institute of Physics.* [S1063-7834(98)01511-1]

Most experimental works on the Faraday effect (FE) in anisotropic crystals without magnetic ordering concern the simplest case, where light propagates along the optic axis. This is due to the fact that it is very difficult to observe the FE for other directions when a large natural linear birefringence (NLB) is present. The picture becomes even more complicated in anisotropic optically active crystals. In Ref. 1 it was shown experimentally that in anisotropic crystals the FE in combination with optical activity (OA) result in a nonreciprocal optical effect similar to the magnetochiral effect (nonreciprocal linear birefringence), first measured experimentally in an optically active lithium-iodate crystal in a transverse magnetic field under conditions with no FE.[2] In the longitudinal configuration with the light propagating perpendicular to the optic axis, the above-mentioned combined manifestation of FE and OA makes it difficult to observe this new effect in pure form. In this case the value of the FE and the OA under conditions of a large NLB is very important. It is well known that in this case the FE will be manifested not as nonreciprocal circular polarization (rotation of the polarization plane), but rather as nonreciprocal elliptical birefringence.[3,4] Under these conditions the effect of the FE on the polarization of light which has passed through the crystal has a very complicated dependence both on the polarization of the incident light and on the length of the crystal and the magnitude of the linear birefringence, as a result of which the effect is very weak. In the conventional procedure, where the FE parameters are studied using crystal samples in the form of plane-parallel plates, not only do serious experimental difficulties arise because of the weakness of the effect, but the parallelism of the plate faces, the divergence and width of the radiation spectrum, and the stabilization of the sample temperature must all satisfy exacting requirements which creates additional problems. For this reason, at the present time there are essentially no experimental data on the anisotropy of the FE constants in paramagnetic and diamagnetic crystals. In the present work, to solve these problems, we use a modulation method and a wedge-shaped sample to measure the FE parameters in the presence of large NLB. The wedge angle is chosen to be large enough so that the ordinary and extraordinary rays in the wedge would not spatially overlap at the exit. Then it is obvious that all information about the FE will be contained in the ellipticity of these waves at the exit. The present work is devoted to the experimental investigation of the anisotropy of the FE in crystalline quartz (α SiO$_2$) with the corresponding parameters measured in a longitudinal magnetic field with light propagating both along and perpendicular to the optic axis.

For crystals in a constant external magnetic field, taking account of only the linear terms, the reciprocal-permittivity tensor can be represented as[5]

$$\varepsilon_{ij}^{-1}(\omega)=\varepsilon_{0ij}^{-1}(\omega)+ie_{ijm}\gamma_{mk}(\omega)H_k(0), \tag{1}$$

where $\varepsilon_{0ij}^{-1}(\omega)$ is the reciprocal-permittivity tensor for the undisturbed crystal, e_{ijk} is the completely antisymmetric unit tensor, $\gamma_{mk}(\omega)$ is a polar tensor, and $\mathbf{H}(0)$ is the constant magnetic field vector. In the absence of absorption $\gamma_{mk}(\omega)$ is a real tensor. For crystals of different symmetry the form of the tensor γ_{ij} is presented in Ref. 6. For trigonal quartz crystals (32)

$$\gamma_{mk}=A\mathbf{e}_i\mathbf{e}_j+B\mathbf{e}_3\mathbf{e}_3. \tag{2}$$

In Eq. (2) an invariant method is used to express tensors of rank 2,[7] where $\mathbf{e}_j$ are unit vectors along the crystallographic axes and $\mathbf{e}_i\mathbf{e}_j$ is a dyadic product of two unit vectors.

Using the results of Ref. 6 we can obtain an expression for the ellipticity (the ratio of the semiaxes of the polarization ellipse) of light for ordinary and extraordinary rays for an uniaxial quartz crystal (32)

$$\alpha=\frac{n_0^2n_e^2}{(n_e^2-n_0^2)[1-(\mathbf{s}\cdot\mathbf{c})^2]}[A(\mathbf{s}\cdot\mathbf{H}(0))+B(\mathbf{s}\cdot\mathbf{c})(\mathbf{c}\cdot\mathbf{H}(0))]. \tag{3}$$

Here $\mathbf{s}$ is a unit vector in the direction of propagation of the light and $\mathbf{c}$ is a unit vector in the direction of the optic axis.

In the case of a longitudinal magnetic field $H(0)=\mathbf{s}\cdot\mathbf{H}(0)$ with light propagating in a direction normal to the optic axis ($\mathbf{s}\perp\mathbf{c}$)

$$\alpha=\frac{n_0^2n_e^2}{n_e^2-n_0^2}AH(0). \tag{4}$$

Equations (3) and (4) were obtained in an approximation where the natural birefringence is large compared with the anisotropy associated with the FE. In the case that the light propagates along the optic axis ($n_1^0=n_2^0=n_0$), the following expression can be obtained for the rotation angle of the polarization plane of the light in a longitudinal magnetic field:[6]

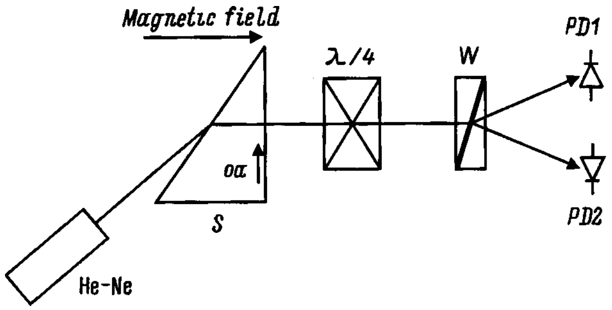

FIG. 1. Experimental arrangement.

$$\theta=\frac{\pi}{\lambda}n_0^3(A+B)H(0)l, \tag{5}$$

where λ is the wavelength of the light and l is the length of the crystal.

In the experiment, a single-pass optical arrangement for measuring the FE with a λ/4 phase plate (Fresnel rhomb) was used in the experiment (see Fig. 1). The crystals investigated were cut out in the form of a wedge, which made it possible to separate the ordinary and extraordinary rays. A LGN-302 helium-neon laser ($\lambda=0.63\ \mu$m) served as a radiation source. A differential detection scheme, constructed on the basis of a Wollaston prism (W) and two photodiodes ($PD1$ and $PD2$), was used to compensate the amplitude noise of the source. The magnetic field was modulated sinusoidally with frequency 65 Hz. Its amplitude was equal to 1–3 kOe. The signal was recorded with a synchronous detector. For a 1 mW laser the sensitivity of the apparatus was 10^{-6} rad with an averaging time $\tau=3$ s.

After passing through the crystal the laser radiation becomes ellipticity-modulated. The λ/4 plate converts the ellipticity modulation into modulation of the rotation angle of the polarization plane $\Delta\theta=\alpha$.

It can be shown that for this optical measurement scheme the signal at the output of the differential amplifier will be

$$\Delta J\sim 2J_0\Delta\theta, \tag{6}$$

where J_0 is the light intensity, $\Delta\theta=\theta_0\cos(\Omega t)$, and Ω is the modulation frequency of the magnetic field of the electromagnet. In the experiment the dependence of θ_0 on the magnetic field amplitude was measured. As expected, this dependence is linear. To increase the measurement accuracy the magnitude of the signal was normalized to that of the signal due to the FE in a fused quartz plate of known thickness. The magnitude of the FE along the optic axis of quartz was measured without the λ/4 plate.

The measured parameters for quartz crystals were

$$A=(2.14\pm0.09)\times10^{-11}\,\mathrm{Oe}^{-1},$$

$$A+B=(2.33\pm0.05)\times10^{-11}\,\mathrm{Oe}^{-1}.$$

Thus the anisotropy of the FE for crystalline quartz is quite small

$$\frac{A}{A+B}=0.92\pm0.06.$$

It is interesting to compare the magnitude of the anisotropy of the FE with the anisotropy of other physical properties of this crystal, specifically, the anisotropy of the magnetic susceptibility. They should be quite close to one another. However, we were not able to find any published experimental data on the anisotropy of the magnetic susceptibility for crystalline quartz.

In conclusion we note that the study of the anisotropy of the FE in crystals is undoubtedly of interest from the standpoint of gaining a deeper understanding of magnetooptic processes. We hope that the method proposed in the present paper for measuring the Faraday constants will make it possible to measure these quantities with adequate accuracy in a wide class of anisotropic crystals.

This work was supported in part by the Russian Fund for Fundamental Research (Grant 95-02-05653).

[1] M. A. Novikov and G. V. Gelikonov, Opt. Spektrosk. **75**(4), 854 (1993) [Opt. Spectrosc. **75**, 506 (1993)].

[2] V. A. Markelov, M. A. Novikov, and A. A. Turkin, JETP Lett. **25**, 378 (1977).

[3] F. F. Sizov and Yu. I. Ukhanov, *Magneto-Optic Faraday and Voigt Effects in Application to Semiconductors* [in Russian], Naukova dumka, Kiev, 1979, 180 pp.

[4] G. A. Smolenskiĭ, V. V. Lemanov, G. M. Nedlin, M. P. Petrov, and R. V. Pisarev, *Physics of Magnetic Insulators* [in Russian], Nauka, Leningrad, 1974, 454 pp.

[5] V. A. Agronovich and V. L. Ginzburg, *Crystal Optics with Spatial Dispersion and Excitons* [Springer-Verlag, N.Y., 1984, 2nd edition; Nauka, Moscow, 1965, 376 pp.].

[6] M. A. Novikov, Kristallografiya **26**(3), 437 (1981) [Sov. Phys. Crystallogr. **26**, 249 (1981)].

[7] G. N. Maloletkin and V. L. Fomin, *Tensor Bases in Crystal Physics* [in Russian], Leningrad University Press, Leningrad, 1972.

Translated by M. E. Alferieff

PHYSICS OF THE SOLID STATE VOLUME 40, NUMBER 11 NOVEMBER 1998

Photorefractive effect in sillenite crystals with shallow traps in a sign-alternating electric field

O. V. Kobozev,*) S. M. Shandarov,†) and R. V. Litvinov

Tomsk State University of Control Systems and Radio Electronics, 634050 Tomsk, Russia

Yu. F. Kargin and V. V. Volkov

Institute of General and Inorganic Chemistry, Russian Academy of Sciences, 117907 Moscow, Russia

(Submitted December 3, 1997; resubmitted April 16, 1998)
Fiz. Tverd. Tela (St. Petersburg) **40**, 2037–2043 (November 1998)

The results of a theoretical analysis of the photorefractive response in crystals with shallow traps to in a sign-alternating, square-wave electric field are presented. The numerical analysis method developed imposes no restrictions on the frequency of the external field and the period of the photorefractive grating. The parameters characterizing deep donor and shallow trap centers are estimated on the basis of investigations of two-beam interaction in a $Bi_{12}SiO_{20}:Cd$ crystal with the application of a sign-alternating, square-wave electric field. © *1998 American Institute of Physics.* [S1063-7834(98)01611-6]

Photorefractive effects in sillenite crystals $Bi_{12}SiO_{20}$, $Bi_{12}GeO_{20}$, and $Bi_{12}TiO_{20}$ have been under intensive investigation for more than 20 years.[1–11] These phenomena are associated with the formation of a space charge field in the crystal under the action of nonuniform illumination and with modulation of the refractive index of the medium by this field as a result of the linear electrooptic effect. The comparatively small electrooptic constants of the sillenites ($\sim$5 pm/V) require the application of external electric fields to the crystals in order to increase the photorefractive response.[3–6] From the technical standpoint it is simpler to use a sign-alternating field.[3]

In Refs. 8 and 9 it was demonstrated that the amplitude of the photorefractive grating in sillenite crystals depends on the frequency f_0 of the external sign-alternating field. In a theoretical analysis of the photorefractive response, taking account of the dependence of the response on the external field frequency,[8–12] an elementary model of charge transport in a crystal with single partially compensated donor level is, as a rule, employed.[13] In Ref. 14 it was noted that a quite complete analysis of photorefractive effects in sillenite crystals is impossible without taking into account their characteristic features, such as the complicated structure of the impurity levels in the band gap.[15,16] In Ref. 17 a model of a photorefractive crystal including deep donor and shallow trap levels was used to explain the dark erasure of photorefractive gratings in a $Bi_{12}SiO_{20}$ crystal. Reference 18 is devoted to a detailed theoretical analysis of photorefractive effects on the basis of this model of a crystal in the absence of an external field and in the approximation of low light intensity. In Ref. 19 the amplitude of the photorefractive grating in the presence of a high-frequency external square-wave field in a crystal with deep donor and shallow trap levels was found on the basis of a probabilistic approach. However, the results obtained there are applicable only to gratings whose spatial period is much greater than the diffusion and drift lengths.

In the present paper we present the results of a theoretical analysis of the space charge field of a photorefractive grating in a crystal with shallow traps, placed in an external electric field of a square-wave form, with no restrictions on the spatial period of the interference pattern. The experimental investigations of the efficiency of two-beam interaction were performed on a sample of acadmium-doped crystal $Bi_{12}SiO_{20}:Cd$, in which in previous work generation of spatial subharmonics of a photorefractive grating[20] and a dependence of the coefficient of two-beam amplification on the light intensity, tentatively attributed to the presence of shallow trap centers,[21] were observed.

1. THEORY

A model of the energy levels of a photorefractive crystal for the dominating electronic photoconductivity, including deep donors and shallow electronic traps, was studied in Ref. 18. This model is described by the material equations

$$\frac{\partial N_D^i}{\partial t} = s_D I (N_D - N_D^i) - \gamma_D n N_D^i, \tag{1}$$

$$\frac{\partial M}{\partial t} = -(s_T I + \beta) M + \gamma_T n (M_T - M), \tag{2}$$

$$\frac{\partial}{\partial t}(N_D^i - M - n) + \frac{1}{e}\nabla \cdot \mathbf{j} = 0, \tag{3}$$

$$\mathbf{j} = e\mu n \mathbf{E} + \mu k_{\mathrm{B}} T \nabla n, \tag{4}$$

$$\nabla \cdot \mathbf{E} = -\frac{e}{\varepsilon}(n - N_D^i + N_A + M), \tag{5}$$

where N_D, M_T, and N_A are the total densities of donors, shallow traps, and acceptors; N_D^i, M, and n are the densities of ionized donors, filled shallow traps, and electrons; $\mathbf{j}$ is the electronic current density; $\mathbf{E}$ is the electric field; s_D, s_T and γ_D, γ_T are the photoionization cross sections and the recombination constants for deep donors (D) and shallow traps (T); β is the coefficient of thermal excitation of shallow traps; μ is the electron mobility; k_B is Boltzmann's constant; T is the temperature; e is the elementary electric charge; and, ε is the static permittivity of the crystal.

Let us examine the space-charge field of the photorefractive grating formed in a crystal in the presence of an interaction of two beams with intensities I_1 and I_2. For the light interference pattern

$$I=I_0[1+m\cos(Kz)], \tag{6}$$

where $I_0=I_1+I_2$ is the average intensity and m is the degree of modulation, we assume that the grating vector $\mathbf{K}=K\mathbf{z}_0$ and the applied field $\mathbf{E}_0=E_0\mathbf{z}_0$ are directed along the Z axis of the coordinate system. If the degree of modulation is small ($m\ll 1$), then Eqs. (1)–(5) can be linearized by representing the solutions for the functions $N_D^i(z,t)$, $M(z,t)$, $n(z,t)$, and $E(z,t)$ in the form[18]

$$F=F_0(t)+0.5[F_1(t)\exp(-iKz)+F_1^*(t)\exp(iKz)]. \tag{7}$$

Representing the average density of the ionized donors as $N_{D0}^i=N_A+N_0$ we employ the approximation of low light intensity I_0, where the average electron density n_0 satisfies the inequalities $n_0\ll N_0$ and $n_0\ll M_0$. In this case the electron recombination time is much shorter than the relaxation time of shallow traps, and the condition of charge conservation $N_0=M_0+n_0$ simplifies to $N_0\approx M_0$, while the average densities of filled traps and electrons can be obtained in the form[18,21]

$$M_0=\frac{1}{2\delta}[(N_D+M_T-N_A\delta)-\sqrt{(N_D+M_T-N_A\delta)^2-4(N_D-N_A)M_T\delta}], \tag{8}$$

$$n_0=\frac{s_D I_0(N_D-N_A-N_0)}{\gamma_D(N_A+N_0)}, \tag{9}$$

where $\delta=1-s_T\gamma_D/(s_D\gamma_T)-\beta\gamma_D/(s_D\gamma_T I_0)$.

2. DYNAMICS OF GRATINGS IN AN EXTERNAL ELECTRIC FIELD

The character of the temporal behavior of gratings of space charge on deep donors and shallow traps will be influenced by the dynamics of the establishment of the average values of these quantities. For incoherent beams (main and signal beams) the analysis can be limited to stationary values for n_0, N_0, and M_0. After the stationary state is reached for n_0, N_0, and M_0, we can restore the coherence of the beams to ensure a two-beam interaction.[22]

In this case, using the expansion (7), we obtain from Eqs. (1)–(5) a system of differential equations for the first spatial harmonics of the space charge

$$\frac{dN_1}{dt}=-\frac{N_1}{\tau_1}-\frac{n_1}{\tau_R'}+mI_0 s_D(N_d-N_A-N_0), \tag{10}$$

$$\frac{dM_1}{dt}=-\frac{M_1}{\tau_T}-\frac{n_1}{\tau_\Delta}-mI_0 s_T M_0, \tag{11}$$

$$\frac{dn_1}{dt}=-N_1\left(\frac{1}{\tau_I}-\frac{1}{\tau_{di}}\right)-M_1\left(\frac{1}{\tau_{di}}-\frac{1}{\tau_T}\right)-n_1\left(\frac{1+R}{\tau_R'}+\frac{1}{\tau_\Delta}\right)+mI_0\{s_D(N_D-N_A-N_0)+s_T M_0\}. \tag{12}$$

The solutions of Eqs. (10)–(12) and (5) with a constant external field have the form

$$F_1(t)=F_{10}+\Delta F_1\exp(p_1 t)+\Delta F_2\exp(p_2 t)+\Delta F_3\exp(p_3 t), \tag{13}$$

$$E_1(t)=i\frac{e}{\varepsilon K}(N_1(t)-M_1(t)-n_1(t)). \tag{14}$$

The function $F_1(t)$ represents the amplitudes of the first spatial harmonics of $N_1(t)$, $M_1(t)$, and $n_1(t)$. The stationary values of the charge densities N_{10}, M_{10}, and n_{10} are determined by the expressions

$$N_{10}=mI_0\tau_I\times\frac{s_D(\tau_R'\tau_T+\tau_{di}\tau_\Delta R)(N_D-N_A-N_0)-s_T\tau_T\tau_\Delta M_0}{\tau_\Delta(\tau_{di}R+\tau_I)+\tau_R'\tau_T}, \tag{15}$$

$$M_{10}=mI_0\tau_T\times\frac{\tau_R'\tau_I s_D(N_D-N_A-N_0)-s_T\tau_\Delta(\tau_{di}R+\tau_I)M_0}{\tau_\Delta(\tau_{di}R+\tau_I)+\tau_R'\tau_T}, \tag{16}$$

$$n_{10}=mI_0\tau_R'\tau_\Delta\frac{s_D\tau_I(N_D-N_A-N_0)+s_T\tau_T M_0}{\tau_\Delta(\tau_{di}R+\tau_I)+\tau_R'\tau_T}, \tag{17}$$

where $E_D=Kk_BT/e$, $E_q'=e(N_A+N_0)(1-(N_A-N_0)/N_D)\varepsilon K$, $\tau_R'=1/\gamma_D(N_A+N_0)$, $\tau_\Delta=1/\gamma_T(M_T-M_0)$, $\tau_I=1/(s_D I_0+\gamma_D n_0)$, and $\tau_T=1/(s_D I_0+\beta+\gamma_T n_0)$. The complex constants p_1, p_2, and p_3 have a negative real part, they determine the dynamics of the space charge gratings, and they are determined by the equation

$$p^3+p^2\left\{\frac{1}{\tau_I}+\frac{1}{\tau_T}+\frac{1}{\tau_\Delta}+\frac{1+R}{\tau_R'}\right\}+p\left\{\frac{R}{\tau_R'}\left(\frac{1}{\tau_I}+\frac{1}{\tau_T}\right)+\frac{1}{\tau_R'}\left(\frac{1}{\tau_T}+\frac{1}{\tau_{di}}\right)+\frac{1}{\tau_\Delta}\left(\frac{1}{\tau_I}+\frac{1}{\tau_{di}}\right)+\frac{1}{\tau_I\tau_T}\right\}+\left\{\left(\frac{R}{\tau_I}+\frac{1}{\tau_{di}}\right)\frac{1}{\tau_T\tau_R'}+\frac{1}{\tau_I\tau_{di}\tau_\Delta}\right\}=0, \tag{18}$$

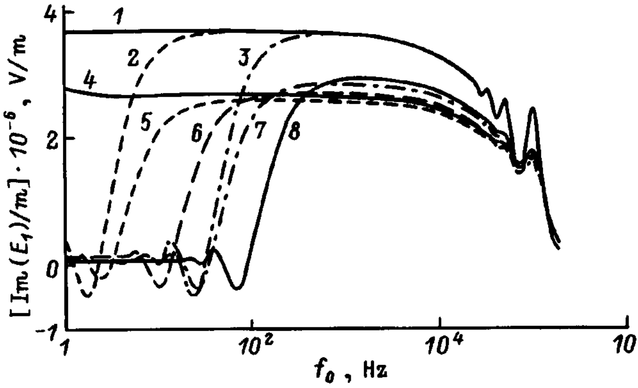

FIG. 1. Frequency dependences of the space-charge field of a photorefractive grating in a crystal with one photoactive level (*1–3*) and in a crystal with a deep donor and shallow trap levels (*4–8*). The curves correspond to average light intensity I_0 (W/m^2): *1, 4* — 2; *2, 5* — 100; *3, 7* — 1400; *6* — 500; *8* — 4000.

where $R=(E_D/E'_\mu+iE_0/E'_\mu+\tau'_R/\tau_{di})$, $E'_\mu=1/(K\mu\tau'_R)$, and $\tau_{di}=\varepsilon/(e\mu n_0)$ is the dielectric relaxation time. The coefficients $\Delta M_{1,2,3}$, $\Delta n_{1,2,3}$, and $\Delta N_{1,2,3}$ are related by

$$\Delta M_{1,2,3}=\left[-\frac{\tau'_R(1/\tau_I+p_{1,2,3})}{\tau_\Delta(1/\tau_T+p_{1,2,3})}\right]\Delta N_{1,2,3},$$
$$\Delta n_{1,2,3}=[-\tau'_R(1/\tau_I+p_{1,2,3})]\Delta N_{1,2,3} \tag{19}$$

and can be found from the initial conditions.

When the beams are coherent and an external square-wave field $E_0(t)$ is applied to the crystal, space-charge gratings build-up in the crystal until a quasistationary state is established. We shall consider only the quasistationary regime, in which the grating amplitudes are periodic functions of time. Using the low-known method of matching the solutions for the positive and negative half-periods of the field $E_0(t)$, we obtained on the basis of the conditions of continuity and periodicity[7] and the relations (19) a system of six linear equations for the coefficients $\Delta N_1^\pm$, $\Delta N_2^\pm$, and $\Delta N_3^\pm$, which we then solved numerically for each desired point.

III. ANALYSIS OF THE FREQUENCY DEPENDENCES OF THE AMPLITUDE OF THE SPACE-CHARGE FIELD

As is well known,[3,4] the imaginary part of the space-charge field of a photorefractive grating determines the two-beam gain

$$\Gamma=\frac{2\pi}{\lambda}n_c^3r_{\mathrm{eff}}\frac{\mathrm{Im}\,(E_1)}{m}, \tag{20}$$

where λ is the wavelength of the light, n_z is the refractive index of the crystal, and r_{eff} is the effective electrooptic constant.

Figure 1 shows the frequency dependences of $\mathrm{Im}(E_1)/m$ for crystals with one deep donor level (curves *1–3*) and for crystals with a deep donor and shallow trap levels (curves *4–8*) with external field amplitude $E_0=10$ kV/cm and photorefractive grating period $\Lambda=15\ \mu$m. In the calculations the material parameters referring to a deep level corresponded to those used in Ref. 11: $N_D=10^{25}$ m^{-3}, $N_A=10^{22}$ m^{-3}, $\mu=3\times10^{-6}$ m^2/(V·s), $\gamma_D=1.65\times10^{-17}$ m^3/s, and $s_D=2\times10^{-5}$ m^2/J. The parameters describing the shallow level were $s_T=s_D$, $\gamma_T=\gamma_D$, $\beta=5$ s^{-1}, and $M_T=0.8\times10^{22}$ m^{-3}.

As noted in Refs. 10 and 11, which are devoted to the analysis of the frequency dependences of the photorefractive response on the basis of a single-level model, here there exist two distinct resonance regions: low- and high-frequency. As the average light intensity I_0 increases, the low-frequency resonances shift to higher frequencies, but the high-frequency resonances are unaffected. Characteristically, there exists an intermediate frequency range with an almost constant amplitude of the space-charge field, which expands as the light intensity decreases. In this region both the low- and high-frequency oscillations of the space-charge field are small and the well-known approximate relations[6] for a crystal with one donor level are valid:

$$E_1=imE_q\frac{E_0^2+E_D(E_D+E_\mu)}{E_0^2+(E_D+E_q)(E_D+E_\mu)}. \tag{21}$$

In a crystal with shallow traps, in contrast to a single-level crystal, the field amplitude E_1 in the intermediate region depends on the average light intensity I_0. The character of this dependence is determined by both the material parameters of the crystal and the conditions of interaction (the spatial period Λ of the grating and the external field amplitude E_0) and will be discussed in greater detail below.

The resonances in the frequency dependence of the photorefractive response at high and low frequencies are related with the oscillatory character of its dynamics in an external electric field.[9,12] The imaginary parts of the constants $p_k\,(k=1,2,3)$ characterizing these oscillations could be comparable to the frequencies ω_k of the waves of charge-transfer on traps,[23,24] studied in Refs. 12 and 25 in application to the photorefractive response of a crystal in the low-frequency region. The quality factor Q_k of the waves of charge transfer on traps, which equals the ratio of the frequency ω_k to the real part of the constant p_k,[12] determines the sharpness of the observed resonances. Table I gives the values of the constants p_k for the conditions considered above for the analysis of the frequency dependences presented in Fig. 1. The constant p_1 in this case describes the low-frequency oscillations of the space-charge field, which are due to charge transfer on deep donor centers. The Q of this wave of charge transfer on traps in a crystal with one photoactive level does not depend on the average light intensity and assumes the value $Q_1\approx3.6$. In a crystal with shallow traps the quality factor is minimum for $I_0=100$ W/m^2 ($Q\approx2.4$) and is essentially independent of the intensity for $I_0>500$ W/m^2 ($Q\approx3$). A lower quality factor leads to less pronounced resonance peaks in the low-frequency region for a two-level crystal than for a one-level crystal (Fig. 1).

The position of the resonances in the high-frequency region depends on the imaginary part of the constant p_2 and can be found from the relation

$$\omega_2T_0/2=2\pi\nu,\quad \nu=1,2,3\ldots. \tag{22}$$

The frequency ω_2 of the high-frequency wave of charge transfer on traps does not depend on the light intensity I_0 and is same for both one- and two-level models of a crystal.

TABLE I. Characteristic constants for crystals with deep donor centers and shallow traps and with one photoactive level with different values of the average light intensity.

	$M_T=0.8\times10^{22}$, m^{-3}			$M_T\approx0$	
I_0, W/m^2	p_1	$p_2\times10^{-6}$	p_3	p_1	$p_2\times10^{-6}$
2	$-0.094+i0.289$	$-0.311-i1.257$	$-4.99-i0.274$	$-0.082+i0.294$	$-0.179-i1.257$
100	$-8.53+i20.8$	$-0.311-i1.257$	$-5.03+i0.255$	$-4.13+i14.9$	$-0.179-i1.257$
500	$-29.3+i87.0$	$-0.311-i1.257$	$-10.9+i0.042$	$-20.5+i73.7$	$-0.179-i1.257$
1400	$-72.3+i220$	$-0.312-i1.257$	$-21.6+i0.0097$	$-57.6+i206$	$-0.180-i1.257$
4000	$-194+i591$	$-0.313-i1.257$	$-51.3+i0.00167$	$-166+i588$	$-0.183-i1.257$

However, the quality factor Q_2 and the sharpness of the resonances at high frequencies decrease when shallow traps are present in the crystal. The constant p_3 characterizes the processes which are associated with the contribution of shallow traps to the photorefractive response and have a very low quality factor $Q_3\ll1$ in the case at hand. For this reason, here no resonances associated exclusively with shallow traps are observed.

4. SPACE-CHARGE FIELD IN THE INTERMEDIATE FREQUENCY RANGE

At intermediate frequencies $-\mathrm{Re}(p_2T_0/2)\gg1$, i.e. the high-frequency oscillations rapidly decay after each switching of the external field and their contribution can be neglected. In this case in Eq. (12) we can set $\partial n_1/\partial t=0$ and in Eqs. (13) $\Delta N_2=0$ and $\Delta M_2=0$. The equation (18) for the constants p_k can be reduced to a quadratic equation and a system of four linear equations for determining the constants $\Delta N_1^{\pm}$ and $\Delta N_3^{\pm}$ can be obtained from the conditions of continuity and periodicity. Moreover, in the intermediate frequency range of the external field $|p_{1,3}T_0/2|\ll1$, and the amplitude of the steady oscillations of the space-charge field is much smaller than the average value of the amplitude of this field. This makes it possible to expand the exponential functions in the solutions (13) for $N_1(t)$ and $M_1(t)$ in a series and to retain only the first two terms of the expansion, and the solution can be sought for any convenient moment in time in the period of the external field.

The amplitude of the first spatial harmonic of the electric field at time $t=0$ on the basis of these assumptions can be represented as

$$E_1(0)=\frac{E_{10}p_1p_3-E_{10}^*p_1^*p_3^*}{p_1p_3+p_1^*p_3^*},\tag{23}$$

where $E_{10}=ie(N_{10}-M_{10})/(\varepsilon K)$. Using below the analytical expressions for the roots p_1 and p_3, the approximation of low light intensity, and the relations (15) and (16) for N_{10} and M_{10} and neglecting small terms of order $\tau_R'/\tau_{di}\ll1$, we obtained an expression for the amplitude $E_1(0)$ in the form

$$E_1(0)=\mathrm{Im}\,E_q'$$

$$\frac{\{E_D[E_D+E_\mu'(1+\tau_R'/\tau_\Delta)]+E_0^2\}(1+\tau_R'\tau_T/(\tau_\Delta\tau_I)s_TI_0/(\beta+s_TI_0))}{\{[E_D+E_\mu'(1+\tau_R'/\tau_\Delta)][E_D+E_q'(1+\tau_R'\tau_T/(\tau_\Delta\tau_I))]+E_0^2\}}.\tag{24}$$

The expression (24) for the amplitude of the first spatial harmonic of the space-charge field in a crystal with shallow traps placed in a square-wave field with an intermediate frequency reduces, as the density M_T of the shallow traps approaches zero, to the well-known expression (21) for a crystal with a single deep trap level.[7] The presence of shallow traps leads mainly to renormalization of the recombination time $\tau_R'=1/\gamma_D(N_A+N_0)$, the drift field $E_\mu'=1/K\mu\tau_R'$, and the saturation field of the traps $E_q\approx e(N_A+N_0)/\varepsilon K$. This is due to the increase in the average density of ionized donors $\tilde{N}_D^+=N_A+N_0$ as a result of electrons settling on shallow traps when the crystal is illuminated. Moreover, the relation (24) takes account of the influence of the thermal generation of electrons from shallow traps into the conduction band on the space-charge field and the redistribution of the recombination rates of electrons on shallow and deep levels as shallow traps are occupied.

5. EXPERIMENTAL PROCEDURE

The investigations were performed on a sample with the dimensions $10.1\times8.1\times7.9$ mm along the [110], [110], and [001] axes. The sample was cut out of a Czochralski-grown $Bi_{12}SiO_{20}$:Cd crystal. The generation of spatial subharmonics of the photorefractive grating[20] and the dependence of the two-beam gain in the absence of an external field on the light intensity[21] have been observed in this crystal. This dependence was attributed to the presence of shallow trap centers.

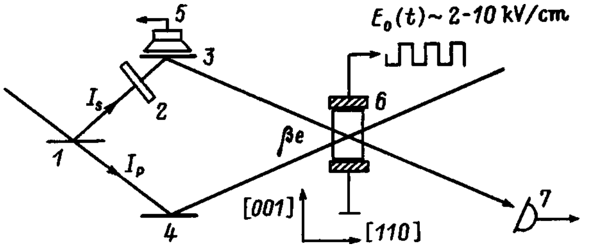

FIG. 2. Diagram of the experimental apparatus.

He–Ne laser radiation with wavelength $\lambda = 0.633$ μm and maximum power $\sim$50 mW was used in the experiments. The experimental setup is shown schematically in Fig. 2. The laser beam was divided into two beams of equal power by half-transmitting mirror *1*. Neutral light filters *2* attenuated the signal beam I_S by a factor of 100–2000. The mirrors *3* and *4* ensured that the signal and reference beams converged in the crystal. The mirror *3* was glued to the dynamic head *5*, making it possible to produce a signal beam which is incoherent with the reference beam I_p by applying to it a sinusoidal voltage with frequency $\sim$400 Hz. The power of the signal beam after passage through the crystal *6* was measured with a calibrated photodiode *7*.

The spatial period of the grating was regulated by varying the convergence angle βe of the beams. In so doing, the bisector of this angle was oriented in the direction normal to the entrance face (110) of the sample, while the photorefractive grating vector was parallel to the [001] axis. A high square-wave voltage was applied to the (001) faces of the crystal using copper electrodes. Two generators, giving a square-wave voltage amplitude from 2.5 to 8 kV, were used to investigate the frequency dependences of the photorefractive response in the range from 100 Hz to 5 kHz.

Signal and reference beams which are incoherent between one another were used in the preparation of the experiment. These beams illuminated the crystal for a time interval during which the average densities N_0, M_0, and n_0 reached stationary values. Then the acoustic generator was switched off to stop the mirrors and the interacting beams became coherent, i.e. they formed in the crystal a stationary interference pattern. Formation of a grating, whose amplitude reached a stationary value in $\sim$200 s, occurred from this moment. The intensities $I_{IN}(d)$ and $I_{CO}(d)$ of the signal beam at the exit from the crystal with incoherent and coherent pump beams, respectively, after the stationary level was reached were used to find the two-beam gain[22]

$$\Gamma = \frac{1}{d} \ln\left(\frac{I_{CO}(d)}{I_{IN}(d)}\right). \qquad (25)$$

VI. EXPERIMENTAL RESULTS AND DISCUSSION

Figure 3 shows the experimental curves of the two-beam gain versus the external field frequency that were measured with a spatial period of the grating $\Lambda = 7.3$ and 42 μm and average light intensity $I_0 = 8800$ W/m^2. The main problem in fitting the theoretical curves presented here to the experimental data was the lack of information about the material parameters of the experimental crystal in the two-level model. We took as a basis the parameters $N_D = 10^{25}$ m^{-3} and $\mu = 2\times10^{-6}$ m^2/(V$\cdot$s) and the condition $N_A \ll N_D$, which are characteristic for a nominally pure $Bi_{12}SiO_{20}$ crystal,[11] and equal photoionization cross sections $s_T = s_D$. In this case we obtain from the experimental value of the absorption coefficient $\alpha_0 = 0.15$ cm^{-1} the value $s_D = \alpha_0/(\hbar\omega N_D) = 4.8\times10^{-6}$ m^2/J. The remaining material parameters were determined by fitting: acceptor density $N_A = 2\times10^{21}$ m^{-3}, total number of shallow traps $M_T = 2\times10^{21}$ m^{-3}, recombination constant on deep donors $\gamma_D = 0.83\times10^{-17}$ m$^3\cdot$s^{-1}, recombination constant on shallow traps $\gamma_T = 4.95\times10^{-17}$ m$^3\cdot$s^{-1}, and thermal excitation rate $\beta = 8$ s^{-1}. We also call attention to the variance in the values employed for the electrooptic constants ranging from $r_{\text{eff}} = 0.64$ pm/V at $E_0 = 8.9$ kV/cm to $r_{\text{eff}} = 0.74$ pm/V at $E_0 = 3.1$ kV/cm ($\Lambda = 42$ μm). These differences could be due to both uncontrollable changes in the state of polarization of the light beams for different experiments and the dependence of the effective electrooptic constants on the external field.[26]

Except for the frequency range below 600 Hz for the curve *4* in Fig. 3, the theoretical frequency dependences agree well with the experimental data. The discrepancy noted for curve *4* could be due to an incorrect choice of the material parameters.

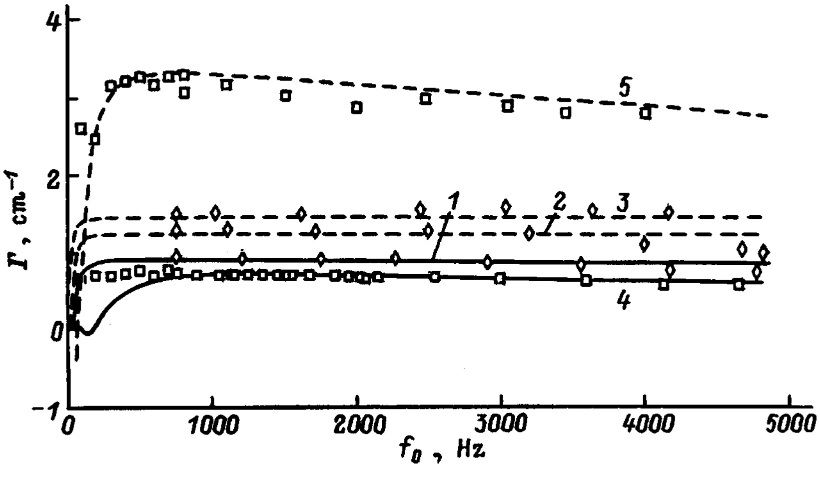

FIG. 3. Frequency dependences of the two-beam gain with a spatial period of photorefractive grating $\Lambda = 7.3$ (*1–3*) and 4.2 μm (*4, 5*). The curves *1–5* correspond to external electric fields $E_0 = 3.1$, 5.2, 8.9, 3.2, and 8.9 kV/cm.

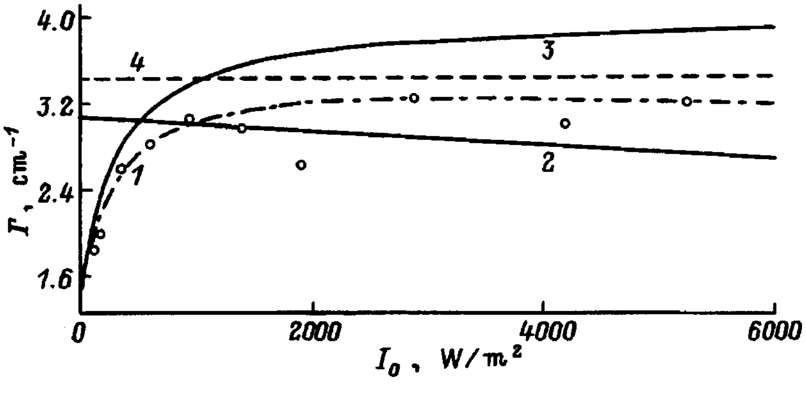

FIG. 4. Two-beam gain versus the average light intensity. *1* and *2* — calculation using the exact method with $M_T=2\times10^{21}$ m^{-3} and $M_T=0$; *3* and *4* — calculation using the approximate Eqs. (24) and (21).

The main argument for the existence of shallow traps in the experimental crystal is that, as observed previously,[12] the two-beam gain depends on the light intensity in the absence of an external field. Analysis of the dependences of the photorefractive response on the external-field frequency, which are presented in Fig. 1, shows that at intermediate frequencies the amplitude of the space-charge field of the photorefractive grating is essentially independent of the average intensity I_0 in a crystal with one photoactive level ($M_T\approx0$). Conversely, in crystals with shallow traps, for $M_T\approx N_A$, such a dependence $E_1(I_0)$ should be quite strong. We investigated experimentally the dependence of the two-beam gain on the total intensity I_0 of the beam for an external field with frequency $f_0=2.025$ kHz and amplitude $E_0=8.9$ kV/cm with a spatial period of the grating $\Lambda=42$ μm. The experimental data presented in Fig. 4 agree well with the computed dependence (curve *1*), obtained for a crystal with shallow trap density $M_T=2\times10^{21}$ m^{-3}. The variance of the experimental points for $I_0>1000$ W/m^2 is due to the measurement errors in the intensity of the amplified signal beam as a result of the substantial photoinduced scattering of the light.

We note that the calculations predict a weak intensity dependence of the two-beam gain even in crystals with no shallow traps also, with $M_T=0$ (curve *2*). The curves *1* and *2* were calculated using the above-described method of numerical analysis on the basis of the relations (15)–(19) and the crystal material parameters used to calculate the frequency dependences $\Gamma(F_0)$ (Fig. 3). The curve *3* was calculated using the approximate formula (24). This approach is valid for low light intensity I_0 and only for intermediate frequencies of the external field. Analysis shows that in the experimental range of light intensities the frequency $f_0=2.025$ kHz at which the experiment was performed falls outside the intermediate region. For this reason, the curve *3* gives too high values of the two-beam gain, qualitatively agreeing with the results of an exact calculation (curve *1*) and the experimental dependence. The straight line *4* in Fig. 4 corresponds to a calculation performed using Eq. (21) for a crystal with one photoactive level.

In summary, in the present work we studied the photorefractive gratings formed in sillenite crystals with shallow traps in the presence of a sign-alternating external electric field in the form of square wave.

We thank A. V. Reshet'ko and S. N. Pitchenko for assisting in the development of the experimental apparatus.

This work was supported in part by the firm ''Stek.''

*)E-Mail: oleg@horizont.tmsk.ru
†)E-Mail: shand@stack.ru

---

[1] J. P. Huignard and F. Micheron, Appl. Phys. Lett. **29**, 591 (1976).
[2] T. G. Pencheva and S. I. Stepanov, Fiz. Tverd. Tela (Leningrad) **24**, 1214 (1982) [Sov. Phys. Solid State **24**, 687 (1982)].
[3] M. P. Petrova, S. I. Stepanov, and A. V. Khomenko, *Photorefractive Crystals in Coherent Optics* [in Russian], St. Petersburg, 1992.
[4] S. I. Stepanov, Rep. Prog. Phys. **57**, 39 (1994).
[5] P. Refregier, L. Solymar, H. Rajbenbach, and J. P. Huighard, J. Appl. Phys. **58**, 45 (1985).
[6] S. I. Stepanov and M. P. Petrov, Opt. Commun. **53**, 292 (1985).
[7] K. Walsh, A. K. Powell, C. Stace, and T. J. Hall, J. Opt. Soc. Am. B **7**, 288 (1990).
[8] C. Besson, J. M. C. Jonathan, H. Villing, G. Pauliat, and G. Roosen, Opt. Lett. **14**, 1359 (1989).
[9] G. Pauliat, A. Villing, J. C. Launay, and G. Roosen, J. Opt. Soc. Am. B **7**, 1481 (1990).
[10] F. Vachss, J. Opt. Soc. Am. B **11**, 1045 (1994).
[11] A. Grunnet-Jepsen, I. Aubrecht, and L. Solymar, Opt. Lett. **20**, 819 (1995).
[12] B. I. Sturman, M. Mann, J. Otten, and K. Ringhofer, J. Opt. Soc. Am. B **10**, 1919 (1993).
[13] N. V. Kukhtarev, V. B. Markov, S. G. Odulov, M. S. Soskin, and V. L. Vinetskii, Ferroelectrics **22**, 949 (1979).
[14] S. I. Stepanov and G. S. Trofimov, Zh. Tekh. Fiz. **55**, 559 (1985) [Sov. Phys. Tech. Phys. **30**, 331 (1985)].
[15] V. I. Berezkin, Fiz. Tverd. Tela (Leningrad) **25**, 490 (1983) [Sov. Phys. Solid State **25**, 276 (1983)].
[16] Yu. F. Kargin and V. M. Skorikov, Ferroelectrics **167**, 257 (1995).
[17] F. P. Strohkendl, J. Appl. Phys. **65**, 3773 (1989).
[18] P. Tayebati and D. Mahgerefteh, J. Opt. Soc. Am. B **8**, 1053 (1991).
[19] I. Biaggio and G. Roosen, J. Opt. Soc. Am. B **13**, 2306 (1996).
[20] R. V. Litvinov, S. N. Pitchenko, A. A. Reshet'ko, S. M. Shandarov, D. V. Yakimov, V. V. Volkov, Yu. F. Kargin, E. P. Shershakov, Pis'ma Zh. Tekh. Fiz. **21**(4), 7 (1995) [Tech. Phys. Lett. **21**, 134 (1995)].
[21] S. M. Shandarov, A. V. Reshet'ko, A. A. Emelyanov, O. V. Kobozev, M. G. Krause, Yu. F. Kargin, and V. V. Volkov, Proc. SPIE **2969**, 202 (1996).
[22] M. H. Garrett, J. Y. Chang, H. P. Jenssen, and C. Warde, J. Opt. Soc. Am. B **9**, 1407 (1992).
[23] R. F. Kazarinov, R. A. Suris, and B. I. Fuks, Fiz. Tekh. Poluprovodn. **6**, 572 (1972) [Sov. Phys. Solid State **6**, 500 (1972)].
[24] V. N. Alimpiev and I. R. Gural'nik, Fiz. Tekh. Poluprovodn. **20**, 811 (1986) [Sov. Phys. Solid State **20**, 512 (1986)].
[25] A. S. Furman, Fiz. Tverd. Tela (Leningrad) **29**, 1076 (1987) [Sov. Phys. Solid State **29**, 617 (1987)].
[26] C. Stace, A. K. Powell, K. Walsh, and T. J. Hall, Opt. Commun. **70**, 509 (1989).

Translated by M. E. Alferieff

External-field-induced formation of stabilized F_2^+ centers in colored LiF crystals

M. G. Abramishvili and V. G. Kvachadze

Scientific-Research Institute of Automatic Systems ''Skhivi'', 380082 Tbilisi, Georgia

Z. G. Akhvlediani, T. L. Kalabegishvili,[a] and Z. K. Saralidze

Institute of Physics, Georgian Academy of Sciences, 380077 Tbilisi, Georgia

(Submitted December 9, 1997; resubmitted April 16, 1998)
Fiz. Tverd. Tela (St. Petersburg) **40**, 2044–2050 (November 1998)

The production of complexes, which are thermally stable at room temperature, with F_2^+ centers in radiation-colored LiF crystals by the combined action of different fields is investigated. The half-life of these laser centers produced by, specifically, hard UV radiation and a shock wave increased by almost two orders of magnitude. © *1998 American Institute of Physics.* [S1063-7834(98)01711-0]

Colored alkali-halide crystals, specifically, LiF with F_2^+ centers, are widely used to produce tunable color-center lasers.[1,2] The main drawback of these centers is their low thermal stability. At room temperature the half-life of these centers does not exceed 12 h. An important role in increasing the thermal stability of F_2^+ centers is played by ions of a divalent metal or products of hydroxyl decomposition,[3,4] which together with the formation of stable electronic traps and additional anionic vacancies stimulate, by virtue of their proximity to F_2^+ centers, the appearance of various perturbing defects.

One method of obtaining F_2^+ centers which are stable at room temperature is irradiation of crystals containing a sufficiently high concentration of hydroxyl ions (>50 ppm).[3–5] At high irradiation doses, reaching almost complete radiolysis of OH^- ions, a substantial density of F_2^+ centers stabilized by oxygen ions can be obtained.

However, it is necessary to take account of the fact that high irradiation doses (especially reactor irradiation), just as high impurity concentrations, can lead to undesirable effects which degrade the lasing characteristics of active centers. It is known, for example, that the energy characteristics of lasers with stabilized centers are at present worse than those of unstable centers: One reason for this fact could be due to a strong distortion of the lattice as a result of a high impurity content or an effect of the radiation. For this reason, in striving to obtain high densities of stable F_2^+ centers the lattice should be perturbed as little as possible so as to avoid harmful ancillary effects.

In Refs. 6 and 7 a new method was proposed for generating F_2^+ centers stable at room temperature, in LiF crystals, that does not require preliminary doping of the crystals with stabilizing impurity ions: lithium fluoride single crystals were preloaded in the region of the yield stress and γ irradiated in the loaded state. Despite the fact that even in this case, just as in Ref. 3 and 4, the increase in the thermal stability of a center is due to the association of an F_2^+ center with a doubly-charged oxygen ion, this method has the advantage that comparatively low concentrations of the hydroxyl ions (<10 ppm) and low γ-ray doses (0.5 Mrad) are adequate.[1)] These are almost ideal conditions for producing a stable active element based on an alkali-halide crystal, especially since the combined action of radiation and mechanical stress greatly increases the resistance of LiF crystals to powerful laser radiation.

It is known that one of the mechanisms leading to the production of F_2^+ centers is two-step ionization of a F_2 center ($F_2+h\nu\rightarrow F_2^*+h\nu\rightarrow F_2+e$). This is ordinarily accomplished by irradiating precolored LiF crystals with UV radiation. However, UV radiation alone is unable to obtain thermally stable F_2^+ centers.

In the present work it is shown that the generation of F_2^+ centers, which are stable at room temperature, in radiation-precolored crystals irradiated in a reactor with doses at which neither F_2^+ centers (in the observed amount) nor their stabilized complexes are formed, is possible under the combined action of UV radiation and a pulsed electric field or a shock wave.

The investigation of such a complex effect is of interest not only from the standpoint of searching for new possibilities for increasing effectively the thermal stability of F_2^+ centers, but also from the standpoint of determining the characteristic features of processes leading to the formation of stable configurations of F_2^+ centers accompanying radiation coloring of stressed crystals even with ''reverse'' processes — bleaching and decay of complicated complexes into simpler formations.

1. EXPERIMENT

The crystals investigated were divided into two basic groups, which were subjected to, respectively, 1) the combined action of UV radiation and a pulsed electric field and 2) the action of a hard UV-radiation pulse accompanied by a shock wave.

A single-crystal block of lithium fluoride was annealed isothermally at a temperature not less than 700 °C for 3 h and then cooled slowly to room temperature. Samples with dimensions of 10×10×0.5 mm were pricked out of this block along the {100} cleavage surfaces, once again annealed under the same conditions and then irradiated in a free state in the channel of an IRT-M reactor at the Institute of Physics of the Georgian Academy of Sciences. The differential flux of thermal neutrons incident on the crystal was $(2.5\pm0.3)\times10^{12}$ n/cm$^2\cdot$s and the integrated dose was 2.4×10^{14} n/cm^2. The absorption spectra were measured after the induced radiation decayed. Together with a F band (250 nm), an intense F_2 band (450 nm) was also observed. The variance in the values of the densities of F and F_2 centers for samples cleared from the same single-crystal ingot and subjected to identical radiation actions was of the order of 3 and 5%, respectively.

The total amount of uncontrollable impurity ions of divalent metal (Au, Sb, Fe, Zn, Co, Ni, Sc) in the crystal did not exceed several ppm (method of activation analysis). Here nickel ions predominate. According to our estimates, the concentration of divalent magnesium ions, which are most easily incorporated into the LiF lattice, was about 10 ppm. The concentration of single hydroxyl ions, estimated from the infrared absorption spectra (3720 cm^{-1} band), was of the order of 100 ppm. Besides the indicated band, bands were also observed at 3635, 3650, and 3670 cm^{-1} (metal-hydroxyl complexes). After irradiation the intensities of all these bands decreased. At the same time, a band appeared at 1970 cm^{-1}, due to interstitial hydrogen ions.[9]

Visible-range and infrared absorption was measured at room temperature using SF-26 and Specord 75 IR spectrometers, respectively. A DRSH-250 high-pressure mercury-quartz lamp was used for UV irradiation. The repetition frequency of the electric field pulses was 100 Hz, the duration and magnitude of the pulses were 200 ns and 20 kV.

The colored LiF crystals were treated with hard pulsed UV radiation and a shock wave in an apparatus in which a creeping discharge on the surface of a dielectric (modification of the ''plasma plateau'') was used as the source of UV radiation.[10] The experimental range of discharge voltages was 10–30 kV (15 kV — threshold for the appearance of a shock wave in this apparatus).

2. RESULTS

1) *UV radiation and pulsed electric field.* When UV radiation and a pulsed electric field are applied separately to the radiation-colored LiF crystals, an F_2^+ band of almost identical intensity arises in both cases with maximum absorption near 645 nm. A gradual decrease of the F_2 band (a result of ionization) is observed as a result of the UV irradiation. The F_2 center density (5.8×10^{17} cm^{-3}) decreased by 20% over the total irradiation time. When a pulsed electric field was applied, however, no changes were observed in the density of F_2 centers. This attests to the fact that in this case the formation of F_2^+ centers is due to a mechanism that does not include ionization of F_2 centers (see Sec. 3). Despite this difference, the absorption spectra near the F_2^+ band are almost completely identical to one another. For this reason, as an illustration we present only the optical absorption spectra (500–1000 nm) for the case of a pulsed electric field (Fig. 1). In this figure the curves 1 and 2 are, respectively, the optical absorption spectra of a colored crystal before and after the action of a pulsed electric field. The application of UV radiation and a pulsed electric field on the crystal was accomplished in two stages. The optical absorption spectra were measured after each stage. The F_2^+ bands (in the case of LiF crystals these bands were nearly Gaussian[11]) were extracted from the complex spectra, and the densities of the F_2^+ centers produced were determined (with an error ~15%) from the areas of these curves (Table I).

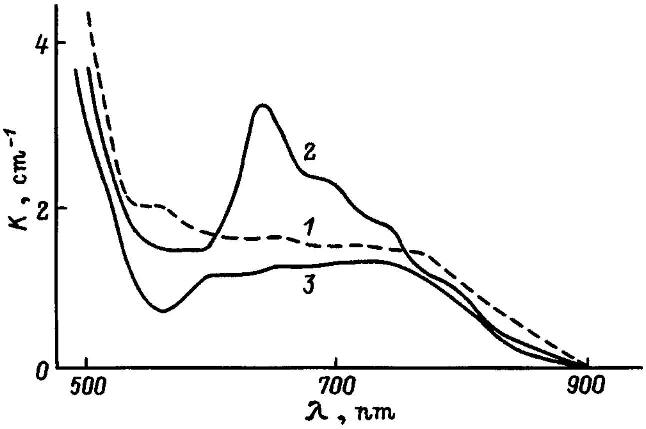

FIG. 1. Optical absorption spectra of colored LiF crystals before (*1*) and after (*2*) the action of a pulsed electric field and after subsequent two-week storage in the dark at room temperature (*3*).

The values obtained are essentially of the same scale. The accumulation of the indicated color centers already saturates at the first stage. Subsequent small changes in the density in one or another direction can be explained by random superposition of partial decoloration and restoration of the experimental centers under repeated actions. In the case when an electric field is applied, a small but pronounced peak appears at 380 nm, which corresponds to $F_3(R_2)$ centers. This peak is also observed subsequently up to merging with the F_2 band, giving rise to broadening of the latter in the short-wavelength direction of the spectrum. For UV-irradiated crystals, this peak appears after the last (fourth) stage of external treatment.

In both cases the thermal stability of the F_2^+ band was found to be equally low: The optical absorption spectra of the experimental crystals after storage for two weeks in the dark at room temperature (curve *3*) are close to the spectra of the initial colored crystals (curve *1*).

The combined effect of UV radiation and a pulsed electric field (for a period of 2 h) on radiation-colored LiF crystal produces F_2^+ centers with an appreciably longer lifetime

TABLE I. Density of F_2^+ centers in colored LiF crystals at different stages of the corresponding actions.

Stage No.	Stage duration, h	After UV irradiation, 10^{16} cm^{-3}	After action of an electric field, 10^{16} cm^{-3}
1	1.5	4.0	3.7
2	2.0	3.3	3.2
3	3.0	3.2	4.1
4	5.0	4.8	3.5

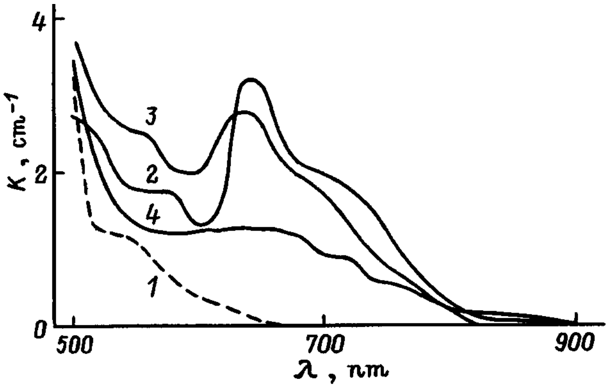

FIG. 2. Optical absorption spectra of colored LiF crystals before (*1*) and after (*2*) the combined action of UV radiation and a pulsed electric field and after subsequent two-week (*3*) and two-month (*4*) storage in the dark at room temperature.

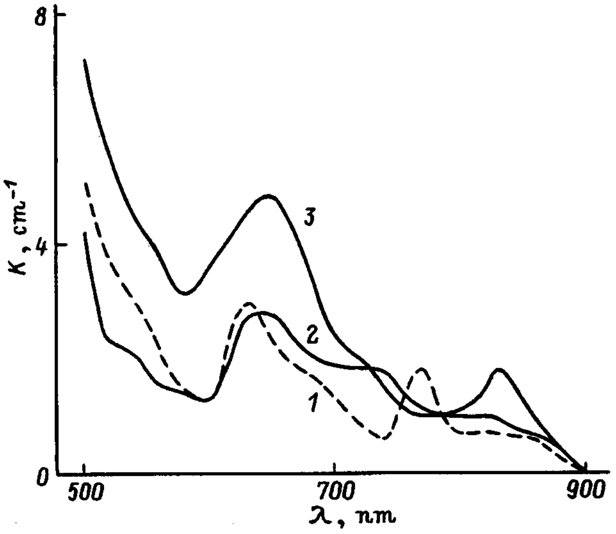

FIG. 3. Optical absorption spectra of colored LiF crystals before (*1*) and after the combined action of a pulsed electric field and UV radiation through a filter (*2*) and without a filter (*3*).

(Fig. 2). For almost the same storage period as above, the density of F_2^+ centers in this crystal decreased negligibly: from 3.7×10^{16} (curve *2*) to 3.0×10^{16} cm^{-3} (curve *3*). The maximum at 645 nm was observed to vanish two months after this action on the experimental crystal, though a sizable continuous absorption remains for a quite long time (curve *4*). In this experiment, together with the formation of F_2^+ centers, a negligible decrease in the density of F_2 centers was observed, after which this density no longer changed during the storage period investigated. Formation of $F_3(R_2)$ centers occurred during storage of the crystal in the dark.

As noted in Sec. 1, hydroxyl ions are the predominant impurity ions in the experimental crystals. The decomposition products of hydroxyl, as is well known, are stabilizing factors for F_2^+ centers. For this reason, to clarify their role in the effect observed above, similar experiments were performed on control LiF crystals, where the number of impurity hydroxyl ions was much smaller than in the samples investigated here (of the order of 10 ppm). In other respects (content of divalent metal ions, dose of preliminary reactor irradiation, and so on) the control samples did not differ much from the experimental samples. The combined effect of UV radiation and a pulsed electric field on the control crystals did not make the F_2^+ centers thermally stable at room temperature. The corresponding absorption bands vanish in less than one day after they are formed. In all cases (combined action of UV radiation and a pulsed electric field, applied in different crystallographic directions [110] and [100]; only UV radiation; electron flux) the maxima of the optical absorption bands of unstable F_2^+ centers in the control LiF crystals are located near 620 nm.

Figure 3 shows the optical absorption spectra of a crystal, which in contrast to the cases described above was subjected to radiation coloring in a stressed state. The applied stress was of the order of the yield stress ($\sim2.3\times10^6$ Pa). According to Refs. 6 and 7, the uniaxial compression which we applied to the crystal during the irradiation process increases the relatiave number of aggregate centers and gives rise to the formation of F_2^+ centers which are stable at room temperature. As expected, a F_2^+ band which is stable at room temperature was also formed in the present case (curve *1*): The density of F_2^+ centers was 3.2×10^{16} cm^{-3}. Besides a F_2^+ band, a band with a maximum at 770 nm, belonging to R_2^- centers, also appeared in this part of the absorption spectrum. Thus, stabilized states of F_2^+ centers were already produced in the experimental crystal prior to the combined external action (UV radiation plus a pulsed electric field). After the indicated combined action (1 h, UFF-1 filter[2)]) the density of the centers investigated increased to 4.3×10^{16} cm^{-3} (curve *2*). In the process, the density of F_2 centers decreased from 8.9×10^{17} to 6.8×10^{17} cm^{-3}. Increasing the time of the external action by another 1.5 h, but this time without using a filter, thereby increasing the intensity of the UV radiation, we observed a substantial growth of the F_2^+ band: The density of F_2^+ centers reached 7.1×10^{16} cm^{-3} (curve *3*), while the intensity of the F_2 band dropped strongly. An appreciable broadening of the F_2 band into the long-wavelength side of the spectrum also occurred — this is a result of the formation of F_3^+ centers. However, the observed increment to the number of F_2^+ centers vanishes during the first two days after the final action (the corresponding optical absorption spectrum is identical to curve *1*). It can be inferred that the number of stabilized states of F_2^+ centers remains unchanged.

Completing the discussion of the first group of experiments, we can draw the following preliminary conclusions: 1) A pulsed electric field[3)] is capable of producing F_2^+ centers in a radiation-colored lithium fluoride crystal; 2) the combined action of UV radiation and a pulsed electric field on radiation-colored LiF crystals increases substantially the room-temperature thermal stability of the F_2^+ centers produced, and the decomposition products of hydroxyls should play a large role in this; 3) the number of stabilizing states of F_2^+ centers formed in a LiF single crystal by the combined action of (n,γ) radiation and an applied mechanical stress is not change much by the subsequent combined action of UV radiation and an alternating electric field on the crystal.

2) *Hard UV radiation and shock wave.* The largest ac-

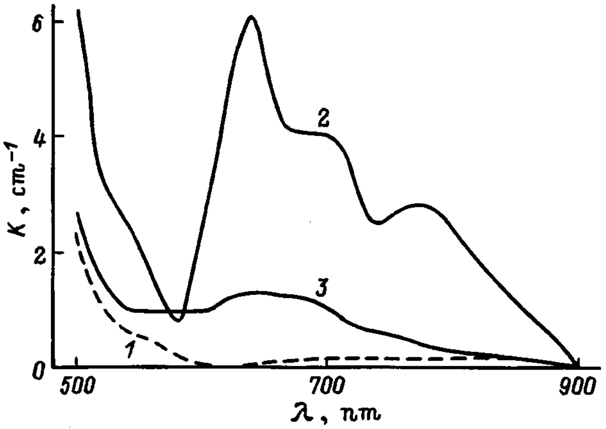

FIG. 4. Optical absorption spectra of colored LiF crystals before (*1*) and after the action of pulsed UV radiation and a shock wave directly on the sample (*2*) and through a quartz plate (*3*).

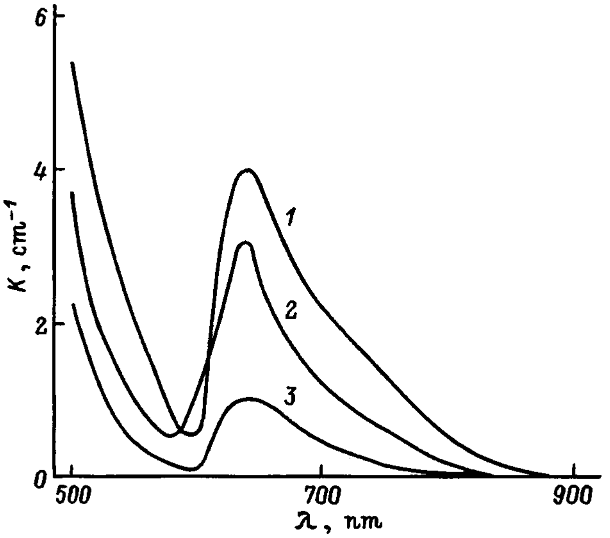

FIG. 5. Optical absorption spectra of colored LiF crystals after one- (*1*), two- (*2*), and four-time (*3*) action of pulsed UV radiation and a shock wave.

cumulation of room-temperature stable F_2^+ centers in (radiation) precolored LiF crystals occurs after the crystals are exposed to pulsed UV radiation accompanied by a shock wave. The corresponding optical absorption spectrum of the experimental crystals is presented in Fig. 4. The curve 1 refers to a sample irradiated in the reactor channel: There are no F_2^+ centers. The curve 2 corresponds to the same sample after exposure to UV radiation and a shock wave. The discharge voltage was 15 kV. A band with a maximum at 645 nm can be seen in this curve — this band is a result of the formation of F_2^+ centers. The maxima at 678 and 786 nm correspond to $F_3^-(R_1^-,R_2^-)$ centers. The latter centers accompany F_2^+ centers in almost all cases (see Figs. 1–3), but the indicated maxima are sharpest in the present experiment.

Exposure to only pulsed UV radiation (through a quartz plate, which protects the sample from the shock wave) sharply decreases the efficiency of generating stable F_2^+ centers (curve *3*).

The largest increment to the absorption coefficient, i.e. the largest number of F_2^+ centers (1.3×10^{17} cm^{-3}) which are stable at room temperature is observed with a discharge voltage of 15 kV. As the discharge voltage increases to 30 kV, the formation efficiency of these centers decreases (when the voltage drops below 15 kV, a discharge is not formed). The accumulation efficiency of stable F_2^+ centers in radiation-colored LiF crystals also decreases under the repeated combined action of hard UV radiation and a shock wave on the experimental crystals with a constant discharge voltage. The optical absorption spectra attest to this — the curves 1–3 in Fig. 5, which correspond to crystals subjected to one-, two-, and four-time action of UV radiation and a shock wave (discharge voltage — 20 kV).

The thermal stability of the F_2^+ centers obtained by the described method was found to be quite high. Despite the fact that half of the centers decay during the first 1.5 weeks, the density of the remaining centers changes slowly during the course of a year and longer (Fig. 6).

Summarizing the results of the second group of experiments, the following can be concluded: 1) The combined action of hard UV radiation and a shock wave on radiation-colored LiF crystals leads to substantial accumulation of stabilized F_2^+ centers; 2) there exists an optimal regime for this combined action (discharge voltage, number of times the action is repeated) for which the largest accumulation of F_2^+ centers which are stable at room temperature obtains.

3. DISCUSSION

Optical characteristics of a center, such as the wavelengths of the absorption and luminescence maxima, the width of the luminescence band, and the Stokes shift, indicate that we are dealing with the complex $F_2^+:\mathrm{O}^{2-}$. Evidently, this model is indeed the most appropriate one for representing a stabilized F_2^+ center as compared with the variants with OH$^-$, O$_2^-$, or O$^-$ ions.[12]

According to Ref. 13, oxygen ions formed as a result of radiolysis of single OH$^-$ ions participate most effectively in the process leading to stabilization of F_2^+ centers (formation of the complexes $F_2^+:\mathrm{O}^{2-}$). It can be estimated from the intensity of the corresponding band that at the (n,γ)-irradiation dosages used in our experiments only 10% of the total number of OH$^-$ ions were subjected to radiolysis. Our estimates show that the total concentration of hydro-

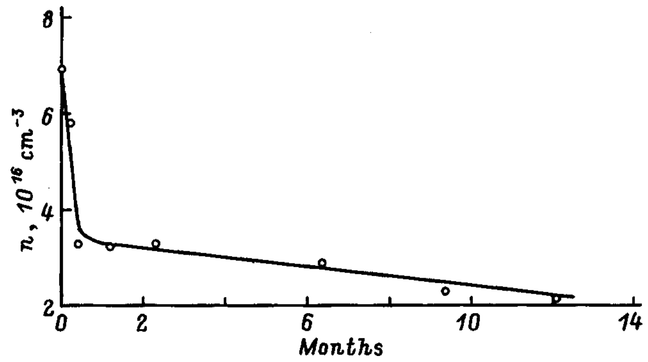

FIG. 6. Density of F_2^+ centers versus storage time of a crystal in the dark at room temperature.

gen products of radiolysis (H_i^-, H_i^0, H_s^-, H_s^0) did not exceed 15 ppm. Therefore the concentration of oxygen ions which are potential stabilizers of F_2^+ centers is approximately the same, but no higher.

The concentration of stabilized F_2^+ centers, formed in irradiated crystals after the complex actions described above, completely corresponds to this value. However, it must be underscored that the presence of the indicated amount of oxygen ions and F_2^+ centers in the crystal in itself is still insufficient for the formation of the experimentally observed quantity of stable $F_2^+:O^{2-}$ complexes, while the combined action of UV radiation and a pulsed electric field or a hard UV pulse and a shock wave leads to the production of thermally stable F_2^+ centers ($F_2^+:O^{2-}$), ''using'' almost completely the store of doubly-charged oxygen ions. The absence of stable F_2^+ centers in the control samples can be easily explained on the basis of these ideas by a deficiency (<1 ppm) of oxygen ions.

In Ref. 7, to explain the effect produced by the combined action of γ irradiation and mechanical stress on a LiF crystal, it was suggested that the factor giving rise to the formation of stable F_2^+ centers is an anisotropic mechanical-stress field with a sharply distinguished direction, produced in the crystal by a uniaxial load. If it is assumed that the formation of the complex $F_2^+:O^{2-}$ requires overcoming an energy barrier, then it has not been ruled out that in an asymmetric stress field in some directions the barrier to formation of a complex, which in itself is a formation with an anisotropic intrinsic elastic field, decreases to such an extent that dynamic overcoming of the barrier in the radiation-perturbed lattice becomes much easier. This will increase the efficiency of the reaction whereby a F_2^+ center combines with an oxygen ion and can lead to the formation of an appreciable quantity of $F_2^+:O^{2-}$ centers even if the concentration of oxygen ions themselves is so low that it is impossible to determine the formation of these centers as a result of only ionizing irradiation without an external stimulating force.

We believe that the pulsed electric field and a shock wave which act on colored LiF crystals during UV irradiation play the same role as an external load applied to the irradiated crystal, producing in the crystal the required anisotropy. This supposition is supported by a correlation between other results of these combined actions.

The effect of asymmetric stresses produced by a uniaxial load can be considerable only if they exceed the internal stresses, which may exist in a crystal because of the presence of structural defects, especially dislocations. The internal stress level near dislocations is substantially higher than that of the stresses that could be produced by external loads, and in certain regions these stresses themselves could stimulate stabilization of F_2^+ centers, as should happen in reality. However, in annealed crystals, because of the low dislocation densities ($\sim 10^{10}$ m^{-2}), the relative fraction of the volume with such stresses is too small, and the average level of internal stresses in a crystal as a whole is very low.

If a crystal is loaded above the yield stress, plastic deformation starts and the dislocation density increases rapidly. This increases the level of the internal stresses. However, since they are a superposition of fields produced by dislocations randomly distributed in both space and over orientations of the axes and Burgers vectors, these stresses are almost isotropic and, not having the required directionality, they cannot give rise to the formation of stable complexes. On the other hand, because of their high level they can weaken the effectiveness of an external field and decrease the accumulation of F_2^+ centers. Indeed, the curve of the absorption coefficient at the maximum of the F_2^+ band versus the applied load (see Fig. 4 in Ref. 8) passes through a maximum when the applied stress equals the yield stress of the sample. Subsequently, as the applied stress increases, the accumulation of stabilized F_2^+ centers becomes much less efficient. As noted above, a decrease of the number of stable F_2^+ centers was also observed with increasing discharge voltage, i.e. with increasing intensity of the combined action of hard UV radiation and a shock wave. Apparently, an appreciable increase in the internal stress level also occurs in this case. This explains the dependence of the accumulation of F_2^+ centers on the multiple action of the UV radiation and shock wave (Fig. 5).

The curve of the decay of F_2^+ centers (Fig. 6) shows that we are dealing with F_2^+ centers of two types: 1) unstable F_2^+ centers which decay mainly during 1.5–2 weeks after the UV radiation with a shock wave have acted on the crystal and 2) stabilized configurations with F_2^+ centers which remain in the crystal for more than one year.

According to Ref. 14, when an electric field is applied to a crystal, vacancies of both types and their clusters are formed. An anionic vacancy, appearing under the acton of an electric field and combining with an existing F center, can form an F_2^+ center. However, an electric field alone is not sufficient for thermal stabilization of the center. Apparently, an anisotropic mechanical-stress field, produced by an electric field in the lattice, with a fixed density of F_2^+ centers is insufficient to form an appreciable number of complexes with stabilizing defects.$^{4)}$ As the F_2^+ center density is increase (by switching on UV radiation), the rate of self-trapping of a center and a perturbing defect should increase and thereby the density of thermally stable configurations of complexes should increase. Indeed, UV irradiation in combination with a pulsed electric field, as seen above, appreciable increase the density of complexes of F_2^+ centers with a perturbing defect which are stable at room temperature.

As perturbing defects, doubly charged oxygen ions ($F_2^+:O^{2-}$) as well as cationic vacancies ($F_2^+:V_c^-$ in the case of a crystal with divalent metal ions), together with increasing the thermal stability of F_2^+ centers, give rise to a displacement of the corresponding absorption and luminescence bands. Table II shows that the displacements of the maxima of the absorption bands, according to data obtained by different groups of investigators, differ not only in magnitude but also in direction, even for the same system of alkali-halide crystals. For example, according to Ref. 15, for NaF they are strongly shifted into the long-wavelength side of the spectrum relative to the absorption band of unperturbed F_2^+ centers, while in Ref. 16 the maximum of the absorption band of $F_2^+:O^{2-}$ centers is shifted in the direction of short

TABLE II. Absorption bands of F_2^+ and similar centers in alkali-halide crystals ($\lambda_{\max}$, nm).

Crystals	Centers			References
	F_2^+	$F_2^+:O^{2-}$	$F_2^+:V_c^-$	
NaF	750	906	870	15
NaF	740	725	–	16
NaF	750	–	880	17
LiF	640	640	580	3
LiF	640	620	–	16
NaCl	1050	1090	–	12

wavelengths (by only 15 nm). For the LiF system, the maximum of the absorption band of $F_2^+:V_c^-$ centers is shifted not in the long-wavelength direction, as in the case of NaF,[15] but rather in the direction of short wavelengths[3] down to 580 nm, and so on. The luminescence bands mainly follow the optical-absorption bands.

This table is incomplete, but it correctly reflects the situation existing at the present time. In the crystals investigated, the absorption band of F_2^+-like centers ($F_2^+:O^{2-}$), both stable and less stable, always lies in the interval 640–650 nm, as, for example, in Ref. 13. We think that in our case an O^2 ion is always present in the environment around an F_2^+ center, while the lifetime is determined by the configuration of the complex $F_2^+:O^{2-}$. In the control crystals, where the number of impurity hydroxyl ions is very small, primarily undisturbed F_2^+ centers are produced and, as expected, vanish in approximately one day. The absorption bands corresponding to undisturbed F_2^+ centers are located at 620 nm.

The methods which we have proposed (besides the present work, we also have in mind Ref. 7) for stabilizing the laser color centers investigated, as remarked above, do not require high impurity concentrations and therefore special doping of the crystal. This is an advantage of these methods, since doping has a bad effect on the laser properties of the active element. For example, according to Ref. 18, an impurity strongly degraded the lasing characteristics of crystals and decreased their radiation resistance.

In closing, comparing the effects obtained using different complex actions it can be concluded that stabilized F_2^+ centers remain for a long time (the effect does not vanish for one year and longer) in irradiated LiF crystals subjected to the combined action of hard UV radiation and a shock wave, just as in crystals irradiated in a mechanically stressed state,[6,7] while F_2^+ centers produced by UV irradiation in an electric field vanish comparatively quickly (mainly within two months).

This work was supported by a grant from the Georgian Academy of Sciences and additional financing from the Georgian Department of Science and Technologies.

[a] E-mail: tlk@physics.iberiapac.ge

[1] A number of characteristic curves from this group of results have been published recently in Ref. 8.

[2] The transmission interval is 220–420 nm.

[3] A constant electric field of the same magnitude was found to be less effective in the phenomena observed in the present work.

[4] We note that the strength of the electric field that we used in combination with UV radiation is 1–2% of the breakdown field in an ionic crystal at room temperature.

---

[1] Yu. L. Gusev, S. P. Marennikov, and V. P. Chebotaev, Pis'ma Zh. Tekh. Fiz. **3**(7), 305 (1977).

[2] L. F. Mollenauer, Opt. Lett. **5**, 164 (1977).

[3] B. D. Lobanov, N. T. Maksimova, V. M. Khulugurov, and I. A. Parfianovich, Zh. Prikl. Spektrosk. **32**, 1079 (1980).

[4] B. D. Lobanov, N. T. Maksimova, and L. I. Shchepina, Opt. Spektrosk. **52**, 163 (1982) [Opt. Spectrosc. **52**, 96 (1982)].

[5] R. A. Sierra and C. R. Collins, Appl. Opt. **21**, 4400 (1982).

[6] V. G. Kvachadze, M. G. Abramishvili, and V. I. Altukhov, J. Low Temp. Phys. **58**, 143 (1985).

[7] M. G. Abramishvili, V. G. Kvachadze, and Z. K. Saralidze, Fiz. Tverd. Tela (Leningrad) **29**, 39 (1987) [Sov. Phys. Solid State **29**, 22 (1987)].

[8] M. G. Abramishvili, Z. G. Akhvlediani, E. M. Barkhudarov, T. L. Kalabegishvili, V. G. Kvachadze, and M. I. Taktakishvili, in *Proceedings Conference on Laser Physics-96*, Ashtarak, Armenia, October 21–25, 1996, p. 95.

[9] Z. G. Akhvlediani and N. G. Politov, Izv. Akad. Nauk SSSR, Ser. Fiz. **35**, 1414 (1971).

[10] M. G. Abramishvili, Z. G. Akhvlediani, É. M. Barkhudarov, T. L. Kalabegishvili, V. G. Kvachadze, and M. I. Taktakishvili, Fiz. Tverd. Tela (St. Petersburg) **37**, 2526 (1995) [Phys. Solid State **37**, 1385 (1995)].

[11] J. Nahum, Phys. Rev. **158**, 814 (1967).

[12] E. Georgiou, J. F. Pinto, and C. R. Pollock, Phys. Rev. B **35**, 7636 (1987).

[13] I. A. Parfianovich, V. M. Khulugurov, N. A. Ivanov, Yu. M. Titov, V. A. Chepurnoĭ, O. P. Varnavskiĭ, V. P. Shevchenko, and A. M. Leontovich, Izv. Akad. Nauk SSSR, Ser. Fiz. **45**, 309 (1981).

[14] S. K. Gupta, H. B. Gon, and K. V. Rao, J. Mater. Sci. Lett. **5**, 792 (1986).

[15] L. F. Mollenauer, in *Defects in Insulating Crystals*, edited by V. M. Tuchkevich and K. K. Shvarts, Riga, 1981, p. 524.

[16] B. D. Lobanov, N. T. Maksimova, E. D. Isyanova, V. N. Lomasov, A. M. Provorov, and P. N. Tsirul'nik, Opt. Spektrosk. **63**, 816 (1987) [Opt. Spectrosc. **63**, 485 (1987)].

[17] D. M. Hofmann, F. Lohse, H. J. Paus, D. Y. Smith, and J.-M. Spaeth, J. Phys. C: Sol. Stat. Phys. **18**, 443 (1985).

[18] T. T. Basiev, Yu. K. Voron'ko, S. B. Mirov, V. V. Osiko, and A. M. Prokhorov, Izv. Akad. Nauk SSSR, Ser. Fiz. **46**, 1600 (1982).

Translated by M. E. Alferieff

PHYSICS OF THE SOLID STATE VOLUME 40, NUMBER 11 NOVEMBER 1998

Temperature dependence of the heat capacity and lattice constant of lanthanum and samarium hexaborides

N. N. Sirota, V. V. Novikov, V. A. Vinokurov, and Yu. B. Paderno

Bryansk Pedagogical Institute, 241036 Bryansk, Russia

(Submitted April 21, 1998)
Fiz. Tverd. Tela (St. Petersburg) **40**, 2051–2053 (November 1998)

The temperature dependence of isobaric heat capacity and [411] interplanar spacing in lanthanum and samarium hexaborides have been determined experimentally within the 5–300 K region. The variation of the lattice parameters and thermal expansion coefficients $\alpha(T)$ with temperature has been calculated. © *1998 American Institute of Physics.* [S1063-7834(98)01811-5]

This work reports an experimental study of the temperature dependence of the heat capacity and lattice periods of lanthanum and samarium hexaborides within the region from helium to room temperatures (4.2–300 K).

The temperature dependences of the heat capacity and electrical resistivity of lanthanum hexaboride were investigated earlier (see, e.g., Refs. 1,2).

Data on the temperature dependence of the physical properties of SmB_6 can be found in Refs. 3–5 and references therein.

At the same time no systematic low-temperature x-ray diffraction measurements of interatomic distances in LaB_6 and SmB_6 have thus far been made.

In the low-temperature domain, SmB_6 exhibits a specific change in the valence state of samarium ions, the character of interatomic interaction, in particular, a transition from semiconducting to metallic conduction, which account for anomalies in the temperature behavior of some of its physical characteristics. This stresses the need for investigating its properties.

Single-crystal and powder samples were prepared for low-temperature calorimetric and x-ray diffraction measurements.

The calorimeter copper ampoule used to measure the heat capacity $C_p(T)$ was filled with pieces of SmB_6 single crystals. The sample for x-ray diffraction measurements was prepared from a single crystal ground to powder.

The temperature dependence of the heat capacity of SmB_6 was measured in a Nernst-Strelkov–type low-temperature calorimeter.[6] The measurements were performed adiabatically with a periodic heat injection by a technique described previously. Within the 5–20 K interval, the measurements were made in 0.5–1 K steps, and from 20 to 300 K, in steps of 2–5 K. The measurement error in the 5–20 K interval was about 1%, and at higher temperatures, 20–300 K, it did not exceed 0.3%.

Figure 1 plots the temperature dependence of the heat capacity of SmB_6 and identifies the experimental points. The scatter of experimental points with respect to the smoothened curve is smaller than the calculated error. Also shown is the temperature dependence of the heat capacity of lanthanum hexaboride obtained by us earlier.[1]

The molar heat capacity of SmB_6, $C_p(T)$, was extrapolated to absolute zero using the relation $C_p \simeq C_v = 3.6 \times 10^{-2} T + 2.61 \times 10^{-4} T^3$, which corresponds to a characteristic temperature at absolute zero $\theta_0 = 374$ K. Ultrasonic measurements yielded for samarium hexaboride $\theta_0 = 373$ K.[7] In contrast to the $C_p(T)$ curves obtained for the hexaborides of praseodymium,[7] neodymium,[8] and most other rare earths, SmB_6 does not exhibit a clearly pronounced magnetic transition within the 5–20 K interval.

The x-ray measurements were carried out in a low-temperature chamber by the technique described elsewhere.[9] The samples were preliminarily tested for being single phase and having no texture. The interatomic spacing was derived from the center of gravity of the (411) reflection. The measurement error did not exceed 6×10^{-5} Å throughout the temperature range covered, 4.2–320 K. The experimental scatter relative to the smoothened curve $d_{411}(T)$ for LaB_6 and SmB_6 was less than the calculated error. Each value of $d_{411}(T)$ was determined in Å to the sixth digit after the decimal point.

Figure 2 displays the experimental values of $d_{411}(T)$ for LaB_6 and SmB_6 obtained in the 4.2–320 K range.

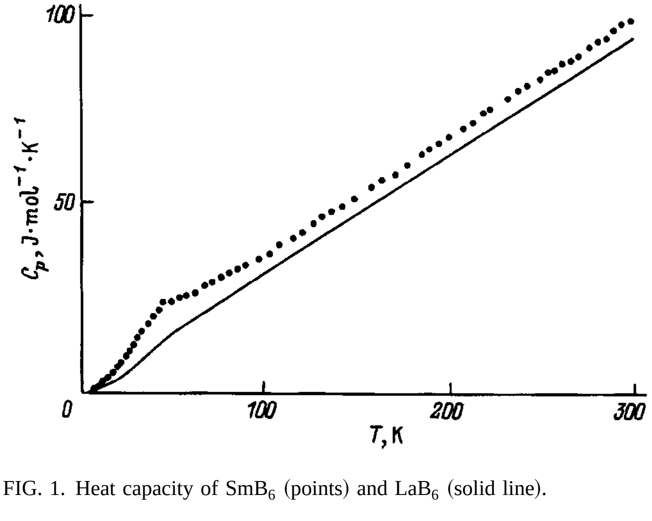

FIG. 1. Heat capacity of SmB_6 (points) and LaB_6 (solid line).

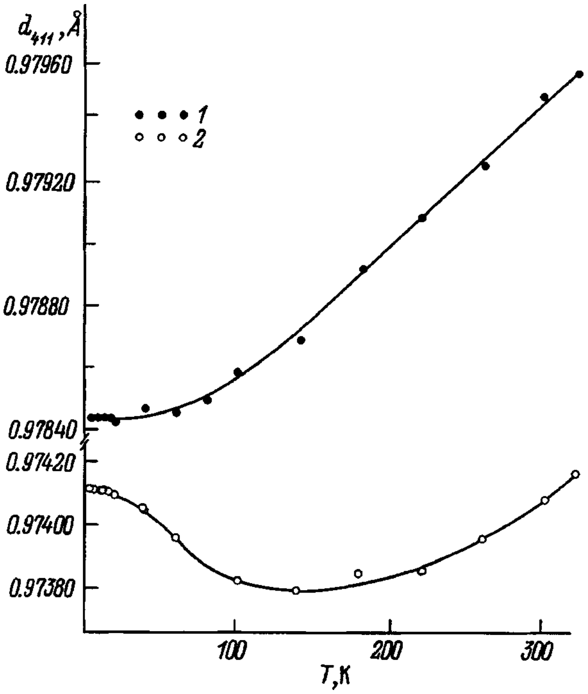

FIG. 2. Interplanar spacing d_{411}. *1*—LaB_6, *2*—SmB_6.

Table I lists the lattice constant *a* of LaB_6 and SmB_6 and volume thermal expansion coefficients calculated for the temperature range studied.

LaB_6 and SmB_6 have similar crystal structures with a CsCl-type cubic unit cell, and the tensor surface of their linear thermal-expansion coefficient has spherical shape with a radius independent of direction.

TABLE I. Lattice parameters *a* and volume thermal-expansion coefficients β of lanthanum and samarium hexaborides.

	LaB_6		SmB_6	
T, K	*a*, Å	$\beta \cdot 10^6$, K^{-1}	*a*, Å	$\beta \cdot 10^6$, K^{-1}
4.2	4.15112	0.15	4.13281	−0.24
10	4.15112	0.27	4.13280	−1.50
20	4.15114	0.72	4.13276	−3.15
30	4.15116	1.44	4.13267	−7.98
40	4.15118	2.16	4.13254	−11.13
50	4.15121	3.21	4.13237	−13.44
60	4.15127	4.26	4.13216	−13.80
70	4.15134	5.43	4.13199	−11.88
80	4.15143	6.75	4.13187	−9.60
90	4.15153	7.92	4.13174	−7.38
100	4.15168	9.09	4.13165	−5.91
120	4.15193	10.89	4.13155	−3.30
140	4.15228	12.66	4.13148	−0.93
160	4.15265	13.77	4.13149	0.99
180	4.15305	14.43	4.13153	2.76
200	4.15345	14.70	4.13163	4.53
220	4.15384	14.85	4.13178	5.91
240	4.15427	15.00	4.13195	6.78
260	4.15471	15.12	4.13216	8.37
280	4.15510	15.30	4.13240	10.08
300	4.15553	15.54	4.13284	13.44
320	4.15597	15.72	4.13305	

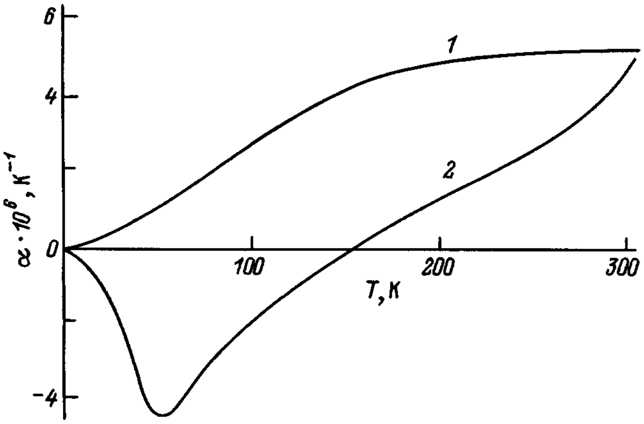

FIG. 3. Linear thermal-expansion coefficient. *1*—LaB_6, *2*—SmB_6.

Figure 3 displays the temperature behavior of the linear thermal-expansion coefficient $\alpha(T)$ of the above hexaborides determined from the (411) reflection. We readily see that the interplanar spacing d_{411} and the linear thermal-expansion coefficient of LaB_6 increase throughout the temperature range of 4.2–320 K, with $\alpha > 0$ everywhere. Above 250 K, $\alpha(T)$ grows more slowly with temperature.

In contrast to lanthanum hexaboride, the interatomic spacing d_{411} and, accordingly, the lattice constant *a* of SmB_6 decrease starting from 8 K, the lattice contracts, and the unit cell volume decreases up to 150 K, after which d_{411} starts to increase. It is only close to 300 K that d_{411} becomes equal to its value for $T \rightarrow 0$.

The linear thermal-expansion coefficient of SmB_6 becomes negative starting from 4 K to reach a minimum at 55 K. At 145 K, $\alpha(T)$ becomes zero, reverses sign, and approaches the value for LaB_6 at about 300 K.

The considerable difference between the temperature dependences of the linear thermal-expansion coefficients α_{LaB_6} and α_{SmB_6} is due primarily to the differences in interatomic chemical bonding in these hexaborides. As seen from a comparison of the temperature dependences of the electrical conductivity of LaB_6 and SmB_6, lanthanum hexaboride exhibits metallic conduction, whereas samarium hexaboride is a donor semiconductor at low temperatures.[2]

The decrease of unit cell volume with increasing temperature and the negative thermal-expansion coefficient at low temperatures shown by SmB_6 is a typical feature of compounds with covalent bonding, including semiconductors of the type of diamond, Si, Ge, III-V, II-VI, and other compounds.[10]

[1] N. N. Sirota, V. V. Novikov, V. A. Vinokurov, and Yu. B. Paderno, Zh. Fiz. Khim. (in press).

[2] Yu. B. Paderno, V. V. Novikov, and E. S. Garf, Porosh. Metall. No. 11, 70 (1969).

[3] E. S. Konovalova, Yu. B. Paderno, V. E. Yachmenyov, and E. M. Dudnik, Izv. Akad. Nauk SSSR, Neorg. Mater. **14**, 2191 (1978).

[4] A. Tamaki, T. Goto, S. Kunii, M. Kasaya, T. Suzuki, T. Fujimura, and T. Kasuya, J. Magn. Magn. Mater. **47–48**, 496 (1985).

[5] S. Nakamura, T. Goto, S. Kunii, T. Fujimura, M. Kasaya, T. Suzuki, and T. Kasuya, J. Magn. Magn. Mater. **76–77**, 312 (1988).

[6] N. N. Sirota, A. M. Antjouchov, V. V. Novikov, and V. A. Fyodorov, Cryst. Res. Technol. **17**, 279 (1982).

[7] T. Kasuya, M. Kasaya, T. Kagehara, T. Fujuta, T. Goto, A. Tamaki, M. Takigawa, and H. Yasuoka, J. Magn. Magn. Mater. **31–34**, 447 (1983).
[8] N. N. Sirota, V. V. Novikov, and S. V. Antipov, Fiz. Tverd. Tela (St. Petersburg) **39**, 913 (1997) [Phys. Solid State **39**, 815 (1997)].
[9] N. N. Sirota and A. A. Sidorov, Dok. Akad. Nauk SSSR **284**, 1111 (1985) [Sov. Phys. Dokl. **30**, 647 (1985)].
[10] S. I. Novikova, *Thermal Expansion of Solids* [in Russian] (Nauka, Moscow, 1974), p. 292.

Translated by G. Skrebtsov

PHYSICS OF THE SOLID STATE VOLUME 40, NUMBER 11 NOVEMBER 1998

Drift mobility of photogenerated current carriers in $Bi_{12}GeO_{20}$ crystals

S. N. Plyaka and G. Kh. Sokolyanskiĭ

Dnepropetrovsk State University, 320625 Dnepropetrovsk, Ukraine

(Submitted May 14, 1998)
Fiz. Tverd. Tela (St. Petersburg) **40**, 2054–2055 (November 1998)

The drift mobility of photogenerated electrons and holes in $Bi_{12}GeO_{20}$ crystals with different degrees of doping is investigated experimentally.
[S1063-7834(98)01911-X]

There are a number of time-of-flight studies of the mobility of photogenerated charge carriers in germanium and silicon sillenites.[1–4] In Refs. 5–7 charge transport is investigated by direct measurement of the distribution of the electric field intensity using the transverse electrooptic effect. A very wide spectrum of values is observed: from 10^{-5} cm^2/(V−s) in samples with empty traps[2] up to values $\geqslant 10$ cm^2/(V−s), obtained in Ref. 3 using a technique with high temporal resolution under conditions of band-band generation. Most investigations studied electron transport. In the present work we report some results of measuring the mobility of photogenerated electrons and holes in $Bi_{12}GeO_{20}$ crystals, both nominally pure and doped with vanadium ions.

The investigations were performed on Czochralski-grown crystals. Doping was performed by introducing into the charge V_2O_5 in quantities of 0.2, 0.5, and 1 mole%. The mobility was measured both by the method of steady space-charge-limited currents (SCLCs) and by the time-of-flight (TOF) method. Samples in the form of plane-parallel plates with thickness $d \leqslant 1$ mm were used. In the SCLC measurements the polished end of a sample was illuminated with $\lambda = 400$ nm light with intensity ~ 10 μW/cm. In the TOF investigations single light pulses from an ISSH-400 lamp used. The pulses passed through a glass light filter with a transmission maximum at $h\nu \approx 3.4$ eV, which is close to the band gap in $Bi_{12}GeO_{20}$. To obtain a reproducible signal in the TOF measurements the sample was first held in the dark with shorted electrodes for 5 min, and a measuring field was applied for not more than 1 min. In this case, the phototransport signal stopped changing appreciably after the sample was illuminated with several flashes. In measuring the current-voltage characteristics (IVCs), each experimental point was recorded 600 s after the light was switched on, when a steady photocurrent was established. In this time a nonuniform field distribution is formed in the interior of the sample.[6,7] Thus, in both cases the measurements were performed in a state of the crystal with filled traps.

Analysis of the IVCs shows[8,9] that in the case of monopolar and with double injection (DI) a quadratic section of the voltage dependence of the current, described by the equation

$$j = \frac{9}{8} \varepsilon \mu_{\mathrm{ef}} \frac{U^2}{d^3}, \tag{1}$$

where d is the sample thickness and μ_{ef} is the effective carrier mobility, can be observed. In the case of DI, for close values of the electron and hole mobilities, μ_{ef} characterizes ambipolar drift. A quadratic voltage dependence of the current is observed in the experimental IVCs, obtained with uniform illumination, after the section of quite rapid growth. The relation (1) gives mobilities $\mu \geqslant 10^{-3}$ cm^2/(V−s) (see Table I).

Both Gaussian and dispersion transport signals were obtained in the TOF investigations.[10] The latter was observed in pure $Bi_{12}GeO_{20}$ at temperature above 60 °C. In crystals with vanadium at temperatures below 80 °C transport is Gaussian. The pulses obtained (see Fig. 1) contain two sections with a decaying photocurrent. We took as the time of flight T_n the time at which the flatter section terminated. The plot $T_n^{-1} = f(U)$ is a straight line, attesting to the field-independence of the mobility. On the second section the signal $I(t)$ drops off exponentially. This makes it possible to determine the lifetime of photogenerated charge carriers. In

TABLE I. Values of the phototransport parameters in $Bi_{12}GeO_{20}$.

Sample	μ, 10^{-3} cm^2/(V−s)	μ_n, cm^2/(V−s)	τ_n, 10^{-4} s	$E_{\mu n}$, eV	μ_p, cm^2/(V−s)	τ_p, 10^{-4} s	$E_{\mu p}$, eV
BGO	1	3.6×10^{-2}	6.5	0.32	1.1×10^{-2}	4.5	0.52
BGO + 0.2 mole% V_2O_5	6.8	1.37×10^{-1}	1.8	0.2	1.95×10^{-1}	1.94	0.2
BGO+0.5 mole% V_2O_5	1.5	6.97×10^{-2}	1.55	0.31	1.12×10^{-1}	1.8	0.29
BGO+1 mole% V_2O_5	1.2	4×10^{-2}	1	0.36	9×10^{-2}	1.3	0.32

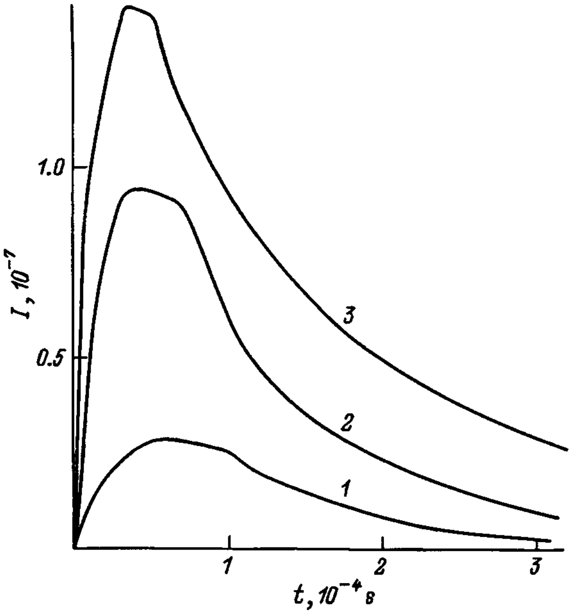

FIG. 1. Time dependence of the photocurrent in a crystal $Bi_{12}GeO_{20}$ $+1$ mole% V_2O_5 at voltages (in V): *1* — 300, *2* — 500, *3* — 600 (temperature 60 °C).

the case of dispersion transport, the time T_n was determined from the kink in the plot $\log I - \log t$. The mobilities determined from both types of signals fall on the same straight line in the Arrhenius plot of $\mu(T)$.

Transport signals for both photogenerated electrons and holes were obtained in all experimental samples. The electron (μ_n, τ_n) and hole (μ_p, τ_p) mobilities and lifetimes are presented in Table I. In undoped $Bi_{12}GeO_{20}$ the product $\mu\tau$ for electrons is somewhat larger than for holes, remaining close in order of magnitude for both types of carriers. The values of μ_n and τ_n agree well with the published data obtained for samples with filled traps.[1,2,4] The introduction of vanadium leads to the reverse relation $(\mu\tau)_p > (\mu\tau)_n$. In all cases the difference between $(\mu\tau)_n$ and $(\mu\tau)_p$ does not exceed one order of magnitude. As the vanadium concentration increases, the mobilities and lifetimes of both electrons and holes decrease. As temperature increases, the mobility of photogenerated charge carriers increases exponentially with activation energy $E_{\mu n}$ and $E_{\mu p}$.

The fact that the mobilities μ obtained by analyzing the IVCs for all crystals are less than the values of μ_n and μ_p determined by the TOF method could be an indication that under uniform illumination both electrons and holes move simultaneously in the sample. Then μ is the ambipolar drift mobility.[11] Mobilities of the order of $10^{-1} - 10^{-2}$ cm^2/(V$-$s) are characteristic for hopping conduction in the tails of the density of states.[12] This agrees with the fact that sillenite crystals have a well-developed optical-absorption shoulder.[13]

[1] S. L. Hou, R. B. Lauer, and R. E. Aldrich, J. Appl. Phys. **44**, *6*, 2652 (1973).

[2] V. Kh. Kostyuk, A. Yu. Kudzin, and G. Kh. Sokolyanskiĭ, Fiz. Tverd. Tela (Leningrad) **22**, 2454 (1980) [Sov. Phys. Solid State **22**, 1429 (1980)].

[3] I. T. Ovchinnikov and É. V. Yanshin, Fiz. Tverd. Tela (Leningrad) **25**, 2196 (1983) [Sov. Phys. Solid State **25**, 1265 (1983)].

[4] A. Ennouri, M. Tapiero, J. P. Vols, J. P. Zielinger, J. Y. Moisan, and J. C. Launay, J. Appl. Phys. **74**, 2180 (1993).

[5] V. N. Astratov, A. V. Il'inskiĭ, V. A. Kiselev, and M. B. Mel'nikov, Fiz. Tverd. Tela (Leningrad) **26**, 743 (1984) [Sov. Phys. Solid State **26**, 449 (1984)].

[6] V. N. Astratov, A. V. Il'inskiĭ, and M. B. Mel'nikov, Fiz. Tverd. Tela (Leningrad) **25**, 3042 (1983) [Sov. Phys. Solid State **25**, 1756 (1983)].

[7] V. V. Bryksin, L. I. Korovin, and V. I. Marakhonov, Zh. Tekh. Fiz. **53**, 1133 (1983) [Sov. Phys. Tech. Phys. **9**, 686 (1983)].

[8] M. Lampert and P. Mark, *Current Injection into Solids*, Academic Press, N.Y., 1970; Mir, Moscow, 1973, 416 pp.

[9] K. Kao and W. Hwang, *Electrical Transport in Solids*, Pergamon Press, N.Y., 1979; Mir, Moscow, 1984, 219 pp.

[10] V. I. Arkhipov, A. I. Rudenko, A. M. Andriesh, M. S. Iovu, and S. D. Shutov, *Nonstationary Injection Currents in Solids* [in Russian], Shtiintsa, Kishinev, 1983, 175 pp.

[11] R. Smith, *Semiconductors*, Cambridge University Press, N.Y., 1959; Mir, Moscow, 1982, 560 pp.

[12] M. Brodsky [Ed.], *Amorphous Semiconductors*, Springer-Verlag, N.Y., 1985; Mir, Moscow, 1982, 420 pp.

[13] R. E. Aldrich, S. I. Hou, and M. L. Marvill, J. Appl. Phys. **42**, 493 (1971).

Translated by M. E. Alferieff

PHYSICS OF THE SOLID STATE VOLUME 40, NUMBER 11 NOVEMBER 1998

DEFECTS. DISLOCATIONS. PHYSICS OF STRENGTH

Scattering of spin waves by a rectilinear edge dislocation

A. N. Kuchko and M. V. Chernyshëva

Donetsk State University, 340000 Donetsk, Ukraine

(Submitted March 2, 1998)
Fiz. Tverd. Tela (St. Petersburg) **40**, 2056–2058 (November 1998)

The propagation of volume spin waves in an unbounded easy-axis magnet containing a rectilinear edge dislocation is studied theoretically. The spin-wave scattering amplitudes are calculated in the Born approximation. It is shown that the spin-wave scattering amplitude vanishes for certain values of the scattering angle. The dependence of the scattering angle on the angle of incidence of the spin waves is found for this case. The transport scattering cross section of spin waves is found. © *1998 American Institute of Physics.* [S1063-7834(98)02011-5]

Recently, there have appeared a number of papers (see, for example, Refs. 1–3) on travelling exchange spin waves (SWs). In these papers, specifically, the methods of SW generation and detection and SW propagation processes in nonuniform materials are examined, mechanisms are proposed for converting electromagnetic oscillations and magnetostatic waves into travelling SWs, and so on. This increased interest in this subject is due to the possibility of using SWs in spin-wave microelectronics devices, obtaining with their help information on the local properties of magnetic layers, and so on.

Extended lattice defects—dislocations,[4,5] which produce in a material deformations which decay slowly with increasing distance from a defect, are always present in real magnetic crystals (propagation medium for SWs). The presence of an interaction between the elastic and magnetic subsystems (magnetostriction) results in the appearance of a nonuniform magnetization distribution in the field of dislocation deformations[6,7] and strongly influences the magnetization dynamics.[8–10] Moreover, the presence of such an interaction also influences the dynamic properties of the dislocation itself. In the present paper, the scattering amplitude of volume SWs scattered by an individual edge dislocation will be calculated.

We shall study the propagation of SWs in an unbounded easy-axis magnet, in a constant uniform magnetic field and containing a single rectilinear edge dislocation. We shall assume that the axis of easy magnetization (AEM) and the constant uniform external magnetic field **H** are parallel to one another, and we orient the z axis of the coordinate in this direction. In such a coordinate system the energy density of the ferromagnet can be written as follows taking account of the smallness of the deformation:[7]

$$w(\mathbf{m})=\frac{\alpha}{2}\frac{\partial m_i}{\partial x_j}\frac{\partial m_i}{\partial x_j}-\frac{\beta}{2}m_z^2-hm_z-\gamma\sigma_{ij}(x,y,z)m_im_j,$$

$$i,j=x,y,z. \qquad (1)$$

Here α, β, and γ are exchange interaction, uniaxial anisotropy, and magnetostriction constants, respectively; $\sigma_{ij}(x,y,z)$ are the components of the tensor of dislocation deformations, whose form depends on the orientation and type of dislocation; $h=H/M_s$; and, $\mathbf{m}(\mathbf{r},t)=\mathbf{M}(\mathbf{r},t)/M_s$ is the dimensionless magnetization distribution.

We shall assume the material in its ground state is magnetized uniformly along the z axis. We shall describe the small deviations of the magnetization from the ground state by the variables $m_\pm=m_x\pm im_y$. We shall consider an edge dislocation with axis parallel to the AEM and Burgers vector directed along the x axis. In this case, only the xx, yy, and xy components of the tensor of dislocation deformations will be different from zero,[5] and the expression for the energy to within terms quadratic in $m_\pm$ will assume the form

$$w(m_+,m_-)=\frac{\alpha}{2}\nabla m_-\nabla m_++\frac{\beta+h}{2}m_+m_-$$
$$+\frac{\gamma}{4}\{\sigma_{yy}[m_+-m_-]^2-\sigma_{xx}$$
$$\times[m_++m_-]^2+i\sigma_{xy}[m_+^2-m_-^2]\}. \qquad (2)$$

We shall obtain the equation of motion of the magnetization using Eq. (2). If $m_\pm(\mathbf{r},t)\sim\exp\{i\omega t\}$, where ω is the SW frequency, then the desired equations describing the propagation of linear SWs against the background formed by the uniformly magnetized material assume the following matrix form:

$$(\hat U+\varepsilon\hat V)X=0. \qquad (3)$$

Here

$$X=\begin{pmatrix}m_-\\ m_+\end{pmatrix},\quad \hat U=\begin{pmatrix}-\Delta-k^2 & 0\\ 0 & \Delta+k^2\end{pmatrix},$$

$$\hat V=\begin{pmatrix}V_0 & V_1+iV_2\\ -V_1+iV_2 & -V_0\end{pmatrix},$$

where the wave number k is determined from the dispersion law for SWs in a homogeneous material (far from a dislocation):[11] $\omega\hbar/2\mu_0 M_s=\alpha k^2+\beta+h$ ($\hbar$ is Planck's constant, μ_0 is the Bohr magneton), $\varepsilon=\gamma b/4\pi\alpha(1-\nu^2)$ (ν — Poisson's ratio, b—modulus of Burgers vector), while the components of the operator $\hat{V}$ in polar coordinates ($x=\rho\cos\varphi$, $y=\rho\sin\varphi$), taking account of the explicit form of the components σ_{ij},[5] satisfy the relations

$$V_0=2(1-\nu-2\nu^2)\frac{\sin\varphi}{\rho},$$

$$V_1=4(1+\nu)\frac{\sin\varphi\cos^2\varphi}{\rho},\qquad V_2=\frac{\cos\varphi\cos 2\varphi}{\rho}. \tag{4}$$

Equation (3) is analogous to the stationary Schrödinger equation. This makes it possible to use the well-developed apparatus of quantum mechanics to solve the equations. Since ε is a small parameter of the problem, we shall employ the Born approximation,[12] according to which in the case of a cylindrically symmetric potential the scattering amplitude can be written, to within the constant phase factor, as

$$F(\mathbf{k}_a,\mathbf{k}_b)=\frac{\varepsilon}{2\sqrt{2\pi k}}\int \tilde{X}^{+}_{\mathbf{k}_b}\hat{V}\tilde{X}_{\mathbf{k}_a}\,d\boldsymbol{\rho}. \tag{5}$$

Here $\tilde{X}_{\mathbf{k}}$ are the solutions of the unperturbed equation (3) with $\varepsilon=0$, which are monochromatic plane waves with a coordinate part

$$\tilde{X}_{\mathbf{k}}(\boldsymbol{\rho})=\begin{pmatrix}\exp(i\mathbf{k}\cdot\boldsymbol{\rho})\\ \exp(-i\mathbf{k}\cdot\boldsymbol{\rho})\end{pmatrix}, \tag{6}$$

$\mathbf{k}_a$ and $\mathbf{k}_b$ are the wave vectors of the incident and scattered waves, respectively, and $\boldsymbol{\rho}$ is a coordinate vector in the xy plane. Substituting the expressions (4) and (6) into Eq. (5), we find

$$F(\mathbf{p},\mathbf{q})=\frac{\varepsilon}{\sqrt{\pi k}}\int_0^{\infty}\int_0^{2\pi}[V_0\cos(\mathbf{q}\cdot\boldsymbol{\rho})-V_1\sin(\mathbf{p}\cdot\boldsymbol{\rho})$$

$$+V_2\cos(\mathbf{p}\cdot\boldsymbol{\rho})]\,d\varphi\,d\rho, \tag{7}$$

where $\mathbf{q}=\mathbf{k}_a-\mathbf{k}_b$ and $\mathbf{p}=\mathbf{k}_a+\mathbf{k}_b$. We shall assume that the scattering of a SW by a dislocation is elastic. In this case $|\mathbf{k}_a|=|\mathbf{k}_b|=k$, $p=2k\cos(\Theta/2)$, and $q=2k\sin(\Theta/2)$, where Θ is the scattering angle (the angle between the wave vectors of the incident and scattered waves).

Next, integrating Eq. (7) with respect to ρ and φ, we obtain finally for the scattering amplitude of a SW scattered by an edge dislocation the expression

$$F(\Theta,\Phi)=\frac{\gamma b}{\sqrt{8\pi}(1-\nu)\alpha k^{3/2}}\Bigg[4\sin(\Phi+\Theta/2)$$

$$\times\cos(2\Phi+\Theta)\cos(\Theta/2)$$

$$-(1-2\nu)\frac{\cos(\Phi+\Theta/2)}{\sin(\Theta/2)}\Bigg], \tag{8}$$

where Φ is the angle of incidence of the SW (the angle between the direction of the incident wave and Burgers vector of the dislocation). Expressions can be obtained similarly for the scattering amplitudes in other cases of the relative arrangement of the Burgers vector, the AEM, and the dislocation axis.

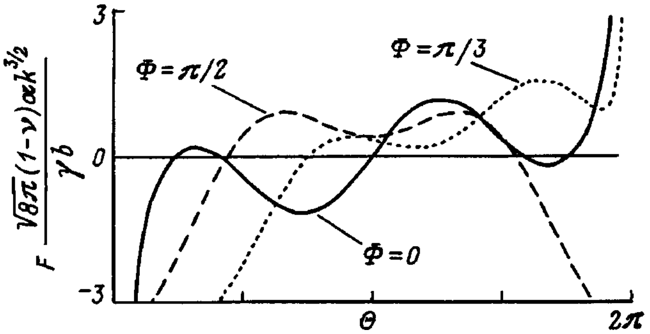

FIG. 1. Modulus of the scattering amplitude versus the angle for different angles of incidence of the spin wave ($\nu=0.3$).

Let us analyze the expression obtained. A plot of the modulus of the scattering amplitude (8) as a function of the scattering angle is displayed in Fig. 1.

Analysis of the function (8) and Fig. 1 shows that the scattering amplitude vanishes for certain scattering angles. Taking account of Eq. (8), such scattering angles must satisfy the equation

$$\tan(\Phi+\Theta/2)\cos(2\Phi+\Theta)\sin\Theta=\frac{1}{2}-\nu. \tag{9}$$

This transcendental equation as a function of the angle of incidence and the Poisson ratio can have up to six different real roots. A plot of the function $\Theta(\Phi)$, obtained by solving Eq. (9) numerically, is shown in Fig. 2.

Let us calculate the total transport SW scattering cross section of a dislocation. Substituting into the expression for the transport cross section

$$\Omega_T=\int_0^{2\pi}|F|^2(1-\cos\Theta)\,d\Theta$$

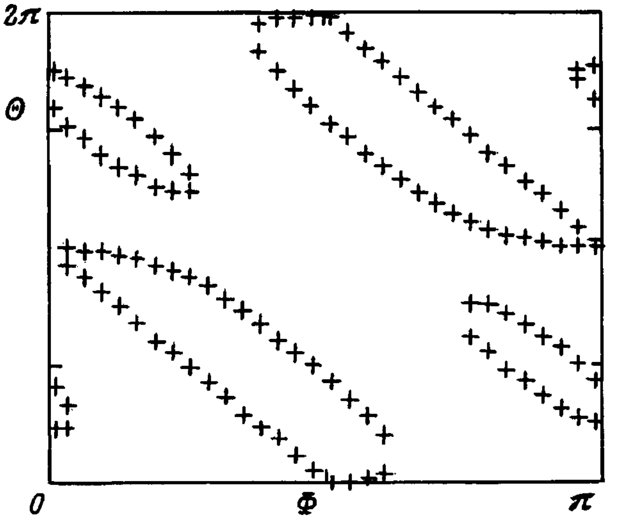

FIG. 2. Scattering angle versus the angle of incidence of the spin wave at which the scattering amplitude is zero.

the expression (8) for the scattering amplitude and carrying out the integration, we find

$$\Omega_T=\frac{\gamma^2}{4(1-\nu)^2}\,\frac{b^2}{\alpha^2 k^3}\left[\frac{1}{2}+(1-2\nu)^2+\sin^2 2\Phi\right]. \qquad (10)$$

As one can see from Eq. (10), SWs are most efficiently scattered by a dislocation for angles of incidence $\Phi=(2n+1)\pi/4$ (n — integer). Numerical estimates for the transport cross section in the case of yttrium iron garnet show that it can reach values of the order of several nanometers near the threshold of SW activity.

Let us discuss the applicability of the expressions obtained above for the scattering amplitudes of spin waves.

One can see from Eq. (8) and Fig. 1 that the spin-wave scattering amplitude grows without bound as $\Theta\to 0$. This is due to the fact that in the present paper the scattering amplitude was obtained on the basis of perturbation theory using the method of successive approximations in the stationary case (Born approximation). The wave functions corresponding to monochromatic plane waves (6) were used to calculate the matrix elements (5). However, if the scattering potential is long-range, then the wave is distorted at infinity and the stationary states will no longer correspond to monochromatic plane waves. Nonetheless, for Coulomb-type fields, which decrease at infinity as $1/\rho$ (which happens in the present case), such a distortion gives only a phase shift of the wave function that depends logarithmically on the coordinate,[12] which is of no consequence for calculating matrix elements appearing in the scattering amplitude for scattering angles sufficiently different from zero. Thus, the expressions obtained for the scattering amplitudes are inapplicable for small scattering angles.

Since the expressions for dislocation deformations are inapplicable for distances $\rho<a$, where a is the lattice constant,[4,5] the range of applicability of the expressions for the scattering amplitudes is limited above with respect to wave numbers at least by the relation $k\ll k_{\max}=1/a$, which is identical to the condition of applicability of the continuum approximation for SWs. The condition of applicability of the exchange approximation for SWs (absence of magnetostatic terms in the expression (1)) is $k\gg k_{\min}=\sqrt{4\pi/\alpha}$.[2] Therefore the expression (8) for the SW scattering amplitude is applicable for wave numbers $k_{\min}\ll k\ll k_{\max}$.

These investigations were performed as part of a project financed by the Ukrainian Ministry of Education.

[1] P. E. Zil'berman, A. G. Temiryazev, and M. P. Tikhomirov, Usp. Fiz. Nauk **165**, 1219 (1995).

[2] A. G. Gurevich and G. A. Melkov, *Magnetic Oscillations and Waves* [in Russian], Nauka, Moscow, 1994, 463 pp.

[3] V. V. Danilov, M. V. Zavislyak, and M. G. Balinskiĭ, *Spin-Wave Electrodynamics* [in Russian], Lybid', Kiev, 1991.

[4] J. P. Hirth and J. Lothe, *Theory of Dislocations*, McGraw-Hill, N.Y., 1967; Atomizdat, Moscow, 1972, 600 pp.

[5] L. D. Landau and E. M. Lifshitz, *Theory of Elasticity* [Pergamon Press, N.Y.; Nauka, Moscow, 1987, 248 pp].

[6] A. M. Kosevich and E. P. Fel'dman, Fiz. Tverd. Tela (Leningrad) **9**, 3415 (1967) [Sov. Phys. Solid State **9**, 2696 (1967)].

[7] V. V. Gann and É. P. Fel'dman, Fiz. Nizk. Temp. **2**, 30 (1976) [Sov. J. Low Temp. Phys. **2**, 14 (1976)].

[8] V. G. Bar'yakhtar, V. A. Sevchenko, and V. V. Tarasenko, Zh. Éksp. Teor. Fiz. **54**, 1603 (1968) [Sov. Phys. JETP **25**, 858 (1968)].

[9] V. K. Vlasko-Vlasov, L. M. Dedukh, and V. I. Nikitenko, Zh. Éksp. Teor. Fiz. **65**, 376 (1973) [Sov. Phys. JETP **38**, 184 (1974)].

[10] L. M. Dedukh, M. V. Indenbom, and V. I. Nikitenko, Zh. Éksp. Teor. Fiz. **80**, 380 (1981) [Sov. Phys. JETP **53**, 194 (1981)].

[11] A. I. Akhiezer, V. G. Bar'yakhtar, and S. V. Peletminskiĭ, *Spin Waves* [in Russian], Nauka, Moscow, 1967, 368 pp.

[12] L. D. Landau and E. M. Lifshitz, *Quantum Mechnics. Non-Relativistic Theory* [Pergamon Press, N. Y.; Nauka, Moscow, 1989, 768 pp].

Translated by M. E. Alferieff

PHYSICS OF THE SOLID STATE VOLUME 40, NUMBER 11 NOVEMBER 1998

Equilibrium configurations of partial misfit dislocations in thin-film heterosystems

M. Yu. Gutkin,[a)] K. N. Mikaelyan, and I. A. Ovid'ko

Institute of Machine Engineering, Russian Academy of Sciences, 199178 St. Petersburg, Russia

(Submitted May 25, 1998)
Fiz. Tverd. Tela (St. Petersburg) **40**, 2059–2064 (November 1998)

The energy characteristics of orthogonal rows of partial misfit dislocations with *V*-shaped stacking faults in thin-film heteroepitaxial systems are analyzed theoretically. It is shown that they should appear only in very thin epitaxial films of nanoscopic thickness and for high values of the mismatch exceeding a definite value. Under these conditions partial misfit dislocations associated with *V*-shaped stacking faults are typical elements of the defect structure of nanolayer heterosystems. For smaller mismatches and larger films thicknesses total misfit dislocations should form. © *1998 American Institute of Physics.* [S1063-7834(98)02111-X]

After nearly three decades the problem of the defectiveness of thin-film systems obtained by different heteroepitaxy methods is still a key problem of semiconductor materials science. Diverse defect structures, whose appearance is an effective channel for relaxation of intrinsic elastic stresses (mismatch stresses), due to the mismatch of the structure and properties of the joined materials, form at the fabrication stage of the heterosystem and often result in the degradation of the basic characteristics of micro- and optoelectronics devices.[1–6] The most common method of relaxation of mismatch stresses is formation of total or partial misfit dislocations (MDs) which form two-dimensional dislocation networks near heteroboundaries. The formation of networks of total MDs is ordinarily preferred, since on the one hand they possess larger Burgers vectors and therefore accommodate more efficiently the lattice mismatch of the contiguous materials while, on the other hand, stacking faults are not formed in the process in the interior of the materials, i.e. far from heteroboundaries the materials possess a higher degree of structural perfection. However, in heterosystems with a large mismatch there often arise situations where the existing sources of total dislocations are inadequate for the degree of accommodation of the initial mismatch that is energetically preferred here. In such cases so-called ''secondary'' relaxation mechanisms come into play[7] and lead to the appearance of a network of partial MDs (PMDs). One of the main mechanisms of nucleation of MDs likewise leads to the formation of PMDs — nucleation on a free surface of a growing epitaxial film and gliding of half-loops of dissociated dislocations toward a heteroboundary.[8–12]

Despite the fact that PMDs are now a frequent object of experimental investigations, their theoretical description is not nearly as detailed as that of total MDs. This pertains specifically to the problem of determining the equilibrium density of MDs and the critical parameters of a heterosystem (critical thickness h_c of an epitaxial film and the critical mismatch f_c for which the formation of MDs becomes energetically favorable (correspondingly, for arbitrary mismatch f and for a monolayer film). For total MDs this problem is most easily solved on the basis of a macroscopic quasiequilibrium approach,[1,13–27], the basic idea of which is to calculate the total energy of a heterosystem with MDs and to minimize this energy with respect to the density of a dislocation ensemble. For this reason, this approach is also said to be an energetic approach.

A review of previous works that are devoted to the analysis of the equilibrium density of total MDs on the basis of the energy approach is contained in Ref. 1. These works all have the drawback that the expression for the total energy does not contain terms describing the energy of interaction of MDs with the elastic field of the initial mismatch, with the free surface of the epitaxial film, and with one another. For an infinite discrete row of edge MDs with Burgers vectors lying in the plane of the heteroboundary, these terms were first taken into account comprehensively in Refs. 14 and 15, the main results of which are also presented in Ref. 16. The macroscopic energy approach was further elaborated in Refs. 17–27. Misfit dislocations of a mixed type with Burgers vector tilted with respect to the plane of the heteroboundary and orthogonal networks of MDs were studied, and the elastic anisotropy of the film and substrate and small differences in their elastic moduli were taken into account.[26] The results obtained in Refs. 17–27 taken together made it possible to apply the energy approach to the analysis of dislocation structures in specific heterosystems taking account of the geometry and the type of MD exactly. Nonetheless, the results did not change qualitatively, and the discrepancy in the theoretical estimates and experimental data was found to be of the same order of magnitude.

It was found that there were significantly fewer theoretical calculations for PMDs. We call attention to Ref. 28, where the formation of a row of parallel PMDs was investigated theoretically using Matthews' simplified energy approach,[13] which neglects the energies of interaction of the dislocations with the stress field of the initial mismatch and with the free surface of the epitaxial film as well as with one another. At the same time, in the case of total MDs these terms have a large effect on the equilibrium density of MDs and on the values of the critical parameters.[14–16] It is natural to expect that similar corrections will also be important for the case of PMDs.

One formation mechanism of PMDs is nucleation on the

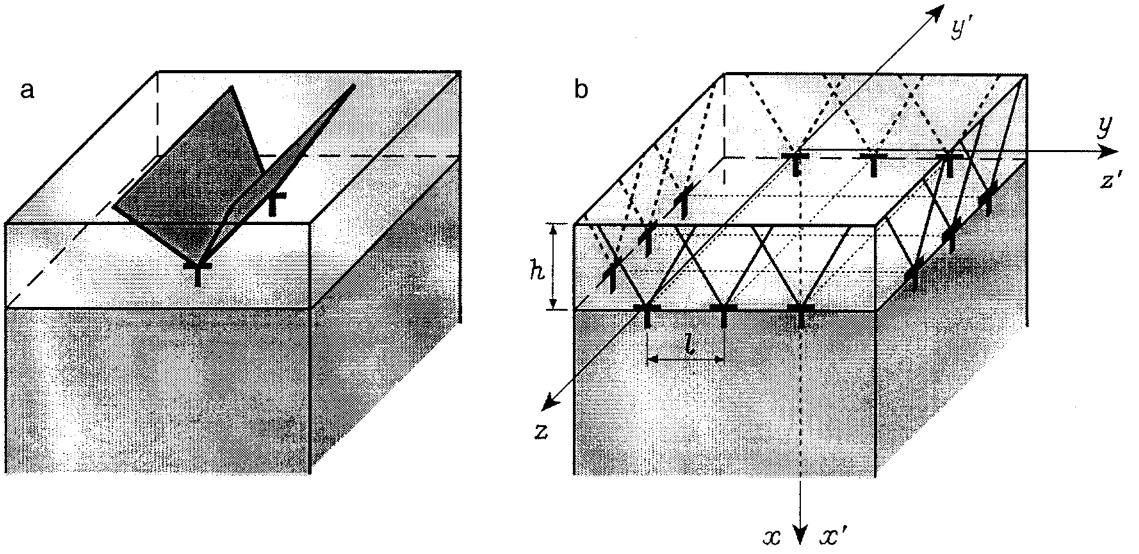

FIG. 1. Partial misfit dislocations with *V*-shaped stacking faults. a — Diagram of the formation of a single PMD; b — orthogonal network of PMDs.

surface of a film and gliding of mixed-type partial dislocations toward the film–substrate interface. For a sufficiently high density of surface sources, these dislocations, reaching a heteroboundary, enter into a reaction with analogous dislocations gliding along neighboring planes, and often form ‘‘sessile’’ PMDs of the Lomer–Cottrell barrier type.[29] The PMDs formed in this manner are located at the vertices of *V*-shaped stacking faults (Fig. 1a). This has been observed in experiments on heterosystems with diamond and sphalerite lattices.[8–12,30]

Thus, our main goal in the present work is to analyze theoretically the energy characteristics of an ensemble of PMDs with *V*-shaped stacking faults, taking account of the indicated components of the total energy and the formation of orthogonal rows of such PMDs. Epitaxial gallium arsenide films on silicon substrates are studied as an example of a specific heterostructure.

To investigate the qualitative differences in the energetics of the formation of total and partial MDs, we shall examine a very simple model — a thin, elastically isotropic film of thickness h obtained by epitaxial growth on a semiinfinite, elastically isotropic substrate. We shall assume the elastic constants, the shear modulus G, and the Poission ratio ν to be the same for the film and substrate materials.

The initial coherent (or pseudomorphous) state of the system is characterized by elastic strain $\varepsilon_1=-f$, where $f=(a_2-a_1)/a_1>0$ is the initial two-dimensional mismatch between the lattice constants of the substrate and the film — a_1 and a_2, respectively. The density of the elastic mismatch self-energy (per unit area of the interface) is given by the expression[1]

$$W^f=2G\frac{1+\nu}{1-\nu}f^2h. \tag{1}$$

As h increases to some critical value h_c, relaxation of the initial mismatch f starts in the film by nucleation of an orthogonal network of PMDs on the boundary with the substrate: The system passes into a semicoherent state (Fig. 1b). This new state is characterized by a residual uniform elastic strain $\varepsilon_2=-(f-\varepsilon_d)<0$, where $\varepsilon_d=b/l$ is part of the initial mismatch accommodated by the introduction of PMDs; b is the magnitude of Burgers vector of the PMD; and, l is the distance between the PMDs. The total energy density of the system in such a semicoherent state can be written in the form (by analogy with the calculation in Refs. 14 and 15)

$$W=W^f+W_{\mathrm{el}}^d+W_n^d+W_{\mathrm{int}}^{fd}+W^{\gamma}, \tag{2}$$

where W_{el}^d is the elastic energy of PMDs, which is obtained by taking account of their interaction with the free surface of the film and with one another; $W_n^d=Gb(f+\varepsilon_2)/[2\pi(1-\nu)]$ is the energy of the nuclei of the PMDs (in the expressions given below we omit the index 2 in ε_2); $W_{\mathrm{int}}^{fd}=-4Gf(f+\varepsilon)(h-b)(1+\nu)/(1-\nu)$ is the energy of interaction of PMDs with the elastic field of the initial mismatch; $W^{\gamma}=4\gamma h(f+\varepsilon)/(b\cos\alpha)$ is the energy of *V*-shaped configurations consisting of bands of stacking faults; γ is the energy of a stacking fault; and, 2α is the opening angle of the *V*-shaped configuration.

The elastic energy of a dislocation system consists of the self-energies of each row of PMDs and their interaction energy

$$W_{\mathrm{el}}^d=W_s+W_{\mathrm{int}}. \tag{3}$$

The self-energy of a dislocation row can be calculated as the work required for its nucleation in its elastic self-field.[14,15] Let one row of PMDs lie along the $0y$ axis of a Cartesian coordinate system (x,y,z), and let a second row lie along the $0y'$ axis of a Cartesian coordinate system (x',y',z') rotated relative to the first one by the angle $\pi/2$ so that the correspondences $x'\to x$, $y'\to -z$, and $z'\to y$ holds (Fig. 1b). Then the self-energy of two orthogonal rows of PMDs can be written in the form

$$W_s=\frac{Nb}{2}\int_0^{h-b}\sigma_{yy}^{(x,y,z)}dx+\frac{Nb}{2}\int_0^{h-b}\sigma_{y'y'}^{(x',y',z')}dx', \tag{4}$$

where $N=1/l$ is the number of PMDs per unit length of a row, $\sigma_{yy}^{(x,y,z)}$ was found in Refs. 14 and 15 and is taken here with the opposite sign of the component of the stress field of the first row in the coordinate system (x,y,z), and $\sigma_{y'y'}^{(x',y',z')}$ is a component of the stress field of the second row in the coordinate system (x',y',z'). Switching to the coordinate system (x,y,z), we have $\sigma_{y'y'}^{(x',y',z')}=\sigma_{yy}^{(x,y,z)}$, and the expression (4) becomes

$$W_s=Nb\int_0^{h-b}\sigma_{yy}^{(x,y,z)}dx. \tag{5}$$

The interaction energy of the rows can be calculated as the work required for nucleation of the first row in the elastic field of the second row

$$W_{\text{int}}=Nb\int_0^{h-b}\sigma_{z'z'}^{(x',y',z')}dx=Nb\int_0^{h-b}\sigma_{zz}^{(x,y,z)}dx. \tag{6}$$

Integrating, taking account of the coordinates of the PMDs $y=\pm nl$, where $n=0,1,2,\ldots$, which gives $\cos(2\pi y/l)=1$ in the expressions for $\sigma_{ij}^{(x,y,z)}$, we find

$$W_s=\frac{Gb}{2(1-\nu)}(f+\varepsilon)^2\left\{\left(\frac{2h}{b}-1\right)\frac{C_1+1}{S_1}-\frac{C_2+1}{S_2}-\frac{h}{b}\left(\frac{h}{b}-1\right)\frac{4\pi(f+\varepsilon)}{C_1-1}-\frac{1}{2\pi(f+\varepsilon)}\ln\frac{C_2-1}{C_1-1}\right\}, \tag{7}$$

$$W_{\text{int}}=\frac{Gb\nu}{2(1-\nu)}(f+\varepsilon)^2\left\{4\frac{h}{b}\left(\frac{C_1+1}{S_1}-\frac{C_3+1}{S_3}\right)-\frac{1}{\pi(f+\varepsilon)}\ln\frac{C_2-1}{C_1-1}\right\}, \tag{8}$$

where

$C_1=\cosh[2\pi(f+\varepsilon)(2h/b-1)]$, $C_2=\cosh[2\pi(f+\varepsilon)]$,

$C_3=\cosh[2\pi(f+\varepsilon)h/b]$,

$S_1=\sinh[2\pi(f+\varepsilon)(2h/b-1)]$, $S_2=\sinh[2\pi(f+\varepsilon)]$,

$S_3=\sinh[2\pi(f+\varepsilon)h/b]$.

Substituting the expressions (7) and (8) into Eq. (3), we obtain

$$W_{\text{el}}^d=\frac{Gb}{2(1-\nu)}(f+\varepsilon)^2\left\{\left(2(1+2\nu)\frac{h}{b}-1\right)\frac{C_1+1}{S_1}-\frac{C_2+1}{S_2}-4\nu\frac{h}{b}\frac{C_3+1}{S_3}-4\pi\frac{h}{b}\left(\frac{h}{b}-1\right)\frac{f+\varepsilon}{C_1-1}-\frac{1+2\nu}{2\pi(f+\varepsilon)}\ln\frac{C_2-1}{C_1-1}\right\}. \tag{9}$$

The resulting expression obtained for the total energy (2) was analyzed numerically taking account of Eqs. (1) and (9) with parameter values characteristic for the heterosystem GaAs/Si (001): $G=32.5$ GPa, $\nu=0.31$, $2\alpha\approx70°$, and $\gamma=0.06$ J/m^2.[28,31] For example, in a heteroboundary with (001) orientation, a Burgers vector of the PMD $\mathbf{b}=\frac{a}{6}[1\bar{1}0]$ can be formed by combining two partial 30° Shockley dislocations, one of which glides in the film along the $(1\bar{1}1)$ plane and can have a Burgers vector $\mathbf{b}_1=\frac{a}{6}[\overline{121}]$ or $\frac{a}{6}[21\bar{1}]$ while the other glides along the plane (111) and can have $\mathbf{b}_2=\frac{a}{6}[211]$ or $\frac{a}{6}[\overline{121}]$. Here a is the interatomic distance in the direction [001], equal to, for example, 0.5635 nm in GaAs. As a result of the dislocation reaction, the screw components of these partial dislocations annihilate, which results in the formation of a sessile purely edge PMD, whose line lies in the plane of the interface (001). In the case of a GaAs film, the standard formula $|\mathbf{b}|=\frac{a}{6}\sqrt{h^2+k^2+l^2}$ with $\mathbf{b}=\frac{a}{6}[hkl]$ give $b=0.133$ nm and $b_1=b_2=0.23$ nm for the values of the Burgers vectors of the partial dislocations participating in these reactions.

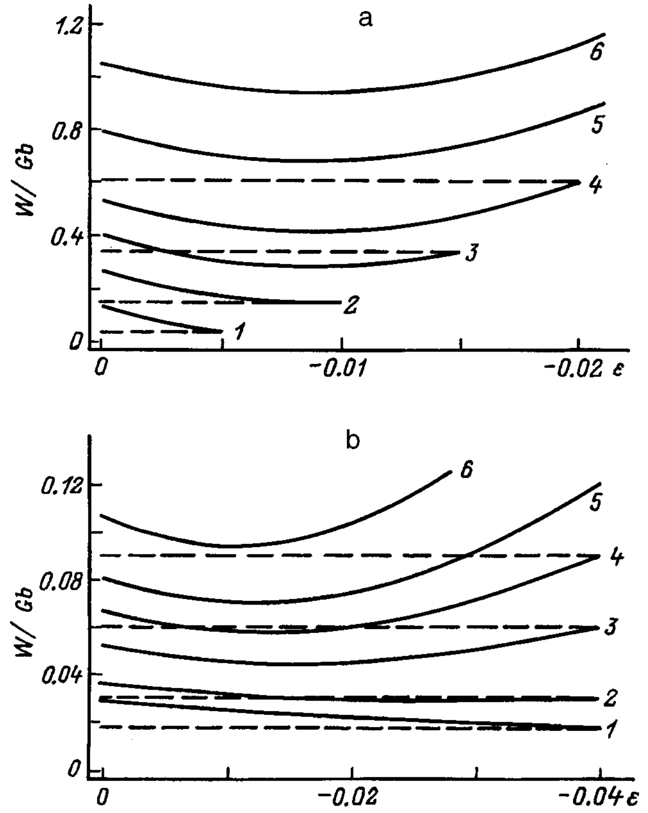

FIG. 2. Total energy density W of a heterosystem versus the residual homogeneous elastic strain ε in the film. a) $h/b=400$ and $f\cdot10^2=0.5$ (*1*), 1 (*2*), 1.5 (*3*), 2 (*4*), 3 (*5*), 4 (*6*); b) $f=0.04$ and $h/b=3$ (*1*), 5 (*2*), 10 (*3*), 15 (*4*), 20 (*5*), and 30 (*6*). The horizontal dashed lines correspond to the values of $W(\varepsilon=-f)$ for a coherent state of the system.

Figure 2 displays the function $W(\varepsilon)$ for a fixed film thickness $h=400b$ and different initial mismatches f as well as for a fixed mismatch $f=0.04$ and different thicknesses h. The dashed lines show the straight lines $W(\varepsilon=-f)$, corresponding to a coherent state of the heterosystem — absence of PDMs in it. One can see that for small f and h (curves *1* in Fig. 2) the energy of the coherent state is less than the energy of the relaxed state, $W(f)<W(\varepsilon)$, i.e. the formation of PMDs is energetically unfavorable. For some critical values of f and h (curves *2* in Fig. 2) there appear on the curves sections where $W(\varepsilon)>W(f)$ — nucleation of PMDs becomes energetically favorable. The strain $\varepsilon=\bar{\varepsilon}$, corresponding to the minimum on the curve $W(\varepsilon)$, is an equilibrium residual elastic strain which is uniform over the cross section of the film. Then the sum $f+\bar{\varepsilon}$, representing the part of the initial mismatch that is removed when the PMDs are formed, determines the equilibrium distance between them $\bar{l}=b(f+\bar{\varepsilon})$. As f and h increase further, the values of $|\bar{\varepsilon}|$ and $\bar{l}$ decrease: The ensemble of PMDs becomes more dense and accommodates a larger part of the initial mismatch f.

The curves $W(\varepsilon)$ (Fig. 2) describing the energetics of a heterosystem with PMDs agree qualitatively well with the similar curves obtained in Refs. 14–16 for total MDs (TMDs). However, the quantitative discrepancies are very large. Setting $\gamma=0$ in Eq. (2) and taking $b=0.385$ nm (the Burgers vector of a total 90° MD $a_{\mathrm{Si}}/2\langle 110\rangle$, lying in the (001) heteroboundary along the directions [110] or $[1\bar{1}0]^{12}$), we obtain an expression for the total energy of a system with two orthogonal rows of TMDs. Analysis of the curves $W(\varepsilon)$ for PMDs and TMDs makes it possible to compare the characteristic features of the formation of their ensembles.

Figure 3 shows $\bar{\varepsilon}$ and $\bar{l}$ versus the mismatch f for a fixed film thickness $h=400b\approx 53.2$ nm (here $b=0.133$ nm — the Burgers vector of the PMDs) and versus the thickness h for fixed $f=0.04$ (characteristic for the heterosystem GaAs/Si). The solid lines show the curves for PMDs and the dashed lines show the curves for TMDs. One can see that for small values of f the functions $\bar{\varepsilon}(f)$ are linear $(\bar{\varepsilon}(f)=-f$, Fig. 3a), while for small h the equilibrium strain $\bar{\varepsilon}(h)$ is constant and likewise equals $-f$ (Fig. 3b), which corresponds to purely elastic accommodation of the mismatch and absence of MDs on the heteroboundary $(\bar{l}=\infty)$. As soon as f or h reaches its critical value f_c or h_c (for fixed h or f, respectively), plastic relaxation — nucleation of MDs — occurs and the equilibrium uniform elastic strain $|\bar{\varepsilon}|$ decreases sharply for $f>f_c$ (Fig. 3a) and for $h>h_c$ (Fig. 3b). Correspondingly, the equilibrium distance $\bar{l}$ between MDs becomes finite and decreases. It is important to note that for the chosen thickness $h\approx 53.2$ nm the critical mismatch f_c is five times smaller for TMDs (~ 0.002) than for PMDs (~ 0.01). The decreasing curves $\bar{\varepsilon}(f)$ (Fig. 3a) rapidly saturate, the modulus of the saturation level being almost two orders of magnitude smaller for TMDs ($\sim 1\cdot 10^{-4}$) than for PMDs ($\sim 85\cdot 10^{-4}$), i.e. for such a film thickness the TMDs give much more complete accommodation of the mismatch than do PMDs. It is interesting that in this case the equilibrium distances between TMDs are approximately two times greater than between PMDs.

In turn, for a chosen mismatch $f=0.04$ the critical film thickness h_c (Fig. 3b) is approximately 1.6 times smaller than for PMDs (~ 0.6 nm) than for TMDs (~ 0.96 nm). This means that as an epitaxial film grows with such a mismatch (for example, a GaAs film on a silicon substrate), first PMDs and then TMDs should nucleate. This sequence of appearance of PMDs and TMDs has been observed in the heterosystems GaAs/Si[11,12] and Pd/Au ($f\approx 0.046$).[32,33]

The diagram in Fig. 4, obtained using the functions $h_c(f)$ for TMDs (curve *1*) and PMDs (curve *2*), gives a more complete picture of the possible regimes of filling of heteroboundaries of PMDs and TMDs in a wide range of mismatches f and thicknesses h. The intersecting curves *1* and *2* divide the phase space (f,h) into four regions with different defect structure of the heteroboundary. Region I, bounded by the upper part of the curve *1* and the lower part of the curve *2*, corresponds to a coherent state of the system with no MDs present. The region II, bounded by the upper parts of the curves *1* and *2*, corresponds to the presence of TMDs on the heteroboundary. The region III, bounded by the lower part of the curve *1* and the upper part of the curve *2*, corresponds to the simultaneous existence of TMDs and PMDs. Finally, the region IV, bounded by the lower parts of the curves *1* and *2*, is the region where PMDs form. One can see that the curves *1* and *2* are considerably different: The function $h_c(f)$ for TMDs (curve *1*) has no asymptotes, while for PMDs (curve *2*) it has a vertical asymptote at the point $f\approx 9\cdot 10^{-3}$. This

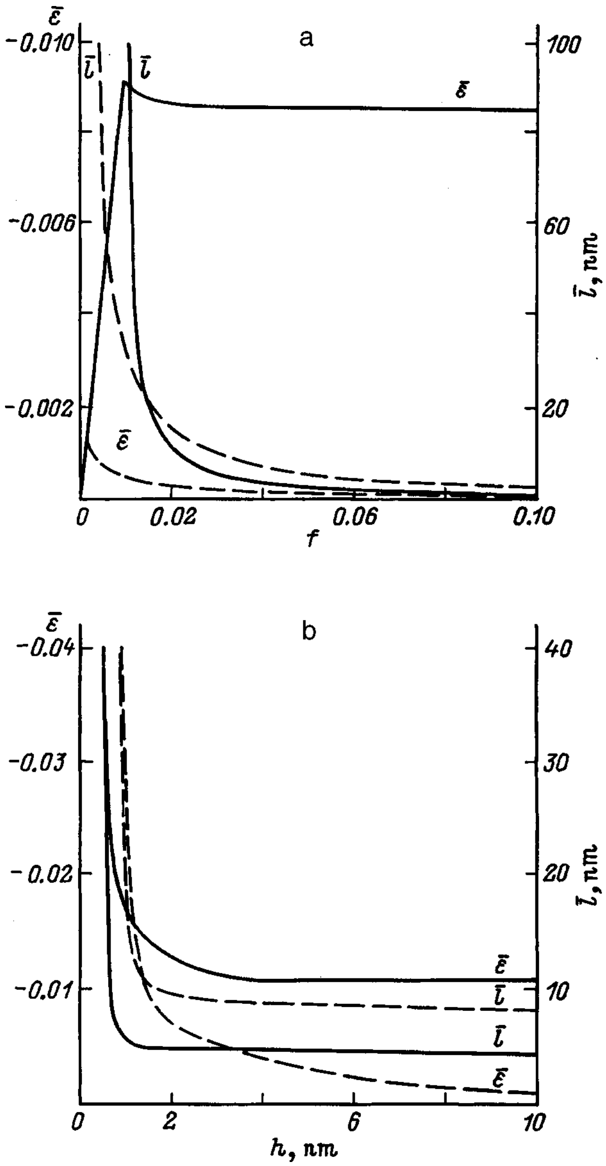

FIG. 3. Equilibrium uniform elastic strain $\bar{\varepsilon}$ of a film and the equilibrium distance $\bar{l}$ between misfit dislocations versus the initial mismatch f with $h=400b\approx 53.2$ nm (a) and versus the thickness h of the epitaxial film with $f=0.04$ (b). The solid lines show the curves for partial and the dashed for total misfit dislocations.

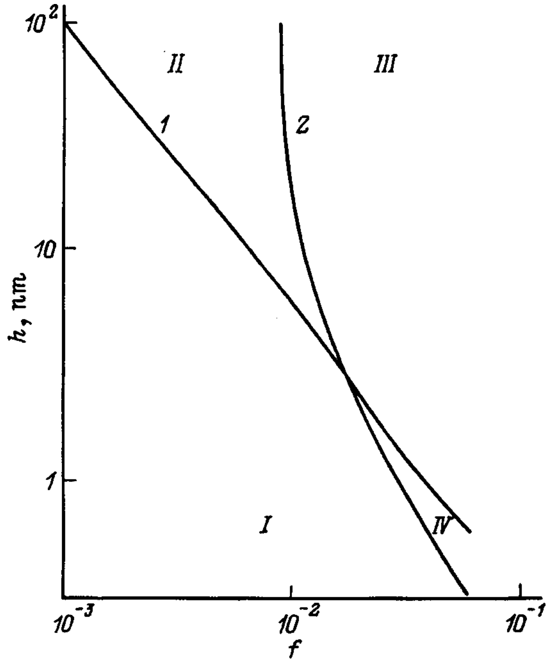

FIG. 4. $f-h$ diagram obtained using the functions $h_c(f)$ for total (*1*) and partial (*2*) misfit dislocations. Four regions are distinguished: I — coherent state of the system, II–IV — total, total and partial, and partial misfit dislocations at a heteroboundary, respectively.

means that in the case of TMDs there should always exist a critical thickness h_c for any, however small, f, i.e. in any heterosystem it is possible to grow a film on a semiinfinite substrate up to a thickness such that nucleation of TMDs becomes energetically favorable. However, this is not so in the case of PMDs: There exists a limiting mismatch f_l ($f_l \approx 9 \cdot 10^{-3}$ for the chosen working parameters) such that for $f < f_l$ the formation of PMDs will remain energetically unfavorable for any film thicknesses. We also note that the range Δh of film thicknesses for which nucleation of PMDs is more favorable than nucleation of TMDs is found to be extremely narrow — $\Delta h \leq 0.3$ nm. For this reason, it should be extremely difficult to observe accommodation of the mismatch by formation of only PMDs. In most cases either PMDs or PMDs and TMDs simultaneously should be observed, and the larger the mismatch and the thicker the film, the lower the relative fraction of PMDs should be. Such an observation is contained in the experimental work Ref. 12, where the percentage fractions of TMDs and PMDs (and also 60° MDs, which we do not study here) are presented as a function of the film thickness. This is explained both by the low efficiency of PMDs from the standpoint of the degree of relaxation of the initial mismatch as a result of the smaller magnitude of their Burgers vector (Fig. 3) and by the large contribution of the stacking-fault energy to the total energy of the system.

Figure 5 displays the equilibrium total energy $\overline{W}$ of the system as a function of the misfit f for a system with TMDs ($\overline{W}^{(1)}(f)$, curve *1*) and with PMDs ($\overline{W}^{(2)}(f)$, curve *2*) with film thickness $h=100$ nm. The initial part of the curve *2* for $f \leq f_c = f_l \approx 9 \cdot 10^{-3}$ is completely determined by the expression (1), and the difference $\overline{W}^{(2)}(f) - \overline{W}^{(1)}(f)$ characterizes here the energy gain as a result of the introduction of TMDs. In the region $f > f_c = f_l \approx 9 \cdot 10^{-3}$ this difference shows the energy gain from formation of TMDs instead of PMDs. In this case it is ≈ 0.06 Ga≈ 1.1 J/m^2, and $\overline{W}^{(2)}(f)$ is more than an order of magnitude greater than $\overline{W}^{(1)}(f)$.

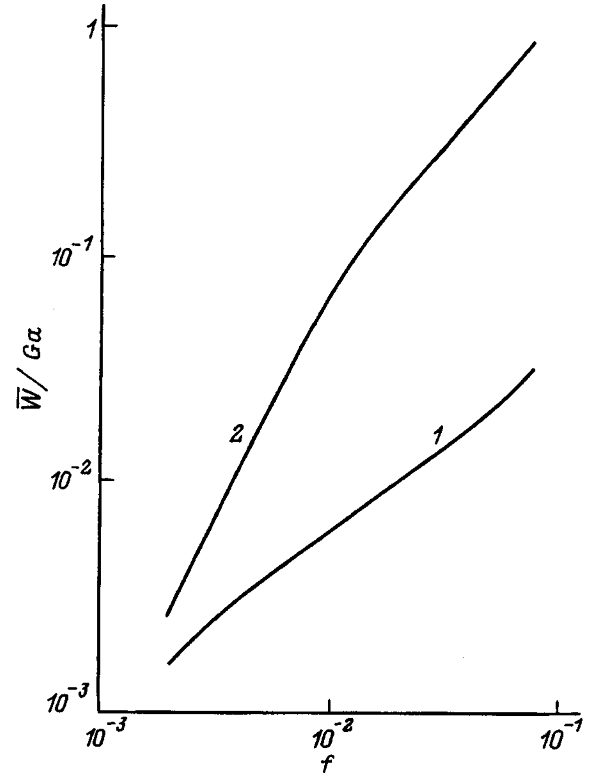

FIG. 5. Equilibrium total energy $\overline{W}$ of a system versus the mismatch f for a system with total (*1*) and partial (*2*) misfit dislocations with film thickness $h=100$ nm.

In summary, our model of PMDs, located at the vertices of *V*-shaped stacking faults that penetrate through the entire film from heteroboundary to the free surface, gives an extremely low probability of observing such defective configurations in quite thick films ($h \approx 10$ nm and thicker). The calculations performed show that they should appear only in very thin epitaxial films of nanoscopic thickness and for large mismatches ($f > 0.01$). Under these conditions the PMDs associated with *V*-shaped stacking faults are typical elements of the defective structure of nanolayer heterostructures observed expermentally in Refs. 11 and 12. For smaller values of f and larger values of h TMDs or PMDs, associated with stacking faults with partial dislocations located in the interior of the film outside the heteroboundary, should form. The investigation of the role and location of such formations in mismatch accommodation processes in heteroepitaxy is a subject of our further investigations.

This work was supported in part by the Russian Fund for Fundamental Research (grant 98-02-16075) and the Russian Scientific Council on the Interdisciplinary Science and Technology Program ‘‘Physics of Solid-State Nanostructures’’ (Grant 97-3006).

[a] E-Mail: gutkin@pgpt.ioffe.rssi.ru; gutkin@def.ipme.ru

---

[1] Yu. A. Tkhorik and L. S. Khazan, *Plastic Deformation and Misfit Dislocations in Heteroepitaxial Systems* [in Russian], Naukova Dumka, Kiev, 1983, 304 pp.

[2] M. G. Mil'vidskiĭ and V. B. Osvenskiĭ, *Structural Defects in Epitaxial Layers of Semiconductors* [in Russian], Metallurgiya, Moscow, 1985.

[3] W. D. Nix, Metall. Trans. A **20**, 2217 (1989).

[4] S. C. Jain, J. R. Willis, and R. Bullough, Adv. Phys. **39**, 127 (1990).

[5] S. C. Jain and W. Hayes, Semicond. Sci. Technol. **6**, 547 (1991).

[6] E. A. Fitzgerald, Mater. Sci. Rep. **7**, 87 (1991).

[7] N. Burle, B. Pichaud, N. Guelton, and R. G. Saint-Jacques, Phys. Status Solidi A **149**, 123 (1996).

[8] B. C. De Cooman and C. B. Carter, Acta Metall. **37**, 2765 (1989).

[9] B. C. De Cooman, C. B. Carter, Kam Toi Chan, and J. R. Shealy, Acta Metall. **37**, 2779 (1989).

[10] J. Zou and D. J. H. Cockayne, Appl. Phys. Lett. **69**, 1083 (1996).

[11] M. Loubradou, R. Bonnet, A. Vila, and P. Ruterana, Mater. Sci. Forum **207–209**, 285 (1996).

[12] M. Tamura, Appl. Phys. A: Solids Surf. **63**, 359 (1996).

[13] J. W. Matthews, J. Vac. Sci. Technol. **12**, 126 (1975).

[14] V. I. Vladimirov, M. Yu. Gutkin, and A. E. Romanov, in *Physical Aspects of the Prediction of the Fracture and Deformation of Heterogeneous Materials* [in Russian], edited by A. M. Leksovskiĭ, Physicotechnical Institute Press, Leningrad, 1987, p. 76.

[15] V. I. Vladimirov, M. Yu. Gutkin, and A. E. Romanov, Pverkhnost'. Fizika, i Mekhanika, No. 6, 46 (1988).

[16] M. Yu. Gutkin, A. L. Kolesnikova, and A. E. Romanov, Mater. Sci. Eng. A **164**, 433 (1993).

[17] J. R. Willis, S. C. Jain, and R. Bullough, Philos. Mag. A **62**, 115 (1990).

[18] A. Rocket and C. J. Kiely, Phys. Rev. B **44**, 1154 (1991).

[19] A. Atkinson and S. C. Jain, Thin Solid Films **222**, 161 (1992).

[20] A. Atkinson and S. C. Jain, J. Appl. Phys. **72**, 2242 (1992).

[21] T. J. Gosling, S. C. Jain, J. R. Willis, A. Atkinson, and R. Bullough, Philos. Mag. A **66**, 119 (1992).

[22] S. C. Jain, T. J. Gosling, J. R. Willis, R. Bullough, and P. Balk, Solid State Electron. **35**, 1073 (1992).

[23] S. C. Jain, T. J. Gosling, J. R. Willis, D. H. J. Totterdell, and R. Bullough, Philos. Mag. A **65**, 1151 (1992).

[24] T. J. Gosling, R. Bullough, S. C. Jain, and J. R. Willis, J. Appl. Phys. **73**, 8267 (1993).

[25] U. Jain, S. C. Jain, J. Nijs, J. R. Willis, R. Bullough, R. P. Mertens, and R. Van Oversraeten, Solid State Electron. **36**, 331 (1993).

[26] T. J. Gosling and J. R. Willis, Philos. Mag. A **69**, 65 (1994).

[27] F. Bailly, M. Barbé, and G. Cohen-Solal, J. Cryst. Growth **153**, 115 (1995).

[28] A. K. Gutakovskiĭ, O. P. Pchelyakov, and S. I. Stenin, Kristallografiya **25**, 806 (1980) [Sov. Phys. Crystallogr. **25**, 461 (1980)].

[29] J. Hirth and J. Lothe, *Theory of Dislocations*, Wiley, N. Y., 1982, 2nd ed.; Atomizdat, Moscow, 1972, 600 pp.

[30] *Defects in Semiconductor Crystals* (Mir, Moscow, 1969), 376 pp.

[31] J. Zou, B. F. Usher, D. J. H. Cockayne, and R. Glaisher, J. Electron. Mater. **20**, 855 (1991).

[32] D. Cherns and M. J. Stowell, Thin Solid Films **29**, 107 (1975).

[33] D. Cherns and M. J. Stowell, Thin Solid Films **37**, 249 (1976).

Translated by M. E. Alferieff

PHYSICS OF THE SOLID STATE VOLUME 40, NUMBER 11 NOVEMBER 1998

Reversible and irreversible magnetic-field-induced changes in the plastic properties of NaCl crystals

Yu. I. Golovin, R. B. Morgunov, D. V. Lopatin, A. A. Baskakov, and Ya. E. Evgen'ev

Tambov State University, 392622 Tambov, Russia

(Submitted January 27, 1998; resubmitted April 27, 1998)
Fiz. Tverd. Tela (St. Petersburg) **40**, 2065–2068 (November 1998)

It is established that a weak magnetic field with induction $B \sim 1$ T gives rise to irreversible changes in NaCl crystals without freshly introduced dislocations, while a strong magnetic field with induction $16 < B < 35$ T gives rise predominantly to reversible changes. It is inferred that there exist two different channels whereby a magnetic field influences the state of point defects. © *1998 American Institute of Physics.* [S1063-7834(98)02211-4]

Dislocation motion stimulated by a weak constant magnetic field (MF) with induction $B \leqslant 1$ T in unloaded crystals with paramagnetic impurities was first reported in Ref. 1. In such a field the energy E imparted to a paramagnetic center with magnetic moment equal to one Bohr magneton μ is $E \approx \mu g B \ll kT$, where $T \sim 300$ K is the experimental temperature, $g \approx 2$ is the Landé factor, and k is Boltzmann's constant. Later it was established that one reason why dislocations move in a MF is that the field influences electronic processes occurring in a subsystem of structural defects.[2–4] At the present time the nature of this ''weak-field'' effect is not known in detail, but there are strong grounds for believing that a MF stimulates spin-dependent intercombination transitions in complexes of paramagnetic defects.[2–5] This speeds up the relaxation of the complexes out of a metastable state[6] and gives rise to depinning of dislocations from stops and subsequent motion of the dislocations in the long-range field due to the internal mechanical stresses of the crystal.[3,7]

In MFs, which we shall conventionally term strong in what follows, such that $E \approx \mu g B \sim kT$, additional channels whereby a field can influence the state of structural defects and in consequence the plastic properties of materials can arise. Our objective in the present work was to create experimental conditions for observing and investigating differences between the effects of weak and strong MFs on the plasticity of NaCl crystals.

Two characteristics of plastic properties were chosen as the response to the action of MFs: the microhardness and MF-induced runs of individual dislocations. The experiments were performed on $3 \times 3 \times 5$ mm NaCl single crystals, quenched in air from 700 K, with Ca impurity-ion concentration of 0.01 at.%. The microhardness of the crystals was measured using a PMT-3 microhardness meter. Each point in the plots is the result of averaging 30–50 individual microhardness measurements performed under identical conditions. In experiments investigating the mobility of edge dislocations introduced by the standard method of making scratches on the surface of the sample, the MF-induced displacement L of a dislocation was measured. The displacement was determined by averaging 100–150 values of the travel distances of individual dislocations, measured by double chemical etching. The procedure of double etching in the absence of external actions produced a background travel distance, identical in all experiments, for freshly introduced dislocations $L_0 = 10 \pm 1$ μm, evident from etch pits at the surface.

Square pulses of a weak field lasting 20 s, leading edge 3 s, and amplitude $B = 2$ T were produced with an electromagnet. Strong MF pulses with the shape of one-half period of a sinusoid of 140 μs and amplitude up to 35 T were generated in a solenoid by discharging a capacitor bank.

In the first series of experiments the influence of a weak MF on the microhardness of crystals was investigated. NaCl samples with no freshly induced dislocations were pretreated with a MF and then, after 1 min, the microhardness H was measured. The value obtained for H was less than the microhardness H_0 of crystals which were not treated with a MF (Fig. 1). Just as in Ref. 8, the value of H, decreased as a result of the preliminary treatment of crystals with a MF, was restored to a value close to the initial value H_0 as the duration τ of the pause between the field pulse and the moment when the microhardness is measured increased (Fig. 1). However, this fact alone cannot be the only evidence of reversibility of the changes produced by a field in a system of structural defects. For this reason, the NaCl samples, held for $\tau = 2 \cdot 10^4$ s after the first exposure in MF, were exposed to an additional field pulse (amplitude $B = 2$ T, duration 20 s) which was applied just before the microhardness was measured. It was established, to within the limits of the experimental error, that this additional pulse did not change the position of the level reached by $H(\tau)$ for $\tau > 2 \cdot 10^4$ s (Fig. 1), i.e. despite the fact that H was restored, the crystal was no longer sensitive to a MF. Therefore the state of crystals was not restored to the initial state even a long time after the first MF pulse during which the microhardness returned to a value close to H_0.

The experiments in the second series differed from experiments in the first series only in that the MF pulses applied to the crystals before indentation had a duration of 140 μm and an amplitude of 20 T. The effect of one such pulse was to decrease the microhardness of the crystals by the same degree as in the case of the crystals exposed to a

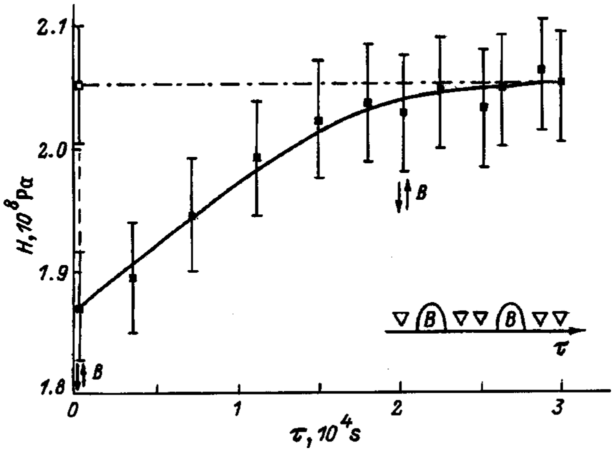

FIG. 1. Microhardness H of crystals versus the pause duration τ between the first measurement (performed before treatment of the crystals in a MF and denoted by the open square) and subsequent measurements of the microhardness. The arrows show the switching on and off of the MF pulse (duration 20 s and amplitude $B=2$ T), performed between successive microhardness measurements. The dot-dashed line shows the microhardness H_0 in crystals which have not been exposed to a MF. Inset: Sequence of procedures: B — MF pulse, triangles — moments at which microhardness measurements were preformed.

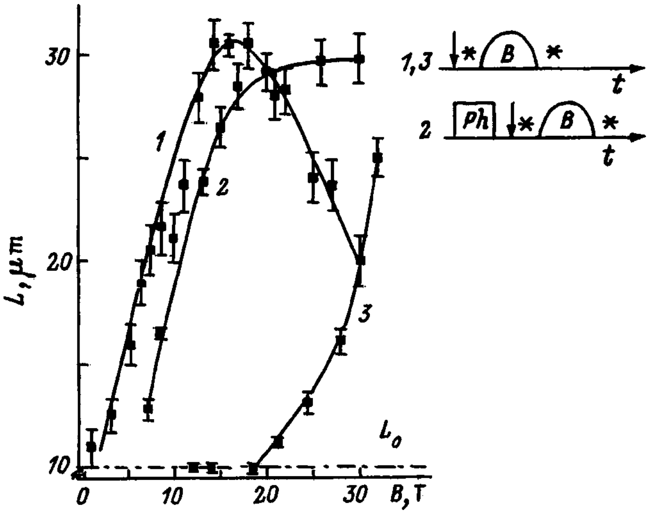

FIG. 3. Average dislocation travel distance L versus the amplitude B of the MF pulse. *1* — in NaCl-I, *2* — in NaCl-II, and *3* — in NaCl-I, exposed to light with wavelength 350 nm before dislocations were introduced. The dot-dashed line shows the value of the travel distance L_0, produced in the crystals by etching in the absence of a MF. Inset: Sequence of procedures in experiments of different types: B — MF pulse, arrow — introduction of dislocations, asterisk — etching, Ph — photoexposure.

weak MF (Fig. 2). It was also observed that H was restored to the value H_0 when the pauses between the MF treatment and indentation increased. However, this restoration occurred approximately 20 times more slowly than in the first series of experiments (see Figs. 1 and 2). Moreover, switching the MF on repeatedly once again decreased H to the same value that existed immediately after the field was switched on the first time (Fig. 2). Therefore a strong MF induced reversible changes in the crystals.

In summary, depending on the conditions of exposure of quenched crystals in MFs, qualitatively different changes arose in the crystals: irreversible in a weak field and reversible in a strong field. In what follows, we shall call crystals in which a weak MF influenced the microhardness NaCl-I. A weak MF did not produce any changes in the microhardness of crystals held at 290 K for one year after quenching (NaCl-II crystals).

Both types of crystals were used in the third series of experiments, where the dependence of the dislocation travel distance L on the amplitude of a MF pulse with duration 140 μm was investigated. In Ref. 7 it was established that virtually the entire run induced by a short MF pulse occurs after the pulse ends and not during the pulse, so that dislocation travel distances actually characterize the aftereffect of a MF, just in measurements of the microhardness. In NaCl-I crystals the dependence $L(B)$ was nonmonotonic: It was an increasing dependence only up to $B=16\pm2$ T, while for $B>16$ T it became a decreasing dependence (Fig. 3). In NaCl-II the dependence $L(B)$ was monotonic, and, to within the experimental accuracy, MFs right up to $B=17\pm1$ T did not increase the dislocation displacements above the background value L_0 (Fig. 3). A field with $B>1$ T initiated dislocations displacements which increased monotonically with the field induction. Therefore, to within the limits of the experimental error, the value of B at which a maximum of $L(B)$ in NaCl-I was observed is the same as the threshold value of the field at which stimulation of dislocation displacements in NaCl-II is first observed.

In NaCl-I crystals it was also possible to observe a monotonic field dependence $L(B)$, if the samples are exposed for 15 min to monochromatic light with wavelength 350 nm before dislocations are introduced and a MF is applied (Fig. 3). In Ref. 4 it was established that such treatment of crystals suppresses the sensitivity of point defects to a weak MF. It follows from Fig. 3 that suppression of the ‘‘weak-field’’ magnetoplastic effect results in the fact that the ‘‘strong-field’’ part of the field dependence $L(B)$ (for $B>16$ T) is no longer decreasing, but rather is increasing. Thus photoexposure of NaCl-I makes the dependence $L(B)$ closer to that observed in NaCl-II without photoexposure.

Switching now to our discussion, we note that the change in the state of the crystals in a weak MF, in principle, could be explained by depinning of growth dislocations from stops and redistribution of internal mechanical stresses in the

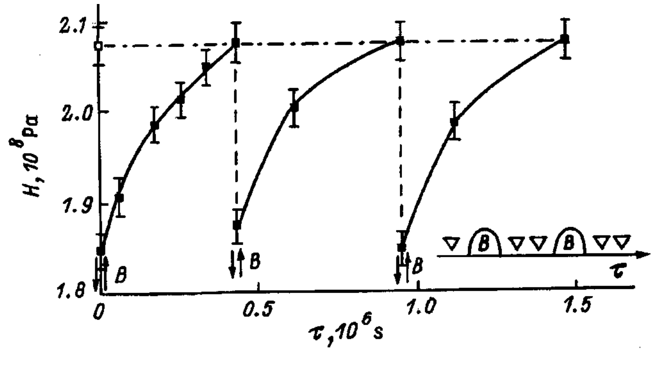

FIG. 2. Same as Fig. 1 with MF pulse amplitude $B=20$ T and duration 140 μm.

crystal (as described in Ref. 3) or by the influence of a MF on the state of complexes of point defects (for example, on the degree of their association). Evidently, in the first case one would expect that the microhardness likewise will change irreversibly. However, according to Fig. 1, the value of the microhardness is restored after the MF pulse ends. The decrease in H in a MF and an increase in H after the field is switched off can hardly be due to the same cause—relaxation of internal stresses. This shows that in a MF the microhardness changes because of the influence of the MF on the state of point defects.

In a weak MF the state of point defects changes irreversibly, since in the opposite case switching on an additional field pulse should put point defects into the same state as that existing immediately after the first MF pulse, which in turn would once again decrease H. The fact that the crystal loses its sensitivity to repeated weak MF pulses (Fig. 1) shows that the a field with $B<16$ T initiates in a subsystem of point defects a multistage relaxation process, which causes the crystals to become insensitive to subsequent exposures to a MF. Therefore the apparent ''restoration'' of the state of point defects after the MF is switched off is apparently the second stage of the field-induced relaxation process, while the first stage proceeds in the MF.

The irreversible character of the changes initiated in the subsystem of point defects by a weak MF attests to metastability of magnetically sensitive states of point defects and means that the role of a MF reduces only to speeding up the relaxation process, which proceeds slowly in the crystal even in the absence of a MF.

In strong MFs, primarily irreversible changes in the states of point defects occur in NaCl-I crystals (Fig. 2). This could be due to the difference in the micromechanisms of the effect of a MF on point defects at $B=2$ and 20 T. The fact that the pause duration τ required to restore H after treatment in strong and weak fields with the same initial value of $\Delta H=H-H_0$ (Figs. 1 and 2) likewise shows that the strong- and weak-field channels whereby a MF incluences the state of point defects are different. The reversibility of the microhardness changes after the action of a strong MF shows that in a strong MF, in contrast to a weak field, enough energy is imparted to point defects so that the defects are transferred into excited states. Therefore the weak and strong field magnetoplastic effects are thermodynamic opposites of one another.

The nonmonotonic dependence of the dislocation travel distances on the amplitude of the MF pulse, varied from 0 to 30 T, shows that a superposition of two very different mechanisms of the effect of a MF on the state of point defects is observed in NaCl-I crystals. One is the weak-field mechanism. In NaCl-I crystals it gives rise to irreversible changes in the point defects. The other is a strong-field mechanism. It becomes effective in fields $B>16$ T and is characterized by reversibility of the changes introduced by a field into the subsystem of point defects. Apparently, only the strong-field channel of the effect of a MF on the state of point defects materializes in NaCl-II crystals, since a monotonic dependence $L(B)$ is observed in them. This point of view is also confirmed by the fact that the ''bleaching'' of point defects which are sensitive to a weak MF by light eliminates the nonmonotonicity of the dependence $L(B)$ (Fig. 3).

In summary, a weak MF with induction $B\sim 1$ T gives rise to an irreversible change in the metastable states of point defects, initiating a multistage relaxation process accompanied by a change in the microhardness of the crystal. A strong MF with induction $B>16$ T reversibly changes the state of point defects. This attests to the fact that in a strong MF energy comparable to the average energy of thermal fluctuations is imparted to point defects. Further investigations are required in order to determine the mechanism of the redistribution of the energy imparted to point defects in a strong MF and the type of these magnetosensitive defects.

This work was supported by the Russian Fund for Fundamental Research (Grant No. 97-02-16074).

[1] V. I. Al'shits, E. V. Darinskaya, T. M. Perekalina, and A. A. Urusovskaya, Fiz. Tverd. Tela (Leningrad) **29**, 467 (1987) [Sov. Phys. Solid State **29**, 265 (1987)].

[2] V. I. Al'shits, E. V. Darinskaya, and O. L. Kazakova, JETP Lett. **62**, 375 (1995).

[3] V. I. Al'shits, E. V. Darinskaya, and O. L. Kazakova, Zh. Éksp. Teor. Fiz. **111**, 615 (1997) [JETP **84**, 338 (1997)].

[4] Yu. I. Golovin, R. B. Morgunov, M. V. Badylevich, and S. Z. Shmurak, Fiz. Tverd. Tela (St. Petersburg) **39**, 1389 (1997) [Phys. Solid State **39**, 1232 (1997)].

[5] M. I. Molotskiĭ, Fiz. Tverd. Tela (Leningrad) **33**, 3112 (1991) [Sov. Phys. Solid State **33**, 1760 (1991)].

[6] Yu. I. Golovin, R. B. Morgunov, and V. E. Ivanov, Fiz. Tverd. Tela (St. Petersburg) **39**, 2016 (1997) [Phys. Solid State **39**, 1803 (1997)].

[7] Yu. I. Golovin, R. B. Morgunov, and S. E. Zhulikov, Izv. Ross. Akad. Nauk, Ser. Fiz. **61**, 965 (1997).

[8] Yu. I. Golovin, R. B. Morgunov, D. V. Lopatin, and A. A. Baskakov, Phosphorus, Sulfur Silicon Relat. Elem. **160**, R3 (1997).

Translated by M. E. Alferieff

PHYSICS OF THE SOLID STATE VOLUME 40, NUMBER 11 NOVEMBER 1998

MAGNETISM AND FERROELECTRICITY

Phase separation in degenerate magnetic oxide semiconductors

É. L. Nagaev

Institute of High-Pressure Physics, Russian Academy of Sciences, 142092 Troitsk, Moscow Region, Russia

(Submitted April 13, 1998)
Fiz. Tverd. Tela (St. Petersburg) **40**, 2069–2073 (November 1998)

A theory of mixed electronic-impurity phase separation in degenerate magnetic oxide semiconductors, including high-T_c superconductors and materials with colossal magnetoresistance (CMR), is developed. Such a separation can occur in materials with excess oxygen, if they are simultaneously doped with an acceptor impurity whose atoms are frozen in position. Oxgyen acts as an acceptor, which can diffuse through the crystal. Then, for example, manganites can break up into ferromagnetic and antiferromagnetic regions with all holes and oxygen ions concentrated in the former and with no holes or oxygen ions in the latter. Such two-phase systems can possess CMR and anomalous thermoelectric power, and they can make a transition from an insulating into a highly conducting state as temperature increases. The reverse insulator–metal transition is also possible. © *1998 American Institute of Physics.* [S1063-7834(98)02311-9]

It has been known for a long time that in the ground state of a number of strongly doped magnetic semiconductors thermodynamically equilibrium phase separation occurs so that the minimum energy of the crystal corresponds to a state where different magnetic phases are mixed with one another. Similar phenomena are also possible in high-T_c superconductors related to them.

Two basic types of magnetic phase separation are distinguished: electronic[1] and impurity[2] (see the monograph Ref. 3 and the review Ref. 4). The first type occurs with fixed positions of the dopant atoms and consists in concentration of all charge carriers in definite regions. In antiferromagnetic (AF) semiconductors the initial order is replaced by ferromagnetic (FM) order in which the carrier energy is lower. The rest of the crystal remains AF and insulating. Together with phase separation, charge separation also occurs here, since both phases are positively charged (excess carriers in one and excess ionized donors or acceptors in the other).

Phase separation of the second type occurs in the materials where donors or acceptors are quite mobile at temperatures below the magnetic-ordering point. For this reason, not only charge carriers but also the defects engendering them and becoming ionized concentrate in one of the phases. As a result, the charge separation and the associated increase of the Coulomb energy of the system vanish. For example, this is the situation in a number of high-T_c superconductors with perovskite structure, where oxygen, playing the role of an acceptor, collects in a definite part of the crystal and makes it superconducting. The rest of the crystal becomes an AF insulator. Impurity AF–MF phase separation with oxygen concentrated in the FM phase is also possible in materials with colossal magnetoresistance (MCMR) such as manganites, if their oxygen content exceeds the stoichiometric level.

However, because of difficulties in monitoring oxygen stoichiometry, often high-T_c superconductors and MCMRs contain as acceptors not only essentially immobile ions specially introduced into them (for example, Ca and Sr in manganites) but also mobile oxygen ions. Mixed electron-impurity phase separation can be expected in such materials. The present paper is devoted to investigating this. In the case of such phase separation, all holes and oxygen ions present in the crystal collect in the FM part and are completely absent from the AF part of the crystal. Although in this case, just as in the case of electronic phase separation, charge separation also occurs, this effect is less pronounced here. The destruction of the two-phase state by a magnetic field is manifested as CMR. The existence of a two-phase AF–FM state in manganites moderately doped with Ca has been confirmed by direct neutron experiments,[5] but its nature has still not been determined.

Mixed phase separation is also possible in high-T_c superconductors. Moreover, there are direct experimental indications that phase separation in lanthanum cuprate combines features of impurity and electronic separation.[6]

1. ELECTRON-IMPURITY PHASE SEPARATION IN THE GROUND STATE

Here a thermodynamically equilibrium phase separation will be considered to be the ground state of the crystal. In reality, of course, we have in mind quite low but finite temperatures at which impurity diffusion is still possible. As noted above, mixed phase separation is accompanied by charge separation. To decrease the Coulomb energy of the phase-separated system, both phases strive to mix with one another. However, the increase in surface energy arising in this case limits their mixing. As a result, in the isotropic crystal the phase with the smaller volume (minor phase) consists of small drops several nm in size, imbedded in the matrix of the host phase, where they form a superlattice.[1,3,4]

As far as impurity phase separation is concerned, despite the absence of Coulomb forces the tendency toward phase mixing exists here also: It decreases the elastic forces which arise as a result of the difference in the elastic properties of both phases. As a result, here, the minimum energy corresponds to plane-parallel geometry (alternating layers of both phases), but under typical conditions their typical sizes are several orders of magnitude larger than the radius of the drops in the presence of electronic phase separation (see Ref. 4). Since Coulomb forces are much stronger than elastic forces, they should determine the geometry of the system in the presence of mixed phase separation also.

Having in mind lanthanum manganites, we shall study the separation of a sample into FM and AF phases. The extension of this analysis to other systems (high-T_c superconductors and so on) is self-evident. The analysis is based on the $s-d$ model with the Hamiltonian

$$\begin{aligned} H=\sum E_{\mathbf{k}} a^*_{\mathbf{k}\sigma} a_{\mathbf{k}\sigma} - \frac{A}{N}\sum (\mathbf{s}\cdot\mathbf{S}_{\mathbf{g}})_{\sigma\sigma'} \\ \times \exp\{i(\mathbf{k}-\mathbf{k}')\cdot\mathbf{g}\} a^*_{\mathbf{k}\sigma} a_{\mathbf{k}'\sigma'} \\ -I\sum \mathbf{S}_{\mathbf{g}}\cdot\mathbf{S}_{\mathbf{g}+\mathbf{\Delta}} - \sum (\mathbf{H}\cdot\mathbf{S}_{\mathbf{g}}) + H_{\mathrm{C}} + H_{\mathrm{el}}, \end{aligned} \tag{1}$$

where $a^*_{\mathbf{k}\sigma}$ and $a_{\mathbf{k}\sigma}$ are s-electron operators modeling conduction electrons or holes with quasimomentum $\mathbf{k}$ and spin projection σ, $\mathbf{s}$ is the s-electron spin operator, and $\mathbf{S}_{\mathbf{g}}$ is the operator for the d-spin of atom $\mathbf{g}$ of magnitude S. The first term in Eq. (1) is the kinetic energy of the s electrons, the second term is the $s-d$ exchange energy, and the third term is direct exchange between d spins ($\mathbf{\Delta}$ is the vector connecting nearest neighbors). Further, H_{C} is the Coulomb interaction energy of s electrons interacting with ionized impurity atoms and H_{el} is the elastic interaction energy between impurity atoms. Only the effect of an external magnetic field $\mathbf{H}$ on the d spins is taken into account. Its indirect effect on the spins of the s electrons via the magnetization of the d spins is much stronger than the direct effect,[3] and for this reason the latter is neglected.

To calculate the energy of the phase-separated state we shall employ a variational principle, generalizing the procedure employed in Ref. 1. All conduction electrons (or holes) are assumed to be concentrated within the FM phase. The number of charge carriers in the AF phase is exponentially small.

It is assumed that the minor phase consists of spheres of radius R, which form a periodic lattice inside the host phase. The second variational parameter X is the ratio of the volumes of the AF and FM phases: $X=V_{\mathrm{A}}/V_{\mathrm{F}}$. If the minor phase is highly conducting, the electronic part of the wave function at $T=0$ is taken in the form of an antisymmetrized product of one-electron wave functions $\psi(\mathbf{r})$, corresponding to the free motion of an electron inside a spherical region of radius R

$$\Psi=(N_{\mathrm{e}}!)^{-1/2}\,\mathrm{Det}\,|\psi_k(\mathbf{R}_i-\mathbf{r}_n)|, \tag{2}$$

where $\mathbf{R}$ are the coordinates of the center of the ith sphere, $\mathbf{r}_n$ are the coordinates of the nth electron, and N_{e} is the total number of electrons. In the ground state the indices of the single-electron states k correspond to the one-electron energies E_k below the Fermi energy μ.

Dirichlet boundary conditions are used for each sphere. This is justified even for not very deep potential wells, if $[2m(U-E_k)^{1/2}]R \gg 1$, where U is the depth of the potential well and m is the electron effective mass ($\hbar=1$). The wave function (2) is exact, if the radius of the potential well is less than the screening radius. For large values of R, it gives an upper estimate for the energy of the phase-separated state.

If $k_F R \gg 1$, then the adiabatic approximation can be used to calculate the kinetic energy E_k. In this approximation, a memory of the spatial quantization of the electronic motion remains in the form of the surface energy E_{S}, which must be added to the volume energy E_{V} (Ref. 3)

$$\begin{gathered} E_{\mathrm{K}}=E_{\mathrm{V}}+E_{\mathrm{S}}, \\ E_{\mathrm{V}}=\frac{3}{5}\mu(n)\,n(1+X)^{2/3}V, \quad \mu(n)=\frac{(6\pi^2 n)^{2/3}}{2m}, \end{gathered} \tag{3}$$

$$E_{\mathrm{S}}=\beta\left(\frac{\pi}{6}\right)^{1/3}\frac{5E_{\mathrm{V}}}{16n^{1/3}(1+X)^{1/3}R}, \quad n=n_{\mathrm{D}}+n_{\mathrm{O}}, \tag{4}$$

where n is the average electron (or hole) density. It consists of the densities n_{D} and n_{O}, related with the divalent ions and excess oxygen, respectively. The quantity $n(1+X)$ is simply the carrier density inside FM drops, V is the total volume of the sample, and $\beta=3$. The volume of the FM phase is $v/(1+X)$, where v is the volume of a unit cell.

The Fermi energy μ can be written in a form corresponding to the total spin-polarization of the charge carriers (if the polarization were incomplete, then the FM region for carriers with one of the spin projections would not be a potential well but rather a potential hump). In the $s-d$ model (1) this means that the inequality $\mu < AS$ must be satisfied, where A is the $s-d$ exchange integral and S is the magnitude of the d spin. Specifically, this inequality holds in the case of double exchange, where the width W of the band for s electrons, modeling conduction electrons or holes, is small compared with AS.

The Coulomb energy is calculated in the jellium model using elementary electrostatics. For ferromagnetic spheres in an antiferromagnetic matrix the result is

$$\begin{gathered} E_{\mathrm{C}}=\frac{2\pi n_{\mathrm{D}}^2}{5\varepsilon}e^2R^2 f(X)V, \\ f(X)=[2X+3-3(1+X)^{2/3}], \end{gathered} \tag{5}$$

where ε is the permittivity. In the case that the host phase is FM and the AF drops are imbedded in the FM matrix, the FM–AFM interfacial energy is given by Eq. (4) with $\beta=3X$, while the Coulomb energy is

$$\begin{gathered} E_{\mathrm{C}}=\frac{2\pi}{5\varepsilon}n_{\mathrm{D}}^2 e^2R^2 g(X)V, \\ g(X)=X[2+3X-3X^{1/3}(1+X)^{2/3}]. \end{gathered} \tag{6}$$

By postulate, the elastic interaction energy of the impurity atoms is small compared with the Coulomb energy and is therefore neglected.

We shall now write out the energy of the d subsystem. In the nearest-neighbors approximation it is given by the expression

$$E_{dd}/V=\frac{|J|S}{(1+X)\nu}-\frac{H^2SX}{4|J|\nu(1+X)}-\frac{HS}{(1+X)\nu},$$
$$J=zIS, \tag{7}$$

where I is the $d-d$ exchange integral and z is the coordination number. The first term in Eq. (7) is the increment to the $d-d$ exchange energy due to AF ordering being replaced by FM ordering, and the second and third terms give the energy of the AF and FM phases in an external magnetic field H.

Finally, we must write out the difference E_{U} in the s-electron energy in the presence of AF and FM ordering.[3,4] Two expressions will be presented. The first one corresponds to magnetic semiconductors with wide s bands and the second corresponds to narrow s bands (so-called double exchange):

$$E_{\mathrm{U}}=-UNV,$$
$$U=\frac{AS}{2},\quad W\gg AS;$$
$$U=zt\left(1-\frac{1}{\sqrt{2S+1}}\right),\quad W\ll AS, \tag{8}$$

where t is the s-electron hopping integral. Many investigators believe that double exchange materializes in lanthanum manganites, although there do exist experimental data for the opposite point of view (see Ref. 7).

2. SPECIFIC FEATURES OF THE MIXED PHASE-SEPARATED STATE

To find the ground state of the system under study, the total energy $E_{\mathrm{t}}=E_{\mathrm{V}}+E_{\mathrm{S}}+E_{\mathrm{C}}+e_{dd}+E_{\mathrm{U}}$ must be minimized with respect to the parameters X and R. As is evident directly from Eqs. (2)–(8), only the surface energy E_{S} and the Coulomb energy E_{C} depend on R. This makes it possible to minimize the total energy with respect to R in an explicit form. In the case of FM drops, the optimized energy and radius are given by the expressions

$$E_R=(E_{\mathrm{S}}+E_{\mathrm{C}})_{\mathrm{opt}}=(2^{-2/3}+2^{1/3})\left(\frac{9m^2}{160\pi}\right)^{1/3}$$
$$\times\frac{e^{2/3}n^{2/3}\mu^{4/3}f(X)^{1/3}(1+X)^{2/9}}{\zeta^{1/3}}, \tag{9}$$

$$R_{\mathrm{opt}}^3=\frac{135\pi^2\zeta(1+X)^{1/3}}{32m^2e^2\mu f(X)}, \tag{10}$$

where the effective permittivity ζ, corresponding to the mixed phase separation,

$$\zeta=\varepsilon\left(1+\frac{n_{\mathrm{O}}}{n_{\mathrm{D}}}\right)^2 \tag{11}$$

has been introduced.

The subsequent procedure of minimizing the energy with respect to X in the general case can be performed only numerically. But, if the energy E_R is small, it influences very little the optimal value of X determined mainly by the energies E_{V} and E_{dd}, which by assumption are much greater than E_R. Then, we obtain for $H\ll|J|$

$$\frac{V_{\mathrm{F}}}{V}=\frac{1}{1+X}=\left[\frac{3\mu(1/\nu)}{5(|J|-H)S}\right]^{3/5}n\nu. \tag{12}$$

It should be noted that the optimal parameters of the system do not include the depth U of the potential well. Nevertheless, it should be large enough to make phase separation energetically favorable.

As one can see from Eqs. (10)–(12), for a fixed total charge-carrier density n the volume of a FM drop increases quadratically, according to Eq. (11), as a function of the weight $n_{\mathrm{O}}/n_{\mathrm{D}}$ of the impurity phase separation. Therefore, here, the size of FM drops cannot be much larger than in the case of purely electronic phase separation. For this reason, these drops can be manifested not in small-angle scattering, but rather in quite sharp ferromagnetic peaks of neutron scattering, which were observed in Ref. 5 in lanthanum manganites.

Obviously, if the FM phase is the minor phase and consists of drops which are isolated from one another, then all charge carriers are locked up inside them and cannot move through the entire crystal. Therefore the crystal behaves like an insulator. But, as one can see from Eq. (12), the volume of the FM phase increases as the total carrier density increases, and the FM phase becomes the major phase. Then the crystal should possess high conductivity, since carriers can move freely through the crystal, by-passing the insulating AF drops.

An alternative to phase separation in $\mathrm{LaDy}_x\mathrm{Mn}_{1-x}\mathrm{O}_{3+y}$ is noncollinear AF ordering, induced by current carriers under double-exchange conditions.[8] But this idea contradicts not only the neutron diffraction data,[5] but also data on the electrical properties of these materials. Unsaturated ferromagnetism was observed for $x<0.17$ and y close to zero, where the crystal as a whole behaved as an insulator (see Ref. 7). But the theory of Ref. 8 is based on the opposite assumption that the crystal is in a high-conductivity state. At the same time, the considerations presented above concerning phase separation make it possible to explain why unsaturated FM ordering is insulating.

The idea of phase separation also makes it possible to explain the anomalous sign of the thermoelectric power α observed in MCMRs.[9,10] Since excess oxygen and divalent doping ions give rise to holes in the crystal, the thermoelectric power should be positive. However, in Ref. 10 it was established that for $x<0.17$, when the crystal is in an insulating state, the low-temperature thermoelectric power is negative, i.e. its sign is anomalous. As temperature increases, the thermoelectric power changes sign to the normal sign.

If phase separation does indeed occur at low temperatures, then the integrated thermoelectric power is determined by that of the insulating (more accurately, semiconducting) phase. If the conductivity σ is intrinsic, then the thermoelectric power can be both positive and negative, depending on the sign of the charge carriers (e or h) making the dominant contribution to α

$$\alpha=\frac{\alpha_e\sigma_e+\alpha_h\sigma_h}{\sigma_e+\sigma_h}. \qquad (13)$$

Therefore, it can be negative if conduction electrons dominate.

At high temperatures, the state with separated phases melts, and all holes previously locked inside the FM phase become distributed uniformly throughout the crystal. For this reason, the high-temperature thermoelectric power is positive.

The temperature dependence of the thermoelectric power should be reproducible under conditions of thermodynamically equilibrium phase separation. Proceeding from this scenario and from the experimental fact that the thermoelectric power is reproducible, phase separation in lanthanum manganites should be thermodynamically equilibrium.

Finally, phase separation leads to one possible channel for colossal magnetoresistance in these materials. It follows from the results obtained above that if the FM phase is the minor phase, then it can become the major phase under the action of a magnetic field. Indeed, according to Eq. (12), the parameter X decreases as the field increases. As follows from Eq. (10), the drop size increases as X decreases. Therefore, according to Eq. (12), the volume of a FM drop increases as the field intensifies. From the same equation it follows that the total volume of the FM phase also increases with the field. For this reason, at some critical value of the field the ferromagnetic drops come into contact with one another and percolation of the s-electron liquid occurs.

An alternative to percolation could be a jump-like transition out of the phase-separated into a uniform highly-conducting state. The field-induced transition from the insulating into a highly-conducting state can be regarded as a manifestation of colossal magnetoresistance.

3. TRANSITION FROM AN INSULATING TO A HIGHLY-CONDUCTING STATE AS TEMPERATURE INCREASES

We shall now investigate phase separation at finite temperatures. Only the spin-wave region is studied, and $s-d$ interaction is assumed to correspond to double exchange. To carry out this program, taking account of the strong degeneracy of the fermion gas the free energies F_m and $F_{\rm O}$ of the magnons and excess oxygen atoms must be added to the energy $E_{\rm t}$. The magnon energy can be represented in the form

$$F_m^{\rm de}(T)=\frac{xG_{\rm de}^{\rm A}(T)}{1+x}+\frac{G_{\rm de}^{\rm F}(T)}{1+x}, \qquad (14)$$

where the index de means double exchange.

The free magnon energy in both the AF state ($G^{\rm A}$) and the FM state ($G^{\rm F}$) is given by the expression

$$G=T\sum \ln\left(1-\exp\left(\frac{\omega_q}{T}\right)\right). \qquad (15)$$

The magnon frequencies in the AF and FM phases are given by the expressions (the derivation of the latter is presented in Ref. 3), respectively,

$$\omega_q=|J|\sqrt{1-\gamma_q^2}, \quad J=IS^2z,$$

$$\gamma_q=\frac{1}{z}\sum \exp(i\mathbf{q}\cdot\mathbf{\Delta}), \qquad (16)$$

$$\omega_q^{\rm E}=(-|J|+J^{\rm de})(1-\gamma_q), \quad J^{\rm de}=\frac{zt}{2SN}\sum \gamma_k f_k, \qquad (17)$$

where f_k is the fermion distribution function at $T=0$.

We shall examine the case $T_{\rm C}/S\ll T\ll T_{\rm C}$, where the spin-wave approximation is still applicable, if $S\gg 1$. The following estimate for the free energy of AS magnons is obtained from Eqs. (15) and (16):

$$G^{\rm A}=TN\left(\ln\frac{|J|}{T}-\frac{1}{12}\right). \qquad (18)$$

The free energy of FM magnons differs from Eq. (18) in that $|J|$is replaced by $(J^{\rm de}-|J|)$.

Moreover, a contribution proportional to the entropy of redistribution of $N_{\rm O}$ oxygen atoms over $N_{\rm F}=N/(1+X)$ unit cells, comprising the FM phase, appears in the temperature-dependent part of the free energy:

$$F_{\rm O}=TN_{\rm F}\{\nu_{\rm O}\ln\,\nu_{\rm O}+(1-\nu_{\rm O})\ln(1-\nu_{\rm O})\},$$

$$\nu_{\rm O}=\frac{N_{\rm O}}{N_{\rm F}}. \qquad (19)$$

However, it is of the order of $N_{\rm O}/N\ll 1$ compared with the magnon free energy and therefore has virtually no effect on the computational results.

At low temperatures the temperature-dependent part of the free energy can be treated as a small correction to the ground-state energy, and then, since $E_{\rm t}$ is minimum for $X=X(0)$, we find that the total free energy of the system $F=E_{\rm t}+F_m+F_{\rm O}$ is minimum when

$$X(T)=X(0)-\frac{d(F_m+F_{\rm O})/dX|_{X=X(0)}}{d^2E_{\rm t}/dX^2|_{X=X(0)}}. \qquad (20)$$

Taking of Eqs. (14) and (18) we have

$$\frac{dF_m}{dX}=\frac{TN}{(1+X)^2}\left[1+\ln\frac{|J|}{J^{\rm de}(n)(1+X)-|J|}\right],$$

$$n=n_{\rm O}+n_{\rm D}. \qquad (21)$$

In writing down Eq. (21) we took account of the fact that because the charge-carrier density is relatively low we can set in Eq. (17) $\gamma_k\approx 1$ and that the carrier density in the FM regions is $1+X$ times greater than the average value in the crystal.

In summary, for given parameters of the system, its behavior with increasing temperature is determined by $X(0)$, which can found by means of numerical calculations, and Eq. (12) can be used for ball-park estimates. Then it follows from Eqs. (12) and (21) that the sign of dF_m/dX in Eq. (21) does not depend on the carrier density and generally speaking can be both positive and negative.

If dF_m/dX is positive, then X decreases with temperature. Therefore the size of the FM part of the crystal increases with temperature. According to Eq. (10), the size of a FM drop increases as X decreases. An increase of V_F and R simultaneously can result in the appearance of contacts between drops, i.e., temperature-induced percolation of FM ordering and an electronic liquid. In other words, a rise in temperature can give rise to a transition from an insulating to a highly conducting state without phase separation being destroyed, and only with a radical change in the topology of the two-phase state. Simultaneously with this transition, the sign of the thermoelectric power can change: If it was anomalous before the transition (see Sec. 3), then after the transition it can become normal, corresponding to holes as the majority charge carriers in manganites.

However, if dF_m/dX is negative and $X(T)$ increases with temperature, then the volume of the FM part of the crystal decreases, while the volume of the AF part increases. Therefore if the crystal was initially in a highly-conducting two-phase state, it can switch into an insulating state. As temperature increases further, when the two-phase state breaks down, the crystal should once again become highly conducting.

This work was supported by Grant 97-1076(072) from the Ministry of Science of the Russian Federation and Grant 98-02-16148 from the Russian Fund for Fundamental Research.

[1] É. L. Nagaev, JETP Lett. **16**, 394 (1972); V. A. Kashin and É. L. Nagaev, Zh. Éksp. Teor. Fiz. **66**, 2105 (1974) [Sov. Phys. JETP **39**, 1036 (1974)].
[2] É. L. Nagaev, Physica C **222**, 324 (1994).
[3] É. L. Nagaev, *Physics of Magnetic Semiconductors* [in Russian], Nauka, Moscow, 1979.
[4] É. L. Nagaev, Usp. Fiz. Nauk **165**, 529 (1995).
[5] E. Wollan and W. Koehler, Phys. Rev. **100**, 545 (1955).
[6] R. Kremer, E. Sigmund, and V. Hizhnyakov, Z. Phys. B **86**, 319 (1992); Z. Phys. B **91**, 169 (1993).
[7] É. L. Nagaev, Usp. Fiz. Nauk **166**, 833 (1996).
[8] P. De Gennes, Phys. Rev. **118**, *1*, 141 (1960).
[9] R. Mahendiran, S. Tiwary, A. Raychaudhura *et al.*, Phys. Rev. B **54**, R9604 (1996).
[10] A. Asamitsu, Y. Moritomo, and Y. Tokura, Phys. Rev. B **53**, R2952 (1996).

Translated by M. E. Alferieff

Nanocrystalline cobalt films prepared under ultrafast condensation conditions

V. S. Zhigalov, G. I. Frolov, and L. I. Kveglis

L. V. Kirenskiĭ Institute of Physics, Siberian Branch of the Russian Academy of Sciences, 660036 Krasnoyarsk, Russia

(Submitted April 13, 1998)
Fiz. Tverd. Tela (St. Petersburg) **40**, 2074–2079 (November 1998)

The magnetic and electrical properties and the temperature dependence of these properties of cobalt films prepared at high condensation rates (10^5-10^6 Å/s) are investigated. Incremented annealing reveals several nonequilibrium states of cobalt in transition from the as-prepared metastable structure to the ordinary hcp structure. The anomalies of the properties are analyzed from the standpoint of the nanocrystalline state of the samples. Model concepts of microcluster formations in the investigated films are also discussed. © *1998 American Institute of Physics.* [S1063-7834(98)02411-3]

Magnetic materials having a nanocrystalline structure are of major interest for several reasons. First, the size of the elementary structural formations (from two to several hundred atoms) is several times smaller than the dimensions of the crystallites in ordinary polycrystalline films. Second, nanocrystalline systems do not constitute a macroscopic system, i.e., the parameters of nanoformations are not a monotonic function of the number of atoms in them. The parameters undergo the most abrupt changes in passage through the so-called ‘‘magic numbers,’’ which increases the probability of the generation of nanoformations having a strictly defined number of atoms. The latter feature dramatically increases the accuracy and selectivity of instruments utilizing these materials and thereby expands the area of their practical application. Third, the structure and properties of nanosystems differ from those of solids, and in our opinion their investigation is far from complete.[1–3]

Many properties of microclusters have been studied fairly extensively to date, but the preparation of film materials having a nanocrystalline structure is usually discussed only in the hypothetical realm. On the one hand, the prediction of the properties of such films is highly problematical, because interactions of microclusters with the substrate and with each other begin to play a major role in this case, and these phenomena have received little attention; on the other hand, the technologies used to prepare free-standing microclusters (specifically low-energy cluster beam deposition, or LECBD) are ineffective in film preparation.[4]

The objective of the present study is to investigate the influence of the preparation conditions and the anneal time and temperature on the structure and properties of cobalt films prepared by pulsed plasma deposition (PPD)[5] in a vacuum of $\sim 10^{-6}$ Torr.

1. TECHNOLOGY AND SAMPLES

A distinctive feature of the usable vacuum deposition method is a high pulsed condensation rate (exceeding 10^5 Å/s) at a pulse duration $\sim 10^{-4}$ s with a condensate cooling rate of the order of 10^8 K/s. Inasmuch as a necessary condition for the preparation of nanocrystalline systems is abrupt supercooling of the vapor,[4] our technology is found to be efficient. The technological process essentially entails the production of a plasma between a water-cooled anode and a sputtered target of pure cobalt by discharging a high-capacitance bank of capacitors in the vapor of the sputtered target. An initial small quantity of vapor is created by preliminary laser evaporation of the target. In the main stage of the process an LTI-207 solid-state laser partially evaporates the cathode to create a medium for the passage of an electric current. Each evaporated atom is ionized in the discharge plasma, i.e., generates one electron and one ion. The resulting target atoms bombard the material to be evaporated, knocking out a new batch of atoms. The sputtering process continues for a period exceeding the duration of the laser pulse by three or four orders of magnitude.

The method is novel in that one can select the direction of maximum dispersion of the crystal structure at ultrahigh condensation rates, when the number of new nucleation centers is so large that the radius of the critical nucleation center is the same as the radius of coalescence.[5] Films prepared by this method are continuous, beginning with a thickness of $10-15$ Å, and comprise a set of nanocrystallites of approximately equal diameter. These data have been established from electrical resistivity measurements and from measurements in high-resolution tunneling and transmission electron microscopes. The electron diffraction pattern appears as a diffuse halo typical of amorphous and nanocrystalline materials.

2. EXPERIMENTAL RESULTS

The electrical and magnetic properties of the prepared samples have been subjected to temperature analyses. Figure 1 shows the thickness dependence of the electrical resistivity $\rho(d)$ of a cobalt film obtained during deposition. Three distinct intervals are visible on this curve. In the first interval (to a thickness $d_1 \leqslant 15$ Å) we observed a sharp decrease in ρ due to the transition from an island structure to a continuous film. This behavior of the curve confirms the continuity of the film

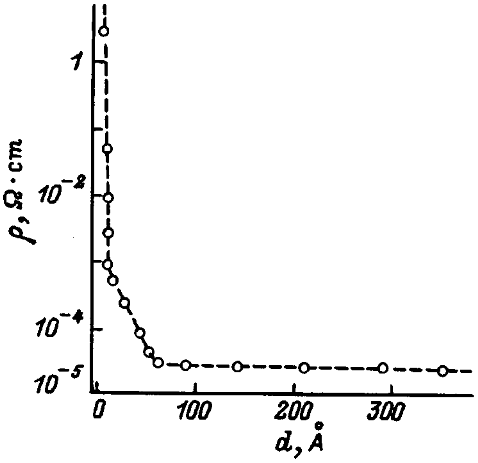

FIG. 1. Electrical resistivity versus thickness of a Co film.

beginning with a monolayer consisting of nanocrystallites. In the second interval (ranging from 15 Å to 60 Å) we observe a somewhat different kind of behavior, which can be identified with the dependence of the effective mean free path of electrons on the sample thickness, i.e., the relation $d < L_q$ (where L_q is the mean free path) holds in the given thickness range. Finally, in the third interval (>60 Å) ρ is essentially independent of d. The value of L_q can be roughly estimated from this dependence and for the given sample is ~60 − 70 Å.

Preliminary studies have also shown that in the initial state the temperature coefficient of the resistance (TCR) of the samples is close to zero, and their resistivity ρ is high, exceeding by more than an order of magnitude the value of ρ for ordinary polycrystalline cobalt films.

Figure 2a shows the characteristic temperature dependence of the resistivity $R(T_n)$. A Co film of thickness $d = 750$ Å, deposited on glass-ceramic, was used in the given situation. The temperature curve exhibits a complex behavior. During initial heating, we observe a slight increase in R up to a temperature ~450 K and then, as T_n increases, two rather sudden drops in the resistivity, which are separated by a short temperature interval (520–600 K) wherein R stabilizes. The resistivity drops differ for different films, but are essentially independent of the initiation temperature and, as a rule, cease at $T_n \sim 670 - 675$ K. The opposite behavior of the $R(T_n)$ is characteristic of metals, i.e., is linear. The total resistivity drops by a factor of 1/5 to 1/15, depending on the sample thickness, and is irreversible.

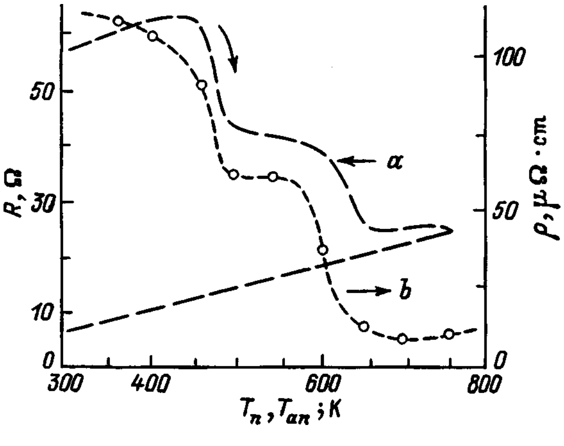

FIG. 2. Variations of the electrical resistance R during heating (a) and the electrical resistivity ρ during annealing (b).

TABLE I. Dependence of the ratio of the electrical resistivities at room temperature and liquid-nitrogen temperature on the thickness of a Co film.

Film thickness, Å	$\rho_{300\ \mathrm{K}}/\rho_{77\ \mathrm{K}}$
70.	1.01
120.	1.015
300.	1.03

It is natural to assume that this behavior is associated with temperature-induced transformation of the nonequilibrium structure of the samples. The influence of temperature on the resistivity was subsequently determined by a series of anneals. A large number of films was subjected to incremented annealing at various temperatures (T_{an}) in the range from 350 K to 850 K in a vacuum of 10^{-5} Torr. The anneal time at each fixed temperature was 1 h. Figure 2b shows the resistivity of a Co film deposited on a glass substrate as a function of the anneal temperature. It is evident from this figure that in the as-prepared state ρ is more than 20 times the resistivity of bulk Co and decreases by almost one half at $T_{\mathrm{an}} = 450$ K. With a further increase in T_{an} in the temperature interval 500 − 650 K ρ decreases to $\cong 12\ \mu\Omega \cdot \mathrm{cm}$. This value is characteristic of polycrystalline cobalt films.

The TCR has also been investigated on Co films in the temperature range 300–77 K. The results are summarized in Table I. These data show that the resistivity depends weakly on the thickness and temperature over a wide range of thicknesses. Control measurements to helium temperatures give the same values of the TRC. These experiments indicate that the character of the carriers does not change and that the variation of the resistance is associated with structural transformation.

The temperature dependence of the magnetization (I_s) and the coercive force has also been investigated. In the as-prepared state the films are magnetic, with the magnetization measured at $T = 300$ K — approximately 800 G, which is much lower than the magnetization of bulk Co. The degree of stability of this equilibrium state of cobalt could be determined from temperature analyses during both the preparation and the annealing of the films.

Figure 3 shows the results of such measurements for films prepared at various temperatures and on various substrates. The substrates were changed to test the influence of their crystalline nature on the magnetic state of the prepared films. It is evident from Fig. 3 that films obtained at room temperature are magnetic, but their magnetization is much lower than that of pure cobalt. An increase in the substrate heating temperature during preparation lowered the value of I_s on glass substrates, caused it to vanish altogether on MgO substrates, and reduced it almost to zero on mica substrates. Raising the substrate temperature above 500 K increased the saturation magnetization, and at $T_n \geqslant 570$ K the magnetization of the films corresponded to the value of I_s for bulk polycrystalline cobalt. The very complex behavior of the

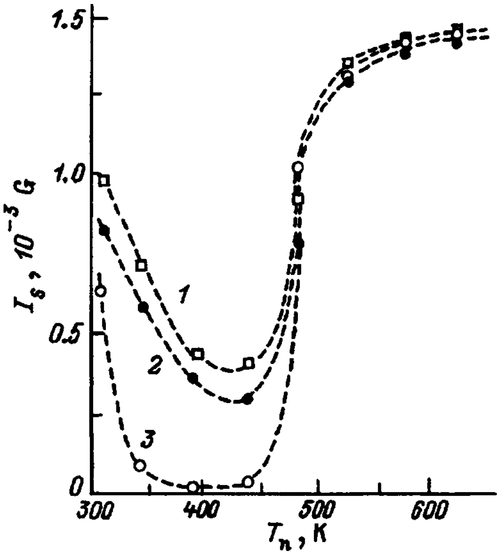

FIG. 3. Influence of substrate temperature during preparation on the magnetization I_s of cobalt films deposited on various substrates: *1*) glass; *2*) MgO single crystals; *3*) mica.

magnetization is evidence of complex structural transformations in the samples under the influence of temperature.

Anomalies in the behavior of the saturation magnetization as the substrate heating temperature is varied during film preparation have been determined from an analysis of the curve representing I_s as a function of the anneal temperature for a specially selected sample of nonequilibrium cobalt. The film in the as-prepared state had a magnetization of 850 G, which is much lower in absolute value than the magnetization of bulk Co. The film was annealed incrementally in 50-K steps for one hour at each fixed temperature in a vacuum of 10^{-5} Torr. The results of the experiment are shown in Fig. 4. It is evident from this figure that I_s decreases almost to zero as T_{an} is increased approximately to 500 K. A further increase in the temperature causes the magnetization to increase almost to the characteristic value for bulk Co (1460 K).

An analysis of the measurements of the magnetic properties has shown that a Co film prepared in the presence of ultrafast condensation has a minimum of three different states, depending on the degree of influence of the temperature both as the condensate is formed during growth and as it is modified during annealing: 1) The film is ferromagnetic, but the saturation magnetization is approximately one third the value in bulk samples; 2) the magnetization of the film is lower than in the first state or is even close to zero; 3) the film has the magnetization of bulk cobalt.

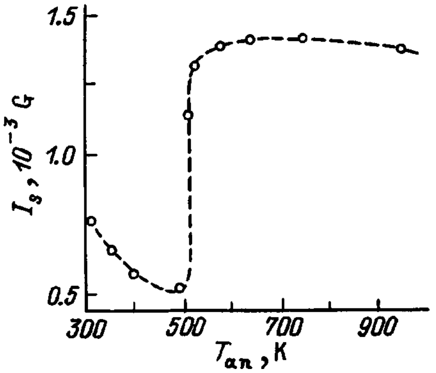

FIG. 4. Influence of high-temperature annealing on the saturation magnetization of a Co film.

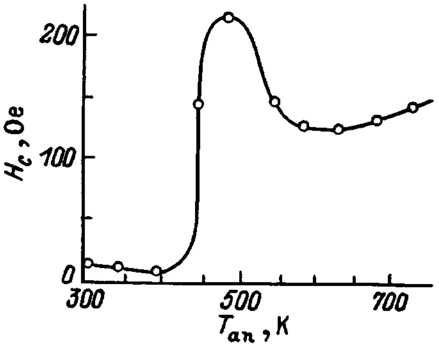

FIG. 5. Influence of high-temperature annealing on the coercive force of a Co film prepared by pulsed plasma deposition on a glass substrate at room temperature.

The coercive force of the investigated films also exhibits a strong temperature dependence. It is evident from Fig. 5 that the variations of H_c take place in the same temperature intervals as in the case of ρ and I_s.

3. DISCUSSION OF THE RESULTS

The reported experimental measurements of the magnetic and electrical properties demonstrate their extraordinary behavior both in the as-prepared state and under the influence of temperature. On the whole, the anomalies of both the magnetic and the electrical properties are associated with the same temperature intervals, and the facts of their temperature dependence and irreversibility attest to structural phase transformations. As shown above, in the as-prepared state the structure is associated with the ultradisperse state and comprises a set of microclusters having a diameter of 20–30 Å. The electron diffraction patterns recorded from samples in the as-prepared state show a diffuse halo typical of the amorphous or ultradisperse state (Fig. 6a). Consequently, the sum-total of our structural measurements along with the measured magnetic and electrical properties show that the as-prepared films exist in a nonequilibrium state and have a microcluster structure.

The current literature contains abundant descriptions of preparation techniques the properties of microclusters of 3*d* metals as well as films having a microcluster structure.[6–8] More often than not cluster technology is largely associated with the application of cluster beams, which are the simplest to create in the case of a freely flowing gas or vapor by sputtering in vacuum. In this case the cluster emerges as an intermediate phase between the gaseous and condensed states. Clusters are efficiently generated under nonequilibrium conditions by converting the gas or vapor into clusters. All cluster generation methods are based on vapor formation, i.e., they utilize the phenomenon of cluster formation from supersaturated vapor as a result of its expansion in a low-pressure region (vacuum). The cooling of the vapor-plasma

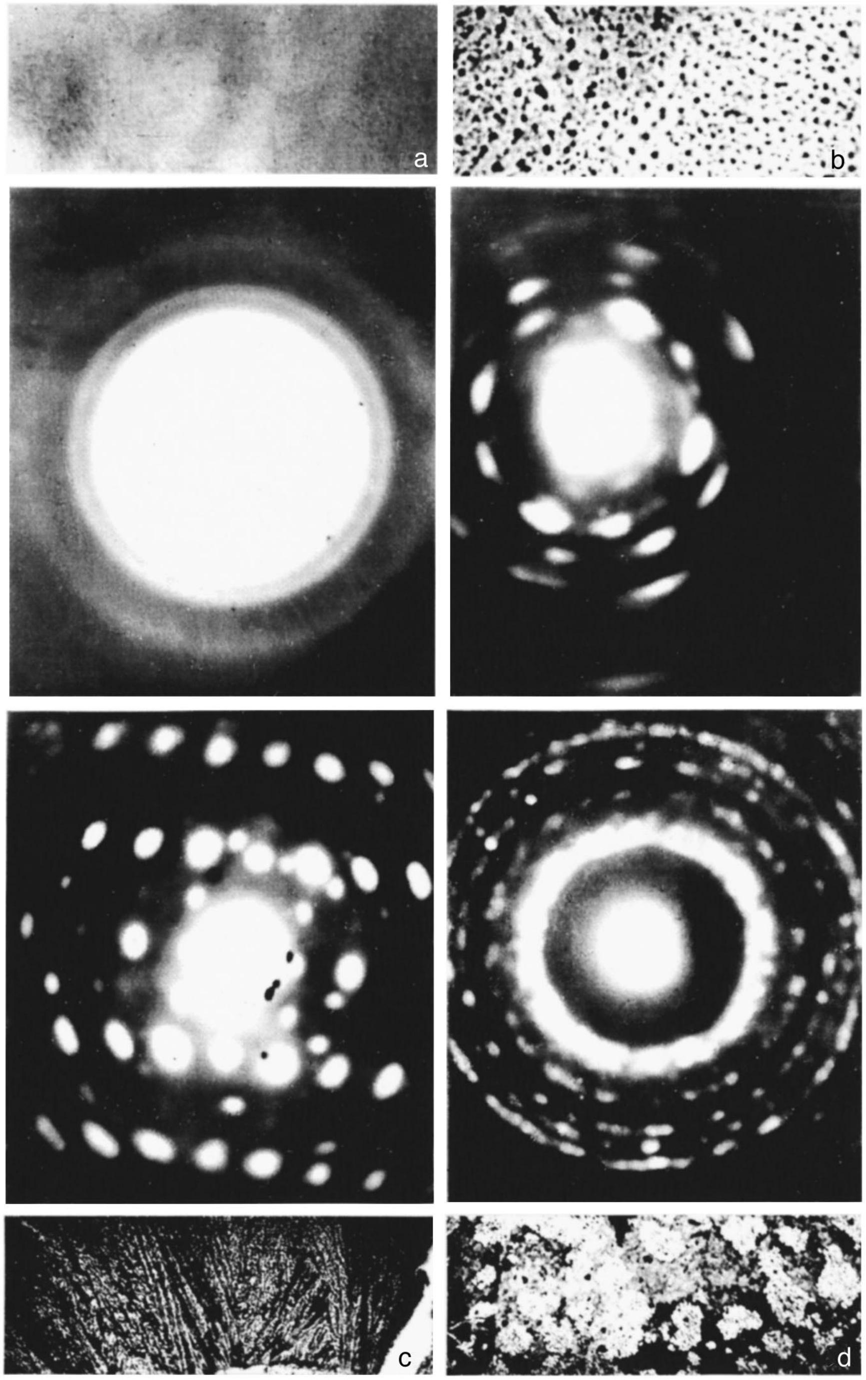

FIG. 6. Results of electron microscope analysis of Co films subjected to various heat treatments. a) Film as prepared at room temperature; b–d) after anneals at: b) 400 K; c) 480 K; d) 650 K. Magnification in the photomicrograph fragments: ×20 000.

mixture during expansion leads to the formation of clusters. Consequently, the most efficient method for the generation of cluster beams is laser evaporation, owing to the high specific surface temperature involved.[4]

The sample preparation technology used by us mainly has the same attributes as those described in the literature and used extensively for the production of cluster beams. However, when films prepared by these technologies are built up from low-energy cluster beams (neutral or unaccelerated), they are similar to ordinary films grown by thermal evaporation. In this case, since the beam has low energy (less than 1 eV/atom), a cluster sticks to the grown film, and its atoms spread out over the surface.[4] In our case a high-energy efficiency of the vapor-plasma mixture is maintained by an applied electric field of 500 V.

Microclusters (including those in films) are preserved if they are separated or exist in a special closed state (as in the case of fullerenes or fullerenelike formations). Since a high specific surface and high reactivity are distinguishing features of clusters, microclusters can be contained in a shell of carbon or nitrogen atoms inherent in a residual vacuum atmosphere.

To test this hypothesis, we have used Auger electron spectroscopy to analyze the chemical composition of cobalt films prepared by PPD. Figure 7 shows the Auger profile of the depthwise distribution of elements in the sample. The

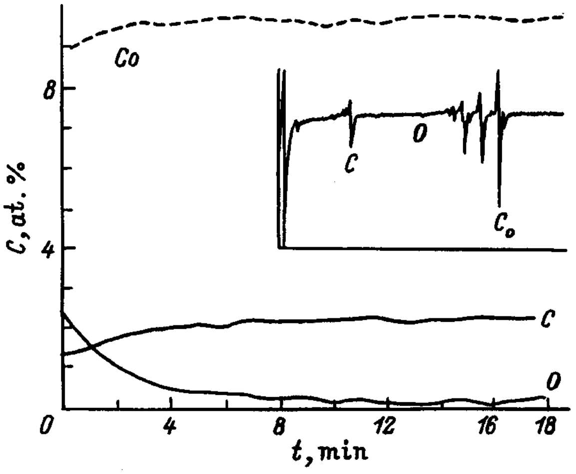

FIG. 7. Auger spectrum of the distribution of elements along the depth of a sample. Inset: panoramic spectrum of the film surface after layer-profiling analysis.

results of estimating the element concentrations with allowance for the element sensitivity factors are shown in Table II. The data in the second row of the table have been obtained for a sample previously etched with an Ar^+ ion beam to the entire measurement depth.

The results of this investigation reveal an extraordinarily high carbon content (more than 30 at. %) in the film. In conventional thermal methods of film preparation in a vacuum of the order of 10^{-6} Torr the carbon content does not exceed 3–4 at. %, and the oxygen content is approximately four times higher than in our case. Such a high C content is clearly associated with the specifics of the PPD method. We can assume that carbon ions are trapped both during the transit time of atoms of the deposited material to the substrate by virtue of the high degree of ionization of the vapor and also during condensate formation as a result of the long spacing between deposition pulses.

Proceeding from the sum-total of data on the magnetic and electrical properties and from structural and spectral measurements, we can assume that the resulting condensate comprises cobalt clusters surrounded by a kind of carbon ''overcoat.'' A substantial transformation of the electron structure can be expected in such structural formations, conducive to variations of the magnetization and other properties.

Figure 6 shows electron diffraction patterns with insets of fragments of photomicrographs of cobalt films subjected to various degrees of heat treatment. Figure 6a shows an electron diffraction pattern of the original film as prepared without preheating of the substrate. The film is x-ray amorphous. Heating to 400 K already produces reflections of the newly formed phase against the background of halo rings (Fig. 6b). It is important to note that the positions of these reflections is confined to the width of the halo rings. Annealing at a temperature of 450–475 K produces a specific electron diffraction pattern of single-crystal reflections (Fig. 6c). The displayed diffraction pattern is one of three typical patterns obtained with dendrites of different configurations and crystallographic orientations. A series of such diffraction patterns has enabled us to calculate the possible structural type of the microclusters. The microstructure of the films is a network of dendrites (Fig. 6c) growing out from the crystallization centers.[9] The crystallization itself exhibits all the signs of an explosive process. Finally, after annealing at 600–650 K the electron diffraction pattern has a series of rings typical of hcp Co. The photomicrograph in this case shows that the nonequilibrium dendritic structure has disintegrated, and the film is now becoming polycrystalline (Fig. 6d).

TABLE II. Element concentrations, calculated with allowance for the element sensitivity factor, on the as-prepared surface and after Ar^+ ion-beam etching to a depth of 150 Å.

Surface	S	Cl	Ar	C	N	O	Co	Na
As-prepared	0.004	0.023	–	0.235	–	0.316	0.422	–
After Ar^+ etch	–	–	0.005	0.304	–	0.009	0.680	–

In several earlier papers we have already investigated the possible structural type of newly formed microclusters.[9–11] A film in the as-prepared state consists of a highly disordered system of microclusters classified as one of the stable nanostructures. It has been substantiated theoretically and experimentally that the most stable structures in the range of dimensions $\leqslant 30$ Å are the octahedron and the cuboctahedron. The rigorous description of the stable structure of certain metal clusters yields the well-known jellium model, or shell model,[3] where metal clusters are regarded as giant macroatoms with electron energy levels that exhibit a shell structure. Because of its high reactivity, such a system can in orderly fashion incorporate carbon atoms, which can reside inside the cluster and also form outer shells. Corroboration for this kind of model can be found in the high carbon concentration actually encountered in our films and in data on the structure of capsulated 3*d* metals.[6,7]

If we assume that the octahedron is the smallest block in a cuboctahedron and take account of the fact that some of the carbon atoms in the system form a carbide configuration, we can then understand the reduced magnetization, high resistivity, zero TCR, and other physical properties of Co films. The initial anneal leads to structural quasiordering of the initially disordered system of microclusters. The possible type of crystallization is the previously observed[12,13] and theoretically calculated ''quasimelting'' mechanism, when the structural blocks, or microclusters, ostensibly rotate about one another under the influence of not too high temperatures of 450–470 K, forming long, drawn-out dendrites. This process occurs within short time periods and resembles explosive crystallization. ''Building blocks'' (microclusters) of these dendrites are genetically assimilated into the initial condensates. This ordering process promotes a further reduction in the magnetization and in some cases causes it to disappear altogether (Fig. 3), and at the same time it has the effect of almost doubling the electrical conductivity (Figs. 2a and 2b).

After high-temperature (above 550–600 K) annealing the film structure relaxes to equilibrium, accompanied by disintegration of the microcluster system, and the saturation magnetization increases to the value inherent in bulk cobalt. Now the film also exhibits all the electrical properties similar to those of a polycrystalline cobalt film.

The authors are deeply indebted to V. G. Myagkov, S. M. Zharkov, and G. V. Bondarenko for invaluable help in carrying out some of the experiments and for suggestions offered in a discussion of the work. We express our gratitude to V. G. Kesler on the staff of the Institute of Semiconductor Physics of the Siberian Branch of the Russian Academy of Sciences for studies conducted on Auger spectroscopy of the cobalt samples.

[1] Yu. E. Lozovik and A. M. Popov, Usp. Fiz. Nauk **167**, 751 (1997).
[2] M. Morse, Chem. Rev. **86**, 1049 (1986).
[3] M. Cohen and W. Knight, Phys. Today **12**, 42 (1990).
[4] B. M. Smirnov, Usp. Fiz. Nauk **167**, 1169 (1997).
[5] G. I. Frolov, V. S. Zhigalov, S. M. Zharkov, and I. R. Yarullin, Fiz. Tverd. Tela (St. Petersburg) **36**, 970 (1994) [Phys. Solid State **36**, 526 (1994)].
[6] Y. Yosida, S. Shida, and T. Ohsuna, J. Appl. Phys. **76**, 4533 (1994).
[7] Y. Saito, T. Yoshikawa, M. Okuda, N. Fujimoto, S. Yamamuro, K. Wakoh, K. Simiyama, K. Suzuki, and A. Kasuya, J. Appl. Phys. **75**, 134 (1994).
[8] Y. Yosida, S. Shida, and N. Ohsuna, J. Appl. Phys. **76**, 4533 (1994).
[9] G. I. Frolov, O. A. Bayukov, V. S. Zhigalov, L. I. Kveglis, and V. G. Myagkov, JETP Lett. **61**, 63 (1995).
[10] S. M. Zharkov, V. S. Zhigalov, L. I. Kveglis, Yu. V. Lisitsa, K. V. Renskaya, and G. I. Frolov, JETP Lett. **65**, 915 (1997).
[11] G. I. Frolov, V. S. Zhigalov, A. I. Pol'skiĭ, and V. G. Pozdnyakov, Fiz. Tverd. Tela (St. Petersburg) **38**, 1208 (1996) [Phys. Solid State **38**, 668 (1996)].
[12] R. M. Ajayan and L. D. Marks, Phys. Rev. Lett. **7**, 585 (1988).
[13] R. M. Ajayan and L. D. Marks, Phys. Rev. Lett. **3**, 279 (1989).

Translated by James S. Wood

Nonlinear interactions of acoustic modes in ferromagnets near magnetoacoustic resonance: effective elastic constants

I. F. Mirsaev

Institute of Metal Physics, Ural Branch of the Russian Academy of Sciences, 620219 Ekaterinburg, Russia

(Submitted April 21, 1998)
Fiz. Tverd. Tela (St. Petersburg) **40**, 2080–2084 (November 1998)

The magnetoelastic contribution $\Delta\hat{C}_{(3)}$ to the effective third-order elastic constants $\hat{C}^{\text{ef}}_{(3)}$ is determined; it describes the additional elastic anharmonicity induced by nonlinear spin-spin and spin-phonon interactions in ferromagnets. In the vicinity of magnetoacoustic resonance, this anharmonicity can be manifested in three-frequency elastic wave interactions, producing magnetoacoustic mode-frequency transformation effects. It is shown that these effects are magnified in resonance as the result of a huge increase (by several orders of magnitude) in the dynamic elastic constants $\Delta\hat{C}_{(3)}$. Quantitative estimates are obtained for yttrium iron garnet.
[S1063-7834(98)02511-8]

The existence of coupled magnetoelastic modes in ferromagnets and antiferromagnets alters their elastic constants. These changes are described by the dynamic magnetoelastic contribution $\Delta\hat{C}$ to the effective elastic constants $\hat{C}\rightarrow\hat{C}^{\text{ef}}=\hat{C}+\Delta\hat{C}$ and are manifested in various magnetoacoustic phenomena.[1–11] In particular, the Faraday and Voigt (or Cotton–Mouton) effects are associated with the second-order constants $\Delta\hat{C}_{(2)}$ (Refs. 3,6, and 8), and various nonlinear effects such as stimulated Raman scattering and acoustic second-harmonic generation are associated with the third-order constants $\Delta\hat{C}_{(3)}$ (Refs. 1,2,7,9–11).

The dynamic constants $\Delta\hat{C}$ in an antiferromagnet are caused by oscillations of the antiferromagnetism vector **L**. Intersublattice exchange interaction enhances the magnetoelastic coupling of these oscillations with elastic strains, inducing giant anharmonicity[1] $\Delta\hat{C}_{(3)}\approx(10^3-10^4)\hat{C}_{(2)}$.

Exchange enhancement does not occur in a ferromagnet. However, strong magnon-phonon coupling can occur in them as a result of magnetoacoustic resonance, which is observed at a wave frequency $\omega\approx\omega_S$, where ω_S is the natural frequency of spin oscillations.

We note that the resonance excitation of spin modes is impeded in an antiferromagnet, because the antiferromagnetic resonance frequency ω_{AFMR} is much higher than the frequency ($\omega_{\text{AFMR}}\gg\omega$) of acoustic waves used in experiments.

In this paper we investigate nonlinear interactions of acoustic waves in a ferromagnet in the vicinity of magnetoacoustic resonance, where spin modes participating in spin-spin and spin-phonon interactions generate additional elastic anharmonicity. The values of the anharmonic constants $\Delta\hat{C}_{(3)}$ at resonance can be several orders of magnitude greater than the lattice nonlinearity of the crystal, thereby ensuring the experimental observability of nonlinear magnetoacoustic phenomena, for example, the magnetoelastic generation of the second harmonic of traveling acoustic waves.[9–11]

1. EQUATIONS OF MOTION

We consider an elastic displacement (**u**) wave and, coupled with it, oscillations of the magnetization $\boldsymbol{\mu}$ (per unit mass) in a ferromagnet magnetized to saturation: $|\boldsymbol{\mu}|=\mu_0=\text{const}$. We adopt Lagrangian coordinates a_i as our independent variables. In this case the equations of motion have the form[12,13]

$$\dot{\mu}_i=-\gamma[\boldsymbol{\mu}\cdot\mathbf{H}^{\text{ef}}]_i, \tag{1}$$

$$\rho_0\ddot{u}_i=\frac{\partial\tau_{ik}}{\partial a_k}+\rho_0\mu_n\frac{\partial H_n}{\partial a_k}\frac{\partial a_k}{\partial x_i}. \tag{2}$$

Here γ is the magnetomechanical ratio, ρ_0 is the mass density before deformation, $\mathbf{H}^{\text{ef}}$ and τ_{ik} are the effective magnetic field and the Piola–Kirchoff stress tensor,

$$H^{\text{ef}}_k=H_k-\frac{\partial F}{\partial\mu_k}+\frac{\partial}{\partial a_S}\frac{\partial F}{\partial(\partial\mu_k/\partial a_S)}, \tag{3}$$

$$\tau_{ik}=\rho_0\frac{\partial F}{\partial\eta_{kp}}\frac{\partial x_i}{\partial a_p}, \tag{4}$$

F is the potential energy per unit mass of the ferromagnet, x_i denotes the Eulerian coordinates, $H_i=H^0_i+h_i$, H^0_i is the internal field, **h** is the magnetostatic field, which is defined by the equations

$$\text{curl}\,\mathbf{h}=0,\quad \text{div}(\mathbf{h}+4\pi\rho\boldsymbol{\mu})=0, \tag{5}$$

$\rho\approx\rho_0(1-\eta_{ii})$ is the mass density after deformation, η_{ik} is the strain tensor,

$$\eta_{ik}=(u_{ik}+u_{ki}+u_{is}u_{ks})/2, \tag{6}$$

$u_{ik}=\partial u_k/\partial a_i$ is the distortion tensor, and $u_i=x_i-a_i$.

The magnetostatic equations (5) are written in Eulerian coordinates. They can be transformed to Lagrangian coordinates by the substitution

$$\frac{\partial}{\partial x_i}=\frac{\partial a_k}{\partial x_i}\frac{\partial}{\partial a_k},\quad \frac{\partial a_k}{\partial x_i}\approx\delta_{ik}-u_{ik}. \tag{7}$$

We consider magnetoelastic waves propagating in one direction. According to Eqs. (5) and (7), the magnetostatic field **h** generated by these waves is

$$h_i = -4\pi\rho n_i n_k \mu_k = -4\pi\rho_0 n_i n_k \mu_k (1-\eta_{ss}). \tag{8}$$

Here **n** is the unit vector in the direction of wave propagation.

Looking at nonlinear magnetoelastic interactions, we write the potential energy $\rho_0 F$ per unit volume of the crystal in the form

$$\rho_0 F = \rho_0 F(0) + K_{ij}\alpha_i\alpha_j + K_{ijkl}\alpha_i\alpha_j\alpha_k\alpha_l + b_{ijkl}\eta_{ij}\alpha_k\alpha_l + \lambda_{ij}\frac{\partial\alpha_s}{\partial a_i}\frac{\partial\alpha_s}{\partial a_j} + \frac{1}{2}C_{ijkl}\eta_{ij}\eta_{kl} + \frac{1}{6}C_{ijklmn}\eta_{ij}\eta_{kl}\eta_{mn}. \tag{9}$$

In Eq. (9) $\alpha_j = \mu_i/\mu_0$, K_{ij} and K_{ijkl} are the magnetic anisotropy constants, b_{ijkl} are the magnetoelastic constants, λ_{ij} are the inhomogeneous exchange constants, and C_{ijkl} and C_{ijklmn} are the second-order and third-order elastic constants.

2. AMPLITUDES OF COUPLED MODES

We now turn our attention to determining the magnetoelastic coupling between the spin and elastic wave amplitudes. A practical approach is to assign $\alpha_i = \alpha_i^0 + \tilde{\alpha}_i$ to a primed coordinate system $\{\alpha_\beta\}$ $(\beta, \gamma, \mu = 1', 2', 3')$, in which the third axis a_3 is parallel to the equilibrium magnetization $\boldsymbol{\mu}_0$. Here $\tilde{\alpha}_i$ is the deviation of the direction cosines from the equilibrium values α_i^0. In this coordinate system $\alpha_\beta^0 = \delta_{\beta 3'}$, and $\tilde{\alpha}_\beta = Q_{k\beta}\tilde{\alpha}_k$ (and, conversely, $\tilde{\alpha}_k = Q_{k\beta}\tilde{\alpha}_\beta$), where $Q_{k\beta}$ is the rotation matrix corresponding to the coordinate transformation. From the condition $|\boldsymbol{\mu}| = |\boldsymbol{\mu}_0| = \mu_0$ we deduce the relation $\tilde{\alpha}_{3'} = -(\tilde{\alpha}_{1'}^2 + \tilde{\alpha}_{2'}^2)/2$, which permits the quantities $\tilde{\alpha}_{1'}$ and $\tilde{\alpha}_{2'}$ to be adopted as independent variables.

Using Eq. (9) in the expression for the effective field $\mathbf{H}^{\mathrm{ef}}$ (3) and limiting the result to the quadratic approximation, we obtain

$$\mathbf{H}^{\mathrm{ef}} = \mathbf{H}_0^{\mathrm{ef}} + \tilde{\mathbf{H}}^{\mathrm{ef}}, \quad \tilde{\mathbf{H}}^{\mathrm{ef}} = \tilde{\mathbf{H}}^L + \tilde{\mathbf{H}}^{NL},$$

$$H_{0\beta}^{\mathrm{ef}} = H_\beta^0 - \frac{2}{M_0}(K_{\beta\gamma} + 2K_{\beta\gamma\mu\nu}\alpha_\mu^0\alpha_\nu^0)\alpha_\gamma^0,$$

$$\tilde{H}_\beta^L = -\chi_{\beta\gamma}\tilde{\alpha}_\gamma - B_{kl\beta}\eta_{kl} + \nu_{kl}\frac{\partial^2\tilde{\alpha}_\beta}{\partial a_k \partial a_l},$$

$$\tilde{H}_\beta^{NL} = -\chi_{\beta\gamma\mu}\tilde{\alpha}_\gamma\tilde{\alpha}_\mu - B_{kl\gamma\beta}\eta_{kl}\tilde{\alpha}_\gamma, \tag{10}$$

where $\mathbf{H}^{\mathrm{ef}}$ is the static part, and $\tilde{\mathbf{H}}^L$ and $\tilde{\mathbf{H}}^{NL}$ are the dynamic parts of the effective field evaluated in the linear (L) and nonlinear (NL) approximations; $M_0 = \rho_0\mu_0$ is the magnetization per unit volume; $\hat{\chi}$ and $\hat{\beta}$ are tensors that take into account the renormalization of the anisotropy and magnetoelastic constants due to the magnetostatic field **h** (8),

$$\chi_{\beta\gamma} = \frac{2}{M_0}(K_{\beta\gamma} + 6K_{\beta\gamma\mu\nu}\alpha_\mu^0\alpha_\nu^0) + 4\pi M_0 n_\beta n_\gamma,$$

$$\chi_{\beta\gamma\mu} = \left(\frac{12}{M_0}K_{\beta\gamma\mu\nu} - \frac{1}{2}\chi_{\beta\nu}\delta_{\gamma\mu}\right)\alpha_\nu^0,$$

$$B_{kl\beta\gamma} = \frac{2}{M_0}(b_{kl\beta\gamma} - 2\pi M_0^2 n_\beta n_\gamma \delta_{kl}),$$

$$B_{kl\beta} = B_{kl\beta\gamma}\alpha_\gamma^0, \quad \nu_{kl} = 2\lambda_{kl}/M_0. \tag{11}$$

Spontaneous statistical strains $\tilde{\eta}_0 \sim M_0$, which lead to insignificant renormalization of the magnetic anisotropy constants, are ignored in Eqs. (10).

We assume that $\tilde{\alpha}_i$ and η_{ij} vary according to the law $\exp\{i(\mathbf{k}\cdot\mathbf{a} - \omega t\}$, where ω and $\mathbf{k}$ are the frequency and wave vector of the magnetoelastic mode. Using expressions (10) in Eqs. (1), in the linear approximation we obtain

$$\tilde{\alpha}_\beta^L = -L_{\beta\gamma}(\omega)H_\gamma^{me}a_{\beta kl}(\omega)\eta_{kl}, \quad \beta, \gamma = 1', 2', \tag{12}$$

where $H_\gamma^{me} = -B_{kl\gamma}\eta_{kl}$ is the effective magnetoelastic field, $a_{\beta kl}$ is the magnetoelastic coupling tensor,

$$a_{\beta kl}(\omega) = L_{\beta\gamma}(\omega)B_{kl\gamma},$$

$$L_{1'1'} = \gamma^2 D(\omega)h_{1'1'}, \quad L_{2'2} = \gamma^2 D(\omega)h_{2'2'},$$

$$L_{1'2'} = \gamma D(\omega)(\gamma h_{1'2'} - i\omega),$$

$$L_{2'1'} = L_{1'2'}^* = \gamma D(\omega)(\gamma h_{1'2'} + i\omega). \tag{13}$$

Here we have introduced the notation

$$h_{1'1'} = H_{03'}^{\mathrm{ef}} + \chi_{2'2'} + \nu_{pq}k_p k_q,$$

$$h_{2'2'} = H_{03'}^{\mathrm{ef}} + \chi_{1'1'} + \nu_{pq}k_p k_q,$$

$$h_{1'2'} = h_{1'1'} = -\chi_{1'2'}, \quad D(\omega) = [\omega^2 - \omega_S^2(k)]^{-1},$$

$$\omega_S^2(k) = \gamma^2(h_{1'1'}h_{2'2'} - h_{1'2'}^2), \tag{14}$$

where ω_S is the natural frequency of the spin mode, and $D(\omega)$ is a factor characterizing the resonance nature of the interaction of spin and elastic waves.

In the investigation of nonlinear magnetoacoustic phenomena it is necessary to know the nonlinear dependence of $\tilde{\alpha}$ on η_{ik}. It can be determined by successive approximations, using the linear magnetoelastic coupling (12) in the nonlinear part of the effective field $\tilde{\mathbf{H}}^{NL}$ (10). In this approximation

$$\tilde{\alpha}_\beta^{NL} = -L_{\beta\gamma}(\omega)(H_{me}^{NL}(\omega))_\gamma, \tag{15}$$

where $\mathbf{H}_{me}^{NL}(\omega)$ is the Fourier representation of the effective magnetoelastic field,

$$\mathbf{H}_{me}^{NL} = \tilde{\mathbf{H}}^{NL} - \tilde{\boldsymbol{\alpha}}^L \tilde{H}_{3'}^L, \tag{16}$$

due to nonlinear spin-spin and spin-phonon interactions. According to Eqs. (10), we have

$$(H_{me}^{NL})_\gamma = -\tilde{\chi}_{\gamma\mu\nu}\tilde{\alpha}_\mu^L\tilde{\alpha}_\nu^L - \tilde{B}_{kl\mu\gamma}\eta_{kl}\tilde{\alpha}_\mu^L,$$

$$\tilde{\chi}_{\gamma\mu\nu} = \chi_{\gamma\mu\nu} - \frac{1}{2}(\chi_{\mu\beta}\delta_{\gamma\nu} + \chi_{\nu\beta}\delta_{\gamma\mu})\alpha_\beta^0,$$

$$\tilde{B}_{kl\mu\gamma} = B_{kl\mu\gamma} - B_{kl\beta}\alpha_\beta^0\delta_{\mu\gamma}. \tag{17}$$

By virtue of the magnetoelastic coupling (12) the field $\mathbf{H}_{me}^{NL}$ is a quadratic function of the strain tensor.

3. DYNAMIC SECOND-ORDER ELASTIC CONSTANTS

The equations of motion (2) for the elastic displacement **u** can be written as follows on the basis of Eqs. (9) and (8):

$$\rho_0 \ddot{u}_i = \frac{\partial \sigma_{ij}}{\partial a_j}, \tag{18}$$

where σ_{ij} is the stress tensor.[12] In the quadratic approximation

$$\sigma_{ij} = C_{ijkl}\eta_{kl} + C_{jpkl}\eta_{kl}u_{pi} + \frac{1}{2}C_{ijklmn}\eta_{kl}\eta_{mn}$$
$$+ M_0 B_{ij\beta}\tilde{\alpha}_\beta + \frac{1}{2}M_0\tilde{B}_{ij\beta\gamma}\tilde{\alpha}_\beta\tilde{\alpha}_\gamma. \tag{19}$$

In the derivation of Eq. (19) it has been assumed that the amplitude of the spin mode $|\tilde{\alpha}|$ and the values of the elastic constants $|\tilde{C}|$ satisfy the relations

$$|\tilde{\alpha}| \gg |\hat{\eta}|, \quad |\hat{C}| \gg 4\pi M_0^2.$$

Using the magnetoelastic coupling (12) and the expression for $\hat{\eta}$ (6) in Eq. (19), we write the linear part of the tensor $\hat{\sigma}$ in the form

$$\sigma_{ij}^L = C_{ijkl}^{\text{ef}} u_{kl}, \quad C_{ijkl}^{\text{ef}} = C_{ijkl} + \Delta C_{ijkl},$$
$$\Delta C_{ijkl}(\omega) = M_0 B_{ij\beta} a_{\beta kl}(\omega) M_0 L_{\beta\gamma}(\omega) B_{ij\beta} B_{kl\gamma}, \tag{20}$$

where C_{ijkl}^{ef} is the tensor of effective second-order elastic constants, and ΔC_{ijkl} are the dynamic elastic constants induced the by magnetoelastic interaction of spin and elastic waves whose amplitudes are related by Eq. (12).

Taking the explicit form of the tensors $L_{\beta\gamma}$ (13) into account, we can separate the symmetric (s) and antisymmetric (a) parts of the tensor $\Delta\hat{C}$:

$$\Delta C_{ijkl} = \Delta C_{ijkl}^s + \Delta C_{ijkl}^a,$$
$$\Delta C_{ijkl}^s = \gamma^2 M_0 D(\omega) h_{\alpha\beta} B_{ij\alpha} B_{kl\beta},$$
$$\Delta C_{ijkl}^a = -i\omega\gamma M_0 D(\omega)(B_{ij1'}B_{kl2'} - B_{kl1'}B_{ij2'}), \tag{21}$$

where $\hat{B}$, $\hat{h}$, and $D(\omega)$ are the quantities defined in Eqs. (11) and (14).

4. FREQUENCY MIXING EFFECTS

A quadratic dependence of the stress tensor σ_{ij} (19) on the distortion tensor u_{pq} corresponds to the lowest-order elastic anharmonicity. This type of nonlinear dependence leads to the mixing of acoustic frequencies,[14] specifically: The interaction of two modes with frequencies ω_1 and ω_2 results in the formation of nonlinear waves with combination frequencies $\omega_1 \pm \omega_2$ or a doubled frequency $2\omega_1$ or $2\omega_2$. Each of these effects corresponds to a certain value of the tensor σ_{ij} (19). To determine these values, we write the elastic displacement **u** and the variable $\tilde{\alpha}_i$ as sums of three modes:

$$\tilde{\alpha}_\beta = \frac{1}{2}\sum_{n=1}^{3}(\tilde{\alpha}_\beta(\omega_n) + \text{c.c.}),$$
$$\tilde{\alpha}_\beta(\omega_n) = \tilde{\alpha}_\beta^{(n)} \exp\{i(\mathbf{k}^{(n)}\cdot\mathbf{a} - \omega_n t)\},$$
$$u_i = \frac{1}{2}\sum_{n=1}^{3}(u_i(\omega_n) + \text{c.c.}),$$
$$u_i(\omega_n) = u_i^{(n)} \exp\{i(\mathbf{k}^{(n)}\cdot\mathbf{a} - \omega_n t)\}, \tag{22}$$

where $\mathbf{k}^{(n)}$ is the wave vector of the magnetoelastic mode at the frequency ω_n.

We first consider the three-frequency processes

$$\omega_1 + \omega_2 = \omega_3, \tag{23}$$

for which the equations of motion (18) acquire the form

$$\rho_0 \ddot{u}_i(\omega_n) = C_{ijkl}^{\text{ef}}(\omega_n)\frac{\partial u_{kl}(\omega_n)}{\partial a_j} + \frac{\partial \sigma_{ij}^{NL}(\omega_n)}{\partial a_j}. \tag{24}$$

Here $\sigma_{ij}^{NL}(\omega_n)$ is the nonlinear part of the tensor σ_{ij}, corresponding to the frequency ω_n $(n=1,2,3)$. Taking the magnetoelastic coupling (12), (15) and relations (22) into account in Eq. (19), we have

$$\sigma_{ij}^{NL}(\omega_1) = \frac{1}{2}C_{ijklmn}^{\text{ef}}(\omega_1;\omega_3,-\omega_2)u_{kl}(\omega_3)u_{mn}^*(\omega_2),$$
$$\sigma_{ij}^{NL}(\omega_2) = \frac{1}{2}C_{ijklmn}^{\text{ef}}(\omega_2;\omega_3,-\omega_1)u_{kl}(\omega_3)u_{mn}^*(\omega_1),$$
$$\sigma_{ij}^{NL}(\omega_3) = \frac{1}{2}C_{ijklmn}^{\text{ef}}(\omega_3;\omega_1,\omega_2)u_{kl}(\omega_1)u_{mn}(\omega_2), \tag{25}$$

where $C_{ijklmn}^{\text{ef}}(\omega_3;\,\omega_1,\,\omega_2)$ are effective third-order elastic constants describing the generation of magnetoelastic waves with the sum frequency $\omega_3 = \omega_1 + \omega_2$ as a result of the nonlinear interaction of pump waves with frequencies ω_1 and ω_2. The constants $C_{ijklmn}^{\text{ef}}(\omega_1;\,\omega_3,\,-\omega_2)$ and $C_{ijklmn}^{\text{ef}}(\omega_2;\,\omega_3,\,-\omega_1)$ describe the feedback effect of the generated wave on the pump waves.

The effective elastic constants $\hat{C}^{\text{ef}}$ contain an elastic part and a magnetic part:

$$C_{ijklmn}^{\text{ef}}(\omega_n;\omega_p,\omega_q)\tilde{C}_{ijklmn} + \Delta C_{ijklmn}(\omega_n;\omega_p,\omega_q),$$
$$\tilde{C}_{ijklmn} = C_{ijklmn} + C_{ijkm}\delta_{ln} + C_{jmkl}\delta_{in} + C_{jkmn}\delta_{il},$$
$$\Delta C_{ijklmn}(\omega_n;\omega_p,\omega_q) = M_0\tilde{B}_{ij\beta\gamma}a_{\beta kl}(\omega_p)a_{\gamma mn}(\omega_q)$$
$$+ M_0 a_{\alpha ij}^*(\omega_n)\{2\tilde{\chi}_{\alpha\beta\gamma}a_{\beta kl}$$
$$\times(\omega_p)a_{\gamma mn}(\omega_q) + \tilde{B}_{kl\alpha\beta}a_{\beta mn}(\omega_q)$$
$$+ \tilde{B}_{mn\alpha\beta}a_{\beta kl}(\omega_p)\}. \tag{26}$$

In Eqs. (26) $\Delta C_{ijklmn}(\omega_n;\,\omega_p,\,\omega_q)$ are the dynamic third-order elastic constants induced by nonlinear interactions between magnetoelastic modes with frequencies ω_p and ω_q $(p,\,q=1,2,3)$. These frequencies satisfy the law of conservation of energy (23), i.e., $\omega_n = \omega_p + \omega_q$ (e.g., for $\omega_n = \omega_1$, according to (23), we have $\omega_p = \omega_3$ and $\omega_q - \omega_2$ or $\omega_p = -\omega_2$ and $\omega_q = \omega_3$).

The elastic constants ΔC_{ijklmn} are symmetric with respect to permutation within each pair of indices and with respect to the permutations

$$\begin{aligned}\Delta C_{IJR}(\omega_n;\omega_p,\omega_q)&=\Delta C_{IRJ}(\omega_n;\omega_q,\omega_p)\\&=\Delta C_{JIR}(-\omega_p;-\omega_n,\omega_q)\\&=\Delta C_{JRI}(-\omega_p;\omega_q,-\omega_n)\\&=\Delta C_{RIJ}(-\omega_q;-\omega_n,\omega_p)\\&=\Delta C_{RJI}(-\omega_q;\omega_p,-\omega_n).\end{aligned}\tag{27}$$

Here $I\leftrightarrow ij$, $J\leftrightarrow kl$, and $R\leftrightarrow mn$ are the indices in contracted notation: $I, J, R=1,2,\ldots,6$, 1–11, 2–22, 3–33, 4–23, 32, 5–13, 31, 6–12, 21.

So far we have discussed the three-frequency processes $\omega_1+\omega_2=\omega_3$. For processes $\omega_1-\omega_2=\omega_3$ it is necessary to change to the opposite sign of the frequency ω_2 in the expressions for $\sigma_{ij}^{NL}(\omega_n)$ (25) and to allow for the fact that $u_{mn}(-\omega_2)=u_{mn}^{*}(\omega_2)$. In the generation of waves with frequency doubling $(\omega+\omega=2\omega)$ it is required to set $\omega_1=\omega_2=\omega$, $\omega_3=2\omega$ and to replace the factor 1/2 by 1/4 in the expression for $\sigma_{ij}^{NL}(2\omega)$.

5. DISCUSSION OF THE RESULTS

Nonlinear spin-spin and spin-phonon interactions in a ferromagnet impart additional anharmonicity to the crystal. The anharmonicity is reflected in nonlinear interactions of elastic waves and, as a result, magnetoacoustic effects that transform the frequency of these waves. In three-frequency processes of interaction of wave modes with frequencies ω_1 and ω_2 nonlinear waves are generated with combination frequencies $\omega_3=\omega_1\pm\omega_2$ or a doubled frequency $2\omega_1$ or $2\omega_2$. The contribution of magnetoelastic interactions to these processes is described by the dynamic third-order elastic constants $\Delta\hat{C}(\omega_3;\omega_1,\pm\omega_2)$ and $\Delta\hat{C}(2\omega;\omega,\omega)$ (26), which depend on the wave frequencies. This dependence exhibits resonance behavior, $\Delta\hat{C}\sim D(\omega_n)=(\omega_n^2-\omega_S^2)^{-1}$ $(n=1,2,3)$. Resonance is possible at the frequencies of the pump waves ω_1 and ω_2 and also at the frequency of the generated wave $\omega_3=\omega_1\pm\omega_2$.

The values of the dynamic elastic constants $\Delta\hat{C}_{(3)}$ are governed by the magnetoelastic coupling coefficients $a_{\alpha kl}$ (13). Estimates for a spherical yttrium iron garnet (YIG) sample show that in low-frequency magnetoacoustic resonance $(\omega\approx\omega_S\gtrsim 10^8$ Hz) these coefficients can attain values of the order of 10^3-10^4, which in YIG correspond to $\Delta\hat{C}_{(3)}\approx 10^{14}-10^{15}\,\mathrm{N/m^2}$.

The variation of the elastic constants as a result of magnetoelastic interactions is not reducible to simple renormalization of the constants, because the magnetic part $\Delta\hat{C}$ of the tensor of effective elastic constants $\hat{C}^{\mathrm{ef}}$ can have additional components not found in nonmagnetic crystals. These components of the tensor $\Delta\hat{C}_{(3)}$ produce new nonlinear interactions of acoustic modes. For example, the components $\Delta C_{i33k3l}(\omega_n;\omega_p,\omega_q)$ $(i,k,l=1,2)$ appear in a cubic ferromagnet, describing interactions of transverse elastic waves propagating along the edge of the cube $(\mathbf{k}\|\langle 100\rangle\|a_3)$. The explicit form of such constants $\Delta C_{i33k3l}(2\omega;\omega,\omega)$, calculated for $\mathbf{M}_0(0,M_2^0,M_3^0)$, are given in the Appendix. We note that in cubic crystals $C_{i33k3l}=0$ $(i,k,l=1,2)$, so that $C_{i33k3l}^{\mathrm{ef}}=\Delta C_{i33k3l}$.

The dynamic constants $\Delta\hat{C}_{(3)}$ depend strongly on the direction of the magnetization $\mathbf{M}_0$, and this dependence is manifested in the angular dependence of $\Delta C_{i33k3l}(\Theta)$ (A1), where Θ is the angle between the vectors $\mathbf{k}$ and $\mathbf{M}_0$. In particular, all the components $\Delta C_{i33k3l}(0)=0$ $(i,k,l=1,2)$ for $\mathbf{k}\|\mathbf{M}_0\|\langle 100\rangle$, whereas for $\mathbf{M}_0\perp\mathbf{k}\|\langle 100\rangle$ only the two components ΔC_{544} and ΔC_{445} have nonzero values.

Estimates for YIG with $\omega/2\pi\approx 25$ MHz, $\omega_S/2\pi=30$ MHz, and $\Theta=5°$, using data from Ref. 15 for the characteristics of YIG, show that in resonance $(\omega_S=\omega_t$, where $\omega_t=(C_{44}/\rho_0)^{1/2}k$ is the natural frequency of the transverse elastic mode) the values of the elastic constants $\Delta C_{i33k3l}(2\omega;\omega,\omega)$ (A1) attain huge values of the order of $10^{15}\,\mathrm{N/m^2}$: $\Delta C_{555}=5i$, $\Delta C_{544}=-2i$, $\Delta C_{554}=4$, $\Delta C_{455}=-6$, $\Delta C_{444}=2$, and $\Delta C_{445}=3i$ in units of $10^{15}\,\mathrm{N/m^2}$. Far from resonance, $\omega=0.1\omega_S$ $(\omega_s/2\pi=30$ MHz), the magnitude of the moduli decreases by one to three orders: $\Delta C_{555}=2i\times 10^{-2}$, $\Delta C_{544}=-i$, $\Delta C_{554}=\Delta C_{455}=-6$, $\Delta C_{444}=-1$, $\Delta C_{445}-5i\times 10^{-2}$ in units of 10^{14} N/m^2. At higher spin-mode frequencies $\omega_S/2\pi=10\omega/2\pi=300$ MHz the elastic constants $\Delta\hat{C}_{(3)}$ are of the order of $10^{11}-10^{12}\,\mathrm{N/m^2}$, which are close to the values of the ordinary second-order elastic constants $\hat{C}_{(2)}$.

The giant elastic anharmonicity due to magnetoelastic interactions has been observed experimentally[9,10] in a study of the generation of second transverse acoustic harmonics in YIG. In the magnetoacoustic resonance region $(\omega_S\approx\omega=2\pi\cdot 30$ MHz) the nonlinear interaction parameter Γ (ratio of the effective third-order elastic constants to the constant $C_{44}=8\times 10^{10}\,\mathrm{N/m^2}$ increases by three orders of magnitude.

Consequently, the dynamic elastic constants $\Delta\hat{C}_{(3)}$ are magnified in the presence of magnetoacoustic resonance $(\omega\approx\omega_S)$; consequently, the efficiency of the nonlinear processes associated with these constants increases. The elastic constants $\Delta\hat{C}_{(3)}(2\omega;\omega,\omega)$ describing second-harmonic generation experience a particularly large increase. This effect is attributable to the occurrence of ''double resonance'' for them in the sense that $\Delta\hat{C}_{(3)}(2\omega;\omega,\omega)\sim D^2(\omega)=(\omega^2-\omega_S^2)^{-2}$. The magnetoelastic generation of acoustic harmonics in connection with these elastic constants will be investigated in the second part of the present study.

In closing, we note that the strong dependence of the elastic constants on the magnitude and direction of the magnetic field $\mathbf{H}^0$ $(\omega_S\sim H^0$, $\mathbf{M}_0\|\mathbf{H}^0)$ opens the door to the possible application of an external magnetic field to control nonlinear processes in ferromagnets.

This work has been supported by the Russian Fund for Fundamental Research (Project No. 96-02-16489).

APPENDIX A: DYNAMIC ELASTIC CONSTANTS $\Delta C_{i33l3n}(2\omega,\omega,\omega)$ $i,l,n=1,2$ FOR CUBIC FERROMAGNETS

For $\mathbf{k}\|\langle 100\rangle\|a_3$ and $\mathbf{M}_0(0,M_2^0,M_3^0)$ these constants have the form

$$\begin{aligned}\Delta C_{555}(2\omega)&=i\omega(\gamma b_2/M_0)^2 b_2\sin 2\theta\,\cos\theta D_1\\&\quad\times\{2D_1D_2\omega^2\Omega_4\cos^2\theta+(D_2-D_1)\Omega_1\},\\\Delta C_{544}(2\omega)&=-i2\omega(\gamma b_2/M_0)^2 b_2\sin\theta\,\cos 2\theta D_1\\&\quad\times\{2D_2\cos^2\theta[(D_1\Omega_4\Omega_2^2-\Omega_3)\cos 2\theta\\&\quad-(\Omega_1+4\Omega_2)]-D_1\Omega_2\cos 2\theta\},\\\Delta C_{554}(2\omega)&=0.5(\gamma b_2/M_0)^2 b_2\sin 2\theta D_1\{D_1\cos 2\theta\\&\quad\times[4D_2\Omega_2\Omega_4\omega^2\cos^2\theta-(\omega^2+\omega_S^2)]\\&\quad-D_2[2(\Omega_1^2+4\omega^2)\cos^2\theta+((\omega_S^2-2\omega^2)\\&\quad+2\Omega_1\Omega_3\cos^2\theta)\cos 2\theta]\},\\\Delta C_{455}(2\omega)&=-(\gamma b_2/M_0)^2 b_2\sin 2\theta D_1\{D_2\cos 2\theta\\&\quad\times[D_1\Omega_2\Omega_4\omega^2\cos^2\theta+(\omega_S^2-2\omega^2)]\\&\quad+D_1\cos^2\theta[\Omega_1\Omega_2\cos 2\theta+\Omega_1^2-2\omega^2]\},\\\Delta C_{444}(2\omega)&=(\gamma b_2/M_0)^2 b_2\sin 2\theta\,\cos^2 2\theta D_1\\&\quad\times\{D_1D_2\Omega_2\cos 2\theta(\Omega_2^2\Omega_4+3\omega^2\Omega_3)\\&\quad-D_1(2\Omega_2^2-\omega^2)-4D_2(\Omega_2^2+\omega^2)\},\\\Delta C_{445}(2\omega)&=i\omega(\gamma b_2/M_0)^2 b_2\sin\theta\,\cos 2\theta D_1\\&\quad\times\{2D_1\cos^2\theta[D_2\cos 2\theta(\Omega_3(\omega_S^2+2\omega^2)\\&\quad+\Omega_2^2\Omega_4)+(\Omega_1-2\Omega_2)]-D_2[\Omega_2\cos 2\theta\\&\quad+4(\Omega_1+\Omega_2)\cos^2\theta]\}.\end{aligned}\tag{A1}$$

Equations (A1) are written without regard for the spatial dispersion of spin waves ($\nu=0$). Here $b_2=2b_{2323}$ is the magnetoelastic constant, θ is the angle between the vectors $\mathbf{k}$ and $\mathbf{M}_0$, $D_n=[(n\omega)^2-\omega_S^2]^{-1}$, and $\omega_S=(\Omega_1\Omega_2)^{1/2}$ is the frequency of the spin mode, where

$$\Omega_1=\gamma\left\{\mathbf{H}_0\cdot\boldsymbol{\alpha}_0+\frac{2K}{M_0}(1-2\sin^2 2\theta)+4\pi M_0\sin^2\theta\right\},$$

$$\Omega_2=\gamma\left[\mathbf{H}_0\cdot\boldsymbol{\alpha}_0+\frac{2K}{M_0}\left(1-\frac{1}{2}\sin^2 2\theta\right)\right],$$

$$\Omega_3=\gamma\left(2\pi M_0-\frac{3K}{M_0}\cos 2\theta\right),$$

$$\Omega_4=\gamma\left(6\pi M_0-\frac{15K}{M_0}\cos 2\theta\right).\tag{A2}$$

Here K is the magnetic anisotropy constant.

[1] V. I. Ozhogin and V. L. Preobrazhenskiĭ, Usp. Fiz. Nauk **155**, 593 (1998).

[2] I. F. Mirsaev, V. V. Men'shenin, and E. A. Turov, Fiz. Tverd. Tela (Leningrad) **28**, 2428 (1986) [Sov. Phys. Solid State **28**, 1357 (1986)].

[3] E. A. Turov, *Kinetic, Optical, and Acoustical Properties of Antiferromagnets* [in Russian] (Izd. UrO AN SSSR, Sverdlovsk, 1990), 130 pp.

[4] I. F. Mirsaev, Fiz. Tverd. Tela (St. Petersburg) **36**, 2430 (1994) [Phys. Solid State **36**, 1321 (1994)].

[5] I. F. Mirsaev and E. A. Turov, Fiz. Met. Metalloved. **81**(4), 68 (1996).

[6] I. F. Mirsaev and E. A. Turov, Fiz. Met. Metalloved. **81**(6), 5 (1996).

[7] I. F. Mirsaev, Fiz. Tverd. Tela (St. Petersburg) **39**, 1432 (1997) [Phys. Solid State **39**, 1271 (1997)].

[8] E. A. Turov, Zh. Éksp. Teor. Fiz. **96**, 2140 (1989) [Sov. Phys. JETP **69**, 1211 (1989)].

[9] L. K. Zar3embo, S. N. Karpachev, and S. Sh. Gendelev, Pis'ma Zh. Tekh. Fiz. **9**, 502 (1983) [Sov. Tech. Phys. Lett. **9**, 217 (1983)].

[10] L. K. Zarembo and S. N. Karpachev, Fiz. Tverd. Tela (Leningrad) **25**, 2343 (1983) [Sov. Phys. Solid State **25**, 1345 (1983)].

[11] A. N. Grishmanovskiĭ, N. K. Yushin, V. L. Bogdanov, and V. V. Lemanov, Fiz. Tverd. Tela (Leningrad) **13**, 1833 (1971) [Sov. Phys. Solid State **13**, 1537 (1971)].

[12] A. I. Akhiezer, V. G. Bar'yakhtar, and S. V. Peletminskiĭ, *Spin Waves* (North-Holland, Amsterdam; Wiley, New York, 1968; Nauka, Moscow, 1967, 368 pp.).

[13] I. F. Mirsaev, G. G. Taluts, and A. P. Tankeev, Fiz. Met. Metalloved. **44**(1), 24 (1977).

[14] L. K. Zarembo and V. A. Krasil'nikov, Usp. Fiz. Nauk **102**, 549 (1970) [Sov. Phys. Usp. **13**, 778 (1970)].

[15] W. Strauss, in *Physical Acoustics*, Vol. 4B, edited by W. P. Mason (Academic Press, New York, 1968, pp. 211–268; Mir, Moscow, 1970, 247 pp.).

Translated by James S. Wood

PHYSICS OF THE SOLID STATE VOLUME 40, NUMBER 11 NOVEMBER 1998

Hall effect in $La_{0.67-x}Ce_xSr_{0.33}MnO_3$

R. I. Zaĭnullina, N. G. Bebenin, V. V. Mashkautsan, and V. V. Ustinov

Institute of Metal Physics, Ural Branch of the Russian Academy of Sciences,
620219 Ekaterinburg, Russia

V. G. Vasil'ev and B. V. Slobodin

Institute of Solid-State Chemistry, Ural Branch of the Russian Academy of Sciences,
620219 Ekaterinburg, Russia

(Submitted May 7, 1998)
Fiz. Tverd. Tela (St. Petersburg) **40**, 2085–2088 (November 1998)

An experimental study of the Hall effect and of magnetoresistance in polycrystalline $La_{0.67-x}Ce_xSr_{0.33}MnO_3$ samples ($x=0, 0.07$) is reported. It is shown that the normal Hall coefficient reverses sign at $T_0=360$ K in both samples and that metallic conduction occurs for $T<T_0$, while for $T>T_0$ the conduction is by mechanisms operative in disordered materials. It has been established that doping with cerium brings about an increase in the metallic phase of the normal and anomalous Hall coefficients. A qualitative interpretation of the observed features is given. [S1063-7834(98)02611-2]

1. The active interest expressed presently in lanthanum manganites is stimulated by the colossal magnetoresistance (CMR) observed in these compounds near the Curie temperature T_c (see reviews Refs. 1 and 2). The mechanism responsible for the CMR remains, however, unclear. Valuable relevant information can be obtained by studying the Hall effect. The data published to date relate primarily to thin-film samples[3–6] displaying a variety of features,[1,2] but only our recent paper[7] reports on a study of bulk, while polycrystalline samples. The features observed in the temperature behavior of the normal Hall coefficient, as well as of electrical resistivity and magnetoresistance, were attributed to a temperature-induced shift of the mobility edge, which results in a change in the number of delocalized carriers. It was posited that this mechanism of the change in conduction type in the vicinity of T_c is a common feature for all heavily-doped $LaMnO_3$-based materials.

The present work is a continuation of our investigation of galvanomagnetic effects in lanthanum manganites. The magnetoresistance and Hall-effect measurements were carried out on polycrystalline samples of the $La_{0.67-x}Ce_xSr_{0.33}MnO_3$ manganites ($x=0, 0.07$); when combined with our previous[7] data on $La_{0.67}Ba_{0.33}MnO_3$, this permits one to isolate common features in the galvanomagnetic phenomena observed in lanthanum manganites, as well as to study the role of cerium as dopant. The latter is of a certain interest, because the effect of cerium doping on the magnetoresistance (but not on the Hall effect) of manganites was investigated apparently only in Ref. 8.

2. Powders of nominal compositions $La_{0.67}Sr_{0.33}MnO_3$ and $La_{0.60}Ce_{0.07}Sr_{0.33}MnO_3$ were prepared by coprecipitation from solutions.[9] Polycrystalline samples were obtained by pressing the powders at room temperature at a pressure of 5×10^3 kg/cm^2 with subsequent annealing in an oxygen flow at 1200 °C for 12 h. X-ray diffraction analysis confirmed the samples to be single phase. The samples intended for galvanomagnetic measurements were parallelepipeds measuring $10\times3\times0.9$ mm. Magnetization curves were measured in a vibration-reed magnetometer on plates, which, while being smaller, had the same side-to-length ratio, in a magnetic field oriented as in the Hall-effect measurements. The Curie temperature was determined potentiometrically in magnetic fields of up to 15 kOe. The indium contacts used were deposited ultrasonically.

3. The magnetization curves have a pattern typical of ferromagnets and, for $T<T_c$ and in fields $H\geqslant6$ kOe, are described by the relation $M=M_s+\chi H$. The values of the spontaneous magnetization M_s and of the paraprocess susceptibility χ obtained in this way were subsequently used to calculate the normal, R_0, and anomalous (spontaneous), R_s, Hall coefficients. The Curie temperatures were found to be 374 K for $La_{0.67}Sr_{0.33}MnO_3$ and 369 K for $La_{0.60}Ce_{0.07}Sr_{0.33}MnO_3$.

Figure 1 displays the temperature dependence of magnetoresistance $MR=[R(H)-R(H=0)]/R(H=0)$, where $R(H)$ is the resistance in a magnetic field H. The curves have a pattern typical of polycrystalline heavily-doped lanthanum manganite samples. The absolute value of magnetoresistance passes through a maximum at a temperature T_{MR} slightly lower than T_c ($T_{MR}=360$ K for $La_{0.67}Sr_{0.33}MnO_3$, and $T_{MR}=358$ K for $La_{0.60}Ce_{0.07}Sr_{0.33}MnO_3$), with the position of the maximum being independent of the field applied.

Figure 2 shows isotherms of the Hall resistivity ρ_{Hall} for $La_{0.60}Ce_{0.07}Sr_{0.33}MnO_3$; similar curves were also obtained for the cerium-free sample. In the ferromagnetic region, one observes in weak fields a strong dependence of ρ_{Hall} on H, and for $H>6$ kOe the $\rho_{\mathrm{Hall}}(H)$ relation becomes linear.

In ferromagnets $\rho_{\mathrm{Hall}}=R_0B+R_sM$, where B is the magnetic field induction in a sample; in our case one may assume $B=H$. Figure 3 plots temperature dependences of R_0 derived from the $\rho_{\mathrm{Hall}}(H)$ isotherms and magnetization curves. The

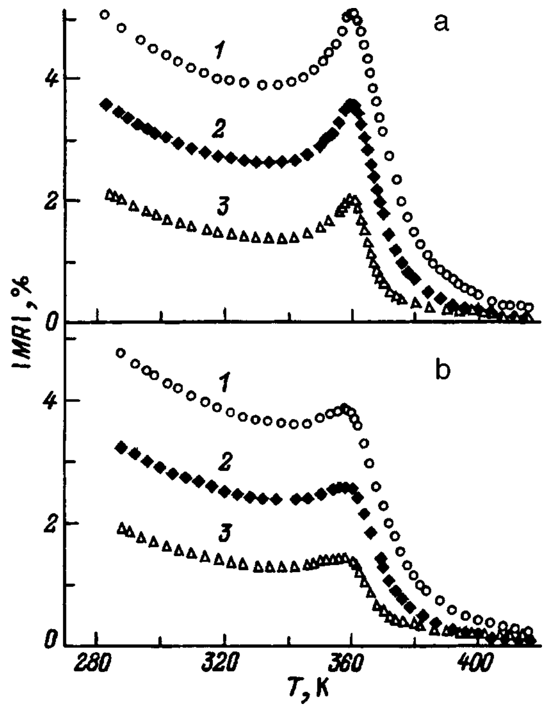

FIG. 1. Temperature dependence of the magnetoresistance of (a) $La_{0.67}Sr_{0.33}MnO_3$ and (b) $La_{0.60}Ce_{0.07}Sr_{0.33}MnO_3$ in fields (kOe): *1*—5, 2—10, 3—15.

normal Hall coefficient reverses sign at $T_0 = 360$ K. For $T < T_0$, this coefficient is positive and temperature independent within experimental error, while for $T > T_0$ a strong temperature dependence is observed. Below T_0 the normal Hall coefficient for the $La_{0.60}Ce_{0.07}Sr_{0.33}MnO_3$ sample ($4.8 \times 10^{-12}\,\Omega \cdot$cm/G) exceeds the value of R_0 for the cerium-free sample ($3.6 \times 10^{-12}\,\Omega \cdot$cm/G) by a factor 1.3.

Figure 4 presents temperature dependences of the anomalous Hall coefficient. In both cases, $R_s < 0$, and $|R_s|$ exceeds $|R_0|$ by two to three orders of magnitude. Doping with cerium increases $|R_s|$. At $T \approx T_0$ the $R_s\,(T)$ curves have minima, and the extremum for the cerium-doped sample is more clearly pronounced.

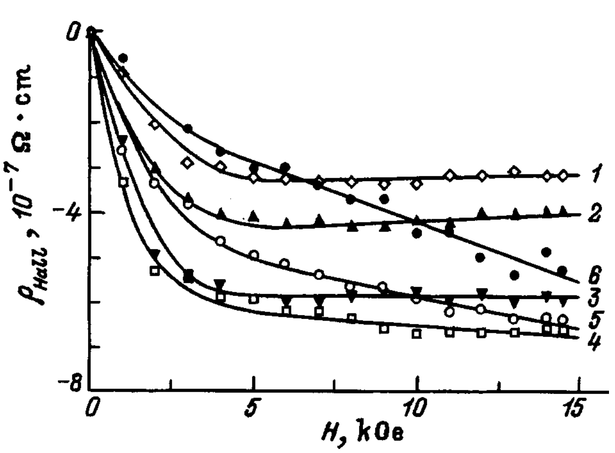

FIG. 2. Hall resistivity isotherms for $La_{0.60}Ce_{0.07}Sr_{0.33}MnO_3$ at T(K): *1*— 194, *2*—310, *3*—335, *4*—350, *5*—361, *6*—370.

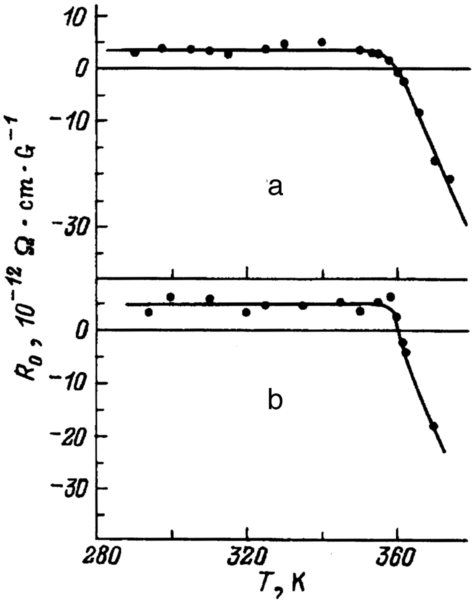

FIG. 3. Temperature dependence of the normal Hall coefficient in (a) $La_{0.67}Sr_{0.33}MnO_3$ and (b) $La_{0.60}Ce_{0.07}Sr_{0.33}MnO_3$.

4. Turning now to a discussion of the results, we notice first of all the slight change ΔT_c of the Curie temperature (by only 5 K) induced by incorporation of 7% Ce. This is close to the shift of the Curie temperature caused by doping $La_{0.67}Ba_{0.33}MnO_3$ with the same amount of trivalent yttrium, where $\Delta T_c = 3$ K,[10] but an order of magnitude smaller than the change in T_c resulting from introduction into a $La_{0.67}Ba_{0.33}MnO_3$ sample of 4% oxygen vacancies,[11] which, like cerium (see below), act as donors in lanthanum manganites but, unlike cerium, are doubly charged. The reasons for these differences in ΔT_c remain unclear.

Note now the features in the temperature dependence of magnetoresistance and Hall coefficients, which are observed both in $La_{0.67}Ba_{0.33}MnO_3$ (Ref. 7) and in $La_{0.67}Sr_{0.33}MnO_3$ and $La_{0.60}Ce_{0.07}Sr_{0.33}MnO_3$. Each sample is characterized, first of all, by a temperature $T_0 < T_c$ at which the normal Hall coefficient becomes zero; we may add that for $T < T_0$ this coefficient is positive and practically temperature indepen-

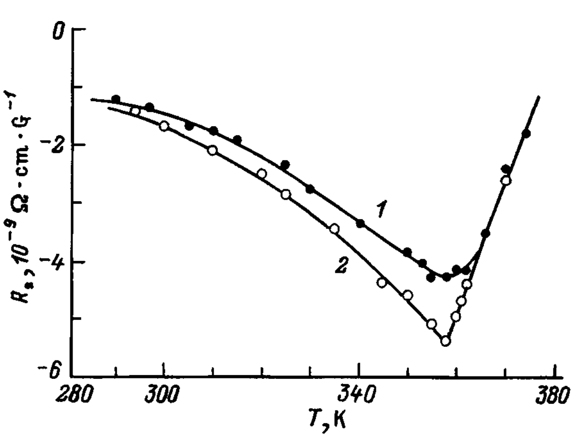

FIG. 4. Temperature dependence of the anomalous Hall coefficient in (*1*) $La_{0.67}Sr_{0.33}MnO_3$ and (*2*) $La_{0.60}Ce_{0.07}Sr_{0.33}MnO_3$.

dent. Second, R_s passes through a minimum at $T \approx T_0$. Third, the absolute value of magnetoresistance reaches a maximum also practically at T_0. The fact that all of the lanthanum manganites studied by us exhibit these features suggests that their interpretation given in Ref. 7 as applied to $La_{0.67}Ba_{0.33}MnO_3$ is valid for all $LaMnO_3$-based materials with a high enough doping level. To wit, the temperature $T_0 < T_c$ is the metal-insulator (MI) transition point at which band conduction, which dominates for $T < T_0$, is replaced by mechanisms typical of disordered materials and involving hopping between localized states and/or activation to the mobility edge. The cross-over between the conduction types originates from the shift of the mobility edge caused by enhancement of magnetic fluctuations in the vicinity of the Curie temperature.

The positive sign of R_0 observed for $T < T_0$ shows that the majority carriers in this temperature region are holes. The hole concentration ratio for samples with and without cerium estimated from the change in R_0 practically coincides with that calculated from the change in the nominal composition. At the same time the values of R_0 derived from the content of strontium and cerium turn out to be substantially larger than the experimental values, which may be due to the presence of minority carriers-electrons. The growth of the normal Hall coefficient induced by a partial substitution of cerium for lanthanum implies a decrease in the hole concentration under such doping. It appears only natural to assign this to the fact that cerium has an extra electron compared to lanthanum, which, when raised to the valence band, reduces the number of holes. In other words, cerium is in our case quadrivalent (as, for instance, in CeO_2) and acts as a singly-charged donor, similar to gadolinium in EuO.[12]

The large value of R_s is in agreement with the conclusion drawn from band-structure calculations[13–15] that the valence band of $LaMnO_3$-based materials is derived primarily from *d* states of manganese. In ferromagnetic single crystals, the anomalous Hall effect is related to resistivity through $R_s = a\rho + b\rho^2$, where *a* and *b* are constants.[16] It may be conjectured that in the polycrystalline materials under study R_s is likewise dominated by ρ, at least near T_0, if one understands by ρ the resistivity in the bulk of the crystallites. For simplicity, we shall consider R_s a monotonic function of ρ; then the increase of $|R_s|$ observed under cerium doping finds an explanation in the fact that a decrease in carrier (hole) concentration results in an increase of ρ. Furthermore, resistance measurements carried out on $La_{1-x}Sr_xMnO_3$ single crystals showed that the resistivity peak in samples exhibiting the MI transition is the sharper, the lower is the hole concentration.[17] Assuming this to be valid for the temperature dependence of the bulk crystallite resistivity as well, one may conclude that the sharpness of the minimum in the $R_s(T)$ relation for the cerium-doped sample is also a result of a decrease in hole concentration. Thus there are grounds to believe that the temperature dependence of the anomalous Hall coefficient in the samples under study is accounted for, in general terms, by that of the crystallite resistivity, at least in the vicinity of the MI transition. Note that such correlation does not, generally speaking, always hold for spatially inhomogeneous systems.[18] In our case the explanation for this correlation lies most likely in the fact that among the parameters determining the anomalous Hall coefficient it is ρ that varies with temperature most strongly near the MI transition.

Thus the Hall effect in various lanthanum manganites exhibits a number of common features, which reflects the existence of a common mechanism responsible for the MI transition. This transition occurs below the Curie temperature. In polycrystalline samples, the temperature dependence of the anomalous Hall coefficient in the vicinity of the above transition is dominated by that of the crystallite bulk resistivity. In La-Ce-Sr-Mn-O manganites, cerium is apparently quadrivalent and plays the part of a singly-charged donor.

Support of the Russian Fund for Fundamental Research (Grant 97-02-16008) is gratefully acknowledged.

[1] É. L. Nagaev, Usp. Fiz. Nauk **166**, 833 (1996).

[2] A. P. Ramirez, J. Phys.: Condens. Matter **9**, 8171 (1997).

[3] G. J. Snyder, M. R. Beasley, T. H. Geballe, R. Hiskes, and S. D. Carolis, Appl. Phys. Lett. **69**, 4254 (1996).

[4] P. Wagner, D. Mazilu, L. Trappeniers, V. V. Moshchalkov, and Y. Bruynseraede, Phys. Rev. B **55**, R 14 721 (1997).

[5] M. Jaime, H. T. Hardner, M. B. Salamon, M. Rubinstein, P. Dorsey, and D. Emin, Phys. Rev. Lett. **78**, 951 (1997).

[6] P. Wagner, I. Gordon, A. Vantomme, D. Dierickx, M. J. Van Bael, V. V. Moshchalkov, and Y. Bruynseraede, Europhys. Lett. **41**, 49 (1998).

[7] N. G. Bebenin, R. I. Zaĭnullina, V. V. Mashkautsan, V. V. Ustinov, A. M. Burkhanov, V. V. Vasil'ev, and B. V. Slobodin, Zh. Éksp. Teor. Fiz. **113**, 981 (1998) [JETP **86**, 534 (1998)].

[8] S. Das and P. Mandal, Z. Phys. B **104**, 7 (1997).

[9] V. G. Vasil'ev, A. A. Ivakin, and A. A. Fotiev, Zh. Neorg. Khim. **39**, 3 (1994).

[10] A. P. Nosov, A. B. Rinkevich, R. I. Zaĭnullina, V. G. Vasil'ev, B. V. Slobodin, N. G. Bebenin, and V. V. Ustinov, Fiz. Met. Metalloved. **85**, No. 4, 72 (1998).

[11] H. L. Ju, J. Gopalakrishnan, J. L. Peng, Qi Li, G. C. Xiong, T. Venkatesan, and R. L. Greene, Phys. Rev. B **51**, 6143 (1995).

[12] É. L. Nagaev, *Physics of Magnetic Semiconductors* [in Russian] (Nauka, Moscow, 1979), 432 pp.

[13] S. Satpathy, Z. S. Popović, and F. R. Vukajlović, J. Appl. Phys. **79**, 4555 (1996).

[14] W. E. Pickett and D. J. Singh, Phys. Rev. B **53**, 1146 (1996).

[15] I. Solovyev, N. Hamada, and K. Terakura, Phys. Rev. B **53**, 7158 (1996).

[16] C. M. Hurd, *Hall Effect in Metals and Alloys* (Plenum Press, New York, 1972), 400 pp.

[17] A. Urushibara, Y. Moritomo, T. Arima, A. Asamitsu, G. Kido, and Y. Tokura, Phys. Rev. B **51**, 14103 (1995).

[18] A. V. Vedyaev, A. B. Granovskiĭ, A. V. Kalitsov, and F. Brouers, Zh. Éksp. Teor. Fiz. **112**, 2198 (1997) [JETP **85**, 1204 (1997)].

Translated by G. Skrebtsov

PHYSICS OF THE SOLID STATE VOLUME 40, NUMBER 11 NOVEMBER 1998

Dependence of the frequencies of magnetostatic waves on the magnetizing field in ferrite films

V. V. Shagaev

Institute of Electronic Engineering Materials, 248650 Kaluga, Russia

(Submitted February 11, 1998; resubmitted May 11, 1998)
Fiz. Tverd. Tela (St. Petersburg) **40**, 2089–2092 (November 1998)

Analytical expressions are derived for the derivatives of the frequencies of magnetostatic waves with respect to the external magnetic field in anisotropic ferromagnetic films. Films having cubic anisotropy and ⟨100⟩, ⟨110⟩, and ⟨111⟩ surfaces are analyzed in detail. The frequency-field relations are used in an experimental determination of the temperature coefficients of the cubic anisotropy field and the saturation magnetization in an yttrium iron garnet film. © *1998 American Institute of Physics.* [S1063-7834(98)02711-7]

The anisotropy of single-crystal ferrite films must be taken into account in the investigation of natural oscillations of their magnetization.[1–6] Magnetic anisotropy makes the parameters of the oscillations dependent on the angles characterizing the orientation of the external magnetic field relative to the crystallographic axes of the ferrite film. It is customary to investigate either the angular dependence of the resonance field at a fixed oscillation frequency or the angular dependence of the frequency at a fixed field strength. Resonance fields are normally studied for homogeneous ferromagnetic resonance,[7–9] and the frequency dispersion curves are studied for waves.[10,11]

On the other hand, the external magnetic field and the natural frequency are interrelated by parameters. This relationship for differentially small field and frequency variations is described by the derivative of one parameter with respect to the other. The derivative can be calculated from experimental frequency-field curves, and its intrinsic angular dependence can be used to determine the magnetic anisotropy parameters. This possibility stresses the need to investigate the frequency-field relations and their derivatives. Of special interest from the theoretical point of view is the problem of ascertaining the analytical form of representation of the derivatives for waves. The problem is that the dispersion relations for spin waves contains the relationship between the frequency and the field in implicit form.

The objective of the present study is to investigate the frequency-field relations for magnetostatic waves (MSWs) in anisotropic ferromagnetic films. Special attention is given to films endowed with cubic and uniaxial anisotropy. The frequency-field relations are investigated for surface MSWs in an yttrium iron garnet (YIG) film.

1. STATEMENT OF THE PROBLEM

We consider a ferrite film for which one of the magnetic symmetric axes is either parallel or perpendicular to the film. Let the film be magnetized to saturation along the designated symmetry axis by an external magnetic field **H**. It follows from the solution of the static problem that for a sufficiently strong field the magnetization vector **M** is parallel to **H**. We shall assume everywhere below that the vectors **H** and **M** and the symmetry axis are mutually parallel and are oriented either tangential to the film or along the normal **n** to it. Let a MSW with wave vector **k**⊥**n** propagate in the film. The functional relations between the MSW frequencies and the magnitude of the magnetizing field can be obtained from the dispersion relations. The dispersion relations given below have been derived from the magnetostatic equations subject to electrodynamic boundary conditions on the surface of the film and from the linearized equation of motion of the magnetization without regard for exchange or losses. Magnetic anisotropy is taken into account by means of the tensor of effective demagnetizing anisotropy factors N_{rs}, where $r,s=x,y,z$ (Ref. 1). The x, y, and z axes form a right-handed orthogonal coordinate system with the z axis parallel to **M** and with the y axis parallel to the film surface.

A. Perpendicularly Magnetized Film, M∥n

Accordingly, we have the axes **z**∥**n** and **x**, **y**⊥**n**. If we choose the direction of the axis **y**∥**k**, the dispersion relation has the form

$$\tan kd(-\mu_{yy}^F)^{1/2} = -\frac{2(-\mu_{yy}^F)^{1/2}}{1+\mu_{yy}^F}, \tag{1}$$

where d is the thickness of the ferrite film, and the component of the magnetic permeability tensor has the form

$$\mu_{yy}^F = 1 + 4\pi M g^2 [H + M(N_{xx} - N_{zz} - 4\pi)] \times \{g^2 [H + M(N_{xx} - N_{zz} - 4\pi)][H + M \times (N_{yy} - N_{zz} - 4\pi)] - (gMN_{xy})^2 - f^2\}^{-1}, \tag{2}$$

where f is the MSW frequency, and $g = 2.8$ MHz/Oe is the gyromagnetic ratio. The dispersion relation describes magnetostatic forward volume waves (MSFVWs). Their frequencies lie in the interval $[H+M(N_{xx}-N_{zz}-4\pi)] \times [H+M(N_{yy}-N_{zz}-4\pi)] - (MN_{xy})^2 < (f/g)^2 < [H+M \times (N_{xx}-N_{zz}-4\pi)][H+M(N_{yy}-N_{zz})] - (MN_{xy})^2$. The lower limit of the interval corresponds to the ferromagnetic resonance frequency, and the upper limit corresponds to the frequency of the short-wavelength edge of the MSFVW spectrum.

B. Tangential Magnetization, $\mathbf{M}\perp\mathbf{n}$ and $\mathbf{k}\parallel\mathbf{M}$.

Accordingly, we have the axes $\mathbf{z}$, $\mathbf{y}\perp\mathbf{n}$ and $\mathbf{x}\parallel\mathbf{n}$, where $\mathbf{z}\parallel\mathbf{k}$ The dispersion relation has the form

$$\tan kd(-\mu_{xx}^{B})^{-1/2}=\frac{2(-\mu_{xx}^{B})^{1/2}}{1+\mu_{xx}^{B}}, \tag{3}$$

where

$$\mu_{xx}^{B}=1+4\pi Mg^2[H+M(N_{yy}-N_{zz})]\{g^2[H+M(N_{xx}-N_{zz})][H+M(N_{yy}-N_{zz})]-(gMN_{xy})^2-f^2\}^{-1}. \tag{4}$$

In this case the dispersion relation describes magnetostatic backward volume waves (MSBVWs). Their frequencies lie in the interval $[H+M(N_{xx}-N_{zz})][H+M(N_{yy}-N_{zz})]-(MN_{xy})^2<(f/g)^2<[H+M(N_{xx}-N_{zz}+4\pi)][H+M(N_{yy}-N_{zz})]-(MN_{xy})^2$. The upper limit of the interval corresponds to the ferromagnetic resonance frequency, and the lower limit corresponds to the frequency of the short-wavelength edge of the MSBVW spectrum.

C. Tangential Magnetization, $\mathbf{M}\perp\mathbf{n}$ and $\mathbf{k}\perp\mathbf{M}$

We now have the axes $\mathbf{z}$, $\mathbf{y}\perp\mathbf{n}$ and $\mathbf{x}\parallel\mathbf{n}$, where $\mathbf{y}\parallel\mathbf{k}$. The dispersion relation can have one of two forms in this case. For magnetostatic volume waves we have

$$\tan\frac{kd[(f_1^2-f^2)(f^2-f_2^2)]^{1/2}}{f_0^2-f^2}=\frac{2[(f_1^2-f^2)(f^2-f_2^2)]^{1/2}}{(f^2-f_2^2)-(f_1^2-f^2)-(4\pi Mg)^2}, \tag{5}$$

and for magnetostatic surface waves (MSSWs) (or a mixed mode when $N_{xy}\neq 0$) has the form

$$\exp\frac{kd[(f^2-f_1^2)(f^2-f_2^2)]^{1/2}}{f^2-f_0^2}=\frac{(4\pi M)^2-[(f^2-f_2^2)^{1/2}-(f^2-f_1^2)^{1/2}]^2}{8\pi Mg(f_3^2-f^2)^{1/2}}, \tag{6}$$

where

$$f_0^2=g^2\{[H^2+HM(N_{xx}+N_{yy}-2N_{zz}+4\pi)]+M^2[(N_{xx}-N_{zz}+4\pi)(N_{yy}-N_{zz})-N_{xy}^2]\},$$

$$f_{1,2}^2=g^2\{[H^2+HM(N_{xx}+N_{yy}-2N_{zz}+4\pi)]+M^2[(N_{xx}-N_{zz})(N_{yy}-N_{zz})-N_{xy}^2]+2\pi M^2(N_{xx}+N_{yy}-2N_{zz})\pm 2\pi M^2\times[(N_{xx}-N_{yy})^2+4N_{xy}^2]^{1/2}\},$$

$$f_3^2=g^2\left\{[H^2+HM(N_{xx}+N_{yy}-2N_{zz}+4\pi)]+\frac{M^2}{4}(N_{xx}+N_{yy}-2N_{zz}+4\pi)^2\right\},$$

f^0 is the ferromagnetic resonance frequency, $f_{1,2}$ are the short-wavelength limits of the MSFVW ($f_0<f<f_1$) and MSBVW ($f_2<f<f_0$) spectra, and f_3 is the short-wavelength limit of the MSSW spectrum ($f_1<f<f_3$). At the frequency f_1 and for the value of the wave vector $kd=2(f_1^2-f_0^2)/[f_2^2-f_1^2+(4\pi Mg)^2]$ the dispersion curves of the fundamental MSFVW and MSSW modes make a smooth transition from one to the other.

2. DIFFERENTIAL RELATIONS

We now consider equations that can be obtained from the above-listed dispersion relations for the derivatives of the MSW frequencies with respect to the magnetizing field.

For MSFVWs with $\mathbf{M}\parallel\mathbf{n}$ and MSBVWs with $\mathbf{M}\perp\mathbf{n}$ and $\mathbf{k}\parallel\mathbf{M}$ these equations are derived from Eqs. (2) and (4), in which μ_{yy}^{F} and μ_{xx}^{B} are treated as constant parameters. It follows from Eqs. (1) and (3) that parametric dependences of the right-hand sides of Eqs. (2) and (4) on *kd* are specified through μ_{yy}^{F} and μ_{xx}^{B}. For both of these dependences it is more convenient to use the single parameter μ given by the equation

$$\tan kd(-\mu)^{1/2}=-\frac{2(-\mu)^{1/2}}{1+\mu}. \tag{7}$$

Now $\mu_{yy}^{F}=\mu$ and $\mu_{xx}^{B}=1/\mu$. Substituting μ into Eqs. (2) and (4), we find explicit functions $f(H)$, which we can then differentiate to obtain simpler relations for the derivatives:

$$\frac{1}{g^2}\frac{d(f^2-g^2H^2)}{dH}=M(N_{xx}+N_{yy}-2N_{zz}-8\pi)+\frac{4\pi M}{1-\mu} \tag{8}$$

for MSFVWs and

$$\frac{1}{g^2}\frac{d(f^2-g^2H^2)}{dH}=M(N_{xx}+N_{yy}-2N_{zz}+4\pi)-\frac{4\pi M}{1-\mu} \tag{9}$$

for MSBVWs.

We note that different coordinate systems are used to treat MSFVWs and MSBVWs. Consequently, the components of the tensor N_{rs} in Eqs. (8) and (9) differ. But the terms $4\pi M/(1-\mu)$ do not depend on the anisotropy fields of the film, and they express the parametric dependence of the derivatives on *kd*. As *kd* varies form zero to infinitely large values, the term $4\pi M/(1-\mu)$ increases monotonically from 0 to $4\pi M$.

We now consider MSWs for $\mathbf{M}\perp\mathbf{n}$ and $\mathbf{k}\perp\mathbf{M}$. The functions $f(H)$ cannot be obtained in explicit form from the dispersion relations (5) and (6). However, f and H enter into these dispersion relations in the combination form $g^2[H^2+HM(N_{xx}+N_{yy}-2N_{zz}+4\pi)]-f^2\equiv U(f,H)$. Hence it follows that for a given value of *kd* the variation of H and the corresponding variation of f must obey the differential equation $dU(f,H)/dH=0$. From this equation we obtain

$$\frac{1}{g^2}\,\frac{d(f^2-g^2H^2)}{dH}=M(N_{xx}+N_{yy}-2N_{zz}+4\pi). \tag{10}$$

The latter does not depend on kd, and it replicates the analogous equation for homogeneous ferromagnetic resonance, which is obtained from the explicit analytical field dependence of the ferromagnetic resonance frequency.

Equations (8)–(10) can be used to find the magnetic parameters of a ferrite film. In fact, combinations of parameters from the right-sides of the equations can be determined from the experimental MSW frequency-external field relations, from which the left-hand sides of the equations are calculated.

3. DERIVATIVES FOR FILMS WITH CUBIC AND UNIAXIAL ANISOTROPY

As an example, we consider the application of the general equations (8)–(10) to YIG films, which are widely used in physical research and engineering. The magnetic anisotropy energy in these films is described by the expression $K_c(\alpha_1^2\alpha_2^2+\alpha_1^2\alpha_3^2+\alpha_2^2\alpha_3^2)+K_u\sin^2\vartheta$, where K_c and K_u are the first cubic and normal uniaxial anisotropy constants, respectively, $\alpha_{1,2,3}^2$ are the squares of the cosines of the angles formed by the vector **M** with the fourfold symmetry axes, and ϑ is the angle between the vectors **M** and **n**. The calculation of the components of the tensor N_{rs} for cases with the vector **M** directed along the symmetry axis $\langle mlp\rangle$ (where $\langle mlp\rangle$ is one of the axes of the type $\langle 100\rangle$, $\langle 110\rangle$, or $\langle 111\rangle$), followed by substitution into Eqs. (8)–(10), yields the relations

$$\frac{1}{g^2}\left[\frac{d(f^2-g^2H^2)}{dH}\right]_{F,\langle mlp\rangle}=H_{\langle mlp\rangle}-8\pi M_{\text{eff}}+\frac{4\pi M}{1-\mu}, \tag{11}$$

$$\frac{1}{g^2}\left[\frac{d(f^2-g^2H^2)}{dH}\right]_{B,\langle mlp\rangle}=H_{\langle mlp\rangle}+4\pi M_{\text{eff}}-\frac{4\pi M}{1-\mu}, \tag{12}$$

$$\frac{1}{g^2}\left[\frac{d(f^2-g^2H^2)}{dH}\right]_{S,\langle mlp\rangle}=H_{\langle mlp\rangle}+4\pi M_{\text{eff}}. \tag{13}$$

The subscript F refers to waves with $\mathbf{M}\|\mathbf{n}$, the subscript B refers to waves with $\mathbf{M}\perp\mathbf{n}$ and $\mathbf{k}\|\mathbf{M}$, the subscript S refers to waves with $\mathbf{M}\perp\mathbf{n}$ and $\mathbf{k}\perp\mathbf{M}$, and the subscript $\langle mlp\rangle$ indicates the crystallographic direction along which magnetization takes place. Here $H_{\langle 100\rangle}=4H_c$, $H_{\langle 110\rangle}=-H_c$, $H_{\langle 111\rangle}=-(8/3)H_c$, $H_c=K_c/M$ is the cubic anisotropy field, $4\pi M_{\text{eff}}=(4\pi M-H_u)$ is the effective magnetization, and $H_u=2K_u/M$ is the uniaxial anisotropy field.

For films having the surface orientations {100}, {110}, and {111} we give relations deduced from Eqs. (11)–(13).

For {100} and {110} we consider directions of magnetization along $\langle 100\rangle$ and $\langle 110\rangle$ axes parallel to the film:

$$\left[\frac{d(f^2-g^2H^2)}{dH}\right]_{S,\langle 100\rangle}-\left[\frac{d(f^2-g^2H^2)}{dH}\right]_{S,\langle 110\rangle}=5g^2H_c, \tag{14}$$

$$\left[\frac{d(f^2-g^2H^2)}{dH}\right]_{S,\langle 100\rangle}+4\left[\frac{d(f^2-g^2H^2)}{dH}\right]_{S,\langle 110\rangle}=5g^24\pi M_{\text{eff}}. \tag{15}$$

For {111} films we consider directions of magnetization along a $\langle 110\rangle$ axis parallel to the film and along a $\langle 111\rangle$ axis directed along the normal:

$$\left[\frac{d(f^2-g^2H^2)}{dH}\right]_{S,\langle 110\rangle}+\left[\frac{d(f^2-g^2H^2)}{dH}\right]_{B,\langle 110\rangle}+\left[\frac{d(f^2-g^2H^2)}{dH}\right]_{F,\langle 111\rangle}=-\frac{14}{3}g^2H_c, \tag{16}$$

$$\frac{11}{3}\left[\frac{d(f^2-g^2H^2)}{dH}\right]_{S,\langle 110\rangle}-\left[\frac{d(f^2-g^2H^2)}{dH}\right]_{B,\langle 110\rangle}-\left[\frac{d(f^2-g^2H^2)}{dH}\right]_{F,\langle 111\rangle}=\frac{14}{3}g^24\pi M_{\text{eff}}, \tag{17}$$

In addition, the derivatives with subscripts B and F correspond to identical modes and identical values of kd. Now the parameter μ in Eqs. (11) and (12) also assumes identical values, and when these equations are summed, terms containing μ cancel each other without introducing a dependence on kd in the final expressions (16) and (17).

Equations (14)–(17) can be used to determine H_c and $4\pi M_{\text{eff}}$ from experimental $f(H)$ curves obtained for any value of k. The value of k itself is not used in the calculations in this case.

The simplest measurements of H_c and $4\pi M_{\text{eff}}$ are performed on films having surface orientation {100} or {110}. It follows from Eqs. (14) and (15) that for these films it is sufficient to obtain two $f(Y)$ curves for a surface wave with magnetization along tangential axes of the type $\langle 100\rangle$ and $\langle 110\rangle$.

4. EXPERIMENTAL

The objective of the experimental investigations was to verify relations (13) for various k, H_c, and $4\pi M_{\text{eff}}$. The investigations were carried out on a YIG film of thickness 9.8 μm grown on a {100}-oriented gallium gadolinium garnet substrate. The magnetic parameters were varied by changing the temperature of the film from 200 K to 360 K. An interference procedure[12] was used to observe MSSWs and to evaluate k.

The film was placed between the poles of an electromagnet in a tangential magnetic field. The orientation of the field relative to the crystallographic axes was set by rotating the film about the normal. The measurements were performed for two positions. In one case the field was aligned with a $\langle 100\rangle$ axis, and in the other case it was aligned with a $\langle 110\rangle$ axis. The alignments were checked against the angular dependence of the frequency interval with the spin-wave spectrum. The lowest and highest frequencies are attained when the direction of the field coincides with the $\langle 100 \rangle$ and $\langle 110 \rangle$ axes, respectively.

The spin-wave frequencies f were measured as the field H was varied in the interval from 200 Oe to 700 Oe and as the wave vector k was varied from $93\,\mathrm{cm}^{-1}$ to $651\,\mathrm{cm}^{-1}$. The quantity $(f^2 - g^2H^2)$ depended linearly on H. The coefficients in this dependence were identical for different values of k and the same field direction. The cubic-anisotropy field H_c and the effective magnetization $4\pi M_{\mathrm{eff}}$ of the film were determined from Eqs. (14) and (15). The values of H_c varied from -92 Oe at 200 K to -32 Oe at 360 K, and $4\pi M_{\mathrm{eff}}$ varied from 2147 G to 1515 G, respectively. In the temperature interval from 220 K to 320 K both magnetic parameters are well approximated by linear temperature dependences with slopes $dH_c/dT = (0.44 \pm 0.02)$ Oe/K and $d(4\pi M_{\mathrm{eff}})/dT = (-4.1 \pm 0.1)$ G/K. These values are consistent with YIG single-crystals data.[13] The dependence of the magnetic parameters on dopant concentration can be similarly investigated.[14,15]

We close with the observation that, in the derivation of the frequency-field relations, the directions of the vectors **H** and **M** have been assumed to coincide in tangentially or perpendicularly oriented films. On the one hand, for this condition to be satisfied, one of the magnetic symmetry axes must be tangentially or perpendicularly oriented, respectively, because the film must be magnetized along such an axis. On the other hand, the magnetizing field must be strong enough for the parallelism of the vectors **H** and **M** not to be disrupted under the influence of the magnetic anisotropy field. These requirements, however, do not impose limitations on the strength of the anisotropy field or the saturation magnetization. The above-derived equations, for example, can be used in the investigation of highly anisotropic films.

When the vectors **H** and **M** are not parallel, an analysis shows that the frequency-field relations in tangentially or perpendicularly magnetized films differ from the analogous relations (8)–(10) only in the replacement of H by the projection H_z of the vector **H** onto **M**. In strong magnetizing fields, when the influence of the anisotropy field on the equilibrium orientation of **M** can be ignored, the frequency-field relations can be used without making any distinction between H and H_z.

The author is grateful to A. V. Maryakhin for furnishing the film sample.

[1] A. G. Gurevich, *Magnetic Resonance in Ferrites and Antiferromagnets* [in Russian] (Nauka, Moscow, 1973), 591 pp.

[2] S. N. Bajpai, I. Rattan, and N. C. Srivastava, J. Appl. Phys. **50**, 2887 (1979).

[3] R. A. Lemons and B. A. Auld, J. Appl. Phys. **52**, 7360 (1981).

[4] A. V. Lugovskoĭ and V. I. Shcheglov, Radiotekh. Elektron. **27**, 518 (1982).

[5] V. V. Danilov and I. V. Zavislyak, Ukr. Fiz. Zh. **26**, 1392 (1981).

[6] A. S. Beregov, Izv. Vyssh. Uchebn. Zaved. Radioélektron. **27**(10), 9 (1984).

[7] R. D. Henry, P. I. Besser, D. M. Heins, and I. E. Mee, IEEE Microwave Guid. Wave Lett. **MAG-9**, 535 (1973).

[8] A. V. Kobelev, M. V. Perepelkina, A. A. Romanyukha, A. P. Stepanov, V. V. Ustinov, V. A. Matveev, and V. G. Tashirov, Zh. Tekh. Fiz. **60**(5), 117 (1990) [Sov. Phys. Tech. Phys. **35**, 605 (1990)].

[9] A. M. Zyuzin, V. V. Radaĭkin, and A. G. Bazhanov, Zh. Tekh. Fiz. **67**(2), 35 (1997) [Tech. Phys. **42**, 155 (1997)].

[10] O. A. Chivileva, A. G. Gurevich, and L. M. Émiryan, Fiz. Tverd. Tela (Leningrad) **29**, 110 (1987) [Sov. Phys. Solid State **29**, 61 (1987)].

[11] S. V. Belyakov, B. A. Kalinikos, and N. V. Kozhus', Élektron. Tekh. Ser. Élektron. SVCh, No. 1(415), 22 (1989).

[12] B. N. Gusev, O. A. Chivileva, A. G. Gurevich, L. M. Émiryan, and O. B. Naronovich, Pis'ma Zh. Tekh. Fiz. **9**, 159 (1983) [Sov. Tech. Phys. Lett. **9**, 70 (1983)].

[13] Yu. M. Yakovlev and S. Sh. Gendelev, *Ferrite Single Crystals in Radio Electronics* [in Russian] (Sov. Radio, Moscow, 1975), 360 pp.

[14] P. Hansen, J. Appl. Phys. **45**, 3638 (1974).

[15] P. Hansen, P. Röschman, and W. Tolksdorf, J. Appl. Phys. **45**, 2728 (1974).

Translated by James S. Wood

Thermal conductivity of $(VO)_2P_2O_7$ single crystals

A. V. Prokof'ev and I. A. Smirnov

A. F. Ioffe Physicotechnical Institute, Russian Academy of Sciences, 194021 St. Petersburg, Russia

W. Assmus and F. Büllesfeld

J.-W.-Goethe-Universität, 60054 Frankfurt a. M., Germany

A. Jezowski

Institute of Low-Temperature and Structural Research, Polish Academy of Sciences,
53-529 Wrocław, Poland

(Submitted May 15, 1998)
Fiz. Tverd. Tela (St. Petersburg) **40**, 2093–2094 (November 1998)

Thermal conductivity $\varkappa$ of single-crystal $(VO)_2P_2O_7$ has been studied within the 4–300 K range. A break was found in the $\varkappa(T)$ relation about 200 K, in the region of the transition from diffuse antiferromagnetic ordering (200–4 K) to a classical paramagnet ($T=200-300$ K). In the low-temperature domain (4–200 K), one may expect an additional contribution to $\varkappa(T)$ from the magnon component of thermal conductivity. © *1998 American Institute of Physics.* [S1063-7834(98)02811-1]

Recent years have been witnessing an increase of interest in investigation of materials with unusual magnetic properties (see, e.g., Ref. 1). A large number of studies deal with $(VO)_2P_2O_7$ (to be referred to subsequently as VOPO), which is a representative of low-dimensional spin systems.

VOPO has a monoclinically distorted orthorhombic structure with space group $P2_1$ and lattice parameters $a=7.73$ Å, $b=16.59$ Å, $c=9.58$ Å, $\beta=89.98°$. Vanadium ion pairs are arranged in the VOPO layered structure one under another in the $\langle 100 \rangle$ direction to form a "ladder" of V^{4+} ions.

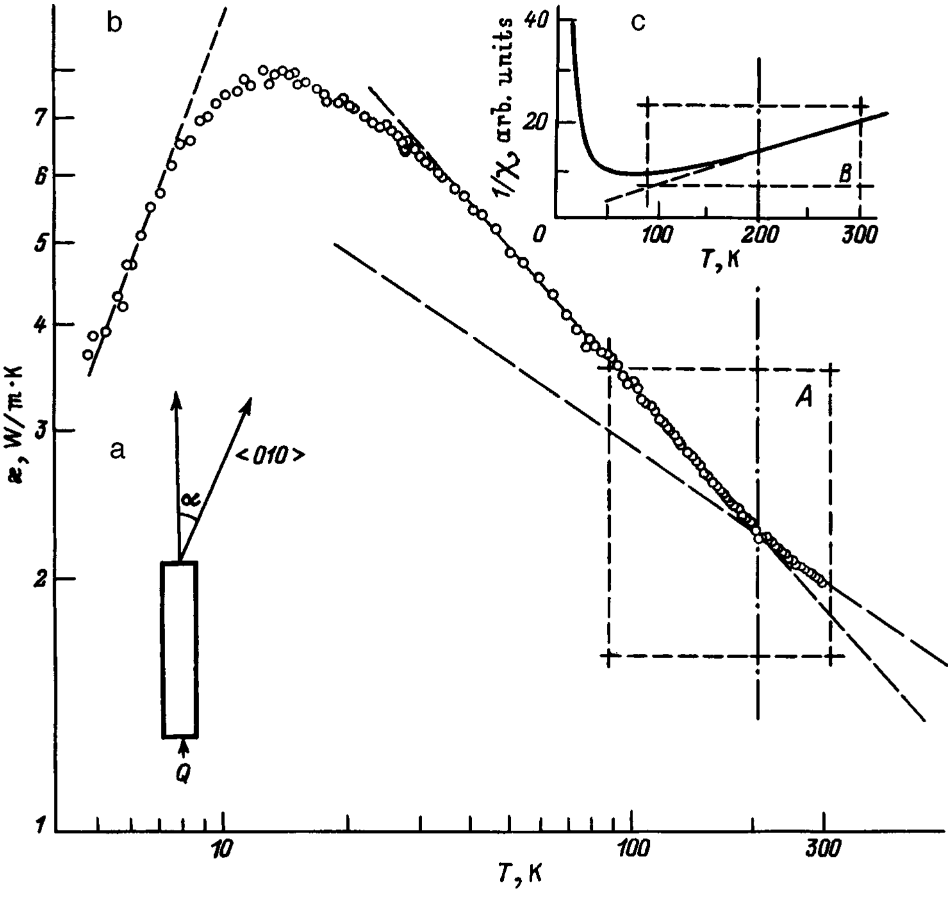

FIG. 1. (a) Sample geometry, (b) $\varkappa(T)$ of single-crystal $(VO)_2P_2O_7$, (c) $1/\varkappa(T)$ of single-crystal VOPO (Refs. 2 and 6).

The first experimental measurements[2] of the VOPO magnetic susceptibility $\varkappa$ were interpreted both within the spin-ladder concept and in terms of antiferromagnetic Heisenberg chains with alternating magnetic order.[2] Subsequent pulsed experiments of inelastic neutron scattering carried out on powder samples provided supportive arguments for the spin-ladder model.[3] At the same time later inelastic neutron-scattering data[4] obtained on an array of 200 oriented crystallites were found to be inconsistent with the $\langle 100\rangle$-oriented spin-ladder model while supporting the model of antiferromagnetic chains directed along $\langle 010\rangle$. Thus the question of which model would adequately describe the magnetic properties of VOPO still remains open.

Recently the authors of this work have developed a method of growing sufficiently large VOPO single crystals,[5] thus broadening the range of investigation of this compound.1)

According to the magnetic susceptibility data obtained on VOPO single crystals, within the 200–300 K interval the $1/\chi(T)$ function behaves in the way typical of conventional paramagnets.[6] For $T<200$ K, the $1/\chi(T)$ relation suggests the onset of gradual antiferromagnetic ordering, which, rather than occurring at a fixed T, takes place within a broad temperature range (200–4 K).

This work reports preliminary data on the thermal conductivity of VOPO. Such data are lacking in the literature, but they are needed for thermodynamic calculations related to this material.

The thermal conductivity of VOPO was measured on a single-crystal sample within the 4–300 K range. The single crystal was grown by the technique described elsewhere.[5] The sample was $5\times3\times2$ mm in size, and the heat flow propagated along the longer side of the crystal, which was at 25° to the $\langle 010\rangle$ direction (Fig. 1a). Measurements of $\varkappa$ were performed on a set-up similar to that described in Ref. 7. VOPO is an insulator and, therefore, the $\varkappa$ obtained in this experiment relates actually to the lattice thermal conductivity.

The objective of the work was (1) to measure the thermal conductivity of VOPO within a broad temperature range, and (2) to study the behavior of $\varkappa(T)$ within the broad region of antiferromagnetic ordering (4–200 K) and at the transition to the classical paramagnet ($\sim$200 K).

Our experimental data on $\varkappa(T)$ are displayed in Figs. 1 and 2. We readily see a break in the relation about 200 K, which is apparently caused by the influence of the magnon subsystem within the 200–4 K range.[4] It may manifest itself in two ways: (1) an additional contribution due to heat transport by magnons ($\varkappa_m$), and (2) a decrease of thermal conductivity because of phonon-magnon scattering. The temperature dependence of $\varkappa$ (the break about 200 K followed by an increase of $\varkappa$ with temperature) argues most likely for the existence within the 200–4 K interval of an additional contribution from $\varkappa_m$ to the measured thermal conductivity.

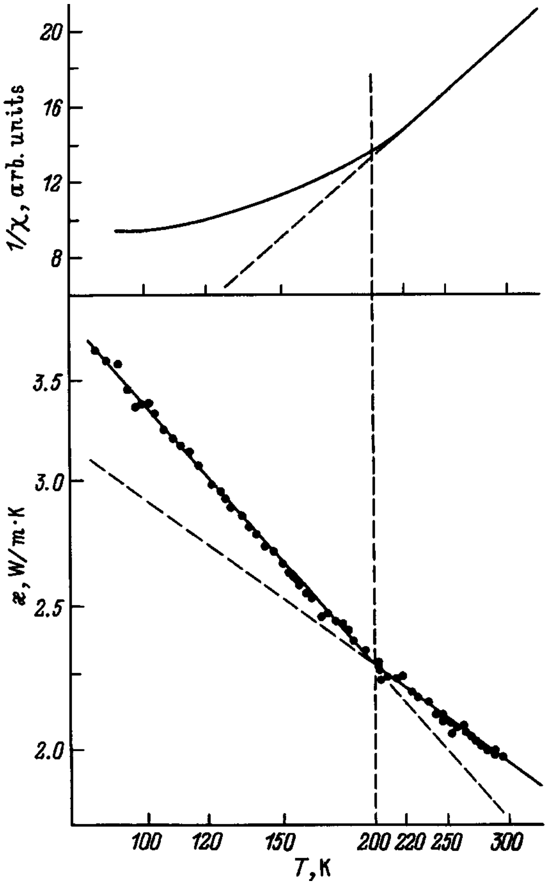

FIG. 2. $1/\varkappa(T)$ (region B) and $\varkappa(T)$ (region A) of VOPO (Fig. 1) shown on an enlarged scale.

It does not presently appear possible to estimate this contribution, because it would even be difficult to choose an appropriate expression for estimation of $\varkappa_m$ for a system with such a strongly diffuse antiferromagnetic transition as VOPO. More definite conclusions can be drawn only after performing $\varkappa(T)$ measurements in a magnetic field, which represent our next objective.

1)All the data available on VOPO in the literature (with the exception of this work and of Ref. 6) were obtained from measurements on powder and polycrystalline samples.

---

[1] E. Orignac and T. Giamarchi, Phys. Rev. B **57**, 5812 (1998).
[2] D. C. Johnston, J. W. Johnson, D. P. Goshorn, and A. J. Jacobson, Phys. Rev. B **35**, 219 (1987).
[3] R. S. Eccleston, T. Barnes, J. Brody, and J. W. Johnson, Phys. Rev. Lett. **73**, 2626 (1994).
[4] A. W. Garrett, S. E. Nagler, D. A. Tennant, B. C. Sales, and T. Barnes, Phys. Rev. Lett. **79**, 745 (1997).
[5] A. V. Prokofiev, F. Büllesfeld, and W. Assmus, Cryst. Res. Technol. **33**, 155 (1998).
[6] A. V. Prokofiev, F. Büllesfeld, W. Assmus, H. Schwenk, D. Wichert, U. Löw, and B. Lüthi, Europ. Phys. J. B (in press).
[7] A. Jezowski, J. Mucha, and G. Pompe, J. Phys. D **20**, 1500 (1987).

Translated by G. Skrebtsov

PHYSICS OF THE SOLID STATE VOLUME 40, NUMBER 11 NOVEMBER 1998

Magnetoelastic interaction in a spatially disordered ferromagnet containing a large number of defects

V. V. Men'shenin

Institute of Metal Physics, Ural Branch of the Russian Academy of Sciences, 620219 Ekaterinburg, Russia

(Submitted February 23, 1998; resubmitted May 21, 1998)
Fiz. Tverd. Tela (St. Petersburg) **40**, 2095–2100 (November 1998)

The description of a continuum with continuously distributed dislocations and disclinations is extended to the case of a spatially disordered ferromagnet. It is shown that the interaction of disclinations with spins can have the effect that the spin-wave frequency is equal to zero for a nonzero wave vector. The variation of the coupled-oscillation frequency is determined in the case of weak coupling between elastic waves and defects. © *1998 American Institute of Physics.* [S1063-7834(98)02911-6]

It is generally known that disordered media lack long-range order in the spacing of their atoms,[1] a condition that significantly alters their spatial distribution from that of crystals. Even though the volume occupied by the atoms of an amorphous material can be partitioned into space-filling Voronoi polyhedra having a configuration similar to that of Wigner–Seitz cells in a crystal, the polyhedra themselves are not mutually congruent,[2] and their symmetry can contain axes of odd order higher than three-fold, which cannot possibly exist in a crystal.[3] Consequently, the structure of disordered media is invariant under local transformations. This means that amorphous materials have a local invariance property.[4]

The presence of odd, fivefold and higher-order symmetry axes in the system is attributable to the existence therein of topologically stable defects called disclinations[4] — structural elements that maintain the amorphous state proper. An important consideration is the fact that here the disclinations cannot be regarded as independent; the hypothesis of an ensemble of interacting disclinations is closer to the truth. If the medium is treated as a continuum, the disclinations can be assumed to have a continuous distribution. In describing the elastic properties of continua, it is assumed that the components of the displacements of points of the medium from the equilibrium position are single-valued functions of the coordinates. This means that a single coordinate system suffices for describing the entire manifold in the medium. When line defects (disclinations and dislocations) are present in the medium, it is impossible to uniquely specify the displacement of points of the medium relative to this single coordinate system. This is the situation in manifolds having torsion and curvature.[5] We can assume therefore that the internal geometry of a medium containing line defects is not Euclidean. In this context the formation of disclinations and dislocations can be attributed to the curving and torsion of space, respectively.[6] A description of the macroscopic dynamics of media having a continuous distribution of line defects without magnetic order is given in Ref. 7. The main approach of this study to formulation of the dynamics is to establish a one-to-one correspondence between the kinematic equations of the defects and the system of Cartan equations for the external forms governing the geometry of the medium. The disclination and dislocation fields are treated as gauge fields generated when the action of the symmetry group of the system loses homogeneity. Grachev *et al.*[8] have extended this approach to systems containing point as well as line defects.

In several papers[9–11] the dynamical magnetic properties of disordered magnets have been investigated using gauge-theoretic methods. However, only magnetic ordering anomalies are taken into account in these papers. The atomic structure is assumed to be defect-free, which is not fully consistent with notions of the amorphous state. Since disclinations in a disordered structure are formations inherent in the structure at the outset, there is a need to investigate their influence on various — including dynamical — properties of the atomic and magnetic subsystems of the structure.

In this paper we discuss the influence of disclinations on dynamical magnetoelastic interaction phenomena in spatially disordered magnets. Our investigation of this problem is based on an extension of the theory[7] to a medium having magnetic degrees of freedom. This extension essentially rests on the fact that, in the presence of line defects, the potential energy of the magnet must be invariant under simultaneous local rotations of spins and the lattice and therefore can be written as a function of quantities that are invariant under the indicated transformations. We also assume that the magnetic properties depend mainly on exchange interactions, which greatly exceed relativistic interactions. This condition enables us, by analogy with Ref. 12, to describe the magnetic properties by introducing the parameters $\boldsymbol{\varphi}=\mathbf{n}\tan(\theta/2)$, which specify spin rotations through angle θ about the axis $\mathbf{n}$.

1. EQUATIONS OF MOTION

To begin, we use the Lagrangian formalism to obtain the dynamical equations of motion. We write the Lagrangian of a disordered ferromagnet in the form

$$L=\frac{1}{2}\alpha_{ik}\omega_i(\boldsymbol{\varphi},\nabla_4\boldsymbol{\varphi})\omega_k(\boldsymbol{\varphi},\nabla_4\boldsymbol{\varphi})+\frac{2}{\gamma}M_i\omega_i(\boldsymbol{\varphi},\nabla_4\boldsymbol{\varphi})$$

$$+\left(\frac{\gamma}{2}\alpha_{ik}\omega_k(\boldsymbol{\varphi},\nabla_4\boldsymbol{\varphi})+M_i\right)H_i+\frac{1}{2}\rho_0(\nabla_4x^i)^2$$

$$-\left\{\frac{1}{2}d_{ij}\omega^*_{i,k}\omega^*_{j,k}+\frac{1}{2}\lambda_{ijkl}\eta_{ij}\eta_{kl}+\frac{1}{2}b_{ijkl}\eta_{ij}M^*_kM^*_l\right.$$

$$\left.+K_{ij}Q^*_{ij}+K_{ijkl}Q^*_{ij}Q^*_{kl}\right\}-\frac{1}{2}s_2c_{\alpha\beta}F^{\alpha}_{ab}g^{ac}g^{bd}F^{\beta}_{cd}$$

$$-\frac{1}{2}s_1\delta_{ij}D^i_{ab}k^{ac}k^{bd}D^j_{cd},$$

$$\omega_i(\boldsymbol{\varphi},\nabla_b\boldsymbol{\varphi})=\frac{(\nabla_i\boldsymbol{\varphi}+[\boldsymbol{\varphi},\nabla_b\boldsymbol{\varphi}])_i}{1+\varphi^2}, \tag{1}$$

$$b=1,2,3,4,\quad i=1,2,3,$$

$$\omega^*_{n,j}=\omega_i(\boldsymbol{\varphi},\nabla_n\boldsymbol{\varphi})\nabla_jx^i,\quad \eta_{ij}=\frac{1}{2}(\nabla_ix^s\nabla_jx^s-\delta_{ij}),$$

$$M^*_k=M_s\nabla_kx^s,\quad Q^*_{ij}=(Q_{rs}-\delta_{rs})\nabla_ix^r\nabla_jx^s,$$

$$F^{\alpha}_{bc}=\partial_bW^{\alpha}_c-\partial_cW^{\alpha}_b+c^{\alpha}_{\beta\gamma}W^{\beta}_bW^{\gamma}_c,\quad \partial_b=\frac{\partial}{\partial a^b},$$

$$D^i_{bc}=\partial_b\mu^i_c-\partial_c\mu^i_b+\gamma^i_{\alpha j}(W^{\alpha}_b\mu^j_c-W^{\alpha}_c\mu^j_b+F^{\alpha}_{ab}x^j),$$

$$b,c=1,2,3,4,\quad i,j=1,2,3, \tag{2}$$

and the covariant derivatives ∇_bx^k and $\nabla_b\varphi^k$ have the form

$$\nabla_bx^k=\frac{\partial x^k}{\partial a^b}+\gamma^k_{nj}W^n_bx^j+\mu^k_b,$$

$$\nabla_b\varphi^k=\frac{\partial\varphi^k}{\partial a^b}+\gamma^k_{nj}W^n_b\varphi^j,\quad \frac{\partial}{\partial a^4}=\frac{\partial}{\partial t}. \tag{3}$$

In Eqs. (1) ρ_0 is the predeformation density of the medium, a_i denotes the Lagrangian coordinates of the initial configuration, $M_i=Q_{ik}(\boldsymbol{\varphi})M^k_0$ is the orientation of the spontaneous magnetization vector $\mathbf{M}_0$ in the nonequilibrium state,

$$Q_{ik}(\boldsymbol{\varphi})=\delta_{ik}+2\frac{(\varphi_i\varphi_k-\varphi^2\delta_{ik}+\varepsilon_{ink}\varphi_n)}{1+\varphi^2}$$

is the matrix of rotations, $c_{\alpha\beta}=c^{\delta}_{\alpha\gamma}c^{\gamma}_{\beta\delta}$ are the structure constants of the Lie algebra of the $SO(3)$ group, γ_{α} are rotation group generators, γ is the gyromagnetic ratio, s_1 and s_2 are positive constants,

$$\alpha_{ik}=\alpha_1\delta_{ik}+\alpha_2n_in_k,\quad n_i=\frac{M_i}{M_0},\quad d_{ij}=d_1\delta_{ij}+d_2n_in_j,$$

$$g^{ac}=-\delta^{ac},\quad a,c=1,2,3;\quad g^{44}=\frac{1}{\zeta},\quad g^{ac}=0,$$

$$a\neq c,\quad \zeta>0,\quad k^{ac}=-\delta^{ac},\quad a,c=1,2,3;$$

$$k^{44}=\frac{1}{y},\quad k^{ac}=0,\quad a\neq c,\quad y>0,\quad K_{ij}=K_0\delta_{ij},$$

$$K_{ijkl}=K^0_1\delta_{ij}\delta_{kl}+K^0_2\delta_{ik}\delta_{jl}+K^0_3\delta_{il}\delta_{jk},$$

$$b_{ijkl}=b^0_1(\delta_{ik}\delta_{jl}+\delta_{il}\delta_{jk})+b^0_2\delta_{ij}\delta_{kl},$$

$$\lambda_{ijkl}=\lambda_1(\delta_{ik}\delta_{jl}+\delta_{il}\delta_{jk})+\lambda_2\delta_{ij}\delta_{kl}, \tag{4}$$

λ_{ijkl} and b_{ijkl} are elastic and magnetoelastic constants, respectively, K_{ij} and K_{ijkl} are anisotropy constants, and $\mathbf{H}$ is the external magnetic field. The physical significance of the quantities s_1, s_2 y, and ζ are clarified in Ref. 7, and W^{α}_n and μ^{α}_n are compensating fields produced in inhomogeneous transformations of the rotation group $SO(3)$ and the translation group $T(3)$, respectively. The right Cartan forms $\boldsymbol{\omega}(\boldsymbol{\varphi}, \delta\boldsymbol{\varphi}$ in Eqs. (1) specify the parameters of relative rotation of spins at the points $\mathbf{x}$ and $\mathbf{x}+d\mathbf{x}$. Here, in contrast with Ref. 12, $\delta\boldsymbol{\varphi}$ incorporates the variations of the parameter $\boldsymbol{\varphi}$ both in its parallel transfer from $\mathbf{x}$ to $\mathbf{x}+d\mathbf{x}$ and as a result of the difference in the coordinate systems at the indicated points.

In Eqs. (2) the quantities $\omega^*_{n,j}$, η_{ij}, M^*_k, and Q^*_{ij} are invariant under simultaneous rotations and translations of spins and the continuum. Their presence is a direct result of the requirement of invariance of the potential energy of the magnet under the above-indicated transformations. The expansion of the potential energy in these combinations of dynamical variables yields the expression in the braces in Eqs. (1).

Invoking the variational least-action principle, from the Lagrangian (1) we obtain the following equations for the dynamical variables of our problem:

$$\partial_bZ^b_i-Z^b_jW^{\alpha}_b\gamma^j_{\alpha i}=R^{ab}_jF^{\alpha}_{ab}\gamma^j_{\alpha i},\quad \partial_bR^{bc}_i-\gamma^j_{\alpha i}R^{bc}_jW^{\alpha}_b=\frac{1}{2}Z^c_i,$$

$$\partial_bN^b_i-\gamma^j_{\alpha i}W^{\alpha}_kN^k_j-\Xi_i=0,$$

$$\partial_bG^{ba}_{\alpha}-c^{\beta}_{\xi\alpha}W^{\xi}_bG^{ba}_{\beta}=R^{ab}_j\gamma^j_{\alpha n}\nabla_bx^n+N^a_i\gamma^i_{\alpha n}\varphi^n,$$

$$a,b=1,2,3,4,\quad i,j,k=1,2,3. \tag{5}$$

The following notation has been introduced in Eqs. (5):

$$\frac{\partial L}{\partial(\nabla_bx^i)}=Z^b_i,\quad \frac{\partial L}{\partial(\nabla_b\varphi^i)}=N^b_i,$$

$$\Xi_i=\frac{\partial L}{\partial\varphi^i}\Big|\nabla_k\varphi^i=\text{const},\quad R^{bc}_i=\frac{\partial L}{\partial D^i_{bc}},$$

$$G^{bc}_{\alpha}=\frac{\partial L_W}{\partial F^{\alpha}_{bc}},\quad L_W=-\frac{1}{2}s_1c_{\alpha\beta}F^{\alpha}_{ab}g^{ac}g^{bd}F^{\beta}_{cd}, \tag{6}$$

and allowance has been made for the fact that variations of the quantities $\mu^i=\mu^i_bda^b$ and $W^{\alpha}=W^{\alpha}_bda^b$ by the amounts $\delta\mu^i=\varepsilon\nu^i$ and $\delta W^{\alpha}=\varepsilon\xi^{\alpha}$ induce the variations

$$\delta F^i=\varepsilon(d\xi^i+c^i_{\beta\gamma}W^{\beta}\wedge\xi^{\gamma}),\quad \delta D^i=\varepsilon(d\nu^i+\Gamma^i_j\wedge\nu^j). \tag{7}$$

In relations (7) the symbol $\wedge$ denotes the exterior product, and $\Gamma^i_j=\gamma^i_{\alpha j}W^{\alpha}_bda^b$.

2. INTEGRABILITY CONDITIONS

Equations (5) cannot be solved for arbitrary values of Z^i_b, R^{bc}_i, G^{bc}_a, N^b_i, and Ξ_i. They must satisfy equations called the integrability conditions. These conditions have been derived[7] for a nonmagnetic continuum by repeated external differentiation of the equations for the dynamical variables after their representation in the form of equations for differential forms. The resulting relations were found to be equivalent to the momentum and angular momentum balance equations for the medium. The momentum balance equation is satisfied identically in this case.

It is well known[13] that the angular momentum balance equation of a system implies invariance of its Lagrangian under rotation of the body as a whole. We make use of this property in the derivation of the indicated equation for a disordered ferromagnet. To do so, we take into account the fact that the quantities Γ, $\boldsymbol{\varphi}$, and $\mathbf{M}$ are transformed under such rotations according to the laws $\Gamma' = Q\Gamma Q^{-1}$, $\boldsymbol{\varphi}' = Q\boldsymbol{\varphi}$, and $\mathbf{M}' = Q\mathbf{M}$, where Q is the matrix of rotations, and the variation δ commutes with the operations of differentiation with respect to time and coordinates. In this case we obtain the following relation from the requirement that $\delta L = 0$ in rotation of the body as a unit whole:

$$\gamma^i_{\alpha j}\left(Z^s_i \nabla_s x^j + \Xi_i \varphi^j + N^a_i \nabla_a \varphi^j + \frac{\partial L}{\partial M^i_0} M^j_0 \right) = 0, \tag{8}$$

which, given the choice of invariants in the form (2), is satisfied identically if $\mathbf{M} \neq 0$. When $\mathbf{M} = 0$, as for example in a spin glass, it follows from Eq. (8) that interaction between the spin and elastic subsystems does not take place in the linear approximation.

We call attention to the following consideration. If the integrability conditions in a disordered ferromagnet are the same as in Ref. 7, we obtain an equation analogous to (8), but without the term $\gamma_{\alpha j}(\partial L / \partial M^i_0) M^j_0$, which differs from the angular momentum balance equation if $\mathbf{M} \neq 0$. It is not an integrability condition in this case.

3. INTERACTION OF SPIN AND ELASTIC WAVES WITH DISCLINATIONS AND DISLOCATIONS

We now consider the interaction of the magnetic moments and atomic displacements with the fields of disclinations and dislocations in a spatially disordered ferromagnet.

We assume that waves propagate in the medium in the direction of axis *3* (axis *3* refers to Lagrangian coordinates). We determine the static displacements without defects. In this case they are attributable to magnetoelastic coupling and can be determined from the minimum of the potential energy of the system. We assume that $\mathbf{M}_0 = \{0, 0, M\}$ and $\mathbf{H}_0 = \{0, 0, H\}$. Only the static displacement u^0_3 has a nonzero value in this case; it is equal to $u^0_3 = -\xi a_3$, where ξ is a constant representing a combination of elastic and magnetoelastic constants. All other components of the displacement are equal to zero. To simplify the problem, we assume that the gauge fields W^α_1, W^α_2, μ^α_1, and μ^α_2 are equal to zero for waves propagating along axis *3*. Substituting the expression for the density of the Lagrangian (1) into Eq. (5), in the linear approximation we obtain a system of coupled equations describing the above-indicated interactions. For right-polarized waves it has the form

$$\alpha_1 \frac{\partial^2}{\partial t^2} \varphi^+ + \alpha_1 \left(-2i\omega_0 \frac{\partial \varphi^+}{\partial t} + \Omega^2_0 \varphi^+ \right) - 2ib^0_1 M^2_0$$

$$\times \left(\frac{\partial u^+}{\partial a_3} + \mu^+_3 \right) - i \frac{2}{\gamma} M_0 W^+_4 - d_1 \frac{\partial^2 \varphi^+}{\partial a^2_3} = 0,$$

$$-\rho_0 \left(\frac{\partial^2 u^+}{\partial t^2} + \frac{\partial \mu^+_4}{\partial t} \right) + \lambda_{\mathrm{ef}} \frac{\partial^2 u^+}{\partial a^2_3} + \lambda_{\mathrm{ef}} \frac{\partial \mu^+_3}{\partial a_3}$$

$$+ 2ib^0_1 M^2_0 \frac{\partial \varphi^+}{\partial a^3} = 0,$$

$$\frac{2s_1}{y} \left(\frac{\partial^2 \mu^+_3}{\partial t^2} - y \frac{\partial^2 \mu^+_3}{\partial a^2_3} + \frac{\lambda_{\mathrm{ef}} y}{2s_1} \mu^+_3 \right)$$

$$= -\lambda_{\mathrm{ef}} \frac{\partial u^+_3}{\partial a_3} + 4ib^0_1 M^2_0 \varphi^+,$$

$$\frac{s_1}{y} \left(\frac{\partial^2 \mu^+_4}{\partial a^2_3} - \frac{1}{y} \frac{\partial^2 \mu^+_4}{\partial t^2} \right)$$

$$= \rho_0 \left(\frac{\partial u^+}{\partial t} + \mu^+_4 \right) + i \frac{s_1}{y} \frac{\partial W^+_4}{\partial a_3} - i \frac{s_1}{y} \frac{\partial W^+_3}{\partial t},$$

$$\frac{s_2}{\zeta} \left(\frac{\partial^2 W^+_4}{\partial a^2_3} - \frac{1}{\zeta} \frac{\partial^2 W^+_4}{\partial t^2} \right) + \frac{s_1}{y} i \left(\frac{\partial \mu^+_3}{\partial t} - \frac{\partial \mu^+_4}{\partial a_3} \right) - i \frac{2}{\gamma} M_0 \varphi^+ = 0,$$

$$\frac{\partial^2 W^+_3}{\partial t^2} - \zeta \frac{\partial^2 W^+_3}{\partial a^2_3} = 0. \tag{9}$$

The following notation has been introduced in Eqs. (9):

$$\varphi^+ = \varphi_1 + i\varphi_2, \quad u^+ = u_1 + iu_2, \quad \mu^+_3 = \mu^1_3 + i\mu^2_3,$$

$$W^+_3 = W^1_3 + iW^2_3, \quad W^+_4 = W^1_4 + iW^2_4, \quad \lambda_{\mathrm{ef}} = \lambda_1 + 2b^0_1 M^2_0,$$

$$\omega_0 = \frac{1}{2\alpha_1} \left[\frac{4M_0}{\gamma} + \gamma H(\alpha_2 - \alpha_1) \right],$$

$$\Omega^2_0 = \frac{1}{\alpha_1} (K_1 + 4M_0 [H + 4b^0_1 M^3_0 \lambda^{-1}_2]),$$

$$K_1 = 8(K^0_2 - K^0_3) - 4K_0,$$

and the following gauge is used as a convenience for our analysis:

$$\frac{\partial \mu^i_3}{\partial a_3} = \frac{1}{y} \frac{\partial \mu^i_4}{\partial t}, \quad y > 0,$$

$$\frac{\partial W^i_3}{\partial a_3} = \frac{1}{\zeta} \frac{\partial W^i_4}{\partial t}, \quad \zeta > 0 \quad (i = 1,2).$$

We note that the gauge fields W^3_3 and W^3_4 are equal to zero for the given direction of wave propagation. Moreover, terms proportional to the product of $u^0_3 + a_3$ and one of the fields W^+_3 or W^+_4 or, equivalently, one of their spatial derivatives

($\partial W_3^+/\partial a_3$, $\partial W_4^+/\partial a_3$) or time derivatives ($\partial W_3^+/\partial t$, $\partial W_4^+/\partial t$) are omitted in Eqs. (9). These terms are omitted for the following reason. Their presence in the equations makes the wave amplitudes dependent on the spatial coordinates. This means that energy exchange takes place between the waves, i.e., they interact nonlinearly. The omitted terms are therefore strongly nonlinear, and their accuracy is greater than that with which Eqs. (9) are formulated in the first place.

The asymmetry of Eqs. (9) with respect to terms containing the disclination fields W_3^+ and uW_4^+ mirrors their role as sources of the dislocation fields μ_3^+ and μ_4^+. Attention has already been called to this fact in Ref. 7.

We now undertake the analysis of the system (9). We first consider the limiting case without magnetoelastic coupling, and we set the dislocation fields μ_3^+ and μ_4^+ equal to zero. We then have interaction between the spins and the disclination fields W_4^+. We seek a solution for the fields φ^+ and W_4^+ in the form

$$\varphi^+=\varphi^+(0)\exp(i[ka_3-\omega t]),$$

$$W_4^+=W_4^+(0)\exp(i[ka_3-\omega t]).$$

The dispersion relation describing the coupled spin and disclination modes can now be written

$$\left(\omega^2+2\omega_0\omega-\Omega_0^2-\frac{d}{\alpha_1}k^2\right)(\omega^2-\zeta k^2)-\frac{4M_0^2\zeta^2}{\gamma^2 s_2\alpha_1}=0. \tag{10}$$

Assuming that the wave vector $k=0$ in Eq. (10), we find an equation characterizing the energy gaps in the wave spectrum. If the condition

$$\frac{4M_0^2\zeta^2}{\gamma^2 s_2\alpha_1}\ll(\omega_s^+(0))^3(\omega_s^-(0)+\omega_s^+(0)),$$

$$\omega_s^\pm(0)=\mp\omega_0+\sqrt{\omega_0^2+\Omega_0^2}$$

holds, where $\omega_s^\pm$ are the activation energies of noninteracting right- $(+)$ and left- $(-)$ circularly polarized spin waves, the uniform precession frequency of spins as a result of interaction with disclinations in the case of right-polarized waves increases by the amount

$$\Delta=\frac{4M_0^2\zeta^2}{\gamma^2 s_2\alpha_1(\omega_s^+(0))^2(\omega_s^+(0)+\omega_s^-(0))}. \tag{11}$$

We note the following. Inasmuch as Eq. (10) does not admit the solution $\omega=0$ for $k=0$, we can infer from this assertion that the spectrum of a disclinationlike mode also acquires a gap as a result of interaction with the spin subsystem. Assuming now that the inequalities

$$\left[\frac{M_0^2\zeta^2}{4\gamma^2 s_2\alpha_1\omega_0^4}\right]^{1/3}\ll1,\quad\left[\frac{\Omega_0^{3/2}\gamma^2 s_2\alpha_1}{\omega_0^2 4M_0^2\zeta^2}\right]^{1/3}\ll1$$

hold, we obtain the following value of the energy gap of a disclinationlike mode:

$$\Delta_d=\left[\frac{2M_0^2\zeta^2}{\gamma^2 s_2\alpha_1\omega_0}\right]^{1/2}. \tag{12}$$

Equation (10) is biquadratic in the wave vector k. Its solution can therefore be found exactly:

$$k_{1,2}^2=\frac{\alpha_1}{2\zeta d}\left[\zeta(\omega^2+2\omega_0\omega-\Omega_0^2)+\frac{d\omega^2}{\alpha_1}\right]\pm\left\{\left(\frac{\alpha_1}{2\zeta d}\right)^2\left[\zeta(\omega^2+2\omega_0\omega-\Omega_0^2)-\frac{d\omega}{\alpha_1}\right]^2+\frac{\omega_0^2\alpha_1^2\zeta}{s_2 d}\right\}^{1/2}. \tag{13}$$

Setting the frequency $\omega=0$ in the latter relation, we find that the square of the wave vector k_1

$$k_1^2=\left\{\left(\frac{\Omega_0^2\alpha_1}{2\zeta d}\right)^2+\frac{\omega_0^2\alpha_1\zeta^2}{s_2 d}\right\}^{1/2}-\frac{\Omega_0^2\alpha_1}{2\zeta d} \tag{14}$$

is nonzero in this case. Consequently, the wave vector k_1 has a value at which the oscillation frequency is equal to zero. We now elucidate the question of the mode with which this solution is associated. Letting $\zeta\to0$ in Eq. (13), we have

$$k_1^2\Big|_{\zeta\to0}=\frac{\alpha_1}{d}(\omega^2+2\omega_0\omega-\Omega_0^2),\quad k_2^2\Big|_{\zeta\to0}=\frac{\omega^2}{\zeta}.$$

It is evident from this result that the value of k_1 at which $\omega=0$ is identified with a spinlike mode. It follows, therefore, that for wave numbers k whose values are smaller than, but close to k_1 the frequency of this mode does not increase with increasing k, as is usually the case, but decreases.

We call attention to the following consideration. In the description of the gauge theory of disordered magnets as a field theory on a principal fiber bundle in Ref. 11, the authors pass to the limit of a slightly less than ideal ferromagnet. A necessary condition for this transition is zero-valued curvature form of a linear connection on a fiber bundle of linear frames.

In this paper we use the traditional approach to gauge theorems, i.e., we work with an associated fiber bundle rather than with a principal fiber bundle. In contrast with Ref. 11, therefore, we do not concern ourselves with the spatial coordinates. Here the spatial coordinates in question are the Lagrangian coordinates of the initial defect-free, undeformed, paramagnetic state of the system. In this situation a limiting transition analogous to the one discussed in Ref. 11 implies that the compensating fields $W_\alpha=0$, because only in this case does the curvature tensor of the final state of the system (''charge'' space) vanish. Accordingly, we go directly to the previously proposed[12] (or in the method of phenomenological Lagrangians) description of long-wavelength spin excitations in a disordered ferromagnet.

We now consider a second limiting situation, wherein we disregard spin degrees of freedom. The dispersion relation describing simultaneous harmonic oscillations of the displacement, dislocation, and disclination fields with wave vector k and frequency ω has the form

$$\begin{aligned}&\left[\rho_0(\omega^2-c^2k^2)\frac{2s_1}{y}\left(yk^2+\lambda_{\mathrm{ef}}\frac{y}{2s_1}-\omega^2\right)+\lambda_{\mathrm{ef}}^2k^2\right]\\&\quad\times\left[\frac{s_1s_2}{y^2\zeta^2}\left(\omega^2-yk^2-\frac{\rho_0y^2}{s_1}\right)(\omega^2-\zeta k^2)-\frac{s_1^2k^2}{y^2}\right]\\&\quad+\omega^2\rho_0\biggl[\frac{2s_1s_2\rho_0}{y\zeta^2}\left(yk^2+\lambda_{\mathrm{ef}}\frac{y}{2s_1}-\omega^2\right)(\omega^2-\zeta k^2)\\&\quad+\frac{s_1^2\lambda_{\mathrm{ef}}k^2}{y^2}\biggr]=0,\quad c^2=\lambda_{\mathrm{ef}}\rho_0^{-1}.\end{aligned}\tag{15}$$

We set the wave vector in Eq. (15) equal to zero. In this case it is evident that modes describing oscillations of the fields W_4^+ and W_3^+ remain nonactivated. The energy gap $\omega_0^2=(\lambda_{\mathrm{ef}}y/2s_1)^2$ acquires a mode associated with oscillations of dislocations. Consequently, the interaction of the disclination fields with elastic waves does not produce an energy gap in the spectrum of a disclinationlike mode.

We now find an approximate solution of Eq. (15), valid only for weak coupling between elastic displacements and defects. In this approximation we can seek a solution of Eq. (15) in the form

$$\omega=ck+\Delta.$$

We then have the relation for Δ

$$\begin{aligned}\Delta=&\biggl\{\frac{4s_1\rho_0ck}{y}\left(\frac{\lambda_{\mathrm{ef}}y}{2s_1}+(y-c^2)k^2\right)\biggl[\frac{s_1s_2}{(y\zeta)^2}\biggl(k^2[c^2-y]\\&-\frac{\rho_0y^2}{s_1}\biggr)(c^2-y)k^2-\frac{s_1^2k^2}{y}\biggr]\biggr\}^{-1}\biggl\{ck\rho_0\biggl[-\frac{s_1\lambda_{\mathrm{ef}}ck^3}{y^2}\\&+\frac{2s_1s_2\rho_0ck}{y\zeta}\left([y-c^2]k^2+\frac{\lambda_{\mathrm{ef}}y}{2s_1}\right)(c^2-\zeta)k^2\biggr]\\&-\lambda_{\mathrm{ef}}^2k^2\left[\frac{s_1s_2}{(y\zeta)^2}\left([c^2-y]k^2-\frac{\rho_0y^2}{s_1}\right)(c^2-y)k^2-\frac{s_1^2k^2}{y^2}\right]\biggr\}.\end{aligned}\tag{16}$$

The general dispersion relation for coupled oscillations of the magnetization, elastic displacements, dislocation field, and disclination field is too cumbersome to write out here and is intractible by analytical methods.

In this paper we have thus proposed a generalization of the macroscopic description of magnetoelastic coupling to spatially disordered ferromagnets, providing a means for describing phenomena of the interaction of magnetization fields not only with elastic displacements of points of the medium, but also with line defects such as disclinations.

To describe the dynamical effects of such interaction, we have used the Lagrangian formalism and, on the basis thereof, have derived coupled equations of motion for the dynamical variables characterizing the medium. The potential energy of the system is found to be invariant under local simultaneous rotations and translations of the magnetic moments and points (atoms) of the medium.

The integrability conditions for the coupled equations of motion are equivalent to the momentum balance equation and the total mechanical angular momentum balance equation of the medium. The second of these equations (8) has been deduced from the requirement that the Lagrangian is invariant under rotation of the body as a whole. It follows from this condition, in particular, that within the framework of the given model interaction between the spin and ''lattice'' subsystems does not occur in a spin glass ($\mathbf{M}_0=0$) in the linear approximation.

Even in the limiting case of zero magnetoelastic coupling the interaction of spins and disclinations significantly influences their dynamics. As a result of this interaction the spectrum of homogeneous vibrations of disclinations acquires an energy gap, and the frequency of uniform precession of the spins changes. In the interval of wave vectors $0<k\leqslant k_1$, where k_1 is given by Eq. (14), the frequency of a spinlike mode of coupled oscillations decreases from the uniform precession frequency to $\omega=0$. The physical causes of the onset of the soft mode (14) require further study. However, indirect evidence exists as to the possibility of its existence. This possibility is indicated by experiments on neutron scattering in the amorphous alloy $\mathrm{Fe}_{0.75}\mathrm{Co}_{0.15}\mathrm{C}_{0.1}$ (Ref. 14), which expose the presence of a minimum in the dispersion law for spin excitations at very high frequencies.

In the second limiting case, where magnetic degrees of freedom are disregarded, the interaction of elastic waves with dislocations and disclinations produces an energy gap only in the spectrum of the dislocation mode, consistent with the results of Ref. 7, whereas disclination modes remain nonactivated. Only in the weak-coupling approximation is it possible to determine the variation of the elastic wave frequency. In closing, we note that the presence of topologically stable defects of the disclination type in the atomic structure of spatially disordered media follows directly from the topological theory of defects[15,16] and is attributable to the nontriviality of the rotation group $SO(3)$, which is not simply connected. The onset of dislocations here is induced by their disclination sources.[7]

[1] J. D. Bernal, Proc. R. Soc. London, Ser. A **280**, 299 (1964).

[2] M. N. Shtogrin, Tr. Mat. Inst. Steklov. **123**, 128 (1973).

[3] G. Ya. Lyubarskiĭ, *The Application of Group Theory in Physics* (Pergamon Press, Oxford-New York, 1960; GITTL, Moscow, 1964, 354 pp.).

[4] N. Rivier, Philos. Mag. **40**, 859 (1979).

[5] P. K. Rashevskiĭ, *Riemannian Geometry and Tensor Analysis* [in Russian] (Nauka, Moscow, 1964), 664 pp.

[6] J. A. Schouten, *Tensor Analysis for Physicists*, 2nd ed. (Clarendon Press, Oxford, 1954; Nauka, Moscow, 1965, 456 pp.).

[7] A. Kadić and D. G. B. Edelen, *A Gauge Theory of Dislocations and Disclinations* (Springer-Verlag, Berlin-New York, 1983; Mir, Moscow, 1987, 168 pp.).

[8] A. V. Grachev, A. I. Nesterov, and S. G. Ovchinnikov, Preprint No. 509F (1988) [in Russian].

[9] I. E. Dzyaloshinskii and G. E. Volovic, J. Phys. (Paris) **39**, 693 (1978).

[10] S. S. Rozhkov, Phys. Lett. A **106**, 309 (1984).

[11] A. I. Nesterov and S. G. Ovchinnikov, Preprint No. 359F (1986) [in Russian].

[12] A. F. Andreev, Zh. Éksp. Teor. Fiz. **74**, 786 (1978) [Sov. Phys. JETP **47**, 411 (1978)].

[13] L. D. Landau and E. M. Lifshitz, *Mechanics*, 3rd ed. [Pergamon Press, New York–Oxford, 1976; Nauka, Moscow, 1973, 203 pp.].

[14] H. A. Mook, N. Wakabayashi, and D. Pan, Phys. Rev. Lett. m **34**, 1029 (1975).

[15] H. R. Trebin, Adv. Phys. **31**, 195 (1982).

[16] N. D. Mermin, Rev. Mod. Phys. **51**, 591 (1979).

Translated by James S. Wood

PHYSICS OF THE SOLID STATE VOLUME 40, NUMBER 11 NOVEMBER 1998

Slow stage in the evolution of an incommensurate ferroelectric superlattice

S. N. Kallaev and V. F. Glushkov

Institute of Physics, Dagestan Science Center, Russian Academy of Sciences, 367003 Makhachkala, Russia

(Submitted March 16, 1998)
Fiz. Tverd. Tela (St. Petersburg) **40**, 2101–2102 (November 1998)

The nature of the slow evolution of a soliton system in an incommensurate phase of a ferroelectric is investigated experimentally. It is shown that the duration of the time interval in which the anomalous permittivity and the corresponding soliton spacings are governed by a logarithmic law increases from a few minutes to several hours as the ferroelectric phase transition is approached. © *1998 American Institute of Physics.* [S1063-7834(98)03011-1]

An incommensurate phase of a ferroelectric with spatially modulated polarization is an example of an inhomogeneous degenerate system, which can be effectively investigated by highly sensitive electrical measurements. At temperatures close to the point of transition to the commensurate polar phase the crystal superlattice begins to resemble the domain structure of ferroelectrics containing narrow domain walls (solitons) separated by adjacent regions (quasidomains) with oppositely directed spontaneous polarizations.[1]

Previously it has been established experimentally[2,3] that, for a small initial deviation from equilibrium of a soliton system in Rb_2ZnCl_4, the dielectric permittivity varies with time in the range from $t_0=1$ s to 10 min according to the logarithmic law

$$\overline{\varepsilon}/\Delta\varepsilon \approx F + G\ln(t/t_0), \tag{1}$$

where $\Delta\varepsilon=|\overline{\varepsilon}-\varepsilon|$, $\overline{\varepsilon}$ is the equilibrium permittivity, $t_0=1$ s, and F and G are constants. The equilibrium value is $\overline{\varepsilon}=(\varepsilon_1+\varepsilon_2)/2$, where ε_1 and ε_2 are the permittivities corresponding to elevated and reduced soliton densities at the same temperature. Equation (1) is consistent with the previously developed[4] interpretation of the relaxation of inhomogeneities of the system as a thermal activation process governed by metastability effects.

We have determined experimentally the nature of the slow evolution of a soliton system in an incommensurate phase of a ferroelectric in a time interval up to several hours for large deviations from the equilibrium state. The investigated object is Rb_2ZnCl_4 (space group *Pmcn*) with structural transitions at $T_i=303$ K and $T_c=195.2$ K (Ref. 1). The intermediate phase is incommensurate, with spatial modulation along the $c(Z)$ axis, and the low-temperature phase is polar ($Pn2_1a$) with spontaneous polarization along the $b(Y)$ axis. The crystal samples were $3\times2.7\times3.8$ mm rectangular bars with their edges oriented along the crystallographic a, b, and c axes.

Nonequilibrium initial states of the soliton structure of the crystal were created in two ways: by the application of uniaxial mechanical stresses (as in Ref. 3) and by varying the temperature of the crystal. The stresses σ_{yy} and σ_{xx} were utilized as a means of abruptly driving the soliton structure into a nonequilibrium state. The stress σ_{yy} shifts the transition point toward lower temperature, i.e., broadens the temperature interval $\Delta T=T-T_c$ increases and increases the equilibrium density of solitons $\overline{n}$, while the stress σ_{xx} has exactly the reverse effect. Consequently, the soliton density can be either raised or lowered relative to the equilibrium state at any temperature point of the incommensurate phase without altering the symmetry of the crystal.

The time dependence of the permittivity was recorded on mechanically free (unconstrained) samples. The measurement procedure in the first technique was as follows: The sample was first cooled at $\sigma_{xx}\approx50$ bar to a specified temperature, and then the stress was lifted. As a result, after stress relief the initial state had a reduced soliton density relative to the equilibrium value $\overline{n}$ and the preloading density n. In the second technique the sample was cooled from the initial phase at $\sigma_{xx}=0$ to a specified temperature corresponding to the temperature point (ΔT) attained by the sample after stress had been lifted in the first case. The evolution of the system was recorded from the variation of the n-dependent anomalous permittivity ε along the b axis. The variations of ε were recorded by means of a capacitance bridge operating at a frequency of 1 MHz. The value of ε was measured within 0.01% error limits, and the temperature was maintained within ~0.005-K error limits.

At the instant of relief of the stress σ previously applied to the sample, the piezocaloric effect causes the temperature of the sample to change by the amount $\delta T=(kT/c)\Delta\sigma$, where k is the coefficient of thermal expansion, c is the specific heat, and $\Delta\sigma$ is the variation of the stress. Estimates for the investigated Rb_2ZnCl_4 sample at $\sigma\approx50$ bar give $\delta T\leqslant0.03$. The variation of ε determined from the experimental data for $\delta T\approx0.03$ does not influence the form of the $\varepsilon(t)$ curves in Fig. 1. The relaxation process can therefore be regarded as isothermal up to the end of the time interval t_0 in which temperature equalization takes place between the sample and the cryostat. When stress is used to create the nonequilibrium state, we have $t_0\approx1$ s, and when the nonequilibrium state is created by varying the temperature, experimental data, obtained at the time $t_0=1$ s after complete temperature stabilization, are used in the calculations.

The results of investigating the relaxation of the per-

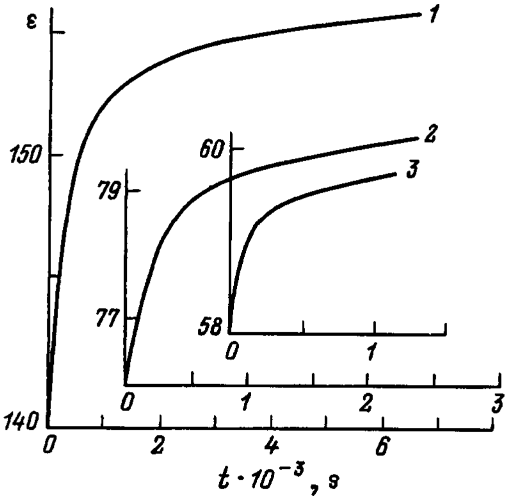

FIG. 1. Time (t) dependence of the permittivity ε of the incommensurate phase of the Rb_2ZnCl_4 crystal at various temperatures $\Delta T=(T-T_c)$. *1)* $\Delta T=0.27$ K; *2)* 0.72 K; *3)* 1.18 K.

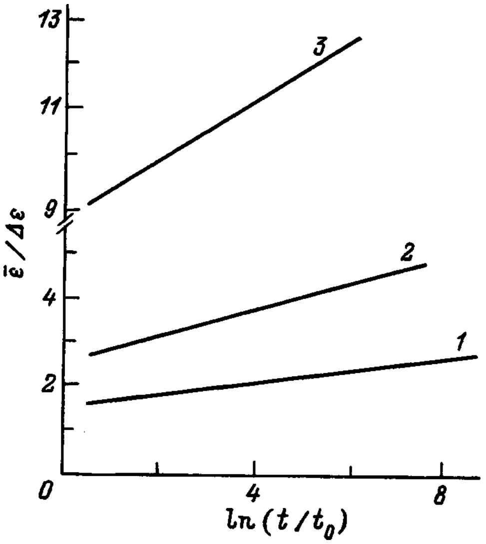

FIG. 2. Dependence of $\bar{\varepsilon}/\Delta\varepsilon$ on $\ln(t/t_0)$ for the incommensurate phase of the Rb_2ZnCl_4 crystal at various temperatures ΔT. *1)* $\Delta T=0.27$ K; *2)* 0.72 K; *3)* 1.18 K.

mittivity of Rb_2ZnCl_4 from various initial nonequilibrium states are shown in Fig. 1. It is evident that ε varies comparatively rapidly in the first few minutes. The results of determining the nature of the evolution of the soliton system are shown in Fig. 2, where the dependence of $\bar{\varepsilon}/\Delta\varepsilon$ on $\ln(t/t_0)$ are plotted using the experimental data. It is evident from this figure that the time dependence of ε for large deviations from equilibrium obeys the logarithmic law described by Eq. (1). It is important to note, in contrast with the data in Ref. 2, that this law is also observed at large times (up to several hours) at temperatures close to T_c, irrespective of what technique has been used to drive the soliton system out of equilibrium. The time interval in which the state of the soliton system varies according to the logarithmic law increases considerably as T_c is approached. It is evident from Fig. 2 that the slopes of the lines relative to the horizontal axis decrease as T_c is approached ($G=0.06$ for $\Delta T=0.27$, and $G=0.6$ for $\Delta T=1.2$, i.e., according to Ref. 1, the relaxation time to a particular value of $\bar{\varepsilon}/\Delta\varepsilon=\text{const}$ increases.

In summary, the results of the experiment indicate that when a large deviation from the equilibrium state is created either by large mechanical stresses $\sigma=50-60$ bar or by a variation of the temperature from the initial phase to a specified temperature in the vicinity of T_c, the anomalous dielectric permittivity and the corresponding soliton spacings (since $\Delta\varepsilon/\bar{\varepsilon}\approx\Delta l/\bar{l}$) of the incommensurate ferroelectric superlattice vary with time according to a logarithmic law, rather than an exponential law as postulated in Ref. 1. This law, which is based on the concepts of relaxation as a thermal activation process, holds in the time interval from a few seconds to several hours.

The authors are indebted to V. V. Gladkiĭ for helpful discussions and deliberations.

This work has received financial support from the Russian Fund for Fundamental Research (No. 97-02-16762).

[1] H. Z. Cummins, Phys. Rep. **185**, 211 (1990).
[2] V. V. Gladkiĭ, V. A. Kirikov, and E. S. Ivanova, Zh. Éksp. Teor. Fiz. **110**, 298 (1996) [JETP **83**, 161 (1996)].
[3] V. V. Gladkiĭ, V. A. Kirikov, and E. S. Ivanova, JETP Lett. **58**, 603 (1993).
[4] E. B. Kolomeĭskiĭ, Zh. Éksp. Teor. Fiz. **99**, 562 (1991) [Sov. Phys. JETP **72**, 314 (1991)].

Translated by James S. Wood

LATTICE DYNAMICS. PHASE TRANSITIONS

Lattice dynamics of crystalline In_4Se_3

D. M. Bercha*) and K. Z. Rushchanskiĭ

Uzhgorod State University, 294000 Uzhgorod, Ukraine

(Submitted April 9, 1998)
Fiz. Tverd. Tela (St. Petersburg) **40**, 2103–2108 (November 1998)

Calculations of the phonon spectrum of crystalline In_4Se_3 in a model of central-pair interactions with neglect of the long-range forces are presented. The model developed contains five unknown parameters, which are determined from experimental values of the elastic moduli without consideration of the internal displacement of the sublattices. The phonon spectrum obtained contains a large number of low-frequency modes, which deform the acoustic branches. Some common features are discovered in the dispersion curves of the electron and phonon spectra. © *1998 American Institute of Physics.* [S1063-7834(98)03111-6]

Crystalline In_4Se_3 is one of the selenides that are promising materials for energy conversion and storage. Its crystal structure was first described by Hogg *et al.*[1] and subsequently by Likformann and Etienne.[2] Some newer data were presented in Walther's book.[3] The unit cell of crystalline In_4Se_3 contains 28 atoms (four formula units) (Fig. 1). The crystal structure is described by the $Pnnm$ (D_{2h}^{12}) space group with the basis vectors $a_1 = 15.296(1)$ Å, $a_2 = 12.308(1)$ Å, and $a_3 = 4.0806(1)$ Å (according to the recent data[3]). The material is composed of chains parallel to the $\mathbf{a}_3$ axis, which lie in two translationally noninvariant layers perpendicular to the $\mathbf{a}_1$ direction. The structure of In_4Se_3 is described by mixed-valence bonds:[3] $In_4Se_3 = [In]^+[(In_3)^{5+}][Se^2]_3$. The In1, In2, and In3 atoms (Fig. 1), which form an $(In_3)^{5+}$ cluster, are joined to the selenium atoms by ionic-covalent bonds. This creates a puckered-layer structure consisting of infinite nonplanar layers of molecules with weakened intermolecular bonding. The stacking of these layers of molecules is similar to the stacking of the molecules in ordinary molecular crystals. Thus, a crystal of In_4Se_3 is not layered in the usual sense, i.e., it does not consist of planar layers joined by van der Waals bonding. The In4 atoms, for which the Debye–Waller temperature factor exceeds that for the other atoms, are located in regions of weakened bonding between the basic frameworks.[1]

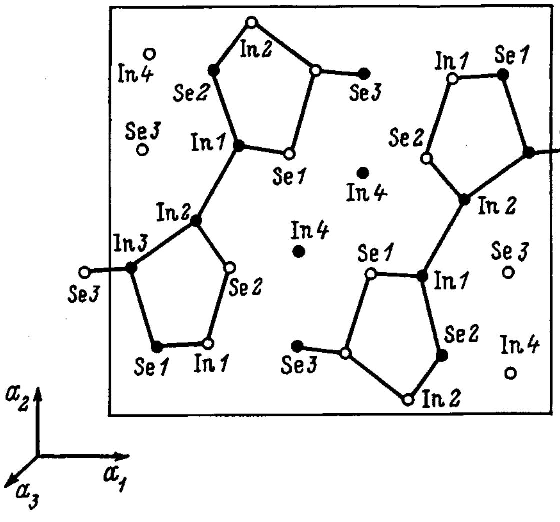

FIG. 1. Structure of crystalline In_4Se_3. The filled circles denote atoms for which $w = 0$, and the unfilled circles denote atoms for which $w = 0.5$.

The x-ray structural investigations in Ref. 4 showed that the scattering of x rays in crystalline In_4Se_3 is anisotropic, possibly due to the presence of one-dimensional translational disorder.[5] The specific features of its structure with a tendency for disordering is apparently the reason for the unusual properties of this material. For example, a deviation from Hooke's law was discovered in In_4Se_3 already at small stresses,[6] but compliance with this law is restored at large stresses. This semiconductor material exhibits an unusual piezoelectric photoresistive effect,[7,8] and anomalous temperature dependences of the kinetic coefficients.[9]

Investigations of the energy spectrum of the charge carriers[10,11] showed that the dispersion laws for both electrons and holes differ drastically from the parabolic laws already in the vicinity of the extremum. It has been theorized that there is a strong electron-phonon interaction in these crystals, which leads to the appearance of condenson states,[12,13] the latter being analogs of polarons. For this reason, an investigation of the lattice dynamics in these crystals, which have scarcely been studied, would be timely. There have only been experimental studies of the polarization IR reflection[14,15] and elastic properties of this material.[16]

This paper proposes a model of the phonon spectrum based on very simple and general approximations, which take into account the structural features of the bonds in crystalline In_4Se_3.

1. SYMMETRY DESCRIPTION OF CRYSTALLINE In_4Se_3 AND ITS NORMAL MODES OF VIBRATION

The $Pnnm$ (D_{2h}^{12}) space group in a reference frame with an origin of coordinates at the center of the unit cell is written in the form (Kovalev's notation)

$$\left(\{h_1|0\},\left\{h_2\left|\frac{1}{2}\,\frac{1}{2}\,\frac{1}{2}\right.\right\},\left\{h_3\left|\frac{1}{2}\,\frac{1}{2}\,\frac{1}{2}\right.\right\},\{h_4|0\},\right.$$

$$\left.\{h_{25}|0\},\left\{h_{26}\left|\frac{1}{2}\,\frac{1}{2}\,\frac{1}{2}\right.\right\},\left\{h_{27}\left|\frac{1}{2}\,\frac{1}{2}\,\frac{1}{2}\right.\right\},\{h_{28}|0\}\right)$$

$$\times T_{n_1\mathbf{a}_1+n_2\mathbf{a}_2+n_3\mathbf{a}_3}, \tag{1}$$

$$n_1,n_2,n_3=0,\pm 1,\pm 2,\ldots .$$

The coordinates of all the atoms in relative units are equal to (u,v,w), $(1/2+u,1/2-v,1/2-w)$, $(1/2-u,1/2+v,1/2-w)$, and $(-u,-v,-w)$, where the values of u, v, and w for In1, In2, In3, In4, Se1, Se2, and Se3 are listed in Table I.

TABLE I. Relative coordinates of atoms in the unit cell.[3] The standard deviations are given in parentheses.

Atom	u	v	w
In1	0.71105 (8)	0.33933 (9)	0
In2	0.81578 (8)	0.52362 (10)	0
In3	0.96733 (7)	0.64423 (11)	0
In4	0.42369 (9)	0.39749 (11)	0
Se1	0.90329 (10)	0.84943 (13)	0
Se2	0.76875 (10)	0.13857 (13)	0
Se3	0.42410 (10)	0.15595 (13)	0

A group-theoretical analysis shows that the 84 normal modes at the Brillouin-zone center, of which 81 are optical, are described by the irreducible representations

$$14\Gamma_1+7\Gamma_2+7\Gamma_3+14\Gamma_4+7\Gamma_5+14\Gamma_6+14\Gamma_7+7\Gamma_8 .$$

At the X, Y, and Z points the modes are doubly degenerate and have $28X_1+14X_2$, $28Y_1+14Y_2$, and $21Z_1+21Z_2$ symmetries, respectively. The irreducible representations of the groups of wave vectors correspond to those given in Ref. 17.

As is usually done, the basis vectors of the normal modes were calculated using a projection-operator procedure. Because there are seven kinds of atoms in the unit cell, each basis vector has 84 components. However, since atoms of different kinds do not transform into one another under the action of the symmetry operators, it is sufficient to consider the components of the basis vector of a normal mode that belong to atoms of one kind. Table II presents the basis vectors of the modes of the In1 atoms for the Γ point of the Brillouin zone. Since the normal modes at the X, Y, and Z points of the Brillouin zone are doubly degenerate, the components of a basis vector form complex functions, which comprise a basis set of two-dimensional irreducible representations. The basis functions corresponding to displacements of the In1 atoms are presented in Table III.

2. MODEL OF CENTRAL-PAIR INTERACTIONS

The model of central-pair interactions for the initial calculations of the phonon spectrum is interesting, because it does not contain a large number of unknown parameters. It has been used repeatedly for highly diverse crystals, including layered crystals.[18,19] In this model the force constants are assigned by the two-parameter expressions

$$\Psi_{\alpha\beta}(lk,l'k')=-\frac{R_\alpha R_\beta}{R^2}(A-B)-\delta_{\alpha\beta}B, \tag{2}$$

where $\mathbf{R}=\mathbf{r}(l)+\mathbf{r}(k)-\mathbf{r}(l')-\mathbf{r}(k')$ is the radius vector of the interacting particles, l labels the cells, k labels the atoms in a cell, R_α and R_β are the α and β components of $\mathbf{R}$, A and B are the radial and tangential force constants,

$$A_i=\left.\frac{\partial^2\varphi}{\partial R^2}\right|_{R=R_i}, \quad B_i=\left.\frac{1}{R}\frac{\partial\varphi}{\partial R}\right|_{R=R_i}, \tag{3}$$

and $\varphi(\mathbf{r})$ is the central pair potential. In our calculations A was assumed to depend both on the chemical species of each atom and on the distance between the interacting atoms according to the expressions

$$A_i=A_{\text{In-Se}}\exp[-\alpha_{\text{In-Se}}(r_i-r_1)], \quad i=1,\ldots,10, \tag{4}$$

$$A_i=A_{\text{In-In}}\exp[-\alpha_{\text{In-In}}(r_i-r_{11})], \quad i=11,\ldots,15. \tag{5}$$

The distances between the atoms are listed in Table IV in accordance with the number i of the pair of interacting particles.

The equilibrium conditions

$$\sum_{l,k} r_\alpha(l,kk')\,B(l,kk')=0 \tag{6}$$

impose fourteen constraints on the fifteen B_i. Only the interacting atoms near the atoms of the selected cell are taken into account in the summation over l. In this case ten In–Se bonds chosen on the basis of the condition $|\mathbf{r}(l,kk')|<3.8$ Å and five In–In bonds with lengths less than 3.9 Å are considered. As a result, the dynamic matrix for calculating the frequencies of the normal modes is determined by five unknown parameters: $A_{\text{In-Se}}$, $\alpha_{\text{In-Se}}$, $A_{\text{In-In}}$, $\alpha_{\text{In-In}}$, and B_{13}.

TABLE II. Basis vectors of the normal modes of four In1 atoms for the Γ point of the Brillouin zone.

Atom No.	Γ_1	Γ_2	Γ_3	Γ_4	Γ_5	Γ_6	Γ_7	Γ_8
1	$x_1,y_1,0$	$0,0,z_1$	$0,0,z_1$	$x_1,y_1,0$	$0,0,z_1$	$x_1,y_1,0$	$x_1,y_1,0$	$0,0,z_1$
2	$x_2,-y_2,0$	$0,0,-z_2$	$0,0,-z_2$	$x_2,-y_2,0$	$0,0,z_2$	$-x_2,y_2,0$	$-x_2,y_2,0$	$0,0,z_2$
3	$-x_3,y_3,0$	$0,0,-z_3$	$0,0,z_3$	$x_3,-y_3,0$	$0,0,-z_3$	$-x_3,y_3,0$	$x_3,-y_3,0$	$0,0,z_3$
4	$-x_4,-y_4,0$	$0,0,z_4$	$0,0,-z_4$	$x_4,y_4,0$	$0,0,-z_4$	$x_4,y_4,0$	$-x_4,-y_4,0$	$0,0,z_4$

TABLE III. Basis functions of the irreducible representations at the X, Y, and Z points of the Brillouin zone.

Irreducible representation	Basis functions	
X_1	$\Psi_{11}=x_1+y_1+i(x_2-y_2)$	$\Psi_{12}=x_4+y_4-i(x_3-y_3)$
	$\Psi_{12}=x_4+y_4+i(x_3-y_3)$	$\Psi_{22}=x_1+y_1-i(x_2-y_2)$
X_2	$\Psi_{11}=z_1-iz_2$	$\Psi_{12}=-z_4-iz_3$
	$\Psi_{22}=z_1+iz_2$	$\Psi_{21}=-z_4+iz_3$
Y_1	$\Psi_{11}=x_1+y_1-x_2+y_2$	$\Psi_{12}=i(-x_3+y_3+x_4+y_4)$
	$\Psi_{22}=x_1+y_1+x_2-y_2$	$\Psi_{21}=i(-x_3+y_3-x_4-y_4)$
Y_2	$\Psi_{11}=z_1+z_2$	$\Psi_{12}=-i(z_3+z_4)$
	$\Psi_{22}=z_1-z_2$	$\Psi_{21}=i(-z_3+z_4)$
Z_1	$\Psi_{11}=x_1+y_1+z_1+i(x_2-y_2-z_2)$ $+i(-x_3+y_3-z_3)-x_4-y_4+z_4$	$\Psi_{12}=-x_1-y_1+z_1+i(x_2-y_2+z_2)$ $+i(-x_3+y_3+z_3)+x_4+y_4+z_4$
	$\Psi_{22}=x_1+y_1+z_1-i(x_2-y_2-z_2)$ $-i(-x_3+y_3-z_3)-x_4-y_4+z_4$	$\Psi_{21}=x_1+y_1-z_1+i(x_2-y_2+z_2)$ $+i(-x_3+y_3+z_3)-x_4-y_4-z_4$
Z_2	$\Psi_{11}=x_1+y_1+z_1+i(x_2-y_2-z_2)$ $-i(-x_3+y_3-z_3)+x_4+y_4-z_4$	$\Psi_{12}=x_1+y_1-z_1-i(x_2-y_2+z_2)$ $+i(-x_3+y_3+z_3)+x_4+y_4+z_4$
	$\Psi_{22}=x_1+y_1+z_1-i(x_2-y_2-z_2)$ $+i(-x_3+y_3-z_3)+x_4+y_4-z_4$	$\Psi_{21}=-x_1-y_1+z_1-i(x_2-y_2+z_2)$ $+i(-x_3+y_3+z_3)-x_4-y_4-z_4$

3. CALCULATION OF THE PHONON SPECTRUM OF In_4Se_3

The parameters of the model were determined from known experimental data: elastic moduli[16] and ranges of observable frequencies in the far-IR reflection spectra (Table V).[14,15]

As we know,[20] the force constants are related to the elastic moduli in the long-wavelength approximation by the expression

$$C_{\alpha\beta\gamma\delta}=\tilde{C}_{\alpha\gamma\beta\delta}+\tilde{C}_{\beta\gamma\alpha\delta}-\tilde{C}_{\beta\alpha\delta\gamma}, \tag{7}$$

where

$$\tilde{C}_{\alpha\beta\gamma\delta}=-\frac{1}{2\Omega}\sum_{l,kk'}\Phi_{\alpha\beta}(l,kk')R_{\gamma}(l,kk')R_{\delta}(l,kk'), \tag{8}$$

and Ω is the unit-cell volume. Since in our case no atom of the crystal structure is an inversion center, the term $\delta\tilde{C}_{\alpha\beta\gamma\delta}$, which takes into account the displacement of the individual sublattices, must be included in (7). In the static approximation, which is valid at high limiting optical frequencies, $\delta\tilde{C}_{\alpha\beta\gamma\delta}$ is calculated according to the expression

$$\delta\tilde{C}_{\alpha\beta\gamma\delta}=\sum_{\substack{kk'\\ \varepsilon\eta}}\tilde{C}^{k}_{\alpha\varepsilon\beta}R^{kk'}_{\varepsilon\eta}\tilde{C}^{k'}_{\gamma\eta\delta}, \tag{9}$$

where

$$\tilde{C}^{k}_{\alpha\varepsilon\beta}=\frac{1}{\Omega}\sum_{l,k'}\Phi_{\alpha\varepsilon}(l,kk')R_{\beta}(l,kk'), \tag{10}$$

and $R^{kk'}_{\varepsilon\eta}$ is a transformation matrix, which is defined in the following manner:

$$R^{kk'}_{\varepsilon\eta}=\begin{cases}[\tilde{C}^{kk'}_{\varepsilon\eta}]^{-1}, & k,k'=1,\ldots,s-1,\\ 0,\ k,\ \ k'=s, & \end{cases} \tag{11}$$

where $[\tilde{C}^{kk'}_{\varepsilon\eta}]^{-1}$ in the inverse matrix of the $(3s-3)\times(3s-3)$ matrix $\tilde{C}^{kk'}_{\varepsilon\eta}$ $(k,k'=1,\ldots,s-1;\ \varepsilon=1,2,3;\ s$ is the number of atoms in the unit cell), which is defined by the expression

TABLE IV. Pairs of interacting particles and interatomic distances.

i	Bond	r, Å
1	In_1-Se_2	2.62384
2	In_3-Se_3	2.63468
3	In_1-Se_1	2.69018
4	In_3-Se_1	2.70891
5	In_2-Se_2	2.79933
6	In_4-Se_3	2.97288
7	In_4-Se_2	3.15856
8	In_4-Se_1	3.39364
9	In_2-Se_3	3.43405
10	In_4-Se_1'	3.73669
11	In_2-In_3	2.75268
12	In_1-In_2	2.77690
13	In_4-In_4	3.43762
14	In_2-In_4	3.78944
15	In_1-In_4	3.83930

TABLE V. Experimental values of the frequencies of optical phonons in crystalline In_4Se_3 determined from the reflection of far-IR radiation with $\mathbf{E}\perp\mathbf{c}$ polarization.[14]

ω_{TO}, cm^{-1}	ω_{LO}, cm^{-1}
40	42
73	76
97	116
158	169
196	209
223	226

TABLE VI. Experimental[16] values of the elastic moduli and values calculated in model 1 (in GPa).

	C_{11}	C_{22}	C_{33}	C_{44}	C_{55}	C_{66}	C_{12}	C_{13}	C_{23}
Exp.	38.2	66.5	64.3	16.6	26.6	19.0	10.8	30.4	22.4
Calc.	39.9	66.9	49.6	18.0	38.1	11.6	9.0	35.9	15.8

$$\tilde{C}^{kk'}_{\varepsilon\eta} = -\frac{1}{\Omega}\sum_{l} \Phi_{\varepsilon\eta}(l,kk'). \qquad (12)$$

The unknown parameters $A_{\text{In-Se}}$, $\alpha_{\text{In-Se}}$, $A_{\text{In-In}}$, $\alpha_{\text{In-In}}$, and B_{13} were adjusted using Eq. (7) without (model 1) and with consideration of the correction $\delta\tilde{C}_{\alpha\beta\gamma\delta}$ (model 2) so that the calculated elastic moduli would correspond to the experimental values (Table VI). A combination of direct search methods and the Gauss–Seidel method was used.[21] The parameters obtained for the modes are listed in Table VII.

4. RESULTS AND DISCUSSION

Figure 2 presents the results of a calculation of the phonon spectrum with the parameters of model 1. We wish to make several comments regarding the parameters of the model and the expected results. As can be seen from Fig. 2, the phonon spectrum of crystalline In_4Se_3 contains numerous low-frequency optical modes (not just hard vibrational modes); therefore, the correction considered in the static approximation, $\delta\tilde{C}_{\alpha\beta\gamma\delta}$, does not completely compensate the displacement of the sublattices, particularly the sublattices belonging to different layers. A large system of differential equations would have to be solved to fully take it into account.[20]

Since the degree of ionic character of the crystal under consideration is small, allowance for the long-range Coulomb interactions cannot influence significantly the general results of the calculation of the phonon spectrum in the fairly rough model of central pair forces.

The exponential dependence of the parameters A_i precludes ensuring exact correspondence between the calculated and experimental values of C_{22} and C_{33} simultaneously. Nevertheless, as can be seen from Table VI, there is satisfactory agreement between the calculated and experimental values of the elastic moduli. A clear picture of the strong anisotropy in the dispersion of the phonon branches in the $\Gamma-Z$, $\Gamma-X$, and $\Gamma-Y$ directions can be traced.

The result of the calculation based on model 2 are not presented, since there was scarcely any improvement in the agreement between the experimental and calculated values of the elastic moduli, and the calculated frequency range significantly exceeded the range of observable IR frequencies, whereas this difference did not exceed 10% in model 1.

TABLE VII. Calculated parameters of models of the phonon spectrum of crystalline In_4Se_3 without (model 1) and with consideration of the internal displacement of sublattices (model 2).

	$A_{\text{In-Se}}$, N/m	$\alpha_{\text{In-Se}}$, Å^{-1}	$A_{\text{In-In}}$, N/m	$\alpha_{\text{In-In}}$, Å^{-1}	B_{13}, N/m
Model I	45.1	0.62	8.9	3.7	0.24
Model II	73	0.7	53	6.5	2.5

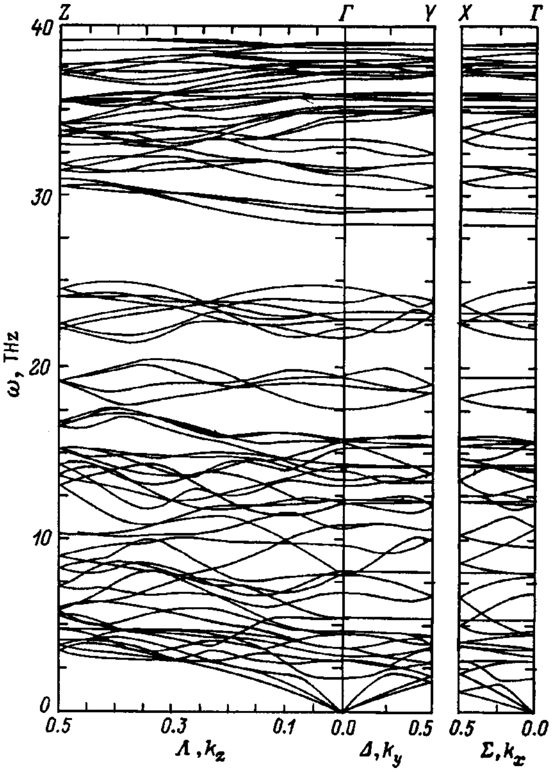

FIG. 2. General form of the phonon spectrum of crystalline In_4Se_3 along the most important directions in the Brillouin zone.

The symmetry of the branches at the high-symmetry points was determined from the compatibility conditions of the irreducible representations of the wave-vector groups listed in Table VIII, as well as by direct calculation of the eigenvectors and determination of their symmetry.

Figure 3 exhibits cross splitting of branches of modes of the same symmetry. At several points of accidental degen-

TABLE VIII. Compatibility conditions of the irreducible representations of the wave-vector groups for the $\Gamma(0,0,0)$, $X(\pi/a_1,0,0)$, $Y(0,\pi/a_2,0)$, and $Z(0,0,\pi/a_3)$ points and the $\Sigma(\mu_1 2\pi/a_1,0,0)$ $(0<\mu_1<1/2)$, $\Delta(0,\mu_2 2\pi/a_2,0)$ $(0<\mu_2<1/2)$, and $\Lambda(0,0,\mu_3 2\pi/a_3)$ $(0<\mu_3<1/2)$ directions.

Γ	Σ	Δ	Λ
Γ_1	Σ_1	Δ_1	Λ_1
Γ_2	Σ_2	Δ_2	Λ_2
Γ_3	Σ_2	Δ_3	Λ_3
Γ_4	Σ_1	Δ_4	Λ_4
Γ_5	Σ_3	Δ_2	Λ_4
Γ_6	Σ_4	Δ_1	Λ_3
Γ_7	Σ_4	Δ_4	Λ_2
Γ_8	Σ_3	Δ_3	Λ_1
X_1		$\Sigma_1+\Sigma_4$	
X_2		$\Sigma_2+\Sigma_3$	
Y_1		$\Delta_1+\Delta_4$	
Y_2		$\Delta_2+\Delta_3$	
Z_1		$\Lambda_1+\Lambda_2$	
Z_2		$\Lambda_3+\Lambda_4$	

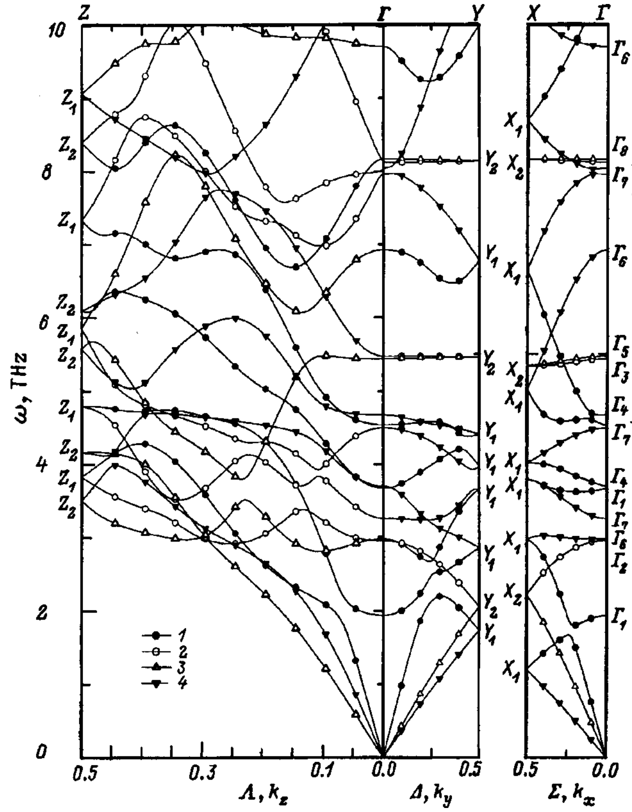

FIG. 3. Low-energy branches of the phonon spectrum of crystalline In_4Se_3 obtained in the model of anisotropic force constants and their symmetry description. *1* — Λ_1, Δ_1, Σ_1; *2* — Λ_2, Δ_2, Σ_2; *3* — Λ_3, Δ_3, Σ_3; *4* — Λ_4, Δ_4, Σ_4.

eracy, the splitting is so small that it could not be depicted in the figure. The acoustic branches undergo splitting already in the low-frequency region, especially in the $\Gamma - Z$ direction, where they are deformed repeatedly as a result of interactions with low-frequency optical modes.

The structure of the phonon spectrum in the $\Gamma - Z$ direction is similar in complexity to the energy spectrum of the charge carriers in the same direction.[10] The entire set of branches in the $\Gamma - Z$ direction is characterized by repeated crossing and bunching.

The dispersion curves of the acoustic branches do not display flexural modes, which would be expected because of the complex structure of an individual layer.[22–24]

The lowest-frequency optical mode at the Γ point has appreciable dispersion, which can be described by the topology of a saddle point.

The abundance of low-frequency modes should influence such integral characteristics as the specific heat and the thermal conductivity,[22,23] which will be the subject of our further studies.

*)E-mail: artem@univ.uzhgorod.ua

---

[1] J. H. C. Hogg, H. H. Sutherland, and D. J. Williams, Acta Crystallogr., Sect. B: Struct. Crystallogr. Cryst. Chem. **29**, 1590 (1973).

[2] A. Likformann and J. Etienne, C. R. Seances Acad. Sci., Ser. C **275**, 1907 (1972).

[3] Ralf Walther, *Beiträge zur Strukturchemic gemischtvalenter Chalkogenide mit Elementen der 3. Hauptgruppe: Neue Verbindungen, Substitutionsversuche an bekannten Phasen, Hochdruckexperimente*, Ralf Walther a1s Ms. gedr. Shaker, Aachen (1995), 263 pp.

[4] O. I. Bodak, Yu. M. Orishchin, V. P. Savchin, and I. M. Stakhira, Kristallografiya **25**, 628 (1980) [Sov. Phys. Crystallogr. **25**, 363 (1980)].

[5] I. M. Stakhira and P. G. Ks'ondzik, Ukr. Fiz. Zh. **26**, 762 (1981).

[6] A. A. Logvinenko, I. M. Spitkovskiĭ, and I. M. Stakhira, Fiz. Tverd. Tela (Leningrad) **16**, 2743 (1974) [Sov. Phys. Solid State **16**, 1774 (1975)].

[7] I. M. Stakhira, R. Ya. Shuvar, and B. M. Pavlishenko, Ukr. Fiz. Zh. **40**, 723 (1995).

[8] I. M. Stakhira, Fiz. Tekh. Poluprovodn. **16**, 175 (1982) [Sov. Phys. Solid State **16**, 108 (1982)].

[9] I. M. Stakhira, V. P. Savchin, and G. M. Demkin, Ukr. Fiz. Zh. **38**, 891 (1993).

[10] D. M. Bercha, O. B. Mitin, L. Yu. Kharkhalis, and A. I. Bercha, Fiz. Tekh. Poluprovodn. **28**, 1249 (1994) [Semiconductors **28**, 711 (1994)].

[11] D. M. Bercha, O. B. Mitin, L. Yu. Kharkhalis, and A. I. Bercha, Fiz. Tverd. Tela (Leningrad) **37**, 3233 (1995) [Phys. Solid State **37**, 1778 (1995)].

[12] D. M. Bercha, L. Yu. Kharkhalis, A. I. Bercha, and M. Snajder, Fiz. Tekh. Poluprovodn. **31**, 1299 (1997) [Semiconductors **31**, 1118 (1997)].

[13] D. M. Bercha, L. Yu. Kharkhalis, A. I. Bercha, and M. Snajder, Phys. Status Solidi B **203**, 427 (1997).

[14] C. Julien, M. Eddrief, and M. Balkanski, Phys. Rev. B **46**, 2435 (1992).

[15] V. P. Zakharov, V. P. Savchin, I. M. Stakhira, and G. P. Sheremet, Fiz. Tverd. Tela (Leningrad) **23**, 1881 (1981) [Sov. Phys. Solid State **23**, 1101 (1981)].

[16] V. Ya. Kuryachiĭ, V. Yu. Bogachev, V. P. Mikhal'chenko, and I. M. Stakhira, Izv. Akad. Nauk SSSR, Neorg. Mater. **22**, 855 (1986).

[17] O. V. Kovalev, *Representations of the Crystallographic Space Groups: Irreducible Representations, Induced Representations, and Corepresentations*, Gordon and Breach, Philadelphia (1993).

[18] V. Ya. Altshul, V. K. Bashenov, D. I. Marvakov, and A. G. Petukhov, Phys. Status Solidi B **98**, 715 (1980).

[19] H. G. Smith and N. Wakabayashi, in *Dynamics of Solids and Liquids by Neutron Scattering (Topics in Current Physics, Vol. 3)*, S. W. Lovesey and T. Springer (ed.) [Springer-Verlag, Berlin–New York (1977); Mir, Moscow (1980), p. 94].

[20] G. Leibfried, ''Gittertheorie der mechanischen und thermischen Eigenschaften der Kristalle,'' in *Handbuch der Physik, Vol. 7/1*, S. F. Flügge (ed.) [Springer-Verlag, Berlin–Göttingen–Heidelberg (1955), pp. 105–324; Fizmatgiz, Moscow (1963), 312 pp.].

[21] D. M. Himmelblau, *Process Analysis by Statistical Methods* [Wiley, New York (1970); Mir, Moscow (1973), 957 pp.].

[22] E. S. Syrkin and S. B. Feodos'ev, Fiz. Nizk. Temp. **8**, 760 (1982) [Sov. J. Low Temp. Phys. **8**, 381 (1982)].

[23] E. S. Syrkin and S. B. Feodos'ev, Fiz. Nizk. Temp. **8**, 1115 (1982) [Sov. J. Low Temp. Phys. **8**, 564 (1982)].

[24] F. V. Motsnyĭ, Doctoral Dissertation, Kiev (1993), 40 pp.

Translated by P. Shelnitz

PHYSICS OF THE SOLID STATE VOLUME 40, NUMBER 11 NOVEMBER 1998

Calorimetric study of phase transitions in the perovskite $BaCeO_3$

V. M. Egorov, Yu. M. Baĭkov, N. F. Kartenko, B. T. Melekh, and Yu. N. Filin

A. F. Ioffe Physicotechnical Institute, Russian Academy of Sciences, 194021 St. Petersburg, Russia

(Submitted April 28, 1998)
Fiz. Tverd. Tela (St. Petersburg) **40**, 2109–2112 (November 1998)

Differential scanning calorimetry was used to study phase transitions (PT) in the perovskite $BaCeO_3$. It is shown that its phase state is determined by a second-order λ transition at $T_{tr}=520-540$ K and a first-order δ transition at $T_{tr}=600-670$ K. Differences in PT parameters between ceramic and fused $BaCeO_3$ have been established.

The present work is a continuation of our earlier studies[1,2] of the thermodynamic properties of ceramic and crystalline (fused) $BaCeO_3$ samples doped with Gd and Y. The interest in these materials is stimulated by their ability of dissolving sizable amounts of hydrogen (water) (up to 10–15 at.% hydrogen), and of acting at high temperatures (700–1200 K) as ionic conductors in hydrogen or oxygen, depending on the actual conditions. High-temperature protonic conductors, including those based on $BaCeO_3$, are presently a subject of intensive investigation in areas of applied interest, namely, as fuel elements, for hydrogen production from water vapor, as hydrogen sensors etc. $BaCeO_3$ and its doped derivatives are, however, of a certain interest also for basic research into the nature of phase transitions (PT) in perovskites and the ways for their control.

Barium cerate is fairly close in structure to barium titanate while being different in basic properties (at any rate we are not aware of publications dealing with the dielectric properties of $BaCeO_3$). $BaTiO_3$ and $BaCeO_3$ exhibit a certain sequence of PTs whose temperatures are, on the average, 2.5 times higher in $BaCeO_3$: 180–280–400 K for the titanate and 530–650–1173 K for the cerate. Besides, the nature of the PTs in $BaCeO_3$ has been studied to a much lesser extent, and there is even disagreement on the symmetry of the modifications preceding the cubic phase.[3–5] We showed also that acceptor doping and thermochemical treatment of $BaCeO_3$ affect considerably its symmetry.[5]

Our previous calorimetric studies[1,2] of $BaCeO_3$ revealed that within the broad temperature range of 400–700 K there are regions where heating produces characteristic thermal effects, namely, a broad endothermal λ peak within the region of 430–570 K, and a narrow, but weaker endothermal δ peak in the 630–700 K interval. We did not succeed in complete characterization of the latter, in particular, the questions concerning the true peak temperature (T_{tr}), temperature hysteresis (ΔT_{tr}), and peak width remained open. A metastable exothermal feature observed only in starting samples[1)] and disappearing after repeated heating was detected within the 430–700 K interval.

The objective of this work was to refine the PT characteristic for ceramic and fused $BaCeO_3$.

1. EXPERIMENTAL TECHNIQUES

We studied ceramic and crystalline[6] (fused) samples of $BaCeO_3$. The thermal properties of the samples were derived from DSC curves obtained on a DSC-2 Perkin-Elmer calorimeter in nitrogen during heating and cooling, performed from 350 to 750 K at rates of 1.25–40 K/min. The samples were preliminarily heated in the calorimeter to 700 K to remove the metastable exothermal effect. The heat flux (heat capacity) scale was calibrated against the heat capacity of sapphire, and the temperature scale, using the melting points of indium (439.78 K), lead (600.65 K), and the solid-state transition in K_2SO_4 (858.2 K). To increase the sensitivity and accuracy of determination of the heat effects, the total heat capacity of the $BaCeO_3$ sample under study was compensated by using amorphous quartz as a reference (in the second chamber).

2. EXPERIMENT

Figure 1 presents DSC curves obtained for $BaCeO_3$ samples heated preliminarily to 700 K. The curves are seen to contain λ and δ endothermal peaks in the above-mentioned temperature regions. There is no exothermal metastable feature in the heating curves, and the curves are reproduced under repeated heating. It turned out that the magnitude of the thermal effects, the enthalpies ΔH, of each peak do not depend on the heating or cooling rates. At the same time there is a considerable difference between the temperatures of the extrema observed during heating (T_{max}) and during cooling (T_{min}) for each peak. This difference changes with the temperature scanning rate (Fig. 2). The observed hysteresis can be associated with that of the PT, ΔT_{tr}, and with the thermal inertia of the instrument, i.e. with the systematic error ΔT, because the position of the extremum on an endotherm (T_{max}) or exotherm (T_{min}) of a transition, T_{extr}, in a DSC curve always differs from that of the true transition temperature T_{tr}. This is due to the existence of thermal resistance R, which results in a thermal lag, i.e. a lag of the temperature of the sample relative to that of the heater by an amount $\Delta T=T_{extr}-T_{tr}$. To remove this systematic error and isolate the hysteresis of the phase transition, one has to apply the following extrapolation procedure.

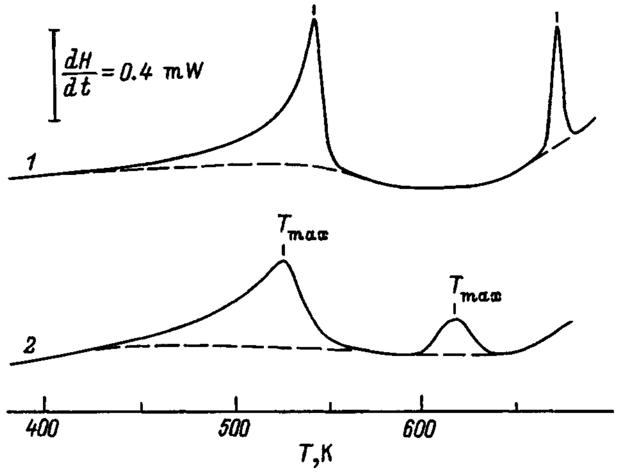

FIG. 1. DSC curves of (*1*) ceramic and (*2*) fused $BaCeO_3$ samples preheated to 700 K. Heating rate 10 K/min.

The error ΔT made in a transition of a pure compound is proportional to the heating/cooling rate V, specific heat of the transition ΔH, sample mass m, and the thermal resistance R:[7]

$$\Delta T = (2m \cdot \Delta H \cdot R \cdot V)^{1/2}.$$

Thus for a constant R and samples of equal mass one should expect a linear relation $\Delta T\,(V^{1/2})$. For $V \to 0$, the difference $\Delta T \to 0$, and $T_{\mathrm{extr}} \to T_{\mathrm{tr}}$. Hence extrapolation of the linear relation $T_{\mathrm{extr}}(V^{1/2})$ to zero heating rate should yield the value of T_{tr}, and the difference between the true temperatures obtained under heating and cooling should give ΔT_{tr}.

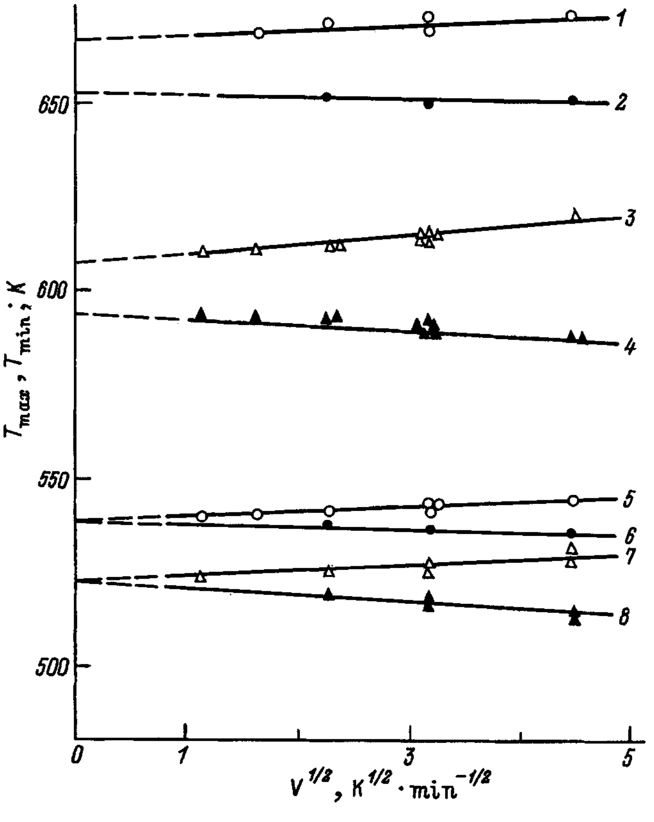

FIG. 2. Dependence of (*1,3,5,7*) T_{max} and (*2,4,6,8*) T_{min} of endothermal peaks obtained on (*1,2,5,6*) ceramic and (*3,4,7,8*) fused $BaCeO_3$ samples preheated to 700 K on the heating and cooling rate.

Figure 2 plots the temperatures T_{max} and T_{min} against $V^{1/2}$. One readily sees that the experimental points for T_{max} and T_{min} fit onto straight lines, and their extrapolation to zero heating rate yields the true temperatures, whose difference gives the true hysteresis ΔT_{tr} for each sample.

The temperatures obtained for the ceramic and fused samples from the λ peak are 538 and 522 K, respectively. Taking into account the extrapolation error of ±1.5 K for the linear relations $T_{\mathrm{max,min}}(V)^{1/2}$, the true hysteresis was found to lie from 0 to 3 K, in other words, ΔT_{tr} is less than 3 K, which is in agreement with previous data[1,2].

For the peaks lying in the 630–700 K interval, the hysteresis obtained for the ceramic and fused samples is the same, despite the difference between the true values of T_{tr}, and, as follows from Fig. 2 (curves *1–4*), is $\Delta T_{\mathrm{tr}} = 15 \pm 1.5$ K. Such a small hysteresis (15 K) is typical of first-order phase transitions.

The data obtained on the hysteresis of the peaks, as well as their λ- and δ-shaped pattern, permit one to assign them to the second- and first-order thermodynamic transitions, respectively, which is in accord with available data. For instance, neutron diffraction showed the transition observed in the 630–700 K interval to be accompanied by an abrupt change in the $BaCeO_3$ lattice parameter characteristic of first-order transitions.[3] This is believed to indicate a transformation of the orthorhombic-II phase to a higher-temperature rhombohedral one.[3] It was also shown[3] that the temperature dependence of the $BaCeO_3$ lattice constant undergoes a break, typical of second-order transitions, at a temperature of 563 K, which is close to T_{max} for the DSC endothermal λ peaks. This transition is accompanied by a symmetry change (orthorhombic-I → orthorhombic-II) of the unit cell, and is connected in this case with the change in oxygen-octahedron orientation angles.[4]

At the same time Raman studies show that the vibrations of oxygen octahedra defreeze above 427 K.[3] These vibrations were called librations, and the experimentally observed appearance of librations was assigned to a second-order PT with $T_{\mathrm{tr}} = 427$ K.[3] It was also pointed out that the DSC and x-ray diffraction techniques are insensitive to this transition. In actual fact, as is evident from Fig. 1, the low-temperature shoulder on the DSC endothermal λ peak clearly deviates from the baseline near 430 K. Thus the DSC method likewise detects the appearance at this temperature of a new "degree of freedom", which absorbs additional energy. Moreover, if one characterizes this transformation as an order-disorder transition, it appears hardly possible to relate the changes in the mutual arrangement of octahedra, observed spectroscopically, with the temperature of the phase transition as such. Indeed, the possibility of observing the above structural changes is determined by the sensitivity of the method, whereas the PT temperature is the temperature at which the energy levels align, and the lattice symmetry changes abruptly without any change in the other lattice parameters. The spectroscopic method is insensitive to such features whereas, in DSC curves, this point corresponds to the maximum of the endothermal λ peak.

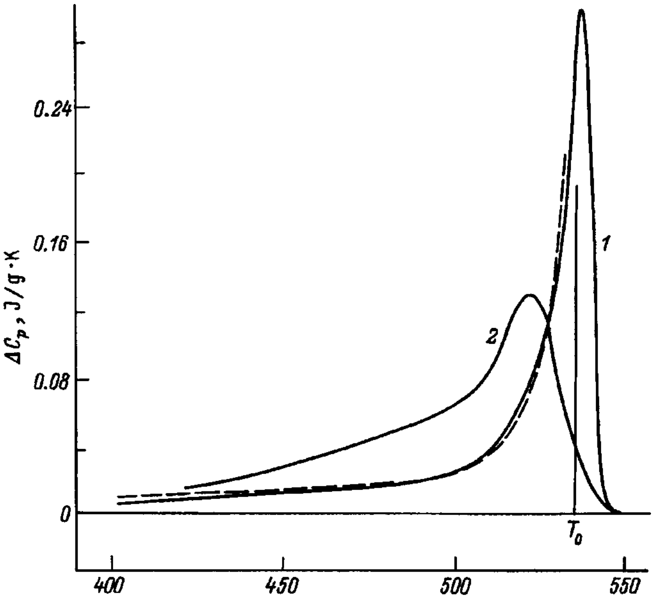

FIG. 3. Temperature dependence of (*1*) ceramic and (*2*) fused $BaCeO_3$ samples in the region of the λ transition obtained from DSC curves (solid lines) and theoretically (dashed line). Heating rate 1.25 K/min.

It is known that in perovskites and related structures the temperature dependence of heat capacity near second-order PTs follows a power-law behavior, $\Delta C_p(T)=A(T-T_0)^{-\alpha}$, where T_0 is the PT temperature, A is a constant, and α is an exponent.[8] Figure 3 shows experimental and calculated temperature dependences $\Delta C_p(T)$ obtained for the ceramic and fused $BaCeO_3$ samples in the vicinity of the transition. The parameters used for the calculation are $A=0.03$ J·K/g, $\alpha=2/3$, and $T_0=535$ K. One readily sees that the calculated and experimental curves measured on the ceramic sample agree fairly well, with the exception of the temperature interval lying in the immediate vicinity of T_0.

Without considering here any particular transition model connected with a physical interpretation of the order parameter, one may assume that the λ transformation belongs to an order-disorder–type second-order transition, in which the order parameter is associated with a particular orientation of the oxygen octahedra. Considered on the microscopic scale, the parameters of the oxygen-octahedron vibrational motion in the orthorhombic-II phase vary smoothly between the transitions.[5]

Phase transitions in ceramic samples of $BaCeO_3$ were studied by neutron diffraction and optical spectroscopy.[3,5] The agreement of the PT temperatures with the calorimetric data may be regarded as quite good. One immediately notices, however, the substantial difference between the δ transition temperatures for the ceramic and fused samples. Besides, one cannot fit the temperature relation $\Delta C_p(T)$ for the fused $BaCeO_3$ sample in the region of the λ transition to a power law (see Fig. 3). The latter is associated with a different polycrystalline structure of the fused $BaCeO_3$ sample, with crystallites ranging widely in size, and with each of them having a different $T_{\max}$, which results in superposition of numerous endothermal effects washed out differently in temperature. The difference in sample texture is a consequence of the technological factor, whose significance should not be ruled out a priori. The selectivity of technology in its effect on PT parameters (the λ peak temperature is the same for all samples) requires careful study. At the present stage of our knowledge one can only conjecture that the observed difference is associated with a different course of chemical processes occurring during the synthesis and caused by the different temperatures of the latter, namely, 1400–1600 K for the solid-state ceramic process and 2400 K for preparation by melting. Arguments for the chemical origin of the technological factor can be obtained from an analysis of doped $BaCeO_3$ samples. For example, doping fused samples with yttrium and gadolinium reduces the molar volume,[1] whereas ceramic samples doped with yttrium retain their molar volume,[9] and doping with gadolinium, conversely, increases it.[10]

As shown earlier,[1,2] in gadolinium-doped $BaCeO_3$ one observes a decrease in intensity and a shift of the above-mentioned endothermal first-order transition toward lower temperatures. At a gadolinium concentration in ceramic samples $\sim 10\%$, this endothermal peak was not present in the DSC curves at all, and at $\sim 20\%$ the low-temperature λ peak disappeared too. In the latter case, x-ray diffraction measurements detected the high-temperature cubic phase in $BaCeO_3$ samples already at room temperature. A similar pattern was observed in yttrium-doped $BaCeO_3$ samples, the only difference being that there were no thermodynamic transitions, and the cubic phase was observed to exist already at an yttrium concentration $\sim 5\%$.

The influence of acceptor doping on the perovskites is traditionally related to substitution of triply charged ions of *Y* or a rare-earth element for the transition-metal ion (Ce^{4+} in $BaCeO_3$), but in a reducing atmosphere self-doping may occur,[11] where part of Ce^{4+} ions reduce to Ce^{3+}, which has another charge and another radius. It is this that may account for the different behavior of ceramic and fused samples at the δ transition. The reducing medium in which the ceramic material is prepared produces a larger fraction of Ce^{3+} ions compared to induction melting in an air ambient, and, accordingly, the mean radius of the Ce ion in a ceramic is larger than it is in a fused sample, and this is what induces a shift of the δ transition toward lower temperatures in the latter. Note that the PTs of barium titanate, which is the closest analog of $BaCeO_3$, and whose Ti^{4+} ion is smaller in radius than Ce^{4+}, are downshifted noticeably on the temperature scale. As another illustration, one can present calorimetric data on $CeAlO_3$, a compound synthesized by the present authors, which may be considered to be the result of substituting of Al for the Ba ions in $BaCeO_3$, with subsequent conversion of the Al and Ce ions. Despite such a radical change of the starting composition ($BaCeO_3$), the DSC curve of a fused $CeAlO_3$ sample (Fig. 4) resembles strongly those of the original $BaCeO_3$ (Fig. 1) in that in both cases one observes two endothermal peaks separated by 130–150 K. There is also a substantial difference in that the whole region of the thermodynamic transitions in $CeAlO_3$ is shifted by 200 K toward lower temperatures compared to $BaCeO_3$.

Thus a DSC study of ceramic and fused $BaCeO_3$

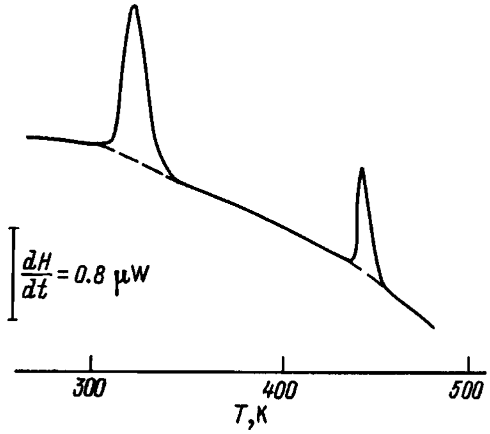

FIG. 4. DSC curve for a fused $CeAlO_3$ sample. Heating rate 20 K/min.

samples revealed the existence of thermodynamic transitions which separate the phase state of $BaCeO_3$ with increasing temperature in the following way: orthorhombic-I phase → second-order λ transition at 538 and 522 K for ceramic and fused samples, respectively, → orthorhombic-II phase → first-order transition with enthalpies of 0.18 and 0.14 J/g and temperatures of 667 and 607 K, respectively, for ceramic and fused samples → rhombohedral phase.

The authors express their sincere thanks to Dr. K. D. Kreuer (Max-Planck-Institut, Stuttgart, Germany) for providing ceramic $BaCeO_3$ samples.

Support of the Russian Fund for Fundamental Research (Grant 97-03-33466a) is gratefully acknowledged.

[1)] We denote here by "starting" the state of the material after its synthesis and subsequent cooling down to room temperature, including an intermediate heat treatment.

[1] B.-T. Melekh, V. M. Egorov, Yu. M. Baikov, N. F. Kartenko, Yu. N. Filin, M. F. Kompan, G. B. Venus, and V. B. Kulik, Solid State Ionics **97**, 465 (1997).
[2] Yu. M. Baĭkov, V. M. Egorov, N. F. Kartenko, B.-T. Melekh, and Yu. N. Filin, Pis'ma Zh. Tekh. Fiz. **22**, No. 11, 91 (1996) [Tech. Phys. Lett. **22**, 476 (1996)].
[3] K. S. Knight, Solid State Ionics **74**, 109 (1994).
[4] C. N. W. Darlington, Phys. Status Solidi A **155**, 31 (1996).
[5] T. Scherban, R. Villeneuve, L. Abello, and G. Lucazeau, J. Raman Spectrosc. **24**, 805 (1993).
[6] E. K. Shalkova, Yu. M. Baĭkov, B.-T. Melekh, T. A. Perevalova, and Yu. N. Filin, Zh. Neorg. Khim. **35**, 262 (1990).
[7] K. Illers, Eur. Polym. J. **10**, 911 (1974).
[8] A. Z. Patashinskiĭ and V. L. Pokrovskiĭ, *Fluctuation Theory of Phase Transitions* [in Russian] (Nauka, Moscow, 1982), 380 pp.
[9] K. D. Kreuer, W. Münch, M. Ise, T. He, A. Fuchs, U. Traub, and J. Maier, Ber. Bunsenges. Phys. Chem. **101**, 1344 (1997).
[10] D. Shima and S. M. Haile, Solid State Ionics **97**, 443 (1997).
[11] Yu. M. Baikov, Solid State Ionics **97**, 471 (1997).

Translated by G. Skrebtsov

Photoinduced instability and semiconductor-metal phase transition in a Peierls system

A. L. Semenov*)

Ul'yanovsk Moscow State University, 432700 Ul'yanovsk, Russia

(Submitted February 3, 1997; resubmitted May 21, 1998)
Fiz. Tverd. Tela (St. Petersburg) **40**, 2113–2118 (November 1998)

A microscopic theory of the appearance of electron-phonon instability and a semiconductor-metal phase transition away from thermodynamic equilibrium in a Peierls system upon the optical excitation of electron-hole pairs is devised. An equation which specifies the dependence of the order parameter of the phase transition and the uniquely related gap width in the electron spectrum, on the concentration n of conduction-band electrons is obtained. The critical concentration $n=n_c$, above which the semiconductor phase of the system is unstable toward the transition to the metallic state, is calculated. A comparison with an experiment on the irradiation of a substrate-supported vanadium dioxide film by a laser pulse is made.

[S1063-7834(98)03311-5]

The Peierls system considered in this paper is a one-dimensional chain of atoms, each of which has one outer electron. In the high-temperature metallic phase the atoms in the chain are equidistant, and the electronic conduction band is half-filled. When the temperature reaches a certain critical value T_0 during cooling, the metallic phase becomes unstable, and a metal-semiconductor phase transition occurs. The atoms in the chain then approach one another in pairs.[1]

Theoretical results obtained on the basis of the Peierls model have been used to describe the experimentally observed properties of numerous quasi-one-dimensional materials: complex compounds of platinum,[1] TaS_3 compounds,[2] organic conductors,[3] vanadium oxide bronzes,[4] $NbSe_3$ materials,[5] etc.[5–7] In particular, the influence of such factors as uniaxial compression,[8] doping,[9,10] phonon-phonon coupling,[8,11] adherence of the VO_2 film to a substrate,[12] adsorption, etc.[13] on the metal-semiconductor phase transition in vanadium dioxide can be explained within this model.

It is known that a phase transition away from thermodynamic equilibrium to a state with a moving charge-density wave is observed in the low-temperature phase of a Peierls system in a constant electric field at a certain threshold value E_t of its intensity.[5] This transition can be either second- or first-order, depending on the specific conditions. For example, the current-voltage characteristic of $NbSe_3$ exhibits a hysteretic dependence typical of a first-order phase transition at $T=26.5$ K, while there is no hysteresis at $T=34$ K (Ref. 5).

The behavior of the low-temperature phase of a Peierls system in response to optical excitation of the nonequilibrium electron-hole pairs in it was studied experimentally in the case of vanadium dioxide.[14,15] It was shown that at sufficiently high levels of photoexcitation there is a loss of stability of the semiconductor state leading to a transition to the metallic state after a characteristic time roughly equal to one picosecond.

This paper proposes a microscopic theory, which describes the behavior of the low-temperature phase of a Peierls system in response to the interband photoexcitation of nonequilibrium electron-hole pairs in it. It is assumed that such excitation can be caused, for example, by dipole transitions of electrons from the valence band to the conduction band under the effect of incident laser radiation.[16] The experiment in Ref. 15 on the irradiation of vanadium dioxide by a laser pulse is interpreted within the theory devised.

1. ELECTRON SPECTRUM OF THE SYSTEM

Let us consider a chain of atoms, on each of which there is one outer electron. We write the Hamiltonian of the electronic subsystem in the tight-binding approximation in the following form:[17]

$$H=\sum_{n\sigma} B_{n,n+1}(a^{+}_{n\sigma}a_{n+1,\sigma}+a^{+}_{n+1,\sigma}a_{n,\sigma})$$

$$+\frac{1}{2}\sum_{n,m,\sigma,\delta} c(n-m)a^{+}_{n,\sigma}a^{+}_{m,\delta}\,a_{m,\delta}\,a_{n,\sigma}, \qquad (1)$$

where n is the number of the atom in the chain, $\sigma=\pm 1$ labels the direction of the spin, $B_{n,n+1}$ is the overlap integral of the wave functions of the nth and $(n+1)$th atoms, $a^{+}_{n,\sigma}$ and $a_{n,\sigma}$ are, respectively, the creation and annihilation operators of an electron with spin σ on atom n,

$$c(n-m)=\langle n,\sigma;m,\delta|U^{(2)}|m,\delta;n\sigma\rangle \qquad (2)$$

is the matrix element of a two-particle interelectronic interaction with the potential $U^{(2)}$.

For narrow-band systems (in particular, for the Peierls model) the distances $r_{n,n+1}$ between neighboring atoms are several times greater than the effective radius R of the atomic wave function of an electron. In this case $B_{n,n+1} \sim \exp(-r_{n,n+1}/R)$.[18] We write the distance $r_{n,n+1}$ in the form

$$r_{n,n+1}=r_0+(-1)^{n+1}R\xi, \qquad (3)$$

where r_0 is the interatomic distance in the metallic phase, and ξ is the period-doubling parameter of a one-dimensional crystal. With consideration of (3) the overlap integral $B_{n,n+1}$ takes the form

$$B_{n,n+1}=b\exp((-1)^n\xi), \tag{4}$$

where b is the overlap integral in the metallic phase ($\xi=0$). In writing (1), the phases of the atomic wave functions were chosen so that b in (4) would be a real quantity.

Using the Heisenberg equation to describe the evolution of a certain operator f (Ref. 17)

$$-i\hbar\frac{\partial f}{\partial t}=[H,f] \tag{5}$$

and using the commutation relations for the second-quantization Fermi operators, from (1) we obtain

$$i\hbar\frac{\partial a_{m,\sigma}}{\partial t}=(B_{m,m+1}a_{m+1,\sigma}+B_{m-1,\,m}a_{m-1,\sigma})$$
$$+\sum_{n,\delta}c(n-m)a^+_{n,\delta}\,a_{n,\delta}\,a_{m,\sigma}. \tag{6}$$

We introduce the Green's function of the system under consideration in the standard form[19]

$$G(m,\sigma,t_1;n,\delta,t_2)=-i\langle Ta_{m,\sigma}(t_1)a^+_{m,\delta}(t_2)\rangle, \tag{7}$$

where T is the chronological ordering operator. Using (6), we find the following equation for the Green's function (7) [the notation $G(m,\sigma,t_1;n,\delta,t_2)=G(m,n)$ is introduced for convenience]:

$$i\hbar\frac{\partial G(m,n)}{\partial t_1}=B_{m,m+1}G(m+1,n)+B_{m-1,m}G(m-l,n)$$
$$-i\sum_{p,\gamma}c(p-m)\langle Ta^+_{p,\gamma}(t_1)a_{p,\gamma}(t_1)a_{m,\sigma}(t_1)$$
$$\times a^+_{n,\delta}(t_2)\rangle+\delta_{n,m}\delta(t_1-t_2). \tag{8}$$

Here $\delta_{m,n}$ and $\delta(t)$ are the Kronecker delta and a δ function.

We continue the analysis of Eq. (8) in the Hubbard approximation, in which only the interaction between electrons located in the same atom is taken into account, i.e.,

$$c(m-n)=c_0\delta_{m,n}. \tag{9}$$

Uncoupling the three-particle correlator in (8) using Wick's theorem,[19] and introducing the antiferromagnetic ordering parameter ζ $(0\leqslant\zeta\leqslant 1)$ according to the equation

$$\langle a^+_{m,\sigma}a_{m,\sigma}\rangle=\frac{1}{2}(1+\sigma(-1)^m\zeta), \tag{10}$$

and going over to Fourier space with respect to the temporal and spatial variables, we obtain a four-component (because of the doubling of the crystal-lattice period in the semiconductor phase of the system) Green's matrix

$$G=\begin{pmatrix}G_{11} & G_{12}\\ G_{21} & G_{22}\end{pmatrix},$$

$$G_{11}(\omega,k)=G_{12}(\omega,k)=\frac{\hbar\omega-c_0(1+\zeta)/2+2b\cosh(\xi)\cos(k)-2ib\sinh(\xi)\sin(k)}{(\hbar\omega-c_0/2)^2-(c_0\zeta/2)^2-(2b\cosh(\xi)\cos(k))^2-(2b\sinh(\xi)\sin(k))^2}. \tag{11}$$

The components $G_{22}=G_{21}$ are obtained from (11) using the replacements $\zeta\to-\zeta$ and $i\to-i$. Taking into account (11), we find the effective one-electron spectrum ε_k of the system

$$\varepsilon_k=\hbar\omega_k=\frac{c_0}{2}\pm\sqrt{4b^2(\cos^2(k)+\sinh^2(\xi))+(c_0\zeta/2)^2}. \tag{12}$$

It can easily be seen that a gap of forbidden energies can form in the spectrum (12) either as a result of doubling the crystal-lattice period [$\xi\neq0$ in (3)] or antiferromagnetic ordering [$\zeta\neq0$ in (10)]. Since there is one electron in each atom, at $T=0$ the states below the band gap in (12) are completely filled with electrons, and the states above it are empty.

2. EQUILIBRIUM EQUATION

Let us consider the behavior of the low-temperature phase of the Peierls system in response to the excitation of nonequilibrium electron-hole pairs in it. We assume that this excitation is caused by forced transitions of electrons from the valence band to the conduction band owing to, for example, a dipolar electron-photon interaction with the incident radiation. It is known that the characteristic intraband relaxation time of electrons $\tau_e\sim10^{-14}$ s is significantly smaller than the interband relaxation time $\tau\sim10^{-11}$ s (Ref. 20). Therefore, when the system is irradiated by a light field of constant amplitude, it can be assumed in an approximation[21] that, within each electronic band, thermodynamic equilibrium is established between the electrons and the quasi-Fermi level corresponding to the respective band. The violation of the thermodynamic equilibrium between the bands caused by external irradiation is manifested by a difference between the corresponding quasi-Fermi levels.

The approach considered above to the description of a system not in thermodynamic equilibrium, consisting of a set of subsystems that are in thermodynamic equilibrium, can be extended to the case where the incident radiation has an adiabatically slowly varying amplitude A (the change in the field amplitude ΔA during the time $\tau_e\sim10^{-14}$ s is much smaller than A). This is because the electronic subsystem within each of the bands manages to completely follow the variation of the field and is, therefore, in a state of thermodynamic equilibrium at any moment in time. This situation is analogous to some extent to the situation usually encountered in the description of systems in thermodynamic equilibrium with adiabatically slow variation of the external parameters.

Below we shall confine ourselves to devising a theory for just such a case. We shall not discuss the transient processes taking place in the system during a time $\tau_e\sim10^{-14}$ s upon passage of the steep leading or trailing edge of the light pulse.

The free energy F_j of the electronic subsystem of the jth band ($j=1,2$) is specified by the relation

$$F_j=\mu_j N_j-k_{\mathrm{B}}T\sum_k \ln\left(1+\exp\left(\frac{\mu_j-\varepsilon_k}{k_{\mathrm{B}}T}\right)\right), \tag{13}$$

where μ_j and N_j are, respectively, the quasi-Fermi level and the number of electrons in the jth band. The summation over k is carried out within the jth band of the spectrum (12) ($|k|<\pi/2$ for $j=1$ and $\pi/2<|k|<\pi$ for $j=2$). We shall henceforth confine ourselves to considering of the case where there is no antiferromagnetic ordering [$\zeta=0$ in (12)].

It is known that the characteristic relaxation time of the phonon subsystem $\tau_p\sim 10^{-13}$ s.[20] Therefore, at times when the amplitude of the incident radiation pulse varies only slightly during a time interval $\tau_p\sim 10^{-13}$ s (adiabatically slow variation of the external parameter) the phonon subsystem manages to relax to its state of dynamic equilibrium, which depends on the instantaneous amplitude of the pulse.

In this case the free energy of the crystal lattice can be described in the harmonic approximation with allowance for the structural distortions (3) by an expression of the following form:

$$F_c=F_0+\frac{\gamma}{2}\sum_m (i_{m,m+1}-I_0)^2, \tag{14}$$

where F_0 is the free energy characterizing the lattice dynamics and γ is the stiffness factor of the lattice for the static displacements (3) of the atoms. Formula (14) was written in the molecular-field approximation,[1] in which it is assumed that the phonon part of F_0 does not depend on ξ, which is responsible for the static distortions. From the physical standpoint, this approximation presumes the absence of any interaction between the dynamic (with a frequency $\omega\neq 0$) and static (with a frequency $\omega=0$) phonon modes.

With consideration of (3), from (14) we obtain

$$F_c=F_0+\frac{A}{2}\xi^2, \tag{15}$$

where $A=\gamma N R^2$.

In order for the system not in thermodynamic equilibrium under consideration to be in a stationary state of dynamic equilibrium, the generalized force f corresponding to the generalized coordinate ξ must be equal to zero:

$$f\equiv-\left(\frac{\partial F_1}{\partial\xi}\right)_{T,N_1}-\left(\frac{\partial F_2}{\partial\xi}\right)_{T,N_2}-\left(\frac{\partial F_c}{\partial\xi}\right)_T=0. \tag{16}$$

Hence, taking into account formulas (13) and (15), we find

$$f=-A\xi+2\sum_{|k|\leqslant\tau/2}\frac{\partial\varepsilon_k}{\partial\xi}\tanh\left(\frac{\varepsilon_k-\mu}{2k_{\mathrm{B}}T}\right)=0. \tag{17}$$

The expression (17) is the equilibrium equation of the Peierls system, which specifies the behavior of ξ in response to the excitation of nonequilibrium electron-hole pairs.

The expansion coefficient A of the free energy F_c of the crystal lattice in a series in the order parameter ξ is expressed in terms of the critical temperature T_0 of the metal-semiconductor phase transition at thermodynamic equilibrium (in the absence of a light field) and other characteristics of the system.[8,10] The condition for an equilibrium metal-semiconductor phase transition is a loss of stability of the metallic phase [$\partial^2F(T_0,\xi=0)/\partial\xi^2=0$, where F is the free energy of the system]. In the absence of a light field, the quasi-Fermi levels of the balance and conduction bands in the spectrum (12) are equal to zero: $\mu_{1,2}=\mp\mu=0$. Hence, with consideration of (17) and (12) we have

$$A=2\sum_{|k|\leqslant\pi/2}\left(\frac{\partial^2\varepsilon_k}{\partial\xi^2}\tanh\left(\frac{\varepsilon_k}{2k_{\mathrm{B}}T_0}\right)\right)_{\xi=0}. \tag{18}$$

Calculating the sum in (18), in an approximation we obtain

$$A=\frac{4bN}{\pi}\left(\ln\left(\frac{\pi b}{2k_{\mathrm{B}}T_0}\right)+1\right). \tag{19}$$

From the physical standpoint, it is convenient to consider the total (including both equilibrium and nonequilibrium excitations) concentration n of electron-hole pairs as the external controllable parameter. For this purpose, in addition to (17) we must write the electroneutrality equation of the system, which relates n to the quasi-Fermi level μ,

$$n=\frac{N}{2}-\sum_{|k|\leqslant\pi/2}\tanh\left(\frac{\varepsilon_k-\mu}{2k_{\mathrm{B}}T}\right). \tag{20}$$

Thus, Eqs. (17) and (12), with consideration of (20), form a closed system for determining the parameter of the structural lattice distortions ξ (3) at an assigned temperature T and concentration of electron-hole pairs n.

3. RELATION BETWEEN THE ORDER PARAMETER ζ OF THE SEMICONDUCTOR–METAL PHASE TRANSITION AND THE CONCENTRATION n OF ELECTRON-HOLE PAIRS

We analyze Eqs. (17) and (20) under the assumption that the Peierls system is a nondegenerate or weakly degenerate semiconductor:

$$\mu-2b\sinh\xi<2k_{\mathrm{B}}T. \tag{21}$$

If Eq. (20) is taken into account, the relation (21), which imposes a bound on the range of variation of the quasi-Fermi level μ, is equivalent to the following approximate inequality, which imposes an upper bound on the concentration n of electron-hole pairs:

$$n<n_1=\frac{8N}{3\pi}\sqrt{\frac{k_{\mathrm{B}}T\sinh\xi}{b}}. \tag{22}$$

Using Eqs. (17) and (20), we find an approximate equation for the order parameter ξ of the metal-semiconductor phase transition:

$$A\xi-4b\left(\frac{N}{\pi}\sinh(\xi)K(\sqrt{1-\tanh^2\xi})-n\cosh(\xi)\right)=0, \tag{23}$$

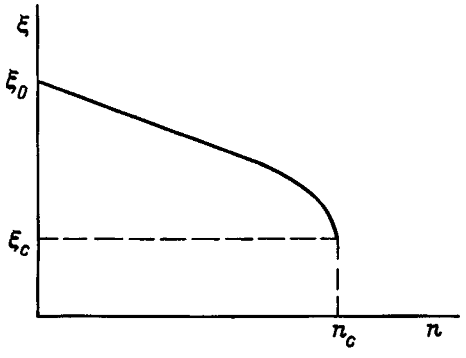

FIG. 1. Schematic plot of the dependence of the order parameter ξ of the metal-semiconductor phase transition on the total concentration n of electron-hole pairs. The quantities ξ_c and n_c are defined by formulas (27).

where $K(x)$ is a complete normal elliptic integral of the first kind.

Inasmuch as the concentration of electron-hole pairs $n \ll N$ in real physical systems and the order parameter of the metal-semiconductor phase transition of such systems $\xi \leqslant 0.5$ (Refs. 1–6), we obtain the following equation in an approximation from (23)

$$n=\frac{N\xi}{\pi}\ln\left(\frac{\xi_0}{\xi}\right), \tag{24}$$

where

$$\xi_0=\frac{\pi}{2}\exp\left\{\arcsin\left(\frac{\pi}{4}\right)-\frac{A\pi}{4bN}\right\} \tag{25}$$

is the order parameter of the metal-semiconductor phase transition for $n=0$.

A schematic plot of $\xi(n)$ with consideration of the condition of stability toward spatially homogeneous fluctuations of the order parameter ξ of the metal-semiconductor phase transition

$$\frac{\partial n}{\partial \xi}<0 \tag{26}$$

is shown in Fig. 1. It is seen that as the concentration n of electron-hole pairs increases to n_c, the order parameter ξ of the metal-semiconductor phase transition decreases smoothly to ξ_c, where

$$n_c=\frac{N\xi_0}{\pi c}, \quad \xi_c=\frac{\xi_0}{c}. \tag{27}$$

At n_c there is an abrupt decrease in ξ from ξ_c to zero (a phase transition to the metallic state).

4. NUMERICAL ESTIMATES, COMPARISON WITH EXPERIMENT, AND DISCUSSION OF RESULTS OBTAINED

The numerical value of the critical concentration n_c of photoexcited electron-hole pairs which initiate the semiconductor-metal phase transition in the Peierls system can be estimated for vanadium dioxide using (27). We adopt typical numerical values of the parameters for VO_2 (Ref. 6): the concentration of vanadium atoms $N \approx 7\times10^{22}\ \mathrm{cm}^{-3}$, the gap width in the semiconductor phase $E_g\approx 0.6$ eV, and the width of the conduction band in the metallic phase $E_0\approx 1.2$ eV. Then, from (12) and (27) we find

$$\xi_0\approx\frac{E_g}{E_0}\approx 0.5, \quad n_c\approx 4\times10^{21}\ \mathrm{cm}^{-3}. \tag{28}$$

The behavior of a vanadium dioxide film on an aluminum substrate in response to irradiation by a laser pulse with a power density $P\approx 7\times10^{8}\ \mathrm{W/cm}^2$ and a duration of 6×10^{-12} s was investigated experimentally in Ref. 15. It was found for an energy of exciting photons $\hbar\omega_0=1.17$ eV that VO_2 passes from the semiconductor state to the metallic state at a time $\tau_0\sim10^{-12}$ s after the onset of the pulse. The metallic phase thereafter remains stable over the course of a fairly long time t ($t>10^{-9}$ s). If the energy of the exciting photons $\hbar\omega_0=2.34$ eV, the loss of stability of the semiconductor phase of vanadium dioxide occurs at a time $t\sim10^{-9}$ s after the onset of irradiation.

To account for the experimentally observed phenomenon just described, we numerically estimate the maximum possible temperature change ΔT in the sample after the application of laser radiation. For this purpose we consider the very thin (~ 1 nm) near-surface, strongly heated region of the film with the neglect of heat-transfer processes under the assumption (which is fairly far-fetched for the short times $t<10^{-12}$ s) that all the radiant energy absorbed manages to be converted into heat. Using the approximate formula

$$\Delta T=\frac{\alpha P\Delta t}{c\rho} \tag{29}$$

(where α, c, and ρ are, respectively, the optical absorption coefficient, the specific heat, and the density of the film material, and Δt is the irradiation time) and adopting numerical values of the parameters that are typical of VO_2 [$\alpha\sim10^{5}\ \mathrm{cm}^{-1}$ (Ref. 6), $c\sim1$ J/(g·K), $\rho\approx10\ \mathrm{g/cm}^3$, and $\Delta t=\tau_0\sim10^{-12}$ s], we obtain $\Delta T\approx 10$ K. Taking into account that the temperature of the semiconductor-metal phase transition at thermodynamic equilibrium in vanadium dioxide $T_0\cong340$ K, we arrive at the conclusion that at room temperature the photoinduced transition to the metallic phase occurring after a time $\tau_0\sim10^{-12}$ s cannot be explained by a thermal mechanism.

At the same time, the stability of the metallic phase of vanadium dioxide after passage of the entire pulse ($\Delta t\sim6\times10^{-12}$ s) is apparently attributable to the fairly high temperature T of the film ($T>T_0\cong340$ K), since, according to formula (29), in this case $\Delta T\approx 60$ K.

We note that, in our opinion, the delay of the semiconductor-metal phase transition by a time $t\sim10^{-9}$ s when the energy of the exciting photons $\hbar\omega_0=2.3$ eV is caused by the large lifetime τ_π of nonequilibrium electrons and holes in the π^* band,[6,15] which slows the film heating process by a corresponding time. Unlike Bugaev *et al.*,[15] we assume that in this case the photoinduced transition to the metallic phase is caused by a purely thermal mechanism, since $t_\pi 10^{-9}\mathrm{s}\gg\tau\sim10^{-11}$ s (Ref. 20) and, therefore, the concentration of nonequilibrium electron-hole pairs in the d band is negligibly small ($n\ll n_c$).

Let us now estimate the concentration n of nonequilibrium electron-hole pairs excited in the d band of vanadium dioxide under the conditions of the experiment in Ref. 15 during irradiation of a film by a pulse with a photon energy $\hbar\omega_0 = 1.17$ eV. For this purpose we use the following approximate kinetic equation:[22]

$$\frac{\partial n}{\partial t} = \frac{\alpha P}{\hbar\omega_0} - \frac{n}{\tau} - \gamma n^3, \tag{30}$$

where γ is the nonlinear Auger recombination constant of the nonequilibrium carriers.

Taking into account that the interband electronic relaxation time in VO_2 $\tau \sim 10^{-11}$ s (Ref. 20) and setting $\gamma \sim 10^{-30}$ cm^6/s [the values of γ for several thoroughly investigated semiconductors, such as Si, GaAs, etc., vary in the range $\gamma \sim 10^{-28} - 10^{-31}$ cm^6/s (Refs. 22–24)], we obtain the approximate solution of Eq. (30)

$$n_0^2 \gamma t = \frac{1}{6} \ln \frac{n_0^2 + n_0 n + n^2}{(n_0 - n)^2} - \frac{1}{\sqrt{3}} \left[\arctan\left(\frac{2n + n_0}{\sqrt{3} n_0} \right) - \arctan\left(\frac{1}{\sqrt{3}} \right) \right], \tag{31}$$

where

$$n_0 = n(t \to \infty) = \sqrt[3]{\frac{\alpha P}{\hbar\omega_0 \gamma}}. \tag{32}$$

During the derivation of (31) we neglected the linear recombination of electron-hole pairs, since the second term on the right-hand side of Eq. (30) is small compared to the sum of the other two terms under the present conditions.[22–24]

Substituting the typical numerical values of the parameters $\alpha \sim 10^5$ cm^{-1}, $P \approx 7 \times 10^8$ W/cm^2, $\hbar\omega_0 = 1.17$ eV, and $\gamma \sim 10^{-30}$ cm^6/s into (31) and (32), we find that the limiting concentration of nonequilibrium electron-hole pairs $n_0 \sim 10^{21}$ cm^{-3} is established after a characteristic time $t \approx 1/(\gamma n_0^2) \approx 10^{-12}$ s.

We note that the numerical value which we obtained $n \sim 10^{21}$ cm^{-3} for the concentration of nonequilibrium electron-hole pairs photoexcited under the conditions of the experiment in Ref. 15 is somewhat smaller than the value given in Ref. 25, where the concentration of nonequilibrium carriers following the irradiation of a VO_2 film on an aluminum substrate by a laser pulse with a power density $P \approx 6 \times 10^8$ W/cm^2 and a duration of 5×10^{-11} s was $n \sim 10^{22}$ cm^{-3}. This difference is apparently due to some arbitrariness in the choice of the values of α and γ in Eq. (32). Moreover, these parameters can vary from sample to sample over a fairly broad range, depending on the method used to fabricate the VO_2 film. In particular, the optical absorption coefficient α varies over a whole order of magnitude.[6]

Nonthermal photoinduced changes in the crystal-lattice structure, such as amorphization[22,24] and a transition to a new crystalline phase,[22,26] can be observed in numerous materials (Si, GaAs, InSb, III–V semiconductors, etc.) and take place at nonequilibrium carrier concentrations $n \sim 10^{21} - 10^{22}$ cm^{-3} under the conditions of irradiation by high-power laser pulses of pico- and femtosecond duration.[22,24,26]

Thus, the microscopic theory of photoinduced instability and the semiconductor-metal phase transition with simultaneous alteration of the crystal structure in a Peierls system developed in this paper is capable of satisfactorily accounting for the set of experimentally observed phenomena occurring when a substrate-supported vanadium dioxide film is irradiated by a short high-power laser pulse.[15] The numerical value estimated from the theory for the critical concentration (28) of nonequilibrium electron-hole pairs initiating this transition coincides in order of magnitude with the value estimated from the experimental data for VO_2 (Refs. 15 and 25) and with the results of other studies on the nonthermal photoinduced alteration of the crystal-lattice structure of semiconductors.[22,26]

Thus, it has been shown in the present work that the semiconductor-metal phase transition taking place away from thermodynamic equilibrium in a Peierls system in an applied constant $(\omega = 0)$ electric field of great intensity[5] can also be observed in the high-frequency optical range $(\omega \neq 0)$. In both cases this transition is caused by excitation of the electronic subsystem. However, while the appearance of the collective properties that lead to the formation of an electron crystal is decisive at $\omega = 0$ (Ref. 27), at $\omega \neq 0$ this phenomenon can also be described successfully in a single-electron approximation, which completely ignores the electron-electron interaction (or takes it into account within the Hartree–Fock method).

*)E-mail: semenov@quant.suniv.simbirsk.su

---

[1] L. N. Bulaevskiĭ, Usp. Fiz. Nauk **115**, 263 (1975) [Sov. Phys. Usp. **18**, 131 (1975)].

[2] V. E. Minakova, Yu. I. Latyshev, and V. A. Volkov, JETP Lett. **62**, 455 (1995).

[3] L. P. Gor'kov, Usp. Fiz. Nauk **144**, 381 (1984) [Sov. Phys. Usp. **27**, 809 (1984)].

[4] A. A. Fotiev, V. L. Volkov, and V. K. Kapustkin, *Vanadium Oxide Bronzes* [in Russian], Nauka, Moscow (1978), p. 151.

[5] G. Gruner, Rev. Mod. Phys. **60**, 1129 (1988).

[6] A. A. Bugaev, B. P. Zakharchenya, and F. A. Chudnovskiĭ, *The Metal-Semiconductor Phase Transition and Its Application* [in Russian], Nauka, Leningrad (1979), 183 pp.

[7] R. O. Zaĭtsev, E. V. Kuz'min, and S. G. Ovchinnikov, Usp. Fiz. Nauk **148**, 603 (1986) [Sov. Phys. Usp. **29**, 322 (1986)].

[8] V. I. Emel'yanov, N. L. Levshin, and A. L. Semenov, Vestn. Mosk. Univ., Ser. 3: Fiz. Astron. **30**(5), 52 (1989).

[9] V. I. Emel'yanov, N. L. Levshin, and A. L. Semenov, Fiz. Tverd. Tela (Leningrad) **31**(10), 261 (1989) [Sov. Phys. Solid State **31**, 1803 (1989)].

[10] A. L. Semenov, Fiz. Tverd. Tela (St. Petersburg) **36**, 1974 (1994) [Phys. Solid State **36**, 1079 (1994)].

[11] A. L. Semenov, Fiz. Tverd. Tela (St. Petersburg) **39**, 925 (1997) [Phys. Solid State **39**, 826 (1997)].

[12] V. I. Emel'yanov and A. L. Semenov, Fiz. Tverd. Tela (Leningrad) **32**, 3083 (1990) [Sov. Phys. Solid State **32**, 1790 (1990)].

[13] V. I. Emel'yanov, N. L. Levshin, S. Yu. Poroĭkov, and A. L. Semenov, Vestn. Mosk. Univ., Ser. 3: Fiz. Astron. **32**(1), 63 (1991).

[14] A. A. Bugaev, B. P. Zakharchenya, and F. A. Chudnovskiĭ, JETP Lett. **33**, 629 (1981).

[15] A. A. Bugaev, V. V. Gudyalis, B. P. Zakharchenya, and F. A. Chudnovskiĭ, JETP Lett. **34**, 430 (1981).

[16] A. L. Semenov, Zh. Éksp. Teor. Fiz. **111**, 2147 (1997) [JETP **84**, 1171 (1997)].

[17] L. D. Landau and E. M. Lifshitz, *Quantum Mechanics: Non-Relativistic Theory*, 3rd ed., Pergamon Press, Oxford (1977), 768 pp.

[18] O. Madelung, *Solid-State Physics: Localized State*, Nauka, Moscow (1985), p. 144.

[19] E. M. Lifshitz and L. P. Pitaevskii, *Statistical Physics*, *Vol. 2*, 2nd ed., Pergamon Press, Oxford–New York (1980), 448 pp.

[20] N. R. Belashenkov, V. B. Karasev, A. A. Solunin, I. A. Khakhaev, K. Sh. Tsibadze, and F. A. Chudnovskiĭ, Fiz. Tverd. Tela (St. Petersburg) **36**, 2475 (1994) [Phys. Solid State **36**, 1347 (1994)].

[21] V. L. Bonch-Bruevich and S. G. Kalashnikov, *Semiconductor Physics* [in Russian], Nauka, Moscow (1977), 688 pp.

[22] V. I. Emel'yanov and D. V. Babak, Laser Phys. **7**, 514 (1997).

[23] V. I. Emel'yanov and I. F. Uvarova, Zh. Éksp. Teor. Fiz. **94**, *8*, 255 (1988) [Sov. Phys. JETP **67**, 1662 (1988)].

[24] S. A. Akhmanov, V. I. Emel'yanov, N. I. Koroteev, and V. N. Seminogov, Usp. Fiz. Nauk **147**, 675 (1985) [Sov. Phys. Usp. **28**, 1084 (1985)].

[25] A. A. Bugaev and A. V. Klochkov, Fiz. Tverd. Tela (Leningrad) **26**, 3487 (1984) [Sov. Phys. Solid State **26**, 2100 (1984)].

[26] Yu. V. Kopaev, V. V. Menyaĭlenko, and S. N. Molotkov, Fiz. Tverd. Tela (Leningrad) **27**, 3288 (1985) [Sov. Phys. Solid State **27**, 1979 (1985)].

[27] S. N. Artemenko, A. F. Volkov, and S. V. Zaĭtsev, Usp. Fiz. Nauk **166**, 434 (1996) [Phys. Usp. **39**, 403 (1996)].

Translated by P. Shelnitz

PHYSICS OF THE SOLID STATE VOLUME 40, NUMBER 11 NOVEMBER 1998

Phonon echo in *L*-alanine

V. V. Lemanov and S. N. Popov

A. F. Ioffe Physicotechnical Institute, Russian Academy of Sciences, 194021 St. Petersburg, Russia

(Submitted May 28, 1998)
Fiz. Tverd. Tela (St. Petersburg) **40**, 2119–2120 (November 1998)

Phonon echo signals have been observed in a finely-dispersed crystalline powder of the *L*-alanine amino acid. Measurements of the relaxation time T_2 have revealed a phase transition in *L*-alanine crystals at a temperature of about 170 K. © *1998 American Institute of Physics.* [S1063-7834(98)03411-X]

Alanine, NH_2CHCH_3COOH, is one of 20 protein amino acids serving as the building blocks for the proteins of living organisms. Alanine molecules, as all protein amino acids with the exception of glycine, can coexist in the form of two mirror antipodes, L and D. Alanine crystals built of such molecules have rhombic symmetry with space group $P2_12_12_1$ (point group D_2).[1] [Interestingly, DL-alanine crystals (racemate) have $Pna2_1$ symmetry,[1] which means that they are polar compounds with point group C_{2v}.] Crystals of protein amino acids are soft, labile objects dominated by hydrogen bonding. These crystals exhibit a high degree of structural order (low symmetry) with a strongly pronounced spatial dispersion (optical activity); application of temperature and pressure apparently can induce phase transformations.

The temperature dependence of NMR spectra[2] and of the spin-lattice relaxation time T_1 (Ref. 3) suggests a phase transition in *L*-alanine crystals at 178 K. Raman spectra do not confirm directly the existence of this transition.[4] At the same time the unusual behavior of the intensity of the lowest-frequency phonon modes (42 and 49 cm^{-1}) led to the conclusion of a mode instability with an activation energy of 500 K, which appears to indicate dynamic localization of vibrational energy in the crystal with a dispersion and nonlinearity (the soliton).[4] The temperature dependence of the thermal conductivity of *L*-alanine single crystals likewise does not contain any anomalies around 178 K,[5] but this characteristic of crystals, in contrast to heat capacity, is known to change very little in a phase transition.

To obtain additional data on a possible phase transition in *L* alanine, we performed measurements of the temperature dependence of the two-pulse phonon echo. As is well known, phonon, or electroacoustical echo consists,[6,7] of the generation in a piezoelectric sample, acted upon by two electromagnetic pulses with rf filling separated by a time τ, of a response in a time 2τ in the form of a pulse of the same duration and with the same filling. The mechanism of phonon echo generation in a powder is as follows. The applied rf pulse initiates, by a reverse piezoelectric effect, vibrations of the grains whose natural frequencies lie within the interval corresponding to the spectral width of the pulse. The system generates a response as a result of a direct piezoelectric effect induced by acoustic vibrations. Because the vibration frequencies of different excited particles are different, the vibration phases, which were initially coupled, become randomized with time to make the vibrations no longer coherent. As a result, the response of the oscillator system damps out, although each of the excited oscillators continues to vibrate. The role of the second pulse is to excite in anharmonic oscillators vibrations whose phases will evolve in the opposite direction. Thus, at time $t=2\tau$, the phases coincide to produce an echo signal.

The echo signal amplitude varies with time τ proportional to $\exp(-2\tau/T_2)$, where the relaxation time T_2 is inversely proportional to the acoustic wave damping in the sample at the given frequency.

We used commercial *L*-alanine powder, finely dispersed, chromatographically homogeneous, Pure Grade, with the content of the main compound not below 98% (REANAL, Budapest). The 100–200-μm fraction used in the measurements was obtained by screening through appropriate sieves. The measurements were performed on an IS-2 pulsed NQR spectrometer interfaced with an AI-1024 multichannel pulse analyzer. The sample with a volume of about 1 cm^3 was placed in the resonant-circuit capacitor. The rf pulse amplitude corresponded to an electric field at the sample of about 5 kV/cm. The operating frequency (pulse filling) was 10 MHz, the pulse duration, 6 μs. The pulse separation was varied from 55 to 165 μs. The pulse-pair repetition frequency was 25 ms.

The ultrasonic velocity in L alanine is 6.2×10^5 and 4×10^5 cm/s for longitudinal waves, and 2×10^5 cm/s for transverse ones.[5] In crystals with D_2 symmetry the xyz, yxz, and zxy piezoelectric coefficients are nonzero, so that an rf electric field excites transverse waves. For particles in the sample ranging from 100 to 200 μm in size, the resonant frequency varies from 10 to 5 MHz, which means that the operating frequency of 10 MHz used in our case coincided with the resonant frequency of 100-μm particles.

Figure 1 presents echo signals generated as the delay time τ between the pulses is varied from 55 to 165 μs at a temperature of 136 K. The exponential echo-signal decay is determined by the relaxation time T_2. Note that, as far as we know, this is the first observation of phonon echo in amino acids.

Figure 2 plots T_2 as a function of temperature within the 100–330 K interval. The time T_2 was found by fitting an exponential to the echo-signal envelope. We readily see that

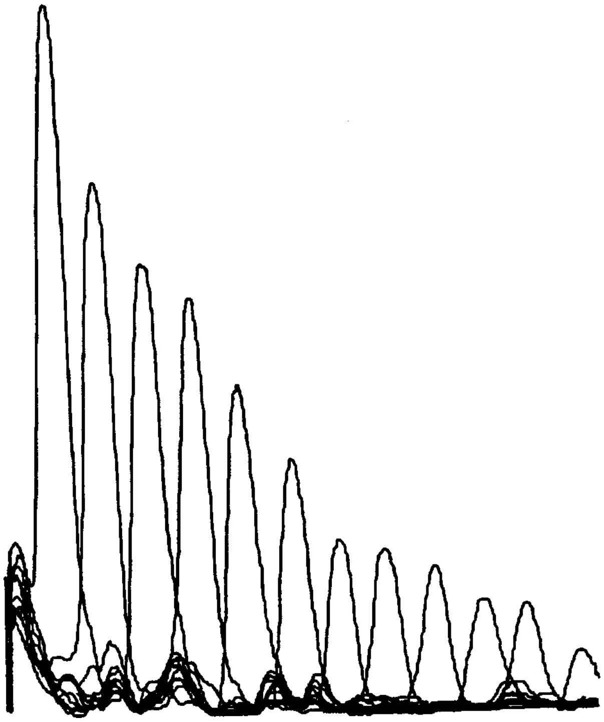

FIG. 1. Phonon-echo signal train obtained in *L*-alanine powder at 136 K. Frequency 10 MHz, pulse duration 6 μs, pulse separation varied from 55 to 165 μs. The scan is gated by the second pulse with a 50-μs delay.

the relaxation time T_2 varies very strongly within the 140–180 K interval. The ultrasonic damping, which is inversely proportional to T_2, changes in this interval approximately from 0.1 to 0.2 dB/μs. Such a strong change in damping within a narrow temperature interval cannot be due to the lattice damping by the mechanism of Akhiezer (which usually is valid for damping in crystals at such frequencies) and is most probably associated with a phase transition.

Note that the existence in this temperature region of a phase transition is supported also by dielectric measurements in the 10^2-10^6-Hz range. The dielectric permittivity of *L*-alanine crystals undergoes a jump at 176 K by about 15% (V. A. Trepakov, private communication).

The echo pulse amplitude at $\tau = 55\,\mu$s decreases slightly with decreasing temperature above the phase-transition point, grows rapidly in the region of the phase transition, and saturates below 150 K.

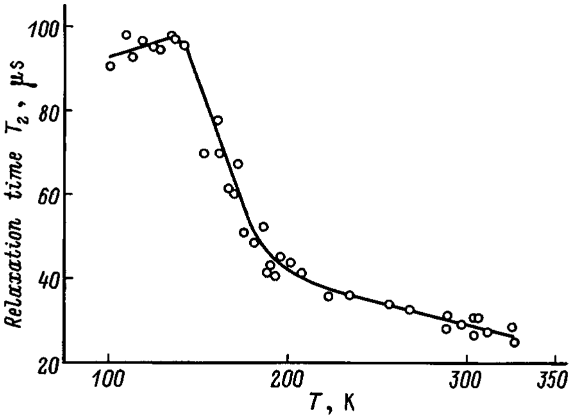

FIG. 2. Temperature dependence of phonon-echo relaxation time T_2.

Thus the totality of available experimental information (NMR data,[2] spin-lattice relaxation times T_1,[3] and our data on phonon echo and dielectric properties) confirm the existence of a phase transition in *L*-alanine crystals at a temperature of about 170 K. Establishment of the mechanisms responsible for this transition requires further, primarily x-ray diffraction, studies.

The authors are grateful to V. A. Trepakov for fruitful discussions.

[1] H. J. Simpson and R. E. Marsh, Acta Crystallogr. **20**, 550 (1966).

[2] K. Beshah, E. T. Olejniczak, and R. G. Griffin, J. Chem. Phys. **86**, 4730 (1987).

[3] P. Jackson and R. K. Harris, J. Chem. Soc., Faraday Trans. **91**, 805 (1995).

[4] A. Migliori, P. M. Maxton, A. M. Clogston, E. Zirngiebl, and M. Löwe, Phys. Rev. B **38**, 13464 (1988).

[5] R. S. Kwok, P. Maxton, and A. Migliori, Solid State Commun. **74**, 1193 (1990).

[6] S. N. Popov and N. N. Kraĭnik, Fiz. Tverd. Tela (Leningrad) **12**, 3022 (1970) [Sov. Phys. Solid State **12**, 2440 (1970)].

[7] A. R. Kessel', I. A. Safin, and A. M. Gol'dman, Fiz. Tverd. Tela (Leningrad) **12**, 3070 (1970) [Sov. Phys. Solid State **12**, 2488 (1970)].

Translated by G. Skrebtsov

PHYSICS OF THE SOLID STATE VOLUME 40, NUMBER 11 NOVEMBER 1998

LOW DIMENSIONAL SYSTEMS AND SURFACE PHYSICS

Interband resonant tunneling in superconductor heterostructures in a quantizing magnetic field

A. A. Zakharova*)

Institute of Physics and Technology, Russian Academy of Sciences, 117218 Moscow, Russia

(Submitted February 3, 1998; resubmitted April 16, 1998)
Fiz. Tverd. Tela (St. Petersburg) **40**, 2121–2126 (November 1998)

The resonant tunneling of electrons through quasistationary levels in the valence band of a quantum well in double-barrier structures based on III-V materials with type-II heterojunctions is considered in a quantizing magnetic field directed perpendicularly to the interfaces. The transmission coefficients of the tunnel structure for transitions from states corresponding to different Landau levels are calculated using the Kane model. It is shown that transitions with a unit change in the Landau level index *n* as a result of mixing of the wave functions of states with opposite spin orientations are possible on the interfaces due to spin-orbit coupling. The probability of such transitions can be comparable to the probability of transitions without a change in the Landau level index for InAs/AlGaSb/GaSb resonant-tunneling structures.

[S1063-7834(98)03511-4]

Resonant tunneling in a quantizing magnetic field is widely used to study the features of the quasiparticle spectrum in low-dimensional structures. Resonant tunneling has been investigated experimentally in double-barrier semiconductor heterostructures in magnetic fields directed both parallel and perpendicularly to the plane of the structure.[1–7] The current-voltage characteristics (IVC's) of resonant-tunneling structures subjected to strong quantization in a perpendicular magnetic field can have several segments of negative differential conductivity due to the possibility of tunneling transitions through quasistationary states corresponding to different Landau levels in the quantum well. A longitudinal magnetic field causes a significant increase in the value of the voltage corresponding to the peak current. Current oscillations were observed in the presence of a quantizing magnetic field perpendicular to the interfaces on the IVC's of GaAs/AlGaAs resonant-tunneling structures with type-I heterojunctions[3,5] and resonant-tunneling structures with type-II heterojunctions, such as double-barrier GaSb/AlSb/InAs structures.[6] In the latter case the resonant tunneling has an interband character, since in these structures electrons tunnel from states in the GaSb valence band through quasistationary states in the conduction band of the InAs quantum well. Interband resonant tunneling was investigated experimentally in a similar InAs/AlSb/GaSb resonant-tunneling structure with a GaSb quantum well in a longitudinal magnetic field in Ref. 7. In the present work the features of resonant tunneling in a quantizing magnetic field perpendicular to the interfaces are investigated theoretically using the multiband Kane model to solve the Schrödinger equation. Employment of the multiband model permits not only a faithful description of the interband tunneling processes, but also the discovery of new qualitative features of the tunneling in conventional GaAs/AlGaAs resonant-tunneling structures due to transitions between states with different Landau level indices without scattering by phonons, impurities, or defects. The interband resonant tunneling in semiconductor heterostructures was previously investigated theoretically in a longitudinal magnetic field in InAs/AlSb/GaSb structures with neglect of the quantization of electrons in the strongly doped InAs layers in the magnetic field.[8]

The nature of the oscillations of the IVC in a perpendicular quantizing magnetic field is different for structures with interband and intraband types of tunneling. In resonant-tunneling structures based on type-I heterojunctions, such as GaAs/AlGaAs, with size quantization of the electrons in the emitter, the principal current peak corresponds to all the possible transitions without a change in the Landau level index upon tunneling.[3,5] The additional peaks on the IVC are caused by tunneling transitions between states corresponding to different Landau level indices. Such transitions can occur either with a change in the total quasiparticle energy due to the emission of polar optical phonons or without a change in energy. In Ref. 4, an analysis of the IVC made it possible to distinguish between transitions with a change in the Landau level index up to 6. Tunneling transitions between states corresponding to different Landau levels without a change in the total quasiparticle energy were treated theoretically in the single-band model in Refs. 9 and 10. Because of the opposite signs of the effective masses of the states in the contact and the quantum well, in resonant-tunneling structures with interband tunneling, the peak current values for tunneling transitions corresponding to each value of the Landau level index correspond to significantly different values of the applied voltage. This leads to pronounced oscillations of the total current, which are not associated with scattering processes.[6] Mendez *et al.*[6] believe that the experimental curves can be explained fairly well under the assumption that the tunneling transitions take place with conservation of the Landau level index and that the additional small peak in a magnetic field equal to 15 T can be attributed to instabilities in the circuit. In this paper the transfer-matrix formalism is used to calculate the transmission coefficients through resonant-tunneling structures for tunneling transitions from states corresponding to each value of the Landau level index n both with and without the conversation of n. Transitions with a unit change in n as a result of the mixing of states corresponding to different values of n on the interfaces due to spin-orbit coupling are possible in the Kane model. Such transitions can lead to the appearance of features not associated with scattering processes on the IVC's of both GaAs/AlGaAs structures and resonant-tunneling structures with interband tunneling. In the case of interband tunneling in InAs/AlGaSb/GaSb resonant-tunneling structures, the calculated probability of transitions with a change in the Landau level index is comparable to the probability of transitions without a change in the Landau level index, and this situation should lead to additional clearly expressed peaks on the IVC's of such structures.

1. THE MODEL

We shall use the envelope-function approximation and the multiband Kane model[11] to describe resonant-tunneling processes. If the z axis is directed perpendicularly to the interfaces of a resonant-tunneling structure, the Hamiltonian can be represented with neglect of the free-electron g factor in the form

$$\hat{H}=\begin{pmatrix} \hat{H}_{+-} & \hat{H}_{--} \\ \hat{H}_{++} & \hat{H}_{-+} \end{pmatrix}, \tag{1}$$

where

$$\hat{H}_{\pm\mp}=\begin{vmatrix} E_C & i\sqrt{\frac{2}{3}}P\hat{k}_z & -i\sqrt{\frac{1}{3}}P\hat{k}_z & P\hat{k}_{\pm} \\ -i\sqrt{\frac{2}{3}}P\hat{k}_z & E_V & 0 & 0 \\ i\sqrt{\frac{1}{3}}P\hat{k}_z & 0 & E_V-\Delta & 0 \\ P\hat{k}_{\mp} & 0 & 0 & E_V \end{vmatrix}, \tag{2}$$

and

$$\hat{H}_{\pm\pm}=\begin{vmatrix} 0 & \sqrt{\frac{1}{3}}P\hat{k}_{\pm} & \sqrt{\frac{2}{3}}P\hat{k}_{\pm} & 0 \\ \sqrt{\frac{1}{3}}P\hat{k}_{\pm} & 0 & 0 & 0 \\ \sqrt{\frac{2}{3}}P\hat{k}_{\pm} & 0 & 0 & 0 \\ 0 & 0 & 0 & 0 \end{vmatrix}. \tag{3}$$

Here $\hat{k}_{\pm}=\mp i(\hat{k}_x\pm i\hat{\hat{k}}_y)/\sqrt{2}$, $\hat{k}_x=-i\partial/\partial x$, $\hat{\hat{k}}_y=-i\partial/\partial y+|e|Bx/(\hbar c)$, $\hat{k}_z=-i\partial/\partial z$, e is the charge of an electron, c is the speed of light, $E_c(z)$ and $E_v(z)$ are the bottom of the conduction band and the top of the valence band, $\Delta(z)$ is the spin-orbit splitting energy, and $P=-\hbar^2\langle s|\partial/\partial z|p_z\rangle/m_0$, where s and p_z are basis states of the conduction and valence bands and m_0 is the free-electron mass. We assume that the magnetic field B is directed along the z axis, so that $B_z=B$ and $B_x=B_y=0$. The components of the vector potential are defined in the following manner: $A_y=Bx$ and $A_x=A_z=0$. We used the same set of basis functions as in Refs. 12 and 13, which were assumed to be identical for all layers of the structure, as was the interband momentum-operator matrix element. We shall disregard heavy-hole states, and we shall neglect the diagonal terms in the Hamiltonian that depend on the operators $\hat{k}_j$. The latter is possible, if the electron effective mass in each layer is much smaller than m_0.

The energy eigenvalues $\overline{E}$ and the envelope functions ψ_i are found from the equations

$$\sum \hat{H}_{ij}\psi_j=\overline{E}\psi_i, \quad i=1,2,\ldots,8. \tag{4}$$

As boundary conditions we use the continuity conditions of the following functions on the interfaces:

$$\psi_1, \quad \sqrt{2}\psi_2-\psi_3, \quad \psi_5, \quad \sqrt{2}\psi_6-\psi_7. \tag{5}$$

These boundary conditions conserve the probability flux density through each interface. The solution of the Schrödinger equation in a heterostructure can be constructed, if the set of eigenfunctions and energy eigenvalues of the electrons in the materials comprising the resonant-tunneling structures is known. We write the envelope functions in the form

$$\psi_i=\varphi_i(x')\exp(ik_y y+ik_z z), \tag{6}$$

where $x'=x+\hbar c k_y/(|e|B)$. Substituting (6) into (4), we can easily obtain two independent equations for φ_1 and φ_5, which specify the spectrum of quasiparticles with different spin orientations.[14] For the energy eigenvalues $E_n^{\pm}$, which correspond to the Landau level index n, we have

$$\frac{E_n^{\pm}(E_n^{\pm}-E_g)(E_n^{\pm}+\Delta)}{P^2 s(E_n^{\pm}+2\Delta/3)}-\frac{k_z^2}{s}\pm\frac{\Delta/3}{E_n^{\pm}+2\Delta/3}=2n+1,$$

$$n=0,1,\ldots\,. \tag{7}$$

In Eq. (7) the energy is calculated relative to the top of the valence band of the layer under consideration, $E_g=E_c-E_v$, and $s=|e|B/(\hbar c)$. The energy eigenvalues $E_n^{\pm}$ correspond to the following functions φ_i:

$$\varphi_1=f_n,\quad \varphi_2=-\frac{i\sqrt{2}Pk_z}{\sqrt{3}E_n^+}f_n,\quad \varphi_3=\frac{iPk_z}{\sqrt{3}(E_n^+ +\Delta)}f_n,$$

$$\varphi_4=\frac{2nP\sqrt{s}}{\sqrt{2}E_n^+}f_{n-1},\quad \varphi_5=0,\quad \varphi_6=\frac{P\sqrt{s}}{\sqrt{6}E_n^+}f_{n+1},$$

$$\varphi_7=\frac{P\sqrt{s}}{\sqrt{3}(E_n^+ +\Delta)}f_{n+1},\quad \varphi_8=0. \tag{8}$$

Here

$$f_n(x')=\exp(-sx'^2/2)H_n(\sqrt{s}x'),\quad n\geqslant 0,$$

$$f_n(x')=0,\quad n<0, \tag{9}$$

where the $H_n(t)$ are Hermite polynomials. The energy eigenvalues E_n^- correspond to the functions

$$\varphi_1=0,\quad \varphi_2=\frac{2nP\sqrt{s}}{\sqrt{6}E_n^-}f_{n-1},\quad \varphi_3=\frac{2nP\sqrt{s}}{\sqrt{3}(E_n^- +\Delta)}f_{n-1},$$

$$\varphi_4=0,\quad \varphi_5=f_n,\quad \varphi_6=-\frac{i\sqrt{2}Pk_z}{\sqrt{3}E_n^-}f_n,$$

$$\varphi_7=\frac{iPk_z}{\sqrt{3}(E_n^- +\Delta)}f_n,\quad \varphi_8=\frac{P\sqrt{s}}{\sqrt{2}E_n^-}f_{n+1}. \tag{10}$$

The tunneling probability is conveniently found using the transfer-matrix formalism, which calls for the replacement of the real distribution of the potential by a piecewise-constant distribution. The wave function in each layer in this case can be represented in the form of a sum of incident and reflected waves of the type (6), and the boundary conditions assign the relationship between the preexponential factors in neighboring layers. With consideration of the continuity of the functions (5) on the interfaces, mixing of states with opposite spin orientations corresponding to the Landau level indices n and $n+1$ takes place in a heterostructure. This leads to the possibility of tunneling processes with a change in the Landau level index.

2. PROBABILITY OF INTERBAND TUNNELING

Let us examine the resonant interband tunneling in double-barrier structures in a quantizing magnetic field perpendicular to the interfaces. An example of a structure with an interband type of tunneling is provided by an InAs/AlGaSb/GaSb resonant-tunneling structure, whose band diagram neglecting band bending is shown in Fig. 1. In this resonant-tunneling structure electrons tunnel from states in the InAs conduction band through quasistationary levels into the valence band of the GaSb quantum well. The spin of the states in the conduction band with the Landau-level energies E_n^+ is parallel to the magnetic field. The spin of the E_n^- states is antiparallel to the magnetic field. The E_0^- states do not mix with states of the opposite spin orientation or with states of other Landau levels. An electron can tunnel from such a state only into a similar state to the right of the resonant-tunneling structure. Each of the $E_n^+(k_z^+)$ states mixes with an $E_{n+1}^-(k_z^-)$ state having an energy equal to $E_n^+(k_z^+)$. The values of k_z^+ for these mixed states are determined from (7). Transitions with a unit change in the Landau level index and spin flip are possible upon tunneling from each such state to the left of the resonant-tunneling structure.

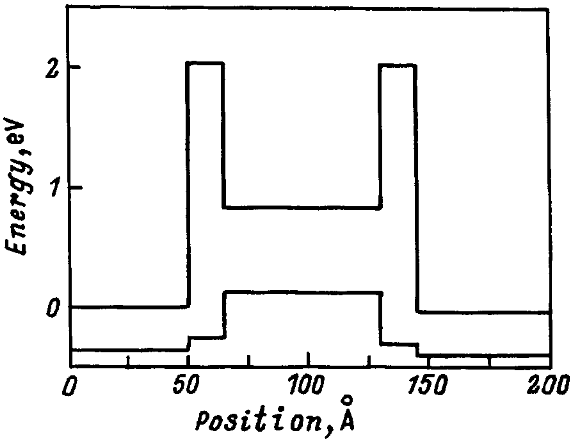

FIG. 1. Band diagram of InAs/AlGaSb/GaSb resonant-tunneling structures.

For the states of the lowest Landau level with spin antiparallel to the magnetic field we assign ψ_5 in layer j in the form

$$\psi_5=A_2^jf_0(x')\exp(ik_yy+ik_{zj}z_j)$$
$$+B_2^jf_0(x')\exp(ik_yy-ik_{zj}z_j). \tag{11}$$

The remaining envelope functions are easily found using (6), (9), and (10). Then the coefficients A_2^j, B_2^j and A_2^{j+1}, B_2^{j+1} are related by the equation

$$\begin{pmatrix}A_2^j\\ B_2^j\end{pmatrix}=M_j\begin{pmatrix}A_2^{j+1}\\ B_2^{j+1}\end{pmatrix}. \tag{12}$$

Here the transfer matrix M_j for $z=z_j$ is specified in the following manner:

$$M_j^{\pm}=\frac{1}{2}\begin{vmatrix}(1+Z_j)e^{-ib_jz_j} & (1-Z_j)e^{-ia_jz_j}\\ (1-Z_j)e^{ia_jz_j} & (1+Z_j)e^{ib_jz_j}\end{vmatrix}, \tag{13}$$

$$Z_j\equiv\frac{k_{z_{j+1}}P_{j+1}}{k_{z_j}P_j},$$

where

$$a_j=k_{zj}+k_{zj+1},\quad b_j=k_{zj}-k_{zj+1}, \tag{14}$$

$$P_j=2/E(z_j)+1/(E(z_j)+\Delta(z_j)). \tag{15}$$

Here $E(z_j)=E-E_v(z_j)$. Then for the amplitudes A_2^0, B_2^0, and A_2^N of the incident, reflected, and transmitted waves we have

$$\begin{pmatrix}A_2^2\\ B_2^0\end{pmatrix}=\prod_{j=0}^{N-1}M_j\begin{pmatrix}A_2^N\\ 0\end{pmatrix}. \tag{16}$$

Here $N-1$ is the number of subdivisions in the structure.

If $n\neq 0$ or the spin of the tunneling electron is parallel to the magnetic field, the solution of the Schrödinger equation can be represented in the form of a superposition of the waves for which $\psi_1 \neq 0$ or $\psi_5 \neq 0$ and which correspond to Landau levels n and $n+1$. For such solutions we set

$$\psi_1 = A_1^j f_n(x')\exp(ik_y y + ik_{zj}^+ z_j) + B_1^j f_n(x')\exp(ik_y y - ik_{zj}^+ z_j), \tag{17}$$

$$\psi_5 = A_2^j f_{n+1}(x')\exp(ik_y y + ik_{zj}^- z_j) + B_2^j f_{n+1}(x')\exp(ik_y y - ik_{zj} z_j). \tag{18}$$

The remaining envelopes are found with consideration of the solutions for them in the bulk materials. We determine the transfer matrix M_j, which relates the coefficients $A_{1,2}$ and $B_{1,2}$ in neighboring layers:

$$\begin{pmatrix} A_1^j \\ B_1^j \\ A_2^j \\ B_2^j \end{pmatrix} = M_j \begin{pmatrix} A_1^{j+1} \\ B_1^{j+1} \\ A_2^{j+1} \\ B_2^{j+1} \end{pmatrix}. \tag{19}$$

Taking into account the boundary conditions, we find the elements of the 4×4 square matrix M_j:

$$M_{j11} = (1 + k_{zj+1}^+ P_{j+1}/(k_{zj}^+ P_j))\exp(-ib_j^+ z_j)/2,$$

$$M_{j12} = (1 - k_{zj+1}^+ P_{j+1}/(k_{zj}^+ P_j))\exp(-ia_j^+ z_j)/2,$$

$$M_{j13} = -i\sqrt{s(n+1)}(Q_j - Q_{j+1})/(k_{zj}^+ P_j)\exp(-ic_j^- z_j),$$

$$M_{j14} = -i\sqrt{s(n+1)}(Q_j - Q_{j+1})/(k_{zj}^+ P_j)\exp(-ic_j^+ z_j),$$

$$M_{j21} = (1 - k_{zj+1}^+ P_{j+1}/(k_{zj}^+ P_j))\exp(ia_j^+ z_j)/2,$$

$$M_{j22} = (1 + k_{zj+1}^+ P_{j+1}/(k_{zj}^+ P_j))\exp(ib_j^+ z_j)/2,$$

$$M_{j23} = i\sqrt{s(n+1)}(Q_j - Q_{j+1})/(k_{zj}^+ P_j)\exp(ic_j^+ z_j),$$

$$M_{j24} = i\sqrt{s(n+1)}(Q_j - Q_{j+1})/(k_{zj}^+ P_j)\exp(ic_j^- z_j),$$

$$M_{j31} = -i\sqrt{s}(Q_j - Q_{j+1})/(2k_{zj}^- P_j)\exp(-id_j^- z_j),$$

$$M_{j32} = -i\sqrt{s}(Q_j - Q_{j+1})/(2k_{zj}^- P_j)\exp(-id_j^+ z_j),$$

$$M_{j33} = (1 + k_{zj+1} P_{j+1}/(k_{zj}^- P_j))\exp(-ib_j^- z_j)/2,$$

$$M_{j34} = (1 - k_{zj+1} P_{j+1}/(k_{zj}^- P_j))\exp(-ia_j^- z_j)/2,$$

$$M_{j41} = i\sqrt{s}(Q_j - Q_{j+1})/(2k_{zj}^- P_j)\exp(id_j^+ z_j),$$

$$M_{j42} = i\sqrt{s}(Q_j - Q_{j+1})/(2k_{zj}^- P_j)\exp(id_j^- z_j),$$

$$M_{j43} = (1 - k_{zj+1}^- P_{j+1}/(k_{zj}^- P_j))\exp(ia_j^- z_j)/2,$$

$$M_{j44} = (1 + k_{zj+1}^- P_{j+1}/(k_{zj}^- P_j))\exp(ib_j^- z_j)/2. \tag{20}$$

Here

$$a_j^\pm = k_{zj}^\pm + k_{zj+1}^\pm, \quad b_j^\pm = k_{zj}^\pm - k_{zj+1}^\pm,$$

$$c_j^\pm = k_{zj}^+ \pm k_{zj+1}^-, \quad d_j^\pm = k_{zj}^- \pm k_{zj+1}^+, \tag{21}$$

$$Q_j = 1/E(z_j) - 1/(E(z_j) + \Delta(z_j)). \tag{22}$$

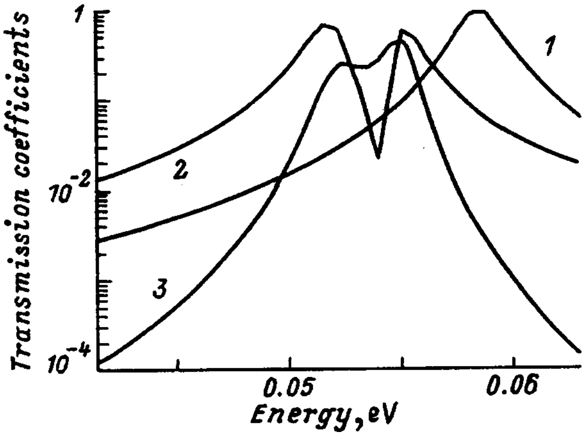

FIG. 2. Transmission coefficients of electrons through InAs/AlGaSb/GaSb resonant-tunneling structures in an 8-T magnetic field.

Then the amplitudes $A_{1,2}^0$, $B_{1,2}^0$, and $A_{1,2}^N$ of the incident, reflected, and transmitted waves are related in the following manner:

$$\begin{pmatrix} A_1^0 \\ B_1^0 \\ A_2^0 \\ B_2^0 \end{pmatrix} = \prod_{j=0}^{N-1} M_j \begin{pmatrix} A_1^N \\ 0 \\ A_2^N \\ 0 \end{pmatrix}. \tag{23}$$

If the spin of the incident wave is parallel to the magnetic field, we have $A_2^0 = 0$ in (23); otherwise, $A_1^0 = 0$. We define the tunneling probability for transitions to each of the Landau bands as the ratio between the probability flux densities through the interface in the transmitted and incident waves averaged over the coordinate x:

$$T_{kl} = \langle J_k^N \rangle / \langle j_l^0 \rangle. \tag{24}$$

Here $k(l) = 1$ corresponds to a wave with spin parallel to the magnetic field, $k(l) = 2$ corresponds to the opposite spin orientation,

$$\langle j_1^{0,N} \rangle \sim 2^n n! |A_1^{0,N}|^2 k_{z0,N}^+ P_{0,N},$$

$$\langle j_2^{0,N} \rangle \sim 2^{n+1}(n+1)! |A_2^{0,N}|^2 k_{z0,N}^- P_{0,N}, \tag{25}$$

where n is the Landau level index for the wave with spin parallel to the magnetic field.

3. DISCUSSION OF RESULTS

The calculated dependences of the transmission coefficients T_{kl} through an InAs/AlGaSb/GaSb/AlGaSb/InAs resonant-tunneling structure with a quantum well thickness equal to 50 Å and thicknesses of the barrier layers equal to 25 Å are shown in Figs. 2 and 3. The same values of the parameters as in Refs. 12, 13, and 15 were used. Figure 2 corresponds to an 8-T magnetic field perpendicular to the interfaces, and Fig. 3 corresponds to a 15-T magnetic field. The voltage applied to the structure equals 0.05 V. Curve *1* in Fig. 2 is a plot of the dependence of the transmission coefficient T on the energy E of the tunneling electron in the left-hand InAs contact layer for states with $n=0$ and spin antiparallel to the magnetic field. These states do not mix with other states, and the transmitted wave also belongs to the zeroth Landau level and has the same spin orientation as the incident wave. Curve *2* is the $T(E)$ curve for transitions from states with $n=0$ and spin parallel to the magnetic field

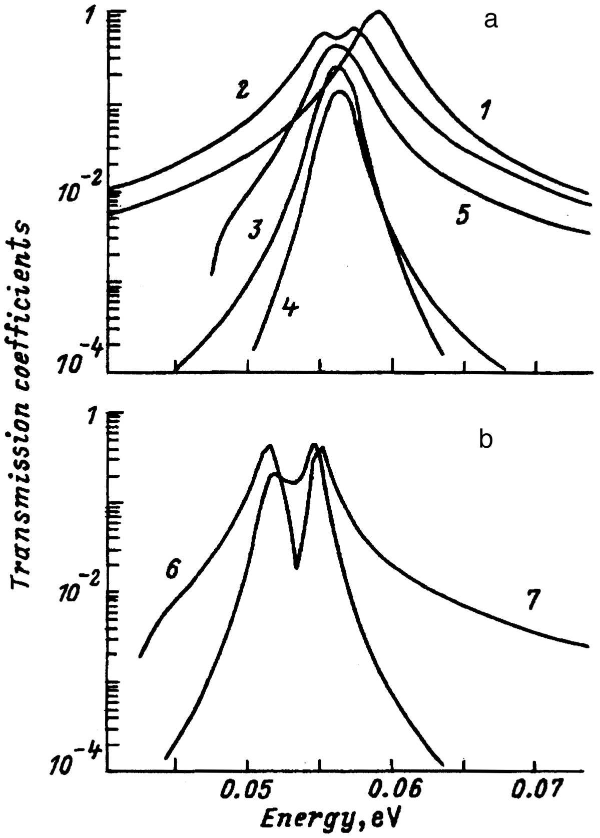

FIG. 3. Transmission coefficients of electrons through InAs/AlGaSb/GaSb resonant-tunneling structures in a 15-T magnetic field.

to the left of the resonant-tunneling structure to analogous states to the right of the resonant-tunneling structure. Curves *3* and *4* correspond to transitions from states with $n=0$ and spin parallel to the magnetic field to states with $n=1$ and spin antiparallel to the magnetic field and vice versa. Curves *5* and *6* describe the $T(E)$ dependence for transitions from states with $n=1$ and spin antiparallel and parallel to the magnetic field, respectively, to the analogous states to the right of the resonant-tunneling structure. Curve *7* refers to the last of the possible interband resonant transitions, i.e., from states with $n=1$ and spin parallel to the magnetic field to states with $n=2$ and spin antiparallel to the magnetic field. All the resonances in Fig. 2 correspond to the single zeroth size-quantization subband in the energy range considered for light holes in the valence band of the quantum well. The probability of interband transitions with a change in the Landau level index is appreciably smaller than the probability of transitions without a change in the Landau level index for an electron tunneling from states with $n=0$ or to states with $n=0$. However, as n increases, the mixing of states belonging to different Landau levels increases, so that the probability of transitions with a change in n becomes comparable to the probability of transitions without a change in n upon tunneling from states with $n=1$ and spin parallel to the magnetic field. In addition, curves *6* and *7* have two pronounced peaks, which are caused by resonant tunneling through quasistationary states in the quantum well with opposite spin orientation and values of n differing by unity.

Figure 3 shows that the mixing of states with different spin orientations intensifies as the magnetic field strength is increased. Curves *1–3* in this field correspond to the same dependences as do curves *1–3* in Fig. 2, but were calculated for $B=15$ T. In this case only three types of interband resonant transitions through quasistationary light-hole levels in the quantum well are possible. Curve *1* in this figure, like curve *1* in Fig. 2, has one maximum, since the states with $n=0$ and spin antiparallel to the magnetic field do not mix with other states. Curves *2* and *3*, which are the plots of $T(E)$ for interband transitions with conservation and a unit change of the Landau level index from states with $n=0$ and spin parallel to the magnetic field, have two sharp peaks. Additional tunneling probability peaks can lead to the appearance of additional peaks on the IVC's of such structures. We note that the mixing of states belonging to different Landau levels is appreciably weaker when the voltage on the structure is zero. We also note that the effects described are significantly weaker for resonant-tunneling structures with type-I heterojunctions, such as GaAs/AlGaAs/GaAs resonant-tunneling structures. However, in this case transitions are possible between states belonging to different Landau levels without scattering and can lead to features on the dependence of the differential conductivity on voltage.

Let us discuss the validity of the approximations used in the calculations. The approximation of continuity of the interband momentum operator matrix element holds quite well for InAs/AlGaSb/GaSb resonant-tunneling structures. Since the values of the effective g factor in the contact layers and the quantum well for all the examples considered were much greater than the free-electron g factor, the latter can be neglected. However, it should be taken into account in GaAs/AlGaAs/GaAs resonant-tunneling structures. The interband tunneling current through quasistationary heavy-hole states in the quantum well is generally significant in the structures considered.[16] Interband tunneling transitions through heavy-hole levels can produce additional peaks on the $T(E)$ curves. However, when $B=0$, the probability of interband tunneling to heavy-hole states is comparable to the probability of interband tunneling to light-hole states only when the kinetic energy of the final state is fairly small and the amplitude of the longitudinal pulse is large.[17] In the energy range considered the mixing of light- and heavy-hole states should not strongly influence the result. However, it should be noted that with consideration of the finite value of the heavy-hole mass, light-hole states with the indices n and $n+1$ and heavy-hole states with the indices $n-1$ and $n+2$ and different spin orientations[18] mix in the valence band of the quantum well when $B\neq 0$ in the case of the isotropic Luttinger model or the model used in Ref. 17. The number of such mixed states is equal to four for each value of n in the range $n\geqslant 1$. The interband resonant tunneling of electrons through each of these mixed states from the states in the InAs conduction band with the index n and spin parallel to the magnetic field or with the index $n+1$ and spin antiparallel to the magnetic field is possible in resonant-tunneling structures.

Thus, interband resonant tunneling has been investigated in semiconductor heterostructures in a perpendicular quantizing magnetic field within the Kane model. The transfer matrices for finding the probability of interband tunneling transitions for states corresponding to different Landau level indices and different spin orientations have been calculated. It has been shown that tunneling transitions with a change in the Landau level index are possible and can produce additional peaks on the IVC.

We thank E. L. Ivchenko for some useful discussions.

This work was supported by the Russian Fund for Fundamental Research (Grant No. 97-02-16438).

*⁾E-mail: chukbar@tapdki.ips.ras.ru

---

[1] E. E. Mendez, L. Esaki, and W. I. Wang, Phys. Rev. B **33**, 2893 (1986).
[2] V. J. Goldman, D. C. Tsui, and J. E. Cunningham, Phys. Rev. B **35**, 9387 (1987).
[3] M. L. Leadbeater, E. L. Alves, L. Eaves, M. Henini, O. H. Hughes, A. Celeste, J. C. Portal, G. Hill, and M. A. Pate, Phys. Rev. B **39**, 3438 (1989).
[4] C. H. Yang, M. J. Yang, and Y. C. Kao, Phys. Rev. B **40**, 6272 (1989).
[5] H. Yoo, S. M. Goodnick, J. R. Arthur, and M. A. Reed, J. Vac. Sci. Technol. B **8**, 370 (1990).
[6] E. E. Mendez, H. Ohno, L. Esaki, and W. I. Wang, Phys. Rev. B **43**, 5196 (1991).
[7] R. R. Marquardt, D. A. Collins, Y. X. Liu, D. Z.-Y. Ting, and T. C. McGill, Phys. Rev. B **53**, 13 624 (1996).
[8] Y. X. Liu, R. R. Marquardt, D. Z.-Y. Ting, and T. C. McGill, Phys. Rev. B **55**, 7073 (1997).
[9] O. E. Raichev and F. T. Vasko, J. Phys.: Condens. Matter **8**, 1041 (1996).
[10] O. E. Raichev and F. T. Vasko, J. Phys.: Condens. Matter **9**, 1547 (1997).
[11] E. O. Kane, J. Phys. Chem. Solids **1**, 249 (1957).
[12] V. Ryzhii and A. Zakharova, Semicond. Sci. Technol. **8**, 377 (1993).
[13] A. Zakharova and V. Gergel, Solid State Commun. **96**, 209 (1995).
[14] R. Bowers and Y. Yafet, Phys. Rev. **115**, 1165 (1959).
[15] A. Zakharova, J. Phys.: Condens. Matter **9**, 4635 (1997).
[16] I. Lapushkin, A. Zakharova, V. Gergel, H. Goronkin, and S. Tehrani, J. Appl. Phys. **82**, 2421 (1997).
[17] A. Zakharova, Semicond. Sci. Technol. **13** (1998) (in press).
[18] D. A. Broido and L. J. Sham, Phys. Rev. B **31**, 888 (1985).

Translated by P. Shelnitz

PHYSICS OF THE SOLID STATE VOLUME 40, NUMBER 11 NOVEMBER 1998

''Horizontal'' and ''vertical'' quantum-dot molecules

N. E. Kaputkina and Yu. E. Lozovik

Institute of Spectroscopy, Russian Academy of Sciences, 142092 Troitsk, Moscow Region, Russia

(Submitted March 31, 1998; resubmitted May 5, 1998)
Fiz. Tverd. Tela (St. Petersburg) **40**, 2127–2133 (November 1998)

An analysis is made of a two-electron system of two adjacent quantum dots (QD) with a two-dimensional parabolic lateral confining potential, and of two coupled or double, spatially separated QDs (a ''horizontal'' and a ''vertical'' QD molecule), and of their behavior in an external transverse magnetic field. The ground-state energies and energy spectra of the system have been determined by various methods (Heitler–London, molecular-orbital, variational approach, and numerical diagonalization of Hamiltonian), with inclusion of electron-electron interaction, and for a broad range of confining-potential steepness, QD-center spacing (interlayer distance), and external magnetic field. © *1998 American Institute of Physics.* [S1063-7834(98)03611-9]

Progress in nanotechnology stimulated intensive studies of new classes of nanoobjects and, in particular, of quantum dots (QD). QDs as quasi-zero-dimensional systems are extremely interesting low-dimension structures. They not only have device potential for nanoelectronics but are promising model objects for basic research, namely, as giant artificial atoms with controllable parameters, such as the form and steepness of the confining potential, the number of particles, and characteristic size of their localization region. The form of the confining potential is determined by the method employed to prepare the QD. The hard-wall and parabolic confining potentials are used most frequently.[1–6] The lateral parabolic-potential model was supported by self-consistent calculations[7] and is applicable to QDs obtained by various methods. Present-day technology permits one to obtain not only single quantum dots but entire QD arrays as well, with each QD in its preset position. Thus, if a single QD is an analog of an atom (a quantummechanical analog of the Thomson atom), then several closely spaced, interacting QDs may be regarded as an artificial giant molecule. The available publications consider primarily single QDs or QD arrays, and interdot coupling is regarded as a small correction resulting in a depolarization shift (of the order of 2–4% for the systems dealt with in experiments).[6,8.9]

There are reports, however, of recent experiments with closely spaced QDs representing giant analogs of molecules (we shall call them horizontal QD molecules) and systems with spatially separated carriers in vertically coupled QDs,[10–13] and in coupled and double QDs (we call such a system a vertical QD molecule).

It appears of interest to consider the physical properties of a QD (2D) system as an artificial molecule. We have analyzed a system of two QDs with two electrons, which is an analog of the hydrogen molecule. In contrast to molecules made up of atoms, in a QD molecule the distance between the QD centers (the interlayer spacing for a vertical molecule) is fixed when one constructs the structure. Being the simplest representative of objects of this kind, such a system permits one to explore the artificial QD molecule with comparatively straightforward calculations. Note that similar methods are applicable to more complex ″molecules″ as well.

1. HORIZONTAL QD MOLECULE

A. Ground-state energy with inclusion of electron-electron interaction

Consider two electrons, with each of them confined in its potential well of the form $U=\alpha r_i^2$ $(i=1,2)$ (parabolic lateral potential), where r_1 and r_2 are reckoned from the closely lying well centers. The Hamiltonian of the system can be written

$$\hat{H}=-\frac{\hbar^2}{2m^*}(\Delta_{\mathbf{r1}}+\Delta_{\mathbf{r2}})+\frac{e^2}{\varepsilon|\mathbf{r}_{12}|}+\alpha(r_1^2+r_2^2)\,, \tag{1}$$

where m^* is the effective electronic mass, ε is the dielectric permittivity, and α is the characteristic steepness of the confining potential.

To transfer to dimensionless variables, introduce the following units of distance, energy, and potential steepness, respectively:

$$r_0=\frac{\hbar^2\varepsilon}{2m^*e^2},\quad E_0=\frac{2m^*e^4}{\hbar^2\varepsilon^2},\quad \alpha_0=\frac{E_0}{r_0^2}, \tag{2}$$

where r_0 and E_0 are the radius and binding energy of the two-dimensional exciton.

We next write the singlet-state wave function in the Heitler–London approximation

$$\Psi=A[\psi_a(\mathbf{r}_1)\psi_b(\mathbf{r}_2)+\psi_a(\mathbf{r}_2)\psi_b(\mathbf{r}_1)]\xi_A(s_1,s_2)\,, \tag{3}$$

where $\xi_A(s_1,s_2)$ is an antisymmetric spin function, and $\psi_a(\mathbf{r})$ and $\psi_b(\mathbf{r})$ are the unperturbed wave functions of a single one-electron QD, $\psi_{a,b}(\mathbf{r})=(\sqrt{\alpha}/\pi)^{1/2}\exp(-\sqrt{\alpha}r_{a,b}^2/2)$. The energy of this state is

$$W=4\sqrt{\alpha}+[1+\exp(-d^2\sqrt{\alpha})]^{-1}(Q+J)\,, \tag{4}$$

where

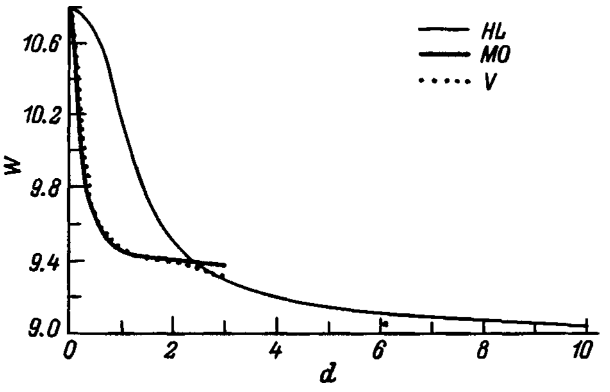

FIG. 1. Energy W of a horizontal QD molecule vs quantum-dot inter-center distance d calculated for a fixed confining-potential steepness $\alpha=5$ by the Heitler–London method (HL), molecular orbital approach with a modified potential (MO), and variational technique (V).

$$Q=(\sqrt{\alpha}/\pi)\int r_{12}^{-1}\exp[-\sqrt{\alpha}(r_{1a}^2+r_{2b}^2)/2]d\tau_1 d\tau_2,$$

$$J=\frac{\sqrt{\alpha}}{\pi}\int\frac{\exp[-\sqrt{\alpha}(r_{1a}^2+r_{2b}^2+r_{1b}^2+r_{2a}^2)/2}{r_{12}}d\tau_1 d\tau_2$$

$$=\sqrt{(\pi/2)}\alpha^{1/4}\exp(-a^2\sqrt{\alpha}).$$

The integral Q is found numerically.

Figure 1 displays the dependence of energy W on the distance between QD centers d for a fixed steepness of the confining potential $\alpha=5$ (curve *HL*). The energy falls off monotonically with increasing spacing d and approaches asymptotically the doubled ground-state energy of a single QD $E_0=2\sqrt{\alpha}$, because the electronic wave-function overlap decreases with increasing distance between quantum-dot centers.

Shown in Fig. 2 is the energy W as a function of the confining-potential steepness α for a fixed distance between the QD centers $d=1.5$. An increase of parameter α localizes the electrons and, thus, reduces the relative contribution of electronic Coulomb interaction, while the electron energy contribution in potential wells (the ground-state energy of a single QD) increases.

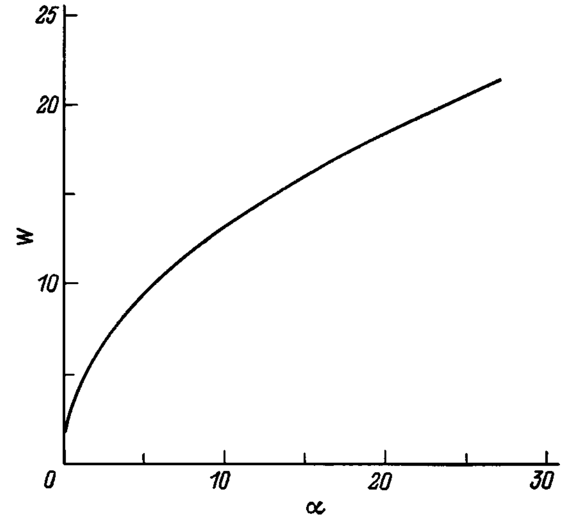

FIG. 2. Energy W of a horizontal QD molecule vs confining-potential steepness α calculated for a fixed quantum-dot separation $d=1.5$.

If the potential steepness α (or the effective confining-potential steepness β^2, see below and Ref. 14) and the QD separation d are both small enough, the Heitler–London method yields an overestimated ground-state energy for the QD molecule. In this case one can use the molecular orbital method.

Assume both electrons to be confined by a potential U_{AB}. In contrast to a molecule made up of atoms, where an electron feels both nuclei, and $U_{AB}=U_A+U_B$, in a QD molecule $U_{AB}=\min(U_A,U_B)$, where $U_{AB}=\alpha r_{A,B}^2$. To estimate the molecule energies by the molecular-orbital method, we use an auxiliary potential $U_0=(\alpha/2)(r_A^2+r_B^2)$. Setting $U_{AB}=U_0+\Delta U$ and using $(r_A^2+r_B^2)/2=r^2+(d^2/2)$, we obtain

$$\Delta U=\alpha\left(\min(r_A^2,r_B^2)-\frac{r_A^2+r_B^2}{2}\right)=-\alpha dr|\cos\Theta|.$$

For $d\to 0$, $U_0\to U_{AB}$.

We take as trial functions a linear combination of unperturbed electron wave functions in potential $U_{A,B}$:

$$\psi_{m0}(\mathbf{r})=\frac{1}{2[1+\exp(-\sqrt{\alpha}d^2/4)]}\left(\frac{\sqrt{\alpha}}{\pi}\right)^{1/2}(e^{-\sqrt{\alpha}r_a^2/2}$$
$$+e^{-\sqrt{\alpha}r_b^2/2}). \tag{5}$$

The corresponding eigenenergies are

$$E_0=2\sqrt{\alpha}+\frac{\alpha d^2}{2[1+\exp(-\sqrt{\alpha}d^2/4)]}. \tag{6}$$

The spin-wave function of a two-electron system in the lowest state is antisymmetric and has a singlet ground state, and the approximate wave function can be written

$$\Psi=\psi_{mo}(\mathbf{r}_1)\psi_{mo}(\mathbf{r}_2)\xi_A(s_1,s_2). \tag{7}$$

Thus

$$W=2\varepsilon_0+I_1+I_2, \tag{8}$$

where

$$I_1=\int\Psi_{mo}^*\Delta U\Psi_{mo}d\tau_1 d\tau_2=-\frac{d\alpha^2\Phi(\alpha^{1/4}d/2)}{2[1+\exp(-\sqrt{\alpha}d^2/4)]}$$
$$-\frac{d\alpha^{3/4}}{\sqrt{\pi}}\frac{2\exp(-\sqrt{\alpha}d^2/4)}{1+\exp(-\sqrt{\alpha}d^2/4)},$$

$$I_2=\int\Psi_{mo}^*\frac{1}{r_{12}}\Psi_{mo}d\tau_1 d\tau_2,$$

and $\Phi(x)$ is the error integral.

For $d\to 0$, $W\to 4\sqrt{\alpha}+\alpha^{1/4}\sqrt{\pi}$, which corresponds to the first approximation in Coulomb interaction of electrons for a two-electron QD.[14] Figure 1 plots the dependence of energy W on distance between the QD centers d for a fixed confining-potential steepness $\alpha=5$, which was obtained using the molecular-orbital method and an auxiliary potential (the *MO* curve).

The variational approach permits one to calculate the QD molecule energy over a broader range of parameters, namely, of the QD center spacing d and the confining-potential steepness α or β (see below). We took for a trial function for small values of parameters α and d functions of the type

$$\psi_0(\mathbf{r})=\frac{\gamma}{\pi}e^{-\gamma r^2/2}, \tag{9}$$

where γ is a variational parameter.

Figure 1 shows plots of the energy of a QD molecule vs QD center separation d for $\alpha=5$ obtained by the Heitler–London method (*HL*), by the molecular-orbital method with a modified potential (*MO*), and by variational techniques (V). For $d>2$, the Heitler–London approximation is seen to be valid. For $d<0.3$ the molecular-orbital approximation gives satisfactory results. Variational calculations performed with the above class of trial functions are applicable for $d<2$.

B. Effect of transverse magnetic field

Let now a two-electron QD molecule be in a transverse magnetic field $\mathbf{B}$. The axial symmetry of each QD allows the use of vector potential $\mathbf{A}$ in symmetric gauge,

$$\mathbf{A}=(1/2)\mathbf{B}\times\mathbf{r}.$$

We use Eq. (2) to introduce dimensionless quantities and choose as a unit of magnetic field

$$B_0=\frac{(2m^*)^2e^3}{\hbar^3\varepsilon^2}c. \tag{10}$$

The Hamiltonian of the system takes on the form

$$\hat{H}=-\left[\Delta_{\mathbf{r}_1}+\Delta_{\mathbf{r}_2}+\frac{i\omega_c}{4}\left(\frac{\partial}{\partial\theta_1}+\frac{\partial}{\partial\theta_2}\right)\right]+\left[\alpha+\left(\frac{\omega_c}{4}\right)^2\right]\times(r_1^2+r_2^2)+\frac{1}{|\mathbf{r}_2-\mathbf{r}_1|}, \tag{11}$$

where ω_c is the cyclotron frequency.

Next we determine the QD molecule energy in a magnetic field in the way we have done it before. The effect of magnetic field reduces to renormalization of the confining-potential steepness.[14] The effective steepness of the confining potential in a magnetic field will be determined by parameter $\beta^2=\alpha+(\omega_c/4)^2$. Accordingly, in place of functions $\psi_a(\mathbf{r})$ and $\psi_b(\mathbf{r})$ we use the unperturbed wave functions of a single one-electron QD in a magnetic field

$$\psi_a(\mathbf{r})=\psi_b(\mathbf{r})=\left(\frac{\beta}{\pi}\right)^{1/2}e^{-\beta r^2/2}. \tag{12}$$

We finally come to

$$W=4\beta+A^2(Q+J). \tag{13}$$

Figure 3 plots energy W vs the cyclotron frequency ω_c for a fixed distance between the QD centers $d=1.5$ and parameter $\alpha=1$. Parameter β grows with magnetic field, which gives rise to electron localization and reduces the contribution of electron Coulomb interaction with increasing electron energy contribution in the potential wells (the ground-state energy of a single QD). Thus the effect of a magnetic field is similar to that of a confining potential. Parameter β is a major parameter of the problem, besides the QD center spacing d.

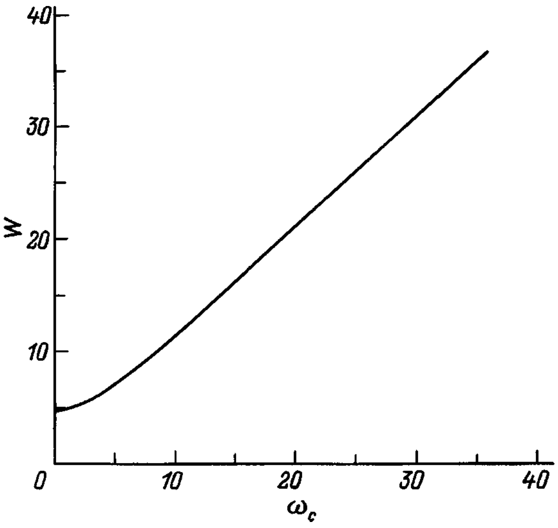

FIG. 3. Energy W of a horizontal QD molecule vs magnetic-field cyclotron frequency ω_c calculated for a fixed quantum-dot center separation $d=1.5$ and confining-potential steepness $\alpha=1$.

Figure 4 displays the dependence of energy W on β for a fixed distance between the QD centers $d=1.5$. The energy W increases with β to approach asymptotically a linear relation for large β.

The relative contribution of QD coupling decreases with increasing parameters β and d. For large β and d, the electron localization region is much smaller than the QD center spacing, so that the QD interaction energy becomes a small correction to the energy of single QDs. For intermediate values of β and d, interaction between QDs yields a noticeable contribution. For both β and d small, the Heitler–London method gives an overestimate for the ground-state energy of

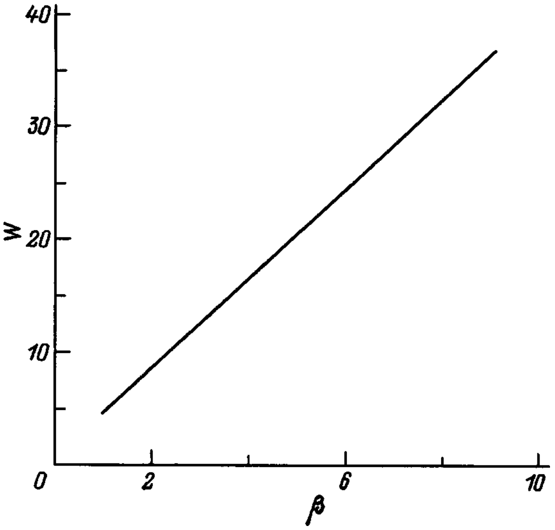

FIG. 4. Energy W of a horizontal QD molecule vs parameter β calculated for a fixed quantum-dot center separation $d=1.5$.

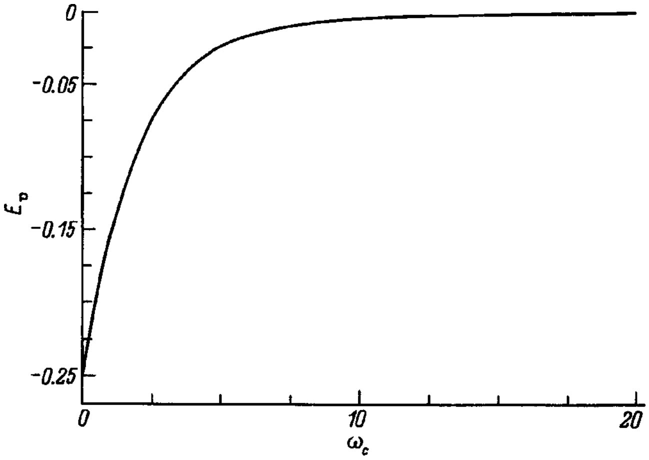

FIG. 5. Dependence of the van der Waals interaction energy for a horizontal QD molecule E_v vs magnetic-field cyclotron frequency ω_c calculated for a fixed quantum-dot center separation $d=1$ and confining-potential steepness $\alpha=1$.

the QD molecule. In this case one can use the molecular-orbital technique. In practice, however, it is very difficult to construct strongly overlapping but still not merging QDs. In the limiting case, two one-electron QDs coalesce to form one two-electron QD. The spectrum of a two-electron QD with inclusion of electron-electron interaction can be obtained by numerical diagonalization of the Hamiltonian in the basis of one-particle functions.[14]

We estimated also the van der Waals energy of two QDs. The QD is a quantum analog of a two-dimensional Thomson atom. The mean dipole interaction energy can be written

$$E_v=\sum_{k,k'}\frac{|(k,k'|V|0,0)|^2}{W_k+W'_{k'}-W_0-W'_0}, \tag{14}$$

where W_0, W'_0, W_k, and $W'_{k'}$ are the ground- and excited-state energies of two QDs. The energies and wave functions of one-electron QDs are

$$E_{nm}=4\beta\left(n+\frac{|m|+1}{2}\right)+\frac{\omega_c}{4}m, \tag{15}$$

$$\psi_{nma,b}=\left(\frac{n!}{\pi(|m|+n)!}\beta^{|m|+1}\right)^{1/2}r_{a,b}^{|m|}\times\exp(-\beta r_{a,b}/2)L_n^{|m|}(\beta r_{a,b}^2)e^{im\theta}, \tag{16}$$

where $L_n^{|m|}$ is the associated Laguerre polynomial. Whence we obtain

$$E_v=-\frac{1}{d^6\beta^2(4\beta+\omega_c/2)}. \tag{17}$$

Figure 5 plots van der Waals energy E_v vs magnetic-field cyclotron frequency ω_c for a fixed distance between the QD centers $d=1$ and a fixed confining-potential steepness $\alpha=1$. We see that $E_v \ll W$ already for $d=1$. E_v decreases with increasing potential steepness and magnetic field, as well as with increasing QD spacing d. Thus within the range of α, ω_c, and d considered here, where the wave-function overlap is small, the contribution of the van der Waals energy E_v is quite small.

Thus molecular-orbital methods have permitted us to determine the ground-state energies of a coupled QD system with inclusion of electron-electron interaction for a broad range of confining-potential steepnesses, QD center separations, and external magnetic fields.

2. VERTICAL QD MOLECULE

We have studied also the energy spectrum of a vertical QD molecule made up of two vertically coupled (or double) two-dimensional QDs separated by a barrier of width d and described, accordingly, by two-electron parabolic potentials $U=\alpha r_{1,2}^2$ ($\mathbf{r}_1,\mathbf{r}_2$ are two-dimensional in-plane position vectors of the first and second QD).

The Hamiltonian of the system can be written

$$\hat{H}=\hat{H}_1+\hat{H}_2+\hat{H}_{\text{int}}, \tag{18}$$

where

$$\hat{H}_1=-\frac{\hbar^2}{2m_e^*}\Delta_{\mathbf{r}_1}+\alpha r_1^2, \quad \hat{H}_2=-\frac{\hbar^2}{2m_e^*}\Delta_{\mathbf{r}_2}+\alpha r_2^2,$$

$$\hat{H}_{\text{int}}=-\frac{e^2}{\varepsilon(|\mathbf{r}_1-\mathbf{r}_2|^2+d^2)^{1/2}}. \tag{19}$$

Introduce dimensionless quantities in accordance with Eq. (2). After a coordinate transformation and separation of the center-of-mass from relative electron motion, $\mathbf{R}=(\mathbf{r}_1+\mathbf{r}_2)/2$, $\mathbf{r}=\mathbf{r}_1-\mathbf{r}_2$, the Schrödinger equation reduces to the following coupled equations:

$$\left(\Delta_{\mathbf{R}}+E_R-\frac{\alpha}{2}R^2\right)\psi_R=0, \tag{20}$$

$$\left(\Delta_{\mathbf{r}}+E_r-\frac{\alpha}{2}r^2+\frac{1}{(r^2+d^2)^{1/2}}\right)\psi_r=0, \tag{21}$$

$$E=E_R+E_r, \tag{22}$$

where $\psi(\mathbf{R},\mathbf{r})=\psi_R(\mathbf{R})\psi_r(\mathbf{r})$. Thus Eq. (20) for the center of mass has in this particular case the form of the harmonic-oscillator equation. We can write now equations for the center-of-mass energy E_R and eigenfunctions ψ_R:

$$E_{R_{nm}}=4(\alpha/2)^{1/2}\left(n+\frac{|m|+1}{2}\right), \tag{23}$$

$$\psi_{R_{nm}}=\left(\frac{n!}{\pi(|m|+n)!}(\alpha/2)^{|m|+1}\right)^{1/2}R^{|m|}e^{-\sqrt{\alpha/2}R^2/2}L_n^{|m|}\times(\sqrt{\alpha/2}R^2)e^{im\theta}. \tag{24}$$

The equation for relative motion (21) differs from that for the center-of-mass motion (20) in the inclusion of electron-electron interaction. In accordance with the symmetry of the problem, the wave function of relative motion can be presented in the form $\psi_r(\mathbf{r})=f_m(r)\exp(im\theta)$, where $m=0,\pm1,\ldots$; and the radial function $f_m(r)$ satisfies the equation

$$\frac{\partial^2 f}{\partial r^2}+\frac{1}{r}\frac{\partial f}{\partial r}+\left(E_r-\frac{\alpha r^2}{2}+\frac{1}{(r^2+d^2)^{1/2}}-\frac{m^2}{r^2}\right)f=0\,. \tag{25}$$

Expand $f_m(r)$ in the basis of eigenfunctions of the problem neglecting the Coulomb interaction among electrons:

$$f_{nm}=\left(\frac{n!}{(|m|+n)!}(\sqrt{\alpha/2})^{|m|+1}\right)^{1/2}r^{|m|}\times\exp(-\sqrt{\alpha/2}r^2/2)L_n^{|m|}(\sqrt{\alpha/2}r^2)\,, \tag{26}$$

$$f_m=\sum_n C_{nm}f_{nm}\,. \tag{27}$$

The solution to Eq. (25) can be found by numerical diagonalization of the Hamiltonian in the basis of these functions. The eigenenergies are determined from the equation

$$\det\{V^m_{nn'}+\delta_{n,n'}(E_{nm}-E_r)\}=0\,, \tag{28}$$

where

$$E_{nm}=4\sqrt{\alpha/2}\left(n+\frac{|m|+1}{2}\right)\,, \tag{29}$$

$$\begin{aligned}V^m_{nn'}=&\left(\frac{n!n'!}{(n+|m|)!(n'+|m|)}!\right)^{1/2}\\&\times\sum_{i=0}^{n}\sum_{j=0}^{n'}\frac{(-1)^{i+j}}{i!j!}\binom{n+|m|}{n-i}\binom{n'+|m|}{n'-j}\\&\times(\alpha/2)^{(|m|+i+j+1)/2}\Gamma(i+j+|m|+1)d^{2(i+j+|m|+1/2)}\\&\times\Psi\left(i+j+|m|+1,\ i+j+|m|+3/2\,;\sqrt{\frac{\alpha}{2}d^2}\right).\end{aligned} \tag{30}$$

Here Γ is Euler's gamma function, and Ψ is Tricomi's confluent hypergeometric function. $V^m_{nn'}$ can be conveniently transformed to

$$\begin{aligned}V^m_{nn'}=&(-1)^{|m|+1}\sqrt{\frac{\alpha^{1/2}}{2^{1/2}\pi}}\left(\frac{n!n'!}{(n+|m|)!(n'+|m|)!}\right)^{1/2}\\&\times\sum_{i=0}^{n}\sum_{j=0}^{n'}\frac{1}{i!j!}\binom{n+|m|}{n-i}\binom{n'+|m|}{n'-j}\\&\times\sum_{l=0}^{\infty}\frac{(\sqrt{\alpha/2}d^2)^l}{l!}\left[-(\sqrt{\alpha/2}d^2)^{s+1/2}\frac{(s+l)!}{\Gamma(s+l+3/2)}\right.\\&\left.+\frac{\Gamma(l+1/2)}{\Gamma(l-s+1/2)}\right],\end{aligned} \tag{31}$$

where $s=i+j+|m|$. The dependences of the lower energy levels E_r on parameter α derived from the solution to Eq. (28) are presented graphically in Fig. 6.

When α is large enough (the case of a strong confining potential or large interlayer spacing), the electron-electron interaction is small compared to the other parameters, and the energies of relative motion E_r approach asymptotically the levels (29) of two-dimensional harmonic oscillator, i.e. they are linear in $\sqrt{\alpha}$, which is readily seen from Fig. 6.

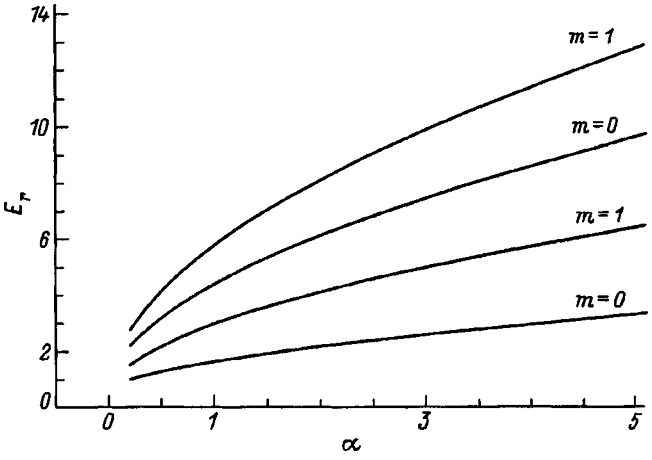

FIG. 6. Dependences of the lower level energies E_r on confining-potential steepness α for a vertical QD molecule.

Figure 7 shows the dependence of the low-lying energy levels on interlayer spacing d. The contribution of Coulomb interaction to the energy decreases with increasing d, and the energies approach asymptotically E_{nm} [see Eq. (29)].

APPENDIX A: EFFECT OF TRANSVERSE MAGNETIC FIELD

If a transverse magnetic field is present, one should add to the Hamiltonian of the system the term

$$\hat{H}_m=\frac{e}{2c}\left(\frac{A_1^2}{m_e^*}-2\frac{i\hbar\nabla_1A_1}{m_e^*}+\frac{A_2^2}{m_e^*}-2\frac{i\hbar\nabla_2A_2}{m_e^*}\right).$$

On separating the center-of-mass motion from the relative motion of the electron and the hole, one obtains coupled equations, which differ from Eqs. (20) and (21) in α being replaced with $\alpha'=\alpha+\omega_c^2/16$, and in $m\omega_c/4$ being added to the energy. The dependences of the lower levels of relative-motion energy on magnetic field are displayed in Fig. 8. The energies increase with the field and approach asymptotically $4\sqrt{\alpha'/2}(2n+|m|+1)+\omega_c m/4$. In the limit of extremely strong magnetic fields, the energy levels approach asymptoti-

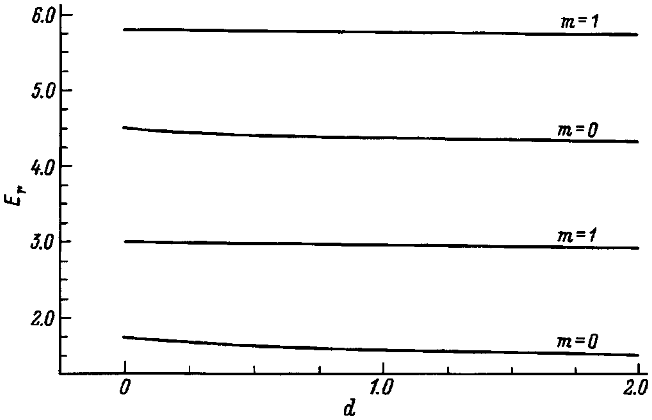

FIG. 7. Dependences of the lower level energies E_r on interlayer spacing d for a vertical QD molecule.

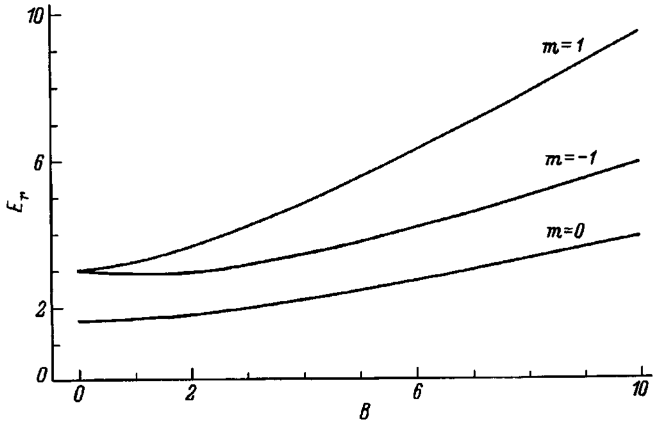

FIG. 8. Dependences of the lower-level relative-motion energy on magnetic field B calculated for $\alpha=1$ for a vertical QD molecule.

cally the Landau levels, as in the case of the absence of a parabolic confining potential (compare, for instance, the hard-wall model).[15,16]

For large interlayer spacings d ($d\rightarrow\infty$), the energies exhibit an asymptotic behavior

$$E\sim 2[(\alpha'/2)(2n+|m|+1)+(\omega_c m)/4+(1/d)$$
$$-(4d^3\sqrt{\alpha'/2})^{-1}].$$

For $d\rightarrow 0$, the matrix element $V^m_{nn'}$ tends to the expression

$$\left(\frac{n!n'!}{(n+|m|)!(n'+|m|)!}\sqrt{\alpha'/2}\right)^{1/2}$$
$$\times\sum_{i=0}^{n}\sum_{j=0}^{n'}\frac{(-1)^{i+j}}{i!j!}\binom{n+|m|}{n-i}\binom{n'+|m|}{n'-j}$$
$$\times\Gamma(i+j+|m|+1/2).$$

The $d=0$ value corresponds to the case of a single quantum well with two carriers.[14]

The authors are grateful to Yu. Kh. Vekilov for fruitful discussions.

Support of the Russian Fund for Fundamental Research , INTAS, and the ‘‘Physics of Solid-State Nanostructures’’ is gratefully acknowledged. The work of N. E. K. was supported by the ISSEP program for post-graduate students.

[1] F. Geerinckx, F. M. Peeters, and J. T. Devreese, J. Appl. Phys. **68**, 3435 (1990).
[2] W. Hansen, M. Horst, J. P. Kotthaus, U. Merkt, and Ch. Sikorsky, Phys. Rev. Lett. **58**, 2586 (1987).
[3] Ch. Sikorsky and U. Merkt, Phys. Rev. Lett. **62**, 2164 (1989).
[4] C. T. Liu, K. Nakamura, D. C. Tsui, K. Ismail, D. A. Antoniadis, and H. I. Smith, Appl. Phys. Lett. **55**, 168 (1989).
[5] T. Demel, D. Heitman, P. Grambow, and K. Ploog, Phys. Rev. Lett. **64**, 788 (1990).
[6] J. Dempsey, N. F. Johnson, L. Brey, and B. I. Halperin, Phys. Rev. B **42**, 11708 (1990).
[7] A. Kumar, S. E. Laux, and F. Stern, Phys. Rev. B **42**, 5166 (1990).
[8] A. O. Govorov and A. V. Chaplik, Zh. Éksp. Teor. Fiz. **99**, 1853 (1991) [Sov. Phys. JETP **72**, 1037 (1991)].
[9] L. Brey, N. F. Johnson, and B. I. Halperin, Phys. Rev. B **40**, 10647 (1989).
[10] A. Zrenner, L. V. Butov, M. Hang, G. Abstreiter, G. Böhm, and G. Weimann, Phys. Rev. Lett. **72**, 3383 (1994).
[11] L. V. Butov, A. Zrenner, G. Abstreiter, G. Böhm, and G. Weimann, Phys. Rev. Lett. **73**, 304 (1994).
[12] L. V. Butov, A. Zrenner, G. Abstreiter, A. V. Petinova, and K. Eberl, Phys. Rev. B **52**, 12153 (1995).
[13] V. D. Kulakovskiĭ and L. V. Butov, Usp. Fiz. Nauk **165**, 229 (1995).
[14] Ya. M. Blanter, N. E. Kaputkina, and Yu. E. Lozovik, Phys. Scripta **54**, 539 (1996); Yu. E. Lozovik and N. E. Kaputkina, Phys. Scripta (in press).
[15] Yu. E. Lozovik and A. M. Ruvinsky, Phys. Lett. A **227**, 271 (1997); Yu. E. Lozovik and A. M. Ruvinskiĭ, Zh. Éksp. Teor. Fiz. **112**, 1791 (1997) [JETP **85**, 979, (1997)].
[16] I. V. Lerner and Yu. E. Lozovik, Zh. Éksp. Teor. Fiz. **78**, 1167 (1980) [Sov. Phys. JETP **51**, 588 (1980)].

Translated by G. Skrebtsov

PHYSICS OF THE SOLID STATE VOLUME 40, NUMBER 11 NOVEMBER 1998

″Spherical″ quantum dots

N. E. Kaputkina and Yu. E. Lozovik

Institute of Spectroscopy, Russian Academy of Sciences, 142092 Troitsk, Moscow Region, Russia

(Submitted March 31, 1998; resubmitted May 5, 1998)
Fiz. Tverd. Tela (St. Petersburg) **40**, 2134–2135 (November 1998)

Quantum dots with a three-dimensional confining potential, i.e. ‘‘spherical’’ quantum dots, are considered with inclusion of electron-electron interaction (a quantum analog of the Thomson atom). The energy spectrum of two-electron parabolic quantum dots has been determined by numerical diagonalization of the full Hamiltonian in a one-particle basis. © *1998 American Institute of Physics.* [S1063-7834(98)03711-3]

Recent years have witnessed intensive studies of quantum dots (QD) with both two-dimensional[1–5] and three-dimensional[6,7] confining potentials. QDs may be considered as a quantum-mechanical analog of a giant Thomson atom (two-dimensional or, for ‘‘spherical’’ QDs, three-dimensional). Present-day nanoscale technology permits one to control at will such parameters as the form and hardness of the confining potential, the number of particles, and characteristic size of their localization region. The form of the confining potential is determined by the method of QD fabrication. The most frequently used are the hard-wall and the parabolic confining-potential models. The model of parabolic lateral potential was confirmed by self-consistent calculations[8] and is applicable to not very large QDs.

This work considers a single QD with a three-dimensional parabolic confining potential

$$U(r,\theta,\varphi)=\alpha r^2\,, \tag{1}$$

where α is the confining-potential steepness, and r, θ, and φ are spherical coordinates reckoned from the QD center.

To transfer to dimensionless quantities, introduce the following units of distance, energy, and potential steepness:

$$a_0=\hbar^2\varepsilon/(2m^*e^2)\,,\quad E_0=2m^*e^4/(\hbar^2\varepsilon^2)\,,$$

$$\alpha_0=E_0/a_0^2\,, \tag{2}$$

where m^* is the effective electronic mass, ε is the dielectric permittivity, and a_0 and E_0 are the radius and binding energy of the two-dimensional exciton.

The one-electron energy spectrum in a parabolic well is given by

$$E_{nl}=\sqrt{\alpha}(4n+2l+3)\,, \tag{3}$$

where n is the radial quantum number ($n=0,1,2,\ldots$), and l is the orbital quantum number ($l=0,1,\ldots$).

The corresponding orthonormalized system of one-particle functions can be written

$$\psi_{nlm}=\frac{1}{\sqrt{2\pi}}e^{im\varphi}\sqrt{\frac{2l+1(l-m)!}{2(l+m)!}}P_l^m$$
$$\times(\cos\theta)\sqrt{\frac{2\alpha^{\frac{l+1+1/2}{2}}n!}{\Gamma(n+l+1/2)}}$$
$$\times\exp(-\sqrt{\alpha}r^2/2)r^lL_n^{l+1/2}(\sqrt{\alpha}r^2)\,, \tag{4}$$

where $P_l^m(x)$ are the associated Legendre polynomials of the first kind, and r, φ, and θ are spherical coordinates.

Consider a two-electron QD with a three-dimensional parabolic lateral potential of type (1).

Introducing the coordinates $\mathbf{r}=\mathbf{r}_2-\mathbf{r}_1$, $\mathbf{R}=\mathbf{r}_2+\mathbf{r}_1$ and assuming $\psi(\mathbf{r}_1,\mathbf{r}_2)=\psi(\mathbf{r},\mathbf{R})=\psi_r(\mathbf{r})\,\psi_R(\mathbf{R})$, we obtain coupled equations

$$\left[\Delta_{\mathbf{R}}+\left(E_R-\frac{\alpha}{2}R^2\right)\right]\psi_R=0\,, \tag{5}$$

$$\left[\Delta_{\mathbf{r}}+\left(E_r-\frac{\alpha}{2}r^2+\frac{1}{|r|}\right)\right]\psi_r=0\,, \tag{6}$$

$$E=E_R+E_r\,. \tag{7}$$

Equation (5) describing center-of-mass motion allows exact solution (this is true also for an arbitrary number of electrons in a parabolic well (see, e.g., Ref. 9). Its solutions have the form of Eqs. (3) and (4) with α replaced by $\alpha'=\alpha/2$.

To solve Eq. (6), expand ψ_r in eigenfunctions of a one-electron QD

$$\psi_r=\sum_{nlm}C_{nlm}\psi_{nlm}\,. \tag{8}$$

The energy spectrum of a two-electron QD with a three-dimensional confining potential is derived from the equation

$$\det\{V_{nn_1lm}+\delta_{n,n_2}(E_{nlm}-E_r)\}=0 \tag{9}$$

with given l and m, where the matrix element of Coulomb interaction has the form

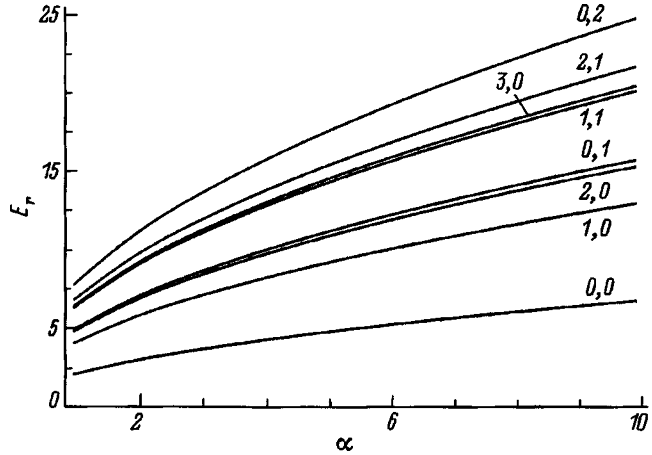

FIG. 1. Position of the lower energy levels E_r vs confining-potential steepness α calculated for two-electron spherical quantum dots with a three-dimensional confining potential. The pairs of numbers at the curves identify the values of l and n.

$$V_{nn_1lm}=\left(\frac{n!n_1!}{\Gamma\left(n+l+1+\frac{1}{2}\right)\Gamma\left(n_1+l+1+\frac{1}{2}\right)}\right)^{1/2}$$

$$\times\alpha\sum_{i=0}^{n}\sum_{j=0}^{n_1}\frac{(-1)^{i+j}}{i!j!}\begin{pmatrix}n+l+1/2\\ n-i\end{pmatrix}\begin{pmatrix}n_1+l+1/2\\ n_1-j\end{pmatrix}$$

$$\times\Gamma\left(i+j+l+\frac{1}{2}\right),$$

where Γ is Euler's gamma function.

Equation (9) can be solved numerically. Because V_{nn_1lm} and E_{nlm} do not depend on m, the degeneracy in m is not lifted (we disregard here the spin). The degeneracy in n and l is removed.

Figure 1 plots the position of the lower energy levels for relative electron motion E_r vs α. The level energies increase monotonically with α. The splitting of the levels with different sets of quantum numbers (n,l) and (n',l') such that $n-n'=2(l'-l)$ results from Coulombic electron interaction (the corresponding one-particle levels coincide). This splitting is clearly seen in Fig. 1 for the levels $(n=0,l=2)$ and $(n=1,l=2)$; $(n=0,l=3)$ and $(n=1,l=1)$. The splitting grows monotonically with increasing α. For α large enough, the electron-electron interaction is small compared to the level spacing in a one-electron problem. In this case the relative-motion energies E_r tend asymptotically to energy E_R (3), i.e. they are linear in $\sqrt{\alpha}$. This is seen from Fig. 1. The levels E_{nl} for a three-dimensional problem lie above those for two dimensions.[10]

Support of the Russian Fund for Fundamental Research and of INTAS and ISSEP is gratefully acknowledged.

[1] Ch. Sikorsky and U. Merkt, Phys. Rev. Lett. **62**, 2164 (1989).
[2] C. T. Liu, K. Nakamura, D. C. Tsui, K. Ismail, D. A. Antoniadis, and H. I. Smith, Appl. Phys. Lett. **55**, 168 (1989).
[3] F. Geerinckx, F. M. Peeters, and J. T. Devreese, J. Appl. Phys. **68**, 3435 (1990).
[4] D. A. Broido, K. Kempa, and P. Bakshi, Phys. Rev. B **42**, 11400 (1990).
[5] J. Weis, R. J. Haug, K. von Klitching, and K. Ploog, in *Quantum Dynamics of Submicron Structures*, edited by H. A. Cerderia, B. Kramer, and G. Schon (Kluwer Academic Publishers, Netherlands, 1995).
[6] S. Schmitt-Rink, D. S. Chemla, and D. A. B. Miller, Adv. Phys. **38**, 89 (1989).
[7] Y. Z. Hu, M. Lindberg, and S. W. Koch, Phys. Rev. B **42**, 1713 (1990).
[8] A. Kumar, S. E. Laux, and F. Stern, Phys. Rev. B **42**, 5166 (1990).
[9] Yu. E. Lozovik and V. A. Mandelshtam, Phys. Lett. A **145**, 269 (1990).
[10] Ya. M. Blanter, N. E. Kaputkina, and Yu. E. Lozovik, Phys. Scripta **54**, 539 (1996).

Translated by G. Skrebtsov

Superradiance of polaritons in finite one-dimensional crystals of increasing length: passage from a dimer to an infinite crystal

O. A. Dubovskiĭ

Institute of Physics and Power Engineering, Russian Academy of Sciences, 249020 Obninsk, Kaluzhskaya Region, Russia

(Submitted May 18, 1998)
Fiz. Tverd. Tela (St. Petersburg) **40**, 2136–2140 (November 1998)

Solutions of the dispersion equations for polariton states in finite one-dimensional crystals of arbitrary length are obtained. The appearance and evolution of the radiative and nonradiative polariton branches are traced as the length varies from two monomers to limiting values, above which the spectrum no longer undergoes significant changes. The dependences of the frequencies and radiative widths on the polariton wave vector are found for various orientations of the dipole moment of the quantum transition. The evolution of superradiance as the length of the crystal increases is traced. Some previously unknown significant features of the polariton spectrum are noted particularly the damping of the branch traditionally termed nonradiative as a consequence of emission from the end faces. © *1998 American Institute of Physics.* [S1063-7834(98)03811-8]

The spectrum of polaritons (mixed Frenkel exciton +photon states) in one- and two-dimensional crystals was first studied theoretically in Refs. 1–3. Strong radiative damping of the polariton states was predicted. This effect was, in fact, subsequently detected experimentally in two-dimensional crystals[4,5] and is presently known as superradiance.[6,7] We note that no complications of fundamental significance were encountered in developing the theory for two-dimensional crystals in Refs. 1–3. However, one question remained open for polaritons in one-dimensional crystals. The complicated, highly nonlinear dispersion equation for the complex polariton frequencies and wave vectors includes a corresponding integral over the photon wave vectors, which converges for two-dimensional crystals, but diverges logarithmically for one-dimensional crystals in the region of large photon wave vectors. This integral was truncated on a definite basis in Refs. 1–3 at the wave vectors corresponding to the Brillouin-zone boundary. Nevertheless, the divergence at large photon wave vectors noted was associated with the interaction of dipoles and the electric field over short distances and with the self-interaction of dipole oscillators interacting with the intrinsic electric field. This self-interaction has not previously been isolated in explicit form. All the calculations in Refs. 1–3 were performed in the Fourier wave representation for one-dimensional crystals of infinite length, and the calculation of the corresponding dipole-dipole sums was difficult.

There have been theoretical and experimental investigations of the polariton spectra in low-dimensional finite crystals such as J aggregates, superlattices, polymer chains, etc.[6–9] The polariton spectrum of a crystal slab of finite thickness with an arbitrary number of monomolecular crystal planes was studied in Refs. 8–10. The entire evolution of the polariton spectrum as the slab thickness increased from one two-dimensional plane to a three-dimensional crystal was traced in Ref. 10.

Modern tools of computer technology provide a previously lacking possibility for directly calculating the corresponding dipole-dipole sums, whose Fourier transforms appear in the complicated nonlinear dispersion equation, and these same tools make it possible to solve directly the dispersion equation using appropriate software. This permits taking the next logical step[10] and tracing the evolution of the polariton spectrum in a one-dimensional system from a single monomer to a dimer, then to a chain of finite length, and, as a limit, to an infinite one-dimensional crystal.

In the present work the polariton spectrum in one-dimensional crystals of finite length was found with consideration of the self-interaction of the dipole oscillators, their Coulomb interaction in the nonwave zone, the interaction in the intermediate zone, and the retarded interaction in the wave zone. The calculations were performed for chains with an increasing number N of monomers in the crystal to a maximum of $N=70$. These calculations confirmed, as expected, the existence of the previously discovered superradiance and, at the same time, permitted tracing its emergence and evolution. As N is increased, the radiative broadening of the polariton terms with maximum damping initially increases as $N\gamma$, where γ is the half-width of the emission line of an isolated monomer, and then tends to the asymptote $\sim \gamma\pi c/\omega_0 a$, where ω_0 is the frequency of the eigenmodes in an isolated monomer and a is the lattice constant. Since $\omega_0 a/c \ll 1$, the half-width significantly exceeds γ, and for two-dimensional crystals the half-width amounts to $\sim(c/\omega_0 a)^2$, i.e., is even greater, and corresponds to superradiance.

At the same time, the calculations revealed features, on which attention was not previously focused. The previous calculations of polariton spectra using various approximations, for example, in isotropic three-dimensional crystals and in the mean- and effective-field approximations, yielded a broad discontinuous range of frequencies of transverse polariton frequencies $0<\omega<\omega_t$, $\omega_l<\omega$, where ω_t and ω_l ($\omega_t<\omega_l$) denote the poles and zeros of the dielectric function $\varepsilon(\omega)=(\omega^2-\omega_l^2)/(\omega^2-\omega_t^2)$, which specifies the dispersion dependence of the wave vector k on the frequency: $k^2=\omega^2\varepsilon(\omega)/c^2$ (Ref. 11). In this case the polariton spectrum has two branches, and each wave vector has two corresponding frequencies. The calculations performed in the present work show that in one-dimensional crystals with a fixed direction for the transition dipole moment each wave vector has only one corresponding frequency on either the radiative ($\omega>kc$) or nonradiative ($\omega<kc$) branch. In one-dimensional crystals with nearly orthogonal inclination of the dipole moment relative to the crystal axis the frequencies of both the radiative and nonradiative polaritons are concentrated in the continuous band $\omega_0-|w|<\omega<\omega_0+|w|$, where w is determined by the characteristic energy of the dipole-dipole Coulomb interaction $\hbar w$. As the number of monomers increases along the series $N=2,3,4,\ldots$, the two polariton terms with different damping for $N=2$ (the dimer) in this bounded continuous band evolve into abutting systems with an increasing number N of k-ordered terms in the radiative region ($\omega>kc$, superradiance) and in the region traditionally termed nonradiative ($\omega<kc$), which have different dependences of the damping on k. As the angle of inclination of the dipoles relative to the axis decreases, the signs of the effective masses at small wave vectors and on the Brillouin-zone boundary change. At large angles the first is negative, and the second is positive, while the opposite is true at small angles. In one-dimensional crystals with nearly zero inclination, as the number of monomers increases from $N=2$ along the series $N=2,3,4,\ldots$, the two terms also evolve into a system of N k-ordered terms with separation of the abutting radiative and nonradiative branches on the light axis. However, at small k the frequency and damping of the radiative branch decrease sharply with decreasing inclination, and the frequency exceeds the band indicated above and tends toward zero frequencies. At the maximum value for our computational capabilities, $N=70$, only the nonradiative branch is observed for zero inclination, and the question of the existence of the radiative branch at zero inclination remains open.

We note one important finding. Two terms for the radiative and nonradiative branches with different frequencies and coinciding or fairly close wave vectors were not observed in any of the calculations from the smallest value $N=2$ to the largest value of N, i.e., the previously assumed passage of the radiative branch above the nonradiative branch was not observed. Each wave vector had one corresponding frequency on either the radiative or nonradiative branch. A similar situation was previously noted at a definite orientation of the dipole moment for a two-dimensional crystal in Ref. 10. In three-dimensional isotropic crystals with two polariton branches of standard form, one above the other, corresponding situations with orthogonal and zero inclination similar to those noted above for a one-dimensional crystal are apparently realized at each value of k, since a triply degenerate dipole-moment transition has ‘‘all the directions’’ of the dipole moment. In one-dimensional crystals a similar situation can be observed only if the excited state is doubly degenerate and the dipole moment has two possible orientations. We note that the calculations demonstrate the occurrence of finite radiative damping $\sim\gamma/2$ of the branch traditionally termed nonradiative in the region of the phase plane $\omega<kc$. This is associated with the possibility of emission from the end faces of a finite one-dimensional crystal into the respective hemispheres, which is lacking in a model infinite crystal. We note that this damping has a clearly expressed minimum at the Brillouin-zone center. It should also be noted that establishing the exact form of the polariton dispersion curves is of great importance for studying the interaction of polaritons with phonons and the kinetics of the transfer of electron excitation energy.[11]

The classical equations of motion for a system of dipole oscillators with a frequency ω at the nodes n with the charge e, the displacement $\mathbf{r}_n$, and the light-particle mass μ have the form[12]

$$(\omega^2-\omega_0^2+2i\gamma_0\omega_0)p_n^i=\frac{e^2}{2\pi^2\mu}\int dq\,\frac{q^iq^i-(\omega^2/c^2)\delta_{ij}}{q^2-(\omega^2/c^2)-i\varepsilon}\times\sum_{m\neq n}p_m^j\exp[iq^1(n-m)];$$

$$i,j=1,2,3;\quad \varepsilon\to+0;\quad \mathbf{p}_n=e\mathbf{r}_n. \tag{1}$$

In (1) $\gamma_0=e^2\omega_0^2/3\mu c^3$ is the intrinsic radiative half-width, the indication of the direction for circumvention of the poles $\varepsilon\to+0$ singles out the retarded interaction, and q^1 is the component of the vector $\mathbf{q}(q^1,q^2,q^3)$ along the crystal axis. The value of γ_0 is specified by the imaginary part of the classical Green's function $(k^2-(\omega^2/c^2)-i\varepsilon)^2$ appearing on the right-hand side of (1). This finite imaginary part of the self-interaction term ($n=m$) gives the intrinsic radiative damping, while the diverging real part (‘‘ultraviolet catastrophe’’) is included in the field mass. Performing the integration over $\mathbf{q}$ in (1), we can obtain the standard relations for the dipole interaction energy with isolation of the terms determining the instantaneous Coulomb interaction at short distances, the interaction in the intermediate zone, and the retarded interaction in the wave zone. For an isotropic three-dimensional crystal, the dispersion equation presented above for transverse waves can easily be obtained from (1) using the standard δ-function formalism.

Determination of the polariton spectrum within the quantum theory of radiation requires diagonalization of the corresponding quadratic Hamiltonian of a Frenkel exciton + transverse photon system[2] for excitons in a nodal representation. The translational motion of excitons and their interaction with transverse photons is specified by the matrix element P of the dipole moment operator of the corresponding quantum transition from the ground state $|0\rangle$ to the excited state $|f\rangle$ of an isolated monomer with the energy $\hbar\omega_0$: $P=|\langle f|e\mathbf{r}|0\rangle|=e(\hbar/2\mu\omega_0)^{1/2}$. The diagonalization procedure for a quadratic Hamiltonian,[2] which is not presented here because of its cumbersomeness, followed by integration over the photon wave vectors with circumvention of the poles conforming to retardation leads to the following system of secular equations corresponding to (1) for the energy

$\hbar\omega$ and the wave functions ψ_n of polaritons in a one-dimensional finite crystal of N monomers ($n=1,2,3,\dots,N$):

$$(\omega^2-\omega_0^2+2i\gamma\omega_0)\psi_n = \frac{2\omega_0|P|^2}{\hbar a^3}\sum_{m\neq n}\left[\left(\frac{1}{|n-m|^3}-\frac{i\omega a/c}{|n-m|^2}\right)\times(1-3\cos^2\theta)-\frac{(\omega a/c)^2}{|n-m|}(1-\cos^2\theta)\right]\times\exp\left[i\frac{\omega a}{c}\left|n-m\right|\right]\psi_m, \tag{2}$$

where θ is the angle of inclination of the dipoles relative to the crystal axis and the half-width $\gamma=2|P|^2\omega_0^3/3\hbar c^3$. On the right-hand side of (2), the first term ($|n-m|^{-3}$) represents the instantaneous dipole-dipole Coulomb interaction at short distances in the nonwave zone, the second term ($|n-m|^{-2}$) takes into account the interaction in the intermediate zone, and the third term ($|n-m|^{-1}$) allows for the retarded interaction in the wave zone.

The orthonormalized eigenfunctions in a system of N nodes has the form

$$\psi_n(k_j)=\left(\frac{2}{N+1}\right)^{1/2}\sin(k_j n);\quad k_j=\frac{\pi j}{N+1};\quad j=1,2,3,\dots,N. \tag{3}$$

The substitution of (3) into (2) followed by multiplication by $\psi_n(k_j)$ and summation over n leads to the following dispersion equation

$$(\omega^2-\omega_0^2+2i\gamma\omega_0) = \frac{4\omega_0|P|^2}{\hbar a^3(N+1)}\sum_{n\neq m}\left[\left(\frac{1}{|n-m|^3}-\frac{i\omega a/c}{|n-m|^2}\right)\times(1-3\cos^3\theta)-\frac{(\omega a/c)^2}{|n-m|}(1-\cos^2\theta)\right]\times\exp\left(i\frac{\omega a}{c}\left|n-m\right|\right)\sin(k_j n)\sin(k_j m). \tag{4}$$

The frequency ω appears in the dispersion equation (4) in a very complex form, and the exact complex damped solutions $\omega=\omega_j=\omega_j'-i\omega_j''$ with real (ω_j') and imaginary (ω_j'') parts for all, including large, N can be determined from two coupled equations for the real and imaginary parts of (4) only using a powerful Pentium computer with appropriate software. We note that only the infinite sums of $\sin(kn)/n$, $\cos(kn)/n^2$, and $\sin(kn)/n^3$ with respect to n, which appear only in part in (4) and only for $N\to\infty$, can be calculated analytically in Eq. (4).[13] Of the sums of $\cos(kn)/n$, $\sin(kn)/n^2$, and $\cos(kn)/n^3$, which also appear in (4), only the first can be calculated analytically, the second is already an untabulated Lobachevsky function, and the third does not have any analytical representation at all.[13] Therefore, the multiple summations in (4) that have been included in the programmed procedure for solving the equation, which is nonlinear with respect to ω, are presently possible only by numerical methods.

For real optical materials the parameter $\omega_0 a/c$ is very small and amounts to $\sim 10^{-3}-10^{-4}$ (Ref. 2). Therefore, the most interesting features of the polariton branches are observed for the wave vectors $k_0\sim\omega_0/c\sim 10^{-3}-10^{-4}/a$, which are far smaller than the Brillouin-zone boundary π/a. For manifestation of the behavior of the radiative branch,[1] there must be at least two polariton branches consisting of N terms arranged equidistantly along k must fall in the range $0<k_j<k_0$. The condition $\pi/(N_c+1)=\omega_0 a/c$ specifies the critical value $N_c\sim 3\times 10^3$. When N is so large, the calculation time increases dramatically and becomes unrealistic for existing personal computers. However, such calculations are not necessary, since all the features of the polariton spectrum can be clearly traced for crystals with smaller values of N. Calculations with $N_r\leqslant 10^2$ are possible on existing Pentium computers. Obviously a large value of the basic parameter $\omega_0 a/c\sim\pi/N_r\sim 0.03$ is needed to obtain a faithful representation of the polariton spectrum. For the purpose of studying the behavior of a radiative branch with at least $5-10$ terms, the calculations of the polariton spectrum as N increases from $N=2$ to N_r were subsequently performed for $\omega_0 a/c=0.3$. The value of the transition dipole moment $|P|$, which specifies the interaction of the excitons and photons, was selected on the basis of the ratio between the width and energy of the exciton band $|P|^2/\hbar\omega_0 a^3=0.1$, which is close to the experimental value.

Figure 1 presents the evolution of the polariton spectrum of crystals with nearly orthogonal inclination of the dipole moment relative to the crystal axis $\theta=\pi/3$ in the ω,k phase plane as N increases. Figure 1a shows the polariton spectrum for $N=2$. Two terms can be seen: both are in the nonradiative region to the right of the $\omega=kc$ light axis (the dashed line). The terms ω_j are depicted in analogy to the representation of the experimental data by vertical segments with the abscissa $k_j a$ ($j=1,2,3,\dots,N$), which are centered at $\omega_j' a/c$ and have a length equal to $(\omega_j'' a/c)^{1/2}$. The square-root representation of the damping is used so that frequencies and dampings of radiative and nonradiative terms differing by an order of magnitude would be visually perceived as being roughly equal. The corresponding curves are drawn through the ends of the segments representing the terms, and the curve drawn through the midpoints of the segments represents the corresponding dispersion dependence. In Fig. 1a the half-width of the $j=1$ term is almost two times greater than the value of γ for the term of an isolated oscillator, which is represented by the thick segment on the vertical axis, and the half-width of the $j=2$ term is significantly smaller than γ. As N is increased, the number of terms increases, and the extreme left-hand terms are displaced toward smaller k in the radiative region, while the right-hand terms are displaced toward the Brillouin-zone boundary. When $N=10$ (Fig. 1b), only the first ($j=1$) term with maximum damping has moved into the radiative region. We note

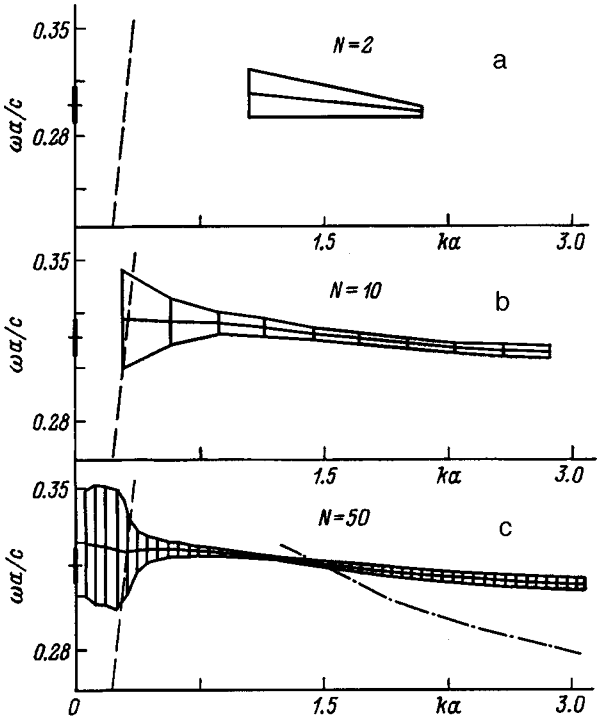

FIG. 1. Evolution of the dispersion curve and damping of polaritons as the length of the crystal is increased. The angle of inclination of the dipoles relative to the crystal axis $\theta = \pi/3$.

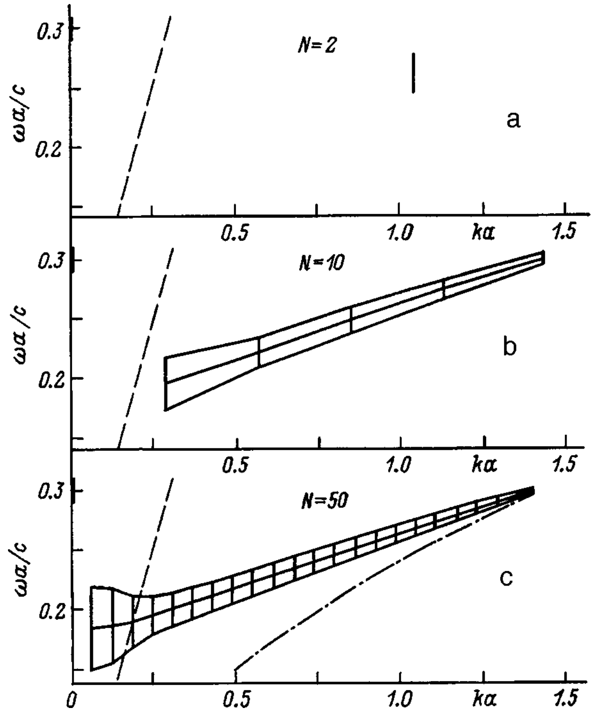

FIG. 2. Evolution of the dispersion curve and damping of polaritons as the length of the crystal is increased. The angle of inclination of the dipoles relative to the crystal axis $\theta = \pi/6$.

that this term approaches $k=0$ as N increases, but fails to reach it, in contradiction to what was previously assumed in several studies. We also note that the damping of terms $j = 2,3,\dots,10$ in the nonradiative region remains approximately the same as that for $j=2$ when $N=2$. At large $N \cong 50$ (Fig. 1c), where a further increase in N no longer significantly alters the results, the polariton terms are represented in the form of segments only in the radiative region, which is of most interest, and such segments are used for the smooth nonradiative branch only at eight reference points. We note that the form of the $\omega_j'(k_j)$ curve corresponds to a negative effective mass at $k \sim 0$ and a positive effective mass at $k \sim \pi/a$. This is consistent with the fact that the energy V of the dipole-dipole Coulomb interaction is positive for the inclination under consideration and the exciton band $E(k) = E_0 + 2V\cos(ka)$ has a form of the type shown in Fig. 1c already, for example, in the approximation of nearest-neighbor interactions. It can be seen that the damping in the radiative region increases with increasing k and reaches a maximum (superradiance) as the light axis is approached, while the frequency drops, as was shown in Refs. 1–3. Upon crossing the light axis, the damping drops, and $\omega_j'(k_j)$ has a discontinuity and becomes a nonradiative branch with small damping. We note that the damping of the nonradiative branch has a clearly expressed minimum at the center of the Brillouin zone and that the damping on its boundary is $\sim \gamma/2$. The very existence of damping on the branch traditionally termed nonradiative is clearly due to the fact that there is a possibility for emission from the end faces of a finite crystal, no matter how long it may be. To demonstrate the character of the variation of the polariton spectrum as a function of θ, the dot-dashed curve in Fig. 1c represents the terminal portion of the nonradiative branch for crystals with $\theta = \pi/2$. To avoid cluttering the figure, the damping and the form of the radiative branch, which have the same features as those shown in detail in Fig. 1c for $\theta = \pi/3$, are not shown for such a crystal. It can be seen that the radiative branch is displaced toward lower frequencies, while the nonradiative branch is displaced toward higher frequencies when θ is reduced. In addition, the maximum damping in the radiative region, which amounts to $\omega'' = 1.24\gamma\pi c/\omega_0 a$ for $\theta = \pi/2$, decreases to $\omega'' = 1.06\gamma\pi c/\omega_0 a$ for $\theta = \pi/3$ (Fig. 1c) and drops further as θ decreases.

Figure 2 shows the evolution of the polariton spectrum as N increases for crystals with nearly zero inclination of the dipoles relative to the axis ($\theta = \pi/6$). In this case the energy V of the dipole-dipole Coulomb interaction is negative, $E(k) = E_0 - 2|V|\cos(ka)$, and the signs of the effective masses at $k=0$ and $k = \pi/a$ are reversed in comparison to Fig. 1. Since the most interesting changes occurring in the polariton spectrum in response to increases in N take place at small k, half of the Brillouin zone is shown in Fig. 2. Figure 2a shows only the term with the greatest damping for $N=2$ (the second term with $k \leqslant \pi/a$ inside the zone). When $N=10$ (Fig. 2b), the number of terms increases, but they remain in the nonradiative region. The damping drops with increasing distance from the light axis. Figure 2c shows the polariton spectrum for $N=50$, which the spectrum no longer varies significantly. It is seen that the damping is large on the radiative branch in the low-frequency region, amounts to $\omega'' = 0.9\gamma\pi c/\omega_0 a$ at the maximum for $j=1$, and then declines sharply inside the zone upon crossing the light axis. To determine the direction of variation in the form of the

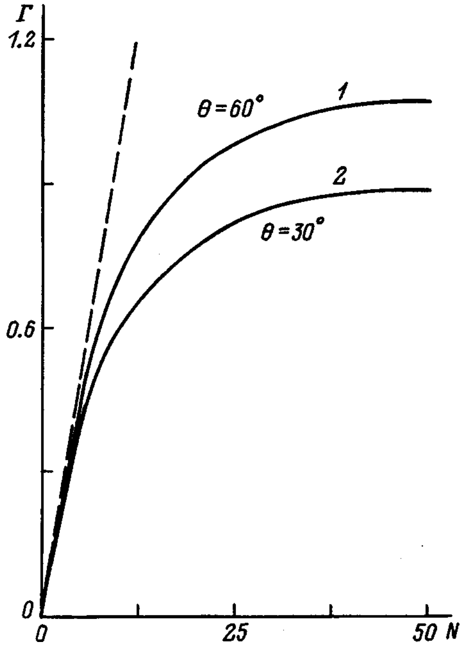

FIG. 3. Dependence of the maximum radiative linewidth of the polariton terms on the length of a one-dimensional crystal for angles of inclination of the dipoles relative to the crystal axis $\theta=\pi/3$ (*1*) and $\pi/6$ (*2*).

polariton branch with θ, the $\omega'(k)$ curve inside the zone for $\theta=0$ is presented as a dot-dashed line in Fig. 2c. The first few terms near $k=0$ were calculated for our largest value $N=70$ and this limiting angle in a separate prolonged procedure. The first term $(j=1)$ has a very low frequency $\omega_1'=0.006c/a$ and a small wave vector $k_1=0.04/a$, i.e., this term, like all the others, is found in the nonradiative region $(\omega_1'<k_1c)$, and the entire $\omega_j(k_j)$ dispersion curve is located near the light axis, having the same form as the standard low-frequency polariton branch of an isotropic three-dimensional crystal.

Figure 3 shows the dependence of the damping $\omega''_{\max}$ of the term with the maximum damping on N. Curve *1* shows the dependence of $\Gamma=\omega''_{\max}(\omega_0 a/c\pi\gamma)$ on N for $\theta=\pi/3$, and curve *2* shows the same dependence for $\theta=\pi/6$. It can be seen that the damping varies according to a $\omega''\sim N\gamma$ law at small N (the dashed asymptote). As N increases further, curves *1* and *2* reach the constant values $\Gamma=1.24$ and 0.8, which, by themselves, specify superradiance. We note, in addition, that in Figs. 1 and 2 the damping is represented as a square-root dependence and that the damping of the terms in the nonradiative region is significantly smaller than the limiting values of Γ, but is, nonetheless, finite.

In conclusion, we express our sincerest gratitude to V. M. Agranovich for some useful comments.

This work was supported by the Russian State Scientific-Technical Program ''Current Trends in the Physics of Condensed Media.'' We thank the Volkswagen Foundation for its partial support in the form of Grant 1/69928.

[1] V. M. Agranovich and O. A. Dubovskiĭ, JETP Lett. **3**, 223 (1966).

[2] V. M. Agranovich, *Theory of Excitons* [in Russian], Nauka, Moscow (1969), 254 pp.

[3] O. A. Dubovskiĭ, Fiz. Tverd. Tela (Leningrad) **12**, 2348 (1970) [Sov. Phys. Solid State **12**, 1874 (1971)].

[4] Ya. Aaviksoo, Ya. Lipmaa, and T. Reĭnot, Opt. Spektrosk. **62**, 706 (1987) [Opt. Spectrosc. **62**, 419 (1987)].

[5] B. Deveaud, F. Clerot, N. Roy, K. Satzke, B. Sermage, and D. S. Katzer, Phys. Rev. Lett. **67**, 2355 (1987).

[6] V. M. Agranovich and S. Mukamel, Phys. Lett. **147**, 155 (1990).

[7] V. M. Agranovich, in *13th General Conference of the Condensed Matter Division of the European Physical Society,* Regensburg (1993).

[8] J. Knoester, Phys. Rev. Lett. **68**, 654 (1992).

[9] L. C. Andreani, Phys. Status Solidi B **188**, 29 (1995).

[10] V. M. Agranovich, O. A. Dubovsky, and D. Basko, J. Chem. Phys. **106**, 3896 (1997).

[11] V. M. Agranovich and V. L. Ginzburg, *Crystal Optics with Spatial Dispersion, and Excitons*, 2nd ed., Springer-Verlag, Berlin–New York (1984).

[12] Ch. Muzikarzh, Zh. Éksp. Teor. Fiz. **41**, 1168 (1961) [Sov. Phys. JETP **14**, 833 (1962)].

[13] I. S. Gradshteyn and I. M. Ryzhik, *Table of Integrals, Series, and Products,* transl. of 4th Russ. ed., Academic Press, New York (1980).

Translated by P. Shelnitz